nagra.

Arbeitsbericht NAB 16-23

FEBEX-DP:
Pre-dismantling THC Modelling

September 2018

M. Birgersson, L. Zheng, J. Samper,
A. Mon & L. Montenegro

National Cooperative
for the Disposal of
Radioactive Waste

Hardstrasse 73
P.O. Box 280
5430 Wettingen
Switzerland
Tel. +41 56 437 11 11

www.nagra.ch

nagra.

Arbeitsbericht NAB 16-23

FEBEX-DP:
Pre-dismantling THC Modelling

September 2018

M. Birgersson[1], L. Zheng[2], J. Samper[3], A. Mon[3] & L. Montenegro[3]

[1)] Clay Technology, Sweden
[2)] Lawrence Berkeley National Laboratory, Department of Energy, USA
[3)] Universidade da Coruña, Spain

KEYWORDS
FEBEX, FEBEX-DP, THC pre-dismantling modelling

National Cooperative
for the Disposal of
Radioactive Waste

Hardstrasse 73
P.O. Box 280
5430 Wettingen
Switzerland
Tel. +41 56 437 11 11

www.nagra.ch

Nagra Arbeitsberichte ("Working Reports") present the results of work in progress that have not necessarily been subject to a comprehensive review. They are intended to provide rapid dissemination of current information.
This report was prepared on behalf of Nagra. The viewpoints presented and conclusions reached are those of the author(s) and do not necessarily represent those of Nagra.

"Copyright © 2018 by Nagra, Wettingen (Switzerland) / All rights reserved.
All parts of this work are protected by copyright. Any utilisation outwith the remit of the copyright law is unlawful and liable to prosecution. This applies in particular to translations, storage and processing in electronic systems and programs, microfilms, reproductions, etc."

Table of Contents

List of Tables

List of Figures

PART A Introduction

Within the FEBEX decommissioning project (FEBEX-DP), "pre-dismantling" modelling tasks were aimed at obtaining predictions of the final state of the FEBEX in-situ test before the dismantling was performed (or before data from the experimental analysis were made available). Two different modelling tasks were conducted, involving several different modelling teams: One task focused exclusively on thermo-hydraulic-mechanical aspects (referred to as the THM modelling), while the other also included – and put focus on – chemical aspects. This report concerns the latter task – referred to as the pre-dismantling THC modelling – and is a collection of individual reports from the participating modelling teams (presented in three appendices). In addition, this report contains a brief description of the FEBEX project as a whole (the remainder of this chapter), as well as a guide/overview for comparing the different modelling contributions (Chapter 2). For reporting on the pre-dismantling THM modelling task, the reader is referred to (Papafotiou et al. 2017).

A.1 The FEBEX Project

FEBEX (Full-scale Engineered Barrier Experiment in Crystalline Host Rock) is a research and demonstration project initiated by ENRESA (Spain).

The aim of the project is to study the behaviour of near-field components in a repository for high-level radioactive waste in granite formations. The main objectives of the project may be grouped in two areas:

Demonstration of the feasibility to construct an engineered barrier system in a horizontal configuration according to the Spanish concept for deep geological storage (DGS) and analysing the technical problems to be solved for this type of disposal method.

To obtain a better understanding of the thermo-hydro-mechanical (THM) and thermo-hydro-geochemical (THC) processes in the near-field, and to develop and validate the modelling tools required for interpretation and prediction of the evolution of such processes.

The project consists of two large-scale tests (see Fig. 1-1) – "in situ" and "mock-up" (the latter is managed by CIEMAT in Spain) –, a series of laboratory tests, and THM and THG modelling tasks.

The full-scale heating test ("in-situ" test), to which this document refers, was performed at the Grimsel underground laboratory in Switzerland, also known as Grimsel Test Site (GTS) or Felslabor Grimsel (FLG in German). A complete description of the FEBEX project objectives and test program may be found in the "FEBEX Full-scale Engineered Barriers Experiment in Crystalline Host Rock. PRE-OPERATIONAL STAGE SUMMARY REPORT" (ENRESA 1998a).

The project started in 1994 and has been supported by the European Commission through consecutive contracts, identified as FEBEX I (contract nº FI4W-CT-95-0006) for the period January 1996 to June 1999, and FEBEX II (contract nº FIKW-CT-2000-00016), from September 2000 to December 2004. The NF-PRO project took over from January 2005 to December 2007. And finally, in January 2008 the "in-situ" test was transferred from ENRESA to a consortium composed by SKB (Sweden), POSIVA (Finland), CIEMAT (Spain), Nagra (Switzerland) and more recently KAERI (South Korea), the FEBEXe Consortium, which supports it currently.

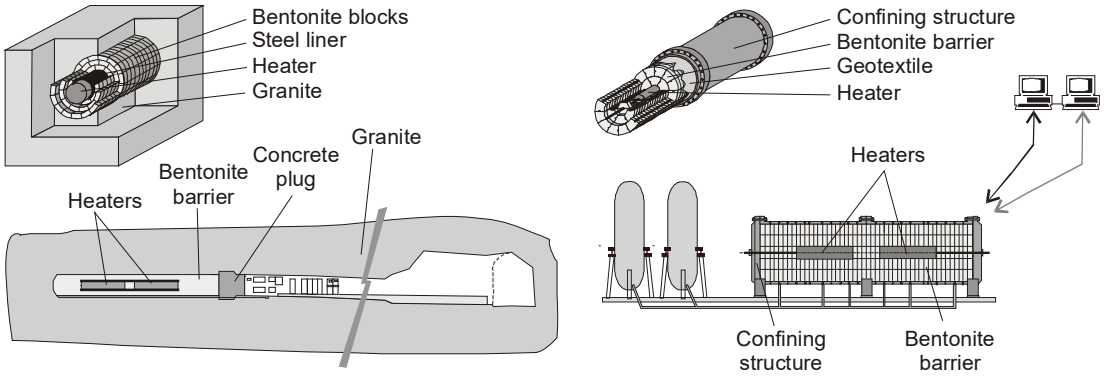

Fig. A-1: Overall layout of FEBEX "in-situ" test (left) and "mock-up" test (right)

The "in-situ" experiment excavation was carried out in 2015 and new partners, interested in taking part in the planned sampling and analysis operations, have been incorporated to the Consortium (now called FEBEX-DP) for that purpose, namely US DOE (USA), OBAYASHI (Japan), RWM (UK), ANDRA (France), BGR (Germany) and SURAO (Chech Republic).

A.2 Test configuration during FEBEX I

The installation of the "in-situ" test was carried out at the GTS. A horizontal drift with a diameter of 2.28 m was excavated in the Grimsel granodiorite especially for this experiment using a tunnel boring machine. Two electrical heaters, of the same size and of a similar weight as the reference canisters, were placed in the axis of the drift. The gap between the heaters and the rock was backfilled with compacted bentonite blocks, up to a length of 17.40 m, requiring a total 115'716 kg of bentonite. The backfilled area was sealed with a plain concrete plug placed into a recess excavated in the rock and having a length of 2.70 m and a volume of 17.8 m^3. Fig. A-2 shows the dimensions and layout of the test components schematically.

A total of 632 instruments were placed in the system along a number of instrumented sections, both in the bentonite buffer and in the host rock, to monitor relevant parameters such as temperature, humidity, total and pore pressure, displacements, ... etc. The instruments were of many different kinds and their characteristics and positions are fully described in the report titled "FEBEX Full-scale Engineered Barriers Experiment in Crystalline Host Rock. FINAL DESIGN AND INSTALLATION OF THE IN-SITU TEST AT GRIMSEL" (ENRESA 1998b).

A Data Acquisition and Control System (DACS) located in the service area of the FEBEX drift collected the data provided by the instruments. This system recorded and stored information from the sensors and also controlled the power applied to the electrical heaters, in order to maintain a constant temperature at the heaters/bentonite interface. The DACS allowed the experiment to be run in an automated mode, with remote supervision from Madrid. Data stored at the local DACS were periodically downloaded in Madrid and used to build the experimental Master Data Base.

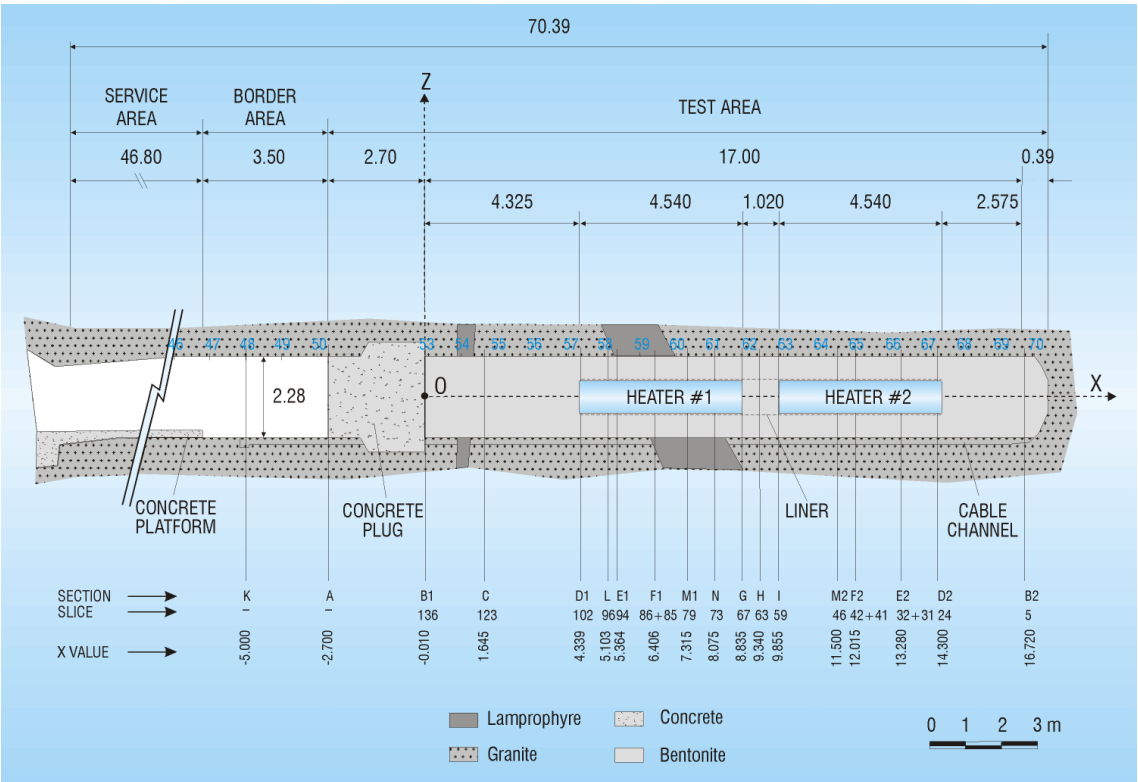

Fig. A-2: General layout of the FEBEX "in-situ" test (FEBEX I configuration)

The construction of the concrete plug was completed in October 1996, and the heating operation started on 28 February 1997. A constant temperature of 100 °C was maintained at the heaters/bentonite interface, while the bentonite buffer slowly hydrated with water naturally seeping from the rock. A complete report that includes both the installation of the test and the results gathered after two years of operation is given in "FEBEX full-scale engineered barriers experiment for a deep geological repository for high level radioactive waste in crystalline host rock FINAL REPORT" (ENRESA 2000).

A.3 Dismantling of Heater #1 and test configuration afterwards (FEBEX II)

A partial dismantling of the FEBEX "in-situ" test was carried out during the summer of 2002, after 5 years of continuous heating. The operation included the demolition of the concrete plug, the removal of the section of the test corresponding to the first heater, and the sealing with a new shotcrete plug. A large number of samples from all types of materials were taken for analysis. A number of instruments were subsequently dismantled, while also some new ones were installed. Accordingly, system design was adapted, and the physical layout was changed in order to ease the partial dismantling operation.

The bentonite buffer and all components were removed up to a distance of 2 metres from Heater #2 to minimize disturbance of the non-dismantled area. A dummy steel cylinder with a length of 1 m was inserted in the void left by Heater #1 in the centre of the buffer. Some new sensors were installed in that one additional metre of bentonite buffer.

Additional sensors were introduced in boreholes drilled in the buffer parallel to the drift. To simplify this operation, the new concrete plug was constructed in two phases: an initial temporary plug measuring just 1 m in length, which was built immediately after dismantling, and a second section to complete the plug length to the 3 m planned in the design of the experiment. Unlike FEBEX I, the new plug was a parallel plug, without a recess excavated in the rock, constructed by shotcreting.

The description of the partial dismantling operation is given by the report titled "Dismantling of the Heater #1 at the FEBEX "in situ" test. Description of operations" (Bárcena et al. 2003). The configuration of the test, after completing the partial dismantling operation and construction of the full plug length, is shown in Fig. A-3.

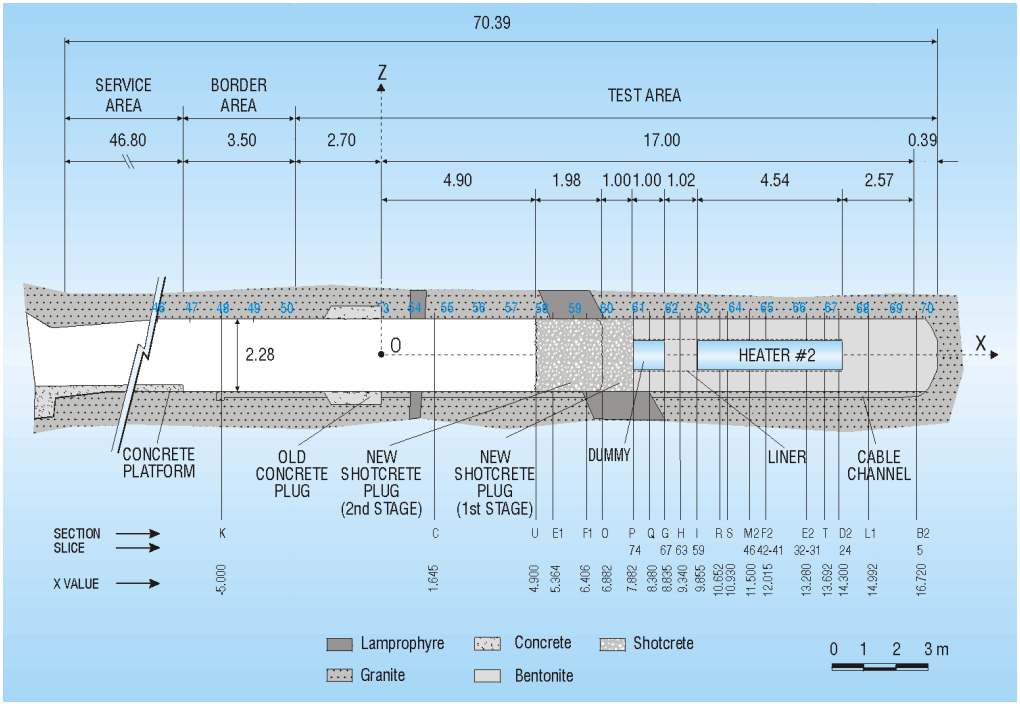

Fig. A-3: Status of the FEBEX "In-situ" test after the partial dismantling (FEBEX II configuration)

A more complete report that describes the test from the conception up to two years of operation after the partial dismantling is given in the document titled "FEBEX Full-scale Engineered Barriers Experiment. UPDATED FINAL REPORT 1994 – 2004" (Huertas et al. 2006).

A.4 Concept of the dismantling of Heater #2

The objective of the second dismantling operation, carried out throughout 2015, was to dismantle all the remaining parts of the "in-situ" test, including Heater #2. This operation includes carrying out a complete sampling of the bentonite, rock, relevant interfaces, sensors, metallic components and tracers to allow the analysis of the barriers' condition after 18 years of heating and natural hydration. The layout for the dismantling sampling is shown in Fig. A-4, including section numbering. Note that this numbering is different from the instrumentation section numbering shown in Fig. A-2 and Fig. A-3.

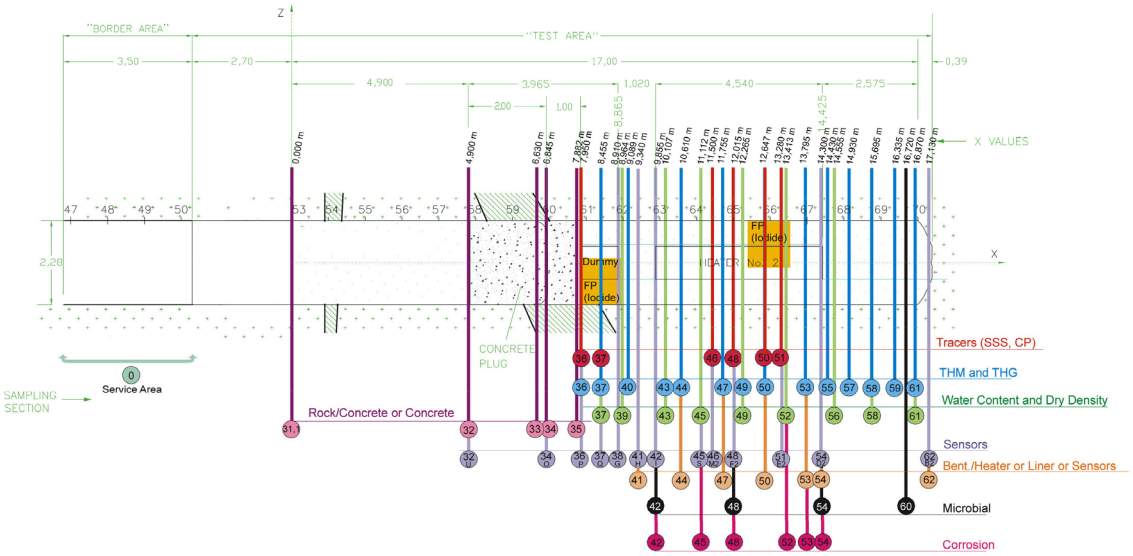

Fig. A-4: Layout for sampling during dismantling (from Bárcena & García-Siñeriz 2015a)

Analytical results will be compared with data obtained from the partial dismantling (Huertas et al. 2006); the monitoring data (Martínez et al. 2016) as well as with the results derived from modelling efforts (Lanyon & Gaus 2016). The results are expected to increase the current knowledge and confidence for the FEBEX-DP partners in bentonite performance with a focus on thermo-hydro-mechanical (THM) and thermo-hydro-chemical (THC) processes as well as on corrosion and microbial activity. The reporting of the laboratory analysis and dismantling results is expected to be complete by the end of 2018 with a final integrated report issued in late 2018.

All details about the planned dismantling operation and sampling program are given in the reference documents: "FEBEX-DP (GTS) Full Dismantling Test Plan" (Bárcena & García-Siñeriz 2015a), "FEBEX-DP (GTS) Full Dismantling Sampling Plan" (Bárcena & García-Siñeriz 2015b) and its update (Rey et al. 2015).

All sample logs of the dismantling operation are documented in AN 15-578 Sample Log Book 34 to 62 FEBEX-DP (Abós & Martínez 2015).

A.5 Objectives and contents of this report

In this report, thermo-hydraulic-mechanical-chemical modelling aspects with a specific focus on the chemical aspects (THM-C), predominantly performed prior to the final dismantling in 2015 of the FEBEX In-Situ Test, will be presented.

PART B provides an overview and summarizes three model approaches conducted by the teams from UPC, LBNL, and Clay Technology, which are self-contained reports presented in PART C, D and E. Given the complexity of the models and codes used, the initial instructions for a pre-modelling exercise were kept very open. Due to the substantially different modelling approaches taken and outcomes to be expected, a direct comparison between them was not foreseen. Additionally, over the course of the reporting, data from the dismantling became aviable and PART B is – beside an attempt to give an overview of the different contributions – also dedicated to point out similarities and differences by some post-dismantling comparison of the predicted and measured chloride and sulphate distributions. A full post-dismantling analysis is foreseen in the currently running EBS task force and the DECOVALEX programs and is beyond the scope of this report.

PART B Oververiew of the different modelling approaches

The main part of this report consists of the collection of reports from three different teams on modelling the FEBEX in-situ test, listed in Tab. B-1 (the teams will be referred to by these labels in the remainder of this document). Considering its unavoidable complexity, the instructions for the pre-THC modelling task were deliberately kept rather "vague", and modelling teams were encouraged to focus on aspects deemed possible to capture, given the available resources (numerical tools, manpower, etc.). As the modelling approaches are substantially different, both conceptually and in terms of scope, it is challenging to make direct comparisons between them. In order to facilitate such comparisons, this chapter is devoted to an overview of the different contributions, and to pointing out similarities and differences.

Tab. B-1: Contributing modelling teams

Team	**Affiliation**	**Contribution**
UDC	University of A Coruña, A Coruña, Spain	PART C
LBNL	Lawrence Berkeley National Laboratory, Berkeley, U.S.	PART D
CT	Clay Technology AB, Lund, Sweden	PART E

Although quite an extensive amount of reported results (from both UDC and LBNL) concerns pure "THM" variables (temperature, RH, density, water content, degree of saturation, etc.), the main focus here will be on comparing the "chemical" aspects, since these are results reported by all three teams, and since these are the additional aspects as compared to the pure pre-THM modelling task (Papafotiou et al. 2017).

Tab. B-2: Overview of the modelling contributions

	UDC	**LBNL**	**CT**
Code	INVERSE-FADES-CORE	THOUGHREACT-FLAC3D	In-house
Geometry	1D/2D axisymmetric	1D axisymmetric	1D planar
Included processes:			
• Thermal	x	x	
• Hydrodynamic	x	x	x (diffusion)
• Mechanical	x	x	
• Chemical	x	x	x
Flow	2-phase	2-phase	No flow
Solute transport	Advection, mechanical dispersion, diffusion	Advection, mechanical dispersion, diffusion	Diffusion
Porewater	Bulk	Bulk	Interlayer
Interlayer	Exchanger	Exchanger	Aqueous phase
Included materials:			
• Bentonite	x	x	x
• Rock	x	x	
• Concrete	x (in separate model)		

B.1 Scope of the individual modelling approaches

This section gives a brief description of the extent of each modelling team's contribution. A summary is also given in Tab. B-2.

B.1.1 UDC

The contribution of UDC is based on coupled THMC models which were developed from the beginning of the FEBEX Project in 1996. The model considers thermal, hydraulic, mechanical, and chemical processes, and considers bentonite and host rock explicitly. UDC provides predictions of the distribution of ions and minerals at different positions of the FEBEX test, including in the interface region at the concrete plug at different times. In addition, predictions are provided for the final concentration distributions in the dedicated tracer diffusion tests. Both 1D and 2D axisymmetric models have been considered. Apart from the predictions of the "C" variables, the UDC contribution provides results regarding both "C" and "THM" variables, which are compared to experimental results both from the dismantling of Heater #1 and Heater #2, as well as with online measurements up until the termination of the test. The contribution from UDC also contains several sensitivity analyses of the presented models.

B.1.2 LBNL

The LBNL contribution is based on previously developed models (for generic disposal systems) and gives a prediction of radial concentration profiles in the "hot" region of the FEBEX test, performed in a 1D axisymmetric model. The model includes bentonite and host rock explicitly, and considers thermal, hydraulic, mechanical, and chemical processes. The contribution also provides results for the "THM" variables, which are compared to online measurements and data from the two heater excavations.

B.1.3 CT

The CT contribution presents a model based on a newly developed numerical prototype code and gives a prediction of concentration profiles of ions and the distribution of gypsum. The model includes only bentonite explicitly, is performed in a planar 1D-geometry, and assumes a water saturated state at constant temperature and density.

B.2 Major processes

Even though the modelling task here reported is named "THC", several of the contributions also include mechanical processes and constitute coupled THMC models (also referred to as THCM). Examples of models in which only a part of these processes are considered – TH, THM, THC, etc. – are also presented. In this section each of the separate process categories (T, H, M, C) are briefly discussed. A summary of included process in each modelling contribution is also given in Tab. B-2.

B.2.1 Thermal

The variable solved for is temperature, as a function of position in the model domain. The evolution of the temperature distribution is governed by dynamic equations, e.g. the diffusion equation for heat conduction. Heat transfer must also be handled in evaporation/condensation processes. Thermal processes are included in the modelling contributions from UDC and LBNL. The thermal problem is not solved in the modelling of CT, for which a uniform and constant temperature is implied.

B.2.2 Hydrodynamic

Hydraulic processes concern fluid mass transfer and include advective transport of water and gas (in case of unsaturated states), which is treated usually with Darcy's law. Also included is diffusion of specific components, in particular diffusion of aqueous species in the pore water, and diffusion of water vapour in the gas phase. The contributions from UDC and LBNL treat unsaturated states and include all of the above-listed processes. The CT contribution assumes water-saturated conditions and only includes the process of diffusion of dissolved aqueous species.

B.2.3 Mechanical

Treating mechanical processes involves solving the evolution of (dry) density by considering deformations. When treating mechanical processes in the case of unsaturated bentonite, swelling – i.e. deformation due to water uptake – is central. Both LBNL and UDC consider a mechanical process (including swelling), while CT does not. Thus, in the LBNL and UDC models, the density distribution evolves as a consequence of water redistribution (and heating), while the density distribution is uniform and constant in the CT model.

Tab. B-3: Chemical components ("primary species") included in the different modelling contributions

	UDC	LBNL	CT
H^+	x	x	
Na^+	x	x	x
Ca^{2+}	x	x	x
Mg^{2+}	x	x	x
K^+	x	x	
Cl^-	x	x	x
SO_4^{2-}	x	x	x
HCO_3^-	x	x	
Fe^{2+}		x	
$SiO_2(aq)$	x	x	
AlO_2	x	x	

B.2.4 Chemical

Chemical processes look at the distribution of mass between different chemical entities, a typical example being precipitation/dissolution reactions, which transfer mass between the pore solution (aqueous species) and a solid mineral phase. The variables involved are the concentrations of the considered aqueous species and the amounts of precipitated phases. Introducing aqueous species usually requires to consider their transport within the pore water (diffusion, advection) as well. Although such transport processes should strictly be viewed as hydrodynamic, they are often referred to as "chemical". Moreover, there is a certain ambiguity as to which processes are considered "chemical", depending on the modelling approach. This applies particularly to the exchangeable cations, which are treated in terms of sorption (a chemical process) in the modelling approaches of UDC and LBNL, while they are treated as diffusive (a hydrodynamic processes) in the CT model. The chemical components included in each contribution are listed in Tab. B-3 and the mineral phases accounted for are summarized in Tab. B-4.

In the following section certain chemical aspects are disucsed in more detail.

B.2.4.1 Definition of bentonite pore water

The properties of water in compacted bentonite have been discussed vividly in the scientific literature for a long time (see e.g. Tournassat & Steefel 2015). Generally, a distinction is made between water in the vicinity of charged surfaces which contains an excess amount of positively charged ions, and water further away, which contain equal amounts of positive and negative ionic charge. These water types will here be referred to as "interlayer water" and "bulk water", respectively (in the bentonite literature there are examples of more detailed categorizations, but these are not needed for the present discussion).

Tab. B-4: Mineral phases included in the different modelling contributions

	UDC*	**LBNL**	**CT**
Calcite	x	x	
Gypsum	x		x
Anhydrite	x		
Quartz		x	
Chalcedony	x		
K-feldspar		x	
Albite		x	
Anorthite		x	
Siderite		x	
Dolomite		x	
Ankerite		x	
Na-Smectite	x	x	
Illite		x	
Chlorite		x	
Kaolinite		x	
Analcime	x		

* In the UDC models dealing with the bentonite/shotcrete interface, a different set of phases are included.

Bentonite models can be characterized according to whether they divide the water into several types (multi-porous models) or if they assume all water to be of a single type (homogeneous models). In this sense, all the contributions here presented adopt homogeneous models. However, while the contributions from UDC and LBNL both assume all water to be bulk water, the contribution from CT assumes all water to be interlayer water. Since interlayer water, by definition, contains the exchangeable cations, the cation pore water concentrations reported by CT are, therefore, not comparable with the cation concentrations reported by UDC and LBNL. For anions, there is no corresponding exchange contribution, and the differently defined pore water concentrations are in some aspects comparable. It must, however, be kept in mind that equilibrium anion concentrations in interlayer water generally differ from the corresponding bulk solution concentration, as a consequence of differences in the electrostatic potential.

The only relevant comparison, when results from these two different modelling approaches are considered, is to compare total amount of ions, expressed e.g. as moles per kg dry clay. Such handling implies that the amounts of exchangeable cations are added to the contribution from the pore water, in models assuming bulk water. A comparison between predicted chloride and sulphate profiles in the different modelling approaches is presented in Section 2.3.

B.2.4.2 Treatment of interlayer pores

A central component to handle when modelling bentonite is the interlayer montmorillonite pores. These are the water-filled, nanometre-wide, slit-like spaces between adjacent individual montmorillonite particles whose width (i.e. amount of water) is a function of the water chemical potential (relative humidity). Treating interlayers is important for the following reasons: it is in these pores that the exchangeable cations reside (compensating negative surface charge of the montmorillonite particles) and incorporation of water in interlayers is the fundamental mechanism behind bentonite swelling phenomena.

The interlayer pores are treated in two fundamentally different ways in the modelling contributions discussed here. In the work presented by UDC and LBNL, the interlayer pores are explicitly represented in form of cation exchange sorption sites. The distribution of the ions associated with these sites – i.e. the exchangeable cations – is derived by requiring local equilibrium with the pore solution in terms of laws of mass action (the pore solution is, in turn, treated as a bulk water solution, as discussed in Section 2.2.4.1). With this representation, the interlayer pores are treated as having zero volume, and the exchangeable cations are given no (diffusive) mass transfer capacity. As the models presented by UDC and LBNL include (coupled) hydro-mechanical processes, the effect of interlayers is also implicitly represented by the water retention curves for the bentonite material.

In the CT contribution, interlayers are represented as pores containing a charged aqueous solution whose net charge precisely compensates that of the negatively charged montmorillonite particles (as discussed in Section 2.2.4.1, this solution is moreover assumed to constitute the entire pore solution). The exchangeable cations are thus treated on equal footing with any other ion, which in particular means that they are ascribed a non-zero diffusivity.

B.2.4.3 Transport of aqueous species

The UDC and LBNL approaches assume aqueous species to be transported both as a consequence of differences in concentration (diffusion) and due to flow of the pore solution (advection, mechanical dispersion), and allow for having different mobility for different chemical species. The CT approach takes only diffusion into account and treats it in terms of Fick's law with a single diffusion coefficient common for all aqueous species. It should be noted that the media in which transport is assumed to take place are different in the models by UDC/LBNL and CT. UDC and LBNL assume advection-diffusion processes to occur in a bulk water phase, while diffusion in the CT approach is assumed to occur in interlayer water (see Section 2.2.4.1). Since corresponding concentration gradients may be very different in these two environments, especially for charged species, diffusion coefficients in the two approaches cannot be directly compared. It should also be noted that charge neutrality is generally not maintained if charged species are given different diffusivities, unless the electrostatic coupling between them is taken into account. Accounting for the electrostatics (by solving e.g. the Nernst-Planck equations) is not done in any of the contributions.

B.2.4.4 Sorption

There are two quite different processes in bentonite which in different contexts are modelled in terms of a sorption mechanism – i.e. the mechanism in which an aqueous species becomes immobilized by "attaching" to a surface. One of these processes is cation exchange, which was discussed in conjunction with treatment of interlayer pores (Section 2.2.4.2) and concerns the fact that montmorillonite carries a permanent negative charge which is compensated for by so-called exchangeable cations. Cation exchange is mainly associated with the basal surfaces of the montmorillonite particles. The other process is protonation/deprotonation of the edge surfaces of the montmorillonite particles (this process in general also applies to species other than the hydrogen ion, e.g. Zn^{2+} or pyrophosphate).

The contributions from UDC and LBNL treat both cation exchange and edge protonation as sorption mechanisms. The contribution from CT instead treats cation exchange in terms of so-called ion equilibrium rather than a sorption process, while it does not consider edge protonation. Thus, the CT contribution does not consider a sorption mechanism as defined at the beginning of this section.

B.3 Comparison of predicted chloride and sulphate distributions

Directly comparing the results from the different modelling contributions is challenging, as discussed in the previous sections, both because of variation in scope and due to differences in conceptual approach. Nevertheless, all teams provide predictions of ion distributions in the radial dimension in a "hot" section of the FEBEX test, calculated in 1D models. This scan line is illustrated in Fig. B-1. Therefore, the predicted chloride and sulphate distributions along this scan line in the different modelling contributions are compared (choosing these ions is motivated simply by the fact that comparing the results for anions can be done without directly involving the exchangeable cations, as discussed in Section 2.2.4.1).

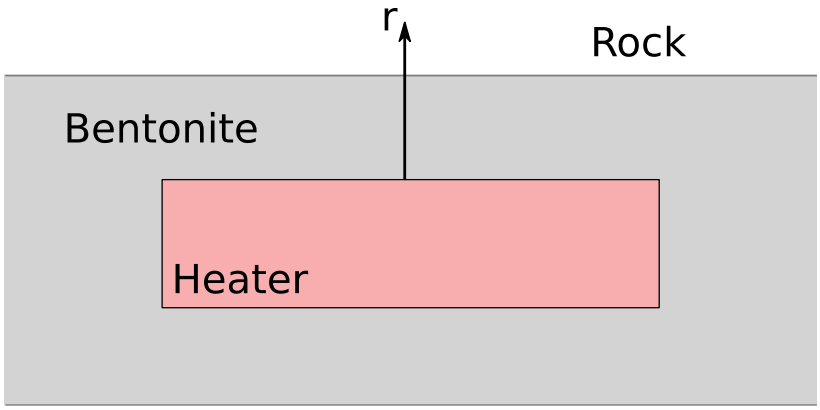

Fig. B-1: Scan line for the compared ion distributions (radial distance r)

The most relevant concentration variable used for this comparison is the amount of ions per mass unit dry clay. The result from CT is reported in this form, while the results from UDC and LBNL were converted to this variable by using the reported values of pore water concentrations, mineral amounts, and water contents. The conversion of the chloride concentration is given by

$$n = c \cdot \frac{w}{\rho}$$

where n denotes the amount of chloride in terms of moles per kg dry clay, c is the pore water concentration (mol/L), w is the water content, and ρ is water density (assumed equal to 1 kg/L). In case of sulphate, the contributions from possible mineral phases should also be added.

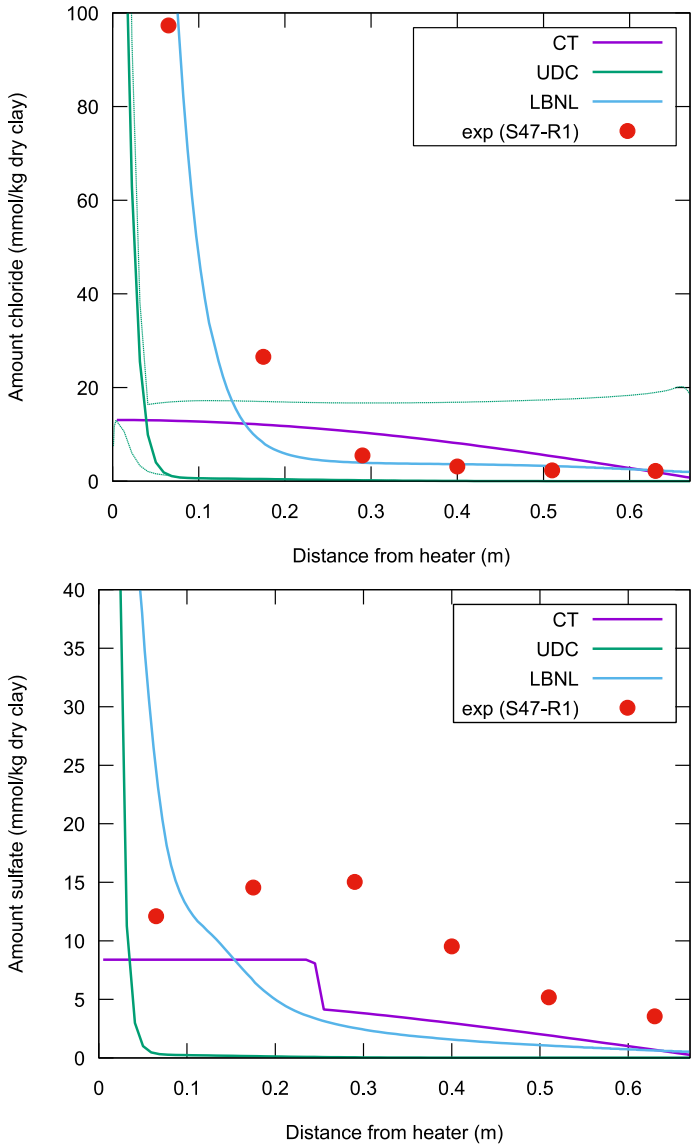

Fig. B-2: Predictions of final radial distributions of chloride and sulphate in a "hot" section, i.e. in a section located at "mid-heater" position and comaprison with measured data.

The plots were based on data shown in figures Fig. A-131, Fig. A-136, Fig. A-140, Fig. A-141 (UDC prediction), Fig. B-47 (LBNL "Model B"), and Fig. C-8 (CT prediction). The green dashed lines in the left plot shows a "prediction band" in the UDC model, accounting for uncertainties within the model with respect to influential input parameters. The experimental data is taken from (Fernández et al. 2017) and represent a section at mid-heater position (Section 47).

Fig. B-2 compares the predicted chloride and sulphate distributions in the three modelling approaches with representative experimental data (Fernández et al. 2017). It is noted that the different models predict significantly different final distributions of chloride and sulphate in the considered section: Both the LBNL and UDC models show substantial enhancement of chloride and sulphate near the heater, while the CT model does not.

The chloride accumulation near the heater is a combined effect of the water saturation process and the presence of a thermal gradient. Both of these issues (water saturation and thermal gradients) are accounted for in the models of UDC and LNBL, which also show qualitative agreement with the experiment. The CT model, on the other hand, which only accounts for diffusion of chloride in a water saturated state, disagrees qualitatively with the experimental result; rather than showing the convex shape of the experimental profile, the CT model shows the characteristic shape of the concentration of a mobile species diffusing out of a domain. Since this process is active probably also (the bentonite initially contains a certain amount of chloride, while the Grimsel groundwater is basically ion free), it can be concluded that out-diffusion is dominated by the process of accumulating chloride at the heater. The experimental result thus reflects a short-term process – in the long run it is expected that all chloride vanishes from the bentonite.

The different "tail" behaviour of the models (i.e. the part of the chloride profiles towards the rock side) reflects differences in how this out-transport of chloride is handled and depends on choices of relevant transport parameters (hydraulic conductivity, permeability, diffusion coefficients, etc.). A comparison with the experimental values in this region shows that the UDC model (base case) overestimates the out-transport – the model is considered chloride free. The CT and LBNL models, on the other hand, show pronounced downhill slopes towards the rock wall, although differently shaped. Note that most of the chloride initially present in the bentonite appears to still be present in this section of the FEBEX test, also at termination. Thus, the chloride has mostly redistributed rather than vanished from the bentonite in this section.

The LBNL and UDC models also predict accumulation of sulphate near the heater, qualitatively similar to their chloride predictions. This is however not in agreement with measurements, which indicate that the sulphate content near the heater equals the initial amount of sulphate in the bentonite. This disagreement indicates that although the water saturation process and thermal gradients are included in the LBNL and UDC models, these processes are not accounted for satisfactorily.

If there is any accumulation of sulphate, it is rather located in the middle of the considered region – the experimental peak is, however, not very pronounced. More distinct is instead the drop in sulphate content towards the rock wall. This drop should – at least partly – be attributed to diffusion out of the bentonite, since the groundwater is almost ion free. The CT model – which includes only mineral dissolution and diffusion in a water-saturated isothermal domain – is in this case seen to have a certain resemblance to the experimental profile. Although this model is too simplistic to draw strong conclusions on the inherently complex processes active in the FEBEX test, this result would indicate that the (re)distribution of sulphate is less sensitive to the water saturation process and to the presence of thermal gradients, compared to chloride. An alternative interpretation is that the processes of sulphate redistribution are more complex compared to chloride and that additional mechanisms must be considered, such as redox processes.

B.4 References to PART B

Abós, H. & Martínez, V. (2015): AN 15-578 Sample Log Book 34 to 62 FEBEX-DP.

Bárcena, I. & García-Siñeriz, J.L. (2015a): FEBEX-DP (GTS) Full Dismantling Test Plan. Nagra Arbeitsbericht NAB 15-15.

Bárcena, I. & García-Siñeriz, J.L. (2015b): FEBEX-DP (GTS) Full Dismantling Sampling Plan. Nagra Arbeitsbericht NAB 15-14.

Bárcena, I., Fuentes-Cantillana, J.L. & García-Siñeriz, J.L. (2003): Dismantling of the Heater #1 at the FEBEX "in situ" test: Description of operations. Publicación técnica 09/2003. ENRESA, Madrid.

ENRESA (1998a): FEBEX Full-scale Engineered Barriers Experiment in Crystalline Host Rock. PRE-OPERATIONAL STAGE: SUMMARY REPORT Publicación tecnica num. 01/98. ENRESA, Madrid.

ENRESA (1998b): FEBEX Full-scale Engineered Barriers Experiment in Crystalline Host Rock. FINAL DESIGN AND INSTALLATION OF THE IN-SITU TEST AT GRIMSEL, Publicación tecnica num. 12/98. ENRESA, Madrid.

ENRESA (2000): FEBEX full-scale engineered barriers experiment for a deep geological repository for high level radioactive waste in crystalline host rock FINAL REPORT, Publicación tecnica 1/2000. ENRESA, Madrid.

Fernández, A.M., Sánchez-Ledesma, D.M., Melón, A., Robredo, L.M., Rey, J.J., Labajo, M., Clavero, M.A., Carretero, S. & González, A.E. (2018): Thermo-hydro-geomechanical behaviour of a Spanish bentonite after dismantling of the FEBEX in situ test at the Grimsel Test Site. Nagra Technical Report NTB 16-25 (in review).

Huertas, F., Fariña, P., Farias, J., García-Siñeriz, J.L., Villar, A.M., Fernández, A.M., Martín, L., Elorza, F.J., Gens, A., Sánchez, M., Lloret, A., Samper, J.& Martínez, M.A. (2006): FEBEX Full-scale Engineered Barriers Experiment. UPDATED FINAL REPORT 1994-2004, Publicación técnica 05-0/2006. Empresa Nacional de Residuos Radiactivos, Madrid.

Lanyon, G. W. & Gaus, I. (2016): Main outcomes and review of the FEBEX In Situ Test (GTS) and Mock-Up after 15 years of operation. Nagra Technical Report NTB 15-04.

Martínez, V., Abós, H. & García-Siñeriz, J.L. (2016): FEBEXe: Final Sensor Data Report (FEBEX "in situ" Experiment). Nagra Arbeitsbericht NAB 16-19.

Papafotiou, A., Li, C. & Kober, F. (2017): FEBEX-DP Pre-THM Modelling. Nagra Arbeitsbericht NAB 16-022.

Rey, M., Bárcena, I. & García-Siñeriz, J.L. (2015): FEBEX-DP (GTS) Full Dismantling Sampling Plan (Rev. 5).

Tournassat, C. & Steefel, C.I. (2015): Ionic Transport in Nano-Porous Clays with Consideration of Electrostatic Effects. Reviews in Mineralogy and Geochemistry 80, 287–329.

PART C

UDC – contribution:
Coupled THCM Model of the FEBEX In-situ Test

Extended summary

Testing and updating the THCM model

FEBEX (Full-scale Engineered Barrier Experiment) is a demonstration and research project for the engineered barrier of high level radioactive waste repository. FEBEX is based on the Spanish reference concept for radioactive waste disposal in crystalline rock according to which canisters are placed in horizontal drifts and surrounded by a compacted bentonite clay barrier made of a Spanish bentonite from Cortijjo de Archidona which is now known as FEBEX bentonite.

A coupled 1D axisymmetric thermo-hydro-chemical and mechanical (THCM) model of the FEBEX tests was developed within the FEBEX Project (Zheng et al. 2011) based on laboratory tests, online data from the FEBEX mock-up test and online and partial dismantling data from the FEBEX in-situ test.

The main objectives of this report include:

1. Reviewing and analysing some aspects of the previous 1D THCM model of the FEBEX in-situ test such as: 1) Extending the previous 1D axisymmetric THCM model of the FEBEX in-situ test to 2D axisymmetric conditions; 2) Quantifying the sensitivity of the chemical predictions to the uncertainties in the retention curve of the bentonite, the vapour tortuosity, the dissolution of smectite, and the changes in the boundary conditions caused by the cooling and the dismantling of the test; and 3) Studying the back-diffusion of solutes from the bentonite into the granite
2. Updating the previous 1D axisymmetric THCM model of the FEBEX in-situ test by: 1) Improving the boundary condition at the heater-bentonite interface; 2) Refining the spatial discretization of the finite element mesh; and 3) Revising the dispersivities of the bentonite and the granite
3. Comparing the updated model with online temperature, relative humidity, water content, and pore water pressure in the granitic rock data collected from 2002 to 2015, with gravimetric water content data measured after the dismantling of Heater #1 in 2002, and with chemical data collected after dismantling Heater #1
4. Performing pre-dismantling THCM model predictions of the geochemical conditions for the hot and cold sections after dismantling Heater #2 in 2015
5. Updating the predictions of the tracer migration
6. Performing pre-dismantling predictions of the geochemical interactions of the bentonite barrier with the concrete plug

Testing and updating the THCM model

The results of these sensitivity runs led to the following conclusions:

1. The computed concentrations of most species in a hot section in 2002 are sensitive to an increase in the α parameter of the van Genuchten retention curve (threshold suction value) of the bentonite. The increase in α leads to larger water evaporation and larger solute concentrations near the heater. The pH and the concentration of HCO_3^- are not sensitive to a change in α. The computed concentrations of most species in the cold section, however, lack sensitivity to a change in α.

2. The computed concentrations are not sensitive to smectite dissolution and analcime precipitation because the cumulative dissolution of smectite and precipitation of analcime in 2002 is extremely small.
3. The computed concentrations in 2002 are not sensitive to a change in the boundary condition of the gas during the dismantling stage. The computed concentrations are sensitive to the cooling because the solubility of the minerals and the chemical parameters depend on temperature.
4. The computed concentrations of dissolved Ca^{2+}, K^{+}, Mg^{2+}, Na^{+} and Cl^{-} near the heater in 2002 increase when the vapour tortuosity increases. However, away from the heater the concentrations decrease when the vapour tortuosity increases. The computed pH and the concentrations of SO_4^{2-} and HCO_3^{-} are less sensitive to changes in vapour tortuosity.
5. Solute diffusion from the bentonite into the granite is very sensitive to the effective diffusion coefficients of the bentonite and the granite. The effective diffusion, D_e, for granite used in the previous model was too small. The computed Cl^{-}, SO_4^{2-}, Na^{+} and Ca^{2+} concentrations in the granite with $D_e = 1 \times 10^{-12}$ m^2/s in the granite and $D_e = 1.4 \times 10^{-10}$ m^2/s in the bentonite are consistent with the Cl^{-}, SO_4^{2-}, Na^{+} and Ca^{2+} concentrations measured in the FUNMIG borehole by Buil et al (2010).

The 1D axisymmetric THMC model of the FEBEX in-situ test was extended to 2D axisymmetric conditions. The temperatures computed with the 2D model in the hot section are smaller than those calculated with the 1D model. The temperatures computed with the 2D model in the cold section are larger than those calculated with the 1D model. The temperatures computed with the 1D model fit the measured data better than the temperatures calculated with the 2D model. The volumetric water contents computed with the 1D model are larger than the water contents calculated with the 2D model at all radial distances. The volumetric water contents computed with the 1D model fit the measured data better than the volumetric water contents calculated with the 2D model. The 1D axisymmetric model outperforms the 2D axisymmetric model because the model parameters used to perform the comparison of both models are the parameters calibrated with the 1D axisymmetric model. A detailed calibration of the parameters of the 2D axisymmetric model will surely lead to model results at least as good as or better than the results of the 1D axisymmetric model.

The concentrations of Cl^{-} in 2002 computed with the 2D model are large near the heaters #1 and #2. The largest concentrations are located at the edge of Heater #2. The contour lines are approximately parallel to the axis of the gallery along heaters #1 and #2. In the edges of the heaters, however, the contour lines are no longer parallel to the gallery axis. The computed contour plots of Cl^{-} concentrations illustrate that the edge effects extend approximately over a distance of 0.5 to 1 m. The concentrations of Cl^{-} in 2015 show a significant decrease compared to the concentrations in 2002 around Heater #2. Large concentrations of Cl^{-} still remain in the bentonite barrier between the dummy and Heater #2 and between Heater #2 and the end of the gallery.

The previous 1D axisymmetric THCM model of the FEBEX in-situ test was updated by: 1) Improving the boundary condition at the heater-bentonite interface; 2) Refining the spatial discretization of the finite element mesh; and 3) Modifying the solute dispersivities of the bentonite and the granite. The revised implementation of the boundary condition leads to more water evaporation than the previous formulation. The computed concentrations of Ca^{2+}, K^{+}, Mg^{2+}, Cl^{-} and Na^{+} near the heater with the updated model are significantly larger than the concentrations calculated with the reference model. The computed pH and the concentrations of SO_4^{2-} and HCO_3^{-} with the updated model are similar to those of the reference model.

The improvement in the boundary condition at the heater-bentonite interface leads to a significant decrease of the mass balance error. The mass balance errors in the model of the cold section are generally smaller than 10 %. At this stage of the project, the mass balance errors of the updated model are deemed acceptable.

The computed concentrations of Ca^{2+}, K^{+}, Mg^{2+}, Na^{+} and HCO_3^{-} become smoother when the diffusion coefficients of the bentonite are increased by a factor of 10. The profiles of Cl^{-} and SO_4^{2-} are less sensitive to the change in the diffusion coefficient because the diffusion coefficients of these species are smaller than the diffusion coefficients of the rest of the species. The computed pH is not sensitive to the change in the diffusion coefficients.

The updated 1D axisymmetric THCM model of the FEBEX in-situ test has been tested with gravimetric water content data measured at the dismantling of Heater #1 in 2002 and Heater #2 in 2015 and online temperature, relative humidity, water content, and pore water pressure in the granitic rock data collected from 2002 to 2015. The comparison of the computed values with the measured data leads to the following major conclusions:

1. The numerical model reproduces the main trends of temperature data. The computed temperatures near the bentonite-granite interface in hot sections are less than the measured temperatures during the first 2000 days and higher than the measured temperatures after 2000 days. The computed temperature in 2015 is 3 °C higher than the measured temperature at the bentonite-granite interface. The computed temperatures in the cold section C located between Heater #1 and the original concrete plug reproduce the steady increase of temperature before the dismantling of the Heater #1 and the sharp decrease of the temperature after switching off this heater.
2. The computed relative humidity values reproduce the general trends of the measured relative humidity data.
3. The computed time evolution of the water contents in the hot section reproduces the time evolution of the measured TDR water content data, except at r = 0.59 m. The best fit of computed values to measured data is achieved at r = 1.04 m, especially at the sensor on the right side of the tunnel.
4. The computed pore water pressures at the granitic rock are smaller than the measured values due to the heterogeneities of the granitic rock, which are not taken into account in the model and the uncertainty in the prescribed pore water pressure at the external boundary.
5. The predicted water content values in a hot section and a cold section at the times of dismantling of Heater #1 (in 2002) and Heater #2 (in 2015) are within the band of measured data and match the general trend of the measured data.
6. The predicted dry density in a cold and hot section at the time of dismantling Heater #1 (in 2002) and Heater #2 (in 2015) are for the most part within the band of measured data. There are some discrepancies in the hot and cold sections in 2002. The computed dry density overestimates the measured dry density near the heater (0.7 m < r < 1 m); this discrepancy is not observed in 2015.

Pre-dismantling THCM model predictions of the geochemical conditions

Pre-dismantling THCM model predictions of the geochemical conditions for the hot and cold sections in June 2015 were performed with the updated 1D axisymmetric THCM model. Prediction uncertainties were quantified by sensitivity runs to key model parameters such as the diffusion coefficients of the chemical species.

The main features of the geochemical predictions in a hot section in 2015 include:

1. The predicted concentrations of Cl^- in 2015 are largest near the heater due to the evaporation of the bentonite pore water and smallest at the granite-bentonite interface due to the hydration of the buffer with granitic pore water, which has a concentration smaller than that of the bentonite. The predicted concentrations of Cl^- in 2015 are much smaller than the concentrations in 2002.
2. The predicted concentrations of dissolved cations (Ca^{2+}, Mg^{2+}, Na^+ and K^+) are also large near the heater.
3. The predicted concentration of SO_4^{2-} in 2015 increases near the heater and decreases in the rest of the bentonite barrier.
4. The computed HCO_3^- is large near the bentonite-granite interface because the hydration of bentonite with granitic water induces the dissolution of calcite at the bentonite/granite interface.
5. The predicted pH in the bentonite in 2015 is 7.5 near the heater and decreases slightly towards the interface with granite.

The predicted concentration of Cl- in a cold section in 2015 shows a diffusion profile with low concentration in the bentonite near the interface with granite and a high concentration of about 0.16 mol/L in the centre of the bentonite barrier. The predicted concentrations of dissolved cations (Ca2+, Mg2+, Na+, K+ and SO42-) show diffusion profiles similar to the profile of the concentration of Cl-. The predicted concentration of HCO3- in the bentonite in 2015 is 10^{-2} mol/L near the granite interface and decreases to 10^{-3} mol/L at the centre of the barrier. The predicted pH in the bentonite remains sTab. Around 7.5.

The predicted concentrations in the hot sections are very sensitive to an increase of the diffusion coefficients by a factor of 10. In general, the profiles of the concentrations of most of the chemical species become smoother when the diffusion coefficient is increased. The concentrations decrease near the heater and increase in the rest of the bentonite barrier. The concentration of dissolved Ca^{2+} increases everywhere in the bentonite because calcite dissolution near the heater is enhanced when the diffusion coefficients of the bentonite are multiplied by 10. Such increase in the concentration is Ca^{2+} is accompanied by a decrease in the concentration of dissolved HCO_3^-.

The predicted radial profiles of the Ca^{2+}-, K^+-, Mg^{2+}-, Na^+- and HCO_3^-- concentrations in the cold sections become smoother when the diffusion coefficients are increased. The profiles of Cl^- and SO_4^{2-} are also sensitive to a change in the diffusion coefficients. Their sensitivity, however, is much smaller than the sensitivity of other species because the diffusion coefficients of Cl^- and SO_4^{2-} are much smaller than the diffusion coefficients of the other species. The predicted pH is slightly sensitive to a change in the diffusion coefficients.

Predictions of tracer migration

Updated predictions of the tracer migration have been produced for: 1) Iodide along several radii in Sections 37, 50 and 51 by using a 1D axisymmetric model; 2) Borate, europium, perrhenate and selenate at the inner blocks of Section 46 by using 2D models in vertical planes; and 3) Caesium and borate at the outer blocks of Section 48 by using 2D models in vertical planes.

The tracer migration was predicted with the most updated version of the THCM model of the FEBEX in-situ test. As a consequence, the accessible porosity of iodide was recalibrated. The following conclusions hold:

6. Large iodide concentrations are predicted near the heater in Sections 50 and 51 located near the Heater #2. The iodide concentration in Section 37 near the Heater #1 decreased after the heater was switched off in 2002 due to the increase in water content caused by vapour condensation and bentonite hydration.
7. The predicted perrhenate concentrations in 2015 show that this tracer has diffused entirely in the full section.
8. The plumes of the point tracers located in the inner blocks are
    a) Almost circular with an approximate diameter of 8 cm for borate
    b) Semi-circular with an approximate diameter of 20 cm for selenate
    c) Slightly anisotropic with an approximate length of 8 cm for europium.

The plumes of the point tracers located in the outer blocks are:

a) Almost circular with an approximate diameter of 7 cm for cesium
b) Almost circular with a diameter of 10 cm for borate

The comparison of the predicted tracer concentrations with measured values will provide the basis for the testing and partial validation of current THCM models for compacted bentonites.

Predictions of the interactions of the bentonite with the concrete plug

The geochemical interactions of the bentonite and the shotcrete plug have been modelled with a non-isothermal variably-saturated 1D numerical water flow and multicomponent reactive transport model normal to the interface at a radial distance from the gallery axis equal to 0.75 m. The computed temperature in the bentonite in 2015 ranges from 24 ºC to 34 ºC in the shotcrete. These temperatures compare well with the temperatures measured along a borehole drilled through the shotcrete plug before switching off the Heater #2

Model predictions show that calcite dissolves in the bentonite and precipitates near the bentonite/shotcrete interface. The precipitation front propagates into the bentonite. Portlandite dissolves in the shotcrete interface. Etringite precipitation is very small and non-uniform. The precipitation of this mineral phase is transient. It redissolves and is present in 2015 only in small amounts. Neither gypsum nor anhydrite precipitate. CSH1.8 dissolves in the shotcrete near the shotcrete/bentonite interface while CSH0.8 precipitation in the shotcrete is extremely small. Brucite precipitates in the bentonite near the interface. The front of brucite precipitation moves from the bentonite/shotcrete interface into the bentonite. Sepiolite shows a similar precipitation front. The model does not predict the precipitation of Friedel salt.

The porosity decreases slightly in the bentonite near the shotcrete/bentonite interface due to the precipitation of brucite, calcite and sepiolite. The porosity in the shotcrete, on the other hand,

increases near the interface due mostly to the dissolution of portlandite. The changes in porosity only affect 2 cm in the bentonite and shotcrete interface on both sides of the interface.

Acknowledgements

The research leading to this work has received funding from Nagra through the Grimsel Phase VI FEBEX-DP Project. Alba Mon enjoyed a research contract from University of A Coruña. We want to thank all the partners of the FEBEX-DP Project for the enjoying and enthusiastic discussions about the scientific and technological challenges of the FEBEX Project. We thank Martin Birgersson form Clay Technology for his review of the first version of this report. His comments, corrections and suggestions have contributed to the improvement of the revised version of the report.

C.1 Introduction

FEBEX (Full-scale Engineered Barrier Experiment) is a demonstration and research project for the engineered barrier of highlevel radioactive waste repository. FEBEX is based on the Spanish reference concept for radioactive waste disposal in crystalline rock according to which canisters are placed in horizontal drifts and surrounded by a compacted bentonite clay barrier made of a Spanish bentonite from Cortijjo de Archidona (EC 2000, ENRESA 2006a, Samper et al. 2008a). This bentonite has been extensively characterized and is well known as the FEBEX bentonite. The main goals of the FEBEX project included: 1) The demonstration of handling and constructing an engineered barrier system; 2) The study and the modelling of the thermo-hydro-mechanic (THM) processes in the near field; and 3) The study and the modelling of the thermo-hydro-geochemical (THG) processes in the near field. The project included two main large-scale tests: the FEBEX in-situ full-scale test performed at Grimsel, Switzerland, and the FEBEX mock-up test operating at Ciemat facilities in Madrid, Spain (ENRESA 2006a; ENRESA 2006b). Both tests started in February 1997. The project also included a wide range of THCM lab tests on samples of different sizes with varying durations.

C.1.1 Previous THCM models of the febex project

The Hydrology group at the Civil Engineering School led by Prof. Javier Samper has a strong background and experience on the development and application of THCM models for coupled water flow, heat and multicomponent reactive nuclide transport through porous media, especially in FEBEX bentonite, thereby taking into account the role of microbial processes. Numerical tools have been developed for the transport of multicomponent reactive chemical and microbial systems under transient, saturated or unsaturated, single or multi-phase non-isothermal flow conditions. The group has been involved in R&D Projects of the EURATOM Program funded by the European Commission for the last 20 years.

The group has developed and tested several powerful computer codes such as CORE, INVERSE-CORE and INVERSE-FADES-CORE some of which were especially developed for the compacted bentonite buffer of the near field. Such models were developed and applied in most European URL's and funded by EU projects since the 3rd EC Program such as CERBERUS, FEBEX I, FEBEX II, BENIPA, NFPRO, FUNMIG, PAMINA and PEBS. Models were also used within the framework of several Performance Assessment projects such as ENRESA 2000, ENRESA 2003, BENIPA and PAMINA. About 5 Masters and 16 PhD dissertations have been completed in this group in this field. This work has been published in technical reports, international conference papers and in more than 60 papers published in journals listed in the prestigious Journal of Citation Reports.

A significant improvement in THM and THC modelling of the clay barrier was achieved during the FEBEX Project. Novel numerical methodologies and sophisticated THM and THC codes were developed during the course of this project which could handle the observed thermo-hydro-geochemical couplings generally and account for the most relevant features of the THC conceptual model. THCM models were constructed by using such codes and relying on: 1) Data provided by a wide range of small-scale laboratory tests such as diffusion, infiltration, permeation and heating and hydration tests; 2) Thermal and hydrodynamic data from the FEBEX mock-up test and; 3) Thermal, hydrodynamic and geochemical data from the partial dismantling of the FEBEX in-situ test during the summer of 2002. The ability of THCM models to reproduce most of the observed THCM patterns under such a large number of conditions enhances the confidence in their predictive capabilities. These models are described in the publications listed in the section

of references. Although complex models have the risk of model over-parameterization, this is not the case for the THCM modes of the FEBEX project because these models were developed over a long period, from a wide range of experimental data at different space-time scales and by adopting the principle of parsimony according to which model complexities are only incorporated when they are fully justified based on experimental observations.

Zheng et al. (2011) presented a 1D axisymmetric coupled THCM model of the FEBEX in-situ test which accounts for bentonite swelling and chemical and thermal osmosis. Model results confirm: (1) The importance of bentonite swelling for the spatial distribution of conservative and reactive chemical species due to its effect on porosity; (2) The relevance of thermal osmosis; (3) The lack of relevance of chemical osmosis; (4) The importance of calcite dissolution-precipitation and cation exchange reactions on the concentrations of dissolved cations; and (5) The significant effect of gypsum/anhydrite dissolution-precipitation on the geochemical evolution of the bentonite barrier. Sensitivity analyses indicate that water content values and dissolved concentrations are strongly sensitive to the intrinsic permeability and the thermal osmotic permeability. Computed concentrations are very sensitive to the initial concentrations because changes in the initial concentrations not only cause differences in the computed concentrations, but also lead to differences in the spatial patterns of concentrations of dissolves species and mineral phases. The model reproduces the measured temperature, relative humidity, water content and inferred geochemical data. However, model results deviate from measured data at the heater-bentonite and bentonite-granite interfaces, because the model does not account for $CO_2(g)$ degassing. The inferred HCO_3^- and pH data cannot be explained by solute transport, calcite dissolution and protonation/deprotonation accounted for in the model, probably because other chemical reactions might be relevant or due to the multiple porosity structure of the bentonite.

The most recent developments in THCM models have addressed the multiple-porosity behaviour of bentonite and the mechanical-geochemical couplings within the context of the PEBS European Project (2010-2014). UDC extended the capabilities of THCM codes to deal with mechanical and geochemical couplings (thus leading to fully coupled THCM models), account for porosity changes caused by swelling phenomena and consider reactive gases (i.e. CO_2 degassing) (Samper et al. 2014a). Some of these developments were tested with data from the FEBEX mock-up test.

Most of the THCM analysis effort has been devoted to constructing thermo-hydro-geochemical models for the main geochemical processes controlling the geochemical evolution of the clay barrier in terms of major ion composition, pH and alkalinity. Some chemical processes which are relevant for performance assessment such as redox reactions and the interactions of corrosion products with bentonite which have not been addressed so far within the FEBEX project.

C.1.2 Objectives

The main objectives of this study include:

1. Reviewing and analysing some aspects of the previous 1D axisymmetric THCM model of the FEBEX in-situ test such as: 1) Extending the previous 1D axisymmetric THCM model of the FEBEX in-situ test to 2D axisymmetric conditions; 2) Quantifying the sensitivity of the chemical predictions to the uncertainties in the retention curve of the bentonite, the vapour tortuosity, the dissolution of smectite, and the changes in the boundary conditions caused by the cooling and the dismantling of the test; and 3) Studying the back-diffusion of solutes from the bentonite into the granite
2. Updating the previous 1D axisymmetric THCM model of the FEBEX in-situ test by: 1) Improving the boundary condition at the heater-bentonite interface; 2) Refining the spatial discretization of the finite element mesh; and 3) Revising the dispersivities of the bentonite and the granite.
3. Comparing the updated model with online temperature, relative humidity, water content, and pore water pressure in the granitic rock data collected from 2002 to 2015, with gravimetric water content data measured after the dismantling of Heater #1 in 2002, and with chemical data from collected after the dismantling of Heater #1.
4. Performing pre-dismantling THCM model predictions of the geochemical conditions for the hot and cold sections after dismantling of Heater #2 in 2015.
5. Updating the predictions of the tracer migration.
6. Performing pre-dismantling predictions of the geochemical interactions of the bentonite barrier with the concrete plug.

C.1.3 Scope

Chapter C.2 presents a brief description of the FEBEX in-situ test. Chapter C.3 presents the mean features of the computer code used for THCM predictions. Chapter C.4 presents the testing of the previous 1D axisymmetric THCM model of the FEBEX in-situ test with data collected in the FEBEX in-situ test from 2002 to 2015. This chapter presents also the extension of the current 1D axisymmetric THCM model to a 2D axisymmetric model which accounts simultaneously for the hot and cold sections of the test. In addition, this chapter presents the updating of the 1D axisymmetric THCM model and the sensitivity analyses of the bentonite retention curve, the vapour tortuosity, the dissolution of smectite, the effect of cooling and the solute back-diffusion from the bentonite into the granite. Chapter C.5 presents the updated pre-dismantling THCM model predictions for the hot and cold sections. Chapter C.6 describes the updated predictions of the migration of the tracers. Predictions have been updated for iodide migration by using a 1D axisymmetric model. The migration of tracers added at point sources has been updated by using 2D axisymmetric models for borate, europium, rhenium, selenate and caesium. Chapter C.7 presents the predictions of the interactions of the bentonite with the concrete plug. The main conclusions of this study are presented in Chapter C.8. Chapter C.9 presents a list of recommendations for future work.

C.2 The febex in-situ test

C.2.1 Description of the febex project

FEBEX (Full-scale Engineered Barrier Experiment) is a demonstration and research project for the engineered barrier of high level radioactive waste repository. FEBEX is based on the Spanish reference concept for radioactive waste disposal in crystalline rock. The compacted bentonite barrier is made of a Spanish bentonite from Cortijjo de Archidona which has been named as FEBEX bentonite (EC 2000, ENRESA 2006a, Samper et al. 2008a). The objectives of the FEBEX project were: 1) The demonstration of handling and constructing an engineered barrier system; 2) The study and the modelling of the thermo-hydro-mechanic (THM) processes in the near field; and 3) The study and the modelling of the thermo-hydro-geochemical (THG) processes in the near field. The project included two main large-scale tests: the FEBEX in-situ full-scale test performed at Grimsel, Switzerland, and the FEBEX mock-up test carried out at Ciemat facilities in Madrid, Spain (ENRESA 2006a, b). Both tests started in February 1997. Numerous lab tests, with different sizes, durations and heating and wetting conditions, were also performed. The project was divided into the following stages: pre-operational (planning, design, characterization of the clay, installation, and modelling); running the test; dismantling of Heater #1 and emplacement of a shotcrete plug in 2002 (extraction, inspection, sampling, and study of the materials); evaluation of the results and verification of the models; extension of the test by using Heater #2; and dismantling of the remaining part of the test in June 2015.

C.2.2 FEBEX lab tests

Heating and hydration lab tests were performed by CIEMAT on blocks of compacted FEBEX bentonite of different sizes and durations. The experiments on CT (*Celdas Termohidráulicas*) cells were performed on cylindrical bentonite blocks 13 cm high and 15 cm in diameter. Compacted bentonite at a dry density similar to that of the barrier in a repository was heated at the top at 100 °C while it was simultaneously hydrated with distilled or granitic water at the bottom. At the end of the test, the bentonite was studied (Fernández et al. 1999, Zheng et al. 2010). The bentonite block was covered with a stainless steel cell with the following dimensions: 15.05 cm in internal diameter, 22.2 cm in external diameter, and 14.6 cm height. Distilled water was injected at a pressure of 1 MPa at the bottom of the cell through a porous stone. A heating system was used at the top of the cell to prescribe a temperature of 100 °C.

The tests on CG (*Celdas Grandes*) cells, i.e. large-scale cells were performed on 60 cm long cells (Villar et al. 2008a). The bentonite thickness in these tests is almost similar to the bentonite thickness in the large-scale tests. This is the reason why the CG cells are denoted as "large-scale lab tests" sometimes. They lasted from 0.5 to 7.6 years. These cells are made of Teflon inside and steel outside to prevent lateral heat conduction and avoid the deformation of the cell by bentonite swelling. The cells were 60 cm in length and have a 7-cm diameter. The bentonite samples were made of several blocks of FEBEX bentonite, 10 cm long and 7 cm diameter. A flat stainless steel heater imposed a constant temperature of 100 °C at the bottom of the cell. Hydration with granitic water took place through the upper surface at an injection pressure of 1.2 MPa. Seven tests were performed: two with a duration a 0.5 years, two with a duration of 1 year, two with a duration of 2 years and another one with a duration of 7.6 years (Villar et al. 2008b). Two tests were performed for each duration, the FQ test which was used for post-mortem determination of hydro-mechanical and geochemical properties, and the HI test which was used for post-mortem determination of geochemistry and extraction of pore water. The longest test, CG3, was used for both types of post-mortem determinations.

C.2.3 Large scale tests

The mock-up test replicates at almost full scale the engineering barrier system of the Spanish reference concept for radioactive waste disposal in granite. The components are two electric heaters, the clay barrier, the instrumentation, the automatic control heating system, and a data acquisitions system. The bentonite buffer is confined in a steel structure which ensures a uniform temperature and water pressure around the external surface of the bentonite (EC 2000, ENRESA 2006a). The clay barrier is made up of highly compacted bentonite blocks. The total bentonite mass installed was 22.5 t. The heating and hydration stage started in February 1997. The hydration of the mock-up test started by filling all the joints and gaps with an initial flooding of six days. Once the joints were closed, bentonite hydration took place at a pressure of 700 kPa. The temperature of the heaters is maintained at 100 °C (Fig. C-1).

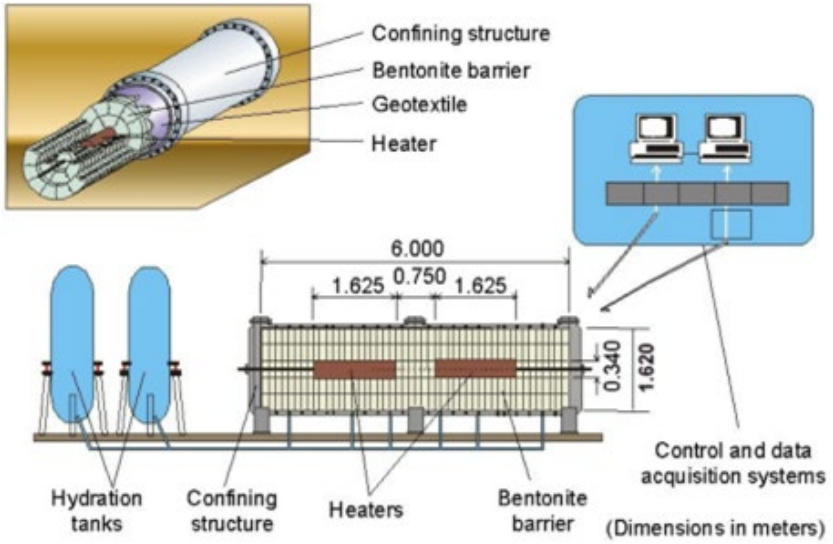

Fig. C-1: Schematic design of the mock up test (Martín et al. 2006)

The FEBEX in-situ test was performed in a gallery excavated in granite in the underground research laboratory operated by Nagra in Grimsel, Switzerland. The test included the heating system, the clay barrier and the instrumentation, monitoring and control system. The drift is 70.4 m long and 2.28 m in diameter (ENRESA 2000). The test zone is located in the last 17.4 m of the drift where heaters, bentonite and instrumentation were installed. The main elements of the heating system are two heaters, separated horizontally by 1.00 m, which simulate full-sized canisters. The heaters were placed inside a cylindrical steel liner, which had been installed concentrically with the drift. Each heater is made of carbon steel, measures 4.54 m in length and 0.90 m in diameter, has a wall thickness of 0.10 m and weighs 11 tons. The heaters were designed to maintain a maximum temperature of 100 °C at the steel liner bentonite interface. The bentonite barrier was made of blocks of highly compacted bentonite. The test began in February 1997. Heater #1 was switched-off in February 2002. After the emplacement of a shotcrete plug, the test continued operating until June 2015 when the bentonite barrier was fully dismantled (Fig. C-2).

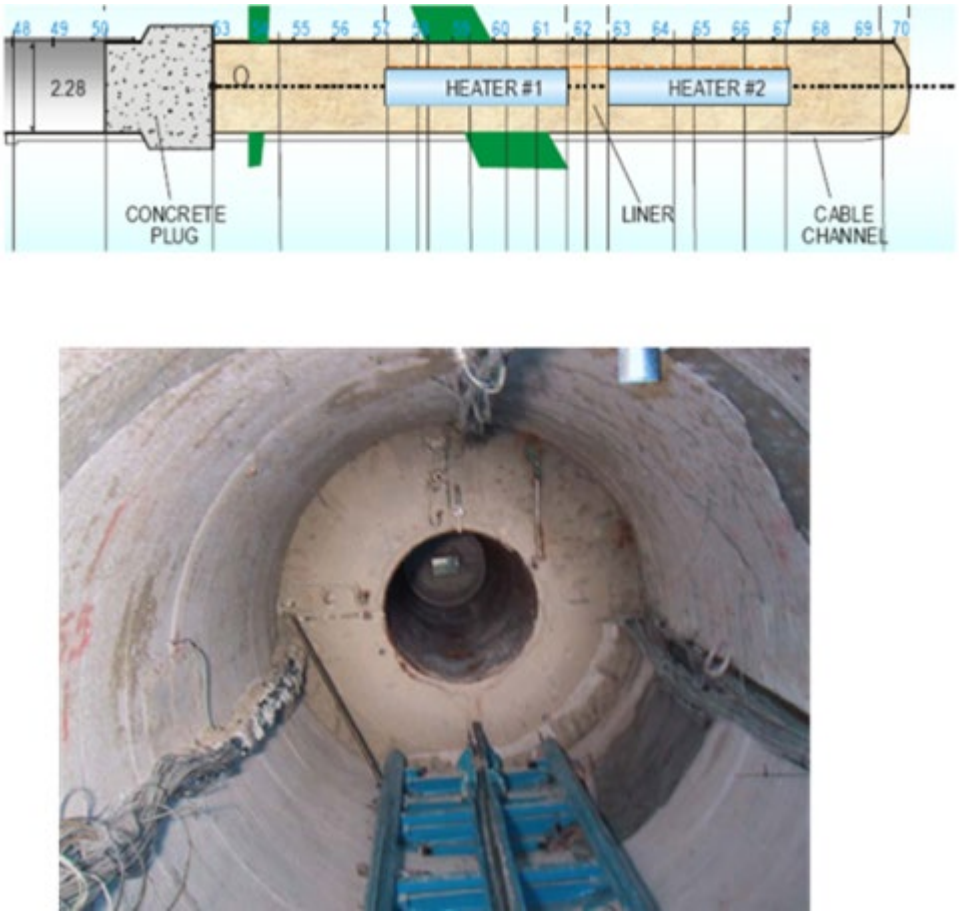

Fig. C-2: Schematic of the FEBEX in-situ test
Vertical lines show the location of the sampling sections (Samper et al. 2008a)

C.2.4 Available data for the FEBEX in-situ test

C.2.4.1 Water content data

Water content was measured with several methods. Volumetric water content was monitored with TDR (Time Domain Reflectometry) sensors. Gravimetric water content data were collected after dismantling of heaters #1 and #2.

C.2.4.2 Temperature data

Thermocouples were installed at several radial distances in several sections to monitor the evolution of the temperature in the bentonite barrier.

C.2.4.3 Chemical concentration data

Compacted bentonites have interlayer pores (2 – 10 Å), intra-aggregate micropores (50 Å), and inter-aggregate macro-pores (50 – 200 Å) which exhibit different hydrodynamic and geochemical properties. The interlayer water is more structured than free water. There are chemical gradients between the interlayer water and the free water.

Bentonite soluble salts were derived from 1:4 aqueous extract tests on samples collected during the dismantling of the Heater #1 of the FEBEX in-situ test. Bentonite pore waters were extracted with squeezing methods in some selected samples. Aqueous extract data were interpreted numerically to infer pore water chemical composition of the bentonite samples because pore water chemistry changes significantly due to dilution and chemical reactions, which take place during extraction. Zheng et al. (2008a) presented an inverse hydrochemical model to estimate pore water chemical composition from measured water content, aqueous extract, and mineralogical data. The model of Zheng et al. (2008a) and the THCM models presented here assume a single bentonite porosity. More complex bentonite porosity models such as that reported by Zheng & Samper (2015) are capable of considering the different chemical characteristics of the free water and the interlayer water. The dissolved concentration of the bentonite pore water was measured with 1:4 aqueous extracts and squeezing methods on samples collected during the dismantling of the Heater #1.

C.2.4.4 Location of sensors and sampling sections

Fig. C-3 shows the layout and the location of the instrumented sections in which water content and temperature were monitored at the FEBEX in-situ test. Water content was measured in sections M1 and M2. Temperature sensors were located in sections D1, G, I and D2. More details about this figure can be found in ENRESA (2000).

Fig. C-4 shows the layout and location of the Sections 7, 12, 19, 28, 29 and 31 at which water content data and pore water chemical data were collected during the dismantling of the Heater #1 of the FEBEX in-situ test (Samper et al. 2008a,b).

Fig. C-5 shows the layout and the location of the new shotcrete plug (first and second stages), the dummy canister and the monitoring sections after dismantling of Heater #1 of the FEBEX in-situ test.

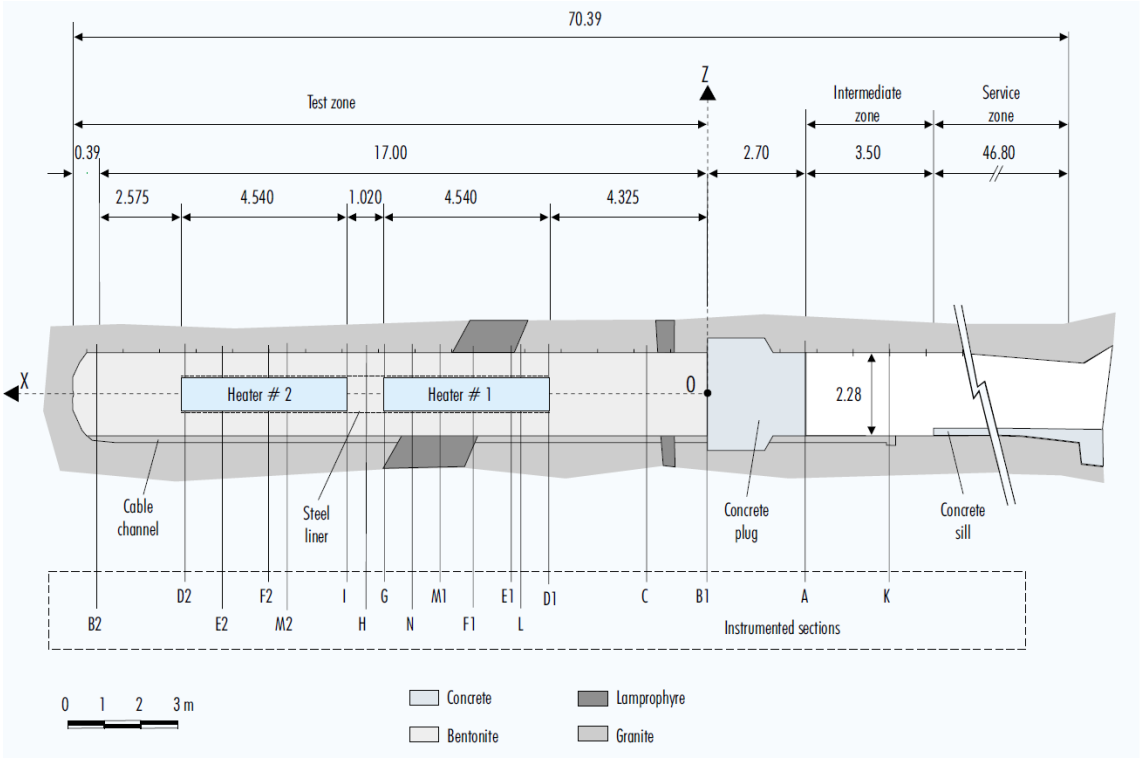

Fig. C-3: Layout and location of instrumented sections. Dimensions in m (ENRESA 2000)
It should be noticed that the tunnel end is at the left of the plot.

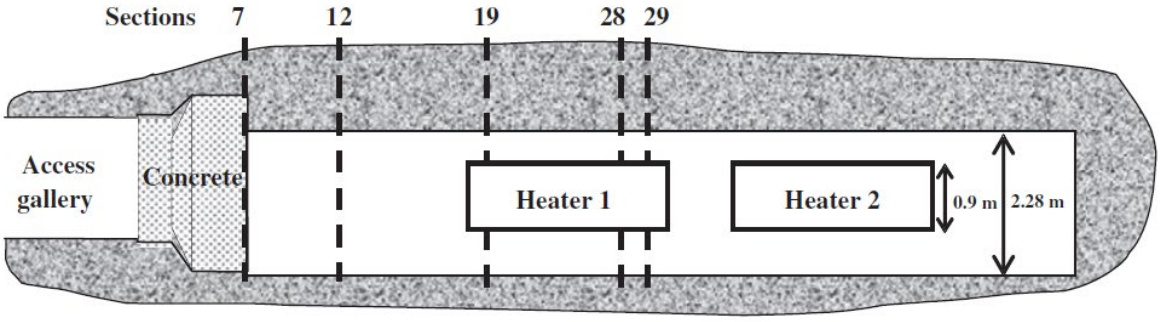

Fig. C-4: Layout and location of Sections 7,12, 19, 28, 29 and 31 in which water content data and pore water chemical data were collected during dismantling of Heater #1 of the FEBEX in-situ test (Samper et al. 2008a,b)

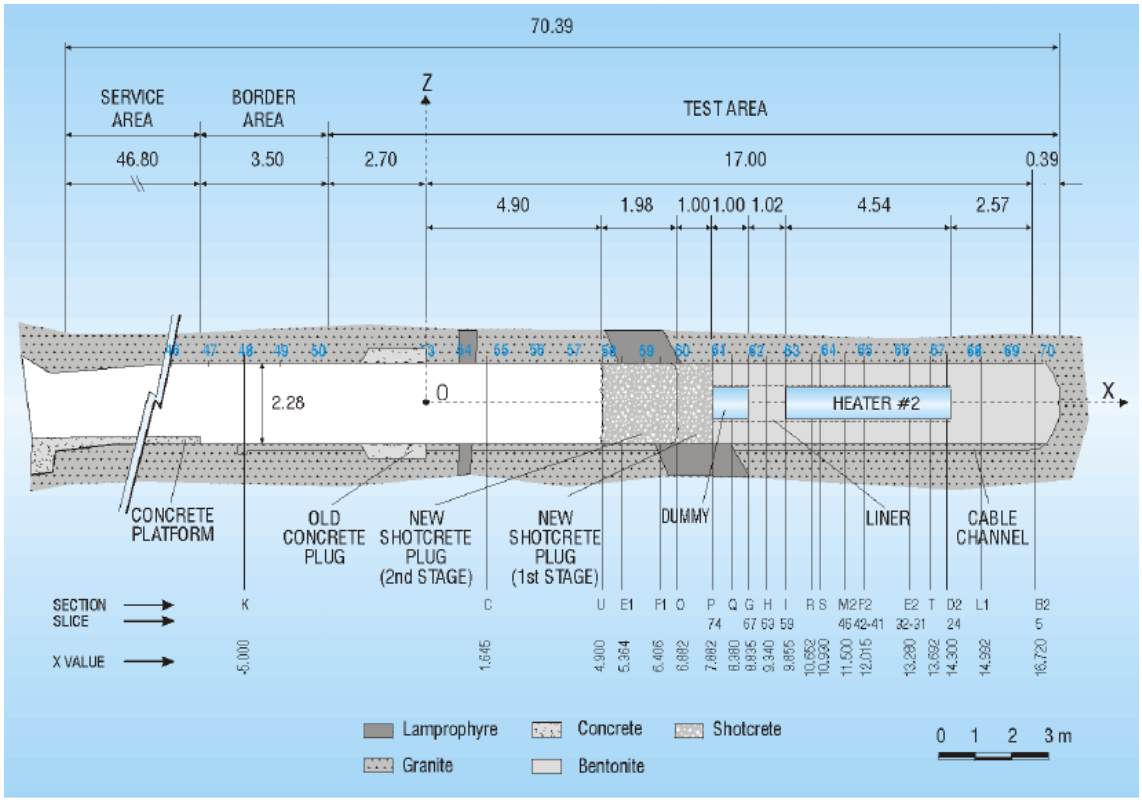

Fig. C-5: Layout and location of the new shotcrete plug (first and second stages), the dummy canister and the monitoring sections after dismantling of Heater #1 of the FEBEX in-situ test

C.3 Computer code

This chapter presents the description of INVERSE-FADES-CORE, the computer code used for the THCM predictions.

INVERSE-FADES-CORE is a finite element code for modelling non isothermal multiphase flow, heat transport and multicomponent reactive solute transport. Chemical reactions can be modelled either with the local equilibrium assumption or by prescribing a kinetic rate law. The code solves the mass balance of water, air, solid and enthalpy, the transport of solids and the mechanical equilibrium equation. INVERSE-FADES-CORE solves direct or forward problems in which the dependent variables such as pressures, temperatures, concentrations and stresses for a given set of model parameters. The code can also solve the inverse problem which estimates model parameters (usually those for which the prior information is not sufficient) from known values of the dependent variables (pressures, temperatures, concentrations) at some given locations and at some selected times. The code can solve for one-dimensional (1D) and two-dimensional (2D) problems in porous and fractured media. It can also handle problems with axial symmetry. Model settings such as the FEBEX in-situ test which show axial symmetry can be modelled in three dimensions (3D) by using 2D axisymmetric finite element grids (Zheng & Samper 2004, 2005).

INVERSE-FADES-CORE integrates the capacities of FADES, a THM code, developed by Navarro (1997), the subroutines of the reactive transport code, CORE^{2D}, (Samper et al. 2003), and the subroutines of the inverse code, INVERSE-CORE, (Dai & Samper 2004). State variables of the forward model include liquid and gas pressures and temperature which are solved by a Newton–Raphson method. A sequential iteration method is used to solve reactive transport equations. The inverse problem is solved by minimizing a generalized least-squares criterion with a Gauss-Newton–Levenberg–Marquardt method (Dai & Samper 2004). The forward routines of INVERSE-FADES-CORE have been widely verified with analytical solutions and tested with THM and THC problems (Navarro & Alonso 2000, ENRESA 2000, Samper et al. 2008a) as well as with THCM processes (Zheng 2006, Zheng & Samper, 2004). Codes of the CORE^{2D} series have been used to model the FEBEX laboratory tests (Samper et al. 2006, 2008b, Zheng et al. 2010), the FEBEX in-situ and mock-up tests (Zhang et al. 2008, Zheng et al. 2011), field studies (Molinero et al. 2004, Dai & Samper 2004, Molinero & Samper 2006, Dai & Samper 2006, Dai et al. 2006), to evaluate the long-term geochemical evolution of radioactive waste repositories in clay (Yang et al. 2008, Samper et al. 2016) and granite (Yang et al. 2007), analyse stochastic transport and multicomponent competitive cation exchange in aquifers (Samper & Yang 2006) and study concrete degradation (Galíndez et al. 2006).

The main applications of INVERSE-FADES-CORE include:

1. the THC model of the FEBEX in-situ test (Samper et al. 2008a)
2. the THCM model of the FEBEX in-situ test (Zheng et al. 2011)
3. the THCM model of the FEBEX mock-up test (Zheng & Samper 2008)
4. the THCM model of a heating and hydration lab experiment performed on compacted FEBEX bentonite (Zheng et al. 2010)
5. the THC model of the Ventilation Experiment on Opalinus Clay (Zheng et al. 2008b)

C.4 Testing and updating the THCM model

This chapter presents the analysis, review, extension, improvement and testing of the previous 1D axisymmetric THCM model of the FEBEX in-situ test reported by Zheng et al. (2011). The first section presents: 1) The results of sensitivity runs performed to quantify the sensitivity of the chemical predictions to the uncertainties in the retention curve of the bentonite, the vapour tortuosity, the dissolution of smectite, and the changes in the boundary conditions caused by the cooling and the dismantling of the test; and 2) The analysis of the back-diffusion of solutes from the bentonite into the granite. The second section presents the results of a 2D axisymmetric THCM model of the FEBEX in-situ test. The previous 1D axisymmetric THCM model of the FEBEX in-situ test has been improved and updated by: 1) Improving the boundary condition at the heater-bentonite interface; 2) Refining the spatial discretization of the finite element mesh; and 3) Revising the solute dispersivities of the bentonite and the granite. The updated model has been used to compare the computed temperatures, relative humidity, water content and pore water pressures with online measured data, collected from 2002 to 2015. The performance of the updated model has been evaluated also by comparing computed values with gravimetric water content data measured after the dismantling of Heater #1 in 2002 and chemical data from aqueous extract tests performed after dismantling Heater #1.

C.4.1 Sensitivity analyses and solute back diffusion analysis

The most updated previous version of the THMC model of the FEBEX in-situ test was reported by Zheng et al. (2011). Fig. C-6 shows the schemes used for the 1D axisymmetric models for the hot and the cold sections. The model for the cold section assumes a constant temperature at r = 0. The value of this temperature was calibrated in order to reproduce the observed temperatures in cold sections C and B2.

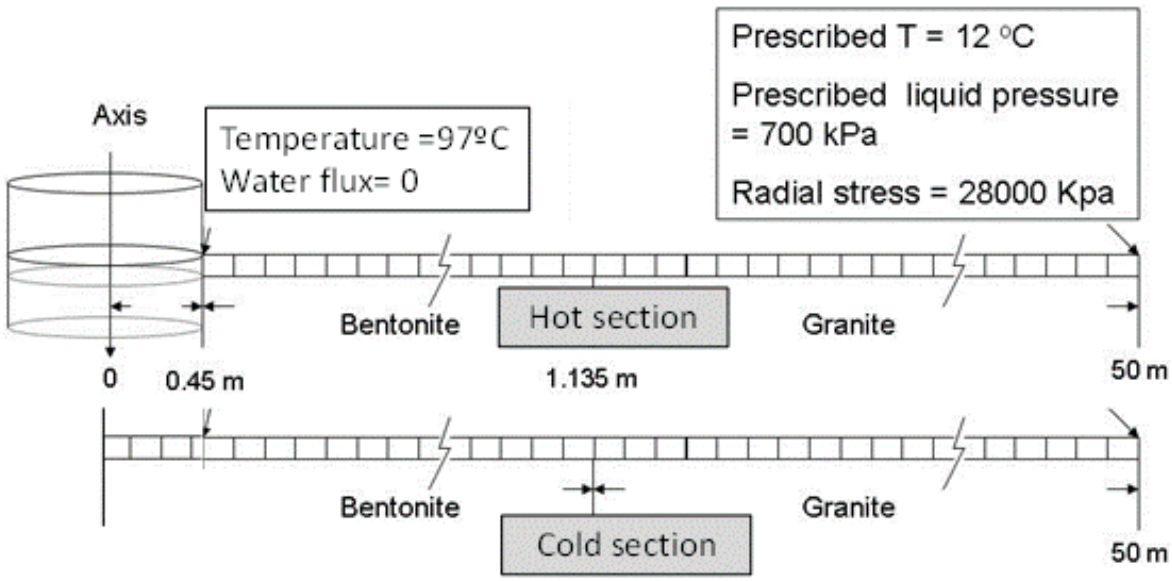

Fig. C-6: Schemes of the 1D axisymmetric models used for the hot and the cold sections

Prior to the update of the previous 1D axisymmetric THCM model of the FEBEX in-situ test reported by Zheng et al. (2011), we performed several model sensitivity runs to quantify the sensitivity of the geochemical predictions to the uncertainties in the retention curve of the bentonite, the vapour tortuosity, the dissolution of smectite, and the changes in the boundary conditions caused by the cooling and the dismantling of the test. We revisited the analysis of the relevance of solute diffusion from the bentonite into the granite. The numerical analyses presented in this section were performed entirely with this THCM model.

C.4.1.1 Sensitivity analyses

C.4.1.1.1 Sensitivity to the retention curve

There are uncertainties in the retention curve of the compacted FEBEX bentonite. Such uncertainties have been recognized also in the THM models of the FEBEX in-situ test (Sánchez et al. 2012) for example for the value of the air-entry pressure P_0. The retention curve used in the base model is given by:

$$S_l = \frac{(1 - 9.11 \times 10^{-7}\psi)^{1.1}}{(1 + (\alpha\psi)^{1.22})^{0.18}}$$

where S_l is the liquid saturation, ψ is the suction (in kPa) and α is the van Genuchten parameter which is equal to the reciprocal of P_0. The value of α in the base model run is equal to 5×10^{-5} kPa^{-1}. A sensitivity run was performed for a value of α equal to 1.4×10^{-4} kPa^{-1}.

Fig. C-7 to A-14 show the sensitivity of the computed concentrations of dissolved Cl^-, Ca^{2+}, K^+, Mg^{2+}, Na^+, SO_4^{2-}, HCO_3^- and pH in 2002 in a hot section after cooling to a change in the value of α. Model results show that computed concentrations of most species are sensitive to a change in the parameter α of the van Genuchten retention curve of the bentonite. The increase in α leads to more water evaporation near the heater and larger solute concentrations near the heater. The pH and the concentration of HCO_3^- are not sensitive to the change in α. We recall that the computed concentrations in this hot section correspond to a generic "hot section", which is a section of the bentonite barrier fully affected by the effect of the heaters. For illustration purposes, the computed concentrations are shown together with the inferred concentrations in Sections 19 and 29. The location of these sections is shown in Fig. C-4.

Fig. C-15 to A-22 show the sensitivity of the computed concentrations of dissolved Cl^-, Ca^{2+}, K^+, Mg^{2+}, Na^+, SO_4^{2-}, HCO_3^- and pH in 2002 in a cold section after cooling to a change in the value of α. Model results show that computed concentrations of most species lack sensitivity to the change in α.

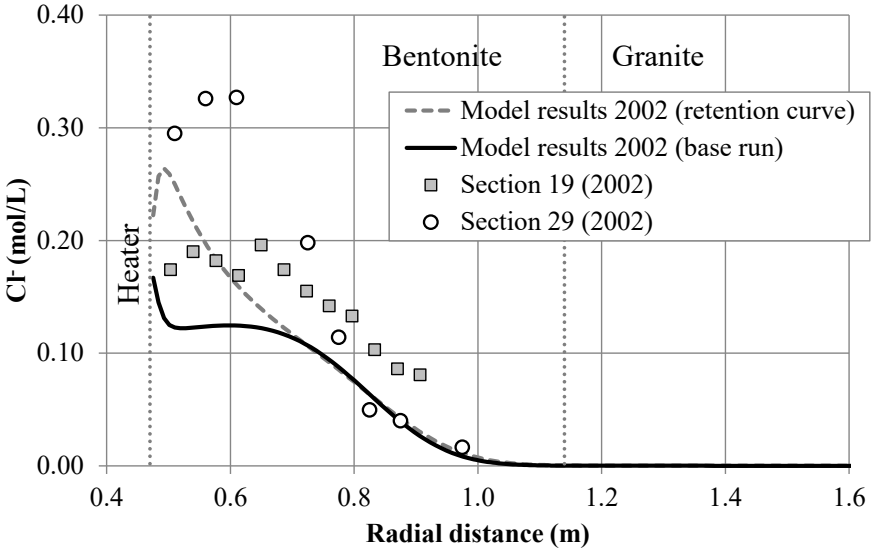

Fig. C-7: Sensitivity of the computed concentrations of dissolved Cl- (lines) in a hot section in 2002 after cooling and dismantling of Heater #1 to a change in the retention curve of the bentonite

Also shown are the inferred Cl- concentrations in Sections 19 and 29 (symbols).

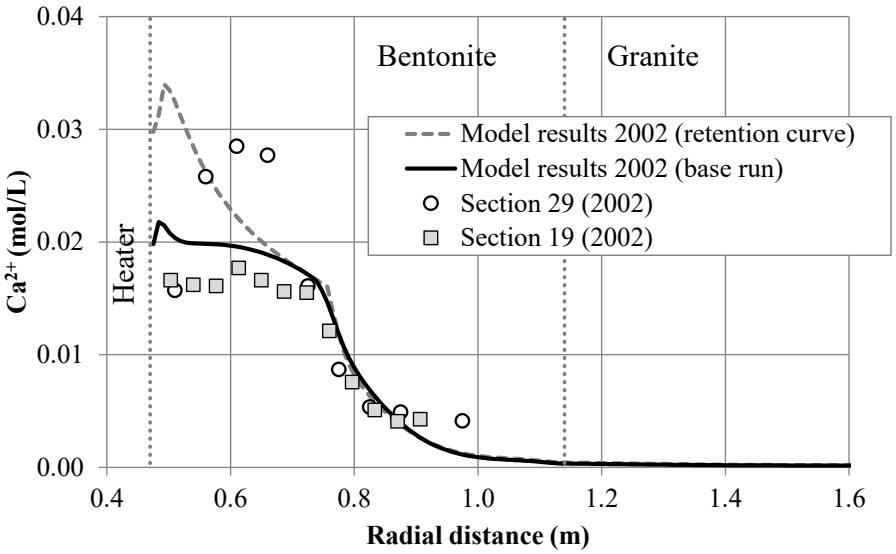

Fig. C-8: Sensitivity of the computed concentrations of dissolved Ca2+ (lines) in a hot section in 2002 after cooling and dismantling of Heater #1 to a change in the retention curve of the bentonite

Also shown are the inferred Ca2+ concentrations in Sections 19 and 29 (symbols).

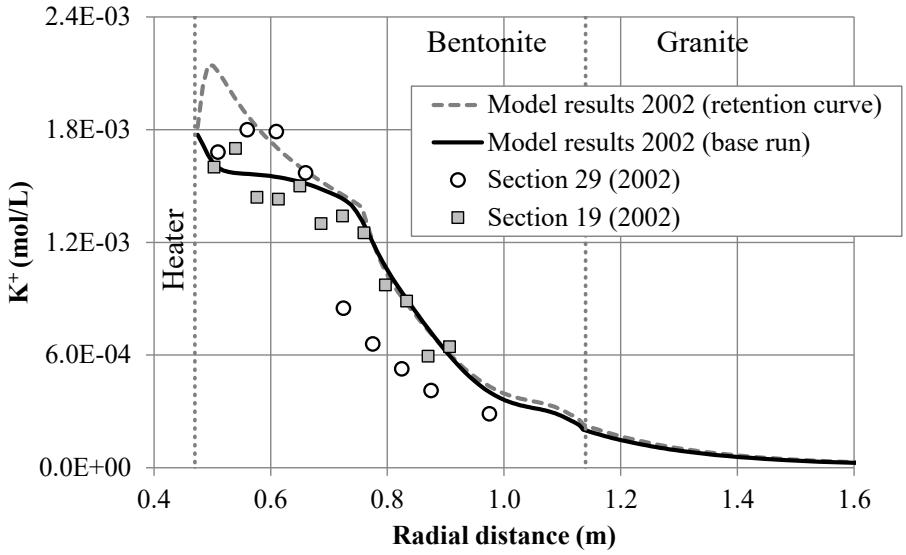

Fig. C-9: Sensitivity of the computed concentrations of dissolved K+ (lines) in a hot section in 2002 after cooling and dismantling of Heater #1 to a change in the retention curve of the bentonite

Also shown are the inferred K+ concentrations in Sections 19 and 29 (symbols).

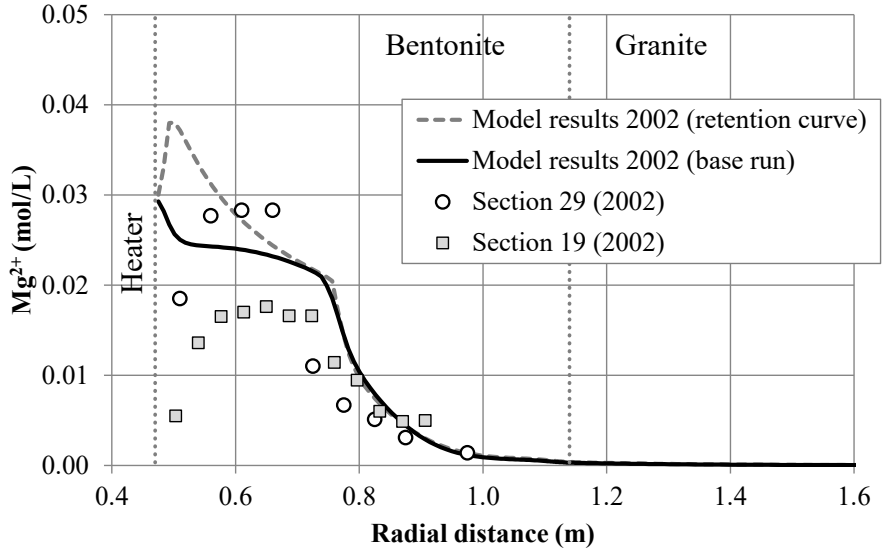

Fig. C-10: Sensitivity of the computed concentrations of dissolved Mg2+ (lines) in a hot section in 2002 after cooling and dismantling of Heater #1 to a change in the retention curve of the bentonite

Also shown are the inferred Mg2+ concentrations in Sections 19 & 29 (symbols).

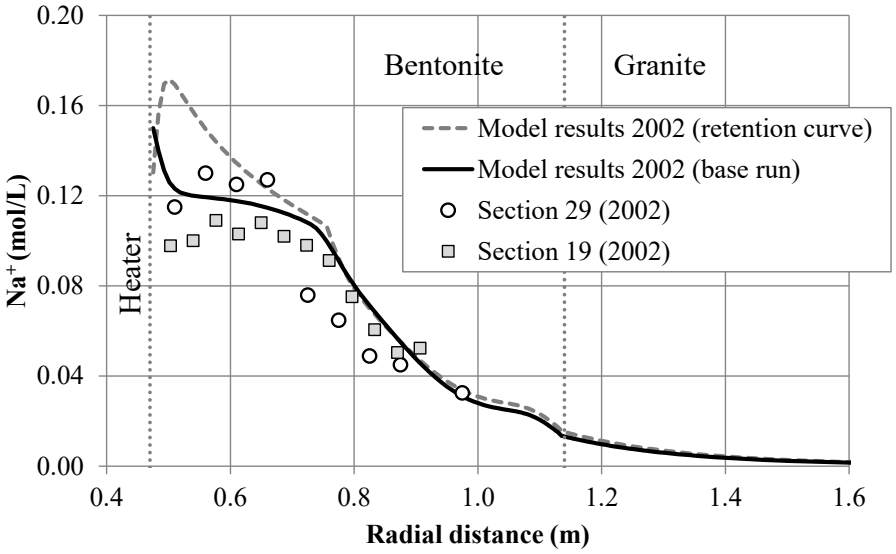

Fig. C-11: Sensitivity of the computed concentrations of dissolved Na+ (lines) in a hot section in 2002 after cooling and dismantling of Heater #1 to a change in the retention curve of the bentonite

Also shown are the inferred Na+ concentrations in Sections 19 and 29 (symbols).

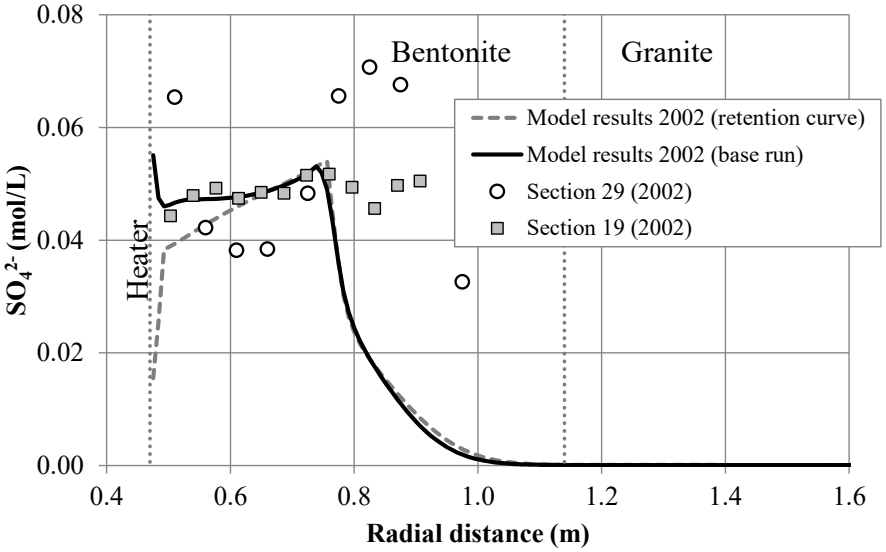

Fig. C-12: Sensitivity of the computed concentrations of dissolved SO42- (lines) in a hot section in 2002 after cooling and dismantling of Heater #1 to a change in the retention curve of the bentonite

Also shown are the inferred concentrations in Sections 19 and 29 (symbols).

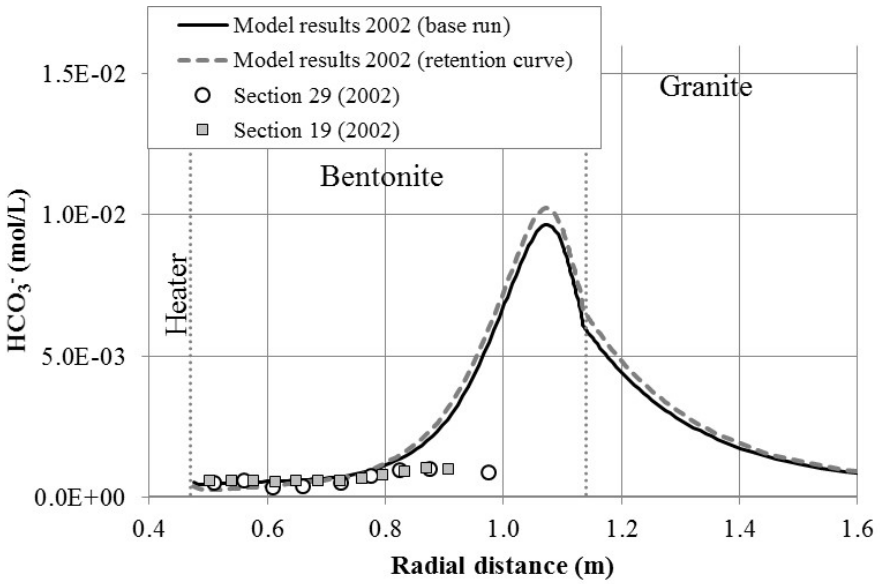

Fig. C-13: Sensitivity of the computed concentrations of dissolved HCO3- (lines) in a hot section in 2002 after cooling and dismantling of Heater #1 to a change in the parameter α of the retention curve of the bentonite

Also shown are the inferred HCO3- concentrations in Sections 19 and 29 (symbols).

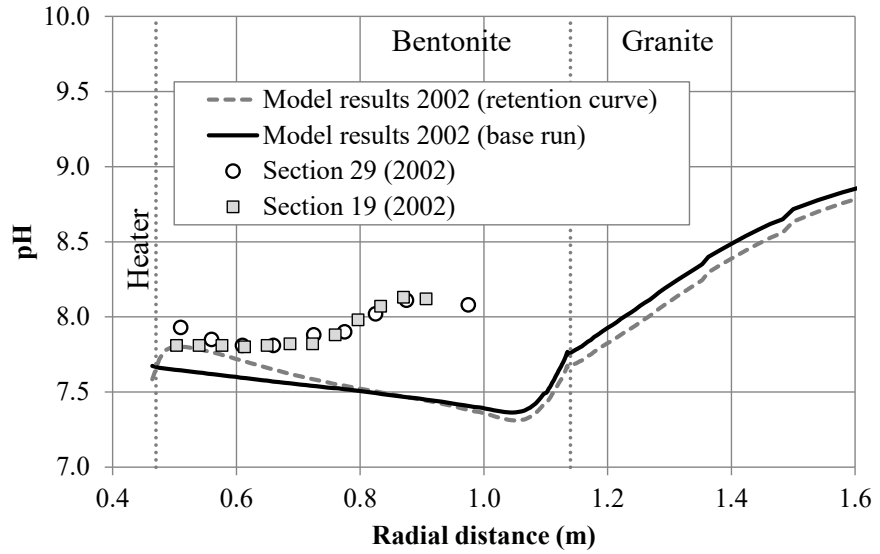

Fig. C-14: Sensitivity of the computed pH (lines) in a hot section in 2002 after cooling and dismantling of Heater #1 to a change in the parameter α of the retention curve of the bentonite

Also shown are the inferred pH in Sections 19 and 29 (symbols).

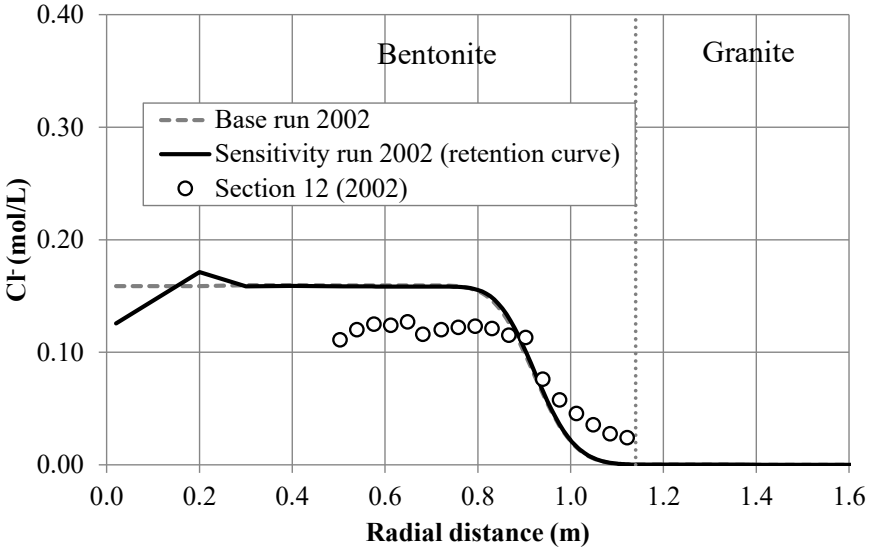

Fig. C-15: Sensitivity of the computed concentrations of dissolved Cl- (lines) in a cold section in 2002 after cooling and dismantling of Heater #1 to a change in the retention curve of the bentonite

Also shown are the inferred Cl- concentrations in Sections 19 and 29 (symbols).

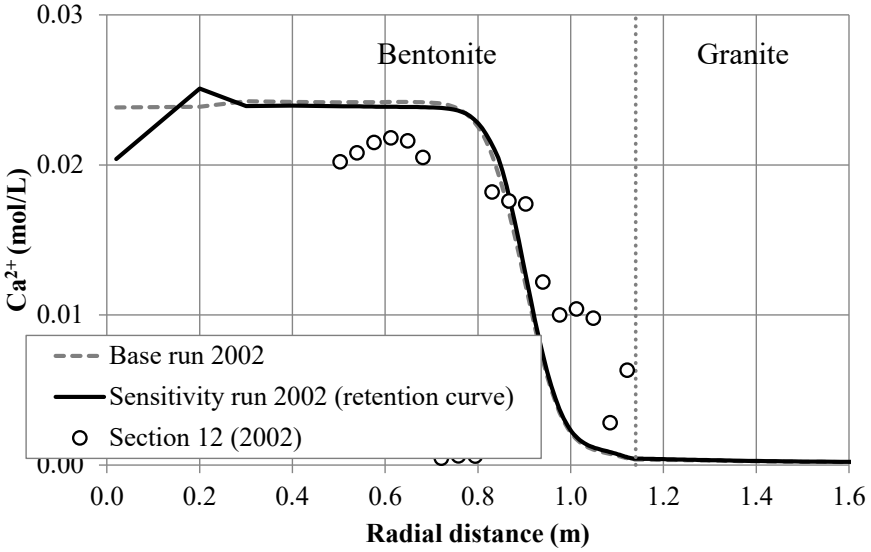

Fig. C-16: Sensitivity of the computed concentrations of dissolved Ca2+ (lines) in a cold section in 2002 after cooling and dismantling of Heater #1 to a change in the retention curve of the bentonite

Also shown are the inferred Ca2+ concentrations in Sections 19 and 29 (symbols).

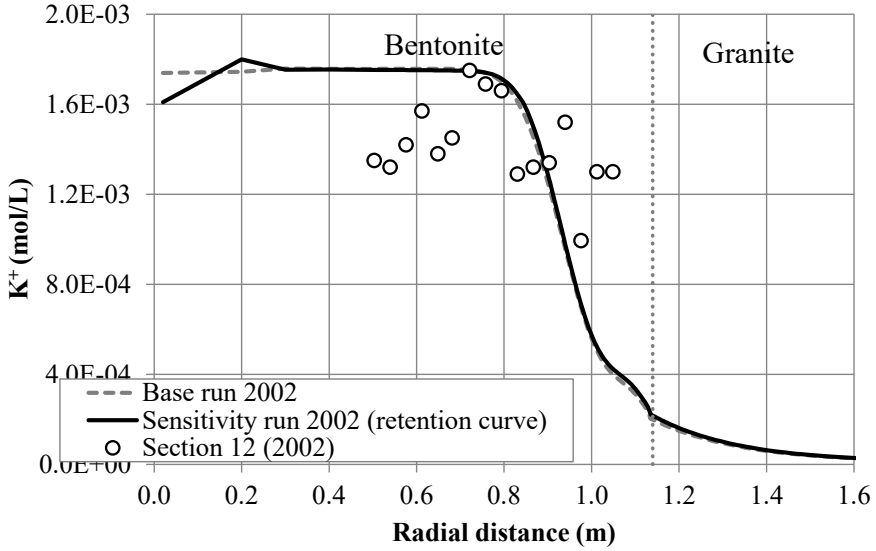

Fig. C-17: Sensitivity of the computed concentrations of dissolved K+ (lines) in a cold section in 2002 after cooling and dismantling of Heater #1 to a change in the retention curve of the bentonite

Also shown are the inferred K+ concentrations in Sections 19 and 29 (symbols).

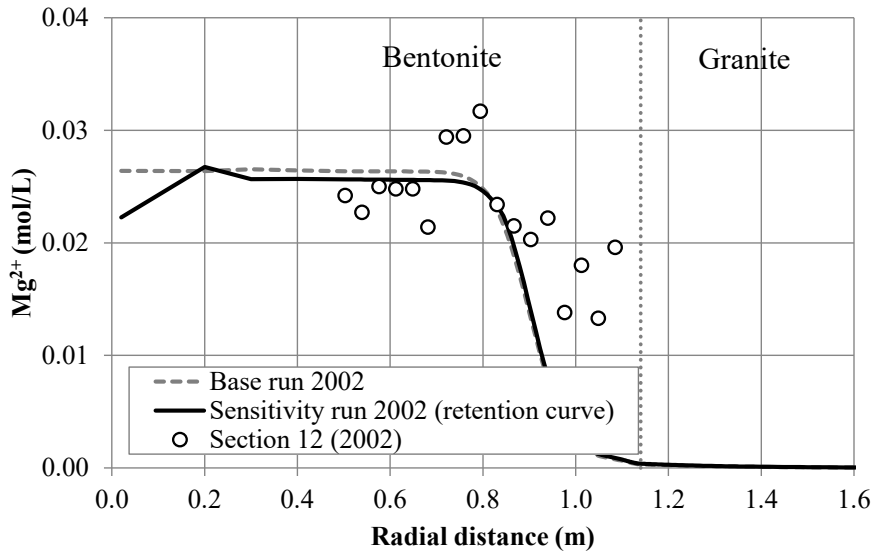

Fig. C-18: Sensitivity of the computed concentrations of dissolved Mg2+ (lines) in a cold section in 2002 after cooling and dismantling of Heater #1 to a change in the parameter α of the retention curve of the bentonite

Also shown are the inferred Mg2+ concentrations in Sections 19 and 29 (symbols).

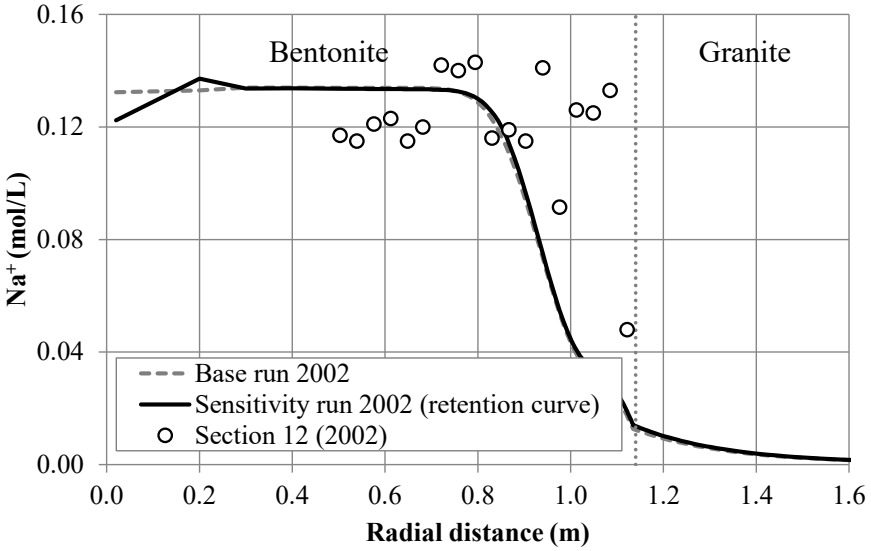

Fig. C-19: Sensitivity of the computed concentrations of dissolved Na+ (lines) in a cold section in 2002 after cooling and dismantling of Heater #1 to a change in the retention curve of the bentonite

Also shown are the inferred Na+ concentrations in Sections 19 and 29 (symbols).

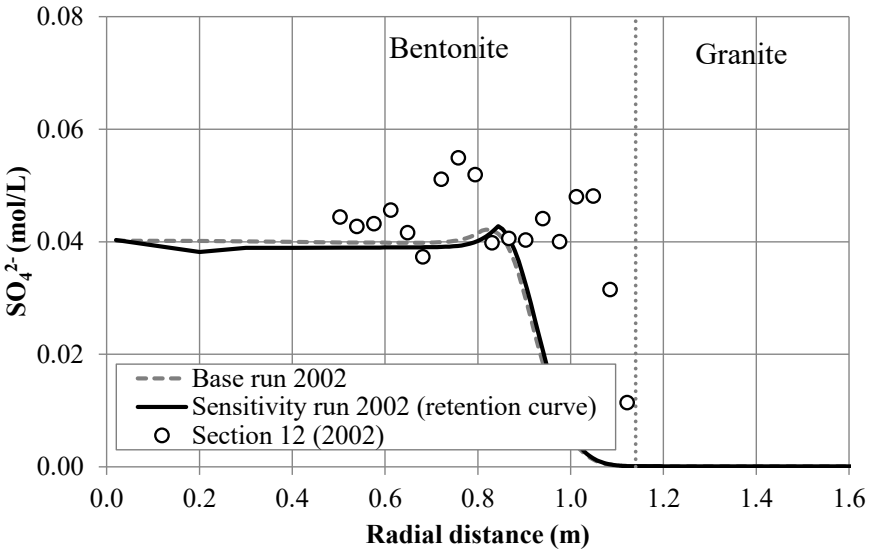

Fig. C-20: Sensitivity of the computed concentrations of dissolved SO42- (lines) in a cold section in 2002 after cooling and dismantling of Heater #1 to a change in the retention curve of the bentonite

Also shown are the inferred concentrations in Sections 19 and 29 (symbols).

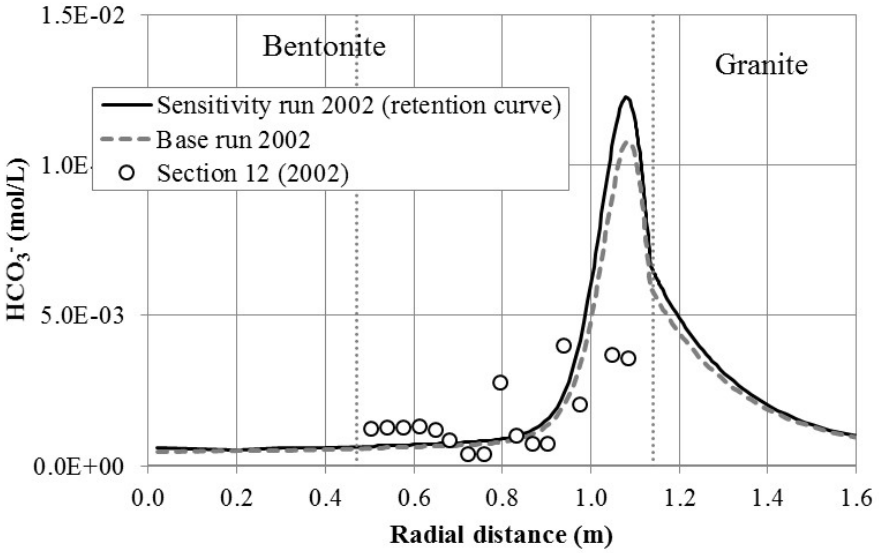

Fig. C-21: Sensitivity of the computed concentrations of dissolved HCO3- (lines) in a cold section in 2002 after cooling and dismantling of Heater #1 to a change in the parameter α of the retention curve of the bentonite

Also shown are the inferred HCO3- concentrations in Sections 19 and 29 (symbols).

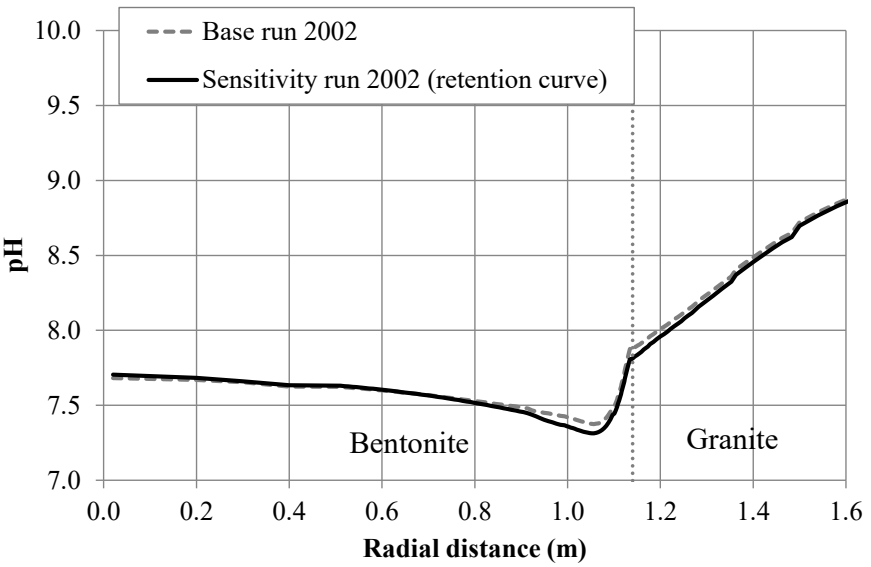

Fig. C-22: Sensitivity of the computed pH (lines) in a hot section in 2002 after cooling and dismantling of Heater #1 to a change in the parameter α of the retention curve of the bentonite

C.4.1.1.2 Relevance of smectite dissolution and analcime precipitation

The base model does not account for smectite dissolution because smectite dissolution is considered to be too slow. Samper et al. (2016) analysed the relevance of smectite dissolution for the long-term performance of the bentonite barrier. The relevance of *smectite dissolution* during the time span of the FEBEX in-situ test has been evaluated by means of a sensitivity run. We took the chemical formulation and kinetic parameters of the FEBEX smectite from the numerical model of Samper et al. (2016). Tab. C-1 shows the reactions and the logK values at 25 °C for smectite dissolution and analcime precipitation. Smectite dissolution is modelled with the following kinetic rate law proposed by Rozalén et al. (2008):

$$r_m = 10^{-14.37} + 10^{-12.30}\left[H^+\right]^{0.40} + 10^{-13.05}\left[OH^-\right]^{0.27}$$

were r_m is the dissolution/precipitation rate in mol/m^2/s which includes first a constant term, a second term which depends on proton activity, [H^+], and a third term which depends on hydroxyl activity, [OH^-]. The reactive surface area is taken equal to 1 m^2/L. Analcime is a zeolite which is not initially present in the bentonite, but it is allowed to precipitate with the following kinetic rate law proposed by Savage et al. (2010):

$$r_m = 10^{-13.9}(\Omega_m - 1)$$

where Ω_m is the saturation index of the mineral. The reactive surface area of analcime is taken equal to 0.01 m^2/L.

Tab. C-1: Dissolution/precipitation reactions of smectite and analcime and equilibrium constants at 25 °C

	Reaction	**Log K** (25 °C)
Smectite (Fernández et al. 2009)	$K_{0.055}Na_{0.135}Ca_{0.125}Mg_{0.1}(Al_{1.545}Mg_{0.425})\cdot(Si_{3.86}Al_{0.145})O_{10}(OH)_2$ $+6.56H^+ \rightleftarrows 0.135Na^+ + 0.055K^+ + 0.125Ca^{2+} + 0.525Mg^{2+} + 1.69Al^{3+}$ $+3.86SiO_2(aq) + 4.82H_2O$	6.26
Analcime (Savage et al. 2010)	$NaAlSi_2O_6\cdot H_2O + 4H^+ \rightleftarrows Na^+ + Al^{3+} + 2SiO_2(aq) + 3H_2O$	6.7833

Fig. C-23 and Fig. C-24 show the computed cumulative dissolution of smectite and precipitation of analcime in the bentonite in 2002 after cooling and dismantling of Heater #1. The cumulative dissolution of smectite and precipitation of analcime in 2002 is extremely small.

Fig. C-25 to A-31 show the sensitivity of the computed concentrations of dissolved Ca^{2+}, K^+, Mg^{2+}, Na^+, SO_4^{2-}, HCO_3^- and pH in 2002 in a hot section after cooling to smectite dissolution and analcime precipitation. Computed Cl^- concentrations are not sensitive to smectite dissolution (not shown here). The concentrations of the rest of the species mostly lack sensitivity to smectite dissolution and analcime precipitation.

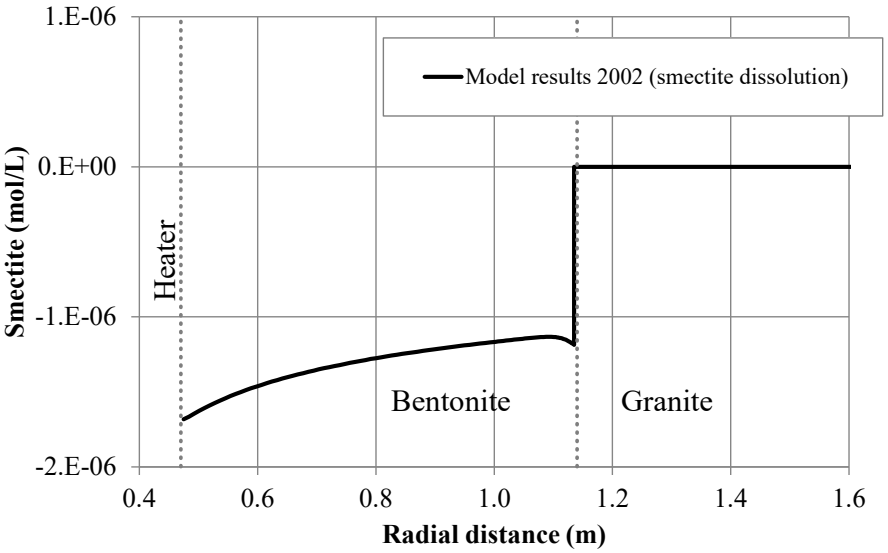

Fig. C-23: Cumulative dissolution of smectite in the bentonite in 2002 after cooling and dismantling of Heater #1

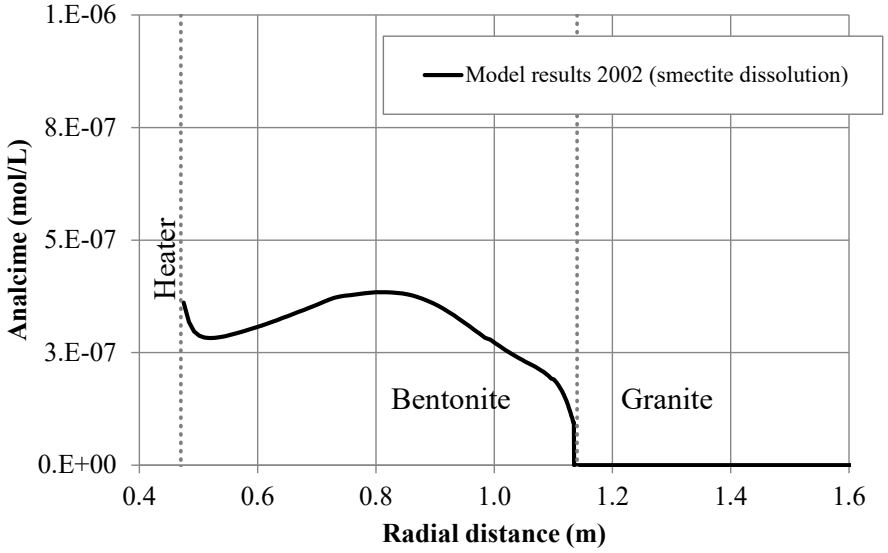

Fig. C-24: Cumulative precipitation of analcime in the bentonite in 2002 after cooling and dismantling of Heater #1

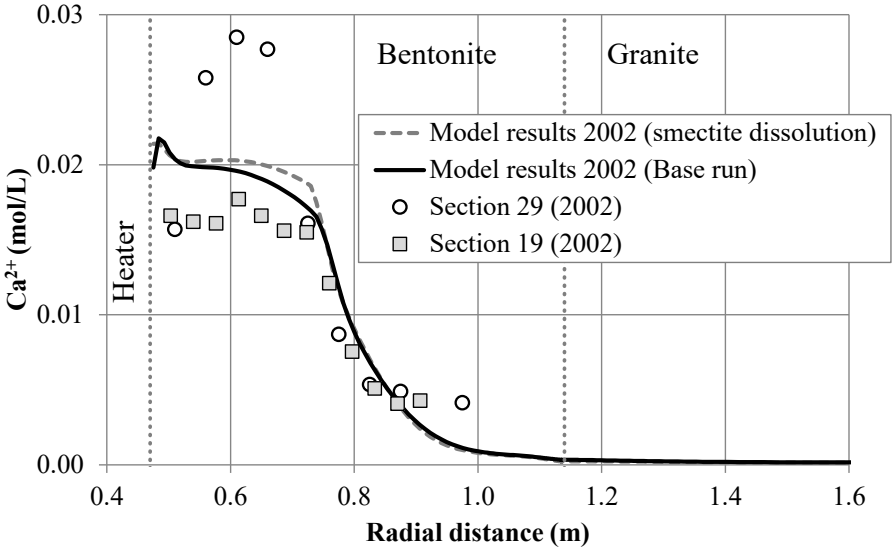

Fig. C-25: Sensitivity of the computed concentrations of dissolved Ca2+ (lines) in a hot section in 2002 after cooling and dismantling of Heater #1 to smectite dissolution and analcime precipitation

Also shown are the inferred Ca2+ concentrations in Sections 19 and 29 (symbols)

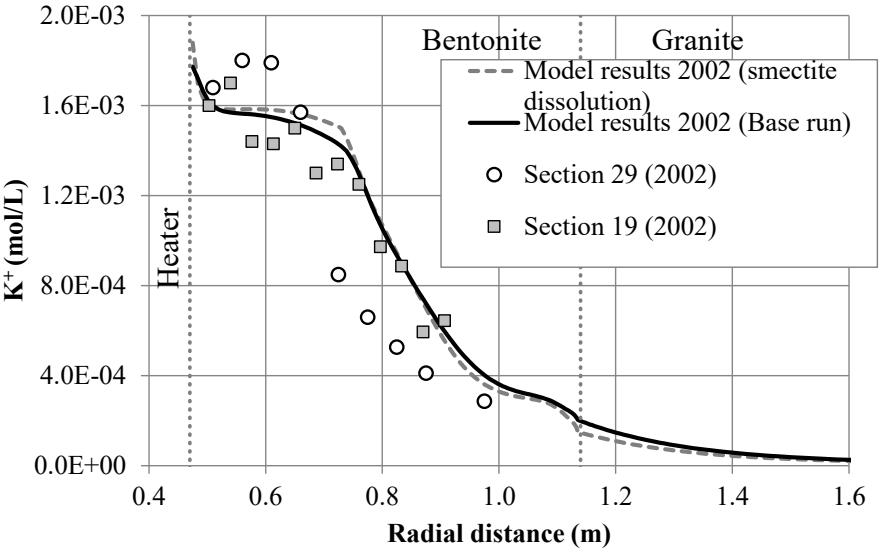

Fig. C-26: Sensitivity of the computed concentrations of dissolved K+ (lines) in a hot section in 2002 after cooling and dismantling of Heater #1 to smectite dissolution and analcime precipitation

Also shown are the inferred K+ concentrations in Sections 19 and 29 (symbols).

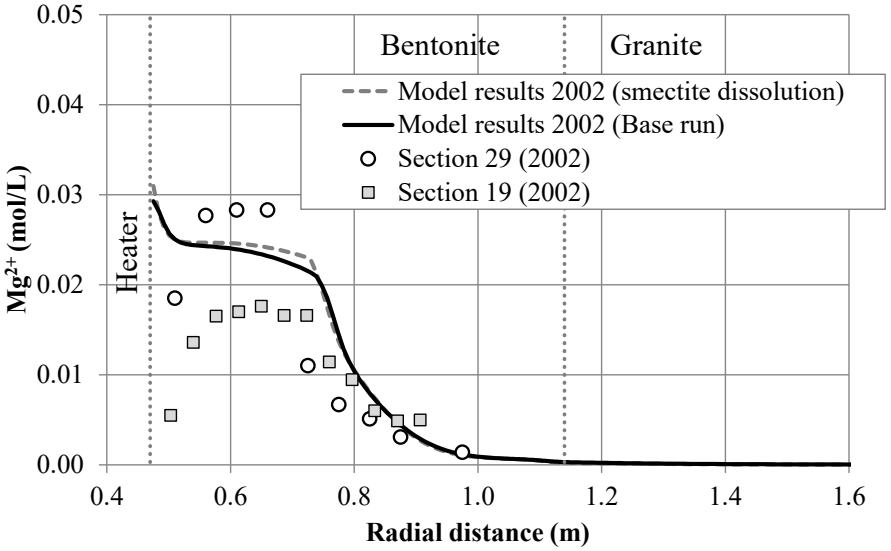

Fig. C-27: Sensitivity of the computed concentrations of dissolved Mg2+ (lines) in a hot section in 2002 after cooling and dismantling of Heater #1 to smectite dissolution precipitation

Also shown are the inferred Mg2+ concentrations in Sections 19 and 29 (symbols).

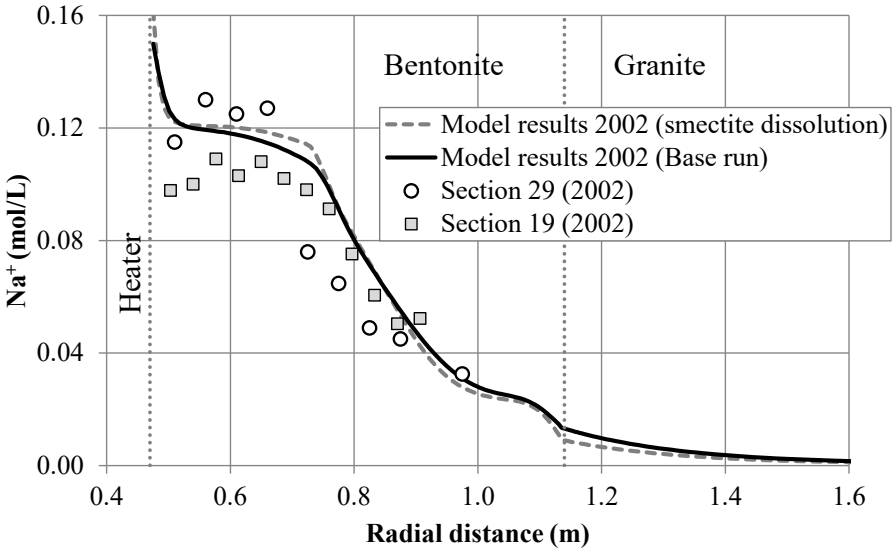

Fig. C-28: Sensitivity of the computed concentrations of dissolved Na+ (lines) in a hot section in 2002 after cooling and dismantling of Heater #1 to smectite dissolution

Also shown are the inferred Na+ concentrations in Sections 19 and 29 (symbols).

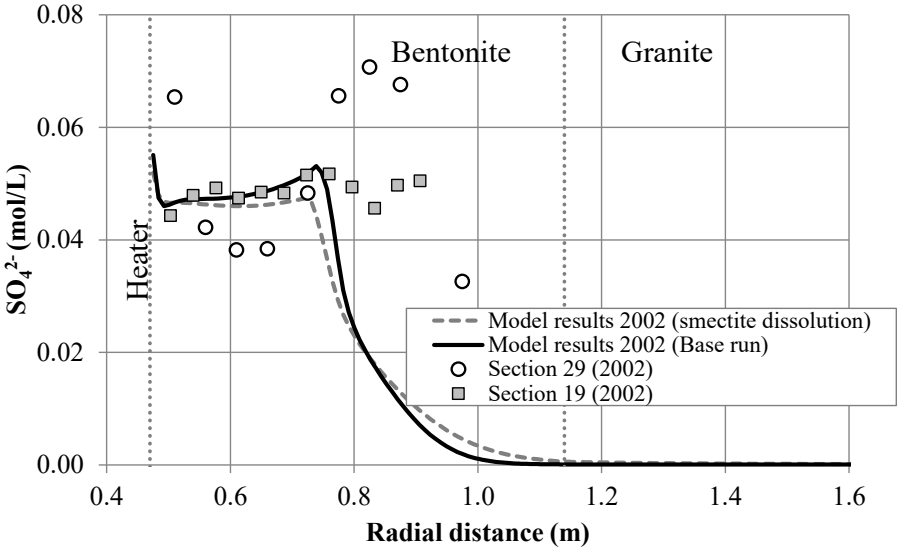

Fig. C-29: Sensitivity of the computed concentrations of dissolved SO42- (lines) in a hot section in 2002 after cooling and dismantling of Heater #1 to smectite dissolution and analcime precipitation

Also shown are the inferred SO42- concentrations in Sections 19 and 29 (symbols).

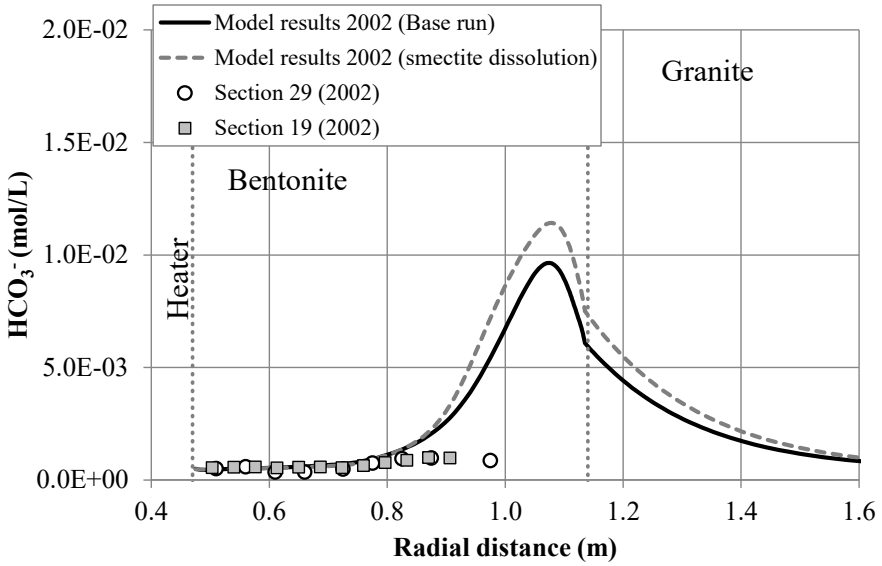

Fig. C-30: Sensitivity of the computed concentrations of dissolved HCO3- (lines) in a hot section in 2002 after cooling and dismantling of Heater #1 to smectite dissolution

Also shown are the inferred HCO32- concentrations in Sections 19 and 29 (symbols).

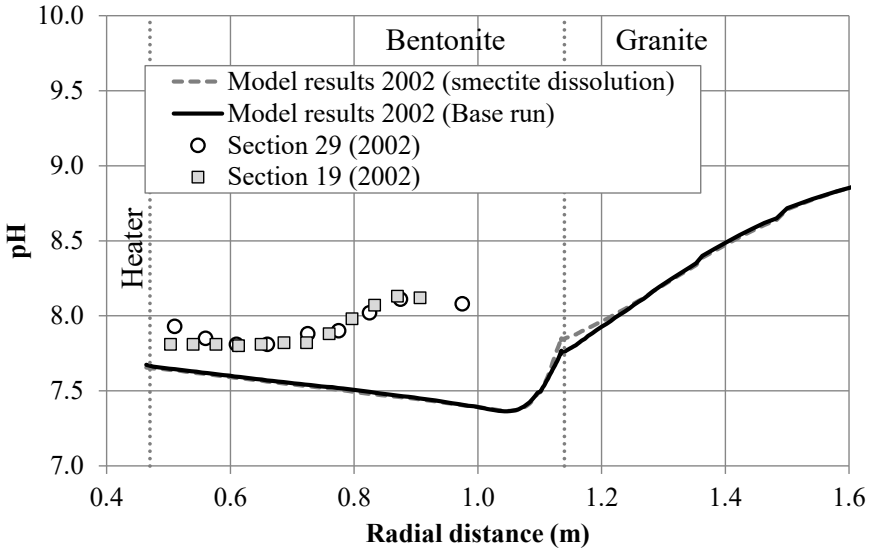

Fig. C-31: Sensitivity of the computed pH (lines) in a hot section in 2002 after cooling and dismantling of Heater #1 to smectite dissolution precipitation

Also shown the inferred pH in Sections 19 and 29 (symbols).

C.4.1.1.3 Changes in boundary conditions during cooling and dismantling of the test

The thermal and hydrodynamic conditions of the bentonite barrier may change after switching off the heaters and during the dismantling of the bentonite blocks. The reference THCM model assumes that the system is closed to gas during all the simulation time. The effects of the changes in the boundary conditions during cooling and dismantling of the test have been evaluated with the following sensitivity runs:

1. "Base run". The simulation ends at t = 1827 days when the Heater #1 was switched off.
2. "Base run & cooling". This run accounts for switching off of Heater #1 at t = 1'827 days and for cooling until t = 1'930 days. The temperature at the heater/bentonite interface drops from 95 °C to 22 °C. The system is closed to gas.
3. "Base run & cooling & open gas". This run accounts for switching off of Heater #1 at t = 1'827 days and for cooling until t = 1'930 days. The system is then open to gas. The gas pressure is fixed at the atmospheric pressure (100 kPa) during the dismantling.

Fig. C-32 to A-39 show the sensitivity of the dissolved Ca^{2+}, K^{+}, Mg^{2+}, Na^{+}, Cl^{-}, SO_4^{2-} computed concentrations, pH and HCO_3^{-} in 2002 in a hot section to changes in the boundary conditions during cooling and dismantling of the test. Model results show that the computed concentrations are not sensitive to a change in the gas boundary condition. The computed concentrations are sensitive to the cooling due to the temperature-dependence of the solubility of the minerals and the chemical parameters.

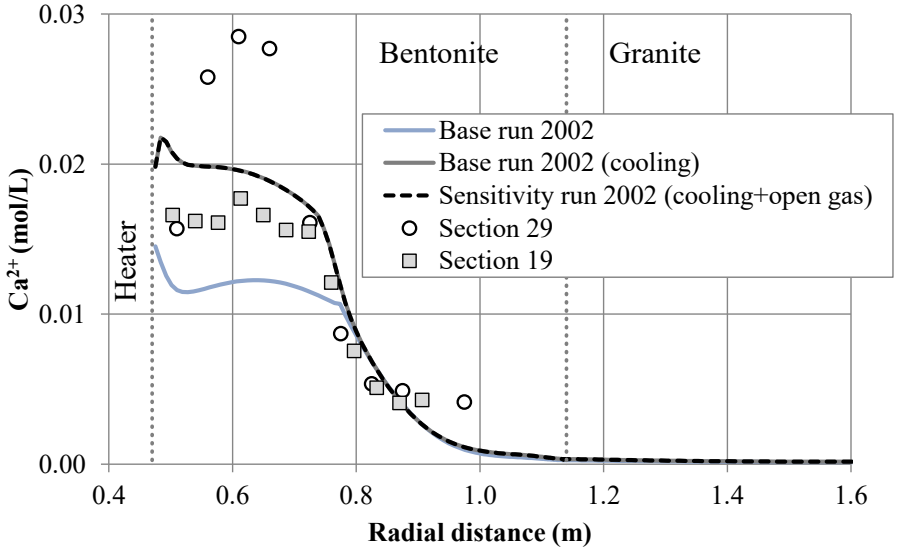

Fig. C-32: Sensitivity of the computed concentrations of dissolved Ca^{2+} (lines) in a hot section in 2002 to cooling and a changing gas boundary condition

Also shown are the inferred Ca^{2+} concentrations in Sections 19 and 29 (symbols).

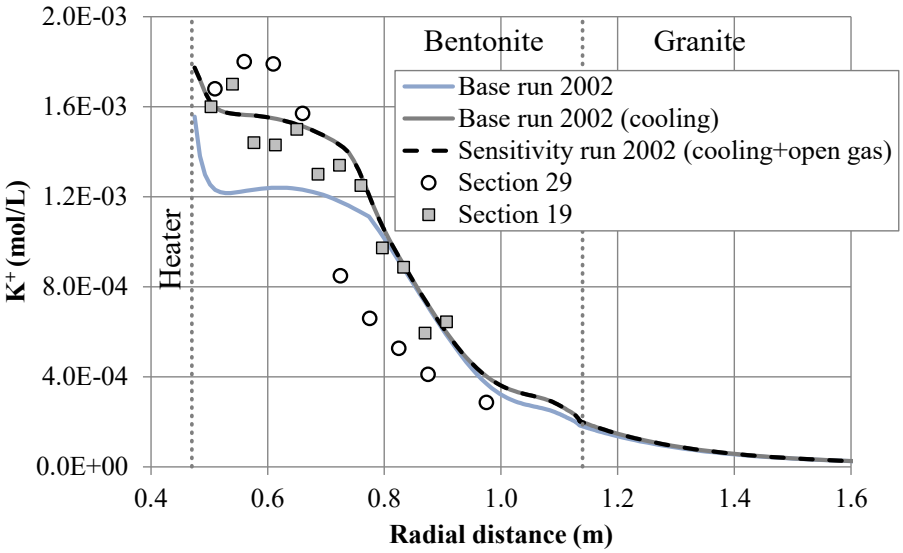

Fig. C-33: Sensitivity of the computed concentrations of dissolved K^+ (lines) in a hot section in 2002 to cooling and a changing gas boundary condition

Also shown are the inferred K+ concentrations in Sections 19 and 29 (symbols).

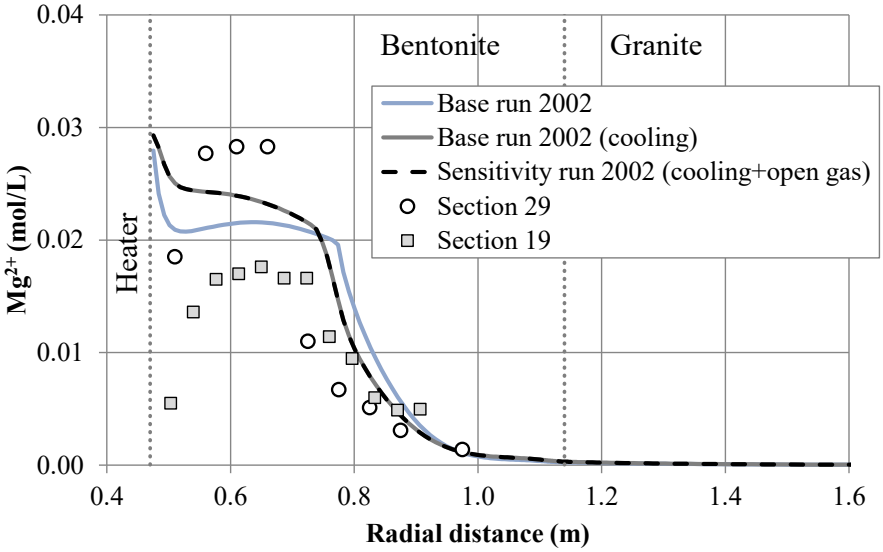

Fig. C-34: Sensitivity of the computed concentrations of dissolved Mg2+ (lines) in a hot section in 2002 to cooling and a changing gas boundary condition

Also shown are the inferred Mg^{2+} concentrations in Sections 19 and 29 (symbols).

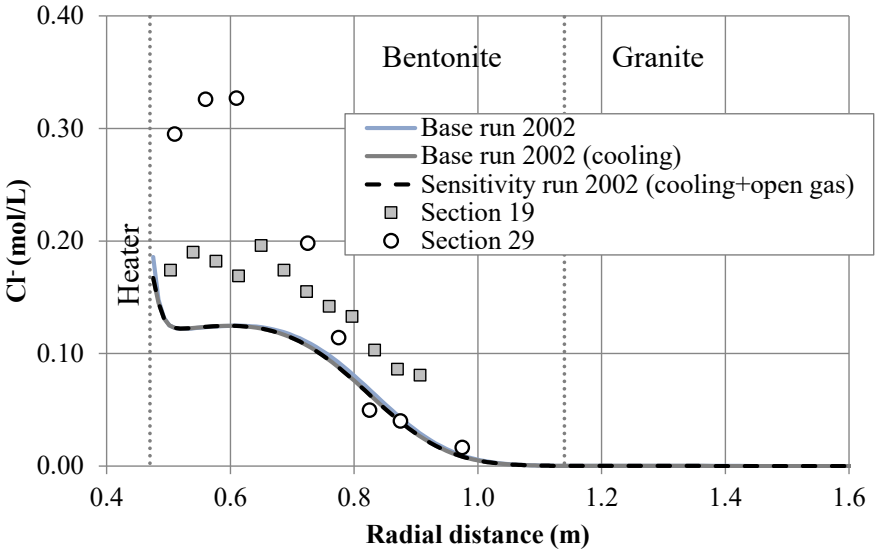

Fig. C-35: Sensitivity of the computed concentrations of dissolved Cl- (lines) in a hot section in 2002 to cooling and a changing gas boundary condition

Also shown are the inferred Cl- concentrations in Sections 19 and 29 (symbols).

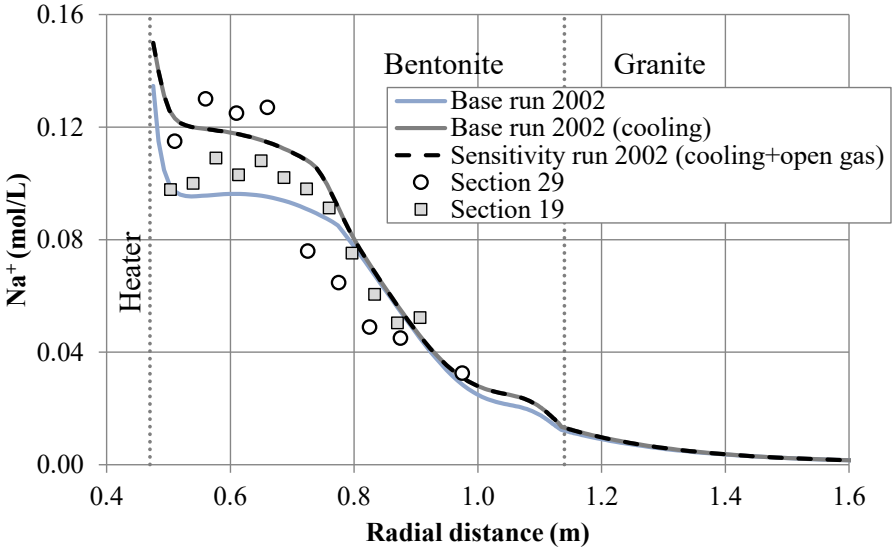

Fig. C-36: Sensitivity of the computed concentrations of dissolved Na^+ (lines) in a hot section in 2002 to cooling and a changing gas boundary condition

Also shown are the inferred Na^+ concentrations in Sections 19 and 29 (symbols).

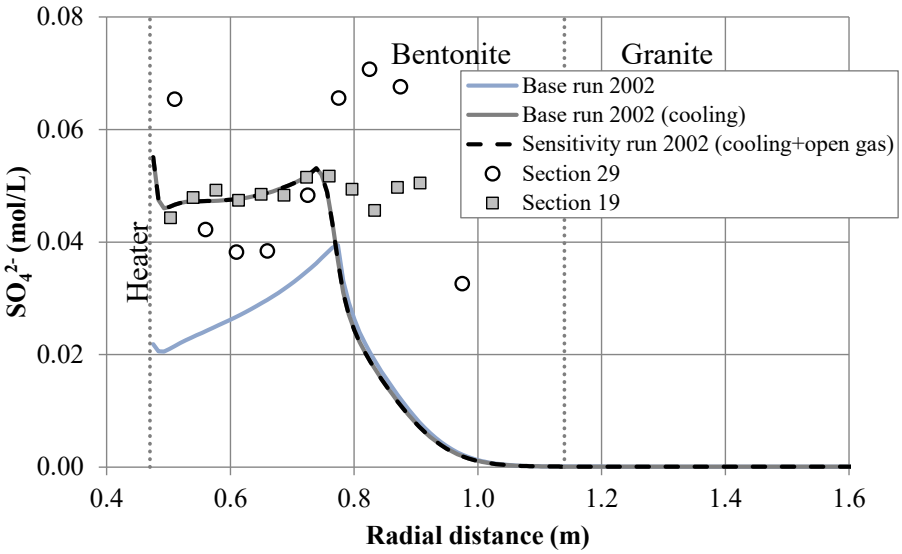

Fig. C-37: Sensitivity of the computed concentrations of dissolved SO_4^{2-} (lines) in a hot section in 2002 to cooling and a changing gas boundary condition

Also shown are the inferred SO_4^{2-} concentrations in Sections 19 and 29 (symbols).

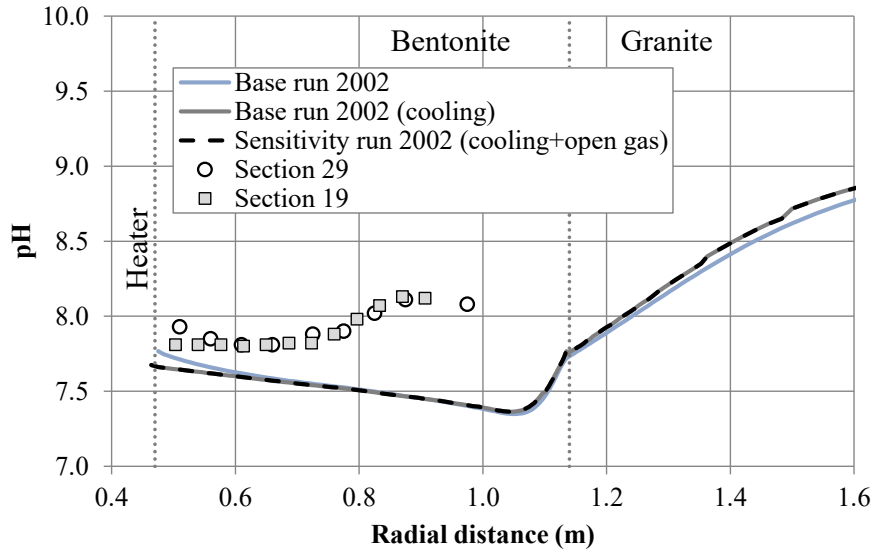

Fig. C-38: Sensitivity of the computed pH (lines) in a hot section in 2002 to cooling and a changing gas boundary condition

Also shown are the inferred pH in Sections 19 and 29 (symbols).

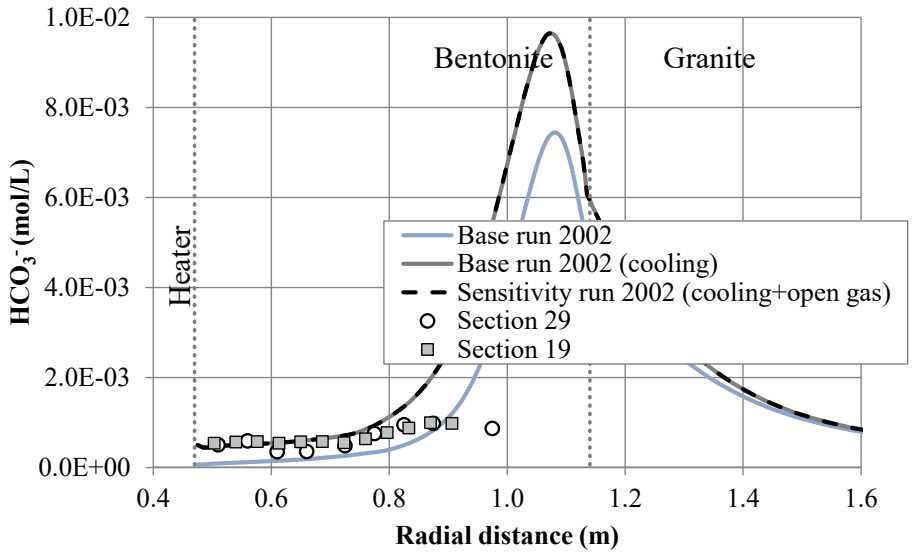

Fig. C-39: Sensitivity of the computed concentrations of dissolved HCO_3^- (lines) in a hot section in 2002 to cooling and a changing gas boundary condition

Also shown are the inferred HCO_3^- concentrations in Sections 19 and 29 (symbols).

C.4.1.1.4 Sensitivity to vapour tortuosity

Vapour transport in the bentonite near the heater is sensitive to vapour tortuosity. This section presents the results of several sensitivity runs to changes in vapour tortuosity in the bentonite from 0.05 to 0.2. The larger the vapour tortuosity, the larger the vapour diffusion coefficient and, consequently, the larger the water evaporation and vapour condensation far from the heater. Water evaporation is strongly dependent on vapour tortuosity. Fig. C-40 to A-47 show the sensitivity of the computed dissolved Ca^{2+}, K^{+}, Mg^{2+}, Na^{+}, Cl^{-}, SO_4^{2-} concentrations, of pH and HCO_3^{-} in 2002 in a hot section to changes in vapour tortuosity. The concentrations of dissolved Ca^{2+}, K^{+}, Mg^{2+}, Na^{+} and Cl^{-} near the heater increase when vapour tortuosity increases. However, away from the heater the concentrations decrease when vapour tortuosity increases. The computed pH and the concentrations of SO_4^{2-} and HCO_3^{-} are less sensitive to changes in vapour tortuosity.

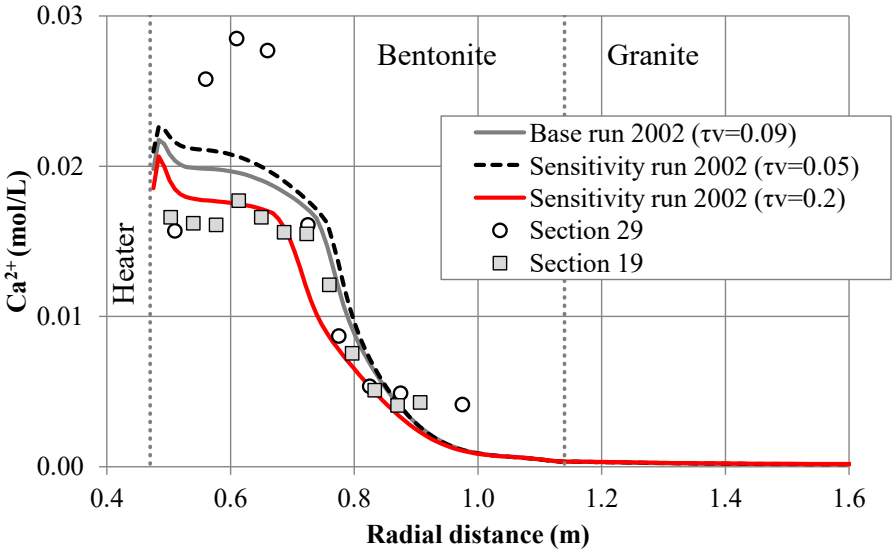

Fig. C-40: Sensitivity of the computed concentrations of dissolved Ca^{2+} (lines) in a hot section in 2002 to changes in vapour tortuosity

Also shown are the inferred Ca^{2+} concentrations in Sections 19 and 29 (symbols).

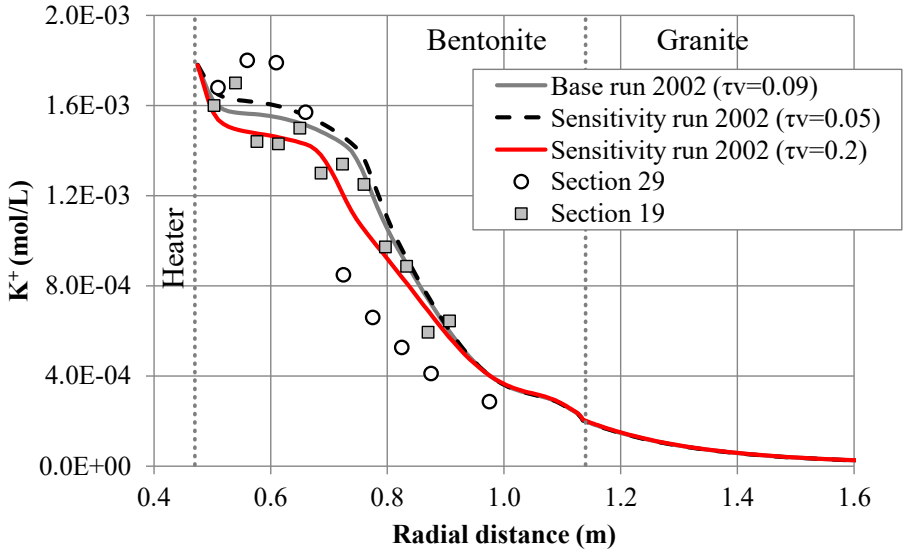

Fig. C-41: Sensitivity of the computed concentrations of dissolved K^+ (lines) in a hot section in 2002 to changes in vapour tortuosity

Also shown are the inferred K^+ concentrations in Sections 19 and 29 (symbols).

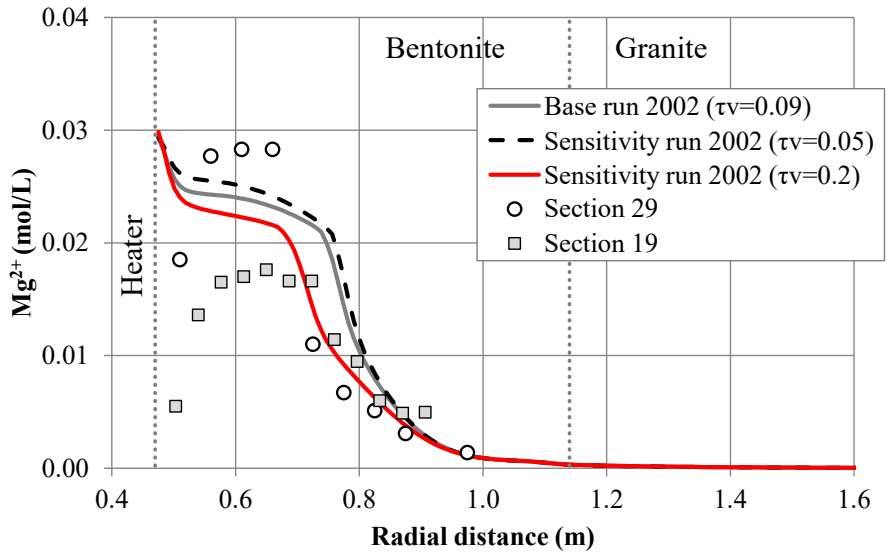

Fig. C-42: Sensitivity of the computed concentrations of dissolved Mg^{2+} (lines) in a hot section in 2002 to changes in vapour tortuosity

Also shown are the inferred Mg^{2+} concentrations in Sections 19 and 29 (symbols).

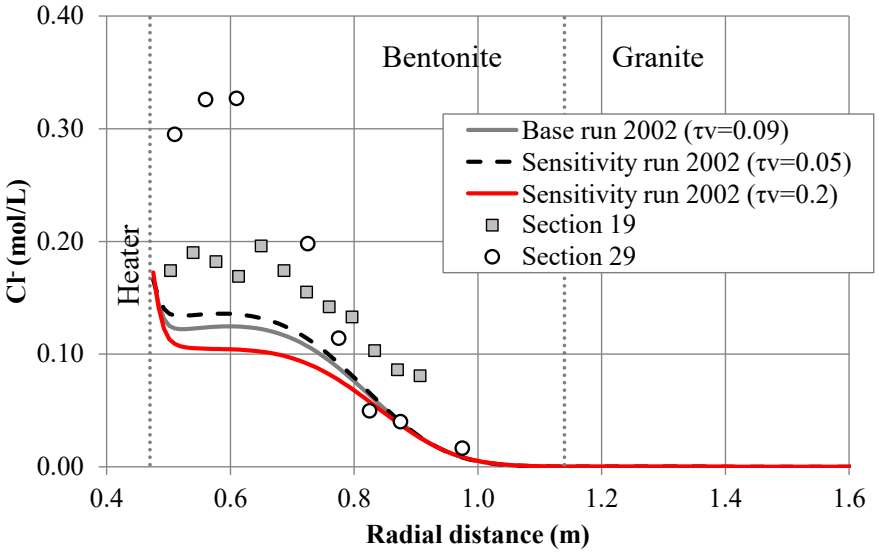

Fig. C-43: Sensitivity of the computed concentrations of dissolved Cl^- (lines) in a hot section in 2002 to changes in vapour tortuosity

Also shown are the inferred Cl^- concentrations in Sections 19 and 29 (symbols).

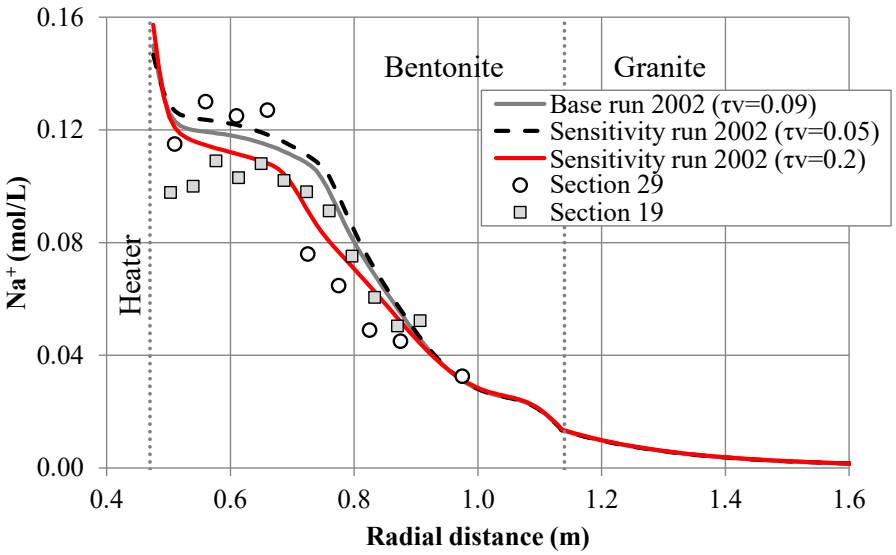

Fig. C-44: Sensitivity of the computed concentrations of dissolved Na^+ (lines) in a hot section in 2002 to changes in vapour tortuosity

Also shown are the inferred Na^+ concentrations in Sections 19 and 29 (symbols).

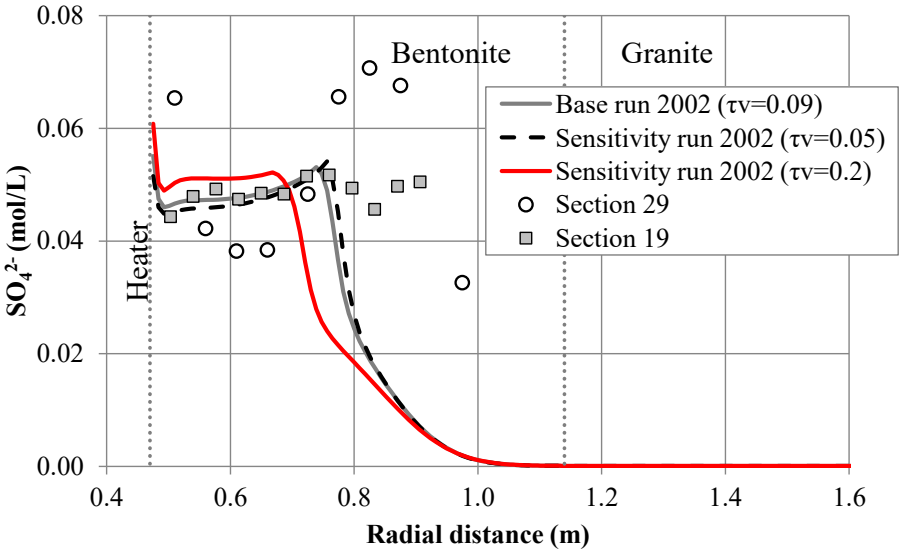

Fig. C-45: Sensitivity of the computed concentrations of dissolved SO_4^{2-} (lines) in a hot section in 2002 to changes in vapour tortuosity

Also shown are the inferred SO_4^{2-} concentrations in Sections 19 and 29 (symbols).

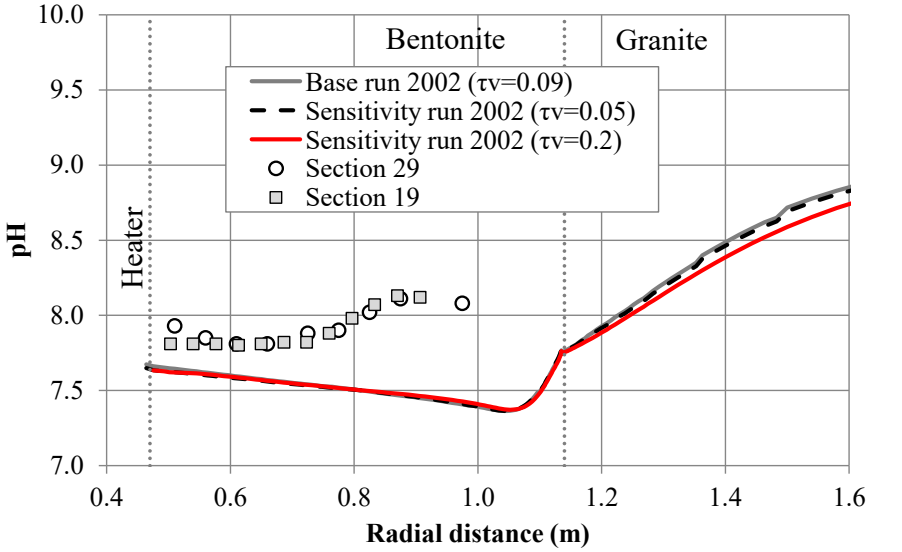

Fig. C-46: Sensitivity of the computed pH (lines) in a hot section in 2002 to changes in vapour tortuosity

Also shown are the inferred pH in Sections 19 and 29 (symbols).

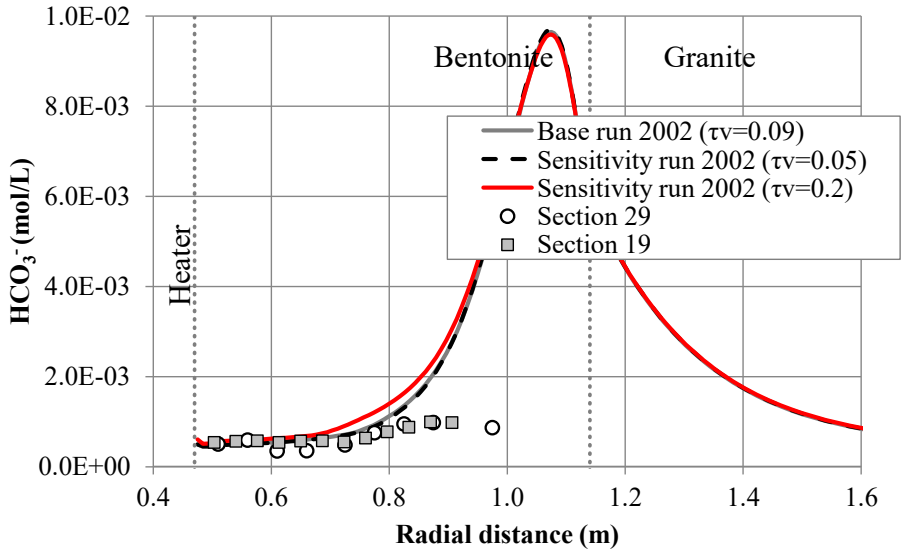

Fig. C-47: Sensitivity of the computed concentrations of dissolved HCO3- (lines) in a hot section in 2002 to changes in vapour tortuosity

Also shown are the inferred HCO3- concentrations in Sections 19 and 29 (symbols).

C.4.1.2 Solute back-diffusion from the bentonite into the granite

During the early stages of bentonite hydration with granitic pore water, solutes migrate from the granite into the bentonite due to solute advection by water flow. The advective flux declines sharply with time. Then, solute diffusion becomes the dominant transport process. As most solute concentrations in bentonite are larger than the concentrations in granite, the solutes may diffuse from the bentonite into the granite. This change in solute transport direction from forward to backward leads to the term "solute back-diffusion".

Two boreholes parallel to the FEBEX drift were drilled 20 and 60 cm away from the granite-bentonite interface to provide data on potential bentonite–granite solute transfer (Buil et al. 2010). Periodic sampling and analysis of the major ions showed: 1) The existence of solute transfer from the bentonite porewater towards the granite groundwater, and 2) That the concentration of the natural tracers coming into the granite groundwater from the bentonite porewater increased with time. Buil et al. (2010) modelled the bentonite–granite solute transfer and confirmed that the increase in Cl^- and Na^+ concentrations of the granite groundwater were indeed caused by diffusive solute migration from the bentonite into the granite. They obtained the best fit to the measured data with an effective diffusion coefficient of granite equal to 5×10^{-11} m^2/s (Buil et al. 2010).

The effective diffusion coefficients of chemical species in the bentonite in the reference THCM model of the FEBEX in-situ test are equal to (Zheng et al. 2011):

1. 9.3×10^{-13} m^2/s for chloride
2. 1.1×10^{-13} m^2/s for sulphate
3. 6.1×10^{-12} m^2/s for the rest of the chemical species. They are all assumed to have the same diffusion coefficient. The optimum value was derived from the calibration of heating and hydration laboratory experiments (ENRESA 2006a).

The effective diffusion coefficient of all chemical species in granite is equal to 4.7×10^{-14} m^2/s.

The reference model considers a longitudinal dispersivity of 0.01 m in the bentonite and 0.2 m in the granite. The dispersivity of the granite affects mostly the solute diffusion from the bentonite into the granite (Zheng et al. 2011). Given the small value of the Peclet number of the bentonite, model results are not sensitive to the bentonite dispersivity.

The previous THCM model of the FEBEX in-situ test accounted for the possibility of solute diffusion across the bentonite/granite interface. However, the effective diffusion coefficients in granite are too small for the solutes to diffuse from the bentonite into the granite. A sensitivity run was performed in which the effective diffusion coefficient in the granite was equal to 1×10^{-12} m^2/s. Fig. C-48 shows the sensitivity of the computed Cl^- concentrations in the granite at a distance of 0.2 m from the bentonite/granite interface to changes in effective diffusion coefficient in the granite and the bentonite. One can see that the computed Cl^- concentrations in the granite with an effective diffusion coefficient of 1×10^{-12} m^2/s in the granite and 1.4×10^{-10} m^2/s in the bentonite are consistent with the Cl^- concentrations reported by Buil et al. (2010).

Fig. C-49 to A-52 show the time evolution of the computed Cl^-, SO_4^{2-}, Na^+ and Ca^{2+} concentrations at several times with an effective diffusion coefficient of 1×10^{-12} m^2/s in the granite and 1.4×10^{-10} m^2/s in the bentonite. Once again, the computed Cl^-, SO_4^{2-}, Na^+ and Ca^{2+} concentrations in the granite with an these effective diffusion coefficients are consistent with the Cl^-, SO_4^{2-}, Na^+ and Ca^{2+} concentrations reported by Buil et al. (2010).

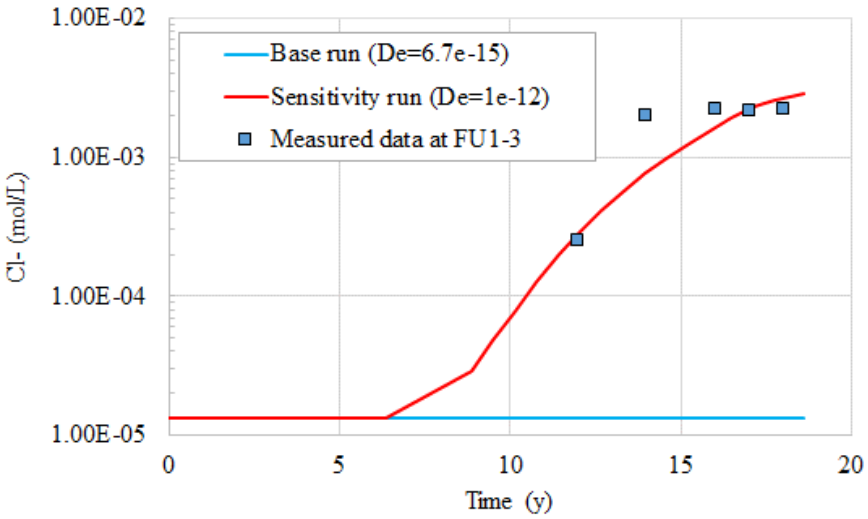

Fig. C-48: Sensitivity of the computed Cl^- concentrations (lines) in the granite at a distance of 0.2 m from the bentonite/granite interface to changes in effective diffusion coefficient in the granite

The measured concentrations were reported by Buil et al. (2010).

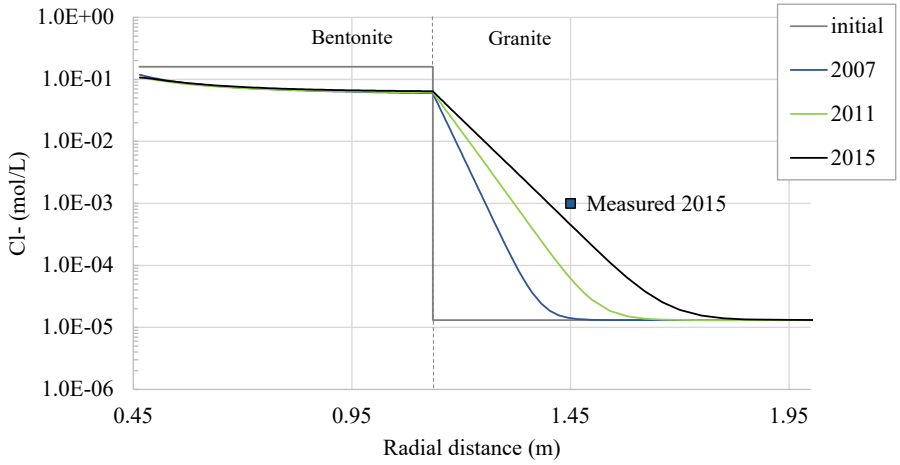

Fig. C-49: Time evolution of the computed Cl^- concentrations at several times (lines) with an effective diffusion coefficient of 1×10^{-12} m^2/s in granite and 1.4×10^{-10} m^2/s in bentonite along with a measured concentration of Cl^- (symbol) in 2015

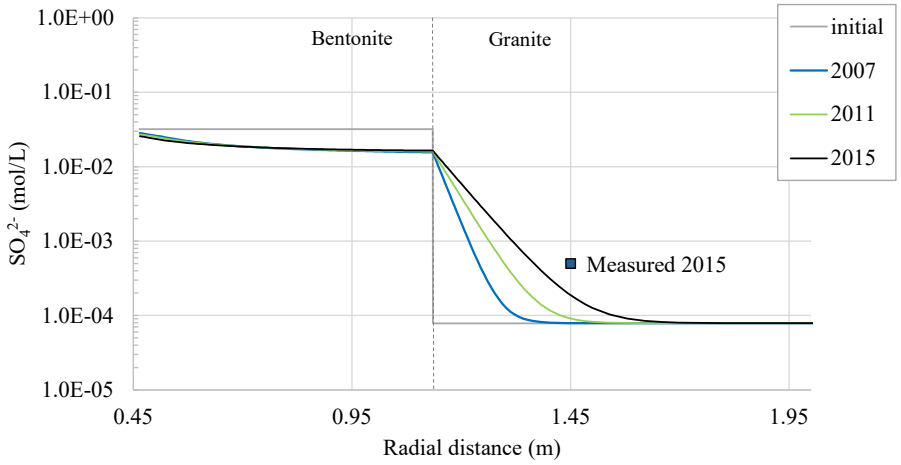

Fig. C-50: Time evolution of the computed SO_4^{2-} concentrations at several times (lines) with an effective diffusion coefficient of 1×10^{-12} m^2/s in granite and 1.4×10^{-10} m^2/s in bentonite and a measured concentration of SO_4^{2-} (symbol) in 2015

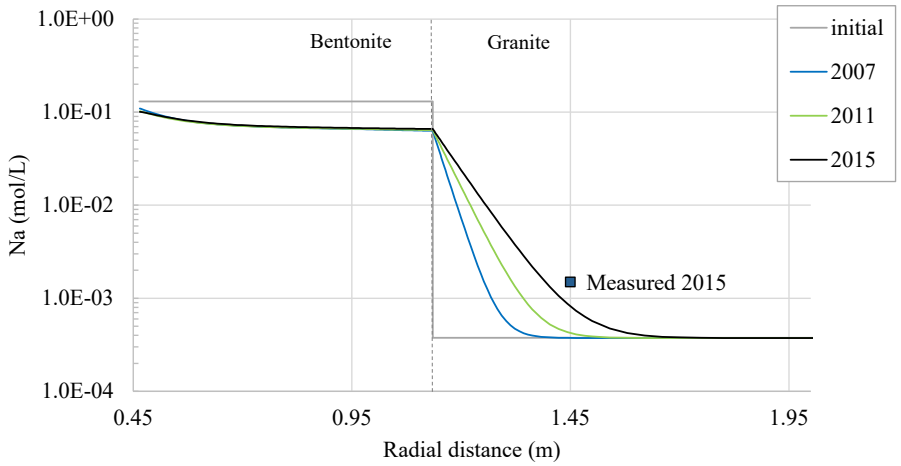

Fig. C-51: Time evolution of the computed Na^+ concentrations at several times (lines) with an effective diffusion coefficient of 1×10^{-12} m^2/s in the granite and 1.4×10^{-10} m^2/s in the bentonite and measured concentration of Na^+ (symbol) in 2015

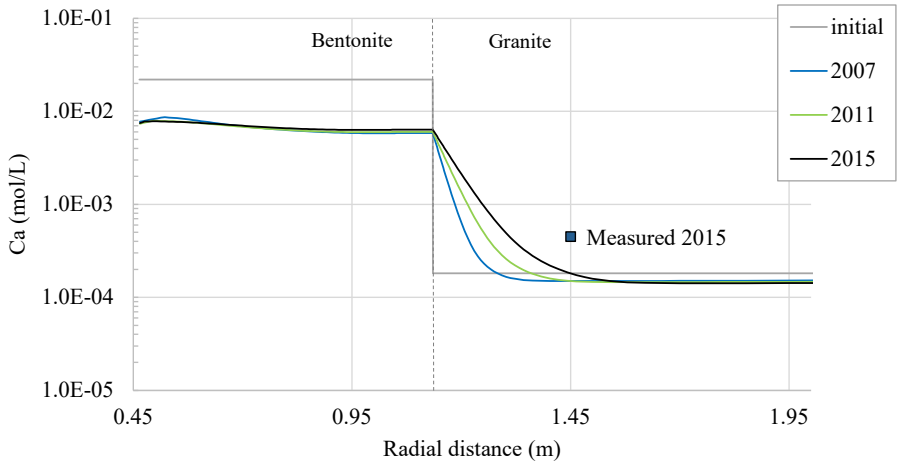

Fig. C-52: Time evolution of the computed Ca^{2+} concentrations at several times (lines) with an effective diffusion coefficient of 1×10^{-12} m^2/s in granite and 1.4×10^{-10} m^2/s in bentonite and measured concentration of Ca^{2+} (symbol) in 2015

C.4.1.3 Conclusions

The sensitivity simulation runs performed on the previous 1D axisymmetric THCM model of the FEBEX in-situ test lead to the following major conclusions:

1. The computed concentrations of most species in a hot section in 2002 are sensitive to an increase in the parameter α of the van Genuchten retention curve of bentonite. The increase in α leads to larger water evaporation and larger solute concentrations near the heater. The pH and the concentration of HCO_3^- are not sensitive to a change in α. The computed concentrations of most species in the cold section, however, lack sensitivity to a change in α.

4. The computed concentrations are not sensitivite to smectite dissolution and analcime precipitation because the cumulative dissolution of smectite and precipitation of analcime in 2002 is extremely small.

5. The computed concentrations in 2002 are not sensitive to a change in the gas boundary condition during dismantling. The computed concentrations are sensitive to cooling because the solubility of the minerals and the chemical parameters depend on temperature.

6. The computed of dissolved Ca^{2+}, K^+, Mg^{2+}, Na^+ and Cl^- concentrations near the heater in 2002 increase when vapour tortuosity increases. However, away from the heater the concentrations decrease when vapour tortuosity increases. The computed pH and the SO_4^{2-} and HCO_3^- concentrations are less sensitive to the changes in the vapour tortuosity.

7. Solute diffusion from the bentonite into granite is very sensitive to the effective diffusion coefficients of both bentonite and granite. The effective diffusion, D_e, f in granite used in the previous model was too small. The computed Cl^-, SO_4^{2-}, Na^+ and Ca^{2+} concentrations in the granite with $D_e = 1 \times 10^{-12}$ m^2/s in the granite and $D_e = 1.4 \times 10^{-10}$ m^2/s in the bentonite are consistent with the Cl^-, SO_4^{2-}, Na^+ and Ca^{2+} concentrations measured in the FUNMIG borehole by Buil et al. (2010).

C.4.2 2D axisymmetric THCM model

The 1D axisymmetric model presented in the previous section has some limitations because it can only be applied to either hot or cold sections. The 1D models are not valid near the edges of the heaters. Some of the limitations of the 1D axisymmetric model are overcome by extending the 1D axisymmetric THCM model of the FEBEX in-situ test to 2D axisymmetric conditions. This section presents the results of a 2D axisymmetric THCM model of the FEBEX in-situ test.

C.4.2.1 Model description

The bentonite surrounding Heater #1 was dismantled in 2002. Next, a shotcrete plug was built. The 2D axisymmetric THCM model of the FEBEX in-situ test considered the geometry of the test from 2002 to 2015. The domain is defined with a finite element mesh with 1'522 nodes and 275 elements (Fig. C-53). The model accounts for the bentonite, the granite and the shotcrete plug.

The simulation time horizon extends from 1997 until 2015. The geometry of the test changed when Heater #1 was dismantled in 2002. Some simplifying assumptions were used to simulate the entire time horizon 1997 – 2015 by using the geometry of the test from 2002 to 2015. The model domain includes the shotcrete plug and the dummy. The simulation period was divided into the following two stages:

1. From 1997 to 2002. During this period, the model assumes that there is a heater with a prescribed temperature of 100 °C at the heater/bentonite interface at the place occupied by the dummy canister.
2. From 2002 to 2015. The dummy canister in this period is assumed to be a no-flow and no heat-flux boundary.

The model parameters, the initial and boundary conditions have been taken from the previous 1D axisymmetric model of Zheng et al. (2011).

To reduce the computation time required for 2D axisymmetric THCM model, the 2D axisymmetric THCM model solves the solute transport of a single species (Cl^-).

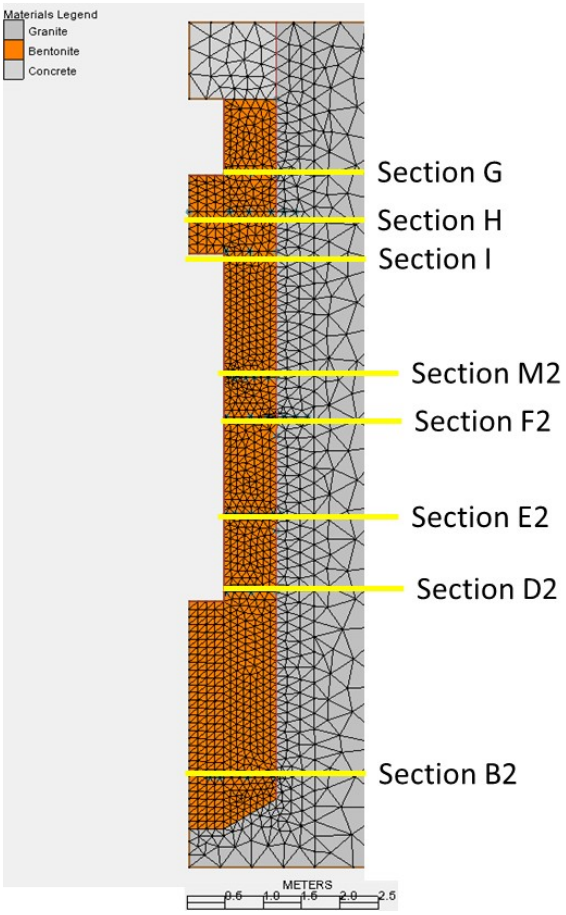

Fig. C-53: Finite element mesh for the 2D axisymmetric THCM model of the FEBEX in-situ test and location of the relevant sections

C.4.2.2 Thermal and hydrodynamic results

Fig. C-54 shows the contour plot of the computed saturation degree at the time of dismantling Heater #1 (in 2002) and dismantling of Heater #2 (in 2015). The computed saturation degrees in the granite and the concrete are equal to 100 %.

Fig. C-55 shows the contour plots of the computed temperatures at the dismantling times of heaters #1 and #2 in 2002 and 2015. The computed temperatures in the granite increase from 2002 to 2015.

Fig. C-56 shows the time evolution of the calculated and measured temperatures in a cold section (section B2) at radial distances r = 0.27 m, r = 0.4 m and r = 1.13 m. Section B2 is located at the end of the FEBEX gallery. One can see that the computed temperatures are slightly higher than the measured values in the cold section B2.

Fig. C-57 shows the time evolution of the calculated and measured temperatures in section D2 located at the edge of Heater #2 near the end of the gallery at radial distances r = 0.48 m, r = 0.81 m and r = 1.14 m. One can see that the computed temperatures fit the measured temperatures.

Fig. C-58 and Fig. C-59 show the time evolution of the calculated and measured temperatures in hot Sections E2 and F2 located near the centre of Heater #2 at radial distances r = 0.48 m, r = 0.8 m and r = 1.05 m. One can see that the computed temperatures fit the measured temperatures near the heater. However, the computed temperatures at r = 1.1 m are 10 °C less than the measured values.

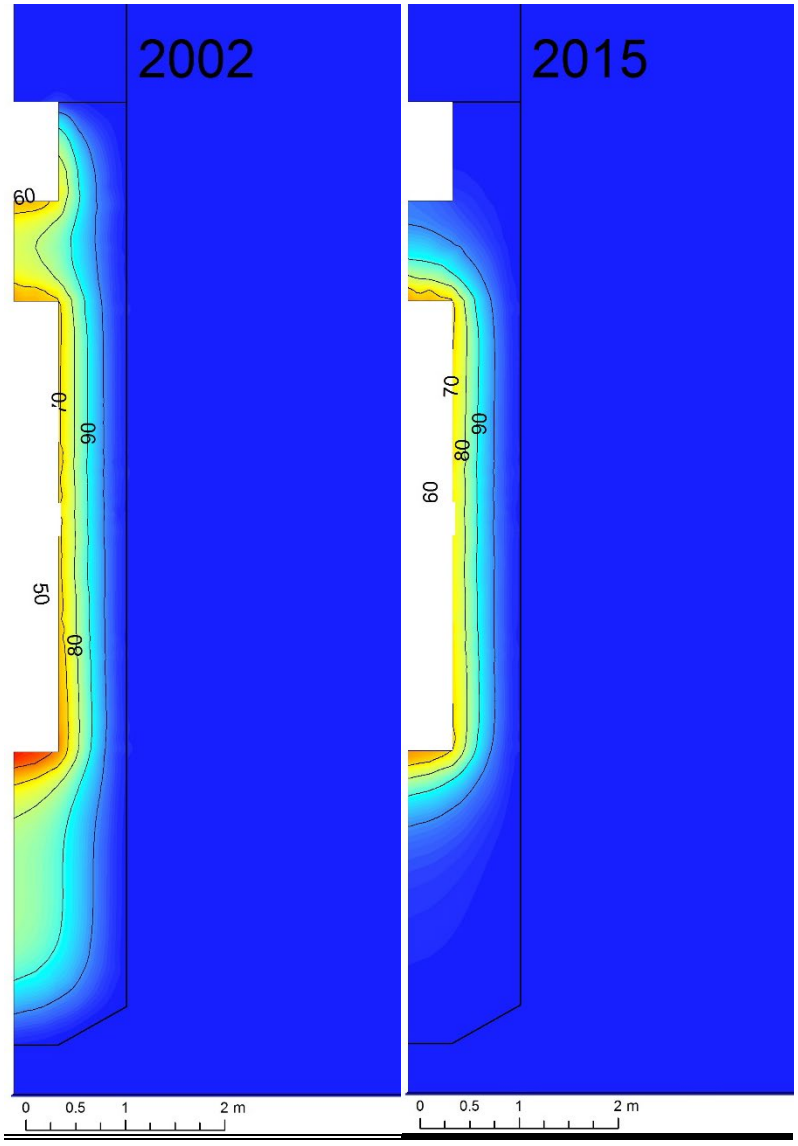

Fig. C-54: Contour plots of computed saturation degrees (%) at the dismantling times of Heater #1 in 2002 (left) and Heater #2 in 2015 (right)

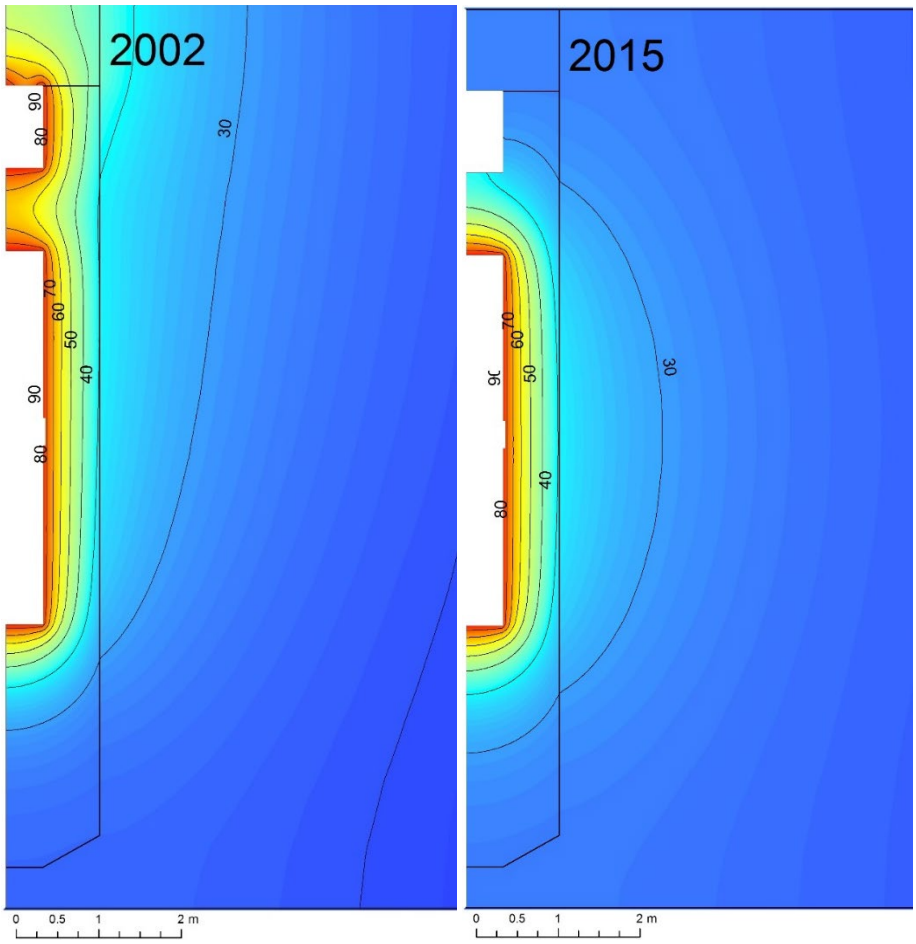

Fig. C-55: Contour plots of the computed temperatures at the dismantling times of Heater #1 in 2002 (left) and Heater #2 in 2015 (right)

Fig. C-60 shows the time evolution of the calculated and measured temperatures in Section I located at the edge of Heater #2 (near Heater #1) at radial distances r = 0.48 m, r = 0.81 m and r = 1.14 m. One can see that the computed temperatures fit the measured temperatures. The sensors in this section reflect temperature decrease caused by the dismantling of Heater #1 only slightly. In general, the computed temperatures fit the measured temperatures.

Fig. C-61 shows the time evolution of the calculated and measured temperatures in section G located at the edge of the dummy at radial distances r = 0.48 m, r = 0.81 m and r = 1.14 m. The sensors in this section reflect a temperature decrease caused by dismantling Heater #1. The measured temperatures at similar radial distances show a large scatter during t < 2'000 days. The computed temperatures fit the measured temperatures for the most part. Fig. C-62 shows the time evolution of the calculated and measured temperatures in section H located between both heaters at radial distances r = 0.78 m and r = 1.07 m. The sensors in this section also reflect a temperature decrease caused by dismantling Heater #1. The measured temperatures at similar radial distances also show a large scatter for t < 2'000 days. The computed temperatures fit the measured temperatures.

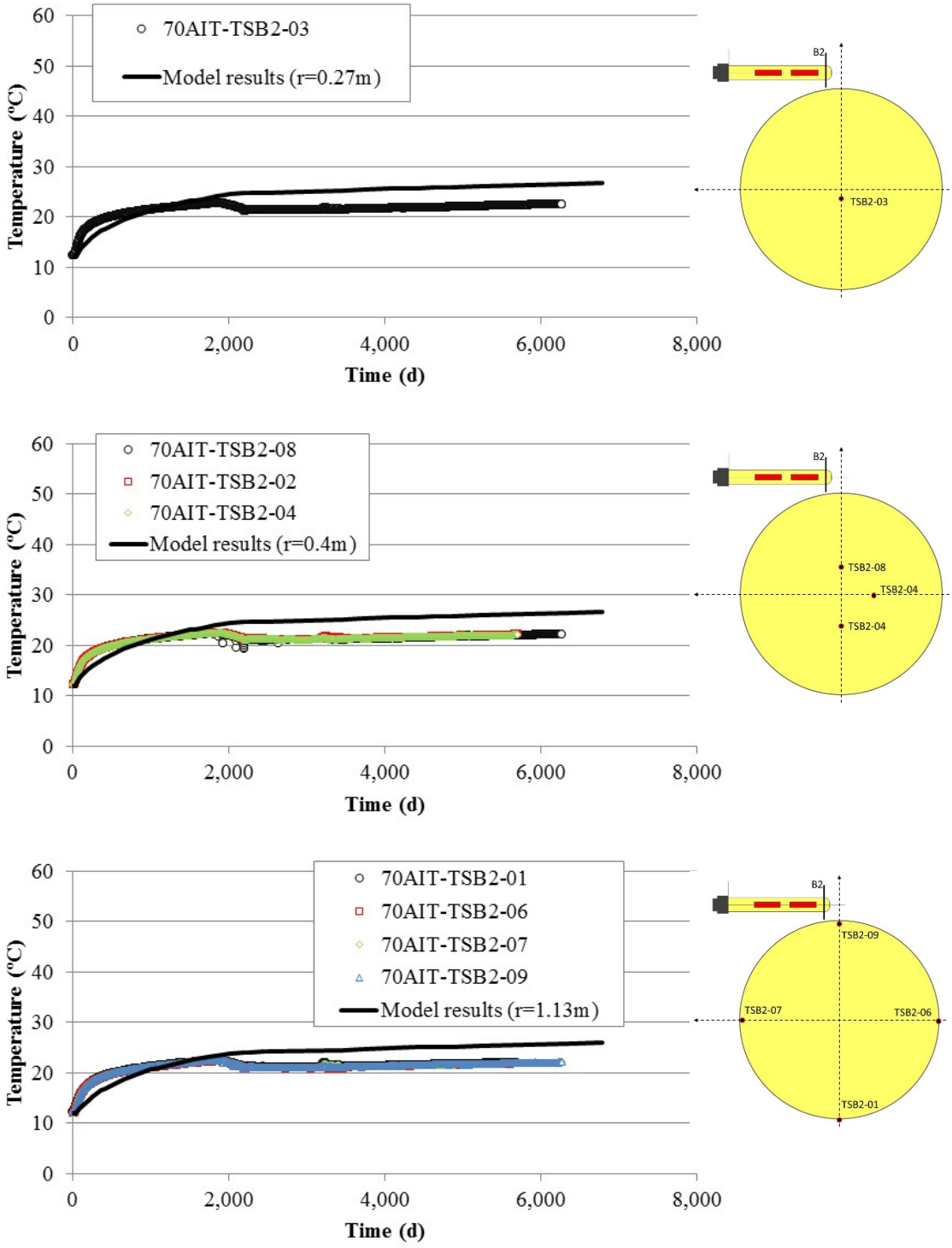

Fig. C-56: Time evolution of the calculated (lines) and measured (symbols) temperatures in section B2 at radial distances r = 0.27 m, r = 0.4 m and r = 1.13 m

Section B2 is located at the end of the FEBEX gallery.

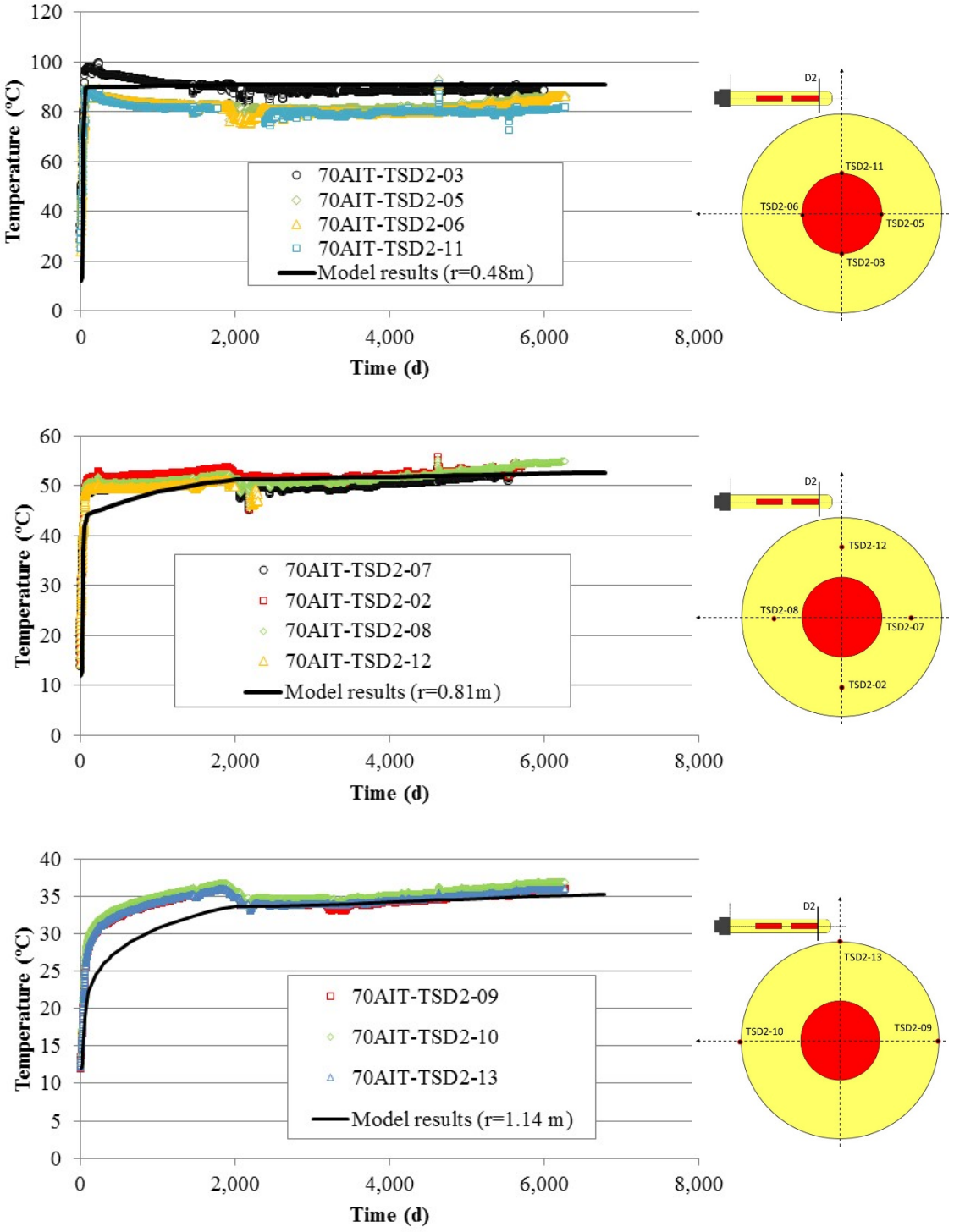

Fig. C-57: Time evolution of the calculated (lines) and measured (symbols) temperatures in section D2 located at the edge of Heater #2 at radial distances r = 0.48 m, r = 0.81 m and r = 1.14 m

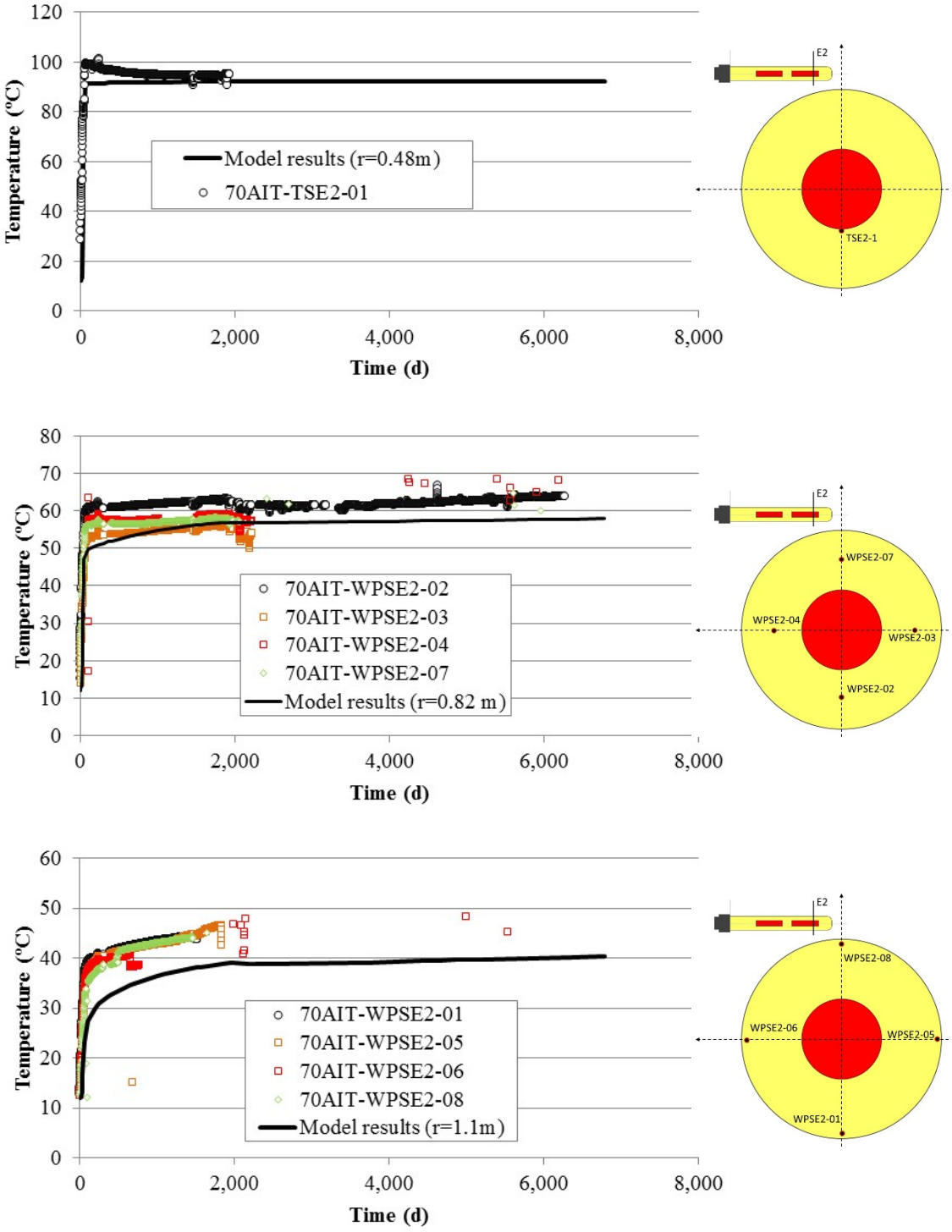

Fig. C-58: Time evolution of the calculated (lines) and measured (symbols) temperatures in hot Section E2 located near the centre of Heater #2 at radial distances r = 0.48 m, r = 0.82 m and r = 1.10 m

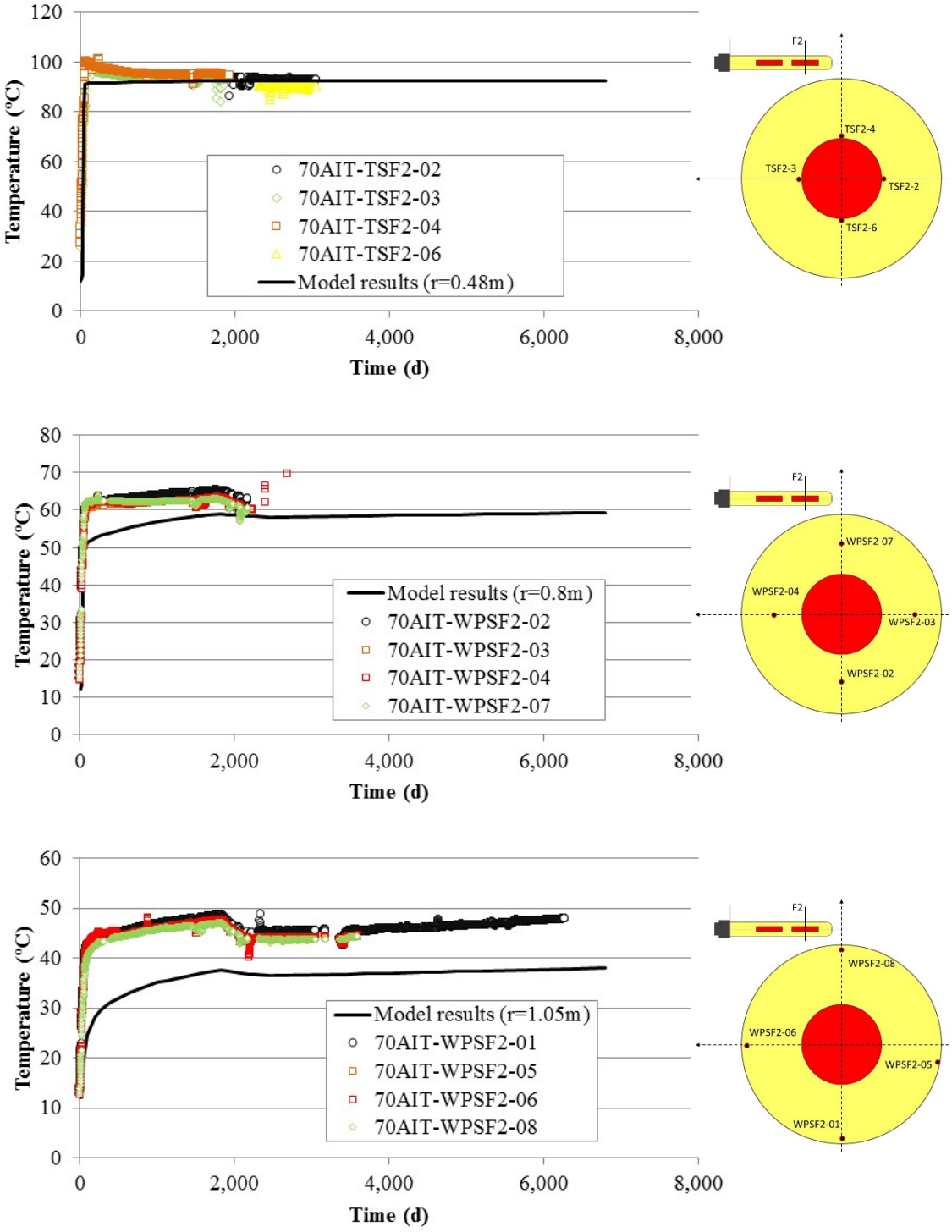

Fig. C-59: Time evolution of the calculated (lines) and measured (symbols) temperatures in hot section F2 located at the mid-point of Heater #2 at radial distances r = 0.48 m, r = 0.8 m and r = 1.05 m

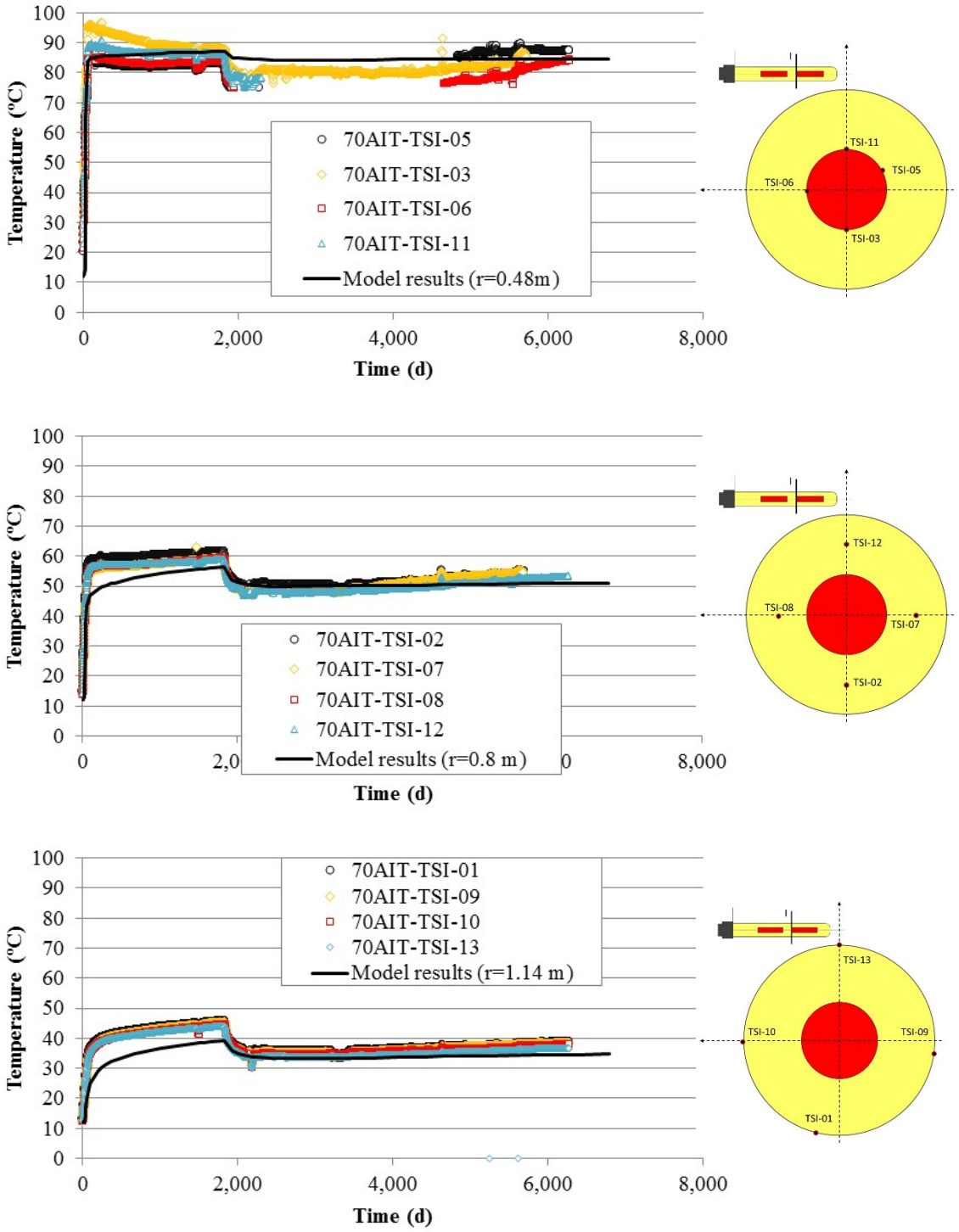

Fig. C-60: Time evolution of the calculated (lines) and measured (symbols) temperatures in section I located at the edge of Heater #2 (near Heater #1) at radial distances r = 0.48 m, r = 0.8 m and r = 1.14 m

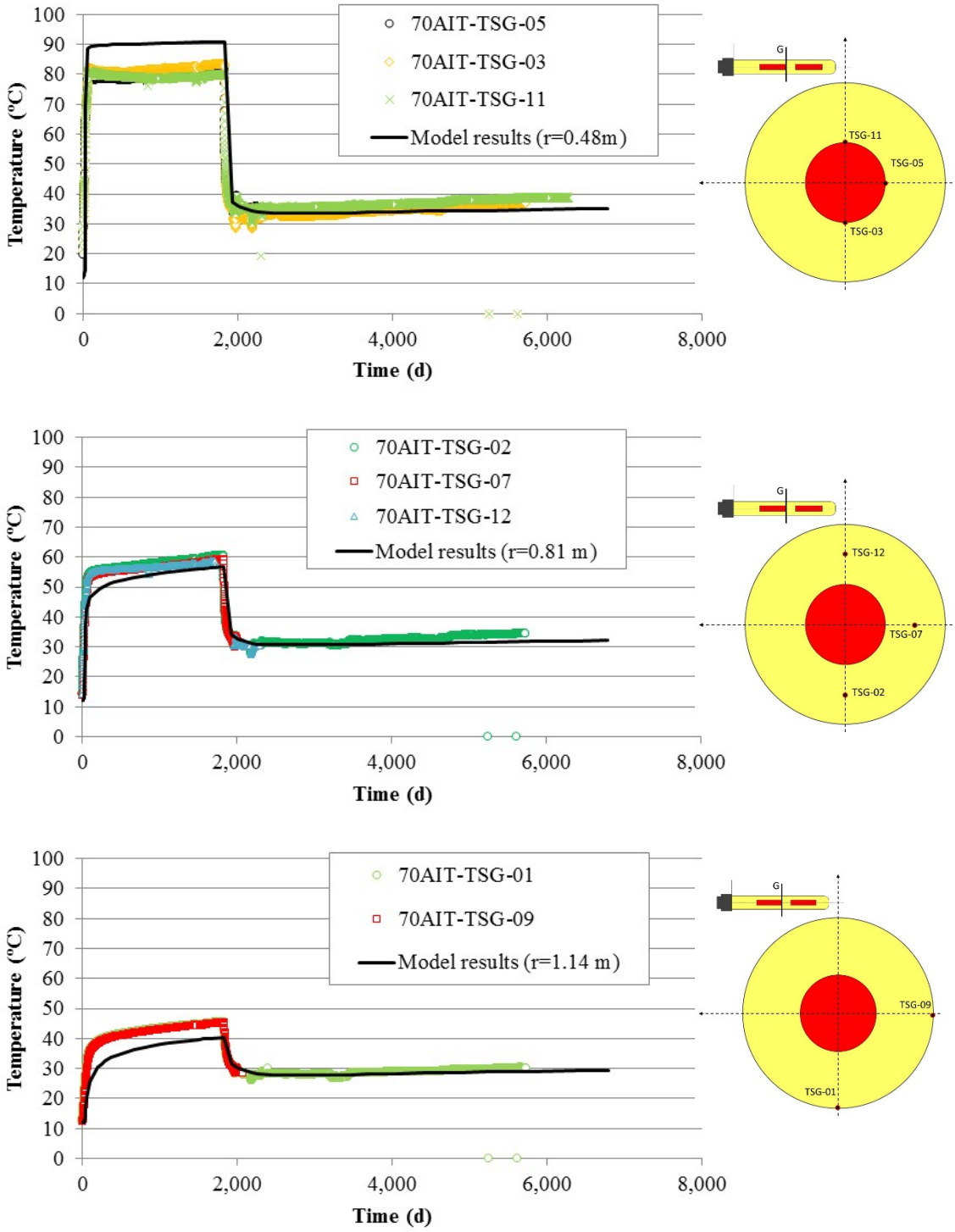

Fig. C-61: Time evolution of the calculated (lines) and measured (symbols) temperatures in section G located at the edge of the dummy at radial distances r = 0.48 m, r = 0.81 m and r = 1.14 m

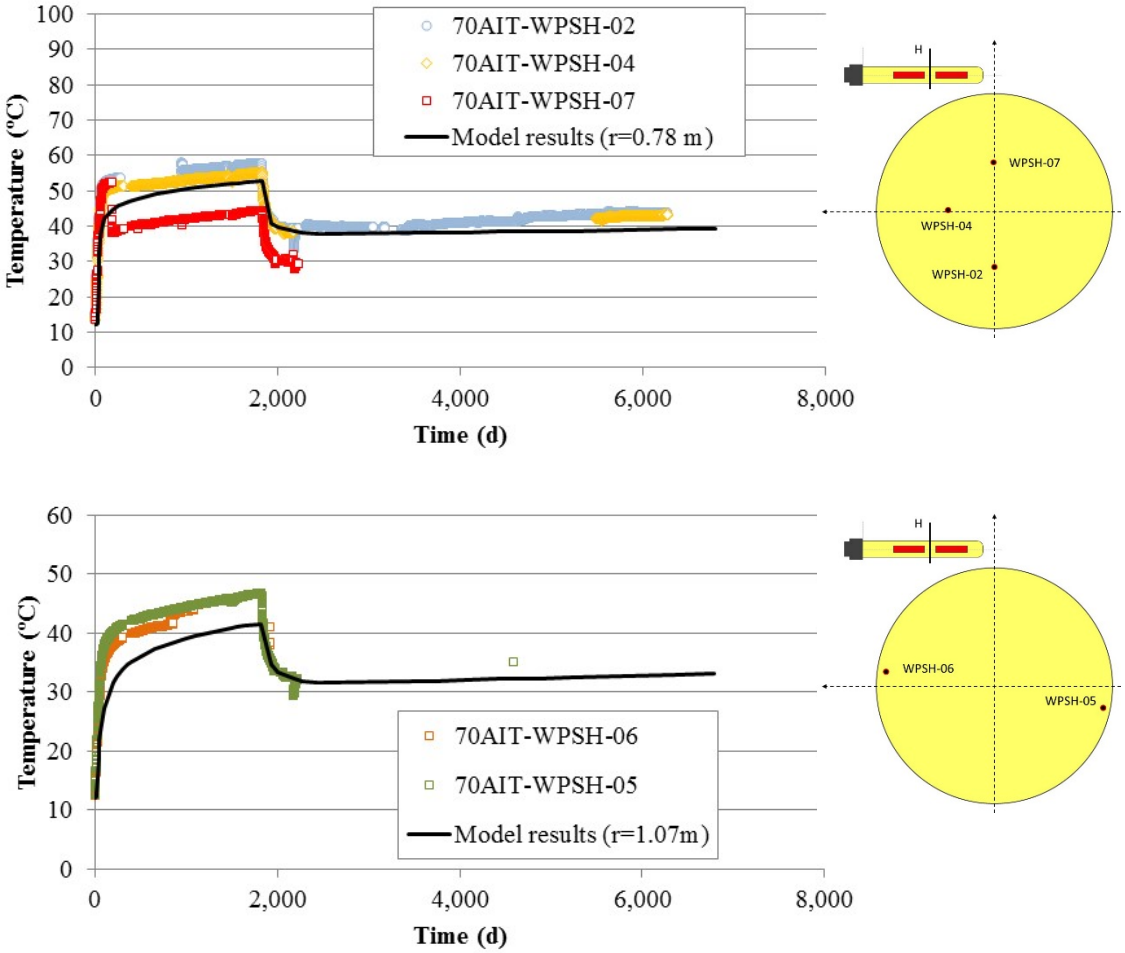

Fig. C-62: Time evolution of the calculated (lines) and measured (symbols) temperatures in section H located between both heaters at radial distances r = 0.78 m and r = 1.07 m

Fig. C-63 and Fig. C-64 show the time evolution of the computed and the measured relative humidity in hot Sections E2 and F2 at radial distances r = 0.8 m and r = 1.05 m. The computed relative humidities reproduce the trends of the measured humidity data.

Fig. C-65 shows the time evolution of the computed and the measured relative humidity in section G at several radial distances. This section is located at the edge of the dummy. Measured data show large and erratic fluctuations. The computed relative humidity reproduces the mean values of the measured humidity data.

Fig. C-66 shows the time evolution of the computed and the measured relative humidity in section G at several radial distances. This section is located at the mid-point between both heaters. The computed relative humidity reproduces the trends of the measured humidity data at radial distances r = 053, r = 0.78 and r = 1.07 m.

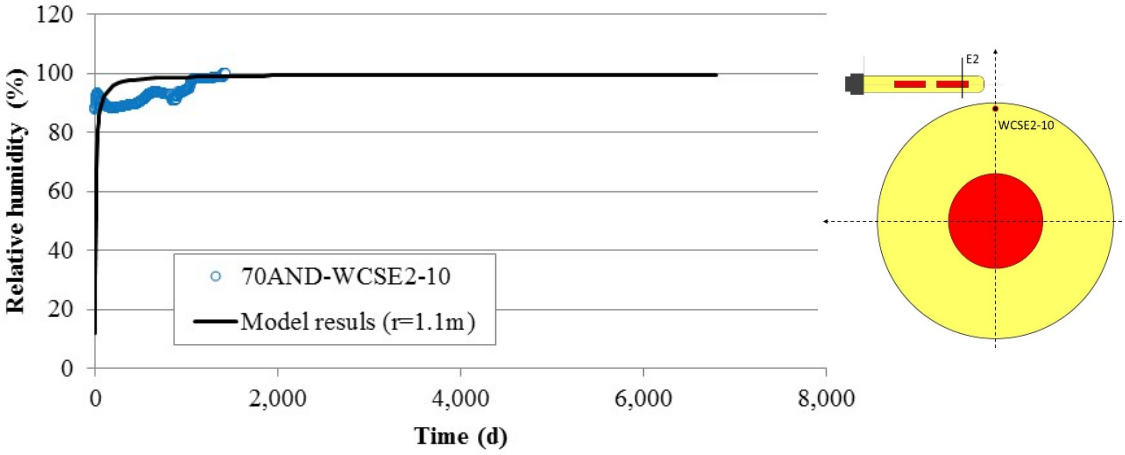

Fig. C-63: Time evolution of the computed (line) and the measured (symbols) relative humidity in the hot Section E2 at radial distance r = 1.1 m

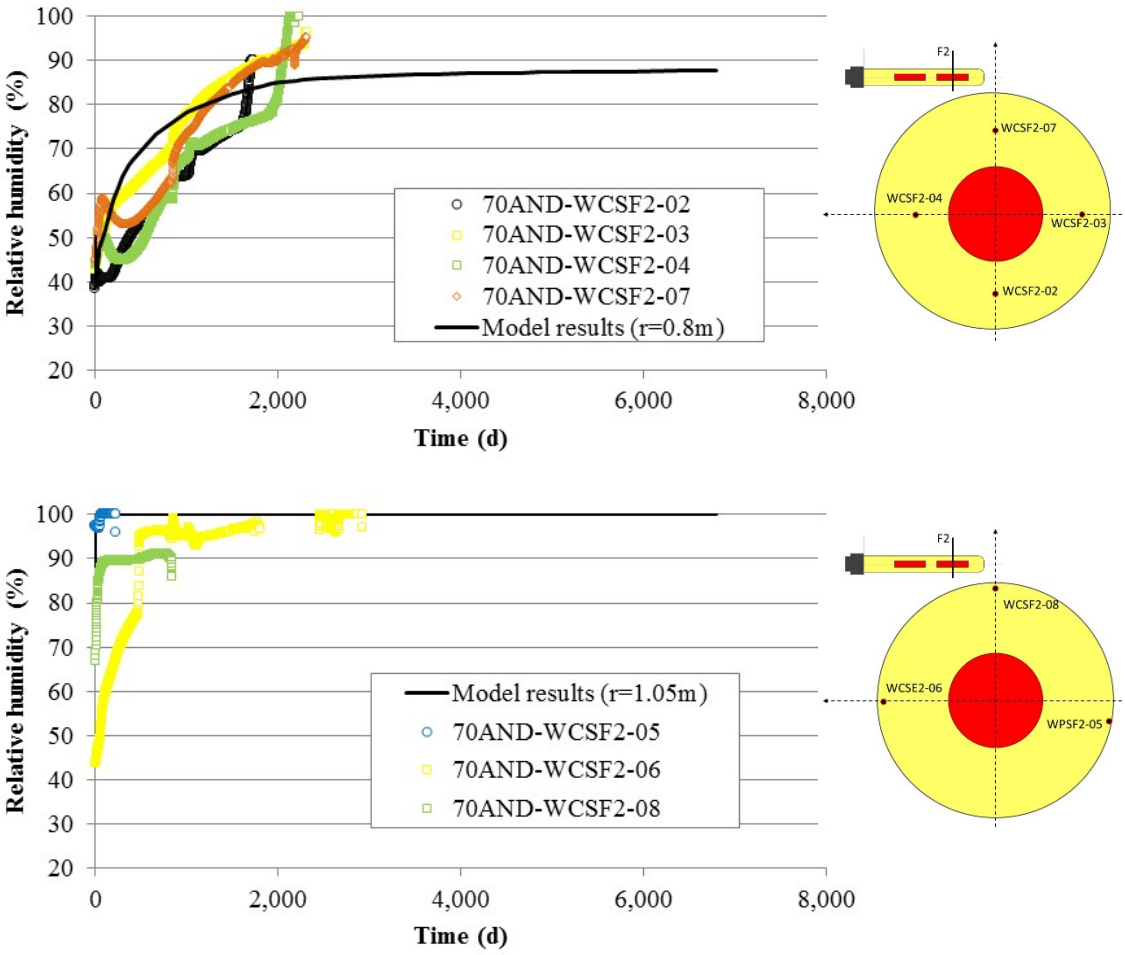

Fig. C-64: Time evolution of the computed (lines) and the measured (symbols) relative humidity in the hot section F2 at radial distances r = 0.8 m and r = 1.05 m

Fig. C-67 shows the time evolution of the computed and the measured relative humidity in section I at several radial distances. This section is located at the edge of Heater #2 (near Heater #1). The computed relative humidity near the bentonite/granite interface fits the measured data. At other locations, however, the measured relative humidity values are higher than the computed relative humidities. The measured relative humidity reaches a value of 100 % after 2'000 days while the computed humidity is 50 % at r = 0.48 m and 90 % at r = 0.8 m. This section has several unique features which may contribute to the lack of agreement between the computed values and the measured relative humidity data. The fact that the measured relative humidity data are high in all radial distances tends to support the hypothesis that the discontinuity at the bentonite/heater surface could facilitate water flow and bentonite hydration. The model, which does not account for such discontinuity, predicts a low relative humidity at the sensor located at r = 0.48 m.

Fig. C-68 shows the time evolution of the computed volumetric water content in Section M2 and the measured TDR water content data in Section M2. This section is located at the mid-point of Heater #2. The computed water content at the bentonite/granite interface fits the measured data. The computed water content near the heater deviates from the measurements. It should be taken into account, however, that the measured data of some sensors near the heater are erroneous. The computed water content at intermediate locations (r = 0.74 and r = 0.85 m) underestimate the measured values.

Fig. C-69 shows the time evolution of the computed pore water pressures in a hot section (F2) and the measured pore water pressures in several packed-off sections of boreholes drilled in the granitic rock surrounding the FEBEX gallery. Measured water pressures show fluctuations caused by water sampling and ambient perturbations and some scatter due to the spatial variability of the permeability of the granitic rock. The computed water pressures reach steady state values very quickly and do not reproduce the transient trend of the measured data. In general, the computed pressures are smaller than the measured values due to the uncertainty in the prescribed water pressure at the outer boundary.

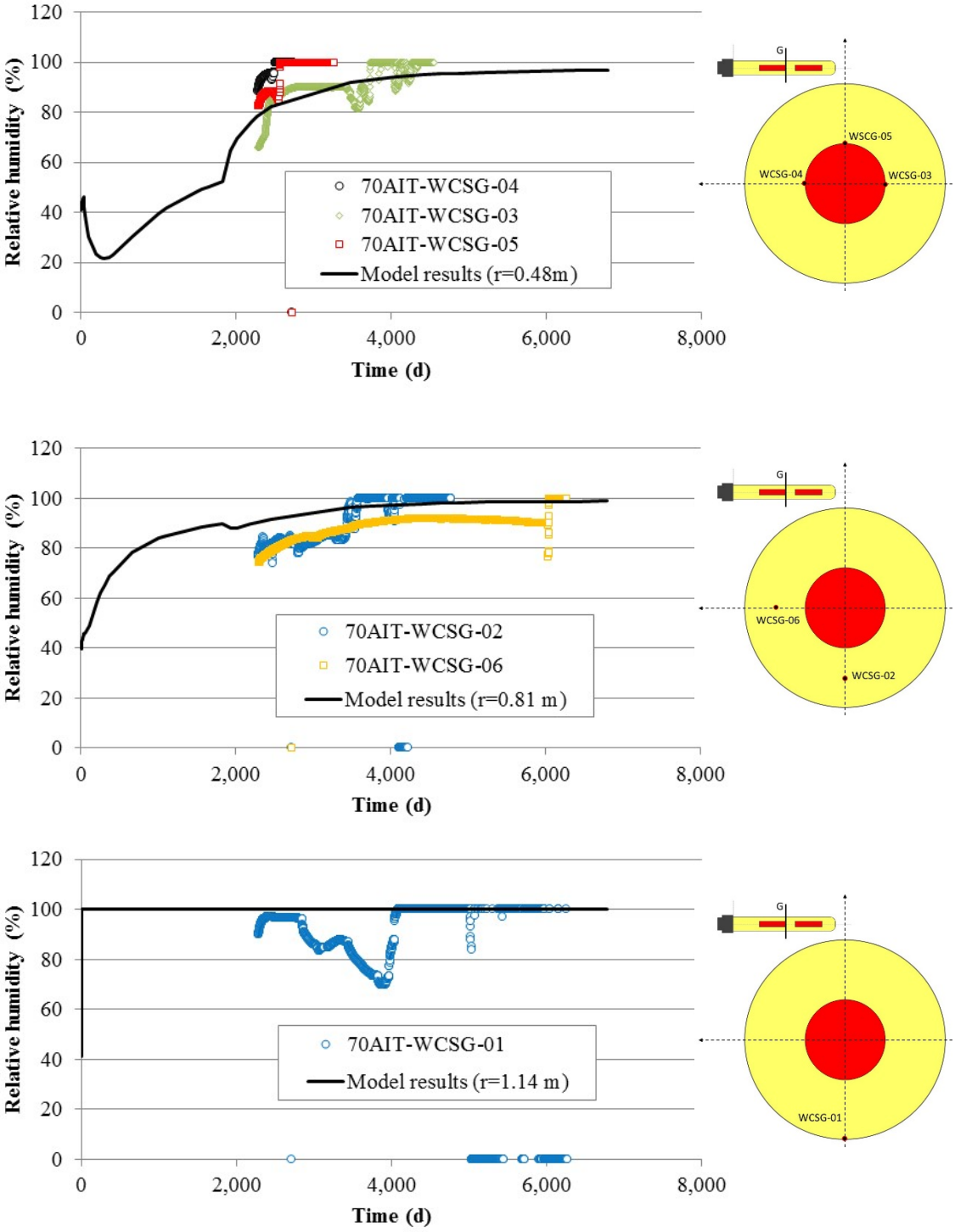

Fig. C-65: Time evolution of the computed (lines) and the measured (symbols) relative humidity in section G at several radial distances

This section is located at the edge of the dummy.

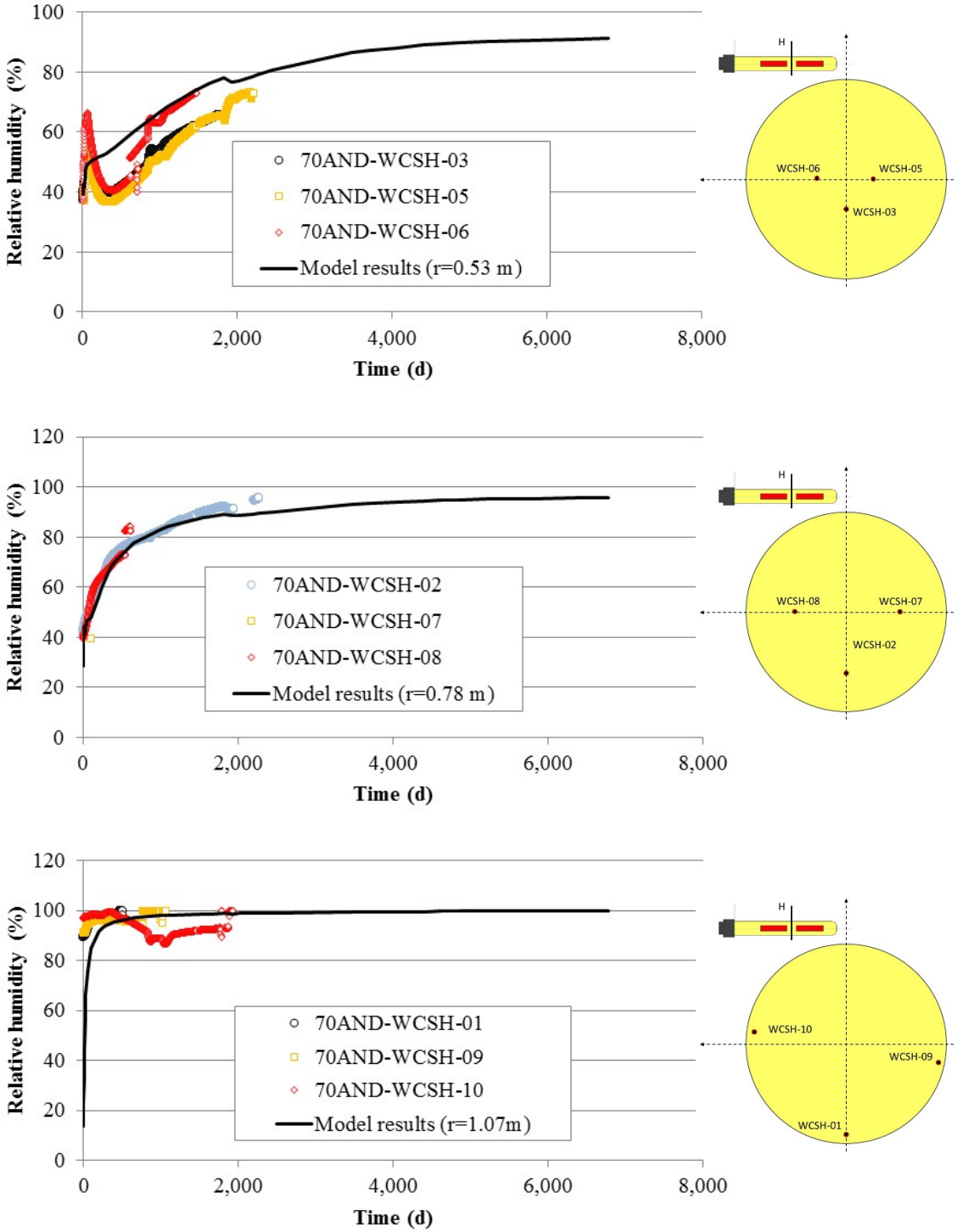

Fig. C-66: Time evolution of the computed (lines) and the measured (symbols) relative humidity in section H at several radial distances

This section is located at the mid-point of between the two heaters.

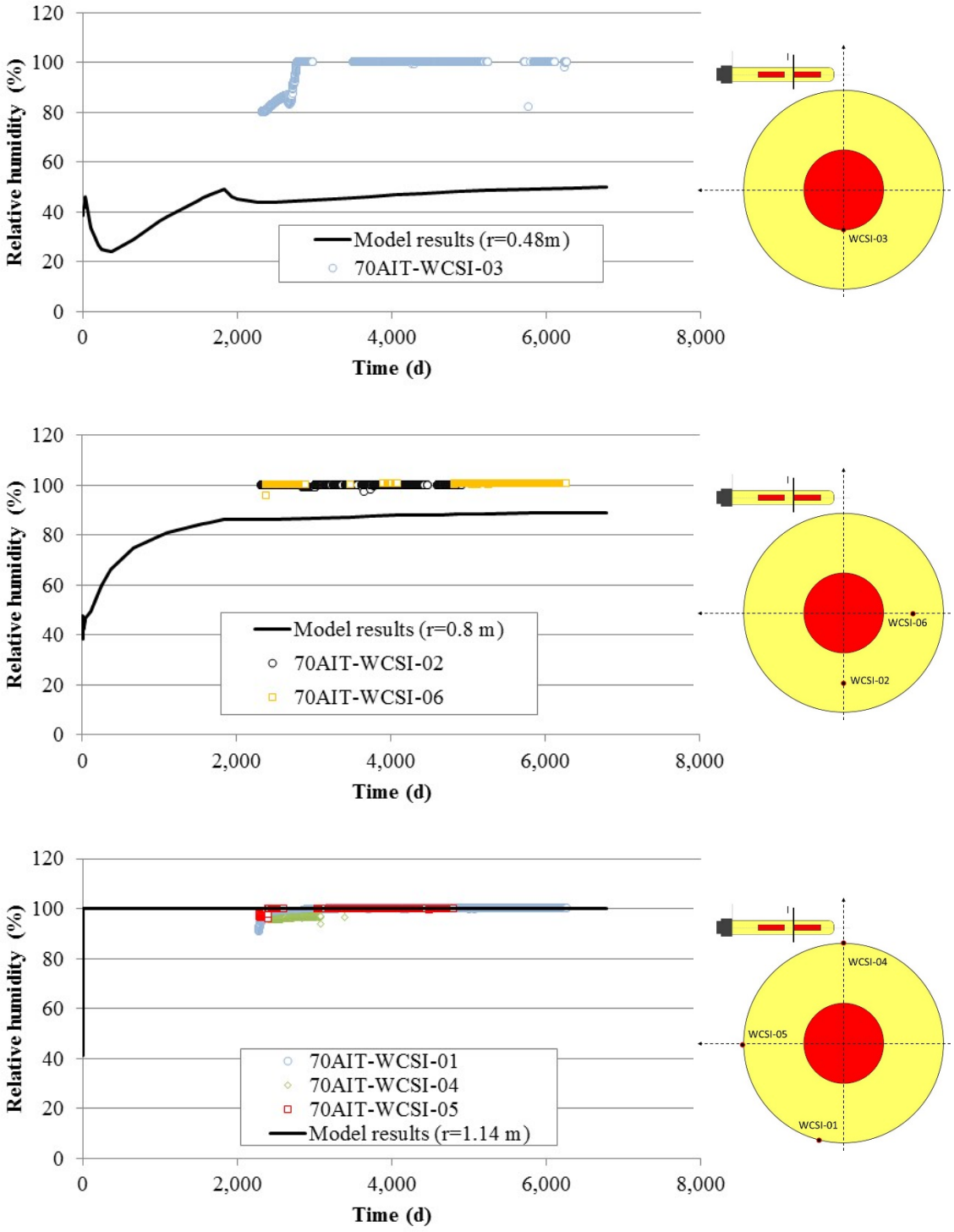

Fig. C-67: Time evolution of the computed (lines) and the measured (symbols) relative humidity in section I at several radial distances

This section is located at the edge of Heater #2 (near Heater #1).

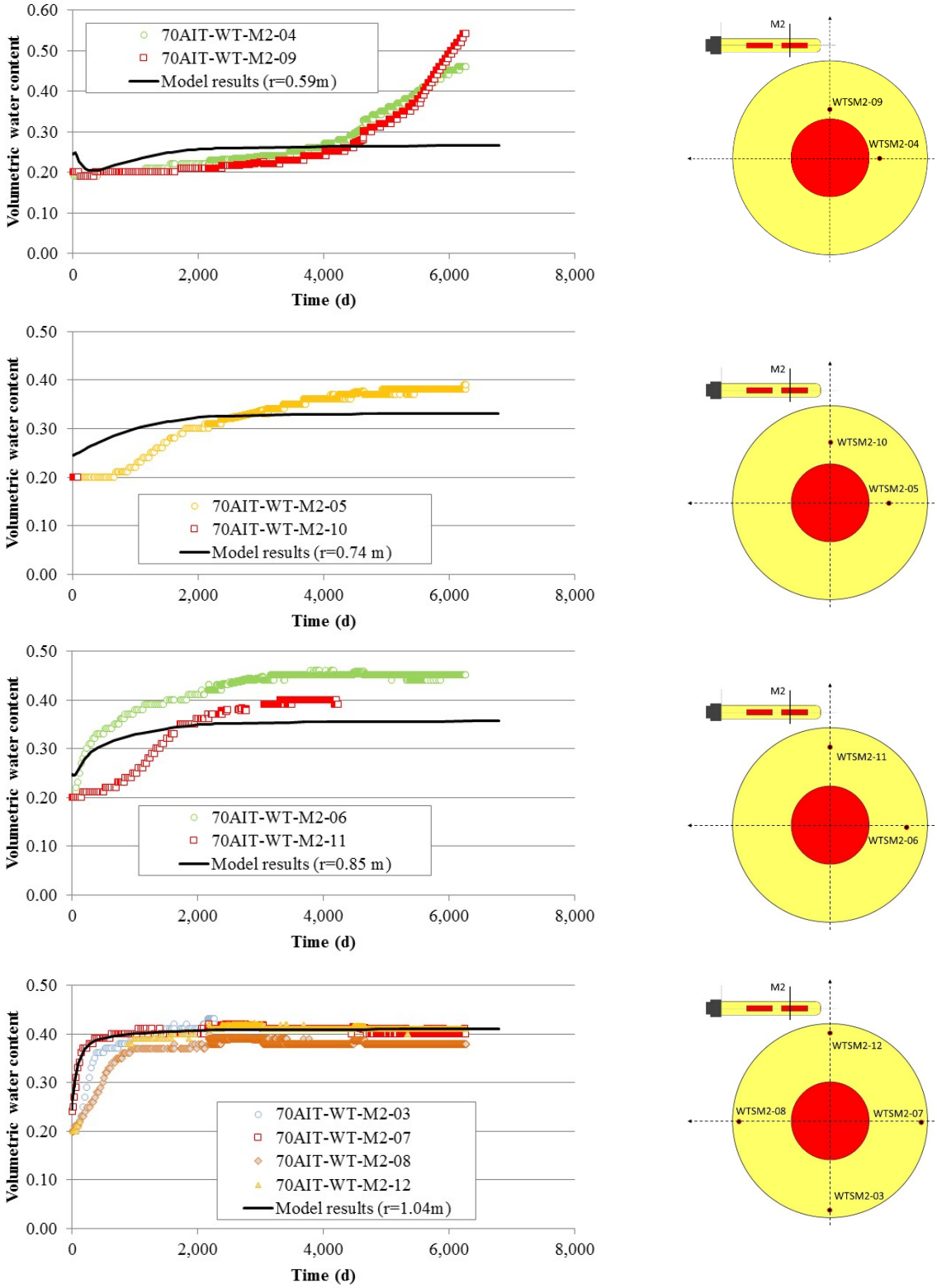

Fig. C-68: Time evolution of the computed (lines) volumetric water content in Section M2 and the measured TDR water content data (symbols)

This section is located at the mid-point of Heater #2.

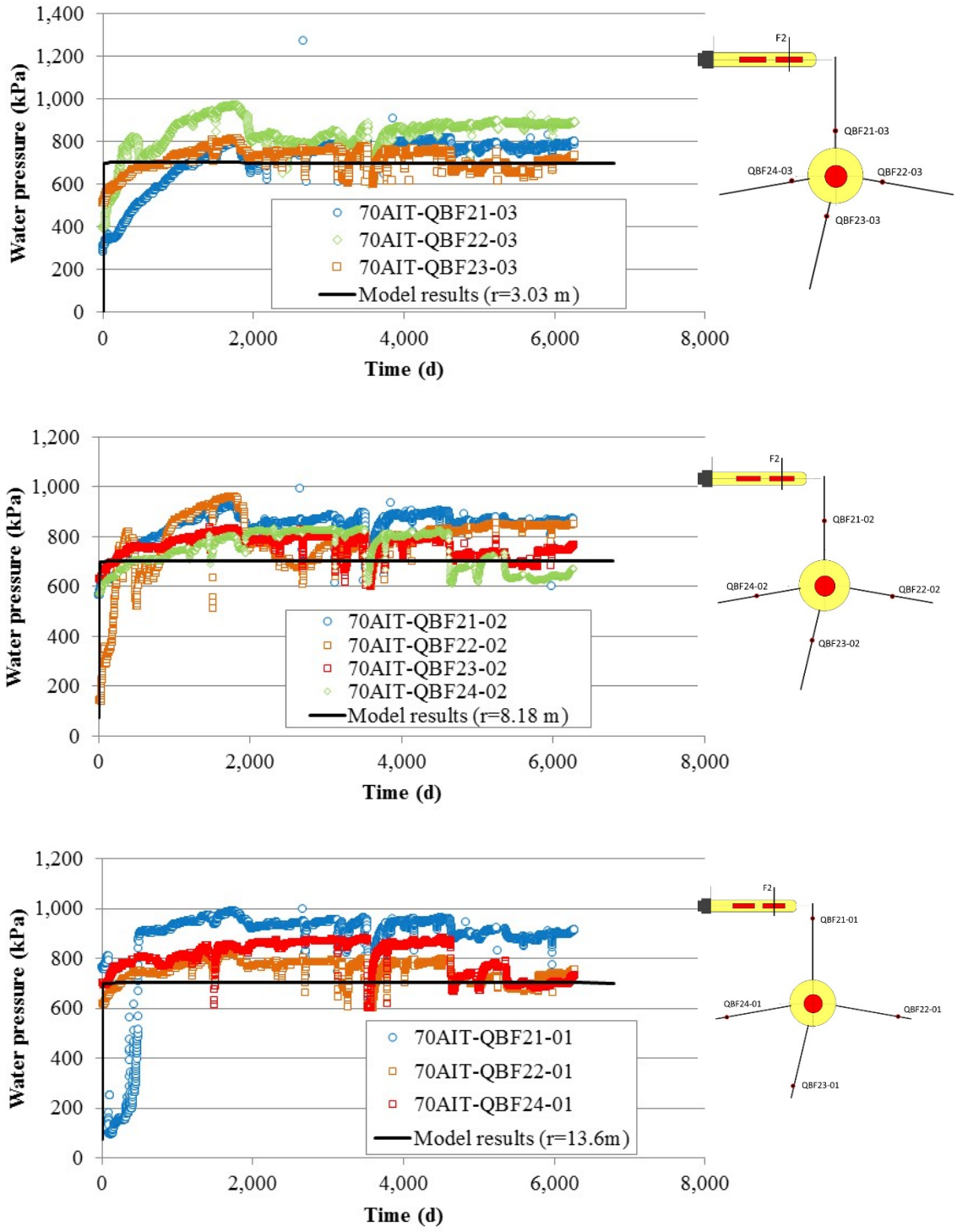

Fig. C-69: Time evolution of the computed (lines) pore water pressures in a hot section (F2) and the measured pore water pressures (symbols) in several packed-off sections of boreholes drilled in the granitic rock surrounding the FEBEX gallery

C.4.2.3 Cl^- concentration results

Fig. C-70 shows the computed concentration of Cl^- after dismantling Heater #1 (2002) and dismantling Heater #2 (2015).

The lowest concentrations of Cl^- are computed in the granite pore water because the initial concentration of Cl^- in granite is much smaller than the concentration in bentonite.

The concentrations of Cl^- in 2002 are large near heaters #1 and #2. It can be noticed that the largest concentrations are located at the edge of Heater #2. The contour lines are approximately parallel to the axis of the gallery along heaters #1 and #2. At the edges of the heaters, however, the contour lines are no longer parallel to the gallery axis. The computed contour plots of Cl^- concentrations illustrate that the edge effects extend approximately over a distance of 0.5 to 1 m.

The concentrations of Cl^- in 2015 show a significant decrease compared to the concentrations in 2002 around Heater #2. Large concentrations of Cl^- still remain in the bentonite barrier between the dummy and Heater #2 and between Heater #2 and the end of the gallery.

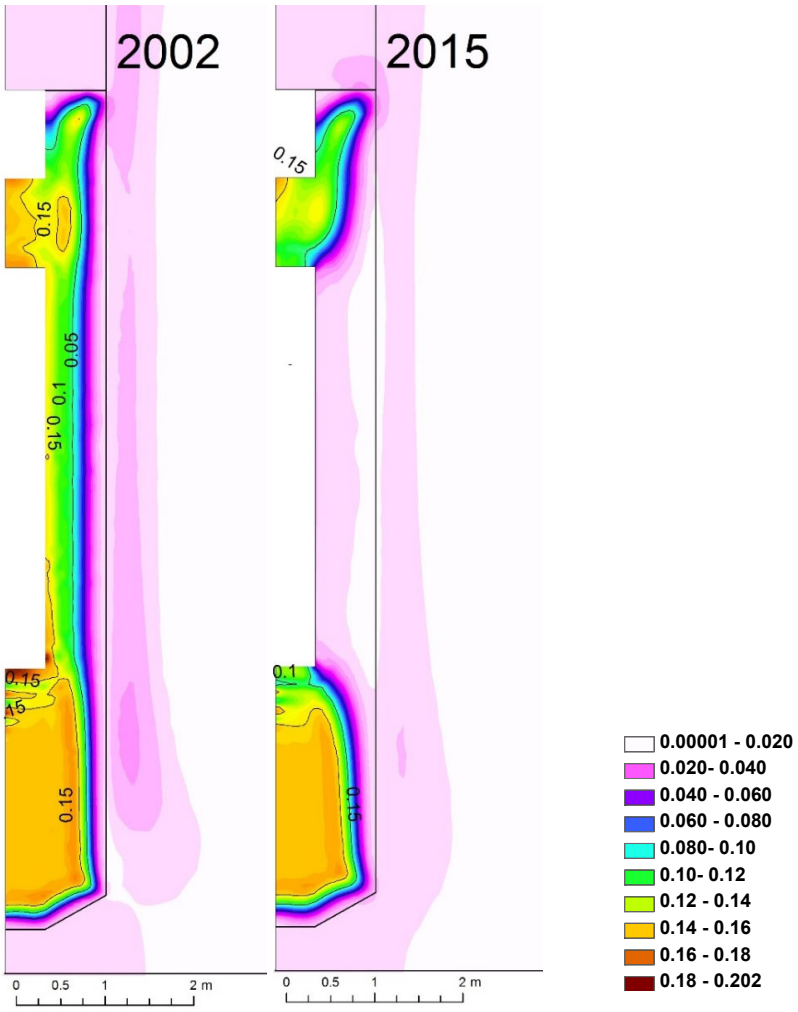

Fig. C-70: Contour plots of the computed Cl^- concentrations at dismantling times of Heater #1 in 2002 (left) and Heater #2 in 2015 (right)

C.4.2.4 Comparison of the results of the 2D and 1D axisymmetric models

The computed temperatures, relative humidity, water content, pore water pressures and Cl^- concentrations computed with the 2D axisymmetric model show some differences compared to the 1D axisymmetric model results. It is beyond the scope of the current THCM modelling to perform a thorough analysis of the differences between the results of the 1D and 2D axisymmetric models. Only the main differences will be described.

C.4.2.4.1 Temperatures

Fig. C-71 shows the time evolution of the calculated temperatures with the 1D and 2D axisymmetric models and the measured temperatures in hot section F2 located at the mid-point of Heater #2. The temperatures computed with the 1D model are larger than those calculated with the 2D model. The differences increase with radial distance to the heater. The maximum differences (more than 10 °C) occur at the bentonite-granite interface. The temperatures computed with the 1D model fit the measured data better than the temperatures calculated with the 2D model.

Fig. C-72 shows the time evolution of the calculated temperatures with the 1D and 2D axisymmetric models and the measured temperatures (symbols) in cold section B2 located at the end of the gallery. The temperatures computed with the 1D model are slightly smaller than those calculated with the 2D model. The temperatures computed with the 1D model fit the measured data better than the temperatures calculated with the 2D model.

The temperatures calculated with the 1D model in the hot section do not account for switching-off Heater #1. The 2D-model does account for the switching-off Heater #1 and the computed temperatures reflect a mild drop in temperature (see Fig. C-71).

The 1D axisymmetric model outperforms the 2D axisymmetric model because the model parameters used to perform the comparison of the two models are the parameters calibrated with the 1D axisymmetric model. A detailed calibration of the parameters of the 2D axisymmetric model, which was not foreseen at this stage of the project, will surely lead to model results at least as good as or better than the results of the 1D axisymmetric model.

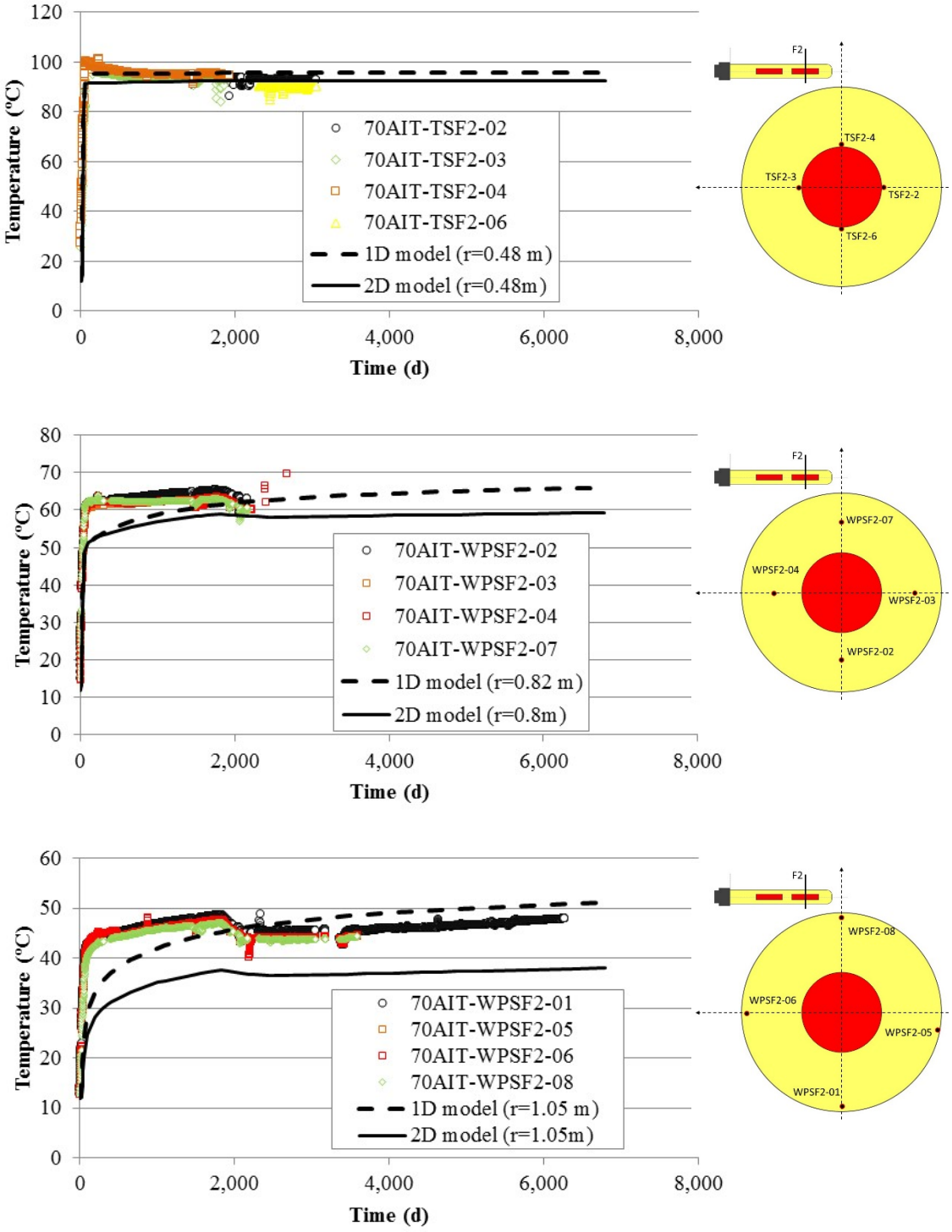

Fig. C-71: Time evolution of the calculated temperatures (lines) with the 1D and 2D axisymmetric models and the measured temperatures (symbols) in hot section F2 located at the mid-point of Heater #2 at radial distances r = 0.48 m, r = 0.82 m and r = 1.05 m

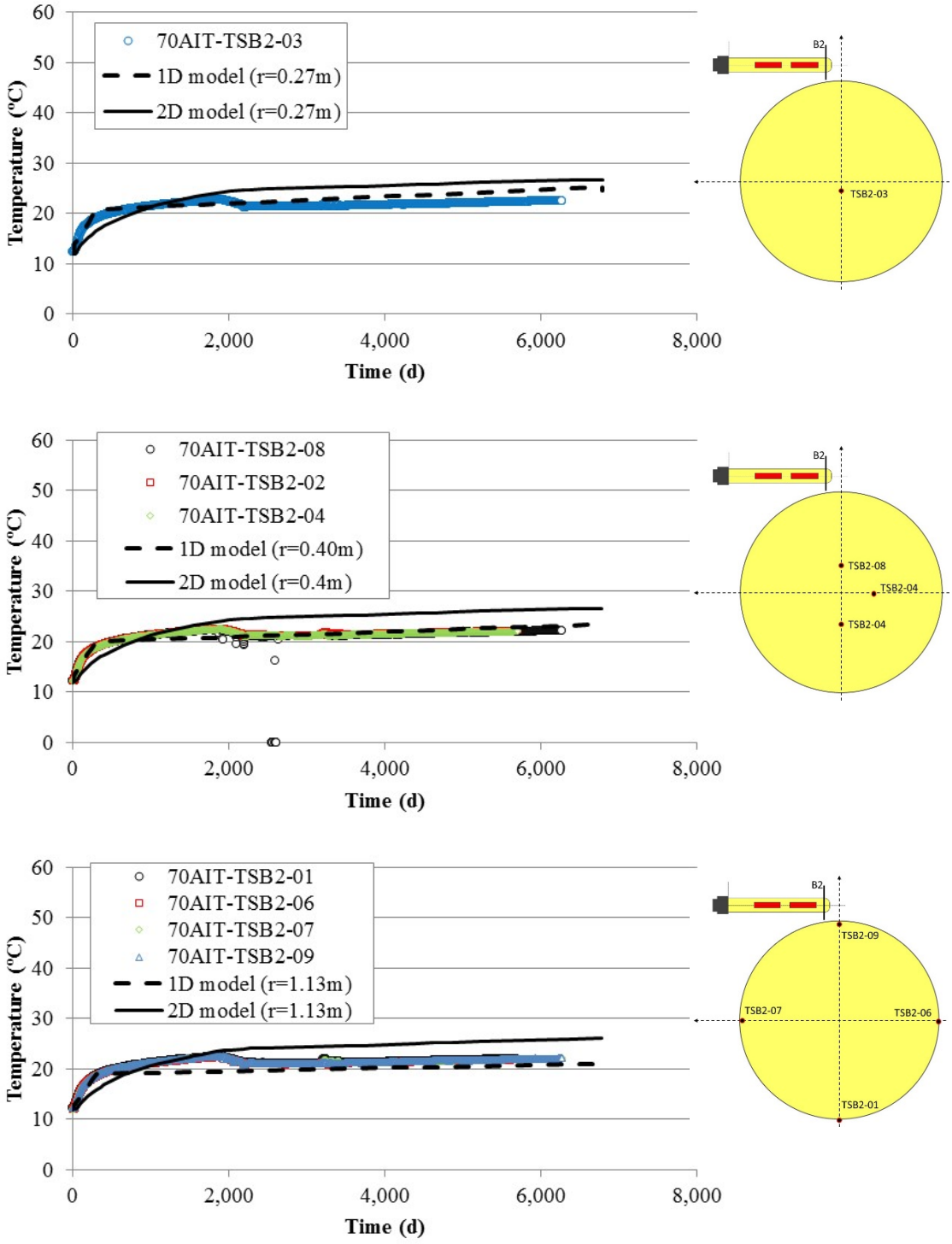

Fig. C-72: Time evolution of the calculated temperatures (lines) with the 1D and 2D axisymmetric models and the measured temperatures (symbols) in cold section B2 located at the end of the gallery

C.4.2.4.2 Relative humidity and water content

Fig. C-73 shows the time evolution of the calculated relative humidity with the 1D and 2D axisymmetric models and the measured relative humidity in hot section F2 located at the mid-point of Heater #2. The relative humidity computed with the 1D model at r = 0.8 m are larger than those calculated with the 2D model. At r = 1.05 m, however, the trend is reversed and the relative humidity computed with the 1D model are smaller than those calculated with the 2D model. The relative humidity computed with the 1D and 2D models fit the measured data equally well because the measured relative humidity data show some scatter. Fig. C-74 shows the time evolution of the computed volumetric water content with the 1D and 2D axisymmetric models in hot Section M2. The volumetric water contents computed with the 1D model are larger than the water contents calculated with the 2D model at all radial distances. The volumetric water contents computed with the 1D model fit the measured data better than the volumetric water contents calculated with the 2D model.

Once again, the water contents computed with the 1D axisymmetric model outperform the water contents computed with the 2D axisymmetric model because the model parameters used to perform the comparison of the two models are the parameters calibrated with the 1D axisymmetric model. A detailed calibration of the parameters of the 2D axisymmetric model will ensure that the results of the 2D model are at least as good as or better than the results of the 1D axisymmetric model.

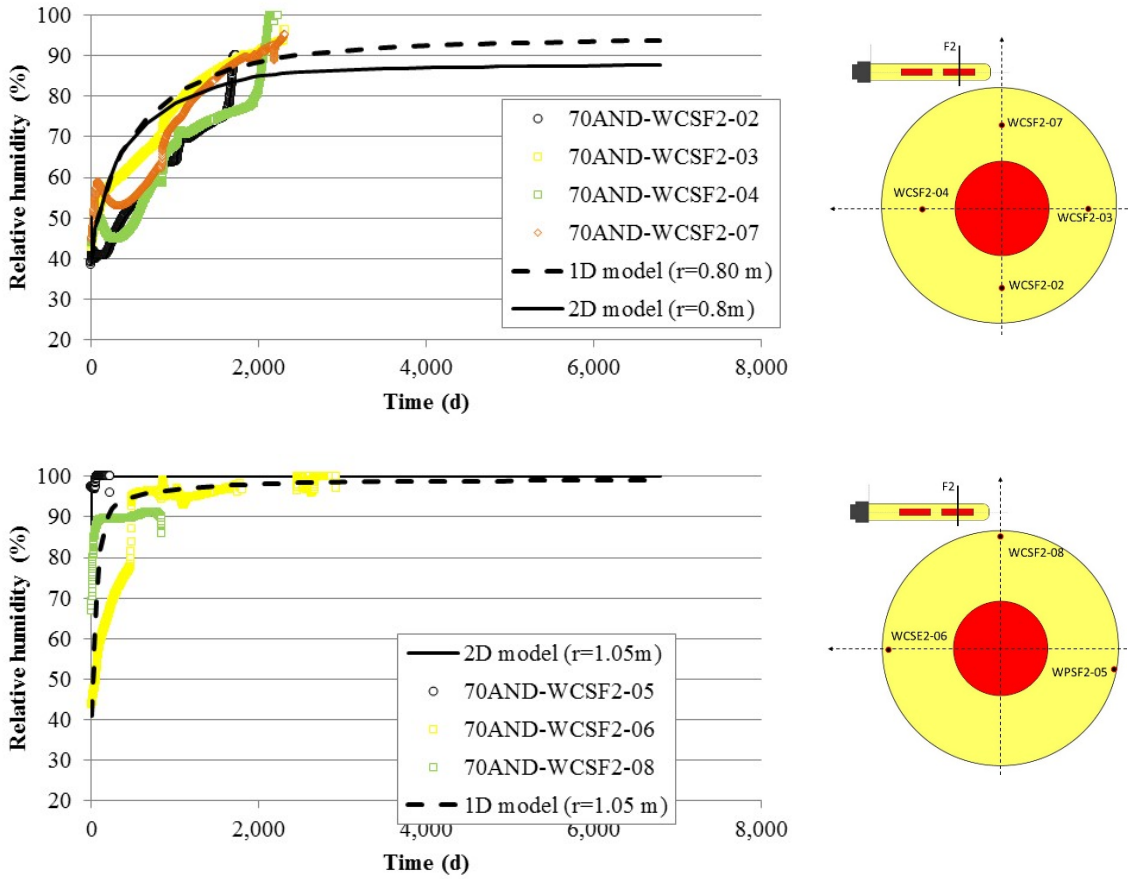

Fig. C-73: Time evolution of the calculated relative humidity (lines) with the 1D and 2D axisymmetric models and the measured relative humidity (symbols) in hot section F2 located at the mid-point of Heater #2

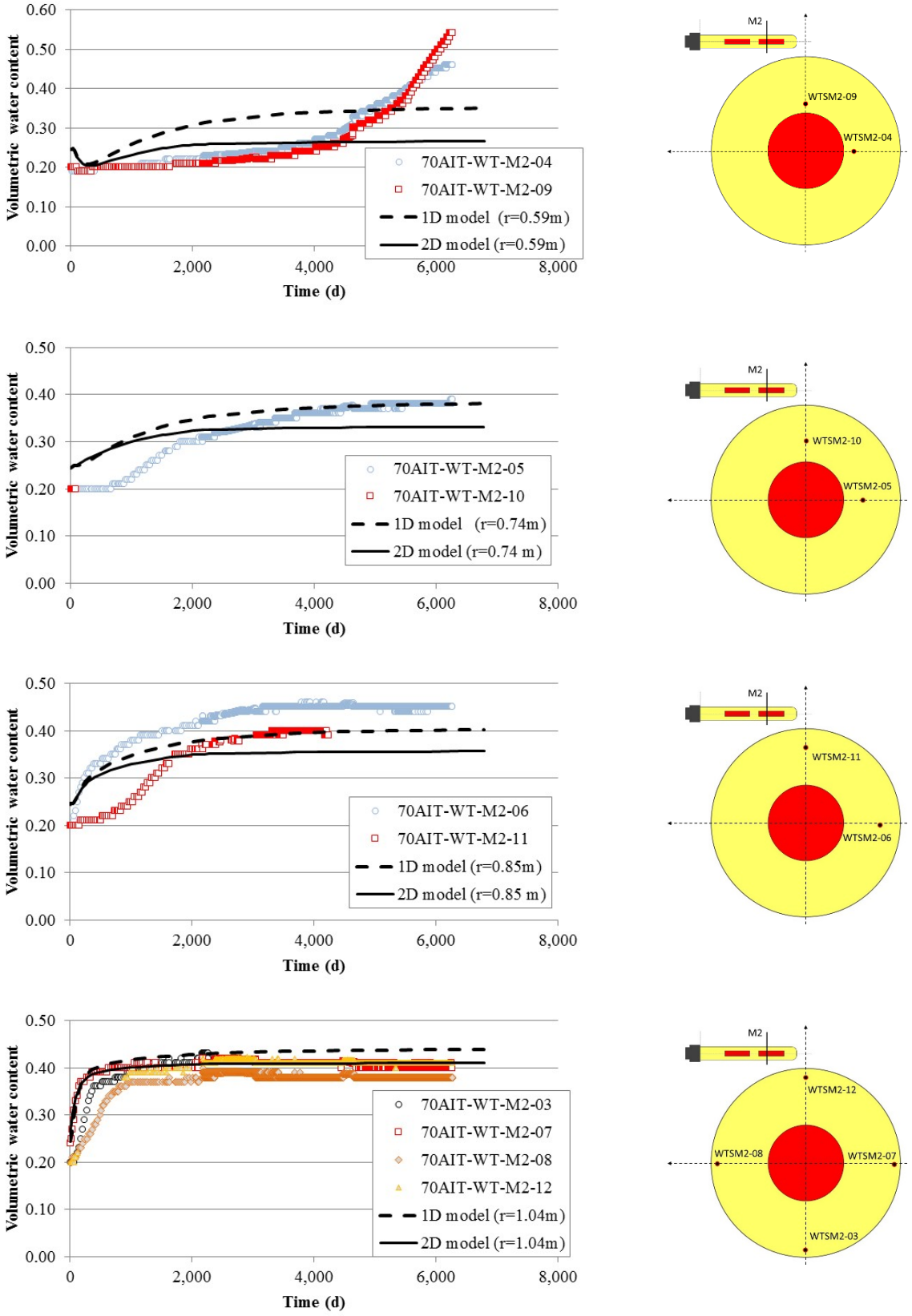

Fig. C-74: Time evolution of the computed water content (lines) with the 1D and 2D axisymmetric models and measured data (symbols) in hot Section M2

C.4.2.4.3 Chloride concentrations

Fig. C-75 shows the concentrations of Cl^- computed with the 1D and 2D axisymmetric models in a hot section in 2002 and 2015. The concentrations computed with the 1D model in 2002 are similar to the concentrations of the 2D model. The computed concentrations with the 1D model in 2015 are smaller than the concentrations calculated with the 2D model because the bentonite hydration rate calculated with the 1D model is slightly larger than the hydration calculated with the 2D model.

Fig. C-76 shows the concentrations of Cl^- computed with the 1D and 2D models in a cold section in 2002 and 2015. The shapes of the concentrations curves of both models are similar, although the concentrations calculated with the 1D model are significantly smaller than the concentrations computed with the 2D model.

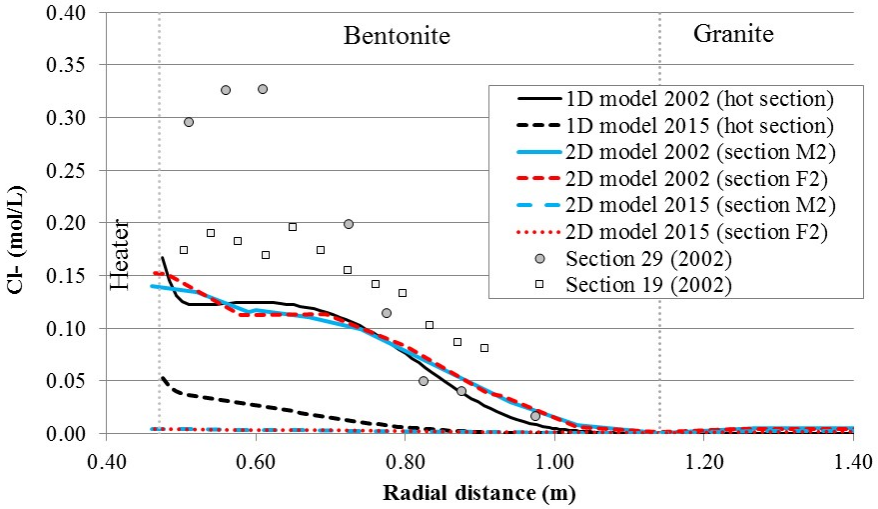

Fig. C-75: Spatial distribution of the concentrations of Cl^- computed with the 1D and 2D axisymmetric models in a hot section in 2002 and 2015 and measured data in 2002 (symbols) in hot sections M2 and F2

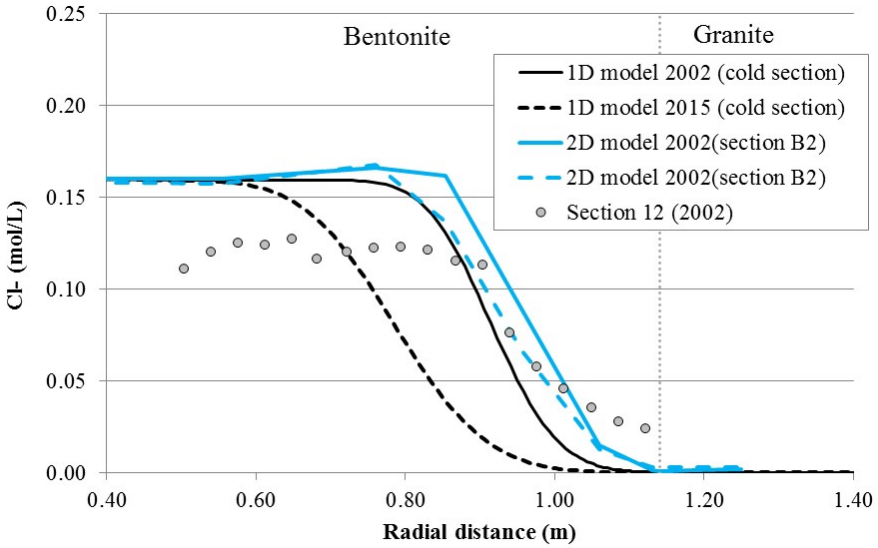

Fig. C-76: Spatial distribution of the concentrations of Cl^- computed with the 1D and 2D axisymmetric models in a cold section in 2002 and 2015 and measured data (symbols) in cold section B2

C.4.2.5 Sensitivity runs

The temperature, water content and relative humidity values computed with the 2D axisymmetric model from the measured data could deviate due to model parameter uncertainties. The key thermal parameters to which temperature results are most sensitive are the thermal conductivities of the bentonite and the granitic rock. On the other hand, bentonite hydration is most sensitive to the liquid permeability of the bentonite.

This section presents the results of sensitivity runs of the computed temperatures and relative humidity to changes in thermal conductivities of the bentonite and the granitic rock and the permeability of the bentonite.

C.4.2.5.1 Sensitivity to the thermal conductivity of the bentonite

Fig. C-77 shows the sensitivity of the temperatures in a cold section computed with the 2D axisymmetric model to a 35 % increase in the thermal conductivity of the bentonite. The figure also shows the temperatures calculated with the base run of the 2D model and the measured temperatures in section B2. As expected, the calculated temperatures in the cold part of the bentonite buffer increase slightly when the thermal conductivity of the bentonite is increased.

Fig. C-78 shows the sensitivity of the temperatures in a hot section computed with the 2D axisymmetric model to a 35 % increase in the thermal conductivity of the bentonite. The figure also shows the temperatures calculated with the base run of the 2D model and the measured temperatures in section F2. Similar to the cold section, the calculated temperatures in the hot part of the bentonite buffer increase when the thermal conductivity of the bentonite is increased. The temperatures of the sensitivity run are greater than those of the base run, but are not sufficiently large to fit the measured temperatures near the bentonite/granite interface.

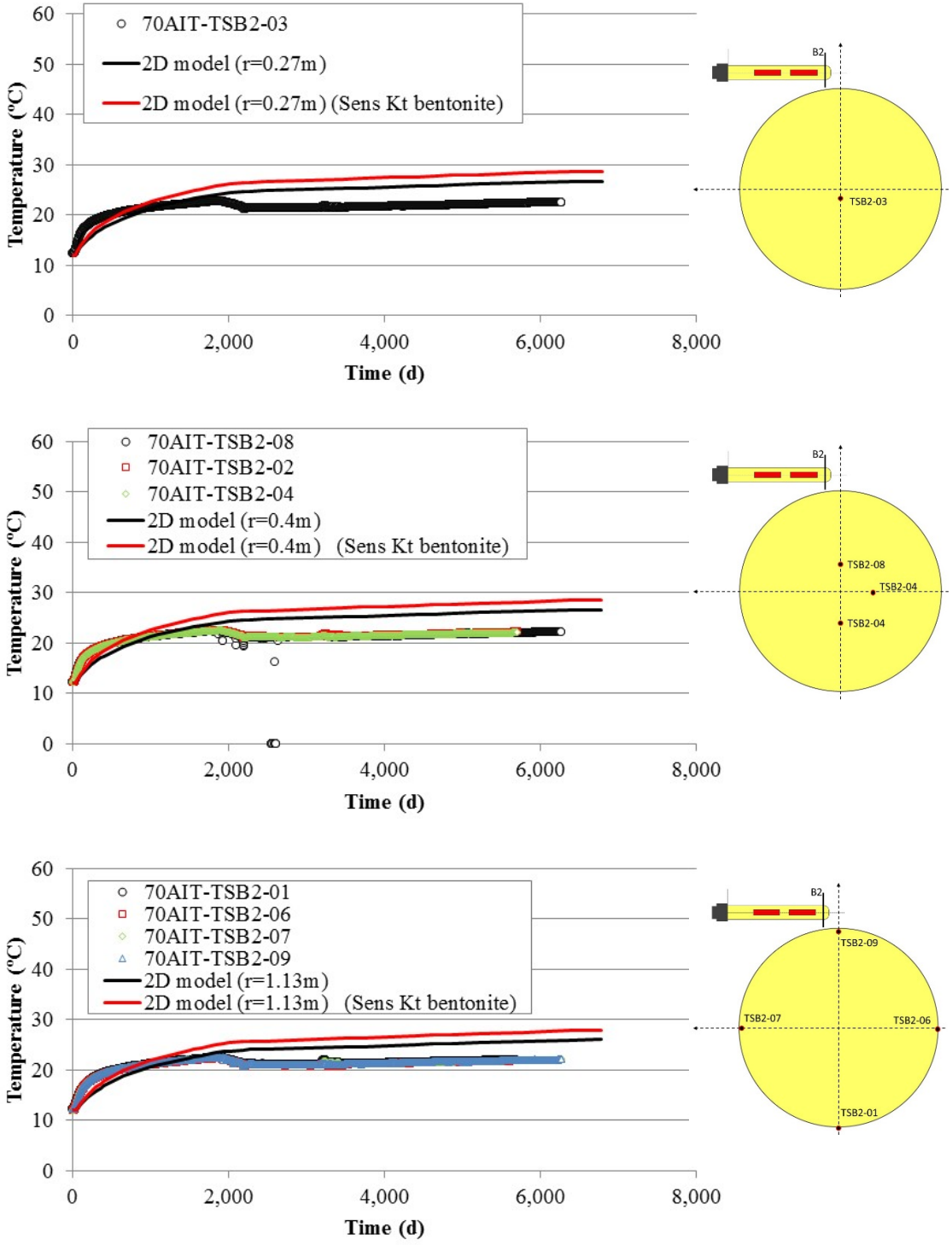

Fig. C-77: Sensitivity of the computed temperature in a cold section with the 2D axisymmetric model to a 35 % increase in the thermal conductivity of bentonite

The figure also shows the temperatures calculated with the base run of the 2D model and the measured temperatures in section B2.

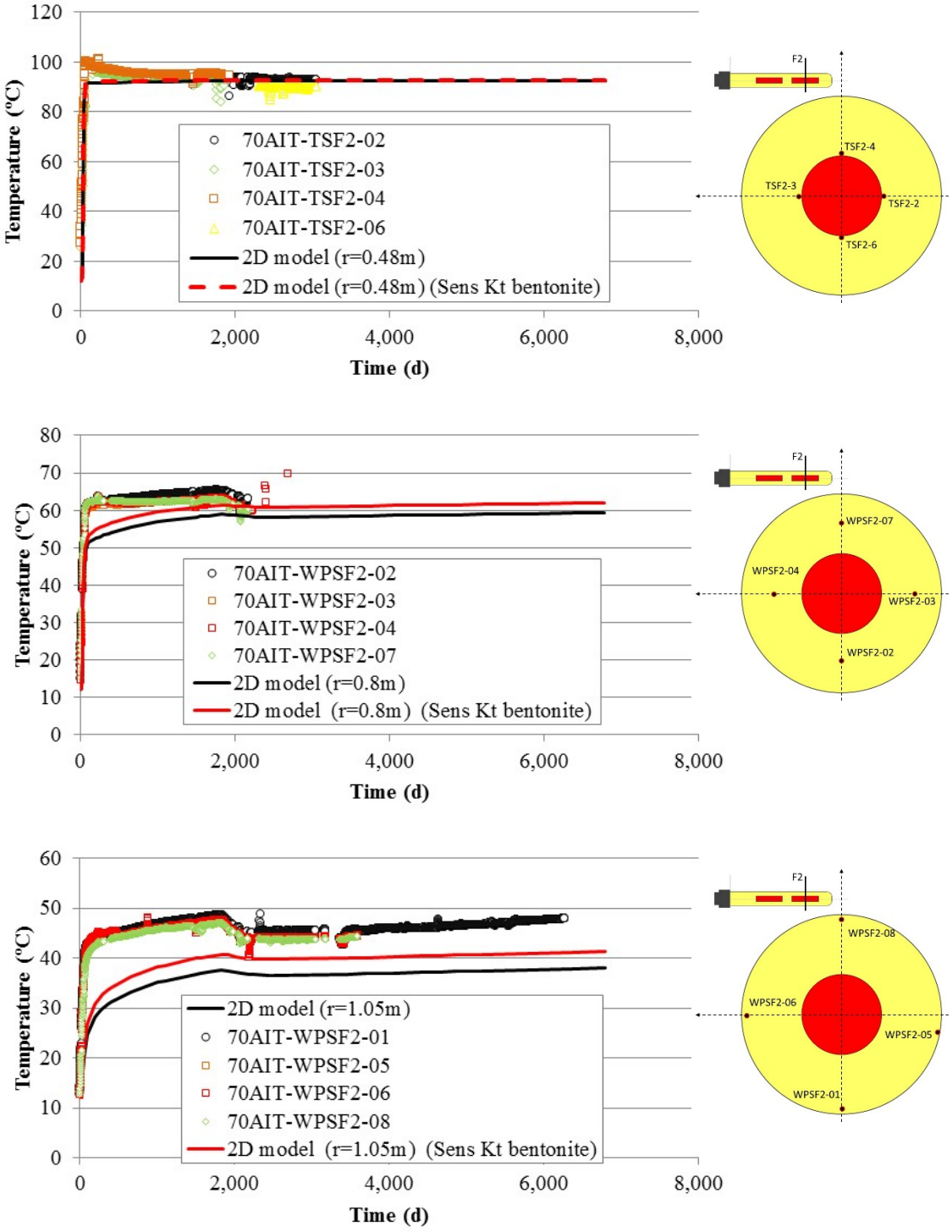

Fig. C-78: Sensitivity of the computed temperature in a hot section with the 2D axisymmetric model to a 35 % increase in the thermal conductivity of bentonite

The figure also shows the temperatures calculated with the base run of the 2D model and the measured temperatures in section F2.

C.4.2.5.2 Sensitivity to the thermal conductivity of the granite

Fig. C-79 shows the sensitivity of the temperatures in a cold section computed with the 2D axisymmetric model to a 20 % increase in the thermal conductivity of the granite. The figure also shows the temperatures calculated with the base run of the 2D model and the measured temperatures in section B2. As expected, the calculated temperatures in the cold part of the bentonite buffer decrease slightly when the thermal conductivity of granite is increased.

Fig. C-80 shows the sensitivity of the temperatures in a hot section computed with the 2D axisymmetric model to a 20 % increase in the thermal conductivity of granite. The figure also shows the temperatures calculated with the base run of the 2D model and the measured temperatures in section F2. The increase in thermal conductivity of granite affects mostly the computed temperatures near the bentonite/granite interface. Similar to the cold section, the calculated temperatures in the external part of the bentonite buffer decrease when the thermal conductivity of the granite is increased. The changes in the computed temperatures in the hot section are larger than those in the cold section.

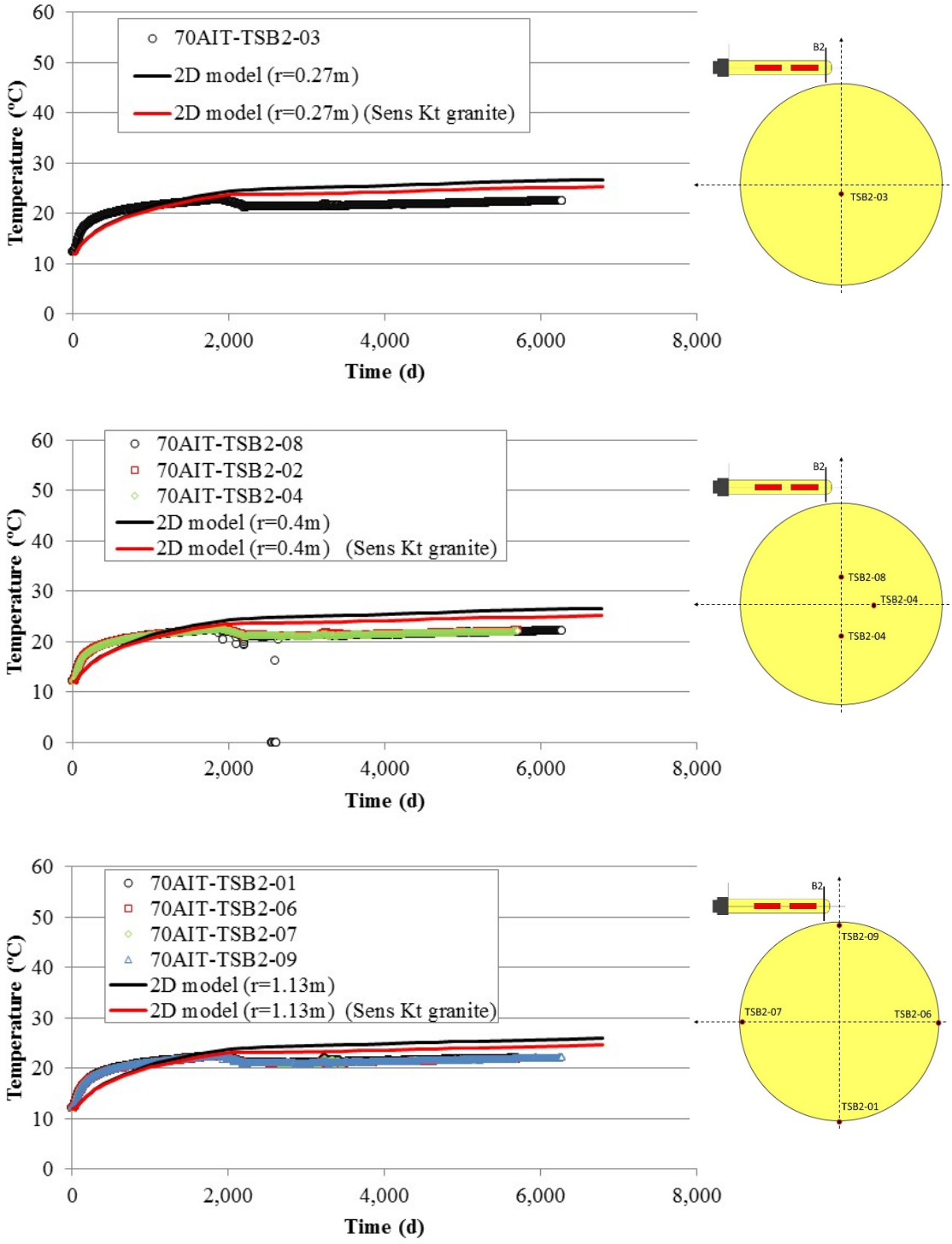

Fig. C-79: Sensitivity of the computed temperature to a 20 % increase in the thermal conductivity of the granite in a cold section with the 2D axisymmetric model

The figure also shows the temperatures calculated with the base run of the 2D model and the measured temperatures in section B2.

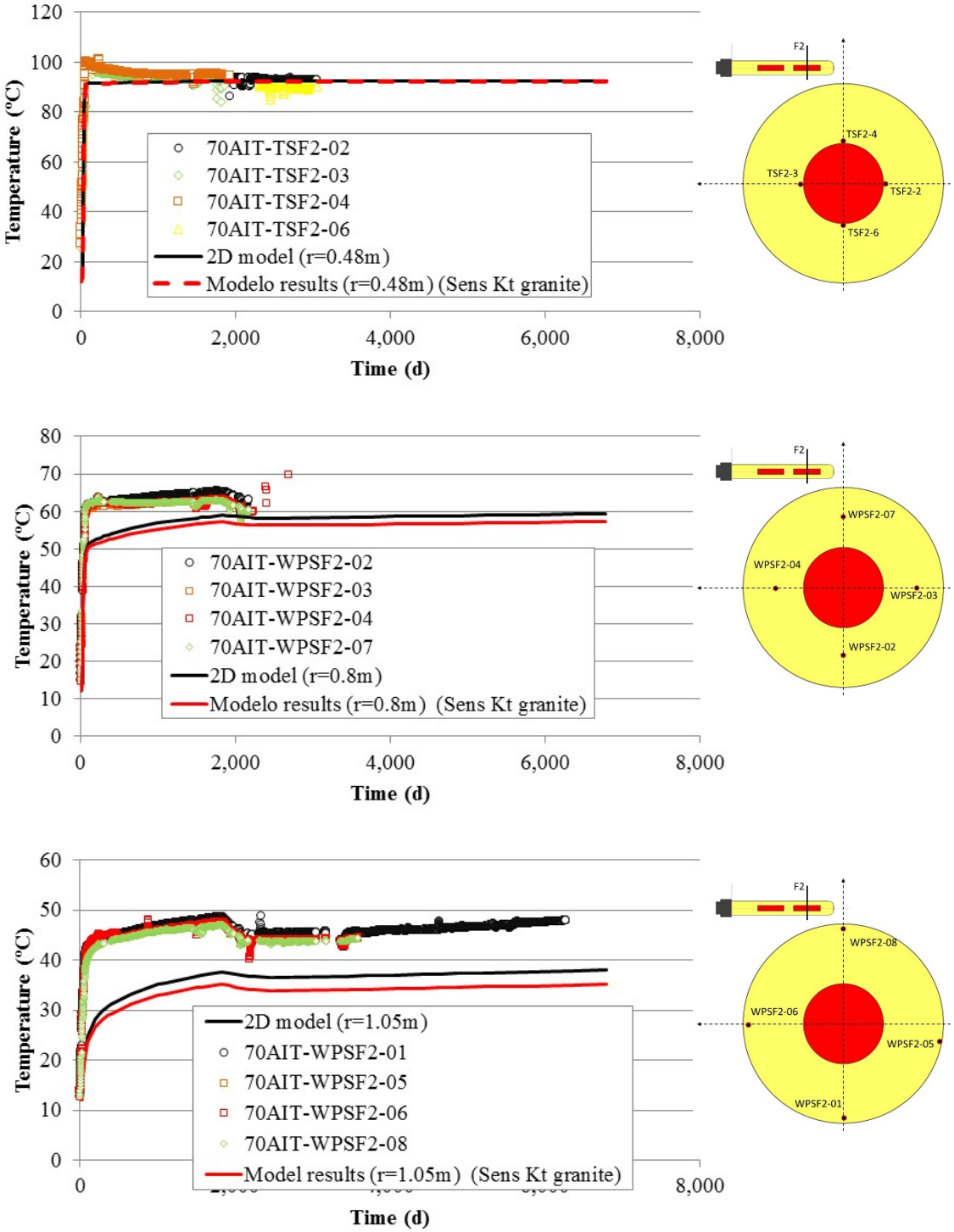

Fig. C-80: Sensitivity of the computed temperature to a 20 % increase in the thermal conductivity of the granite in a hot section with the 2D axisymmetric model

The figure also shows the temperatures calculated with the base run of the 2D model and the measured temperatures in section F2.

C.4.2.5.3 Sensitivity to the permeability of the bentonite

Fig. C-81 shows the sensitivity of relative humidity to a 26 % increase in the permeability of bentonite in a hot section computed with the 2D axisymmetric model. The figure also shows the relative humidity calculated with the base run of the 2D model and the measured relative humidity in section F2. The increase in permeability of bentonite affects the computed relative humidity most at r = 0.8 m which increase when the permeability of bentonite is increased.

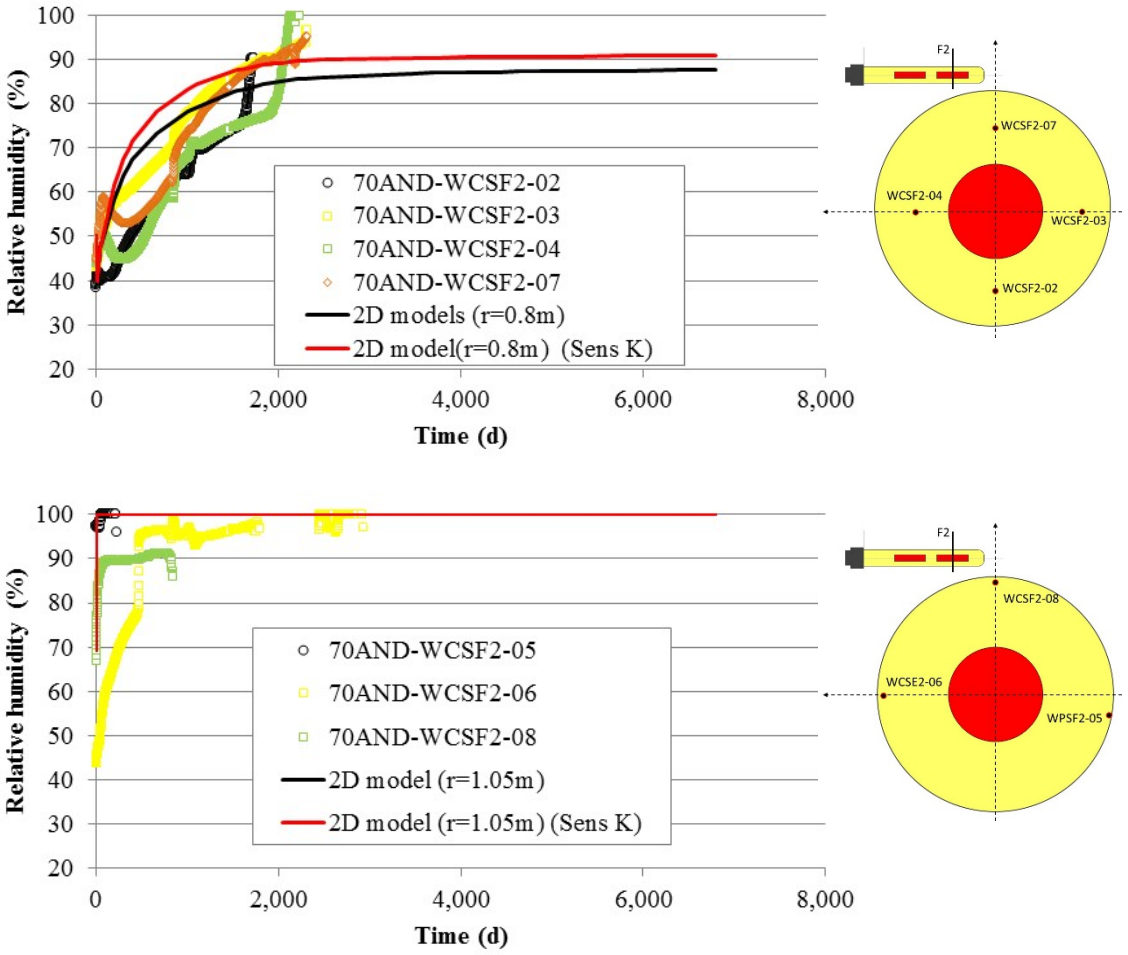

Fig. C-81: Sensitivity of the relative humidity in a hot section computed with the 2D axisymmetric model to a 26 % increase in the permeability of the bentonite

The figure also shows the relative humidity calculated with the base run of the 2D model and the measured relative humidity in section F2.

C.4.2.6 Conclusions

The 1D axisymmetric THMC model of the FEBEX in-situ test was extended to 2D axisymmetric conditions.

The temperatures computed with the 2D model in the hot section are less than those calculated with the 1D model. The temperatures computed with the 2D model in the cold section are higher than those calculated with the 1D model. The temperatures computed with the 1D model fit the measured data better than the temperatures calculated with the 2D model.

The volumetric water content values computed with the 1D model are larger than the water content values calculated with the 2D model at all radial distances. The volumetric water contents computed with the 1D model fit the measured data better than the volumetric water content values calculated with the 2D model.

The 1D axisymmetric model outperforms the 2D axisymmetric model because the model parameters used to perform the comparison of both models are the parameters calibrated with the 1D axisymmetric model. A detailed calibration of the parameters of the 2D axisymmetric model will surely lead to model results at least as good as or better than the results of the 1D axisymmetric model.

The main conclusions of the sensitivity runs include:

1. The calculated temperatures in the cold part of the bentonite buffer increase slightly when the thermal conductivity of the bentonite is increased. Similar to the cold section, the calculated temperatures in the hot part of the bentonite buffer increase when the thermal conductivity of the bentonite is increased.
2. The calculated temperatures in the cold part of the bentonite buffer decrease slightly when the thermal conductivity of the granite is increased.
3. The increase in thermal conductivity of the granite affects the computed temperatures near the bentonite/granite interface most. Similar to the cold section, the calculated temperatures in the external part of the bentonite buffer decrease when the thermal conductivity of the granite is increased. The changes in the computed temperatures in the hot section are larger than changes in the cold section.

The concentrations of Cl^- in 2002 are high near heaters #1 and #2. The largest concentrations are located at the edge of Heater #2. The contour lines are approximately parallel to the axis of the gallery along heaters #1 and #2. At the edges of the heaters, however, the contour lines are no longer parallel to the gallery axis. The computed contour plots of Cl^- concentrations illustrate that the edge effects extend over a distance of 0.5 to 1 m approximately. The concentrations of Cl^- in 2015 show a significant decrease compared to the concentrations in 2002 around Heater #2. High concentrations of Cl^- still remain in the bentonite barrier between the dummy and Heater #2 and between Heater #2 and the end of the gallery.

The concentrations of Cl^- computed with the 1D model in a hot section in 2015 are smaller than the concentrations calculated with the 2D model because the bentonite hydration rate calculated with the 1D model is slightly larger than the hydration calculated with the 2D model. In a cold section the concentrations calculated with the 1D model are significantly smaller than the concentrations computed with the 2D model.

C.4.3 Updated THCM model

The previous 1D axisymmetric THCM model of the FEBEX in-situ test has been improved and updated. This section presents the improvements and updates of the model which include: 1) Improving the boundary condition at the heater-bentonite interface; 2) Refining the spatial discretization of the finite element mesh; and 3) Revising the solute dispersivities of bentonite and granite.

C.4.3.1 Improvements and updates of the THCM model

The boundary condition at the heater-bentonite where the heat source is applied was revised because the mass balance errors of the numerical solution near this boundary was large in some runs. Such errors were already detected and overcome by Samper et al. (2013) within the PEBS Project when modelling the CIEMAT infiltration and heating experiments on CG cells.

The numerical implementation of this boundary condition has been improved by refining the grid near the heater and by applying the heat flux directly on the bentonite. The revised implementation of the boundary condition leads to more water evaporation than the previous implementation of the boundary condition.

The dispersivities of the reference model were revised and updated. The dispersivities of the bentonite and granite in the reference model were equal to 1 cm and 2 cm, respectively. The dispersivities of the bentonite and granite in the updated model are equal to 0.8 cm and 0.1 cm, respectively.

In a closed system as the FEBEX in-situ test, the mass balance error, ε_m, of a given chemical species is computed as the difference between the initial and the final mass in the system. The initial and final masses are calculated by integrating numerically the mass stored in the elements of the finite element grid. This integration involves numerical approximations which in turn introduce numerical errors in the estimate of ε_m. It is well-known that these integration errors are especially large when the water content and the concentration profiles show large radial gradients.

The mass balance errors of the updated THCM model of the FEBEX in-situ test have been reduced significantly compared to the previous model. The mass balance error for Cl^- is reduced from 150 % in the previous model to about 20 % in the updated model. The mass balance errors in the model of the cold section are generally less than 10 %.

The mass balance errors could be reduced by refining the finite element grid. However, the computation time increases sharply with the spatial discretization. For this reason, at this stage of the project, the mass balance errors of the updated model are deemed acceptable. They will be reduced in future studies.

C.4.3.2 Updated model calculations in a hot section

The updated model is an improvement of the previous model. We claim that the previous model provides acceptable numerical results except for a small area near the heater. Next, the differences between the results of the previous and the updated models are presented.

Fig. C-82 to Fig. C-86 show the concentrations of Ca^{2+}, K^{+}, Mg^{2+}, Cl^{-} and Na^{+} computed with the previous and the updated models in a hot section in 2002. The computed concentrations in a hot section correspond to a generic "hot section", which is a section of the bentonite barrier fully affected by the effect of the heaters. For illustration purposes, the computed concentrations in the hot section are compared to the inferred concentrations in Sections 19 and 29. The location of these sections is shown in Fig. C-4.

The concentrations of Ca^{2+}, K^{+}, Mg^{2+}, Cl^{-} and Na^{+} computed with the updated model near the heater are significantly larger than the concentrations calculated with the previous model.

The concentrations of SO_4^{2-} (Fig. C-87) and HCO_3^{-} (Fig. C-88) and the pH (Fig. C-89) of the bentonite computed with the updated model are similar to the concentrations of the previous model because the pH and the concentrations of these species are buffered by surface complexation and mineral dissolution/precipitation reactions, respectively. The pH and concentration of HCO_3^{-} in the granite in the updated model are different from those calculated with the previous model due to the update in the dispersivity of the granite.

Fig. C-90 and Fig. C-91 show the cumulative calcite and gypsum dissolution/ precipitation for the previous and updated models. The computed cumulative mineral dissolution/precipitation is similar in both cases, except for a strong peak of mineral precipitation near the heater due to the evaporation.

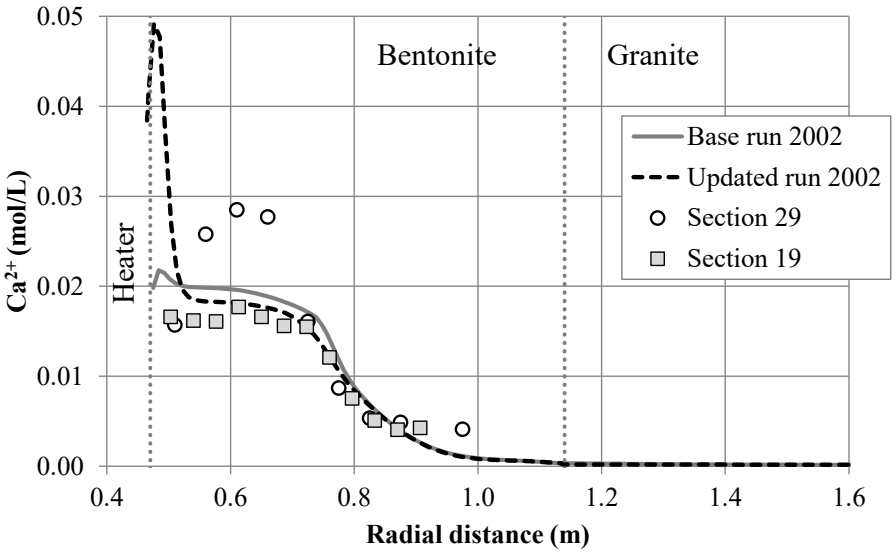

Fig. C-82: Computed Ca^{2+} concentrations (lines) with the previous (base run) and the updated (updated run) models in a hot section in 2002 and inferred data (symbols) in Sections 19 and 29 (symbols)

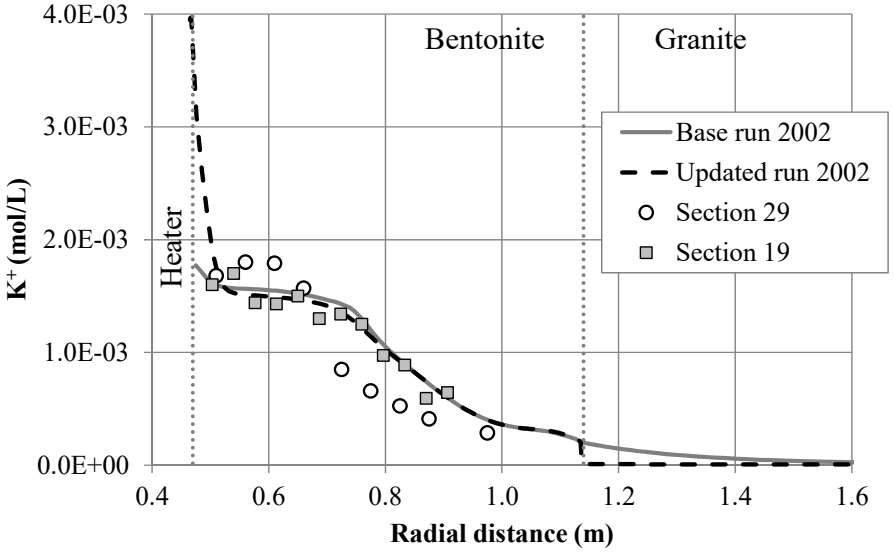

Fig. C-83: Computed K^+ concentrations (lines) with the previous (base run) and the updated (updated run) models in a hot section in 2002 and inferred data (symbols) in Sections 19 and 29 (symbols)

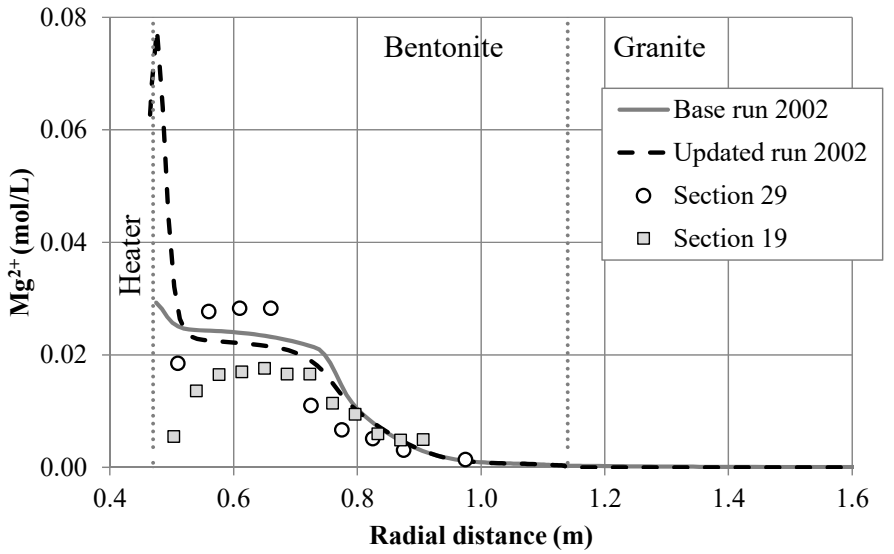

Fig. C-84: Computed Mg^{2+} concentrations (lines) with the previous (base run) and the updated (updated run) models in a hot section in 2002 and inferred data (symbols) in Sections 19 and 29 (symbols)

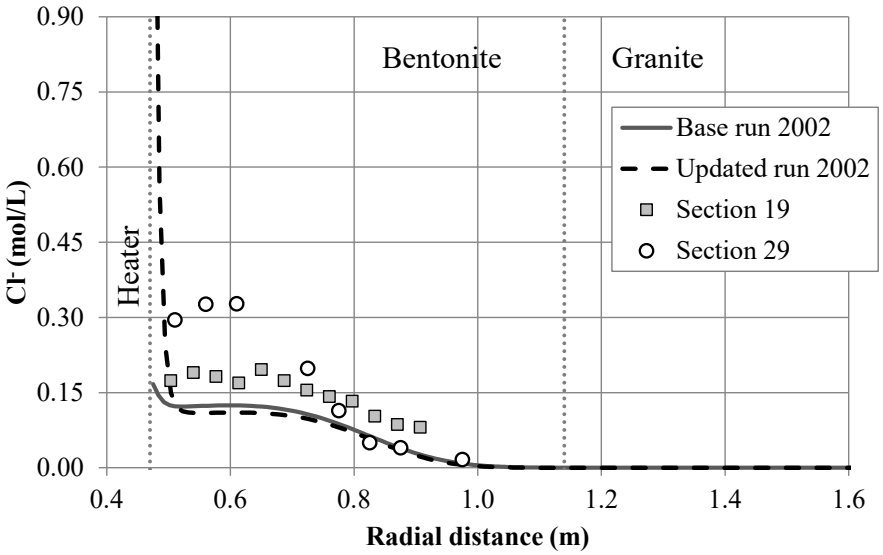

Fig. C-85: Computed Cl^- concentrations (lines) with the previous (base run) and the updated (updated run) models in a hot section in 2002 and inferred data (symbols) in Sections 19 and 29 (symbols)

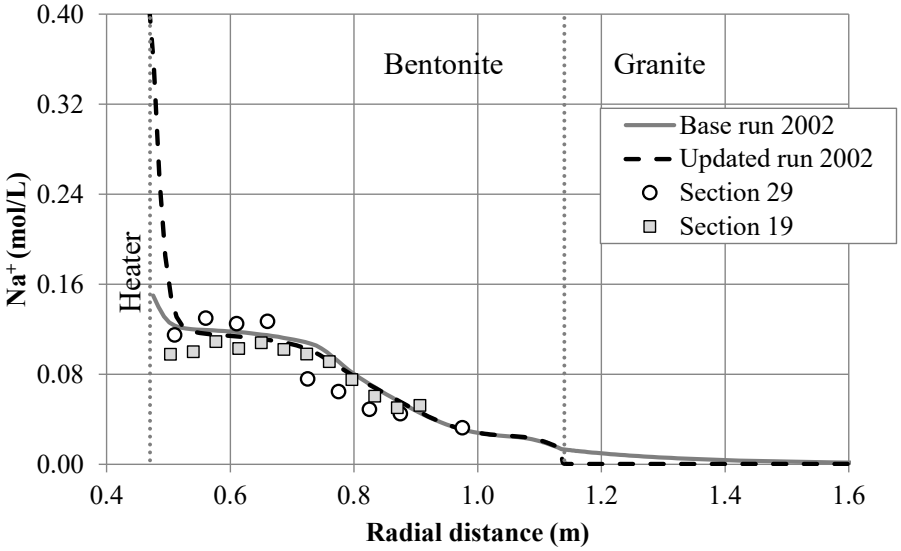

Fig. C-86: Computed Na^+ concentrations (lines) with the previous (base run) and the updated (updated run) models in a hot section in 2002 and inferred data (symbols) in Sections 19 and 29 (symbols)

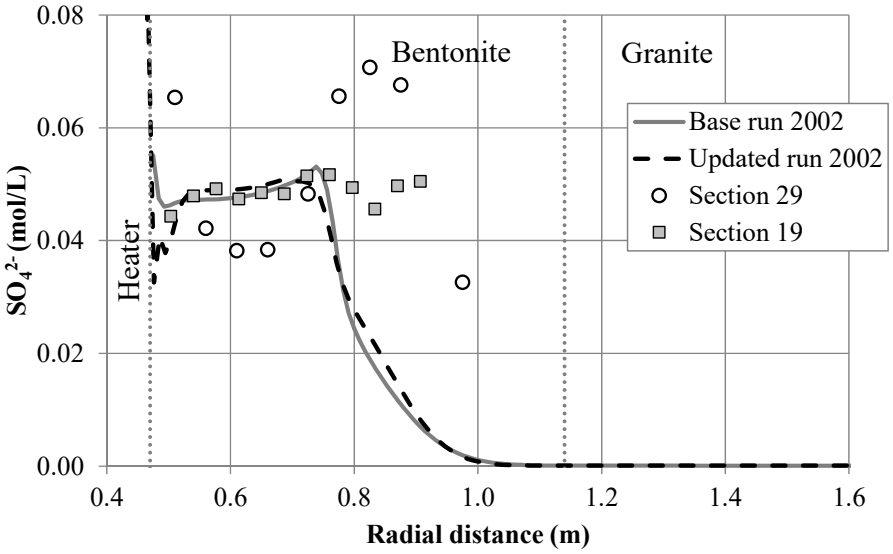

Fig. C-87: Computed SO_4^{2-} concentrations (lines) with the previous (base run) and the updated (updated run) models in a hot section in 2002 and inferred data (symbols) in Sections 19 and 29 (symbols)

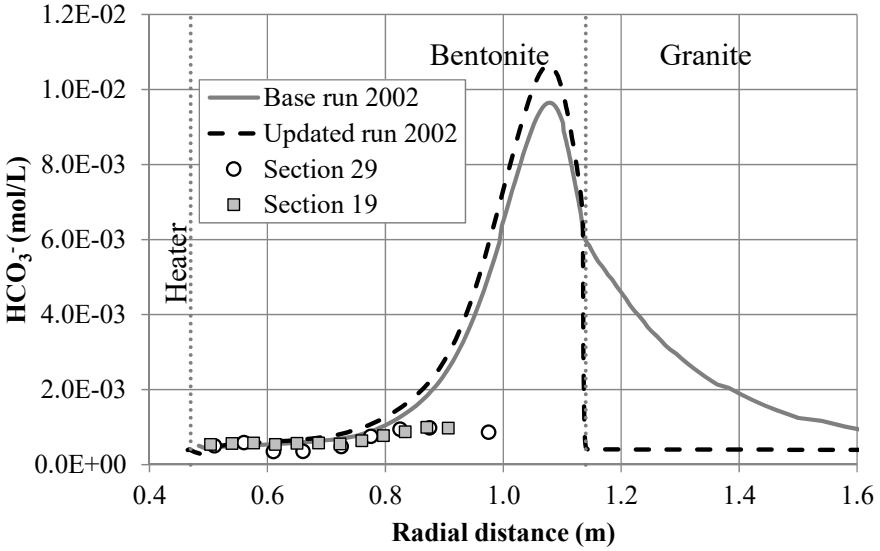

Fig. C-88: Computed $HCO3^-$ concentrations (lines) with the previous (base run) and the updated (updated run) models in a hot section in 2002 and inferred data (symbols) in Sections 19 and 29

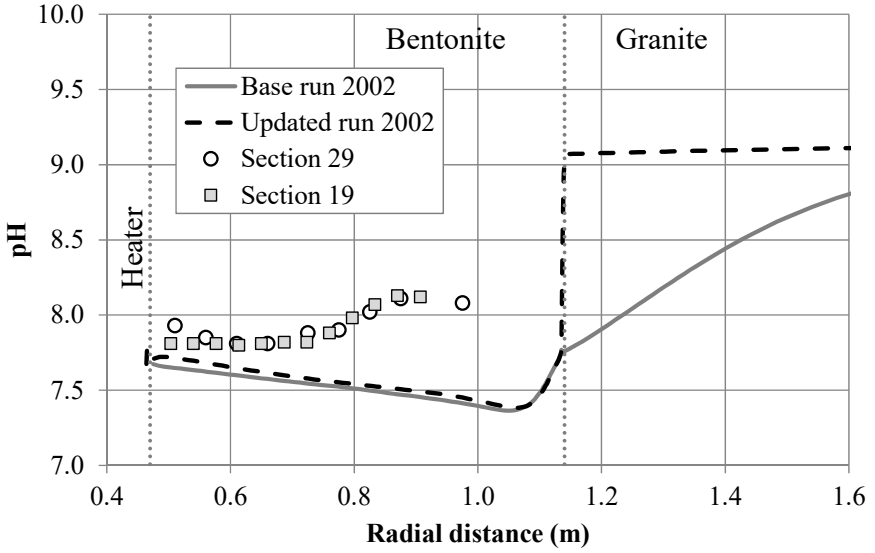

Fig. C-89: Computed pH (lines) with the previous (base run) and the updated (updated run) models in a hot section in 2002 and inferred data (symbols) in Sections 19 and 29 (symbols)

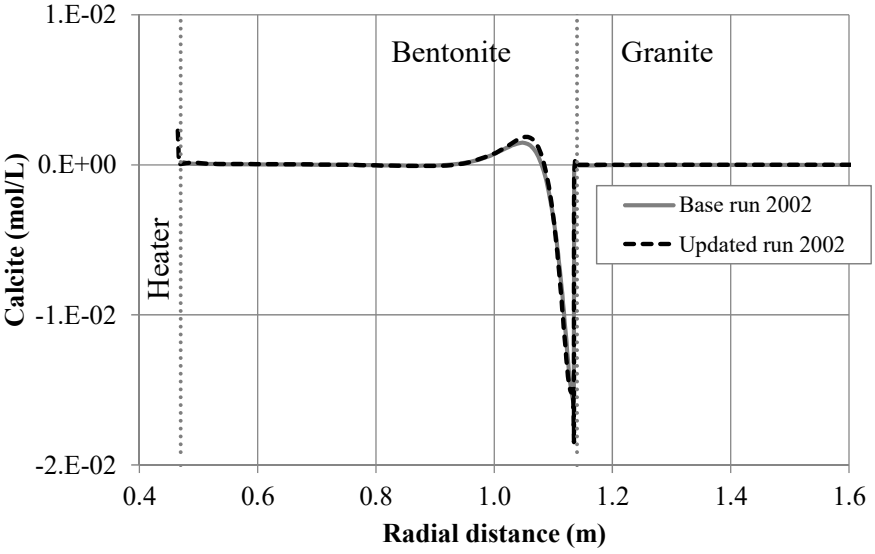

Fig. C-90: Cumulative calcite precipitation/dissolution computed with the previous (base run) and the updated (updated run) models in a hot section in 2002 (negative for dissolution and positive for precipitation)

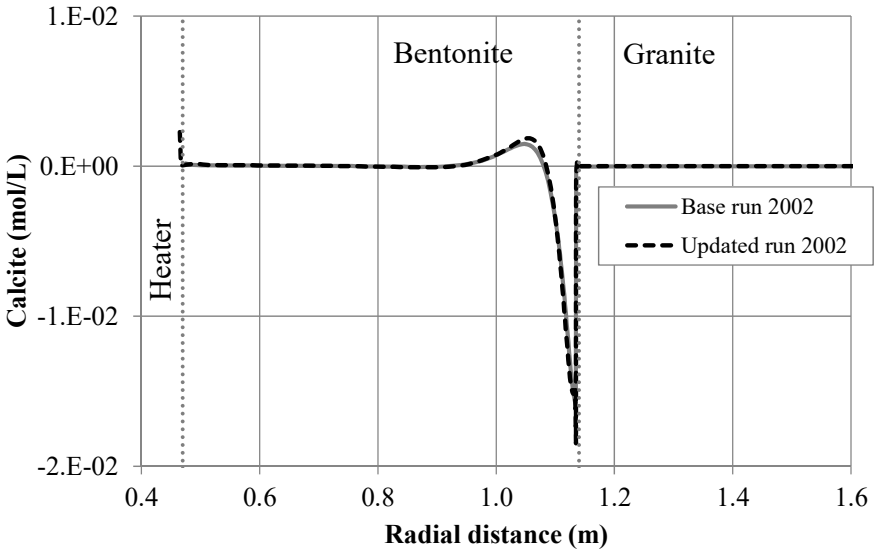

Fig. C-91: Cumulative gypsum precipitation/dissolution computed with the previous (base run) and the updated (updated run) models in a hot section in 2002 (negative for dissolution and positive for precipitation)

The computed relative humidity, temperature and water content with the previous and the updated models do not show relevant differences. The largest differences occur near the heater. Fig. C-92 shows the water content computed with the previous and the updated models and the measured data in 2002. It can be seen that the gravimetric water content of the previous model near the heater is slightly larger than the water content of the updated model because the computed water evaporation with the updated model is larger than the evaporation computed with the previous model.

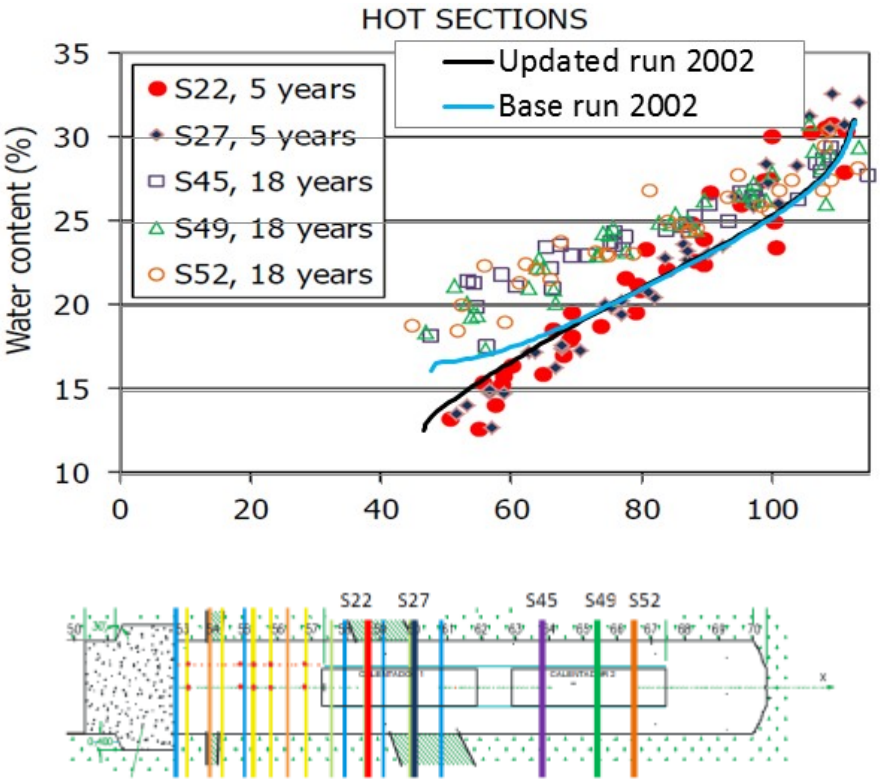

Fig. C-92: Comparison of the gravimetric water content computed (lines) in a hot section in 2002 with the previous model (base run) and the updated model (updated run) and measured gravimetric water content data (symbols) in sections S22, S27, S45, S49 and S52 at the times of dismantling of Heater #1 (year 2002). The plot at the bottom shows the location of the sections where water contents were measured.

C.4.3.3 Sensitivity analyses of the updated THCM model

The sensitivity of the computed concentrations in 2002 to a change in the bentonite diffusion coefficient was analysed by multiplying the bentonite solute diffusion coefficients by 10. Tab. C-2 lists the diffusion coefficients in pure water for the base run and the sensitivity run performed with the updated model.

Tab. C-2: Diffusion coefficients in pure water for the base run (taken from Zheng et al. 2011) and the sensitivity run

Component	**Base run** (m^2/s)	**Sensitivity run** (m^2/s)
Cl^-	3.1×10^{-12}	3.1×10^{-11}
SO_4^{2-}	3.6×10^{-13}	3.6×10^{-12}
Rest of species	2×10^{-11}	2×10^{-10}

Fig. C-93 to A-100 show the sensitivity of the computed concentrations of dissolved Ca^{2+}, K^+, Mg^{2+}, Cl^-, Na^+, SO_4^{2-} and HCO_3^- and pH in a hot section in 2002 to changes in the bentonite diffusion coefficient. These figures also show the inferred concentrations in Sections 19 and 29. The radial profiles of the concentrations of Ca^{2+}, K^+, Mg^{2+}, Na^+ and HCO_3^- become smoother when the diffusion coefficient of the bentonite is increased. The profiles of Cl^- and SO_4^{2-} are less sensitive to a change in the diffusion coefficient because the diffusion coefficients of these species are smaller. The computed pH is not sensitive to the change in the diffusion coefficient.

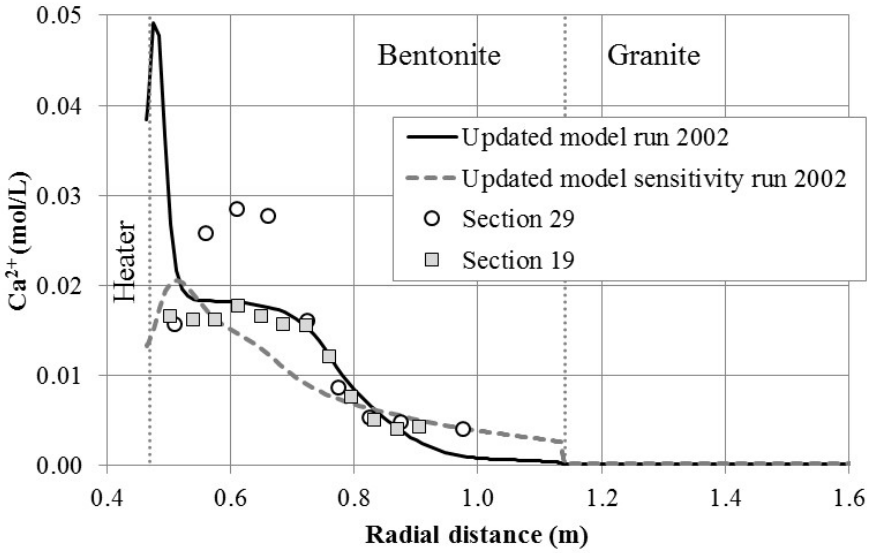

Fig. C-93: Sensitivity of the dissolved Ca^{2+} concentrations computed (lines) with the updated model in a hot section in 2002 to changes in the bentonite diffusion coefficient

Also shown are the inferred Ca^{2+} concentrations in Sections 19 and 29 (symbols)

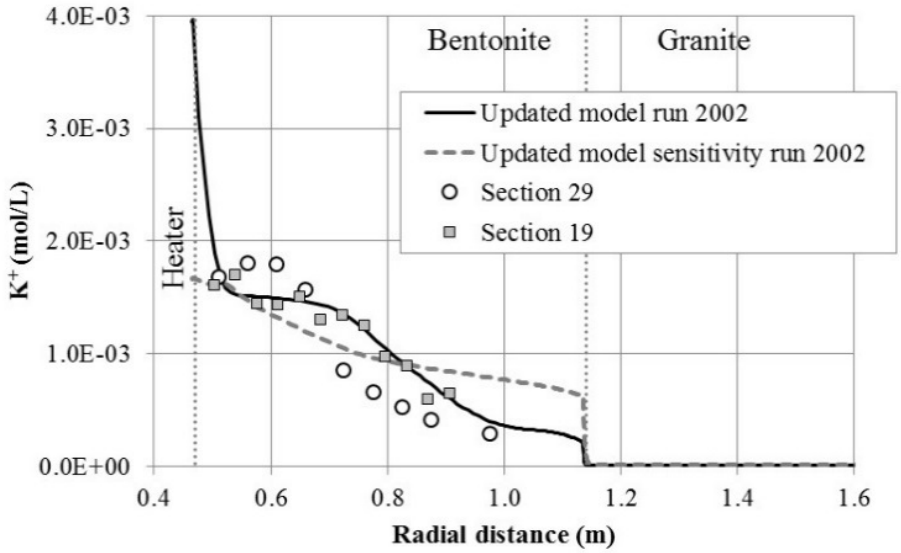

Fig. C-94: Sensitivity of the dissolved K^+ concentrations computed (lines) with the updated model in a hot section in 2002 to changes in the bentonite diffusion coefficient

Also shown are the inferred K^+ concentrations in Sections 19 and 29 (symbols).

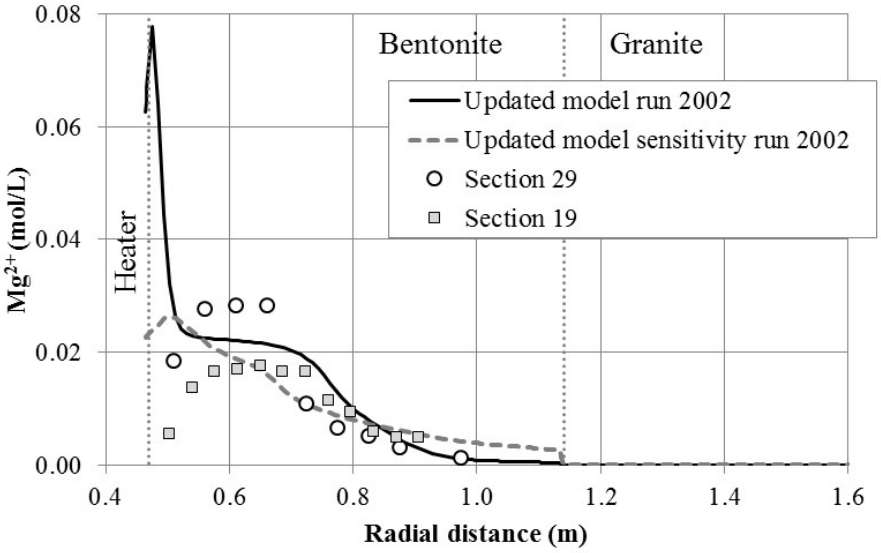

Fig. C-95: Sensitivity of the dissolved Mg^{2+} concentrations computed (lines) with the updated model in a hot section in 2002 to changes in the bentonite diffusion coefficient

Also shown are the inferred Mg^{2+} concentrations in Sections 19 and 29 (symbols).

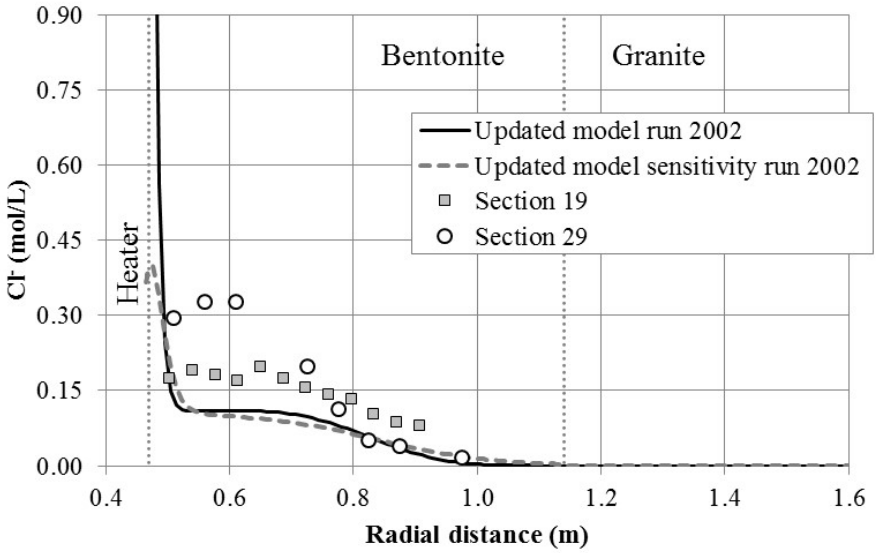

Fig. C-96: Sensitivity of the dissolved Cl^- concentrations computed (lines) with the updated model in a hot section in 2002 to changes in the bentonite diffusion coefficient

Also shown are the inferred Cl^- concentrations in Sections 19 and 29 (symbols).

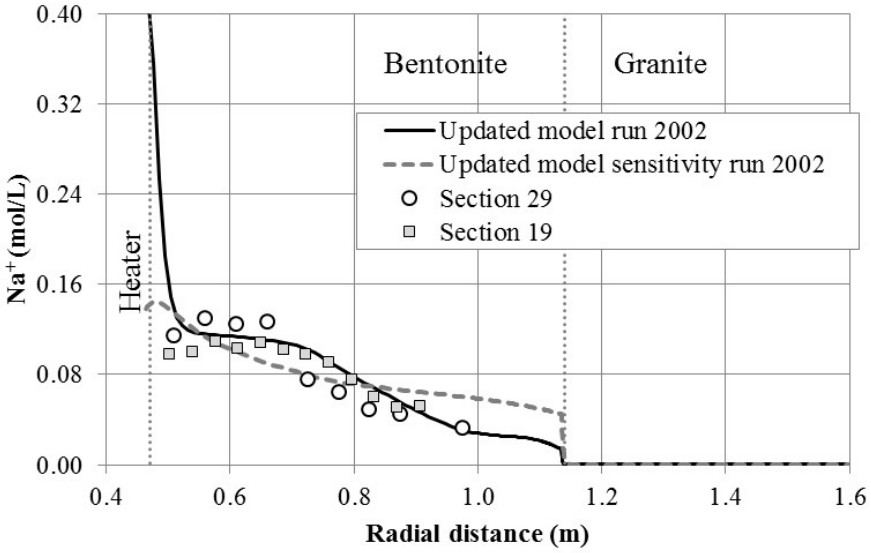

Fig. C-97: Sensitivity of the dissolved Na+ concentrations computed (lines) with the updated model in a hot section in 2002 to changes in the bentonite diffusion coefficient

Also shown are the inferred Na+ concentrations in Sections 19 and 29 (symbols).

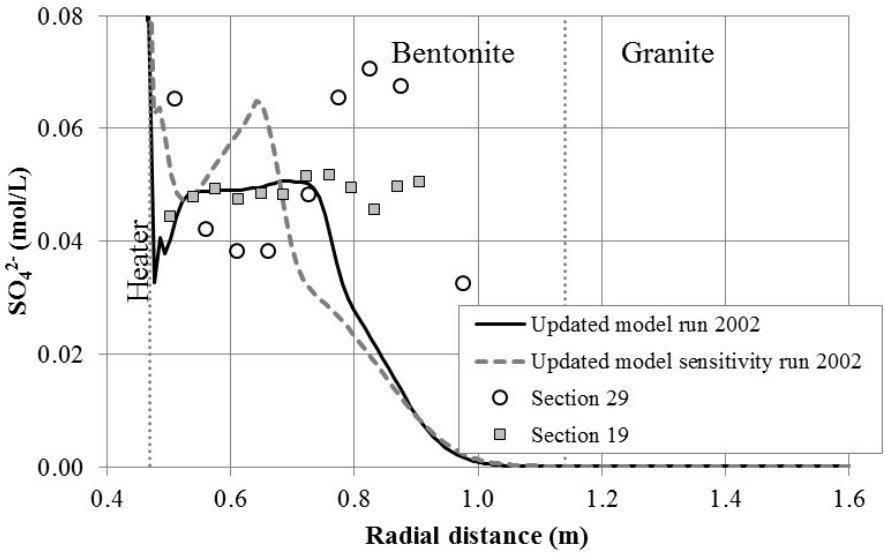

Fig. C-98: Sensitivity of the dissolved SO_4^{2-} concentrations computed (lines) with the updated model in a hot section in 2002 to changes in the bentonite diffusion coefficient

Also shown are the inferred SO_4^{2-} concentrations in Sections 19 and 29 (symbols).

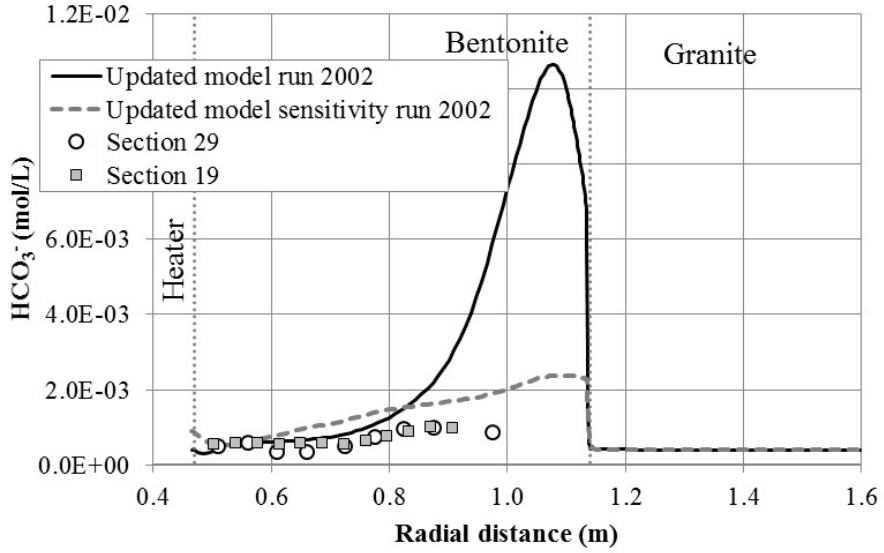

Fig. C-99: Sensitivity of the dissolved HCO_3^- concentrations computed (lines) with the updated model in a hot section in 2002 to changes in the bentonite diffusion coefficient

Also shown are the inferred HCO_3^- concentrations in Sections 19 and 29 (symbols).

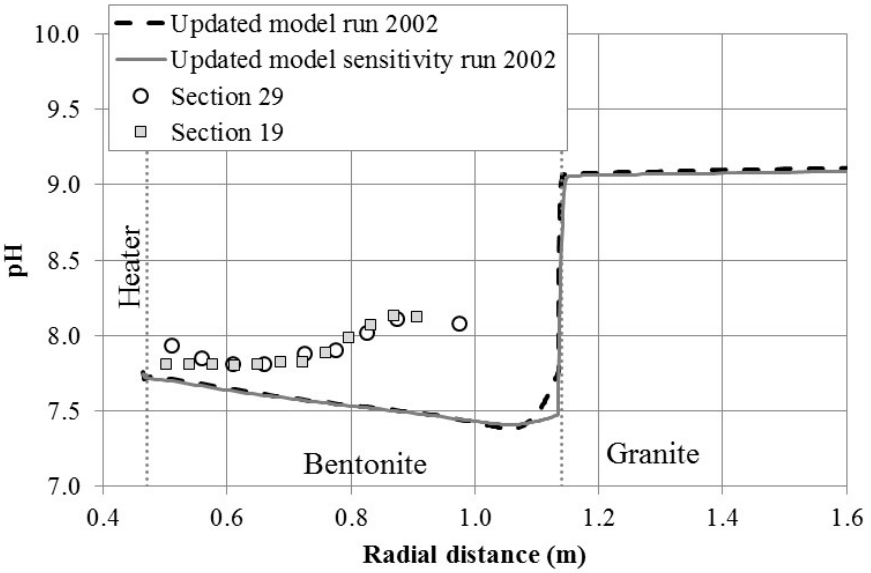

Fig. C-100: Sensitivity of the pH computed (lines) with the updated model in a hot section in 2002 to changes in the bentonite diffusion coefficient

Also shown is the inferred pH in Sections 19 and 29 (symbols).

Sensitivity runs in the cold section

Fig. C-101 to A-108 show the sensitivity of the computed concentrations of dissolved Ca^{2+}, K^{+}, Mg^{2+}, Cl^{-}, Na^{+}, SO_4^{2-} and HCO_3^{-} and pH in a cold section in 2002 to changes in the bentonite diffusion coefficient. The computed concentrations in a cold section correspond to a generic "cold section", which is a section of the bentonite barrier unaffected by the heaters. For illustration purposes, the computed concentrations in the cold section are compared to the inferred concentrations in Section 12 (see Fig. C-4 for the location of Section 12).

These figures also show the inferred concentrations in Section 12. As expected, the radial profiles of the computed concentrations of Ca^{2+}, K^{+}, Mg^{2+}, Na^{+} and HCO_3^{-} become smoother when the bentonite diffusion coefficient is increased. The profiles of Cl^{-} and SO_4^{2-} are less sensitive to a change in diffusion coefficient because the diffusion coefficients of these species are smaller. The computed pH is not sensitive to the change in the diffusion coefficients.

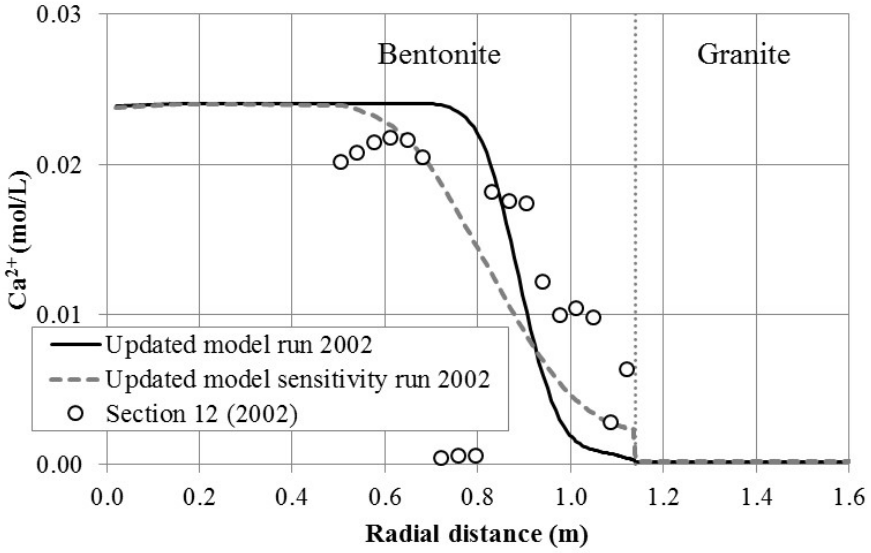

Fig. C-101: Sensitivity of the dissolved Ca^{2+} concentrations computed (lines) with the updated model in a cold section in 2002 to changes in the bentonite diffusion coefficient

Also shown are the inferred Ca^{2+} concentrations in Section 12 (symbols).

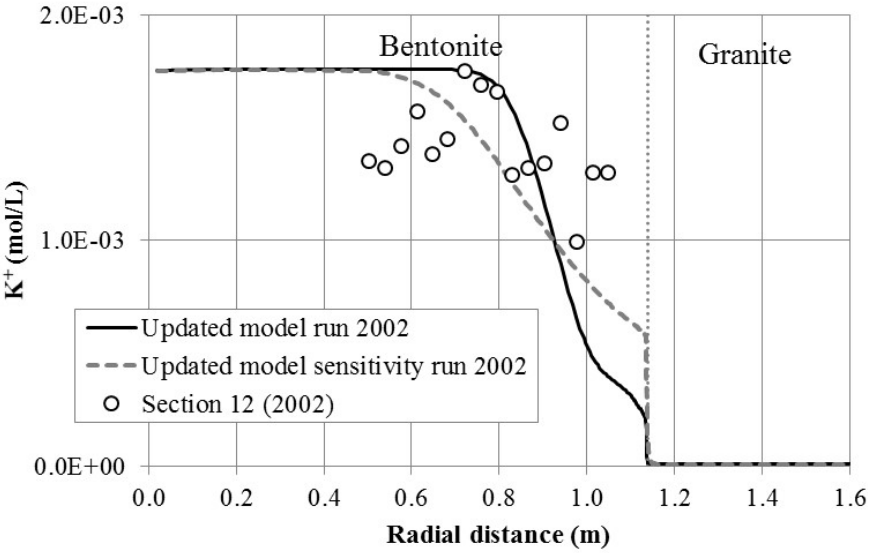

Fig. C-102: Sensitivity of the dissolved K^{+} concentrations computed (lines) with the updated model in a cold section in 2002 to changes in the bentonite diffusion coefficient

Also shown are the inferred K^{+} concentrations in Section 12 (symbols).

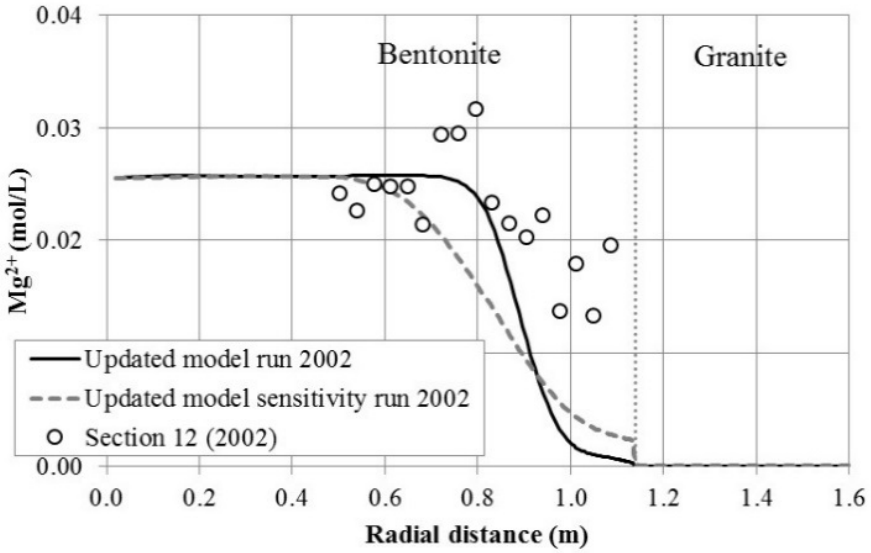

Fig. C-103: Sensitivity of the dissolved Mg^{2+} concentrations computed (lines) with the updated model in a cold section in 2002 to changes in the bentonite diffusion coefficient

Also shown are the inferred Mg^{2+} concentrations in Section 12 (symbols).

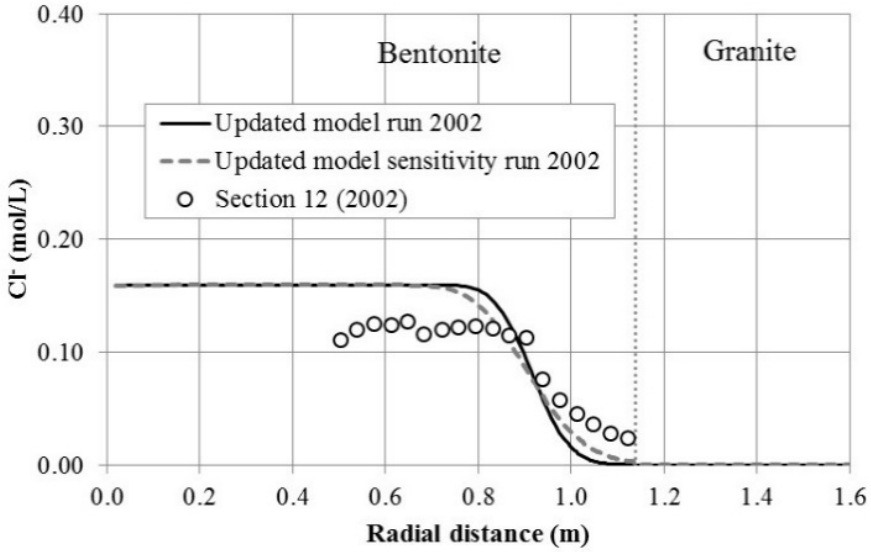

Fig. C-104: Sensitivity of the dissolved Cl^- concentrations computed (lines) with the updated model in a cold section in 2002 to changes in the bentonite diffusion coefficient

Also shown are the inferred Cl^- concentrations in Section 12 (symbols).

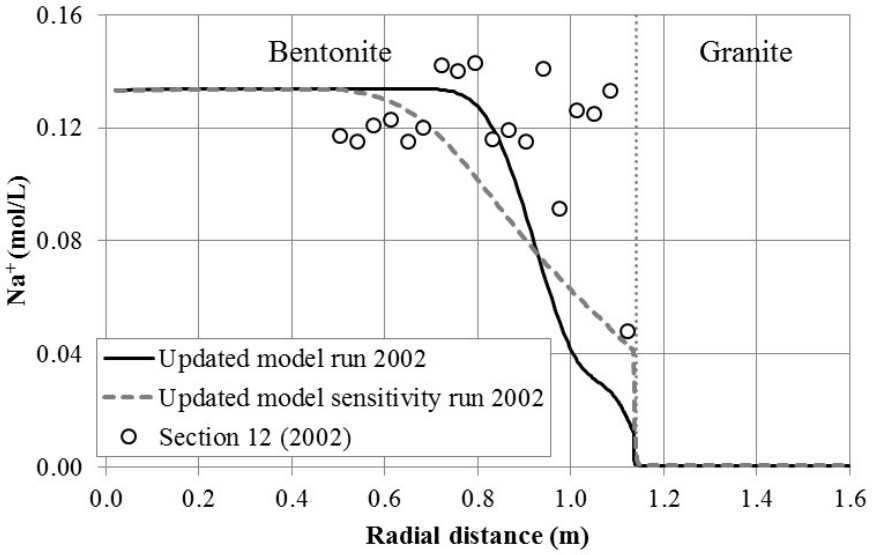

Fig. C-105: Sensitivity of the dissolved Na^+ concentrations computed (lines) with the updated model in a cold section in 2002 to changes in the bentonite diffusion coefficient

Also shown are the inferred Na^+ concentrations in Section 12 (symbols).

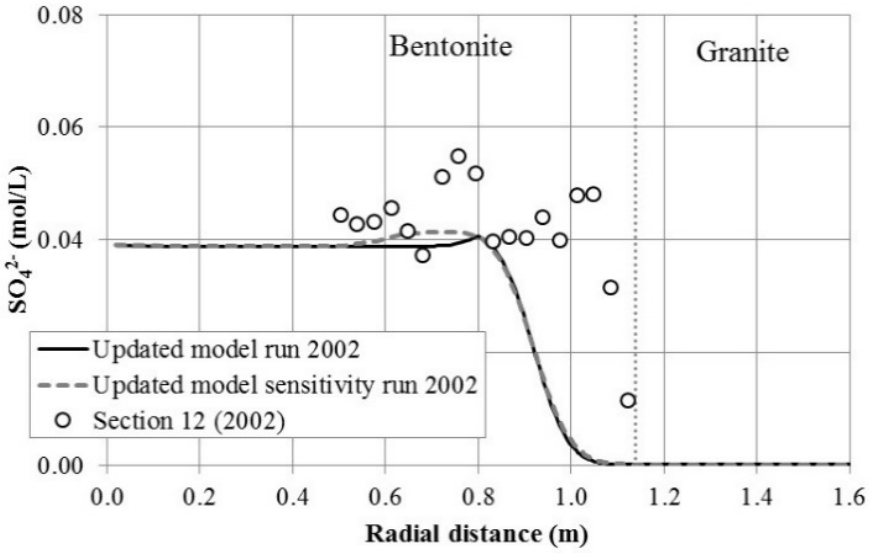

Fig. C-106: Sensitivity of the dissolved SO_4^{2-} concentrations computed (lines) with the updated model in a cold section in 2002 to changes in the diffusion coefficient of the bentonite

Also shown are the inferred SO_4^{2-} concentrations in Section 12 (symbols).

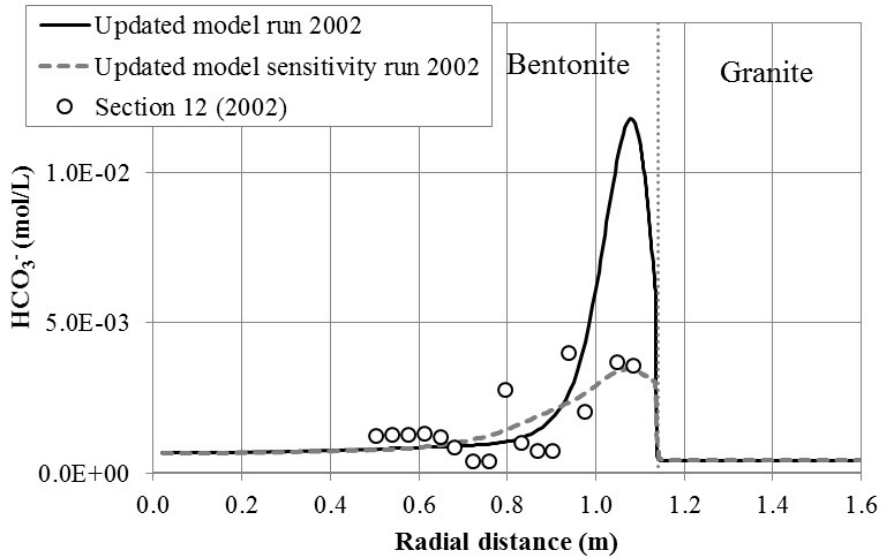

Fig. C-107: Sensitivity of the dissolved HCO_3^- concentrations computed (lines) with the updated model in a cold section in 2002 to changes in the bentonite diffusion coefficient

Also shown are the inferred HCO3- concentrations in Section 12 (symbols).

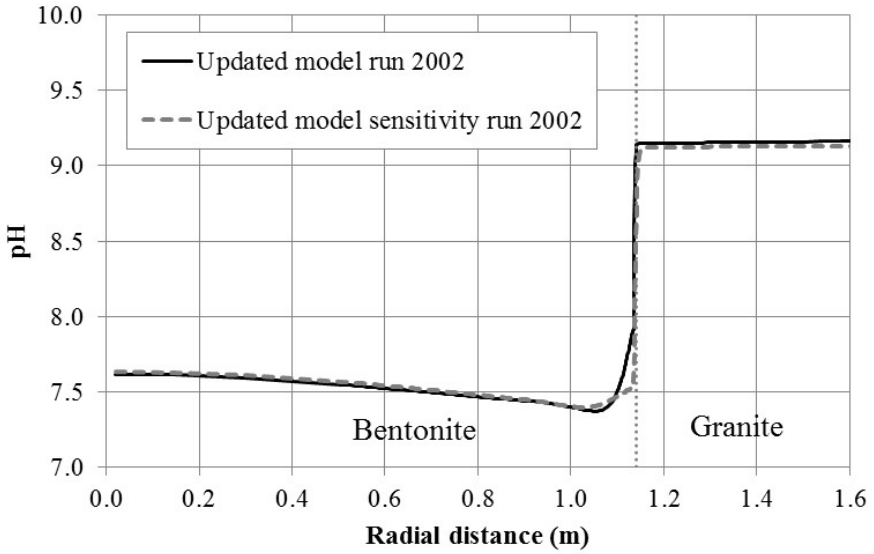

Fig. C-108: Sensitivity of the pH computed (lines) with the updated model in a cold section in 2002 to changes in the bentonite diffusion coefficient

Also shown is the inferred pH in Section 12 (symbols).

C.4.3.4 Conclusions

The previous 1D axisymmetric THCM model of the FEBEX in-situ test has been improved and updated by: 1) Improving the boundary condition at the heater-bentonite interface; 2) Refining the spatial discretization of the finite element mesh; and 3) Modifying the solute dispersivities of the bentonite and granite. The revised implementation of the boundary condition leads to more water evaporation than the previous formulation. The computed concentrations of Ca^{2+}, K^{+}, Mg^{2+}, Cl^{-} and Na^{+} near the heater with the updated model are significantly larger than the concentrations calculated with the reference model. The computed pH and the concentrations of SO_4^{2-} and HCO_3^{-} with the updated model are similar to those of the reference model.

The improvement in the boundary condition at the heater-bentonite interface led to a significant decrease of the mass balance error. The mass balance error for Cl^{-} is reduced from 150 % in the previous model to about 20 % in the updated model. The mass balance errors in the model of the cold section are generally smaller than 10 %. The mass balance errors could be reduced further by refining the finite element grid. However, the computation time increases sharply with the spatial discretization. For this reason, at this stage of the project, the mass balance errors of the updated model are deemed acceptable. They will be reduced in future studies.

The computed concentrations of Ca^{2+}, K^{+}, Mg^{2+}, Na^{+} and HCO_3^{-} become smoother when the bentonite diffusion coefficients are increased by a factor of 10. The profiles of Cl^{-} and SO_4^{2-} are less sensitive to a change in the diffusion coefficient because the diffusion coefficients of these species are smaller than the diffusion coefficients of the rest of the species. The computed pH is not sensitive to the change in the diffusion coefficients.

C.4.4 Comparison of the predictions of the updated model with measured thermal and hydraulic data collected from 2002 to 2015

The updated THCM model presented in the previous section has been used to compare the computed temperatures, relative humidity, water content values and pore water pressures with online measured data collected from 2002 to 2015. The performance of the updated model has been evaluated also by comparing computed values with gravimetric water content data measured after the dismantling of Heater #1 in 2002.

Model predictions have been compared to:

1. Online temperature data
2. Online relative humidity data from capacitive sensors
3. Online water content data from TDR probes
4. Water content data measured after dismantling of Heater #1
5. Water content data measured after dismantling of Heater #2

C.4.4.1 Temperatures

Fig. C-109, Fig. C-110 and Fig. C-111 show the time evolution of the predicted temperatures in a hot section and the measured temperature data in Sections E2 and F2 at the following radial distances: r = 0.48 m, r = 0.82 m and r = 1.10 m.

The temperatures initially increase very fast. This is the thermal transient stage related to heat conduction through the bentonite. Later, the temperatures increase more slowly, which reflects the effect of the heat conducted from the bentonite into the host rock.

One can see in Fig. C-109 that the computed temperatures fit the measured temperature data in hot Sections E2 and F2 at r = 0.48 m. The measured data at r = 0.82 m shows some scatter. The computed temperatures are within the band of measured data and reproduce the increase of temperature from the initial value of 15 °C to about 65 °C at about t = 6'500 days (Fig. C-110).

The computed temperatures near the bentonite-granite interface (r = 1.1 m) reproduce the trends of the measured temperatures. However, the computed temperatures are less than the measured temperatures during the first 2'000 days and higher than the measured temperatures after 2'000 days. At the end of the simulation (t = 6'500 days) the computed temperature is 3 °C higher than the measured temperature (Fig. C-111). This discrepancy could be due to the formulation of the thermal conductivity's dependence of bentonite on water saturation.

The computed temperatures in Fig. C-109, Fig. C-110 and Fig. C-111 correspond to a hot section. They do not show the effect of removing Heater #1, because the 1D THCM model of the hot section does not take into account switching-off Heater #1.

Fig. C-112 and Fig. C-114 show the time evolution of the predicted temperatures in a cold section and the measured temperature data in sections C and B2 at r = 0.6 m and r = 1.10 m. Section C is located between Heater #1 and the original concrete plug, while section B2 is located near the end of the FEBEX gallery. The 1D model for the cold sections was solved by prescribing a time function for the temperature at r = 0. The temperature was set equal to 30 °C before switching-off Heater #1. This temperature was calibrated in order to reproduce the measured temperatures in sections C and B2. The temperature at r = 0 is set equal to the ambient temperature of 12 °C

after switching-off Heater #1. The computed temperatures capture the trends of the measured temperatures. The computed temperatures in section C reproduce the steady increase of temperature before dismantling Heater #1 and the sharp decrease of temperature after switching-off this heater (Fig. C-112 and Fig. C-114).

The computed and the measured temperatures show that the temperature of bentonite near the heater increases instantaneously and then remains sTab. At a value of 97 °C. The temperature decreases with radial distance. The average temperature of the bentonite near the granite contact is around 50 °C. There are small differences between the temperatures registered in the sensors located at the same radial distances, but at different angles. The temperatures are highest in the sensors below the heater. This may induce more water evaporation in these areas.

The measured temperatures data show a decrease of a few degrees caused by switching-off heater#1. This behaviour is not captured by the 1D axisymmetric model.

The measured data of temperature responds faster to the presence of a heat source than the computed temperatures. The slow response to the heat source could be corrected by updating the thermal conductivity law.

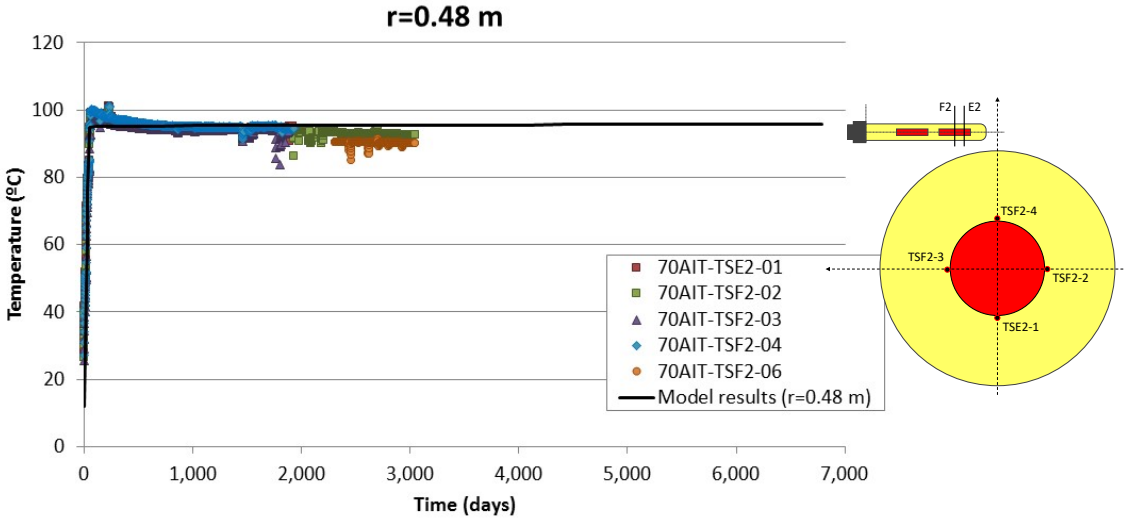

Fig. C-109: Time evolution of the computed (line) and measured temperature data (symbols) in "hot" Sections E2 and F2 at a radial distance r = 0.48 m

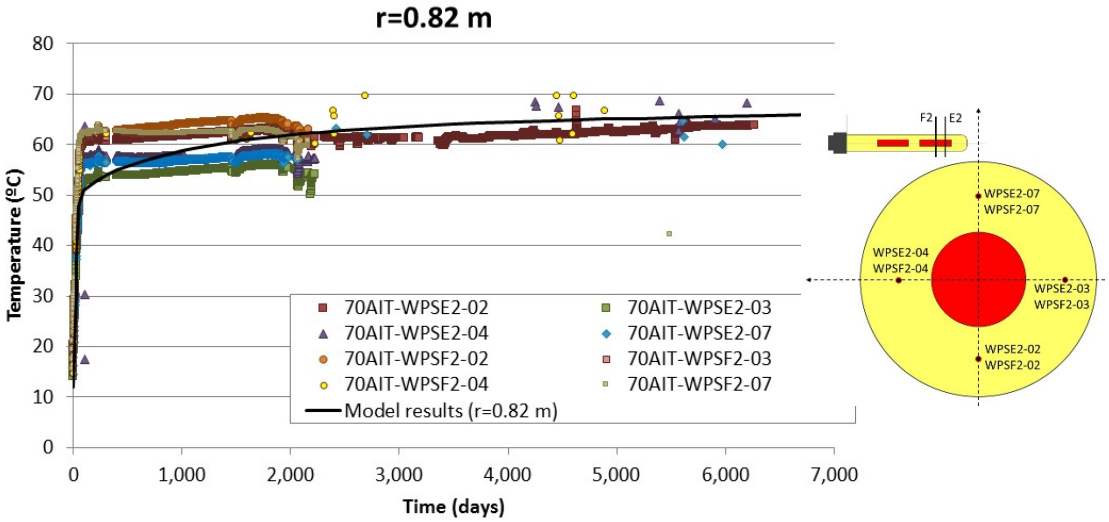

Fig. C-110: Time evolution of the computed (line) and measured temperature data (symbols) in hot Sections E2 and F2 at a radial distance r = 0.80 m

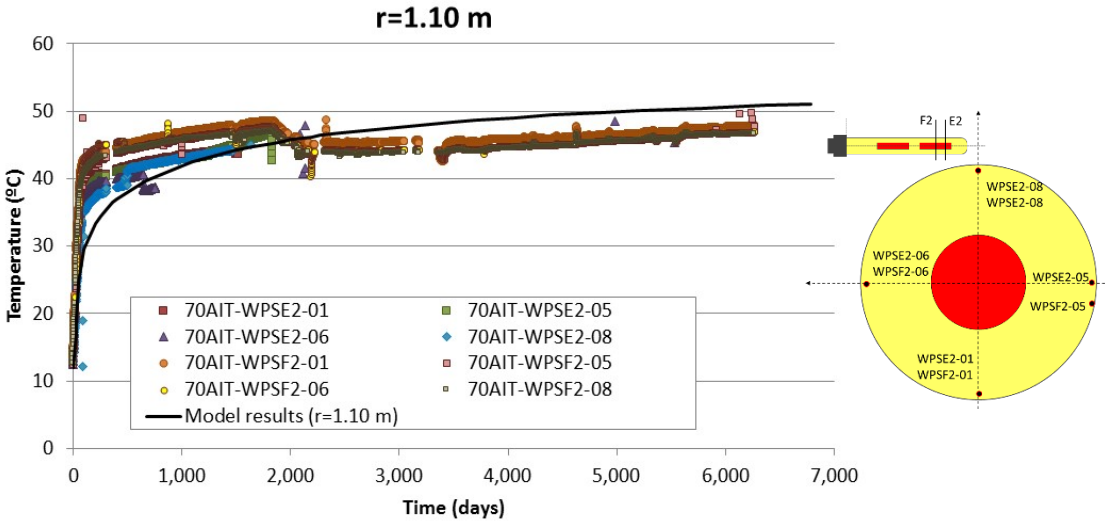

Fig. C-111: Time evolution of the computed (line) and measured temperature data (symbols) in hot Sections E2 and F2 at a radial distance r = 1.10 m

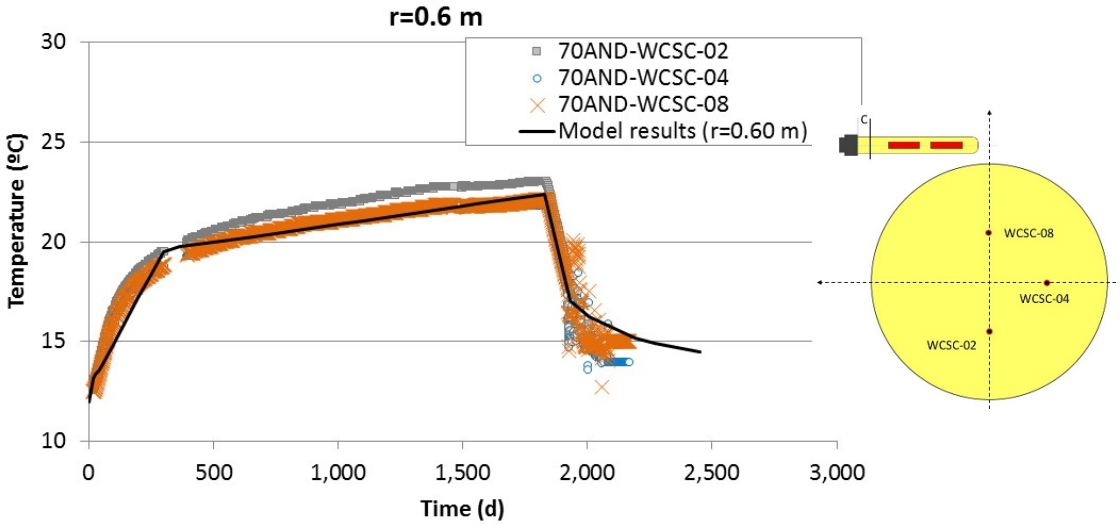

Fig. C-112: Time evolution of the computed (line) and measured temperature data (symbols) in cold section C at a radial distance r = 0.6 m

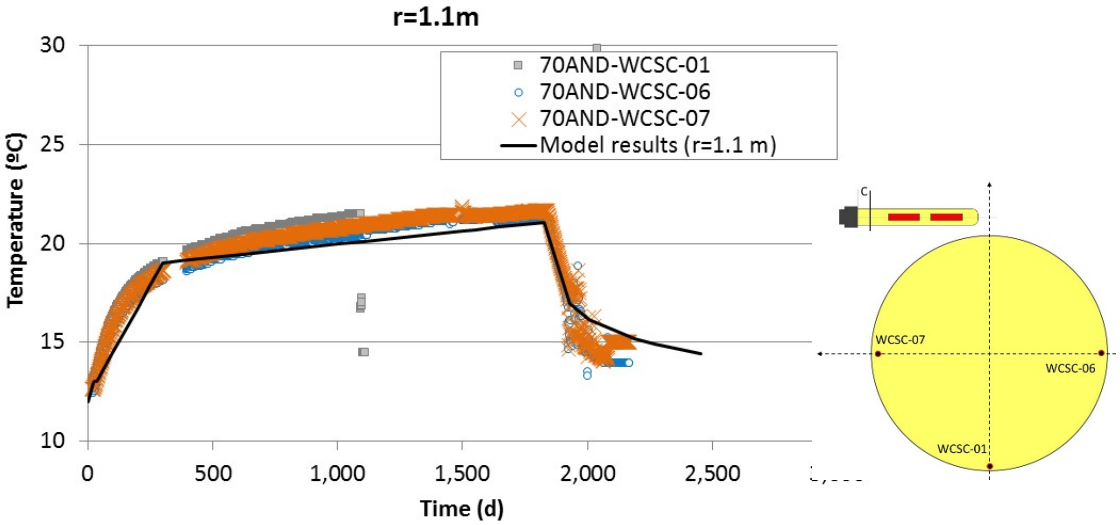

Fig. C-113: Time evolution of the computed (line) and measured temperature data (symbols) in cold section C at a radial distance r = 1.1 m

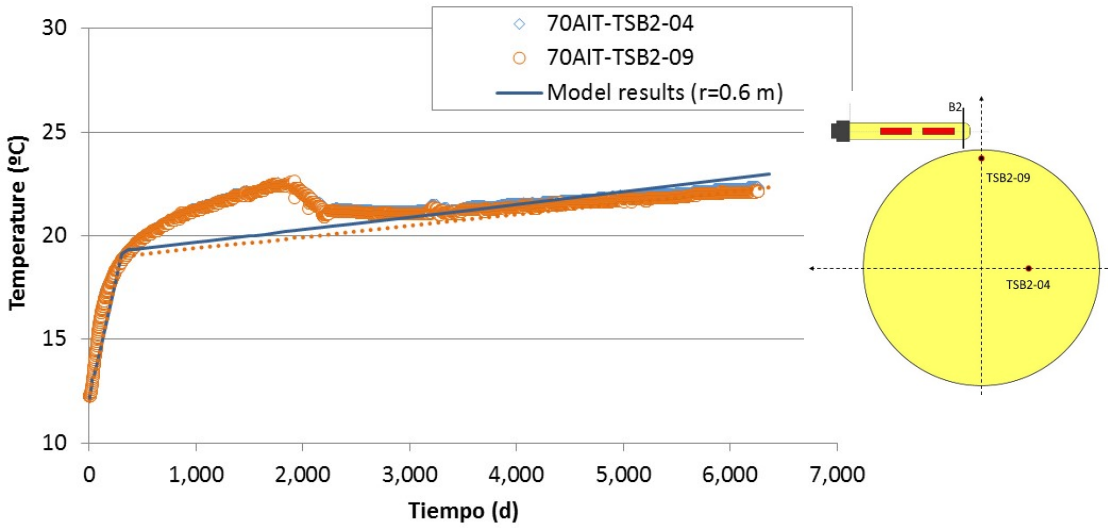

Fig. C-114: Time evolution of the computed (line) and measured temperature data (symbols) in cold section B2 located at the end of the FEBEX gallery at a radial distance r = 1.1 m

C.4.4.2 Relative humidity and water content

Fig. C-115 and Fig. C-116 show the time evolution of the computed and measured relative humidity in the hot Sections E2 and F2 at radial distances r = 0.8 m and r = 1.05 m. Data at r = 0.8 m show a large scatter. Relative humidity increases with time. The computed relative humidity reproduces this trend. The relative humidity near the bentonite-granite interface also has a large scatter and reaches about 100 % after 2'000 days. The computed relative humidity increases quickly and reaches a value above 95 % after 1'000 days.

Fig. C-117, Fig. C-118 and Fig. C-119 show the time evolution of the computed relative humidity in a cold section and the measured relative humidity data in section C at radial distances r = 0, 0.6 and r = 1.10 m. Data are available for t < 2000 days because this section was dismantled in 2002. The computed relative humidity reproduces the increasing trends of the measured values. Relative humidity is slightly overestimated at r = 0 and r = 0.6 m. Measured and computed relative humidity near the bentonite-granite interface reach a value of about 100 % very quickly.

The measured relative humidity data show some fluctuations. In some cases, some sensors provide erroneous data when they fail. For the most part, relative humidity data show axial symmetry. However, the data at some locations are slightly larger or smaller than the average.

Water content was measured with TDR sensors in the hot Section M2. These sensors were available until the dismantling of Heater #2. Sakaki et al. (2016) analysed the TDR water content measurements in the bentonite blocks for 18 years. They concluded that the volumetric water content data derived from TDRs showed a good agreement with on-site sample results. The 18-year water content evolution was captured reasonably well with TDR. According to Sakaki et al. (2016), sensor 4 failed to provide accurate data. Fig. C-120, Fig. C-121, Fig. C-122 and Fig. C-123 show the time evolution of the computed volumetric water content in a hot section and the measured TDR water content data in Section M2. The computed water content values reproduce the time evolution of the measured water content data, except at r = 0.59 m. One of the sensors at

this location gave erroneous signals. Therefore, these measured data should be taken with caution. The computed values achieve the best fit to measured data at r = 1.04 m.

The water content data measured at r = 0.59 m could be erroneous because these data show different trends than other sensors. The measured water content at the same radial distance from the heater shows different values at different locations. The largest water content values were measured in sensors located on the right side of the tunnel. This could be due to a larger water inflow from the granite in this section.

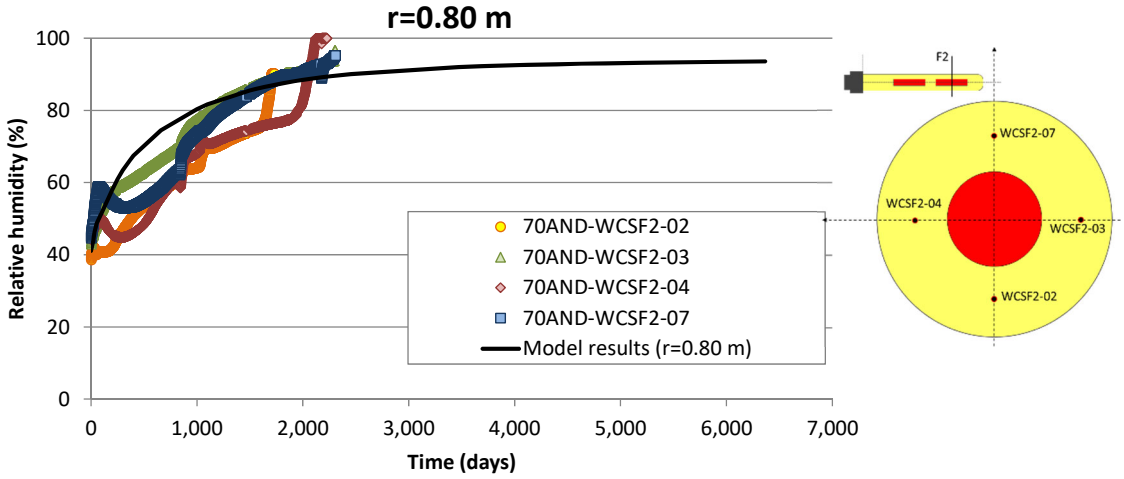

Fig. C-115: Time evolution of the computed (line) and measured relative humidity data (symbols) in hot section F2 at a radial distance r = 0.8 m

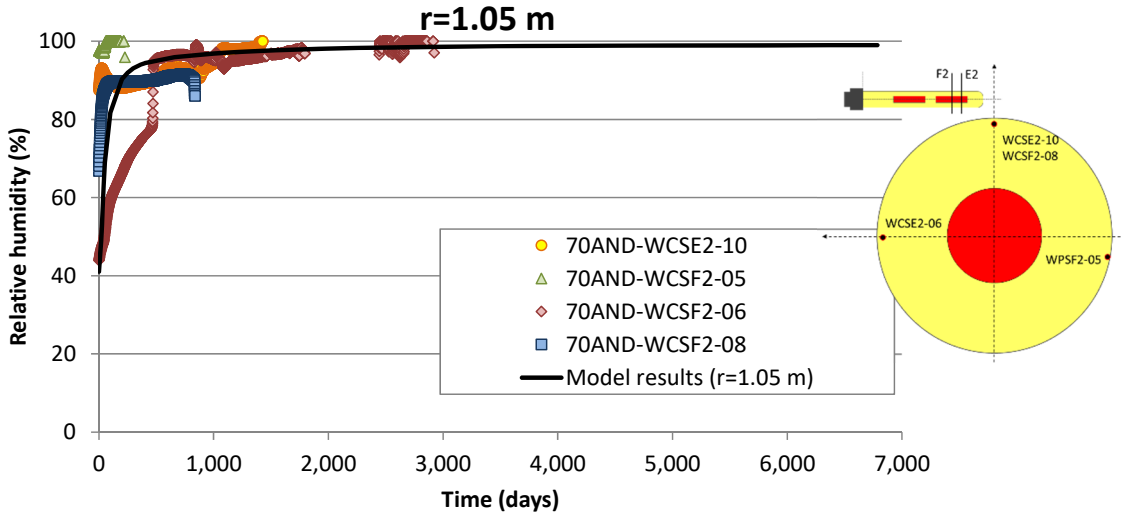

Fig. C-116: Time evolution of the computed (line) and measured relative humidity data (symbols) in hot Sections E2 and F2 at a radial distance r = 1.05 m.

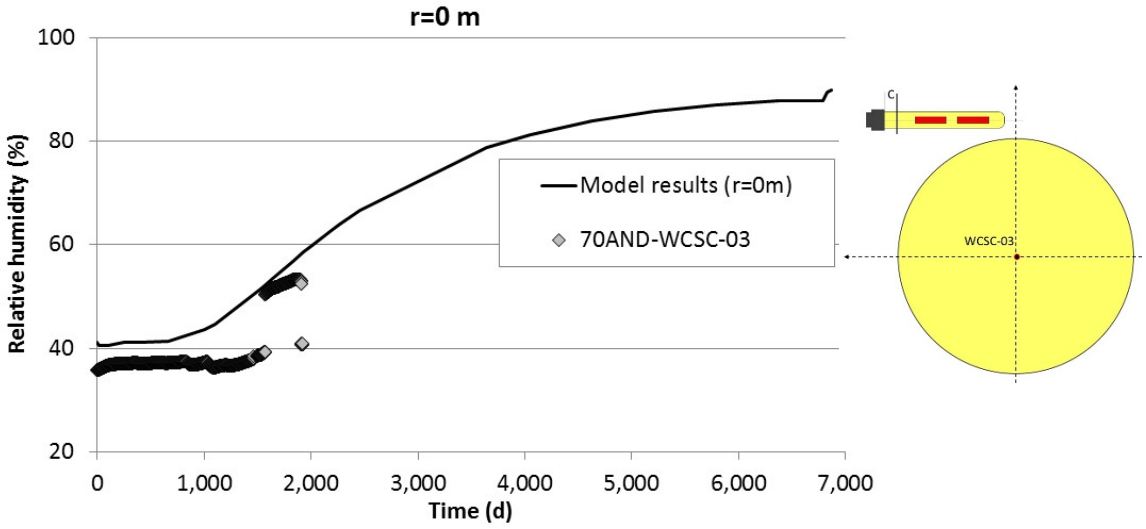

Fig. C-117: Time evolution of the computed (line) and measured relative humidity data (symbols) at the centre (r = 0) of cold section C located between Heater #1 and the original concrete plug

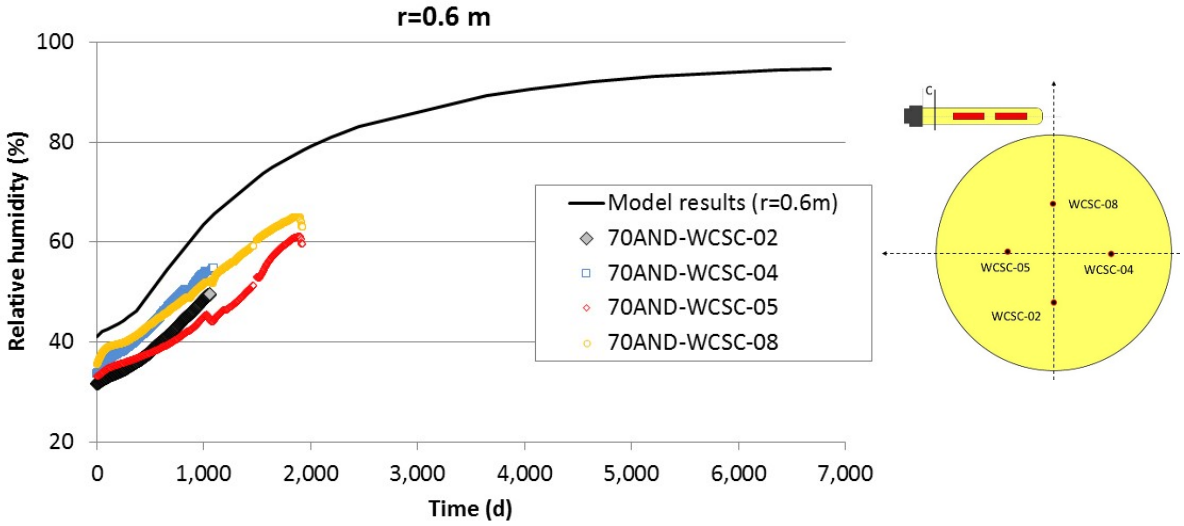

Fig. C-118: Time evolution of the computed (line) and measured relative humidity data (symbols) in cold section C located between Heater #1 and the original concrete plug at a radial distance r = 0.6 m

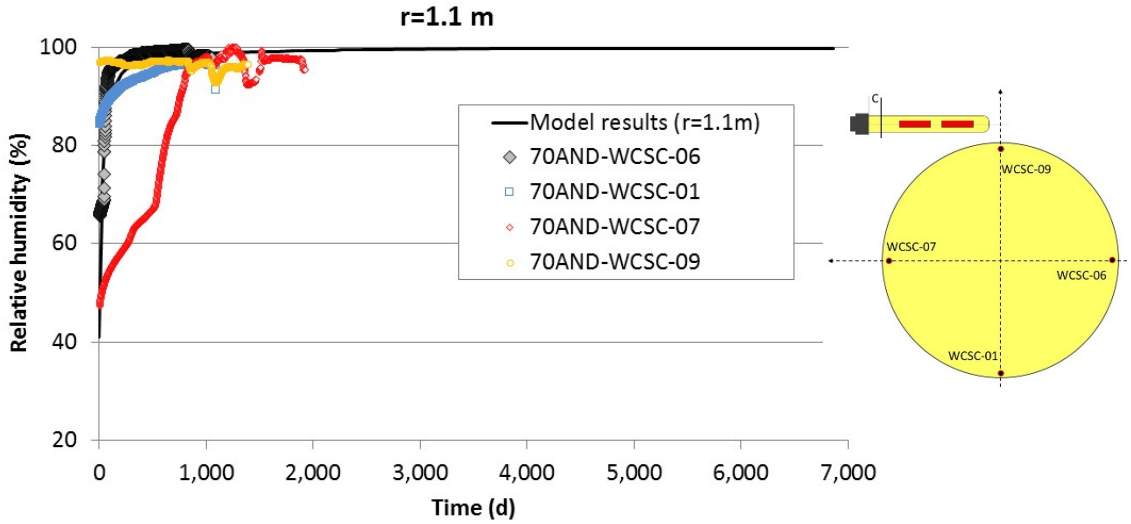

Fig. C-119: Time evolution of the computed (line) and measured relative humidity data (symbols) in cold section C located between Heater #1 and the original concrete plug at a radial distance r = 1.1 m

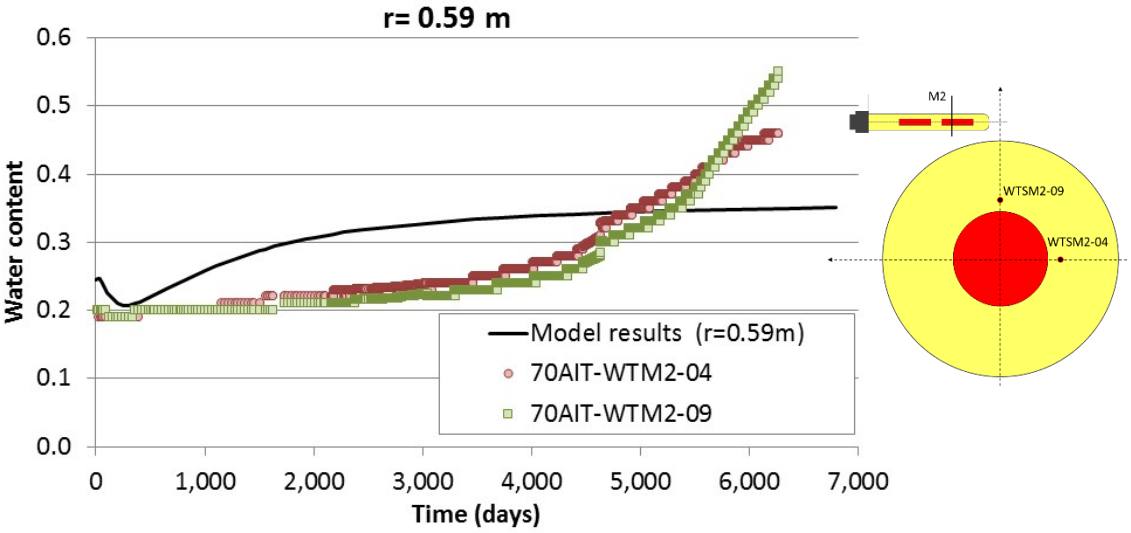

Fig. C-120: Time evolution of the computed (line) and measured TDR water content data (symbols) in hot Section M2 at a radial distance r = 0.59 m

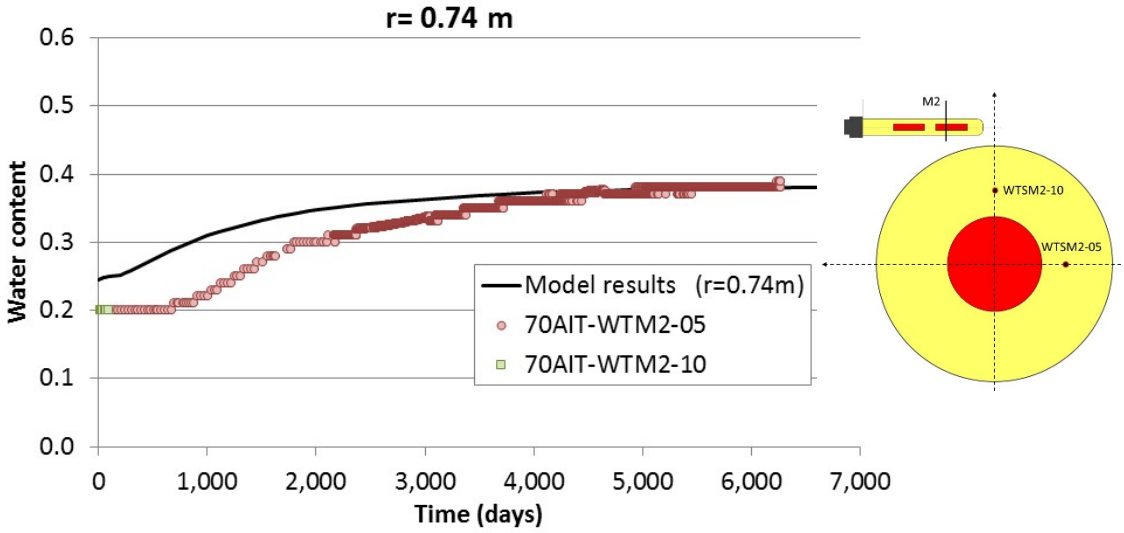

Fig. C-121: Time evolution of the computed (line) and measured TDR water content data (symbols) in hot Section M2 at a radial distance r = 0.74 m

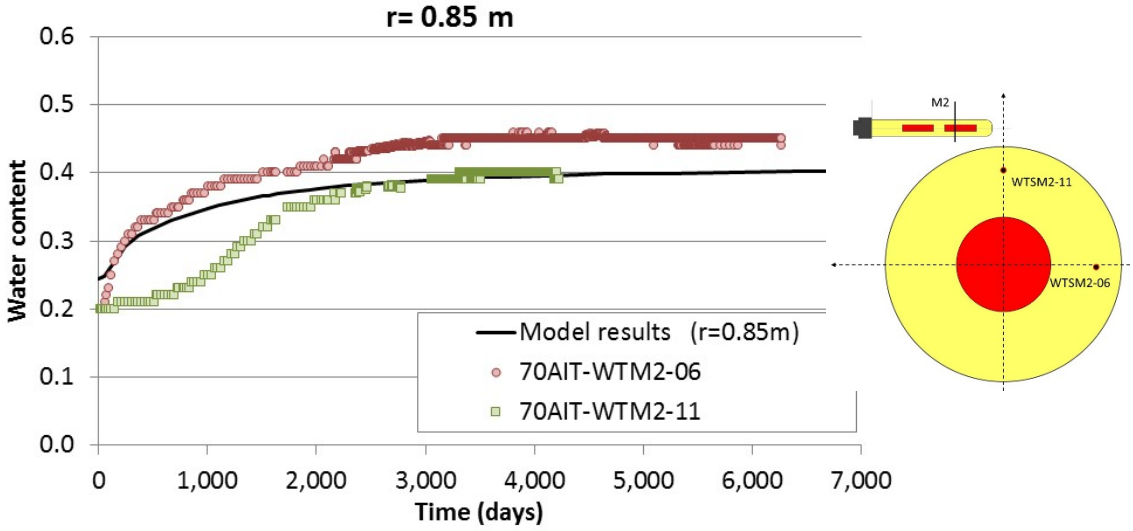

Fig. C-122: Time evolution of the computed (line) and measured TDR water content data (symbols) in hot Section M2 at a radial distance r = 0.85 m

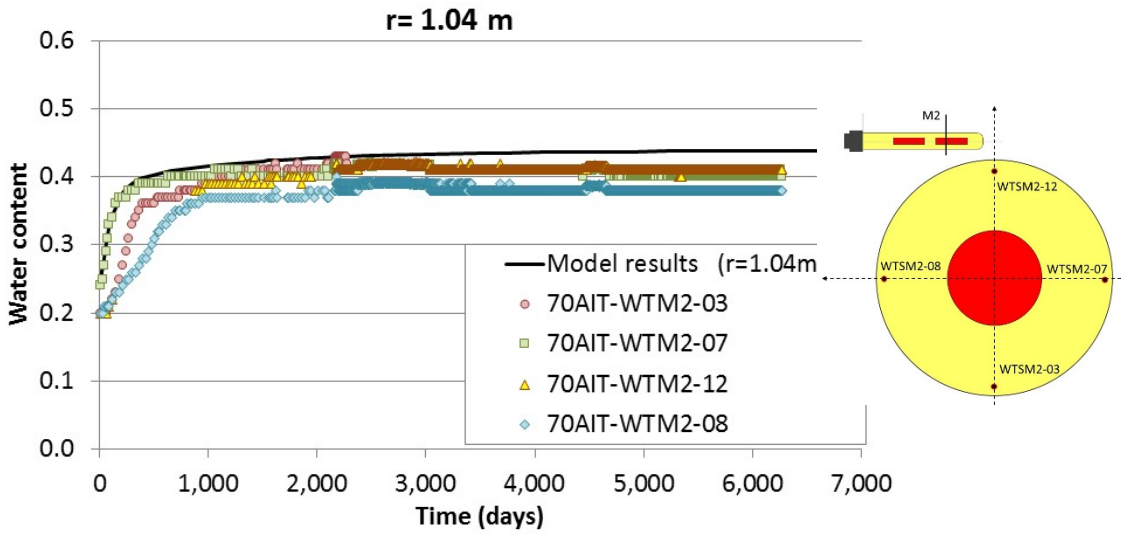

Fig. C-123: Time evolution of the computed (line) and measured TDR water content data (symbols) in hot Section M2 at a radial distance r = 1.04 m

C.4.4.3 Pore water pressures

Fig. C-124, Fig. C-125 and Fig. C-126 show the time evolution of computed pore water pressures in a hot section and the measured pore water pressures in several packed-off sections of boreholes drilled in the granitic rock surrounding the FEBEX gallery in section F2. Measured water pressures show fluctuations caused by water sampling and ambient perturbations and a large scatter due to the spatial variability of the permeability of the granitic rock. The computed water pressures decrease sharply at the beginning and then increase steadily with time in a manner similar to the measured data. The computed pressures at r = 3.03 m are slightly smaller than the measured values due to heterogeneities of the granitic rock, which are not taken into account in the model. The discrepancies in the water pressures increase with radial distance. These discrepancies could also be due to the uncertainty in the prescribed water pressure at the outer boundary.

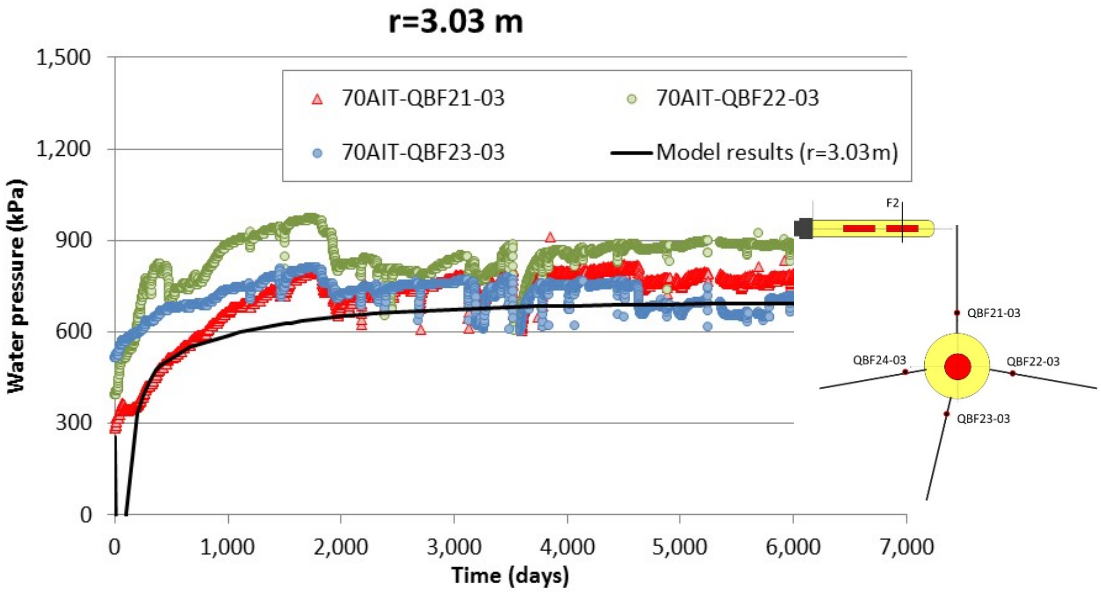

Fig. C-124: Time evolution of the computed (line) and measured pore water pressure (symbols) in the granite rock at a radial distance of 3.03 m

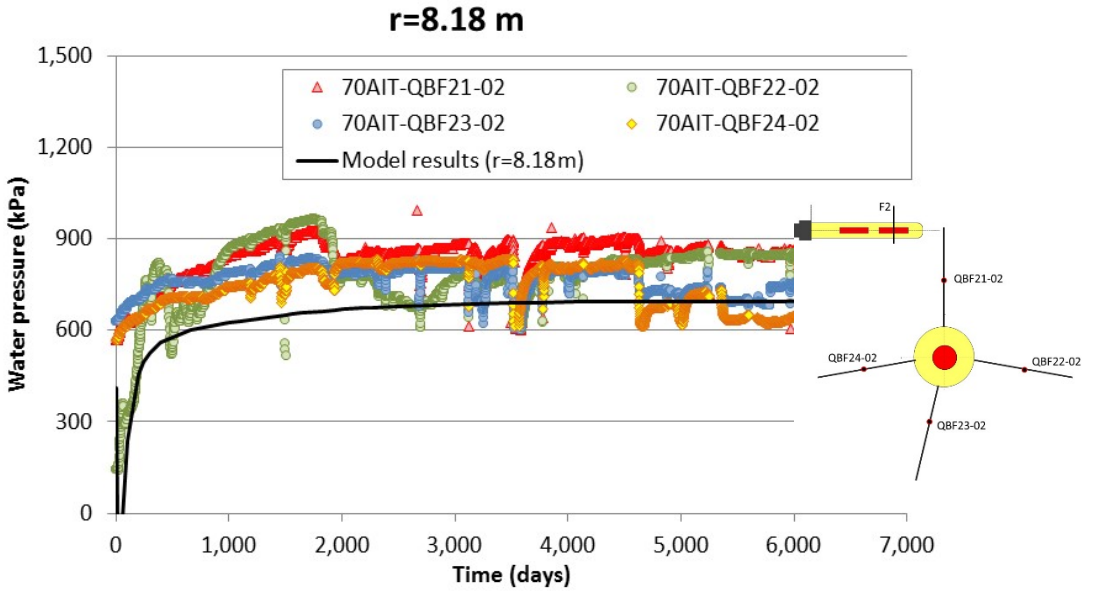

Fig. C-125: Time evolution of the computed (line) and measured pore water pressure (symbols) in the granite rock at a radial distance of 8.18 m

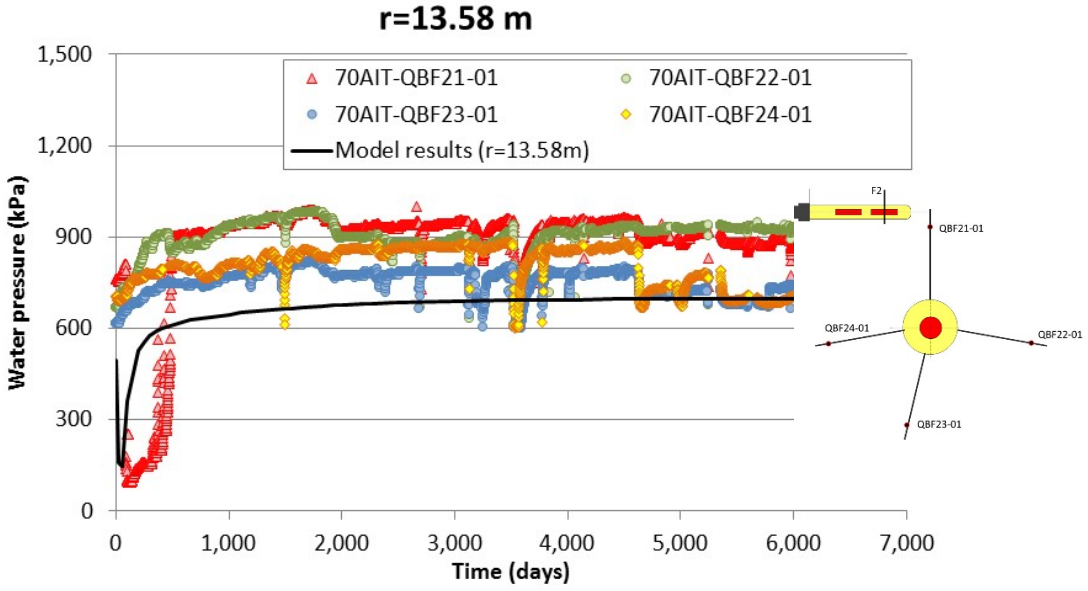

Fig. C-126: Time evolution of the computed (line) and measured pore water pressure (symbols) in the granite rock at a radial distance of 16.58 m

C.4.4.4 Water content and dry density after dismantling

Fig. C-127 compares the predicted gravimetric water content in a hot section and the measured water data in sections S22, S27, S45, S49 and S52 located at the centre of the heaters at the time of dismantling Heater #1 (in 2002) and Heater #2 (in 2015). One can see that the predicted water contents are within the band of measured data and match the general trends.

Fig. C-128 compares the predicted and measured dry density in hot sections S22, S27, S45, S49 and S52 at the time of dismantling Heater #1 (in 2002) and Heater #2 (in 2015). The predicted dry density in 2015 increases slightly compared to the density in 2002. The predicted dry densities are within the band of measured data which show a large scatter.

Fig. C-129 compares the predicted gravimetric water content and the measured gravimetric water data in cold sections S9, S15 and S58 at the time of dismantling Heater #1 (in 2002) and Heater #2 (in 2015). One can see that the predicted water content values are, mostly, within the band of measured data.

Fig. C-130 compares the predicted and the measured dry densities in cold sections S9, S15 and S58 at the time of dismantling Heater #1 (in 2002) and Heater #2 (in 2015). The predicted dry density in 2015 increases significantly compared to the density in 2002. The predicted dry density values in 2015 are larger than measured data for $0.40 < r$ 1.1 m. The predicted dry densities for $r < 0.40$ m are within the band of measured data.

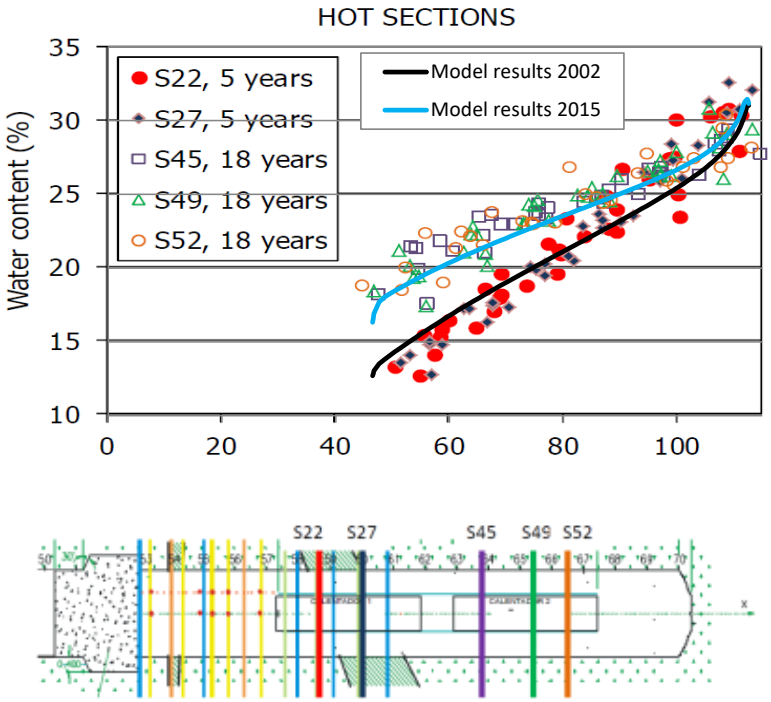

Fig. C-127: Comparison of predicted gravimetric water content (lines) in a hot section and the measured gravimetric water content data (symbols) in Sections S22, S27, S45, S49 and S52 at the time of dismantling Heater #1 (year 2002) and Heater #2 (year 2015)

The plot at the bottom shows the location of the sections where water contents were measured.

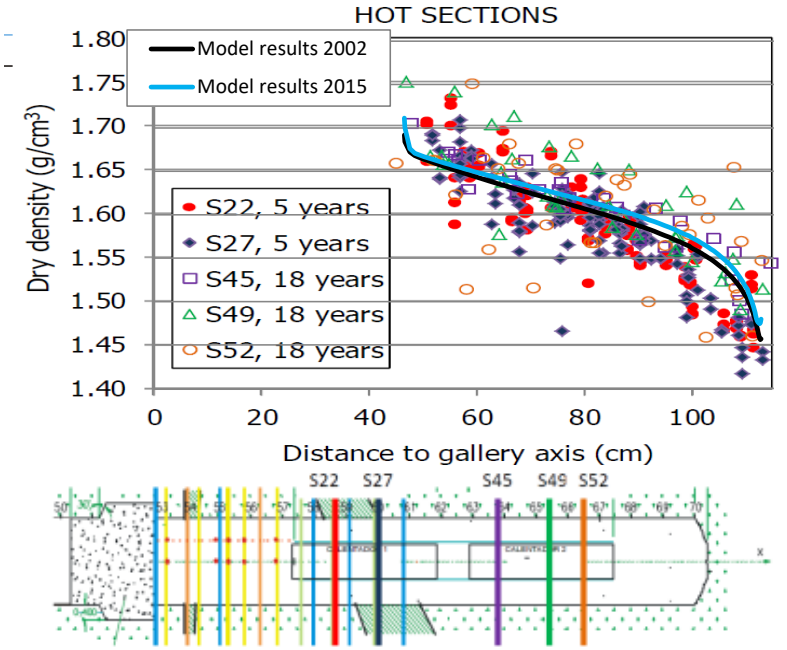

Fig. C-128: Comparison of predicted dry density (lines) in a hot section and the measured dry density data (symbols) in Sections S22, S27, S45, S49 and S52 at the time of dismantling Heater #1 (year 2002) and Heater #2 (year 2015)

The plot at the bottom shows the location of the sections where dry densities were measured.

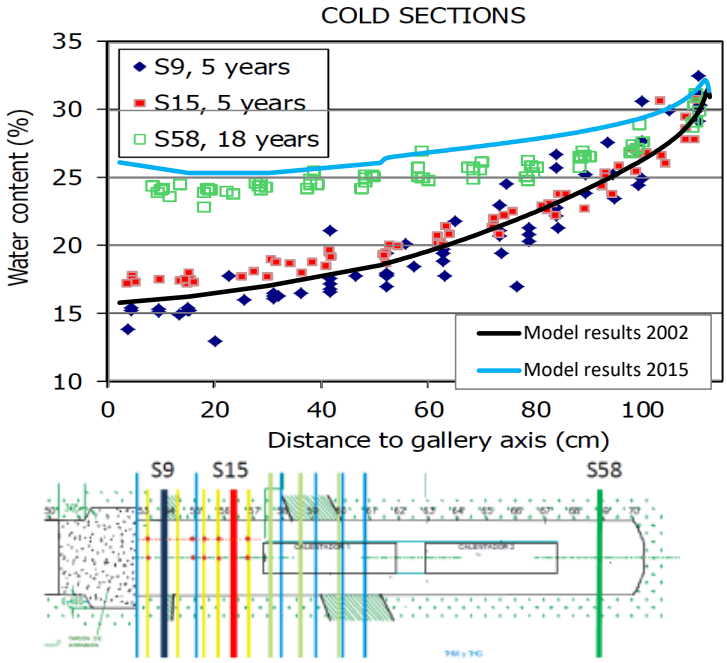

Fig. C-129: Comparison of predicted gravimetric water content (lines) in a cold section and the measured gravimetric water content data (symbols) in Sections S9, S15 and S58 at the time of dismantling Heater #1 (year 2002) and Heater #2 (year 2015)

The plot at the bottom shows the location of the sections where water contents were measured.

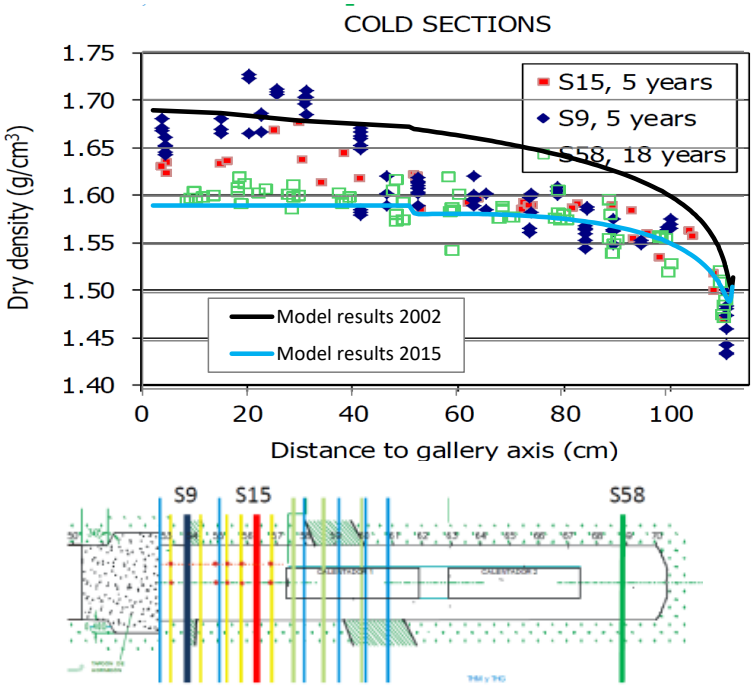

Fig. C-130: Comparison of predicted dry density (lines) in a cold section and the measured dry density data (symbols) in Sections S9, S15 and S58 at the time of dismantling Heater #1 (year 2002) and Heater #2 (year 2015)

The plot at the bottom shows the location of the sections where dry densities were measured.

C.4.4.5 Conclusions

The updated 1D axisymmetric THCM model of the FEBEX in-situ test was tested with gravimetric water content data measured at the dismantling of Heater #1 in 2002 and Heater #2 in 2015 as well as online temperature, relative humidity, water content, and pore water pressure in the granitic rock data collected from 2002 to 2015.

The comparison of the computed values with the measured data leads to the following major conclusions:

1. The numerical model reproduces the main trends of the temperature data. The computed temperatures near the bentonite-granite interface in hot sections are less than the measured temperatures during the first 2000 days and higher than the measured temperatures after 2000 days. The computed temperature in 2015 is 3 °C higher than the measured temperature at the bentonite-granite interface. The computed temperatures in the cold Section C, located between Heater #1 and the original concrete plug, reproduce the steady increase of temperature before dismantling Heater #1 and the sharp decrease of temperature after switching-off this heater.
2. The computed relative humidity reproduces the general trends of the measured relative humidity data.
3. The computed time evolution of the water content in the hot section reproduces the time evolution of the measured TDR water content data, except at r = 0.59 m. The best fit of computed values to measured data is achieved at r = 1.04 m, especially at the sensor on the right side of the tunnel.
4. The computed pore water pressures at the granitic rock are smaller than the measured values due to the heterogeneities of the granitic rock, which are not taken into account in the model and the uncertainty in the prescribed pore water pressure at the external boundary.
5. The predicted water content values in a hot section and a cold section at the time of dismantling Heater #1 (in 2002) and Heater #2 (in 2015) are within the band of measured data and match the general trend of the measured data.

The predicted dry density in a cold and hot section at the time of dismantling Heater #1 (in 2002) and Heater #2 (in 2015) is, generally, within the band of measured data. There are some discrepancies in the hot and cold sections in 2002. The computed dry density overestimates the measured dry density near the heater ($0.7\ m < r < 1\ m$); this discrepancy is not observed in 2015.

C.5 Pre-dismantling THCM model predictions

The THCM model of Zheng et al. (2011) was extended by improving the boundary condition at the heater/bentonite interface, refining the spatial discretization of the finite element mesh near the heater, revising the dispersivities of the bentonite and the granite and revisiting the back-diffusion of solutes from the bentonite barrier into the granite. This extended model simulated the two operation periods of the FEBEX in-situ test. The results of the revisited THCM model were compared to gravimetric water content data measured at the end of the 1st and 2nd operational periods and online data of temperature and volumetric water content in the bentonite and pore water pressure in the granitic rock collected from 2002 to 2015. Blind predictions of the geochemical conditions at the end of the 2nd operation period were performed with the revisited THCM model.

This chapter presents the pre-dismantling predictions of the geochemical conditions in hot and cold sections of the bentonite barrier at the time of dismantling Heater #2 (June 2015). Prediction uncertainties have been quantified by sensitivity runs to key model parameters such as the diffusion coefficients.

C.5.1 Predictions for the hot section

Fig. C-131 to A-138 show the pre-dismantling THCM predictions of the dissolved Cl^-, Ca^{2+}, K^+, Mg^{2+}, Na^+, SO_4^{2-}, HCO_3^- concentrations and pH in 2002 and 2015 in a hot section. The computed concentrations of the chemical species in 2002 and 2015 correspond to the end of the cooling phase. Model predictions in 2002 are compared to data derived from aqueous extract data at Sections 19 and 29. The comparison between model calculations and aqueous extract data show that the model reproduces the trends of the measured data for the most part, but there are some deviations at the heater-bentonite and bentonite-granite interfaces.

The spatial distribution of the concentration of a conservative species such as Cl^- depends on the inward displacement of the hydration front, the water evaporation at the heater-bentonite contact, solute diffusion within the bentonite barrier and backwards diffusion from the bentonite into the granite. Fig. C-131 shows the computed radial distribution of Cl^- concentrations in 2002 and 2015 and the derived aqueous extract data in 2002 in Sections 19 and 29. The measured Cl^- concentration is small close to the bentonite-granite interface and then levels off closer to the heater. The computed Cl^- concentrations are largest near the heater due to the evaporation of the bentonite pore water and smallest at the granite-bentonite interface due to the hydration of the buffer with granite pore water, which has a concentration smaller than that of the bentonite. The predicted concentrations of Cl^- in 2015 show a pattern similar to that of the computed concentrations in 2002, but are much smaller than those of 2002.

The predicted Cl^- diffusion into the rock is small for the adopted effective diffusion of the granite, D_e. The experimental observation of Cl^- backwards diffusion from the bentonite into the granite seems to indicate that the actual D_e of the granite diffusion is probably larger than the D_e used in the model.

The concentrations of dissolved cations (Ca^{2+}, Mg^{2+}, Na^+ and K^+) show trends similar to those of the concentration of Cl^-. Mineral dissolution/precipitation and cation exchange affect their concentrations. Fig. C-132 represents the predictions of the dissolved Ca^{2+} concentration in 2002 and 2015 in a hot section. Water evaporation near the heater causes an increase in the dissolved

Ca^{2+} concentration, which in turn results in calcite precipitation. Consequently, the dissolved Ca^{2+} concentration decreases near the heater-bentonite interface.

The concentrations of other dissolved cations such as Mg^{2+} (Fig. C-133), Na^{+} (Fig. C-134) and K^{+} (Fig. C-135) in 2015 are also large near the heater and decrease towards the bentonite-granite interface.

Fig. C-136 shows the measured and computed radial distribution of SO_4^{2-} concentrations in 2002 and 2015 and the comparison with derived aqueous extract data (Sections 19 and 29) at 2002. The computed SO_4^{2-} concentrations in 2002 underestimate the derived aqueous extract data near the bentonite-granite interface, possibly due to uncertainties in the initial amount of gypsum in the bentonite. Model predictions show that the concentration of SO_4^{2-} in 2015 will increase near the heater and decrease in the rest of the bentonite barrier compared to the concentration of SO_4^{2-} in 2002.

The hydration of bentonite with granite water induces the dissolution of calcite near the bentonite/granite interface. Consequently, the computed HCO_3^{-} concentration increases near the bentonite-granite interface (Fig. C-137). There is a front of high concentrations of HCO_3^{-} which diffuses into the bentonite causing calcite precipitation and a decrease of pH. This can be seen in the low pH computed near the granite-bentonite interface (Fig. C-138). Model predictions show that the concentration of HCO_3^{-} in 2015 will increase due to the dissolution front of the calcite. The concentration will increase near the heater due to significant calcite precipitation.

The pH in the bentonite is buffered by surface protonation reactions and calcite dissolution-precipitation (see Fig. C-139). The pH evolution is the result of the combined effect of several chemical reactions. There are uncertainties in: 1) The initial pH of bentonite pore water and 2) The degassing of $CO_{2(g)}$ from the liquid which is not taken into account in the model. The $CO_{2(g)}$ released near the heater could migrate through the gas phase and re-dissolve in the condensation zone. $CO_{2(g)}$ degassing and dissolution could affect pH, the concentration of dissolved HCO_3^{-} and calcite dissolution and precipitation. The predicted pH in 2015 is similar to that in 2002.

Fig. C-139 shows the predictions of cumulative calcite dissolution (negative)/precipitation (positive) in 2002 and 2015 in a hot section. Calcite dissolves near the bentonite/granite interface and precipitates near the heater.

The initial volume fraction of anhydrite is zero. Anhydrite starts to precipitate after heating because anhydrite is more stable than gypsum at temperatures above 43 °C. At 1'827 days, near the granite-bentonite interface, the initially precipitated anhydrite is dissolved, but near the heater there is still some anhydrite (Fig. C-141). When Heater #1 was switched off after 1'827 days, the bentonite barrier was cooled and anhydrite dissolved due to the temperature decrease. Gypsum shows the opposite trend: all the gypsum was dissolved before cooling ($t < 1'827$ days). Anhydrite converted into gypsum near the heater after cooling at 1'930 days (Fig. C-140).

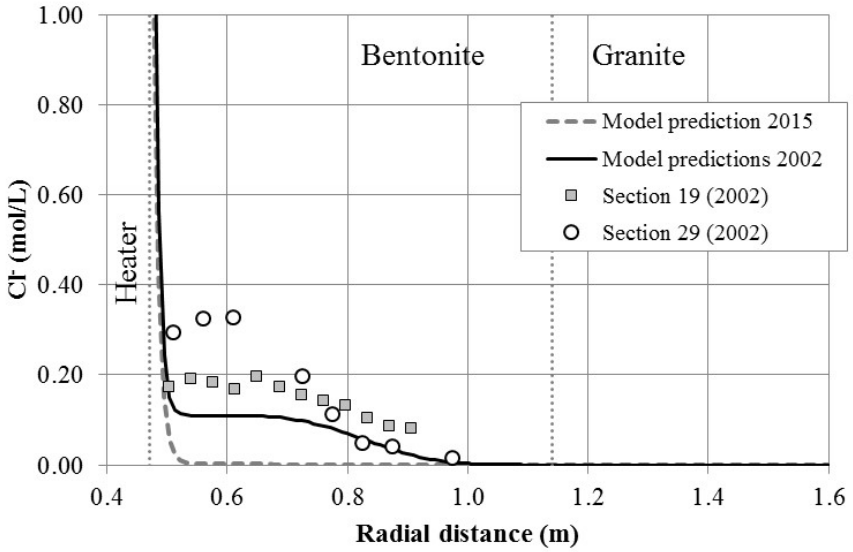

Fig. C-131: Pre-dismantling predictions of Cl^- concentrations (lines) in 2002 and 2015 in a hot section

The graph also shows the derived Cl^- concentrations in Sections 19 and 29 (symbols) in 2002.

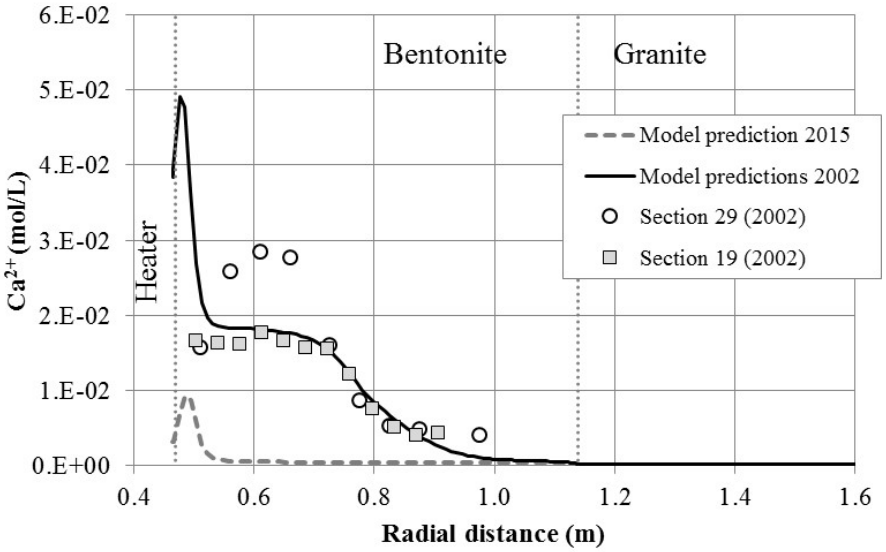

Fig. C-132: Pre-dismantling predictions of Ca^{2+} concentrations (lines) in 2002 and 2015 in a hot section

The graph also shows the derived Ca^{2+} concentrations in Sections 19 and 29 (symbols) in 2002.

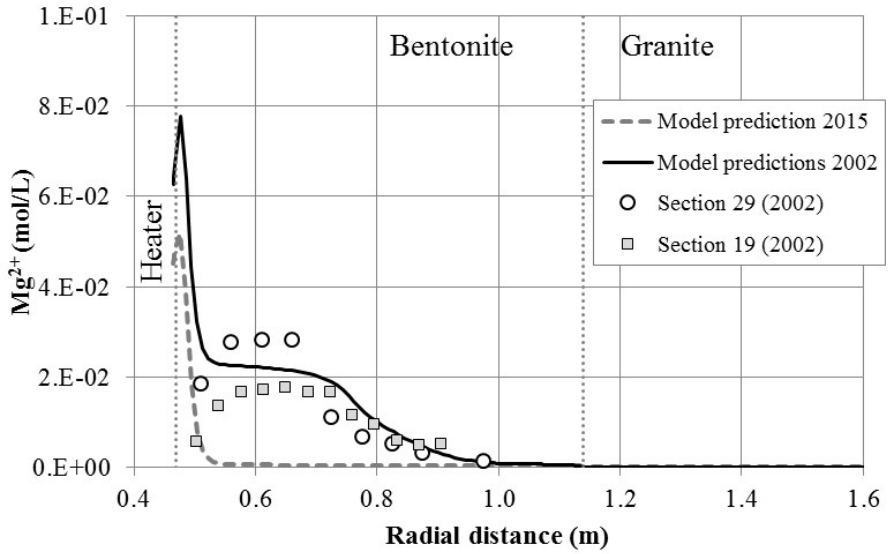

Fig. C-133: Pre-dismantling predictions of Mg^{2+} concentrations (lines) in 2002 and 2015 in a hot section

The graph also shows the derived Mg^{2+} concentrations in Sections 19 and 29 (symbols) in 2002.

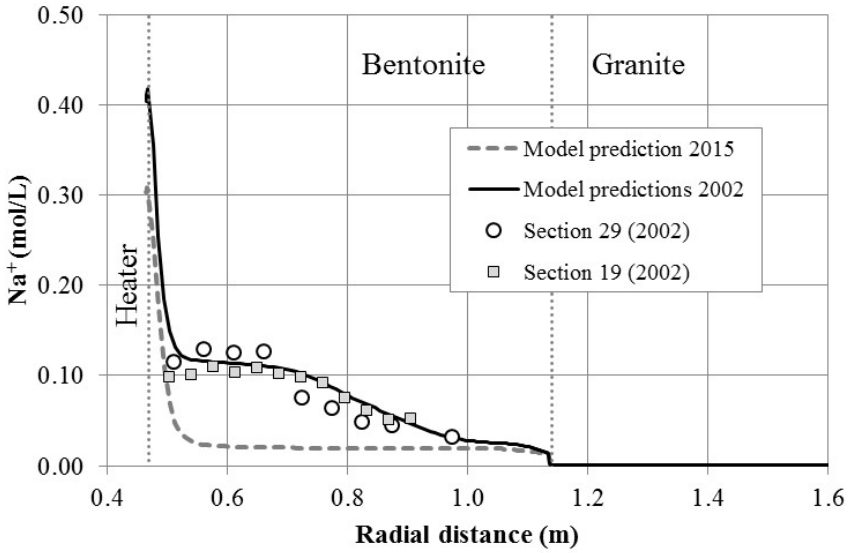

Fig. C-134: Pre-dismantling predictions of Na^{+} concentrations (lines) in 2002 and 2015 in a hot section

The graph also shows the derived Na^{+} concentrations in Sections 19 and 29 (symbols) in 2002.

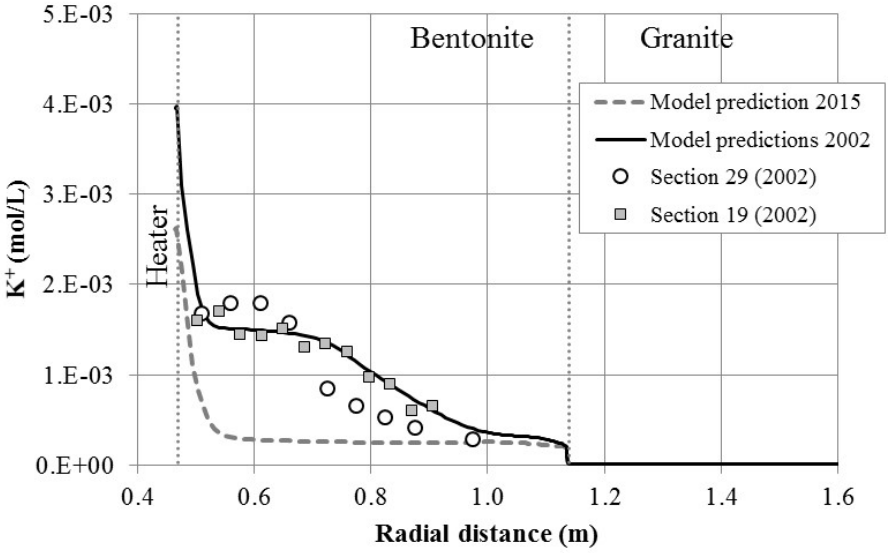

Fig. C-135: Pre-dismantling predictions of K^+ concentrations (lines) in 2002 and 2015 in a hot section.

The graph also shows the derived K^+ concentrations in Sections 19 and 29 (symbols) in 2002.

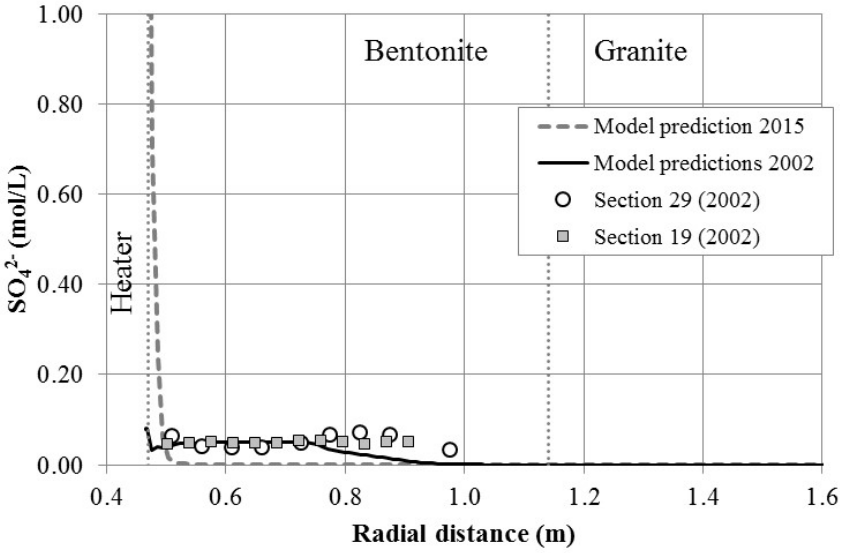

Fig. C-136: Pre-dismantling predictions of SO_4^{2-} concentrations (lines) in 2002 and 2015 in a hot section

The graph also shows the derived SO_4^{2-} concentrations in Sections 19 and 29 (symbols) in 2002.

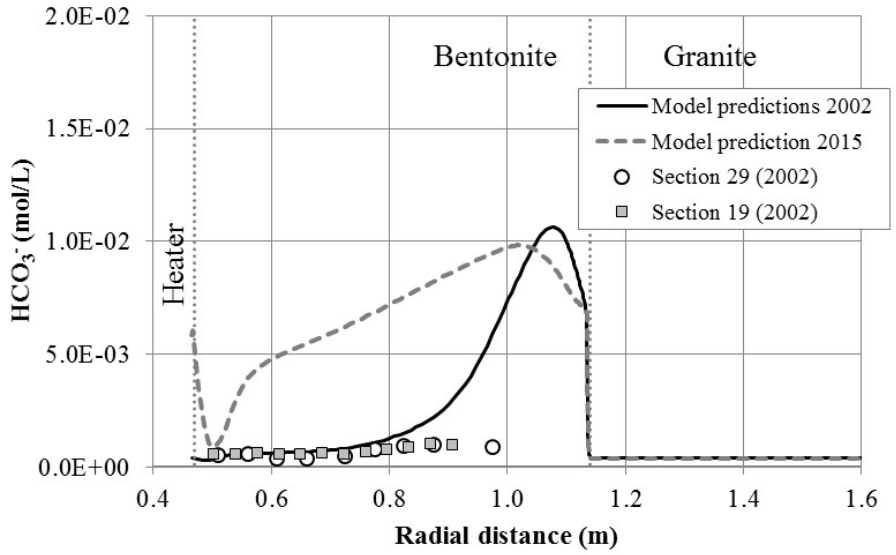

Fig. C-137: Pre-dismantling predictions of HCO_3^- concentrations (lines) in 2002 and 2015 in a hot section

The graph also shows the derived HCO_3^- concentrations in Sections 19 and 29 (symbols) in 2002.

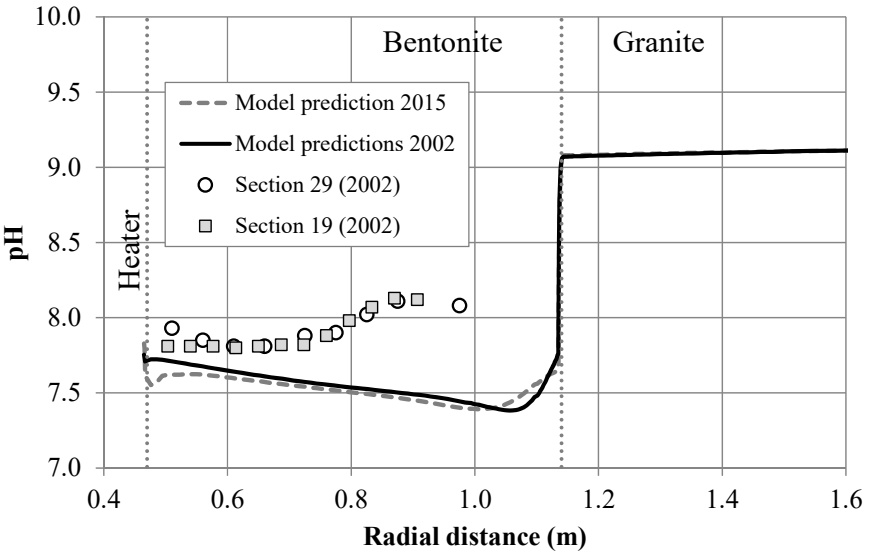

Fig. C-138: Pre-dismantling predictions of pH (lines) in 2002 and 2015 in a hot section

The graph also shows the derived pH in Sections 19 and 29 (symbols) in 2002.

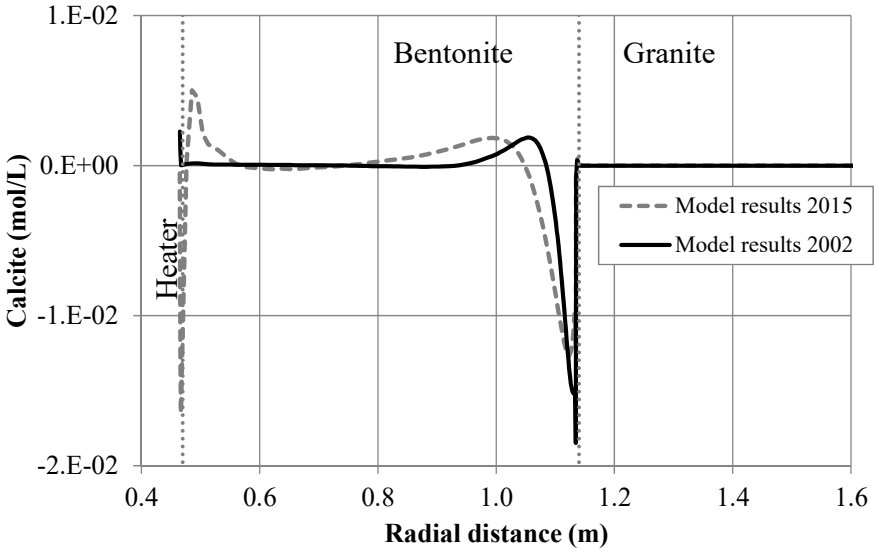

Fig. C-139: Pre-dismantling predictions of cumulative calcite dissolution (negative)/ precipitation (positive) (lines) in 2002 and 2015 in a hot section

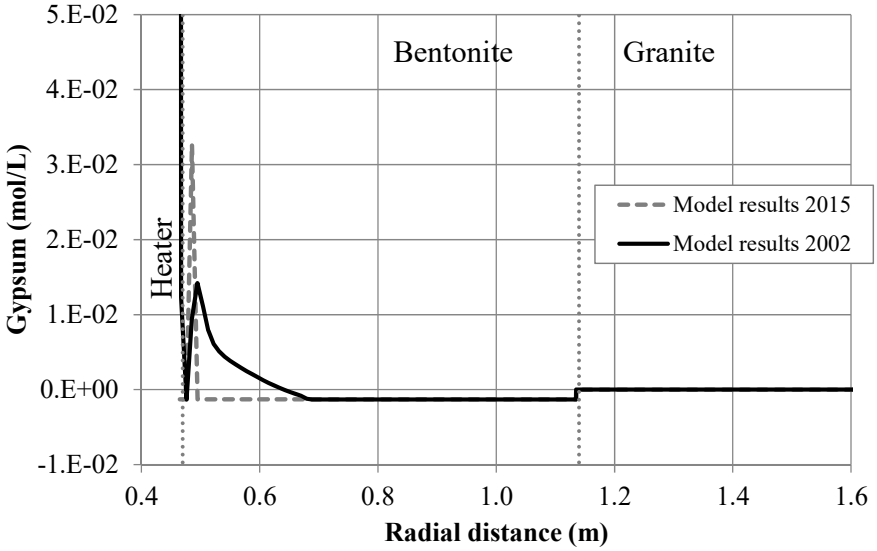

Fig. C-140: Pre-dismantling predictions of cumulative gypsum (negative)/precipitation (positive) (lines) in 2002 and 2015 in a hot section

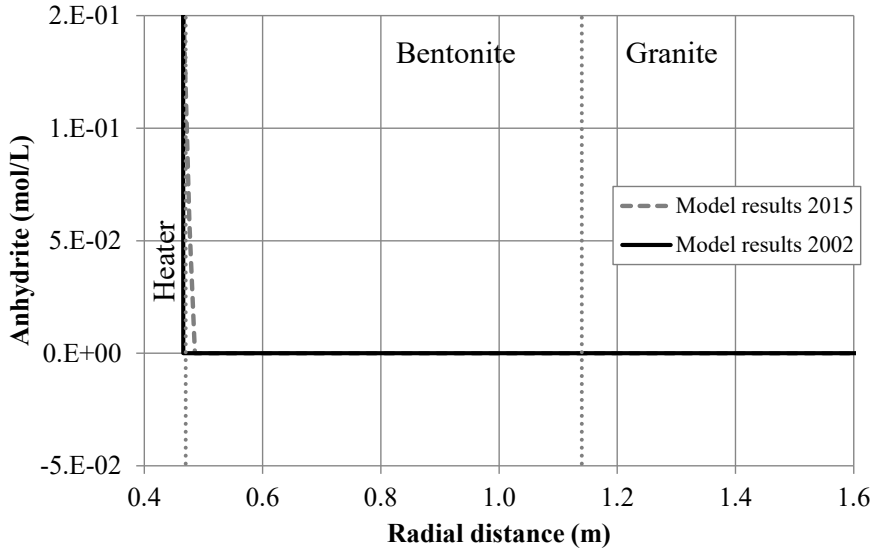

Fig. C-141: Pre-dismantling predictions of cumulative anhydrite (negative)/precipitation (positive) (lines) in 2002 and 2015 in a hot section

C.5.2 Predictions for the cold section

Fig. C-142 to A-149 show the pre-dismantling THCM predictions of the dissolved Cl^-, Ca^{2+}, K^+, Mg^{2+}, Na^+, SO_4^{2-}, HCO_3^- concentrations and pH in 2002 and 2015 in a cold section. The predicted concentrations in 2002 are compared to the derived concentration data in Section 12.

The concentrations in the inner part of the bentonite barrier (i.e. for small radial distances) remain constant and equal to the initial concentrations. Therefore, the chemical changes in the cold section are smaller than in the hot section. The concentrations near the bentonite-granite interface decrease due to water hydration. The comparison of model calculations and derived aqueous extract data show that the model reproduces, generally, the trends of the derived data. However, the model overestimates the measured data in the middle of bentonite barrier and underestimates the measured data near the bentonite-granite interface. At this stage of the project, the comparison of model calculations with measured data was made only visually. Objective and quantitative criteria such as that of Nash-Sutcliffe will be used in the future as reported by Mon et al. (2015).

The concentrations predicted in 2015 are smaller than the concentrations calculated in 2002 due to the advective and diffusive transport. The concentrations fronts move approximately 0.2 m into the bentonite barrier during the period from 2002 to 2015.

Fig. C-142 shows the measured and computed radial distribution of Cl- concentrations in 2002 and 2015 and the comparison with derived aqueous extract data (Section 12) in 2002. The derived Cl- concentration is small close to the bentonite-granite interface, increases and then levels off towards the centre. The inward displacement of the hydration front and solute diffusion govern the spatial distribution of this conservative species. The computed Cl- concentrations in 2015 show a pattern similar to those computed in 2002 but are much smaller than in 2002. The Cl-concentration front moves less than 0.2 m from 2002 to 2015.

The concentrations of dissolved cations (Ca2+, Mg2+, Na+ and K+) show trends similar to those of the Cl-concentration (see Fig. C-143 to Fig. C-146).

Fig. C-147 shows the measured and computed radial distribution of SO42- concentrations in 2002 and 2015 and the comparison with derived aqueous extract data (Section 12) in 2002. The computed SO42- concentrations in 2002 underestimate the derived aqueous extract data near the bentonite-granite interface, possibly due to uncertainties in the initial amount of gypsum in the bentonite. The concentration of dissolved SO42- is affected by gypsum dissolution. A small increase in the SO42-concentration can be seen in 2002 just ahead of the dilution front which is due to gypsum dissolution (see Fig. C-147 and Fig. C-151). Model predictions show that the SO42-concentration in 2015 will decrease compared to those in 2002 within the interval $0.6 < r < 1.2$ m and increase for $r < 0.6$ m. It should be noticed that anhydrite does not precipitate in the cold section because the temperature in this section is below the stability temperature for anhydrite.

Fig. C-148 shows the measured and computed radial distribution of HCO3- concentrations in 2002 and 2015 and the comparison with derived aqueous extract data (Section 12) in 2002. The model results in 2002 fit the general trend of the measures data, except near the granite-bentonite interface where model results underestimate the measured data. The concentration of HCO3- is affected by the calcite dissolution front which advances from the bentonite-granite interface (Fig. C-150). The concentration increases near the bentonite-granite interface due to calcite dissolution. The predicted concentrations of HCO3- in 2015 are larger than those in 2002 because the calcite dissolution front moves inwards.

Fig. C-149 shows the predictions of pH in 2002 and 2015. The computed pH in the bentonite will decrease slightly in the bentonite due to calcite dissolution. Near the bentonite-granite interface, however, the pH will increase due to calcite precipitation and proton diffusion from the bentonite into the granite.

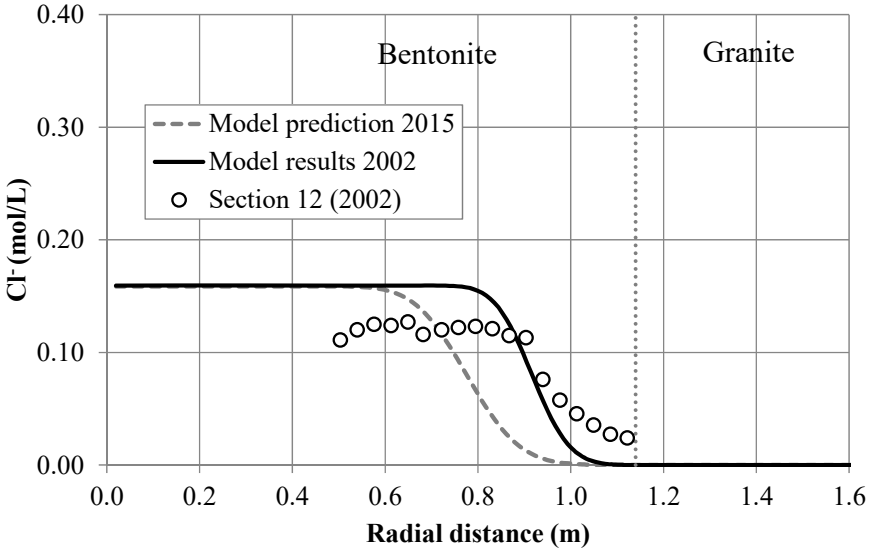

Fig. C-142: Pre-dismantling predictions of Cl^- concentrations (lines) in 2002 and 2015 in a cold section

The graph also shows the derived Cl^- concentrations in Section 12 (symbols) in 2002.

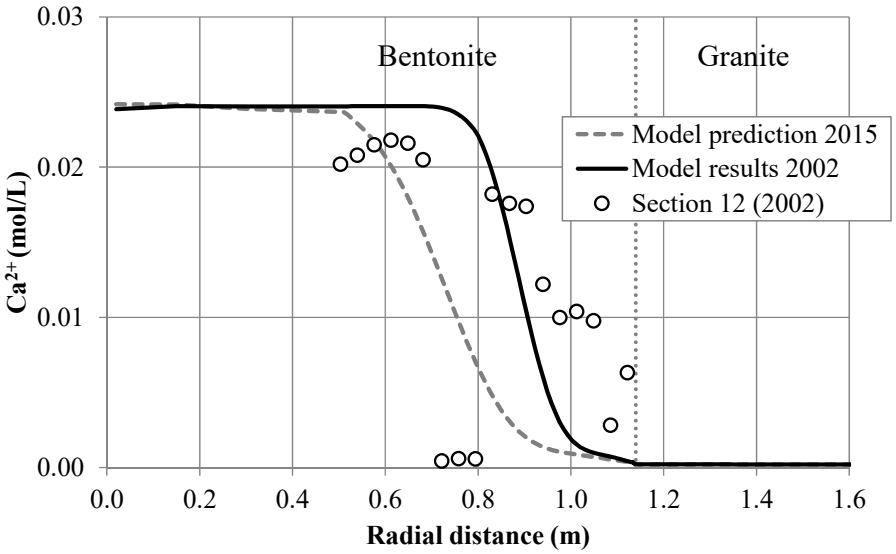

Fig. C-143: Pre-dismantling predictions of Ca^{2+} concentrations (lines) in 2002 and 2015 in a cold section

The graph also shows the derived Ca^{2+} concentrations in Section 12 (symbols) in 2002.

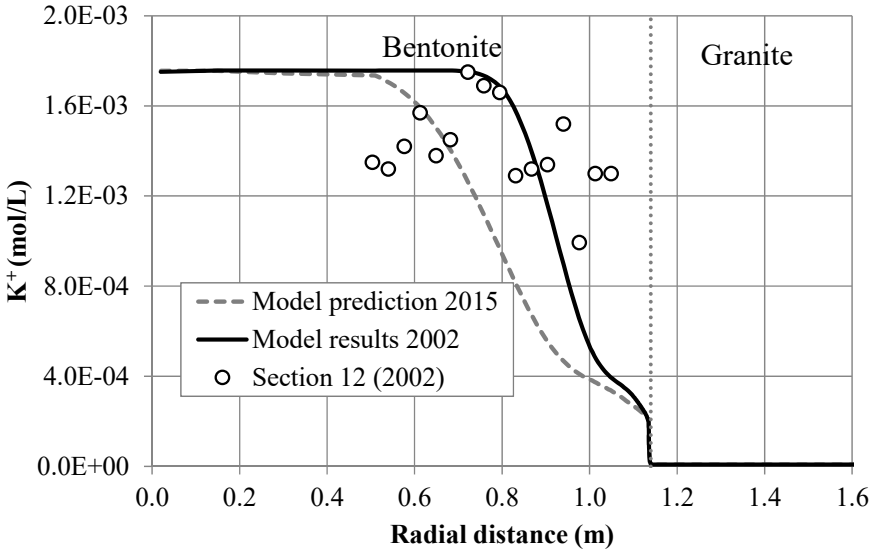

Fig. C-144: Pre-dismantling predictions of K^+ concentrations (lines) in 2002 and 2015 in a cold section

The graph also shows the derived K^+ concentrations in Section 12 (symbols) in 2002.

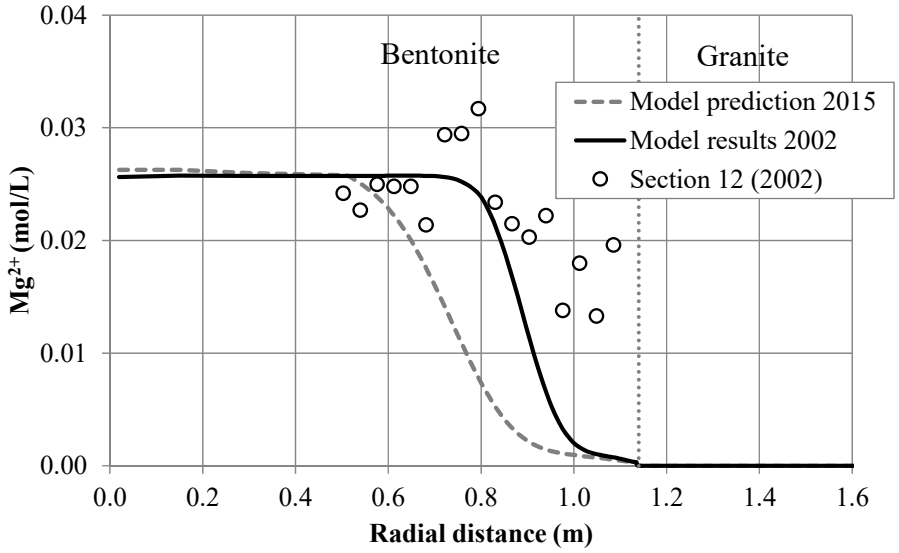

Fig. C-145: Pre-dismantling predictions of Mg^{2+} concentrations (lines) in 2002 and 2015 in a cold section

The graph also shows the derived Mg^{2+} concentrations in Section 12 (symbols) in 2002.

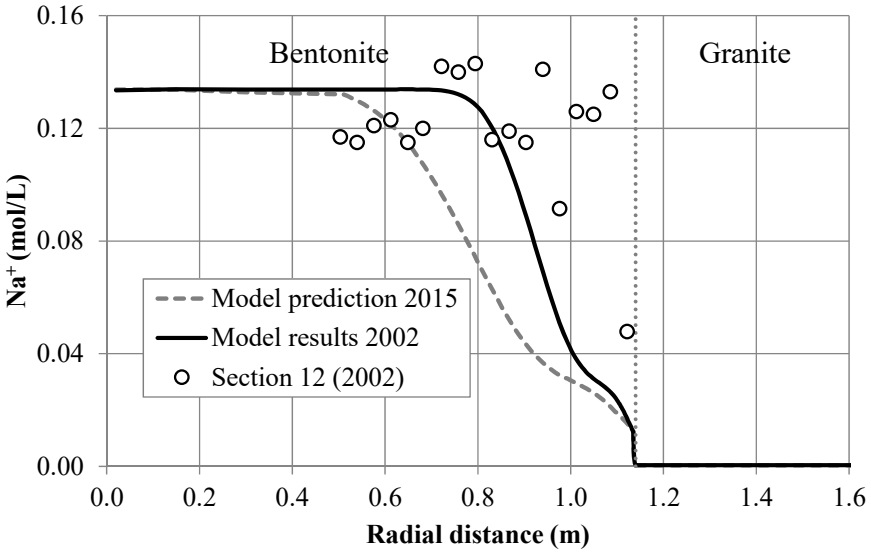

Fig. C-146: Pre-dismantling predictions of Na^+ concentrations (lines) in 2002 and 2015 in a cold section

The graph also shows the derived Na^+ concentrations in Section 12 (symbols) in 2002.

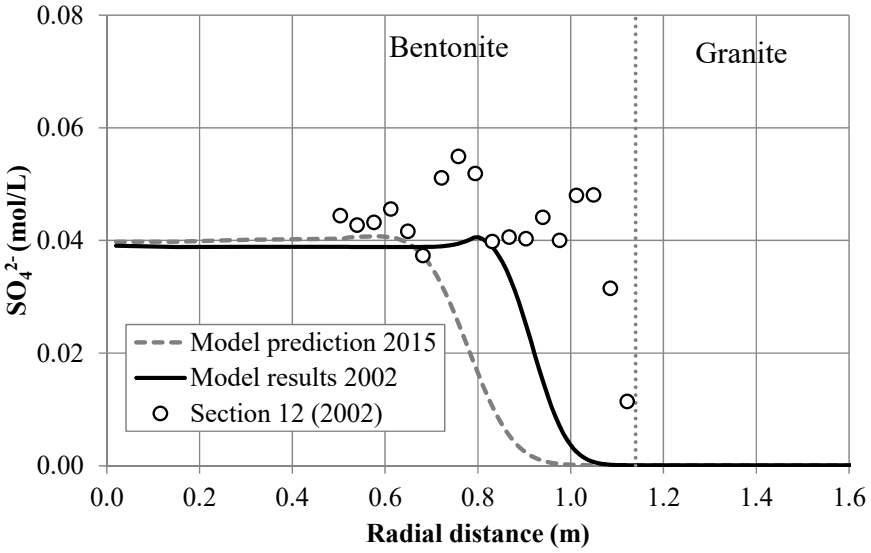

Fig. C-147: Pre-dismantling predictions of SO_4^{2-} concentrations (lines) in 2002 and 2015 in a cold section

The graph also shows the derived SO_4^{2-} concentrations in Section 12 (symbols) in 2002.

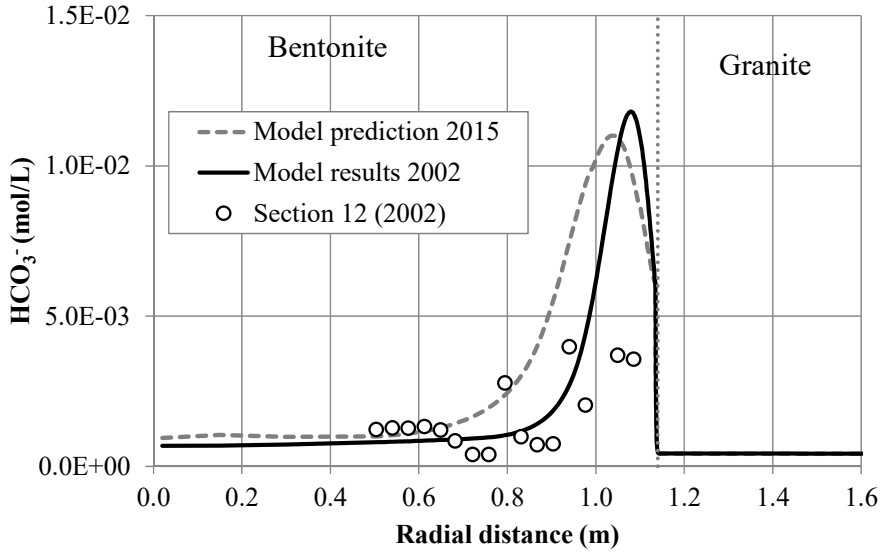

Fig. C-148: Pre-dismantling predictions of HCO_3^- concentrations (lines) in 2002 and 2015 in a cold section

The graph also shows the derived HCO_3^- concentrations in Section 12 (symbols) in 2002.

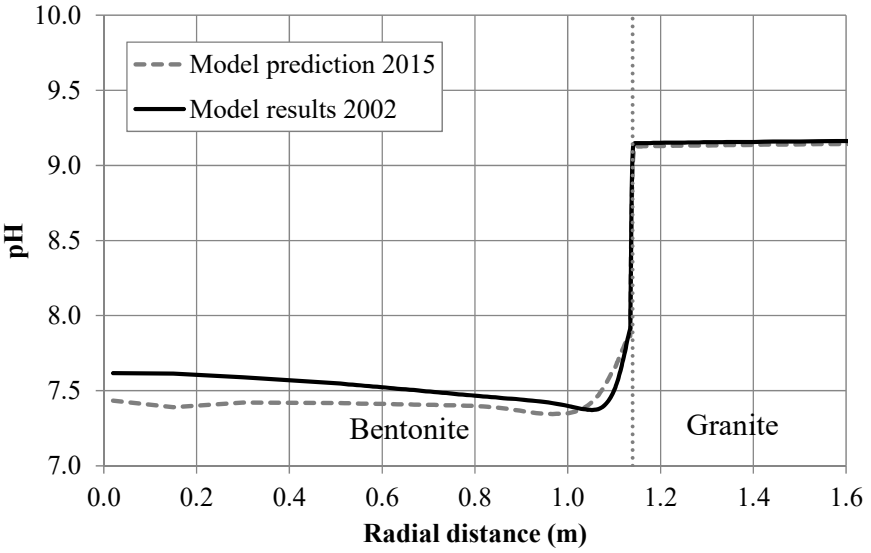

Fig. C-149: Pre-dismantling predictions of pH (lines) in 2002 and 2015 in a cold section.

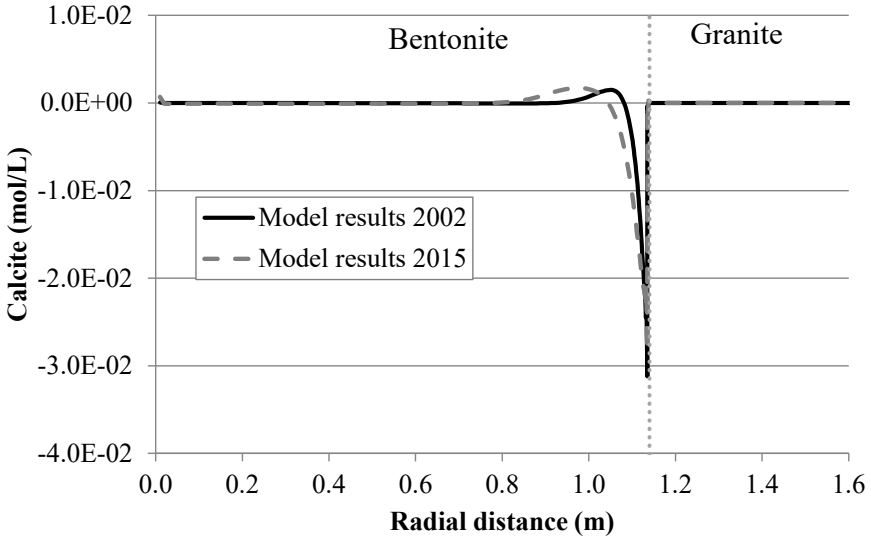

Fig. C-150: Pre-dismantling predictions of cumulative calcite dissolution (negative)/ precipitation (positive) (lines) in 2002 and 2015 in a cold section

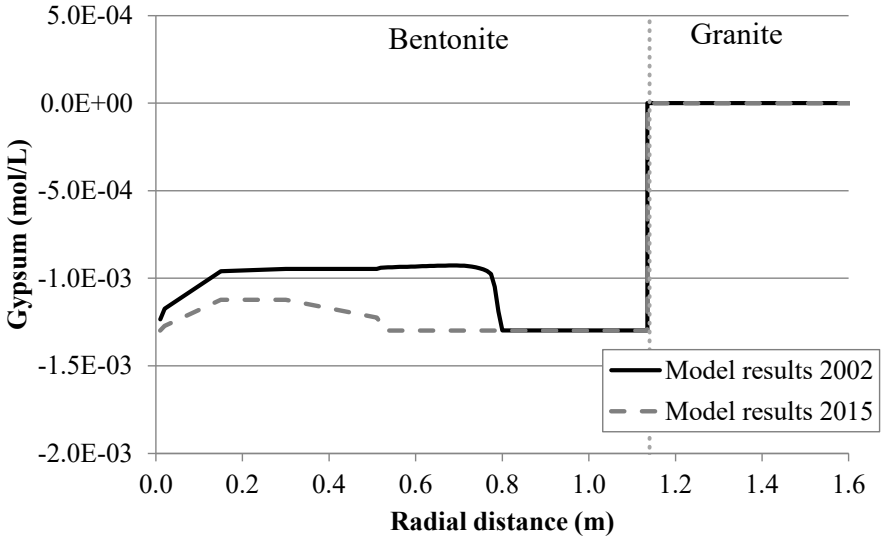

Fig. C-151: Pre-dismantling predictions of cumulative gypsum dissolution (negative)/ precipitation (positive) (lines) in 2002 and 2015 in a cold section

C.5.3 Sensitivity of the predictions to the diffusion coeficients

The prediction uncertainties of the concentrations in 2015 have been quantified by performing an additional simulation run in which the diffusion coefficients in both bentonite and granite are increased by a factor of 10. The changes in the predicted concentrations in 2015 provide a measure of the predictions' uncertainties caused by parameter uncertainties.

Tab. C-3 lists the diffusion coefficients in pure water for the base run and for the sensitivity run. The diffusion coefficients of the sensitivity run are ten times higher than those of the base run and are similar to the values used in previous models of the FEBEX bentonite by Zheng & Samper (2008) and Zheng et al. (2010).

Tab. C-3: Diffusion coefficients in pure water for the base run (taken from Zheng et al. 2011) and the sensitivity run

Component	**Base run** (m^2/s)	**Sensitivity run** (m^2/s)
Cl^-	3.1×10^{-12}	3.1×10^{-11}
SO_4^{2-}	3.6×10^{-13}	3.6×10^{-12}
Rest of species	2×10^{-11}	2×10^{-10}

C.5.3.1 Hot section

Fig. C-152 to A-159 show the sensitivity of the computed dissolved Ca^{2+}, K^+, Mg^{2+}, Cl^-, Na^+, SO_4^{2-} and HCO_3^- concentrations and pH in a hot section in 2015 to an increase of the diffusion coefficients by a factor of 10. The computed concentrations are very sensitive to the change in the diffusion coefficients. In general, the concentration profiles of most of the chemical species become smoother when the diffusion coefficient is increased. The concentrations decrease near the heater and increase in the rest of the bentonite barrier. The concentration of dissolved Ca^{2+} increases everywhere in the bentonite because calcite dissolution near the heater is enhanced when the diffusion coefficients of the bentonite are multiplied by 10. Such an increase in Ca^{2+} concentration is accompanied by a decrease in the concentration of dissolved HCO_3^-.

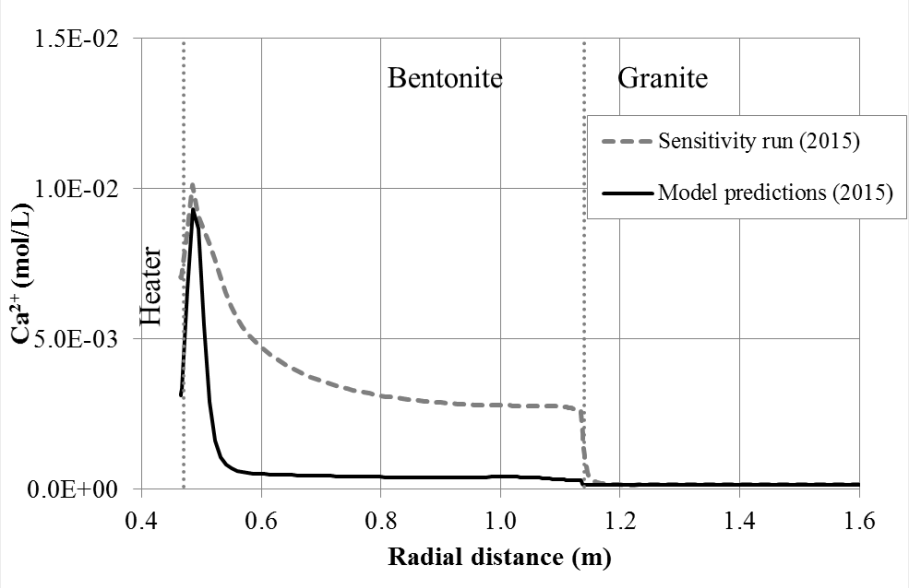

Fig. C-152: Sensitivity of the computed concentrations of dissolved Ca^{2+} in a hot section in 2015 to an increase of the diffusion coefficients

The coefficients of the sensitivity are 10 times larger than those of the reference prediction run.

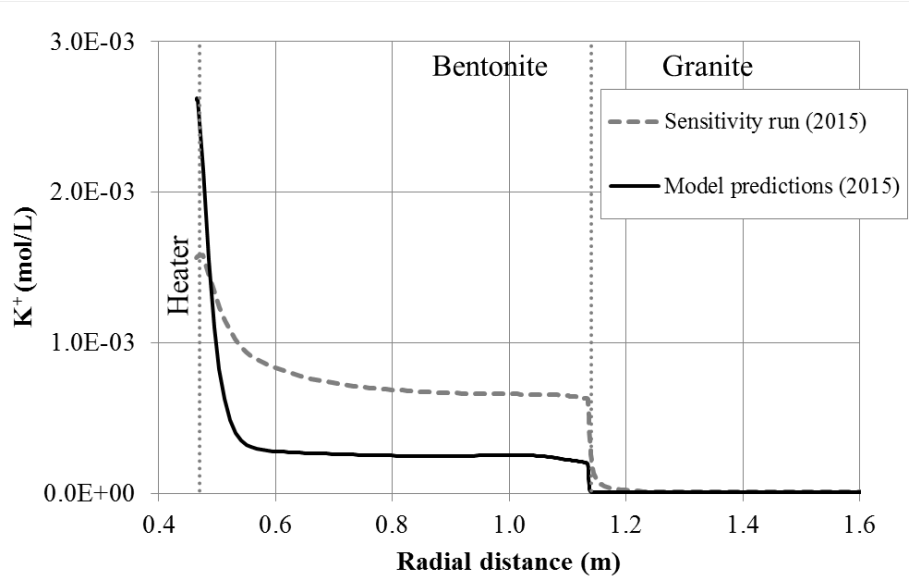

Fig. C-153: Sensitivity of the computed concentrations of dissolved K^{+} in a hot section in 2015 to an increase of the diffusion coefficients

The coefficients of the sensitivity are 10 times larger than those of the reference prediction run.

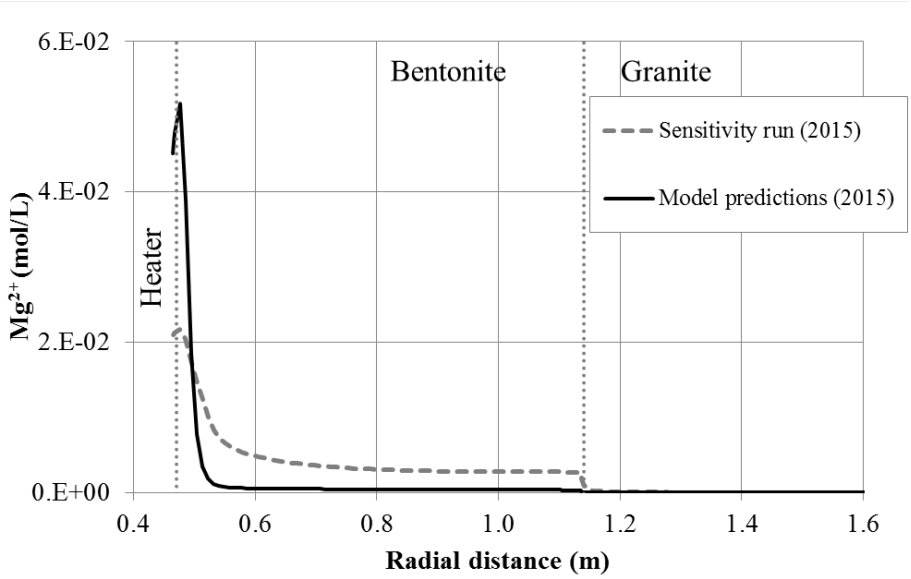

Fig. C-154: Sensitivity of the computed concentrations of dissolved Mg^{2+} in a hot section in 2015 to an increase of the diffusion coefficients

The coefficients of the sensitivity are 10 times larger than those of the reference prediction run.

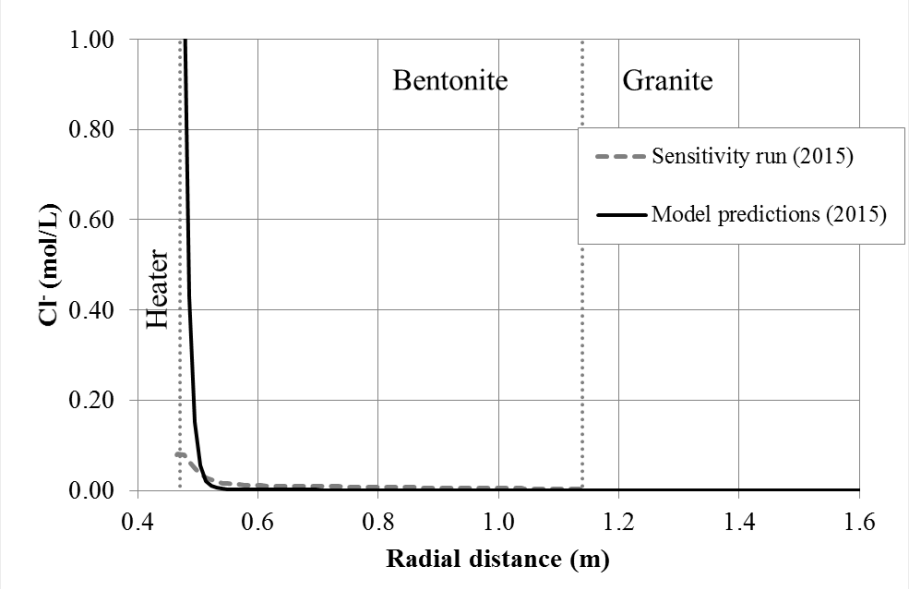

Fig. C-155: Sensitivity of the computed concentrations of dissolved Cl^- in a hot section in 2015 to an increase of the diffusion coefficients

The coefficients of the sensitivity are 10 times larger than those of the reference prediction run.

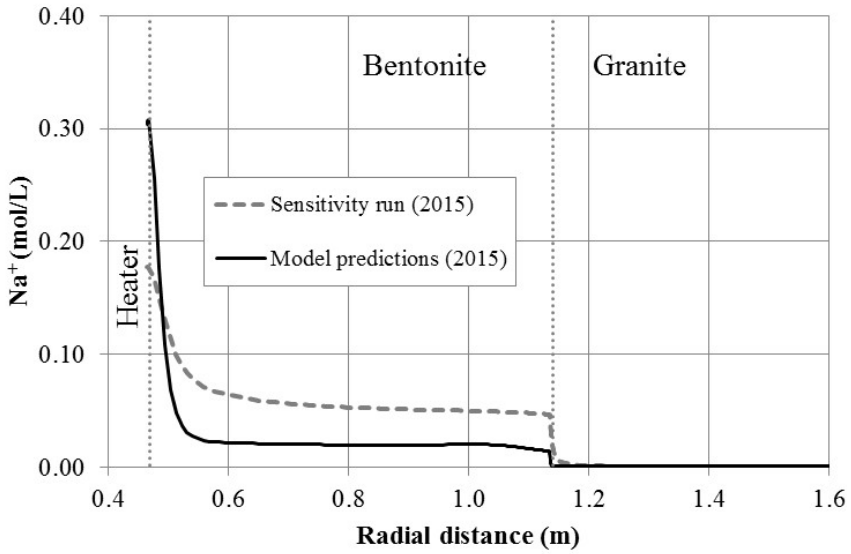

Fig. C-156: Sensitivity of the computed concentrations of dissolved Na^+ in a hot section in 2015 to an increase of the diffusion coefficients

The coefficients of the sensitivity are 10 times larger than those of the reference prediction run.

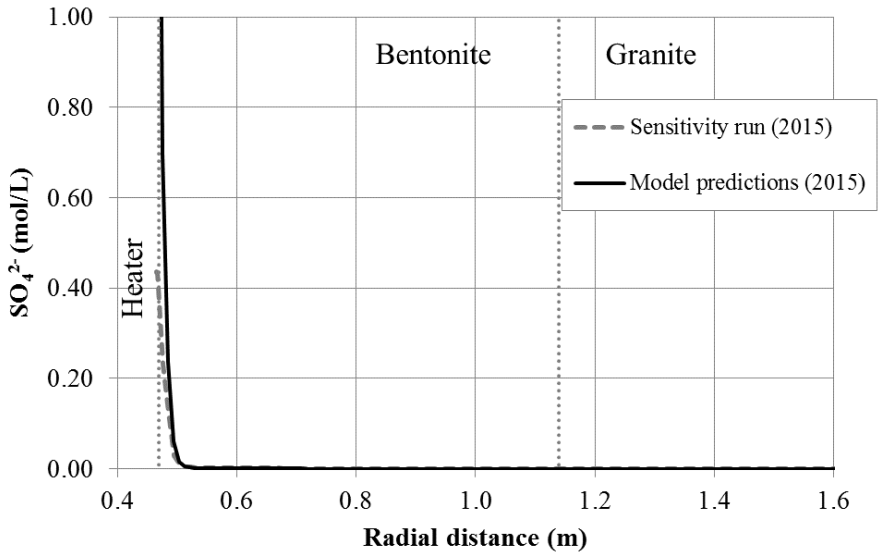

Fig. C-157: Sensitivity of the computed concentrations of dissolved SO_4^{2-} in a hot section in 2015 to an increase of the diffusion coefficients

The coefficients of the sensitivity are 10 times larger than those of the reference prediction run.

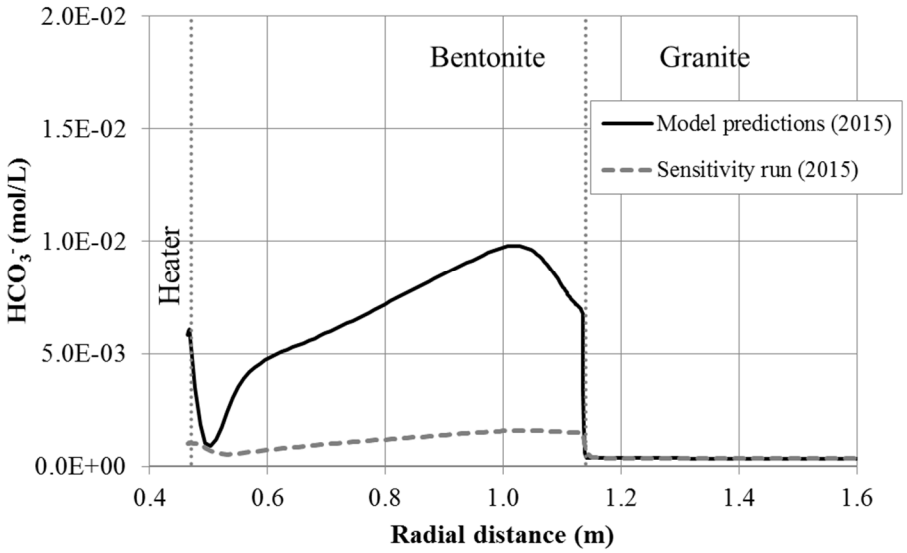

Fig. C-158: Sensitivity of the computed concentrations of dissolved HCO_3^- in a hot section in 2015 to an increase of the diffusion coefficients

The coefficients of the sensitivity are 10 times larger than those of the reference prediction run.

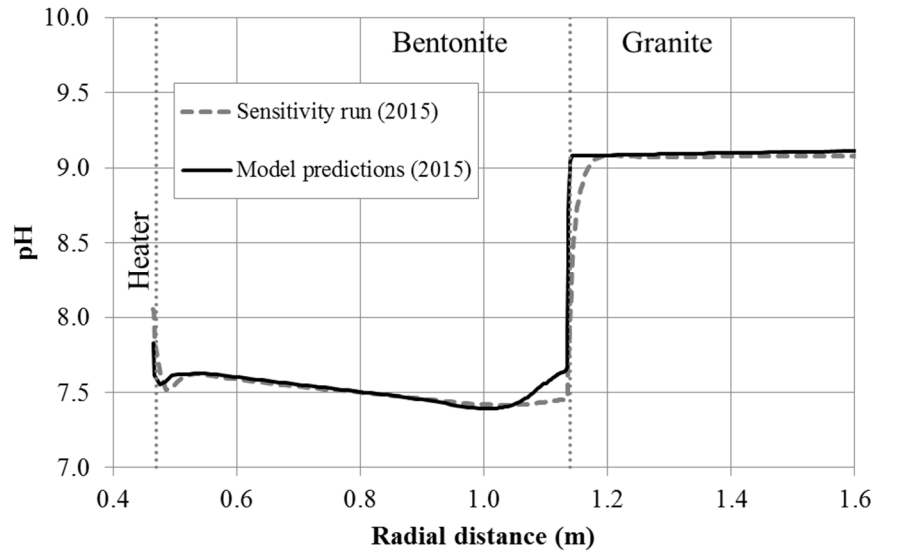

Fig. C-159: Sensitivity of the computed pH in a hot section in 2015 to an increase of the diffusion coefficients

The coefficients of the sensitivity are 10 times larger than those of the reference prediction run.

C.5.3.2 Cold section

Fig. C-160 to A-167 show the sensitivity of the computed dissolved Ca^{2+}, K^{+}, Mg^{2+}, Cl^{-}, Na^{+}, SO_4^{2-} and HCO_3^{-} concentrations and pH in a cold section in 2015 to an increase of the diffusion coefficients by a factor of 10. The radial profiles of the concentrations of Ca^{2+}, K^{+}, Mg^{2+}, Na^{+} and HCO_3^{-} become smoother when the diffusion coefficients are increased. The profiles of Cl^{-} and SO_4^{2-} are also sensitive to the change in the diffusion coefficients. However, their sensitivity is much smaller than the sensitivity of other species because the diffusion coefficients of Cl^{-} and SO_4^{2-} are much smaller than the diffusion coefficients of the rest of the species. The computed pH is slightly sensitive to the change in the diffusion coefficients.

The sensitivity of the concentration of dissolved Ca^{2+} in the cold section is different from the sensitivity in the hot section. While the concentration of dissolved Ca^{2+} in the hot section increases everywhere in the bentonite when the diffusion coefficients are multiplied by 10, the concentration of dissolved Ca^{2+} in the cold section decreases for $r < 0.8$ m and increases for $r > 0.8$ m. The main reason for the different sensitivities is attributed to the enhancement of calcite dissolution near the heater in the hot section when the diffusion coefficient is increased.

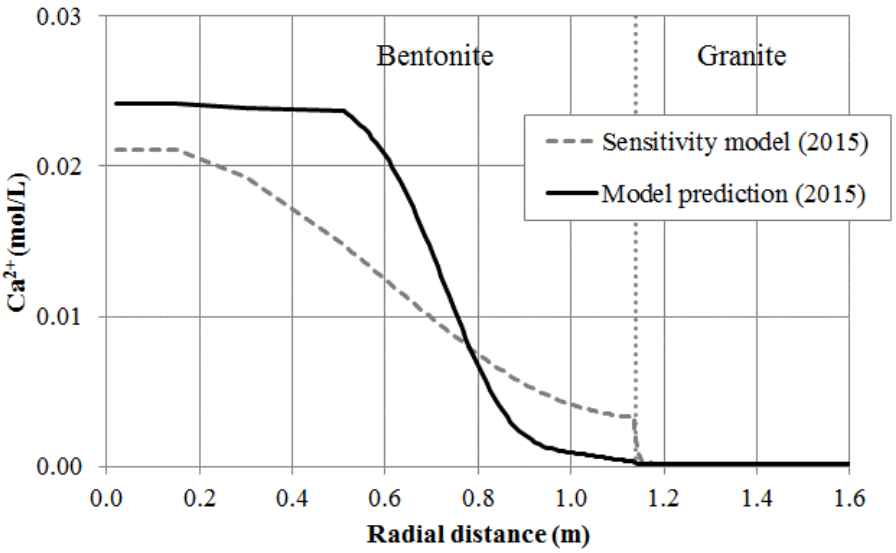

Fig. C-160: Sensitivity of the computed concentrations of dissolved Ca^{2+} in a cold section in 2015 to an increase of the diffusion coefficients

The coefficients of the sensitivity are 10 times larger than those of the reference prediction run.

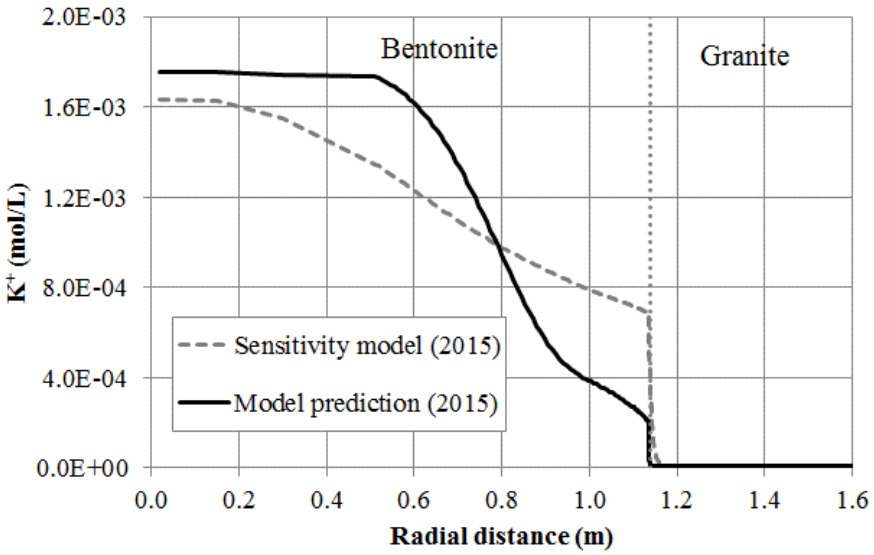

Fig. C-161: Sensitivity of the computed concentrations of dissolved K^+ in a cold section in 2015 to an increase of the diffusion coefficients

The coefficients of the sensitivity are 10 times larger than those of the reference prediction run.

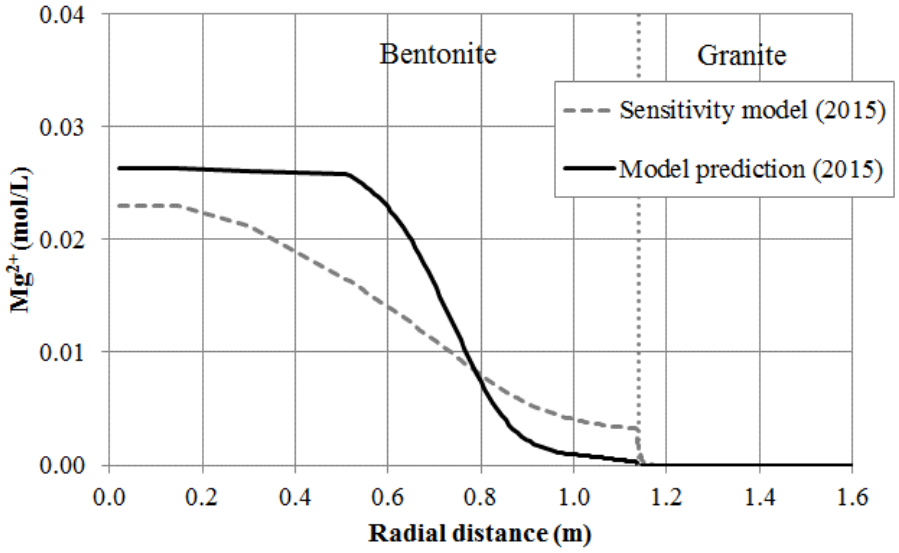

Fig. C-162: Sensitivity of the computed concentrations of dissolved Mg^{2+} in a cold section in 2015 to an increase of the diffusion coefficients

The coefficients of the sensitivity are 10 times larger than those of the reference prediction run.

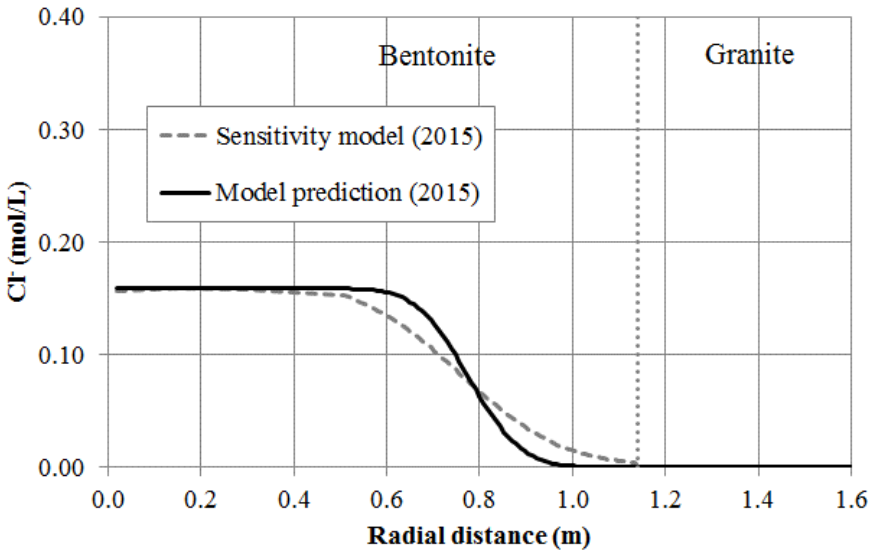

Fig. C-163: Sensitivity of the computed concentrations of dissolved Cl^- in a cold section in 2015 to an increase of the diffusion coefficients

The coefficients of the sensitivity are 10 times larger than those of the reference prediction run.

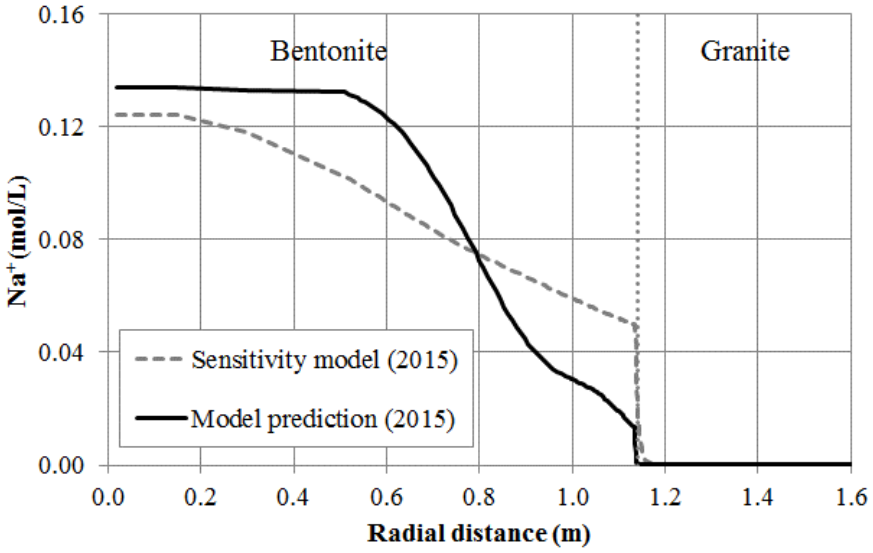

Fig. C-164: Sensitivity of the computed concentrations of dissolved Na^+ in a cold section in 2015 to an increase of the diffusion coefficients

The coefficients of the sensitivity are 10 times larger than those of the reference prediction run.

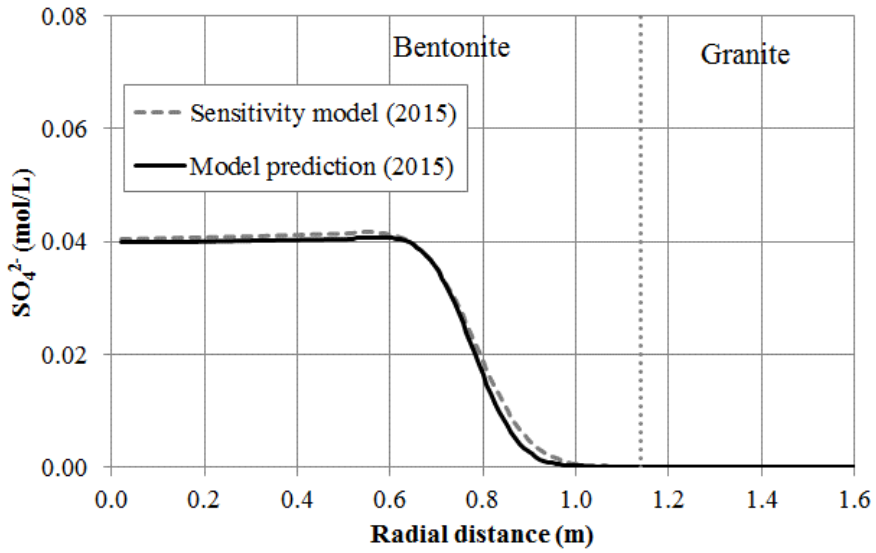

Fig. C-165: Sensitivity of the computed concentrations of dissolved SO_4^{2-} in a cold section in 2015 to an increase of the diffusion coefficients

The coefficients of the sensitivity are 10 times larger than those of the reference prediction run.

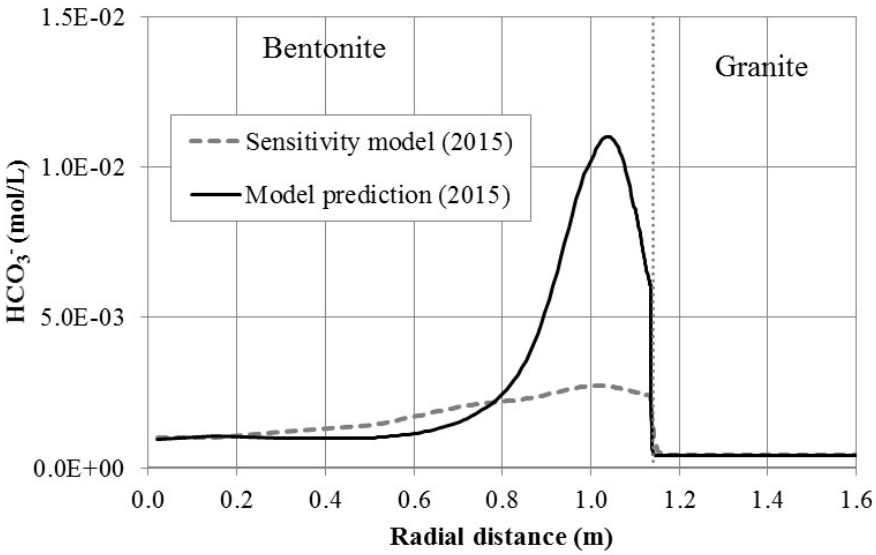

Fig. C-166: Sensitivity of the computed concentrations of dissolved HCO_3^- in a cold section in 2015 to an increase of the diffusion coefficients

The coefficients of the sensitivity are 10 times larger than those of the reference prediction run.

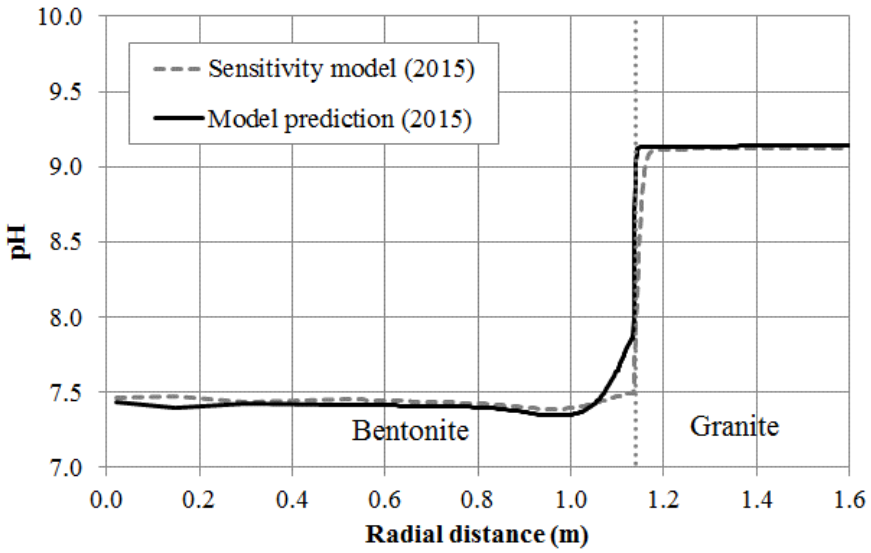

Fig. C-167: Sensitivity of the computed pH in a cold section in 2015 to an increase of the diffusion coefficients

The coefficients of the sensitivity are 10 times larger than those of the reference prediction run.

C.5.4 Transport of a conservative species from the granite into the bentonite

In order to quantify the mass transfer from granite into bentonite, a tracer initially present in the granite but not present in the bentonite pore water was selected; it was studied with the evolution of the F^-concentration. This chemical species has a concentration in granite pore water of 2.247×10^{-4} mol/L, which is much higher than that in the bentonite barrier (5.26×10^{-6} mol/L according to ENRESA 1998).

The migration of F-was simulated with the updated model. The diffusion coefficient of fluoride in pure water was taken equal to 2×10^{-11} m^2/s.

Water flows from the granite into the bentonite. Therefore, F-will migrate by advective transport from the granite into the bentonite. Fig. C-168 shows the radial distribution of the computed log-concentrations of F-in a hot section at selected times. It can be seen that the concentration increases in the bentonite near the heater due to the evaporation. On the other side, the F-concentrations increase in the bentonite near the interface due to advection and diffusion from the granite. After 18 years, the F-concentration is nearly uniform in the bentonite and granite, except near the heater where the F-concentration is large due to the evaporation. Fig. C-169 shows the computed F-concentration in linear scale. The zoom at the bentonite-granite interface shows that the F-concentration decreases slightly in the granite near the bentonite/granite interface.

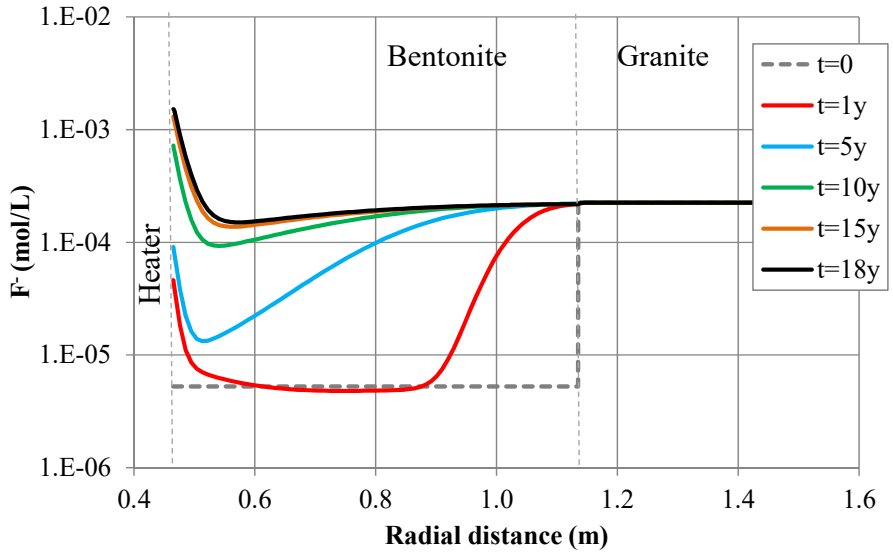

Fig. C-168: Radial distribution of the computed log-concentrations of F-in a hot section at selected times

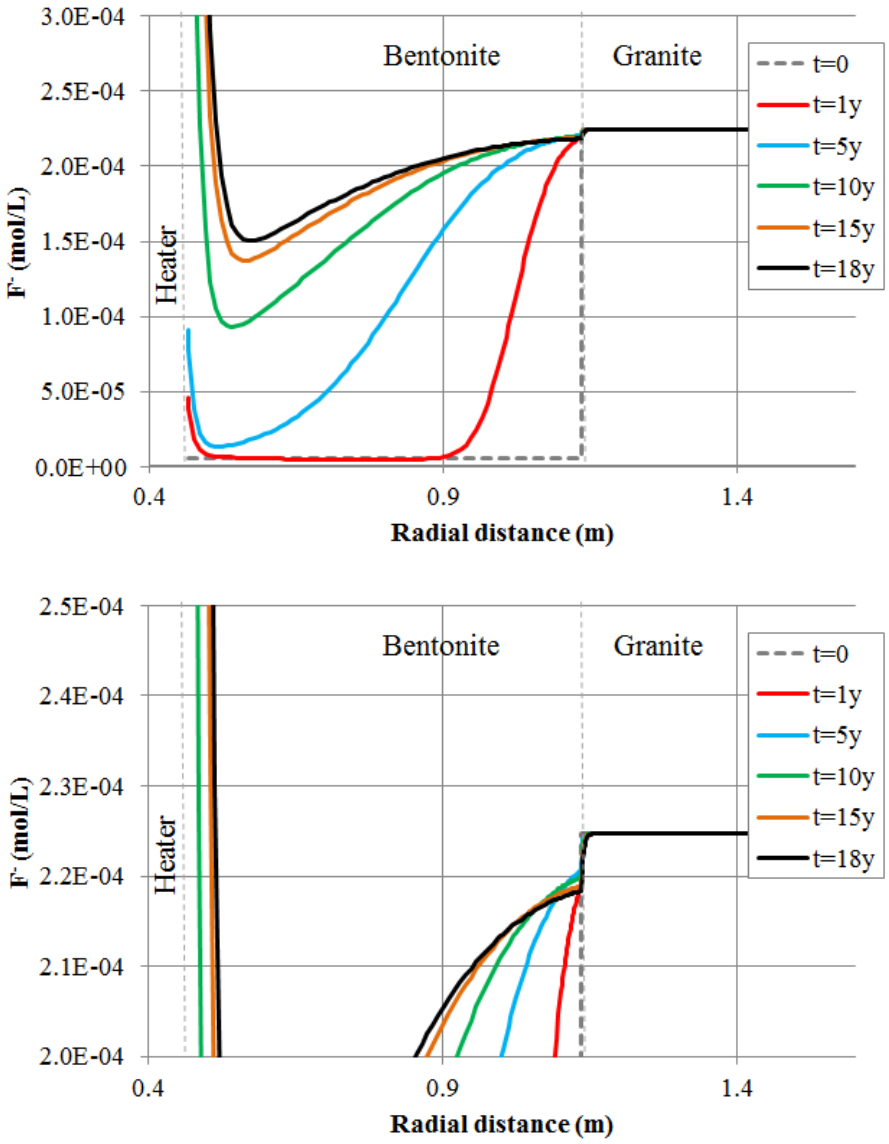

Fig. C-169: Radial distribution of the computed concentrations of F-in a hot section at selected times

The plot at the bottom shows a zoom of the concentrations near the bentonite/granite interface.

C.5.5 Conclusions

Pre-dismantling THCM model predictions of the geochemical conditions for the hot and cold sections in June 2015 were performed with the updated 1D axisymmetric THCM model. Prediction uncertainties were quantified by sensitivity runs to key model parameters such as the diffusion coefficients of the chemical species.

The main features of the geochemical predictions in a hot section in 2015 include:

1. The predicted concentrations of Cl^- in 2015 are largest near the heater due to the evaporation of the bentonite pore water and smallest at the granite-bentonite interface due to the hydration of the buffer with granite pore water, which has a concentration smaller than that of bentonite. The predicted concentrations of Cl^- in 2015 are much smaller than the concentrations in 2002.
2. The predicted concentrations of dissolved cations (Ca^{2+}, Mg^{2+}, Na^+ and K^+) are also large near the heater
3. The predicted concentration of SO_4^{2-} in 2015 increases near the heater and decreases in the rest of the bentonite barrier
4. The computed HCO_3^- is large near the bentonite-granite interface because the hydration of bentonite with granite water induces the dissolution of calcite at the bentonite/granite interface
5. The predicted pH in the bentonite in 2015 is 7.5 near the heater and decreases slightly towards the granite interface

The main features of the geochemical predictions in the cold sections in 2015 include:

1. The predicted concentration of Cl^- in 2015 shows a diffusion profile with low concentration in granite and a high concentration of about 0.16 mol/L in the centre of the bentonite barrier.
2. The predicted concentrations of dissolved cations (Ca^{2+}, Mg^{2+}, Na^+, K^+ and SO_4^{2-}) show diffusion profiles similar to the profile of the concentration of Cl^-.
3. The predicted concentration of HCO_3^- in bentonite in 2015 is 10^{-2} mol/L mol/L near the granite interface and decreases towards 10^{-3} mol/L in the centre of the barrier.
4. The predicted pH in bentonite remains sTab. Around 7.5.

The predicted concentrations in the hot sections are very sensitive to an increase of the diffusion coefficient by a factor of 10. In general, the profiles of the concentrations of most of the chemical species become smoother when the diffusion coefficient is increased. The concentrations decrease near the heater and increase in the rest of the bentonite barrier. The concentration of dissolved Ca^{2+} increases everywhere in the bentonite because calcite dissolution near the heater is enhanced when the diffusion coefficients of the bentonite are multiplied by 10. Such an increase in the Ca^{2+} concentration is accompanied by a decrease in the concentration of dissolved HCO_3^-.

The predicted radial profiles of Ca^{2+}, K^+, Mg^{2+}, Na^+ and HCO_3^- concentrations in the cold sections become smoother when the diffusion coefficients are increased. The profiles of Cl^- and SO_4^{2-} are also sensitive to the change in diffusion coefficients. However, their sensitivity is much smaller than the sensitivity of other species because the diffusion coefficients of Cl^- and SO_4^{2-} are much smaller than the diffusion coefficients of the rest of the species. The predicted pH is slightly sensitive to the change in the diffusion coefficients.

The mass transfer from granite into bentonite was quantified with F^-. This chemical species has a concentration in the granite pore water much higher than that in the bentonite barrier. After

18 years, the predicted concentration of F-is nearly uniform in the bentonite and the granite, except near the heater where the predicted concentration of F-is large due to water evaporation. The predicted concentration of F-decreases slightly in the granite.

C.6 Updating the predictions of tracer migration

The predictions for tracer migration were also adapted in line with the updated 1D axisymmetric model. This chapter presents the numerical models performed for: 1) Iodide along several radii in Sections 37, 50 and 51 by using a 1D axisymmetric model; 2) Borate, europium, perrhenate and selenate at the inner blocks of Section 46 by using 2D models in vertical planes; and 3) Caesium and borate at the outer blocks of Section 48 by using 2D models in vertical planes.

C.6.1 Tracers used in the FEBEX in-situ test

C.6.1.1 Types of tracers

Two types of tracers were used in the in-situ FEBEX experiment: (1) conservative tracers (those that travel with water without chemical interactions with either dissolved species nor solid phases) and (2) non-conservative tracers. Conservative tracers provide valuable independent information about the bentonite hydration front. The spatial distribution of a conservative tracer at the end of the experiment provides information on: (1) the main areas of water flow into the clay buffer, (2) the role of clay heterogeneities (such as the contact between clay blocks) on water flow through the buffer, and (3) the patterns of water distribution within the clay buffer. Non-conservative tracers are delayed with respect to conservative tracers due to geochemical processes such as cation exchange, surface complexation and mineral precipitation. This delay is calculated from the distribution coefficient of the tracer, K_d.

The tracers, the compounds used and the expected soluble form used in the in-situ FEBEX experiment are listed in Tab. C-4. Iodide, perrhenate, and selenate are considered "conservative" tracers although they could have some mild sorption. Borate has a significant K_d value. Anionic tracers such as iodide could suffer anion exclusion if they are excluded from some parts of the total porosity. The rest of the tracers are used to characterize sorption (Cs^+, Eu^{3+}, and $^{10}BO_3^{2-}$), and study the role of redox processes and the evolution of redox conditions at the vicinity of the heaters ($Eu^{2+/}Eu^{3+}$, and selenates).

Two different tracer emplacement procedures were considered. Some tracers were added in an extensive way (diffuse sources) while others were located at point locations as shown in Fig. C-170.

For extensive tracer application on the outer rim of the buffer, tracers were added by impregnating a filter paper (FP) which covers the external surface of the clay buffer. Point sources were implemented by: (1) constructing small clay plugs (a few cm size) made of a mixture of clay powder and the tracer (CP); and (2) sintered stainless steel porous capsules containing the tracer inside (SSS). Total masses of tracer compounds used in the FEBEX in-situ experiment are listed in Tab. C-5 (García-Gutiérrez 1997).

Tab. C-4: Tracers used in the FEBEX in-situ experiment

Tracer	**Compound**	**Expected soluble form**
Iodide	NaI	I-
Perrhenate	NaReO4	ReO4-
Borate	H3BO3	H3BO3 (aq)
Selenate	Na2SeO4:10H2O	SeO42-
Europium	Eu(NO3)2:5H2O	Eu2+/Eu3+
Cesium	CsCl	Cs+

Tab. C-5: Total masses of tracer compounds used in the FEBEX in-situ experiment
More details can be found in García-Gutiérrez (1997).

	Mass/point
Na I	4'560 mg
Na Re O4	536.8 mg
H3 BO3	5'430.5 mg
Na2SeO4:10H2O	1'536.7 mg
Eu(NO3)2:5H2O	447.5 mg
CsCl	248.3 mg

C.6.1.2 Tracer location

Fig. C-170 shows the traced sections in the FEBEX in-situ test and the sections containing point tracers (García-Gutiérrez 1997).

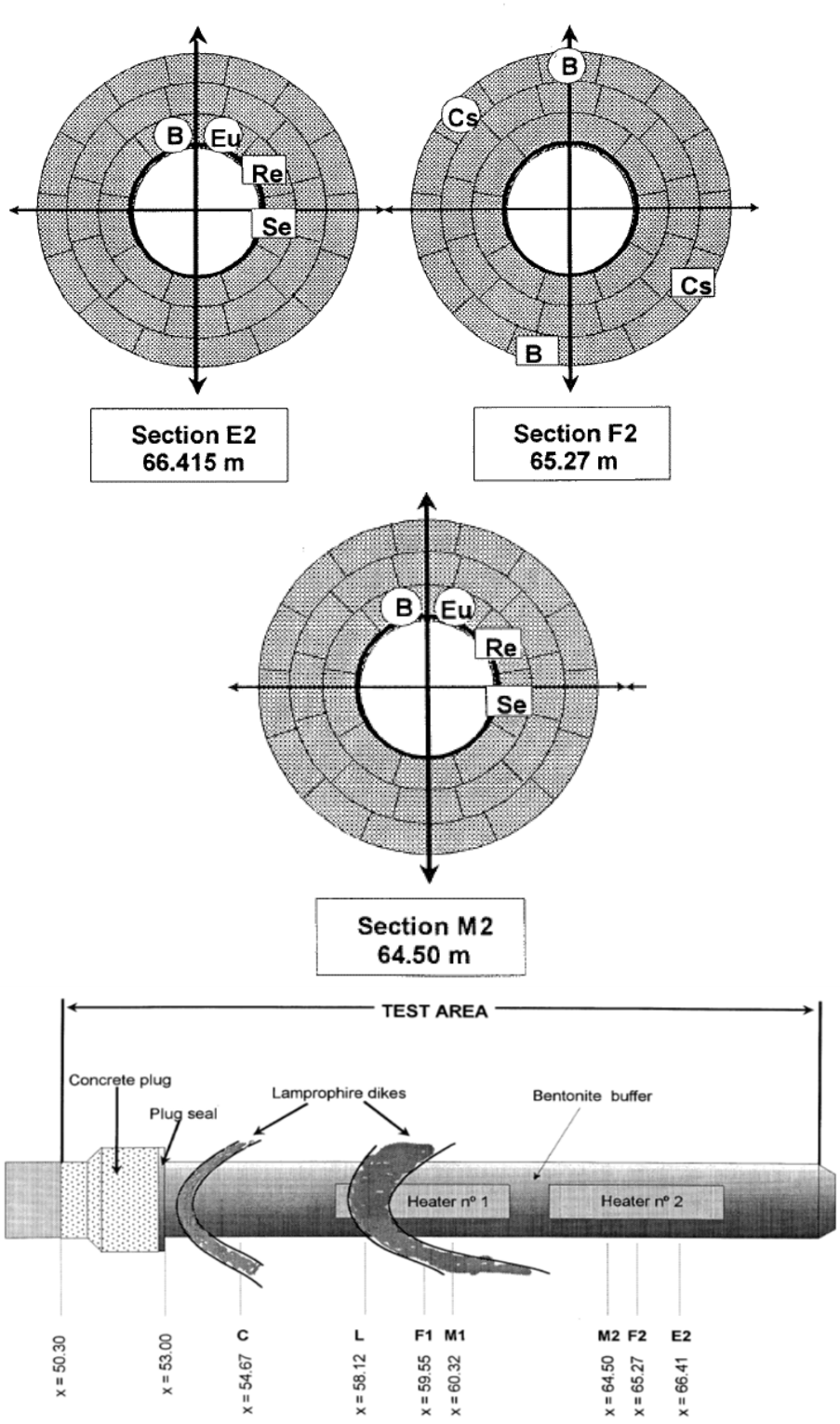

Fig. C-170: Traced sections in the FEBEX in-situ test and sections containing point tracers (García-Gutiérrez 1997).

C.6.1.3 Tracer sampling plans

The sections, which contain tracers, and were dismantled in 2015 include: 36, 37, 46, 48, 50 and 51. The Dismantling Sampling Plan (AITEMIN 2015) accounted for the following sampling sections:

1. Section 37. This section contains iodide which was added on a filter paper. The Sampling Plan considers radial profiles of iodide concentrations in bentonite blocks 37-1 to 37-3 (see Fig. C-171).
2. Section 46 which contains the following point tracers: borate, europium, selenate and perrhenate (see Fig. C-172).
3. Section 48 which contains borate and cesium (see Fig. C-173).
4. Section 50 which contains iodide added in a filter paper. The Sampling Plan considers radial profiles of iodide along 3 bentonite blocks (see Fig. C-174).
5. Section 51 which contains iodide added in a filter paper. The Sampling Plan considers radial profiles of iodide along 3 bentonite blocks (see Fig. C-175). This section contains also borate, europium, selenate and perrhenate.

Point tracers were added in Sections 46, 48 and 51. Point tracers in Sections 46 and 51 were located in the blocks near the heater. These tracers are not likely to migrate beyond the blocks in which they were placed. Consequently, only sampling these blocks should be sufficient for the migration analysis.

Point tracers in Section 48 were located in the outer blocks close to the granite (see Fig. C-173). Cesium is a tracer which undergoes cation exchange with high selectivities (Tachi & Yotsuji 2014). Its migration plume at the dismantling time is not expected to extend beyond the block in which it was placed. Borate sorption, however, is less strong than that of cesium. UDC proposed to collect an additional block in Section 48 above the block B-B-48-2 (see Fig. C-173).

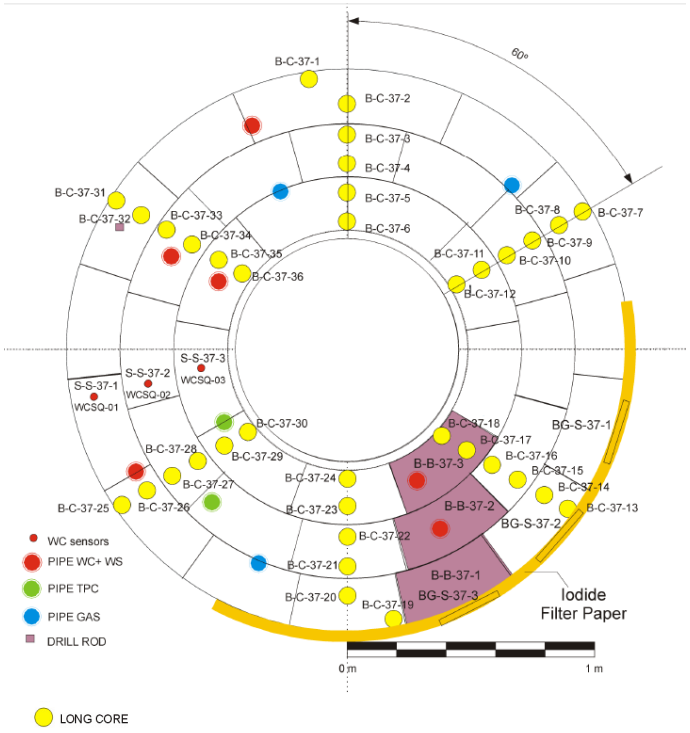

Fig. C-171: Sampling Section 37

This section contains iodide which was added on filter paper. The Sampling Plan considers radial profiles of iodide concentrations along the coloured bentonite blocks 37-1 to 37-3 (see AITEMIN 2015 for more details).

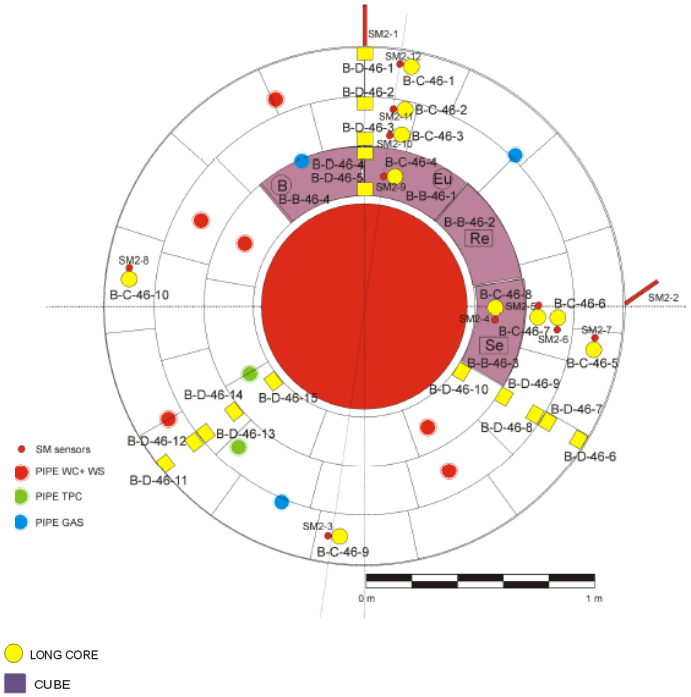

Fig. C-172: Bentonite blocks (coloured blocks) selected for sampling the point tracers in Section 46, which contains borate, europium, selenate and perrhenate (see AITEMIN 2015 for more details)

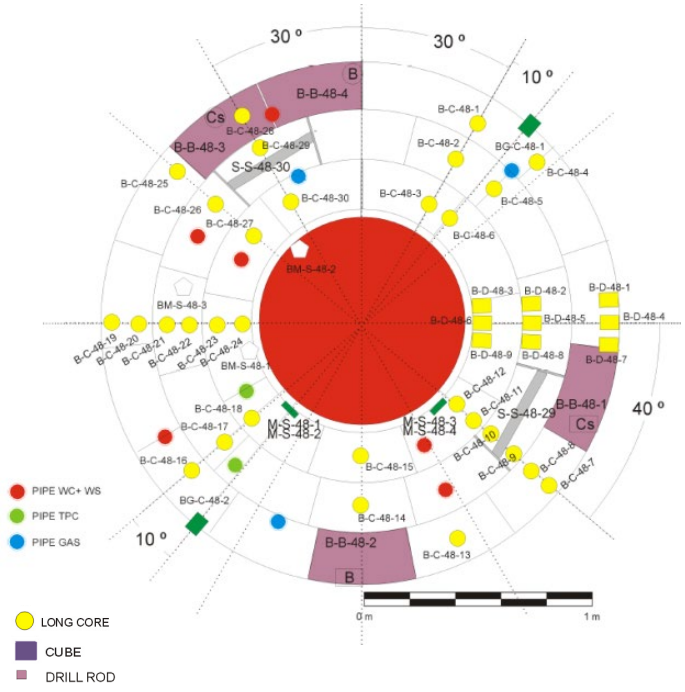

Fig. C-173: Bentonite blocks (coloured blocks) selected for sampling the point tracers (borate and cesium) located in Section 48 (see AITEMIN 2015 for more details)

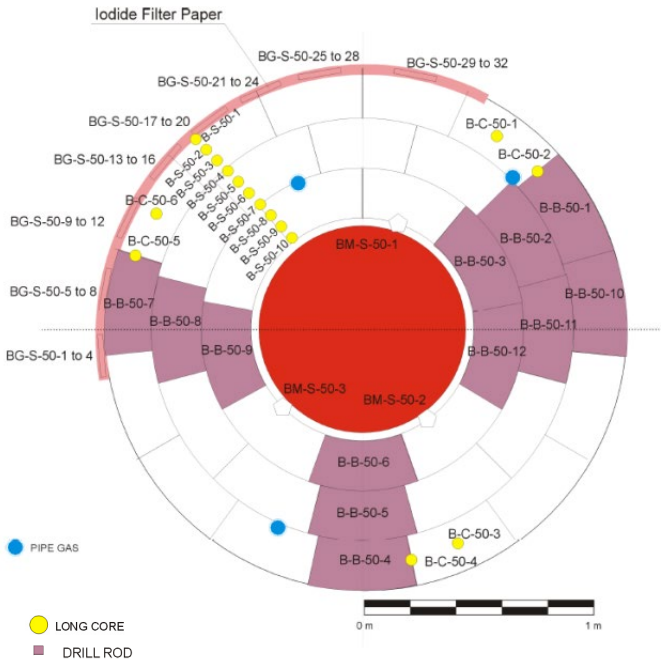

Fig. C-174: Sampling Section 50

This section contains iodide which was added on filter paper. The Sampling Plan considers radial profiles of iodide concentrations along 3 bentonite blocks (see AITEMIN 2015 for more details).

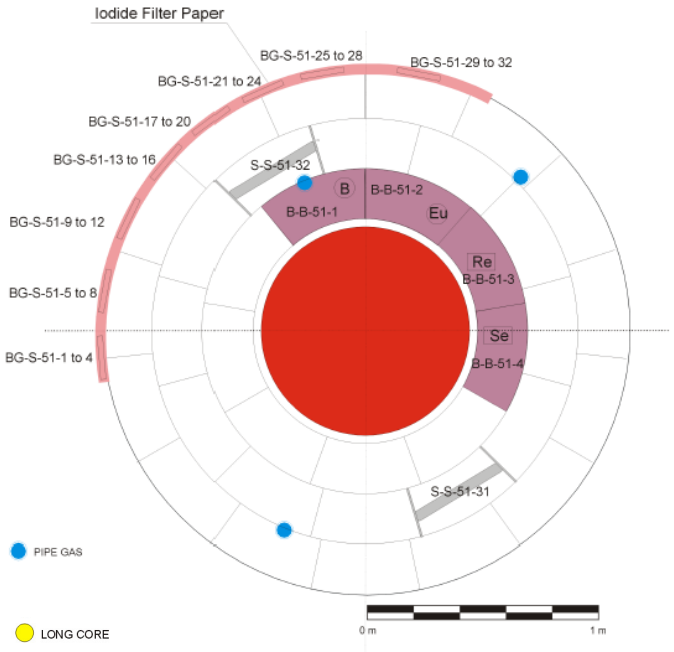

Fig. C-175: Sampling Section 51

This section contains iodide which was added on filter paper. The Sampling Plan considers radial profiles of iodide concentrations along 3 bentonite blocks (modified from AITEMIN 2015). This section contains also borate, europium, selenate and perrhenate in the coloured bentonite blocks (see AITEMIN 2015 for more details).

C.6.2 Predictions of iodide migration

C.6.2.1 Previous iodide migration modelling

Concentrations of iodide were analysed in clay samples along a radius of the clay buffer during the dismantling of Heater #1 to study iodide migration through Section 37.

Zheng (2006) performed a 1D axisymmetric THCM model to predict iodide migration. It was assumed that the tracer was readily available to migrate through the bentonite at t = 0. This was achieved by assigning an initial iodide concentration at the nodes located at the bentonite-granite interface.

Zheng (2006) reported a first inverse model (*inverse model 1*) with a diffusion coefficient, D_o, equal to 8.3×10^{-13} m^2/s and an accessible porosity equal to 61.4 % of the total porosity. Fig. C-176 shows the measured and computed concentrations for the optimum parameters. One can see that the iodide concentration near the heater is unrealistically large, possibly because the evaporation at heater/bentonite contact is too large. Zheng (2006) performed a second inverse run in which the vapour tortuosity was estimated in addition to the diffusion coefficient and accessible porosity (inverse model 2). The parameter estimates in this case were:

1. $D_o = 1.3 \times 10^{-12}$ m^2/s
2. Accessible porosity = 57.2 % of total porosity
3. Vapour tortuosity = 0.099

The fit of computed results to measured data improved by decreasing the vapour tortuosity (Fig. C-176). Zheng (2006) noticed that the optimum values of the diffusion coefficient and accessible porosity could be correlated.

C.6.2.2 Updated iodide migration

The previous simulation of iodide migration reported by Zheng (2006) for Heater #1 in 2002 was updated by using the most updated version of the INVERSE-FADES-CORE code and by using the most updated THMC model parameters and boundary conditions. The accessible porosity was increased from 57.2 % to 95 % of the total porosity to fit the iodide measured data in 2002. The updated accessible porosity is equal to 0.39. The vapour tortuosity was updated to 0.2.

Pre-dismantling predictions of iodide migration in Sections 50 and 51 were performed with the updated 1D axisymmetric model presented in Chapters C.4 and C.5.

Fig. C-177 shows the pre-dismantling predictions of iodide concentrations in 2015. These predictions apply to Sections 50 and 51 (Heater #2). The predictions for Sections 50 and 51 located near the Heater #2 were performed by assuming that the heater was switched off in 2015. Fig. C-178 shows the pre-dismantling predictions of iodide concentrations in 2015 in Section 37 located near Heater #1. The predictions were performed by taking into account that the Heater #1 was switched off in 2002 (after 5.5 years of heating). It can be seen that the model calculates a large evaporation near the heater and the concentrations near the heater increase with time (Fig. C-177). The iodide concentration near Heater #1 decreases after 2002 after the heater was switched off due to the increase in water content caused by vapour condensation and bentonite hydration.

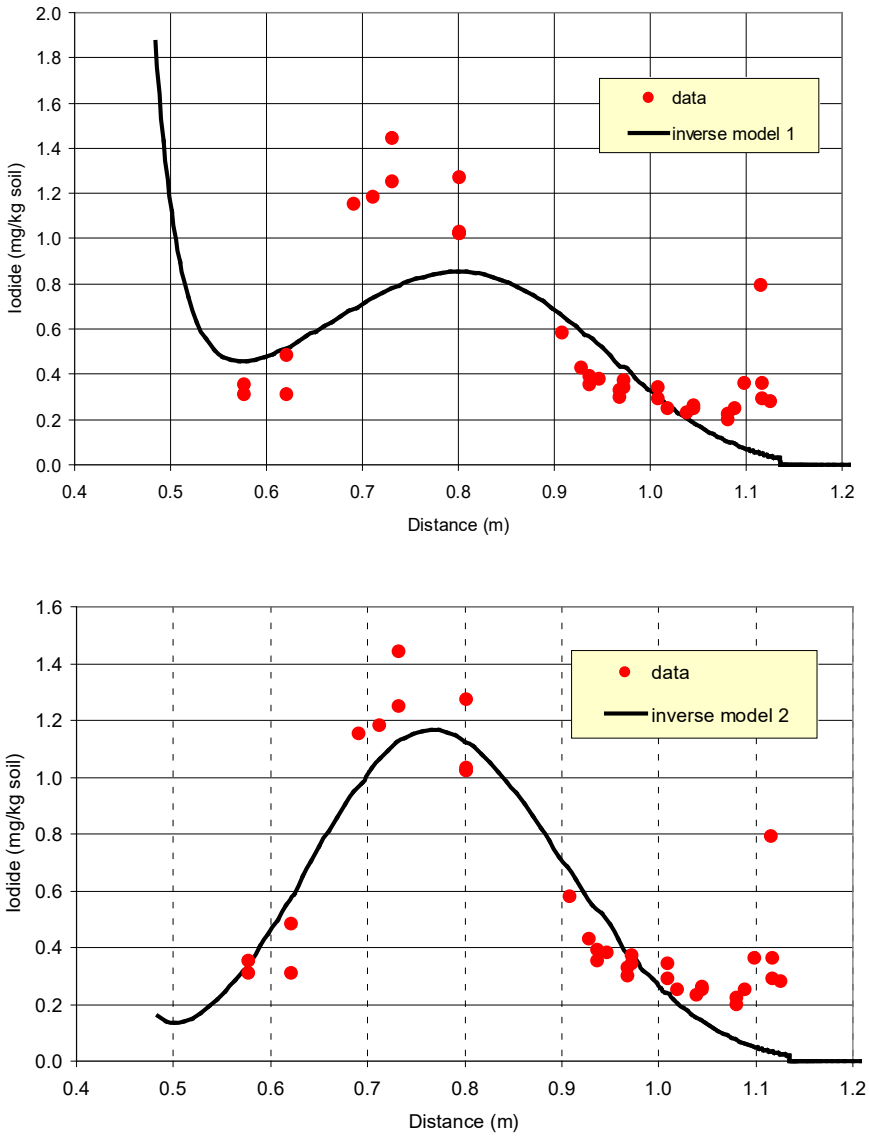

Fig. C-176: Inverse modelling results of inverse model 1 (top plot) and inverse model 2 (bottom plot) (from Zheng 2006)

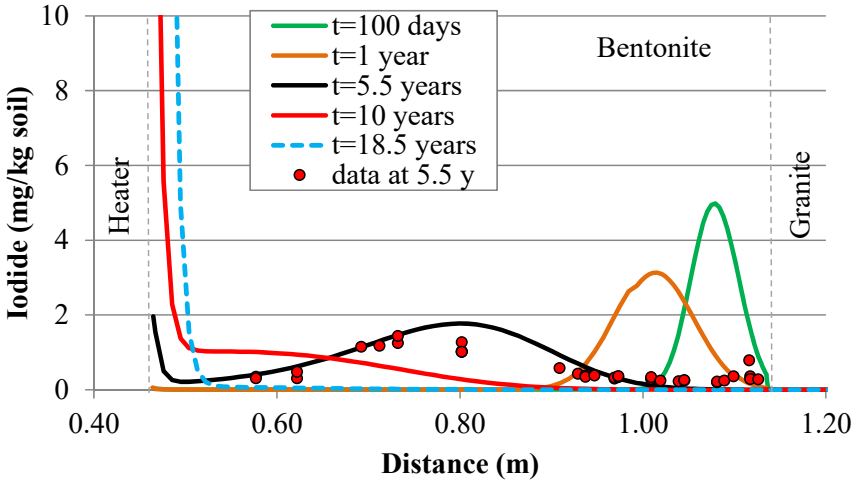

Fig. C-177: Radial distribution of the calculated iodide concentrations at selected times and pre-dismantling prediction of iodide concentrations in 2015 (t = 18.5 years) for Sections 50 and 51

Also shown are the measured iodide data in 2002.

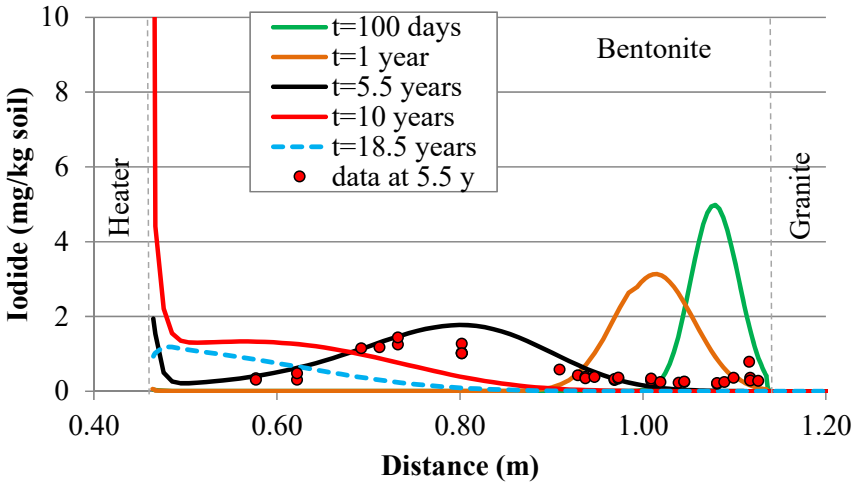

Fig. C-178: Radial distribution of the calculated iodide concentrations at selected times and pre-dismantling prediction of iodide concentrations in 2015 (t = 18.5 years) for Section 37

Also shown are the measured iodide data in 2002.

C.6.2.3 Sensitivity analyses

Given the lack of data on some relevant parameters, predicted iodide concentrations may contain uncertainties. These uncertainties were quantified by means of sensitivity runs with respect to the diffusion coefficient, the accessible porosity, the distribution coefficient and the initial iodide concentration. The set of parameter values used for the sensitivity runs are listed in Tab. C-6.

Tab. C-6: Parameter values used for the sensitivity runs of iodide migration in Section 37 of the FEBEX in-situ test

Parameter	**Base run**	**Sensitivity run**
Accessible porosity, ϕ_a	0.39	0.245 0.41 0.37
Pore water diffusion coefficient, D_o (m^2/s)	1.3×10^{-12}	1.3×10^{-11} 1.3×10^{-13}
Initial iodide concentration in bentonite, C_o (mol/L)	1.57×10^{-7}	7.85×10^{-8} 1.57×10^{-9}
Distribution coefficient, K_d (m^3/kg)	0.0	1.0×10^{-4} 1.0×10^{-3}
Vapour tortuosity	0.2	0.2

C.6.2.3.1 Sensitivity to the accessible porosity

Fig. C-179 shows the sensitivity of the computed iodide concentrations in Section 37 after 5.5 years (2002) to changes in the accessible porosity of the bentonite. The following values of the accessible porosity were considered: ϕ_a = 0.41, ϕ_a =0.39, ϕ_a = 0.37 and ϕ_a = 0.245. The predicted iodide concentrations with an accessible porosity of 0.245 do not fit the measured data. One can see that the best fit to measured data is obtained with the accessible porosity of the base run. However, the computed concentrations underestimate the measured values near the bentonite-granite interface.

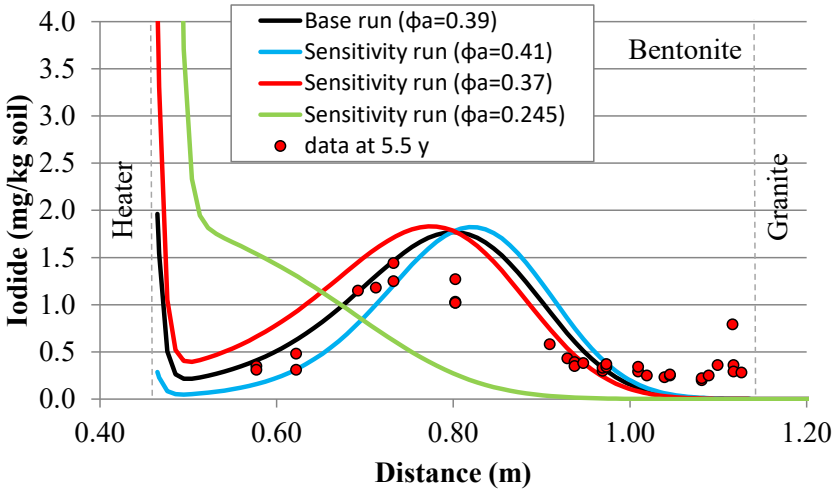

Fig. C-179: Sensitivity of the computed iodide concentrations in Section 37 after 5.5 years (2002) to changes in the accessible porosity of the bentonite

C.6.2.3.2 Sensitivity to the initial concentration of iodide in bentonite

Fig. C-180 shows the sensitivity of the computed iodide concentrations in Section 37 after 5.5 years (2002) to changes in the initial iodide concentration in the bentonite. The predicted iodide concentrations in 2002 are not sensitive to a decrease of the initial iodide concentration in the bentonite pore water.

C.6.2.3.3 Sensitivity to the distribution coefficient

Fig. C-181 shows the sensitivity of the computed iodide concentrations in Section 37 after 5.5 years (2002) to changes in the distribution coefficient in the bentonite, K_d. The computed iodide concentrations are very sensitive to an increase of K_d from 0.1 to 1 mL/g. It can be seen that the tracer pulse is clearly retarded when the K_d is increased.

C.6.2.3.4 Sensitivity to the diffusion coefficient

Fig. C-182 shows the sensitivity of the computed iodide concentrations in Section 37 after 5.5 years (2002) to changes in the diffusion coefficient of the bentonite, D_0. The computed iodide concentrations are sensitive to changes in D_0. The concentrations are more sensitive to an increase

of D_0 than to a decrease of D_0. The computed iodide concentrations are less sensitive to a decrease in the diffusion coefficient because iodide spreading is dominated by hydrodynamic dispersion when the diffusion coefficient is decreased by a factor of 10. The dispersivity of iodide in the bentonite was set equal to 8 mm.

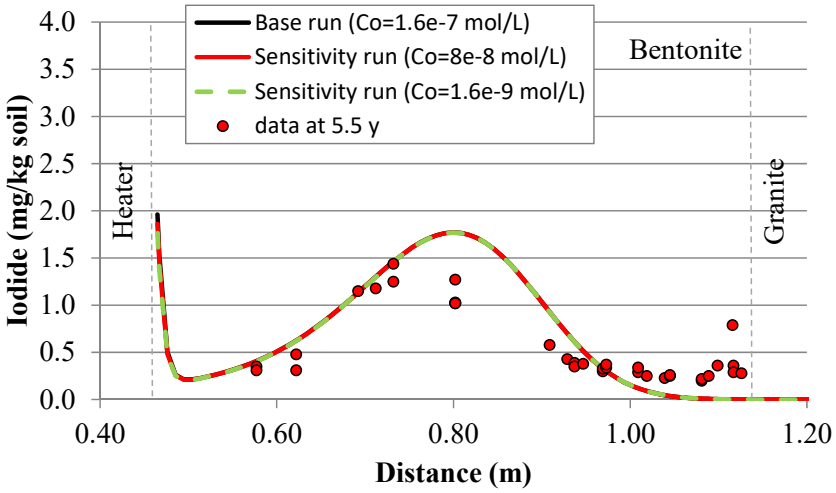

Fig. C-180: Sensitivity of the computed iodide concentrations in Section 37 after 5.5 years (2002) to changes in the initial iodide concentration in the bentonite

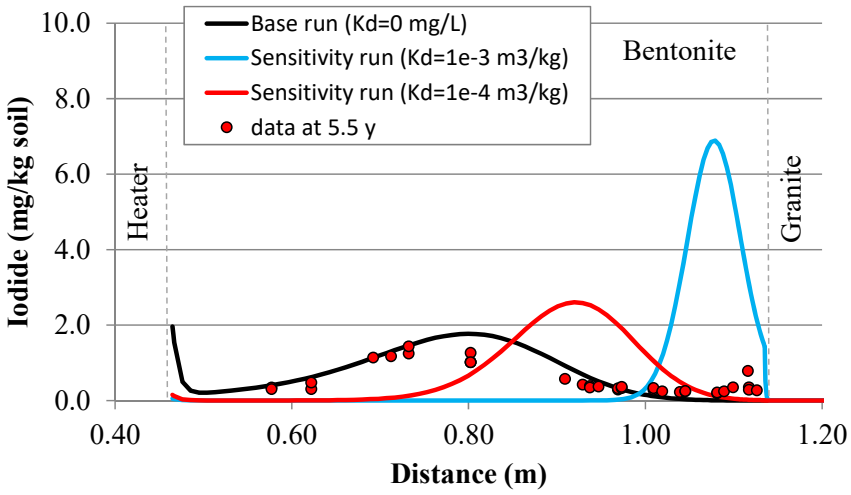

Fig. C-181: Sensitivity of the computed iodide concentrations in Section 37 after 5.5 years (2002) to changes in the distribution coefficient of the bentonite

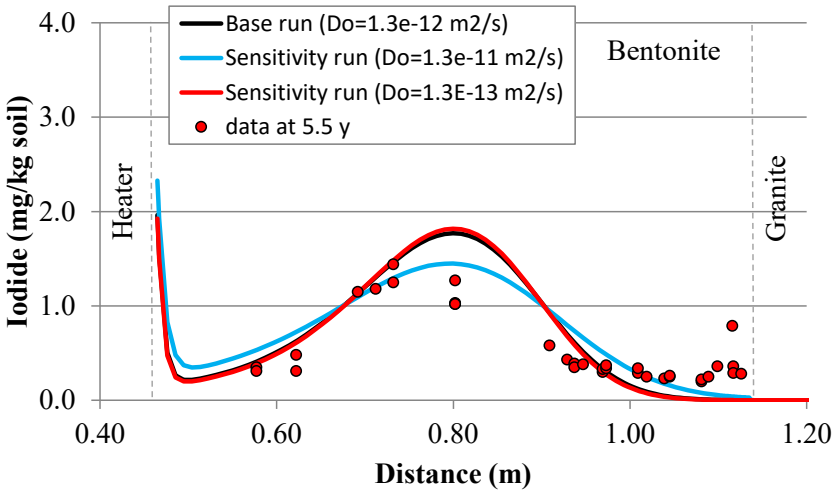

Fig. C-182: Sensitivity of the computed iodide concentrations in Section 37 after 5.5 years (2002) to changes in the diffusion coefficient of the bentonite

C.6.3 Predictions for the migration of point tracers

This section presents the updated predictions of the migration of point tracers by using 2D models in vertical planes perpendicular to the axis of the gallery. Predictions have been performed for the following tracers:

1. Borate, europium, perrhenate, and selenate at the inner blocks of Section 46 which is equivalent to Section E2
2. Cesium and borate at the outer blocks of Section 48 which is equivalent to section F2

C.6.3.1 Numerical model

2D THMC numerical models in vertical planes perpendicular to the axis of the gallery corresponding to Sections E2 and F2 of Heater #2 were carried out. Tracer migration took place in a quadrant of this section. The model accounts for the bentonite barrier which extends up to r = 1.14 m and for a circular annulus of granitic rock of 0.55 m thickness. Fig. C-183 shows the finite element grid of the 2D numerical model used for tracer migration and the approximate location of the points where the tracers were emplaced. The mesh has 1'362 nodes and 2'652 elements.

The boundary condition of the granite at a radial distance of 1.69 m (model boundary) was taken from the 2D axisymmetric model (see Chapter C.4). The simulation time horizon covers the entire duration of the test from February 1997 to June 2015. The model parameters and initial conditions were taken from previous models.

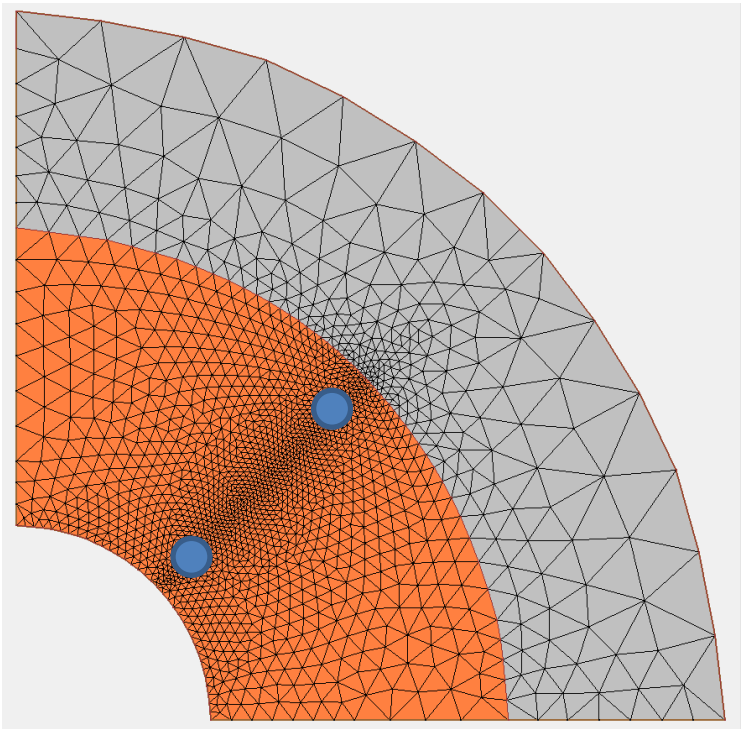

Fig. C-183: Finite element grid of the 2D numerical model in a vertical plane perpendicular to the axis of the gallery used for tracer migration

Blue circles indicate the approximate location of the tracers when they were placed.

C.6.3.2 Tracer parameters

The transport and sorption parameters of the tracers are listed in Tab. C-7. Data for Cs and selenite were taken from Samper et al. (2006). Data for europium were derived from García-Gutiérrez et al. (2011). Data for borate and perrhenate were taken from Samper et al. (1998b). Dispersion processes are mainly caused by molecular diffusion rather than by hydrodynamic dispersion. For this reason, a small dispersivity of 2 mm was adopted.

Tab. C-7: Main transport and sorption parameters of the tracers used in the FEBEX in-situ test

Data for cesium and selenite were taken from Samper et al. (2006). Data for europium were derived from García-Gutiérrez et al. (2011) and Zhou et al (2013). Data for other tracers such as borate and perrhenate were taken from Samper et al. (1998b). CP = Clay Plug; SSS = Sintered Stainless Steel.

Tracer	**Tracer type**	**Mass** (mg)	**D_e** (m^2/s)	**K_d** (mL/g)	**Accessible porosity**
Borate	CP	606	1.95×10^{-10}	100.00	0.41
Europium	CP	88.6	3.88×10^{-12}	26.5	0.41
Perrhenate	SSS	76.9	6.00×10^{-11}	0	0.41
Selenate	SSS	307.5	2.50×10^{-13}	2.17	0.41
Cesium	CP	59	6.00×10^{-10}	925.1	0.41

C.6.3.3 Numerical model results

Fig. C-184 shows the computed temperatures at t = 0, 5, 10 and 18 years. One can see that the computed temperatures exhibit axial symmetry. The temperature increases with time in the bentonite and granite. The measured temperature at t = 18 years in the sensors located near the bentonite/granite interface in Sections E2 and F2 is around 46 °C. The calculated temperature with the 2D model at this interface is 44 °C. Therefore, the 2D numerical model reproduces the measured temperatures at such interface.

Fig. C-185 shows the computed water saturation at t = 0, 5, 10 and 18 years. One can see that the computed saturations exhibit axial symmetry. The initial saturation is 59 % in bentonite and 100 % in granite. The saturation in bentonite increases with time. The bentonite is not fully saturated after 18 years.

Perrhenate is a conservative tracer. The model predictions of this tracer (not shown here) indicate that this tracer should have diffused entirely in the full section so that gradients of the concentration of perrhenate in 2015 are extremely small.

Borate has a moderately large K_d value of 100 mL/g. Fig. C-186 shows the computed concentrations of dissolved borate at t = 0, 5, 10, 15 and 18 years with the 2D model. One can see that the borate plume has moved a few cm after 18 years. The tracer plume migrates mainly by molecular diffusion. Its apparent diffusion coefficient, however, is much smaller than that of a non-sorbing tracer.

Fig. C-187 shows the computed concentrations of dissolved selenate at t = 0, 5, 10 and 18 years. The selenate plume does not diffuse in an isotropic manner due to the thermal field created by the heater and the water flow which pushes the tracer inwards.

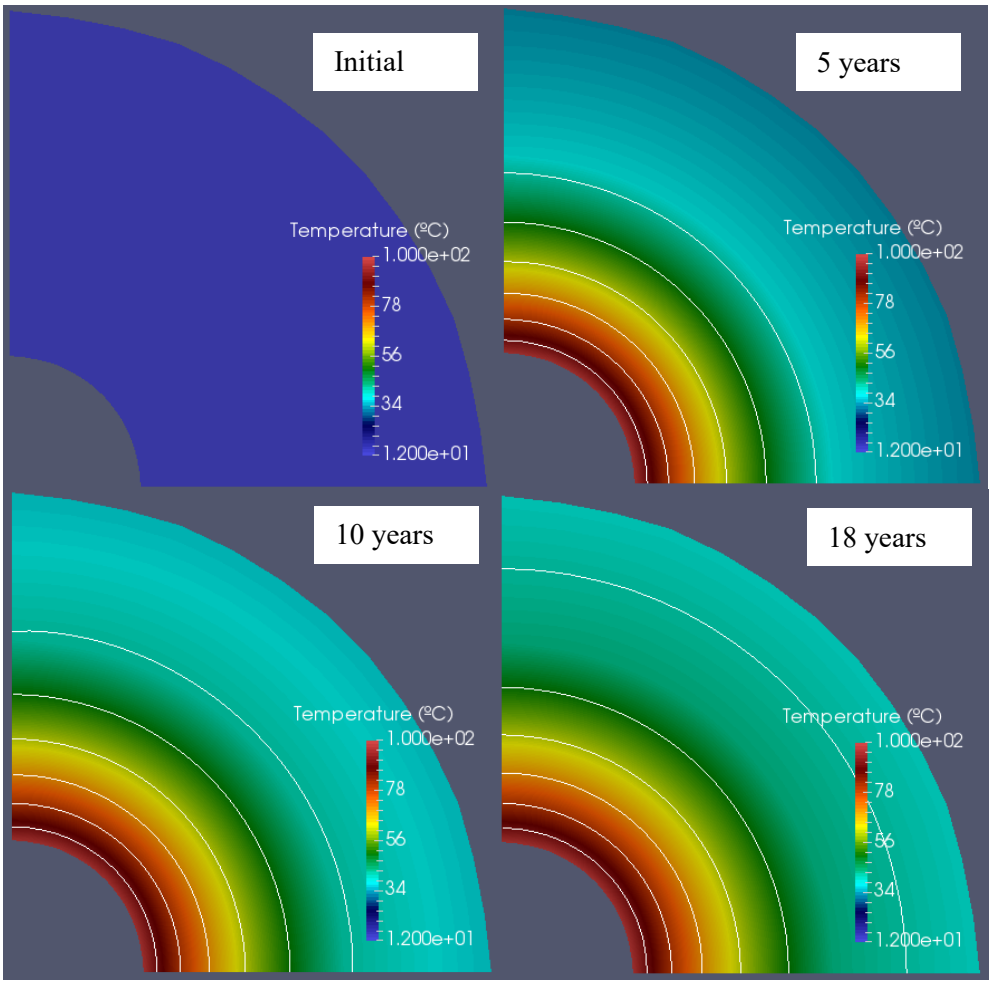

Fig. C-184: Computed temperatures at t = 0, 5, 10 and 18 years with the 2D numerical model in a vertical plane normal to the axis of the gallery

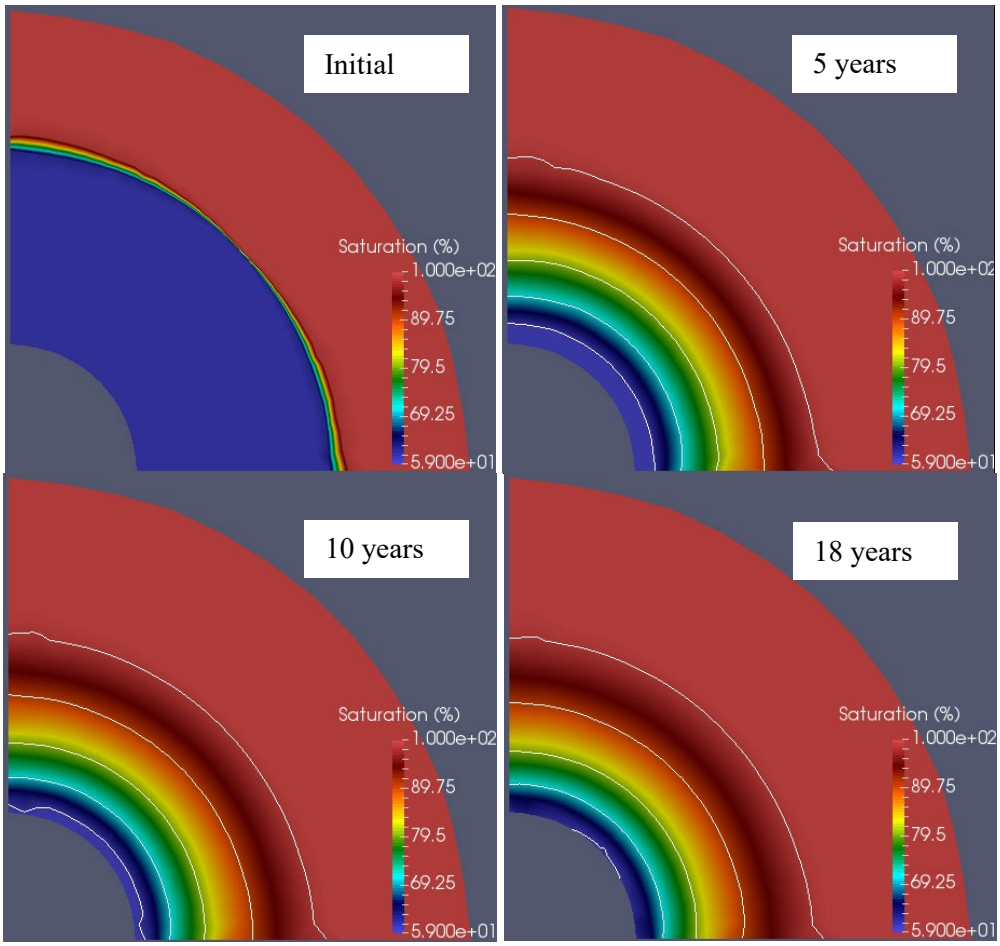

Fig. C-185: Computed water saturation at t = 0, 5, 10 and 18 years with the 2D numerical model in a vertical plane normal to the axis of the gallery

Fig. C-188 shows the computed concentrations of dissolved europium at t = 0, 5, 10, 15 and 18 years. The K_d of europium is sufficiently large so that europium barely migrates after 18 years.

Fig. C-189 the computed concentrations of dissolved cesium at t = 0, 5, 10, 15 and 18 years. This tracer was emplaced in an outer block. The tracer plume in 2015 has a few cm.

Fig. C-190 shows the computed concentrations of dissolved borate at t = 0, 5, 10, 15 and 18 years. The borate concentration contours reveal a small migration and diffusion of this tracer due to the large distribution coefficient of borate.

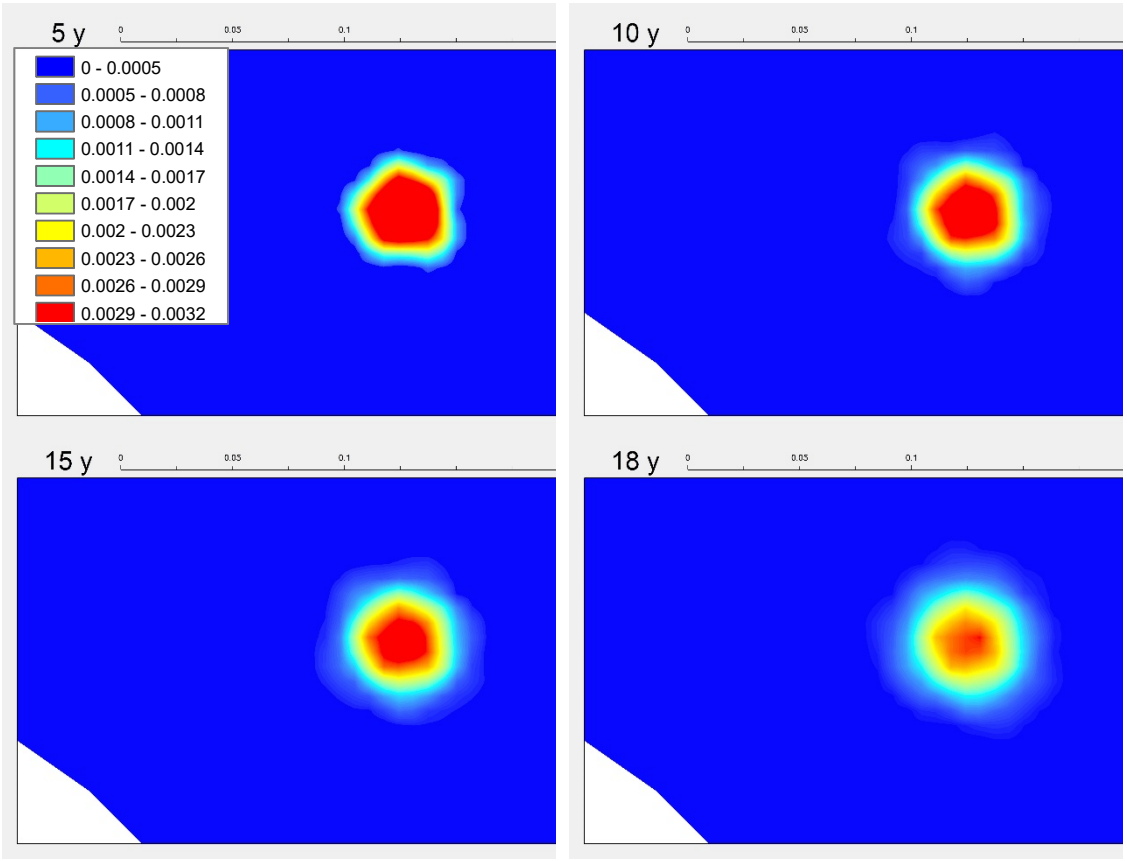

Fig. C-186: Computed concentrations of dissolved borate (mol/L) at:5 years (top left); 10 years (top right); 15 years (bottom left) and 18 years (bottom right) with the 2D numerical model in a vertical plane normal to the axis of the gallery

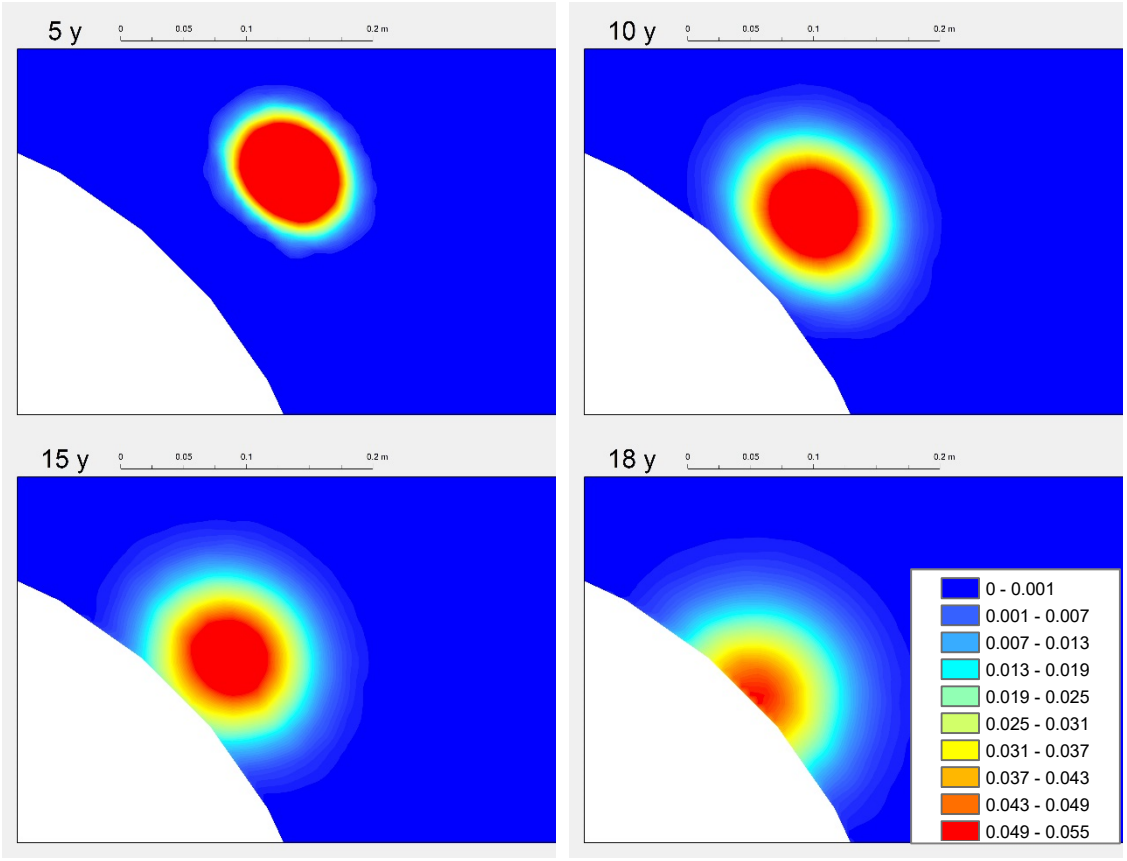

Fig. C-187: Computed concentrations of dissolved selenate (mol/L) at:5 years (top left); 10 years (top right); 15 years (bottom left) and 18 years (bottom right) with the 2D numerical model in a vertical plane normal to the axis of the gallery

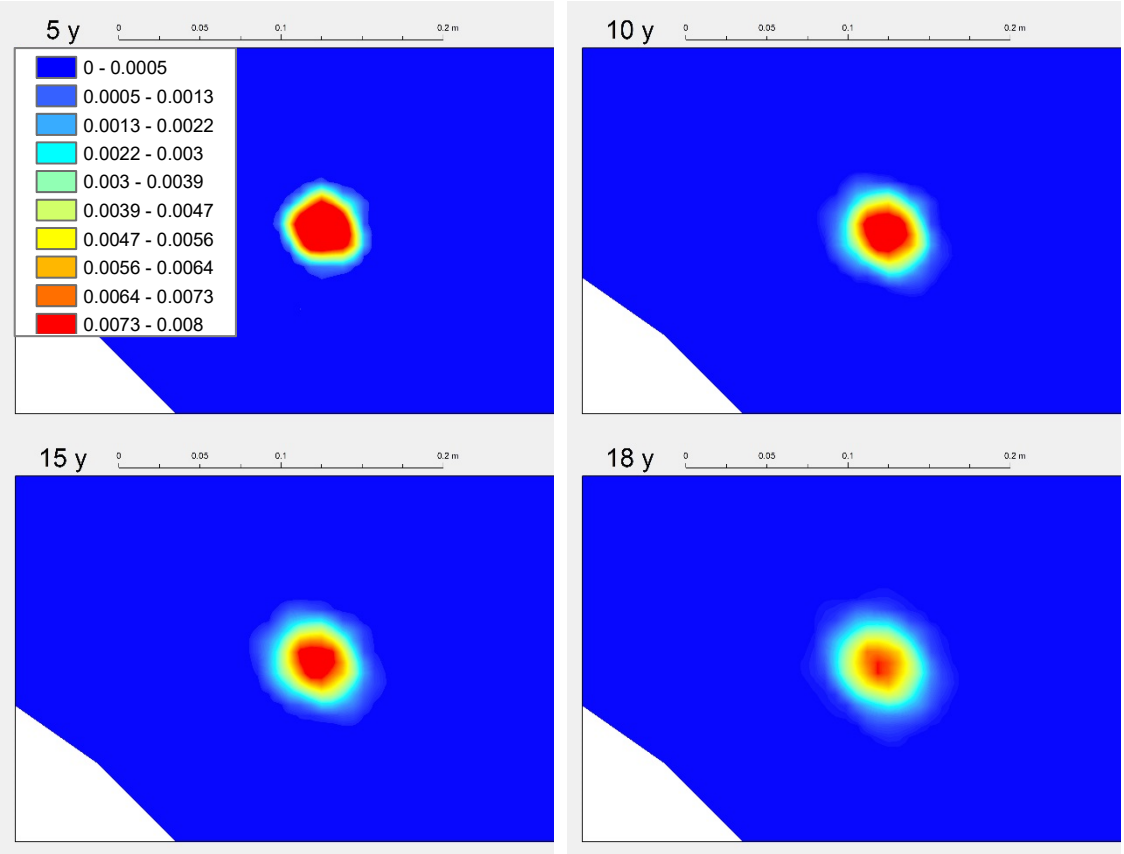

Fig. C-188: Computed concentrations of dissolved europium (mol/L) at:5 years (top left); 10 years (top right); 15 years (bottom left) and 18 years (bottom right) with the 2D numerical model in a vertical plane normal to the axis of the gallery

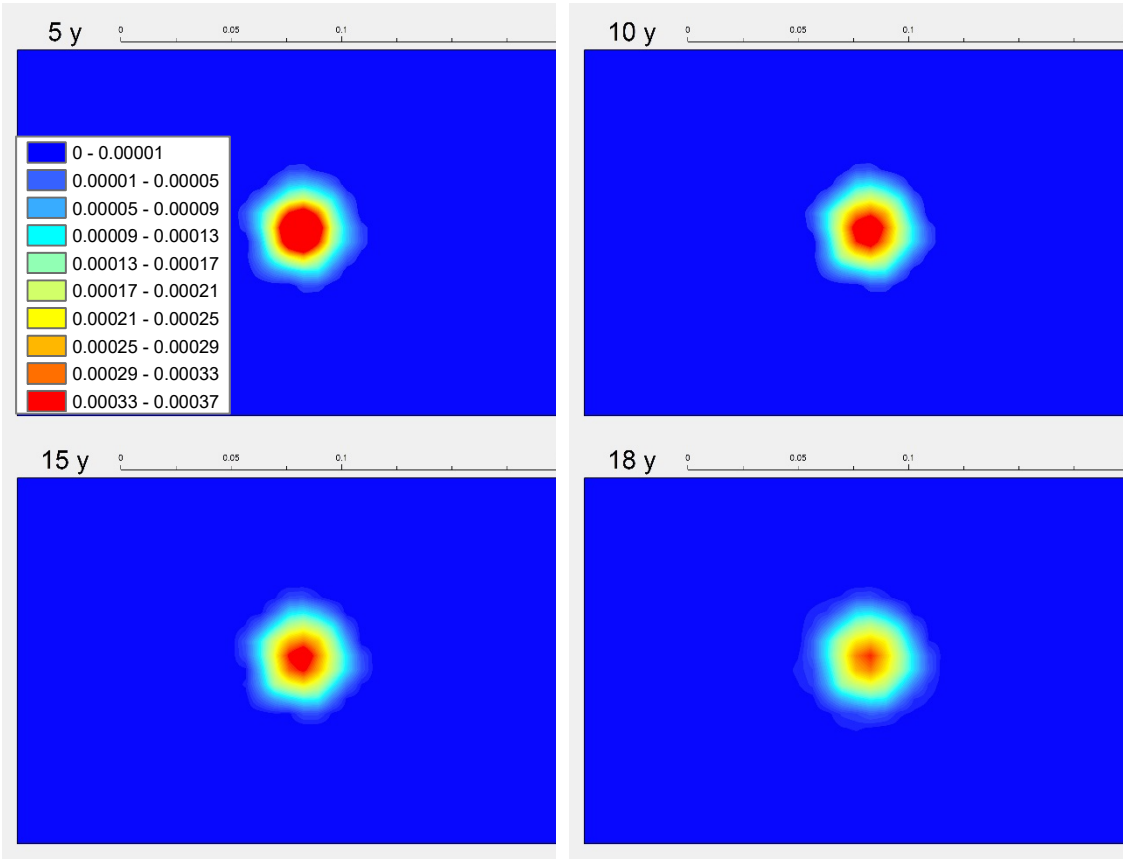

Fig. C-189: Computed concentrations of dissolved cesium (mol/L) at:5 years (top left); 10 years (top right); 15 years (bottom left) and 18 years (bottom right) with the 2D numerical model in a vertical plane normal to the axis of the gallery

This tracer was placed in an outer block near the bentonite/granite interface.

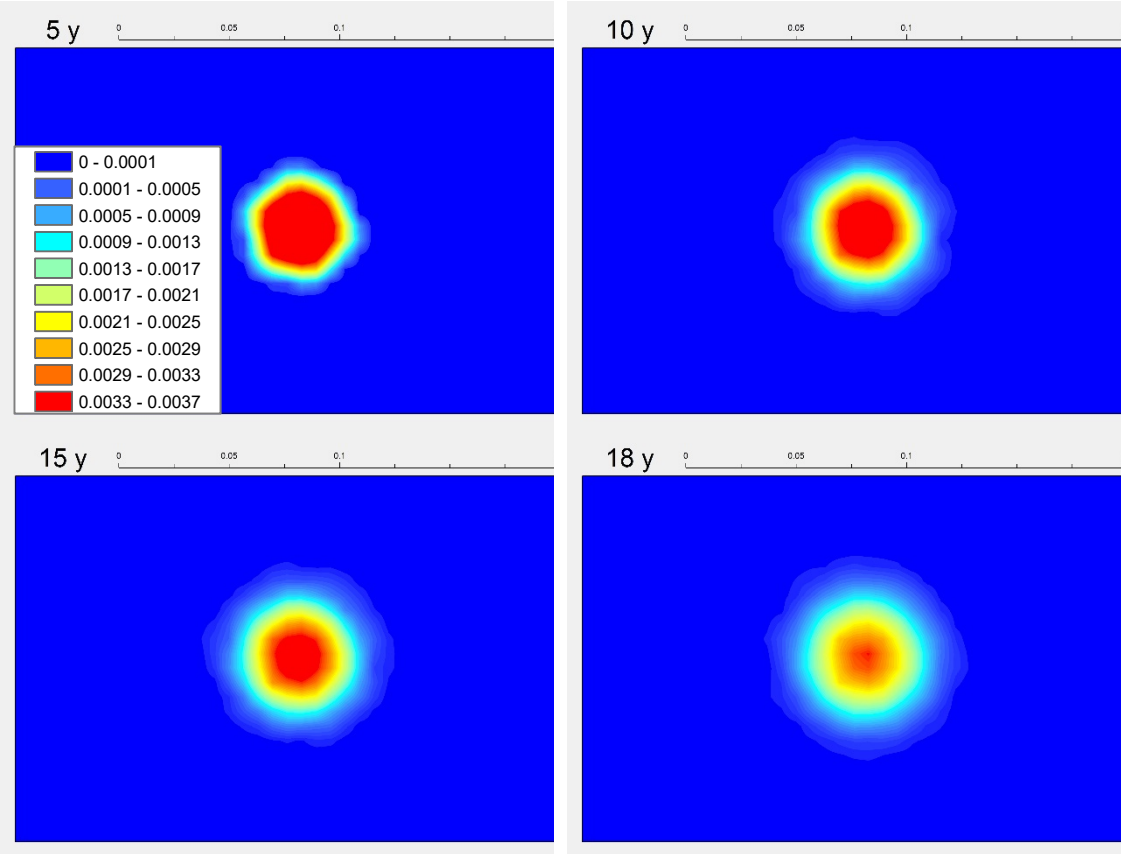

Fig. C-190: Computed concentrations of dissolved borate (mol/L) at:5 years (top left); 10 years (top right); 15 years (bottom left) and 18 years (bottom right) with the 2D numerical model in a vertical plane normal to the axis of the gallery

This tracer was placed in an outer block near the bentonite/granite interface.

The plume of dissolved borate in the inner block is almost circular with an approximate diameter of 8 cm. The dissolved selenate in the inner block reaches the heater and shows a semicircular plume with an approximate diameter of 20 cm. The plume of dissolved europium in the inner block is slightly anisotropic with an approximate length of 8 cm.

The plume of dissolved caesium in the outer block is almost circular with an approximate diameter of 7 cm. Finally, the plume of dissolved borate in the outer block is almost circular with a diameter of 10 cm.

C.6.4 Summary and conclusions

Updated predictions of the tracer migration have been presented for: 1) iodide along several radii in Sections 37, 50 and 51 by using a 1D axisymmetric model; 2) borate, europium, perrhenate and selenate at the inner blocks of Section 46 by using 2D models in vertical planes; and 3) caesium and borate at the outer blocks of Section 48 by using 2D models in vertical planes.

The migration of each tracer was simulated separately by taking into account its transport and chemical parameters (accessible porosity, effective diffusion coefficient, distribution coefficient), initial concentration and location.

The predictions of iodide migration reported by Zheng (2006) for Heater #1 in 2002 have been updated. The predictions of I migration have been computed with most updated version of the THCM model of the FEBEX in-situ test. The accessible porosity of iodide has been recalibrated. The predictions for Sections 50 and 51 located near Heater #2 were performed by assuming that the heater was switched off in 2015. The pre-dismantling predictions of iodide concentrations in 2015 in Section 37 located near Heater #1 were performed by taking into account that Heater #1 was switched off in 2002.

The model predictions of tracer migration lead to the following conclusions:

1. Large iodide concentrations are predicted near the heater in Sections 50 and 51 located near Heater #2. The iodide concentration in Section 37 near Heater #1 decreased after the heater was switched off in 2002 due to the increase in water content caused by vapour condensation and bentonite hydration.

2. The predicted perrhenate concentrations in 2015 show that this tracer has diffused entirely in the full section.

3. The plumes of the point tracers located in the inner blocks are
   a) Almost circular with an approximate diameter of 8 cm for borate
   b) Semicircular with an approximate diameter of 20 cm for selenate
   c) Slightly anisotropic with an approximate length of 8 cm for europium.

4. The plumes of the point tracers located in the outer blocks are:
   a) Almost circular with an approximate diameter of 7 cm for caesium
   b) Almost circular with a diameter of 10 cm for borate

C.7 Predicting the interactions of shotcrete and bentonite

C.7.1 Introduction

The updated THCM model has been used to perform predictions of the interactions of bentonite with the shotcrete plug.

C.7.2 Methodology

The geochemical interactions between bentonite and the shotcrete plug were modelled with a non-isothermal variably-saturated 1D numerical water flow and multicomponent reactive transport model normal to the interface at a radial distance from the axis of the gallery equal to 0.75 m. The simulation extends from 2002, when the shotcrete plug was constructed, to 2015.

A telescopic approach was followed to derive the initial and boundary thermal and hydrodynamic conditions for this 1D model. First, a detailed 2D axisymmetric THM model of the bentonite/shotcrete interface was performed. This detailed model considered a slice of shotcrete plug 0.25 m thick and a slice of bentonite buffer 0.32 m thick. Fig. C-191 shows the finite-element mesh of the 2D axisymmetric model of the entire test and the finite element grid for the detailed 2D axisymmetric model selected for modelling the interactions of bentonite and shotcrete. The THM boundary and initial conditions for the detailed 2D axisymmetric THM model of the bentonite/shotcrete interface were derived from the results of the 2D axisymmetric THM model of the entire FEBEX in-situ test presented in Chapter C.4.

Fig. C-192 shows the location of the 1D profiles normal to the bentonite/shotcrete interface at radial distances r = 0.55 m, 0.75 m and 1 m.

Fig. C-193 shows the finite-element mesh of the 1D numerical model used to simulate the geochemical interactions at the bentonite/shotcrete interface.

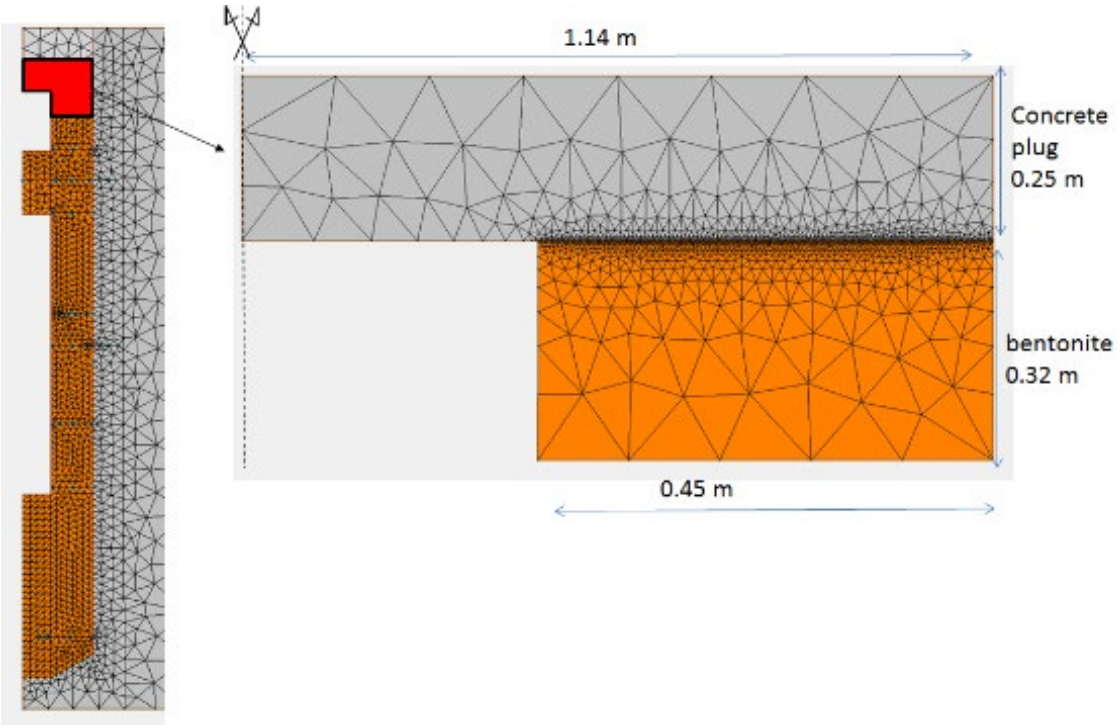

Fig. C-191: Finite-element mesh of the 2D axisymmetric model of the entire test (left) and finite-element grid for the detailed 2D axisymmetric model selected for modelling the interactions of bentonite and shotcrete

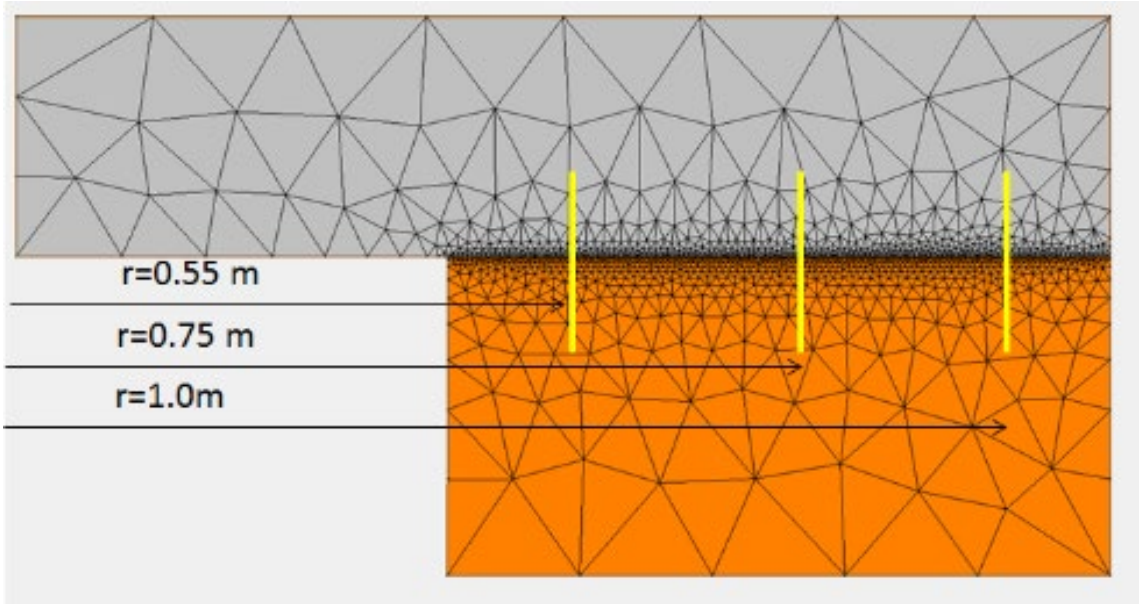

Fig. C-192: Detailed 2D axisymmetric model selected for modelling the interactions of bentonite and shotcrete and location of the 1D profiles normal to the bentonite/shotcrete interface at radial distances r = 0.55 m, 0.75 m and 1 m

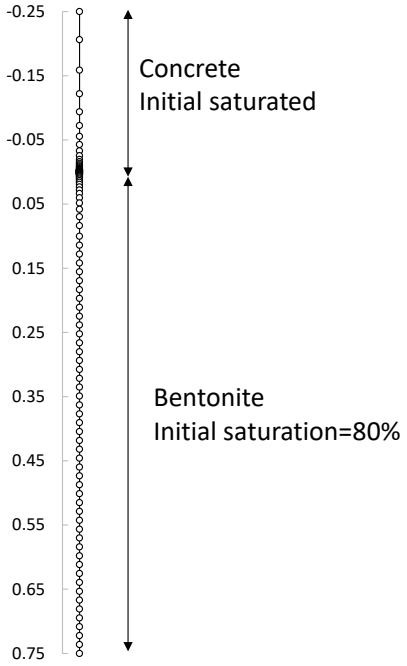

Fig. C-193: Finite-element mesh of the 1D numerical model used to simulate the geochemical interactions at the bentonite/shotcrete interface

C.7.3 Detailed 2D axisymmetric model

The detailed 2D axisymmetric THM model of the bentonite/shotcrete interface was run for the period from 2002 to 2015. Fig. C-194 shows the temperature computed with the detailed 2D axisymmetric THM model of the bentonite/shotcrete interface along a horizontal line normal to the interface at a radial distance of r = 0. 75 m. Model results show that the computed temperature after 13 years of simulation (from 2002 to 2015) ranges from 24 ºC in shotcrete to 34 ºC in bentonite. These computed temperatures compare well with temperatures measured along the boreholes drilled through the shotcrete plug before switching off Heater #2 (Fig. C-195).

Fig. C-196 shows the computed saturation degree with the detailed 2D axisymmetric THM model of the bentonite/shotcrete interface in 2015 and a zoom of the bentonite/shotcrete interface. The shotcrete is always saturated. The saturation degree in the bentonite increases from the granite to the dummy canister.

Fig. C-197 shows the saturation degree computed with the detailed 2D axisymmetric THM model of the bentonite/shotcrete interface along several horizontal lines normal to the interface at radial distances of r = 0.55 m, 0.75 m and 1 m. Fig. C-192 shows the location of the profiles. Again, the shotcrete is fully saturated the entire simulation. The saturation degree in the bentonite increases with time. The saturation at r = 1 m increases faster than it does at r = 0.5 m. After 13 years the bentonite is almost fully saturated.

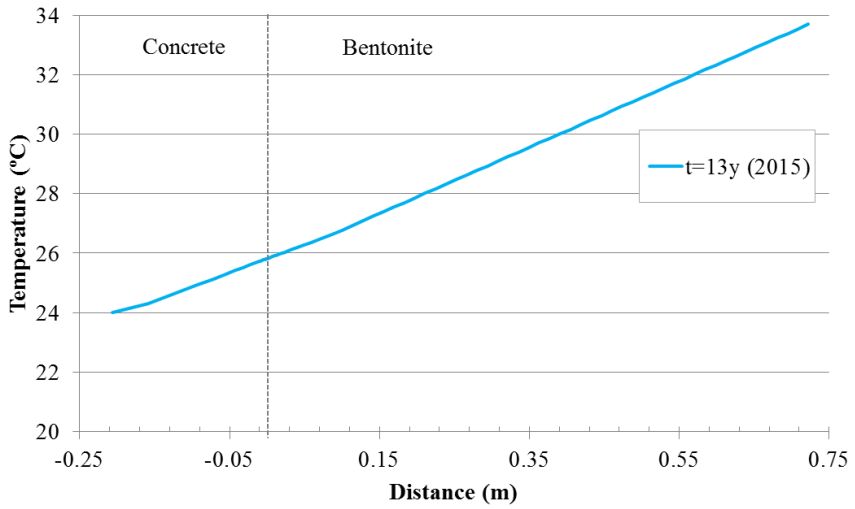

Fig. C-194: Temperature computed with the detailed 2D axisymmetric THM model of the bentonite/shotcrete interface along a horizontal line normal to the interface at a radial distance of r = 0.75 m

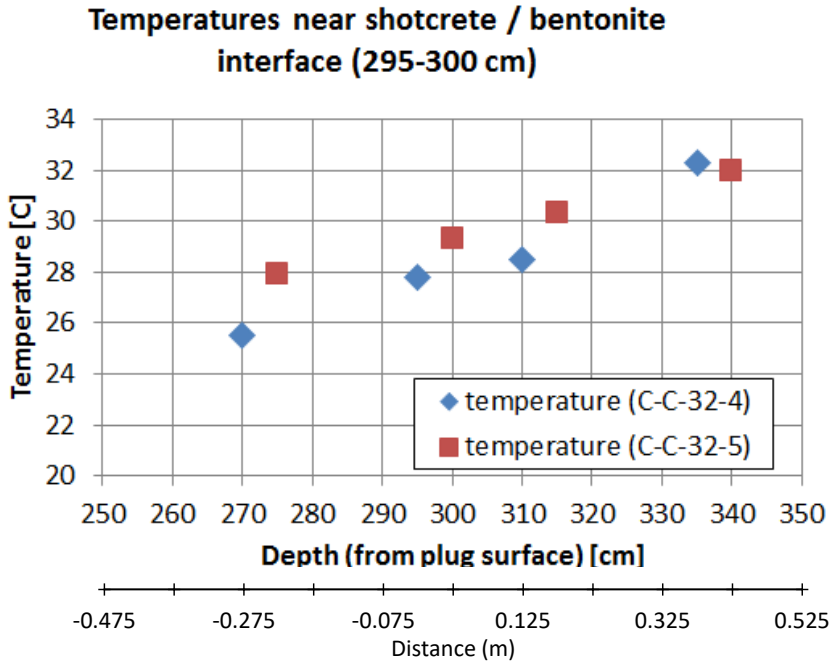

Fig. C-195: Measured temperatures along two boreholes drilled through the shotcrete plug before switching off Heater #2 (Nagra 2015)

The lower x-axis shows the distance measured from the shotcrete/bentonite interface.

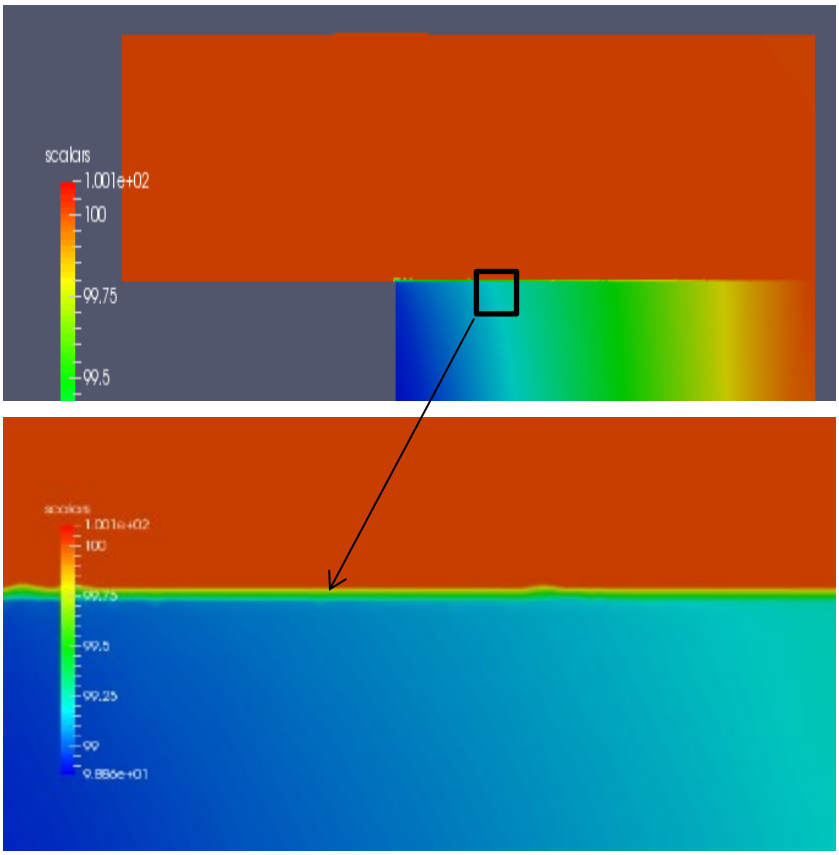

Fig. C-196: Computed saturation degree in 2015 (top plot) and a zoom of the bentonite/shotcrete interface (below)

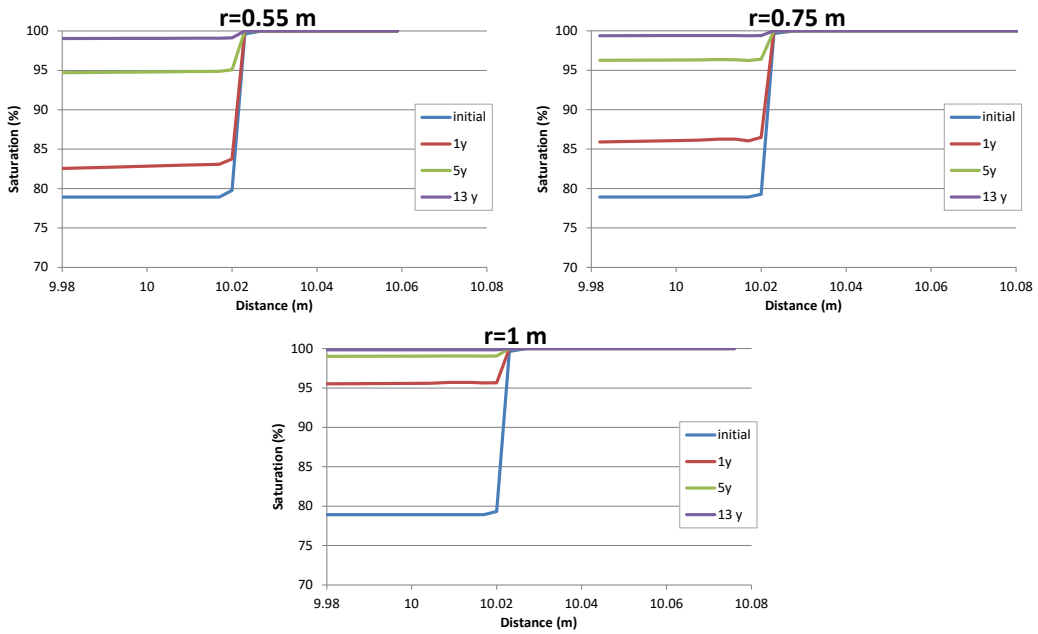

Fig. C-197: Saturation degree computed with the detailed 2D axisymmetric THM model of the bentonite/shotcrete interface along horizontal lines normal to the interface at radial distances of r = 0.55 m, 0.75 m and 1 m

C.7.4 1D model of the geochemical interactions

C.7.4.1 1D model description

The geochemical interactions between bentonite and the shotcrete plug were modelled with a non-isothermal variably-saturated 1D numerical water flow and multicomponent reactive transport model perpendicular to the bentonite/shotcrete interface at a radial distance from the axis of the gallery equal to 0.75 m. Fig. C-193 shows the finite-element mesh of the 1D numerical model.

Fig. C-198 shows the time evolution of the liquid pressure and bentonite saturation taken from the 2D model results, which was prescribed at all the nodal points within the bentonite in the 1D model of the geochemical interactions.

The initial porosity and the concentrations of the bentonite pore water were taken from the model results reported by Zheng et al. (2011) at a radial distance of r = 0.75 m for the dismantling of Heater #1 in 2002. Given the lack of relevant data for the shotcrete, the porewater composition of the shotcrete was taken from Samper et al. (2013). Tab. C-8 lists the initial chemical composition of the bentonite and shotcrete pore water.

The geochemical model accounts for 11 primary species, 46 aqueous complexes, 12 minerals, the exchange of 4 cations and the proton surface complexation reactions on strong and weak sorption sites (Tab. C-9). The initial volume fractions of the minerals are listed in Tab. C-10.

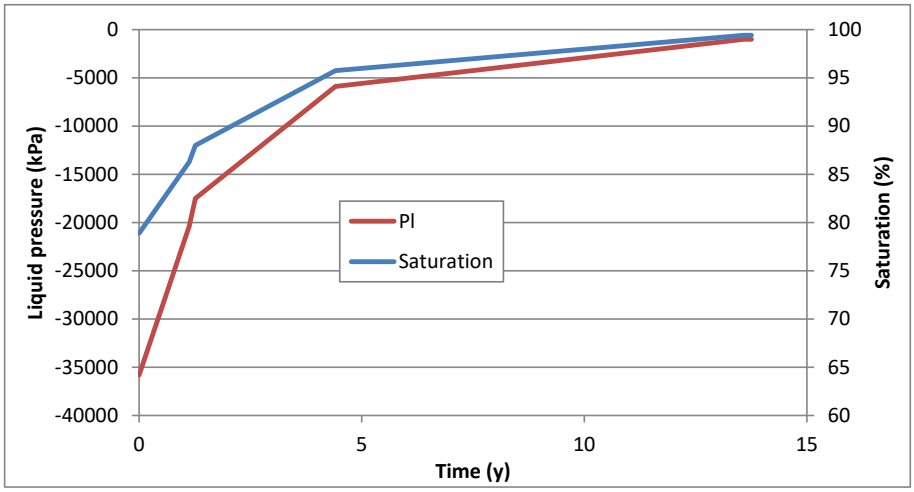

Fig. C-198: Time evolution of the liquid pressure and bentonite saturation prescribed at all the nodal points within the bentonite in the 1D model of the geochemical interactions

Tab. C-8: Initial chemical composition of the bentonite and shotcrete pore water taken from Zheng et al. (2011) and Samper et al. (2013)

	pH	Cl^-	HCO_3^-	SO_4^{2-}	Na^+	K^+	Mg^{2+}	Ca^{2+}	SiO_2	Al^{3+}
Bentonite (Zheng et al. 2011)	7.51	8.1×10^{-2}	9.6×10^{-4}	2.9×10^{-2}	8.5×10^{-2}	1.1×10^{-3}	1.2×10^{-2}	9.9×10^{-3}	2.5×10^{-4}	1.0×10^{-8}
Shotcrete (Samper et al.. 2013)	13 × 2	1.0×10^{-5}	1.7×10^{-5}	2.0×10^{-3}	1.6×10^{-2}	1.0×10^{-1}	1.8×10^{-8}	7.2×10^{-3}	3.1×10^{-3}	1.8×10^{-5}

Tab. C-9: List of primary species, aqueous complexes, minerals, exchange cations and surface complexation sorption sites of the 1D geochemical reactive transport model

Primary species	H_2O, H^+, Ca^{2+}, Mg^{2+}, Na^+, K^+, Cl^-, SO_4^{2-}, HCO_3^-, $SiO_2(aq)$, Al^{3+}
Aqueous complexes	OH-, CO_3^{2-}, $CaCO_3(aq)$, $CaHCO_3^+$, $CaSO_4(aq)$, $CaOH^+$, $CaCl^+$, $CaCl_2(aq)$, $Ca(H_3SiO_4)_2(aq)$, $CaH_2SiO_4(aq)$, $CaH_3SiO_4^+(aq)$, $MgCO_3(aq)$, $MgHCO_3^+$, $MgSO_4(aq)$, $MgCl^+$, $MgOH^+$, $Mg(OH)_4^{4+}$, $MgH_2SiO_4(aq)$, $MgH_3SiO_4^+$, $NaOH(aq)$, $NaCl(aq)$, $NaCO_3^-$, $NaHCO_3(aq)$, $NaH_3SiO_4^+(aq)$, $NaHSiO_3(aq)$, $CO_2(aq)$, $KOH(aq)$, KSO_4^-, $KHSO_4^-$, $NaSO_4^-$, $H_3SiO_4^-$, $H_2SiO_4^{2-}$, $HSiO_3^-$, $H_4(H_2SiO_4)_4^{4-}$, $H_3SiO_3^-$, $H_6(H_2SiO_4)_4^{2-}$, $HCl(aq)$, HSO_4^-, $Al(OH)_4^-$, $Al(OH)_3(aq)$, $Al(OH)_2^+$, $AlOH^{2+}$
Minerals	calcite, quartz, gypsum/anhydrite, portlandite, brucite, sepiolite, CSH1.8, CSH0.8, anortithe, ettringite, Friedel salt
Exchanged cations	Ca^{2+}, Mg^{2+}, Na^+, K^+
Sorption sites	S^sOH^{2+} , S^sO^- , S^{w1} OH^{2+} , S^{w1} O^- , S^{w2} OH^{2+} , S^{w2} O^-

Tab. C-10: Initial mineral volume fraction (%) in the bentonite and shotcrete

Bentonite	Volume fraction	Shotcrete	Volume fraction
Calcite	1.0	Calcite	0.1
Cristobalite	5	Portlandite	7.4
Unreactive smectite	54	Brucite	1.0
		C1.8SH	14.6
		Quartz	64.4

C.7.4.2 1D model results

C.7.4.2.1 TH results

Fig. C-199 shows the computed temperature profile along the shotcrete and the bentonite after 13 years. The computed temperatures are consistent with the measured temperatures (Fig. C-195).

Fig. C-196 and Fig. C-197 show the computed water contents and saturation degrees at t = 0 (2002), 5 years, 10 years and 13 years (2015). The saturation degrees calculated with the 1D model reproduce the computed saturations calculated with the detailed 2D model.

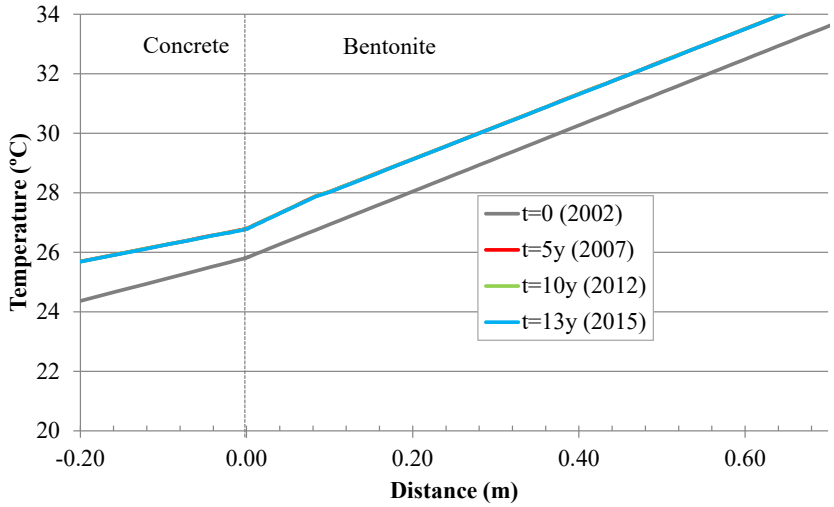

Fig. C-199: Computed temperature at selected times

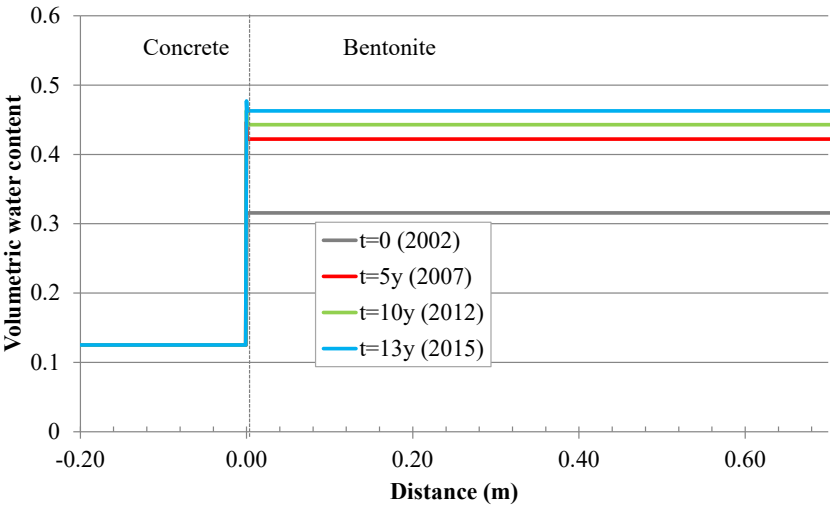

Fig. C-200: Computed water content at selected times

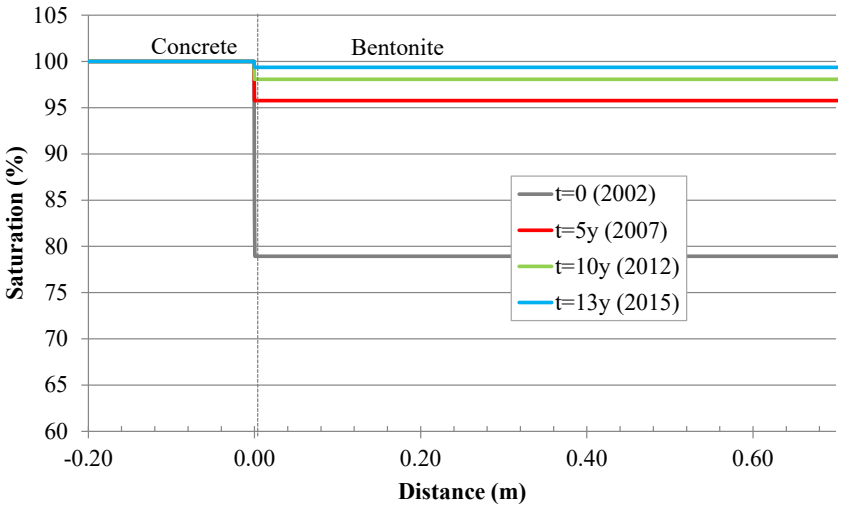

Fig. C-201: Computed saturation degree at selected times

C.7.4.2.2 Geochemical results

The concentration data in the shotcrete were measured with the aqueous extract method (Sacchi & Michelot 2000). The aqueous extract method is often used to quantify the soluble salts of soil, clay or shotcrete samples. An 1:R aqueous extract consists of adding a mass of distilled water equal to R times M_s to a mass M_s of the powdered soil or shotcrete sample.

CSIC performed aqueous extract tests on shotcrete samples collected near the shotcrete/bentonite interface (see Nagra 2015). They used a solid to liquid ratio of 1:1 (10 g of shotcrete in 10 ml of water). The concentration of a conservative species in the shotcrete pore water, c_i, can be derived from the concentration of the aqueous extract, c_{ae}, performed on a shotcrete sample of mass M_s, from the species mass balance. The gravimetric water content of the aqueous extract, w_{ae}, is related to the gravimetric water content of shotcrete sample, w_i, through:

$$w_{ae} = w_i + R(w_i + 1) \qquad \text{A–1}$$

The dilution factor, F, which relates c_i to c_{ae} is given by:

$$F = \frac{c_i}{c_{ae}} = 1 + R + \frac{R}{w_i} \qquad \text{A–2}$$

The dilution factor was calculated for the species to derive an estimate of the chemical composition of the shotcrete pore water. The role of the chemical reactions taking place during the aqueous extraction tests has been neglected. Future analyses should be made to deduce the shotcrete pore water concentrations from the aqueous extract data by means of inverse geochemical models. Tab. C-11 shows the measured aqueous extract and inferred concentrations in the shotcrete.

Tab. C-11: Measured aqueous extract data and derived concentrations in the shotcrete (Nagra 2015)

Derived concentrations have been derived by neglecting the role of chemical reactions

	Aqueous extract data (ppm)									**%Cl total mass**
Distance (m)	**pH**	**Al**	**Ca**	**Fe**	**Mg**	**S**	**Si**	**Na**	**K**	
-0.01	12.02	6.9×10^{-4}	5.75×10^{-1}	1.40×10^{-4}	1.20×10^{-4}	7.73×10^{-2}	2.92×10^{-3}	1.8×10^{-1}	1.91×10^{-1}	9.20×10^{-1}
-0.03	12.27	9.0×10^{-4}	4.80×10^{-1}	1.40×10^{-4}	1.30×10^{-4}	2.47×10^{-2}	2.05×10^{-3}	1.02×10^{-1}	1.24×10^{-1}	1.08
	Inferred concentrations (mol/L)									**Cl (mol/L)**
Distance (m)	**pH**	**Al**	**Ca**	**Fe**	**Mg**	**S**	**Si**	**Na**	**K**	
-0.01	12.02	6.3×10^{-7}	3.54×10^{-3}	6.18×10^{-8}	1.22×10^{-7}	5.95×10^{-5}	2.57×10^{-6}	1.94×10^{-4}	1.21×10^{-4}	1.74×10^{-1}
-0.03	12.27	8.2×10^{-7}	2.96×10^{-3}	6.18×10^{-8}	1.32×10^{-7}	1.90×10^{-5}	1.80×10^{-6}	1.10×10^{-4}	7.82×10^{-5}	2.04×10^{-1}

Figures A-202 to A-211 show the predicted concentrations of dissolved species and pH along the bentonite/shotcrete interface at selected times and the approximate derived aqueous extract data in the shotcrete.

The dissolved Ca^{2+} concentration increases in shotcrete due to the dissolution of portlandite in the shotcrete and solute diffusion from the bentonite. The Ca^{2+}concentration decreases near the bentonite/shotcrete interface due to the precipitation of calcite near the bentonite/shotcrete interface (Fig. C-202).

The computed dissolved K^+ concentration in shotcrete decreases due to K^+ diffusion from the shotcrete into the bentonite. Dissolved K^+ diffuses also within the bentonite towards the shotcrete interface because the concentration of dissolved K^+ decreases at the shotcrete interface due to K^+ cation exchange (Fig. C-203).

The computed HCO_3^- concentration decreases near the bentonite/shotcrete interface due to the precipitation of calcite and sepiolite. The HCO_3^- concentration in bentonite, however, increases with time due to the calcite dissolution front which displaces into the bentonite (Fig. C-204).

The dissolved Mg^{2+} concentration decreases due to the precipitation of brucite and sepiolite near the bentonite/shotcrete interface (Fig. C-205).

The computed Cl^- concentration decreases in the bentonite due to diffusion of Cl^- from the bentonite into the shotcrete (Fig. C-206).

The concentration of dissolved SiO_2(aq) in the shotcrete increases due to the dissolution of CSH1.8 and the diffusion of silica from the bentonite into to the shotcrete. The concentration decrease of dissolved silica in the bentonite is caused also by the precipitation of sepiolite near the bentonite/shotcrete interface (Fig. C-207).

Fig. C-208 shows the computed concentration of Na^+. The computed dissolved sulphate concentration shotcrete decreases due to the precipitation of ettringite (Fig. C-209). The computed aluminium concentration in shotcrete decreases due to the precipitation of ettringite and the diffusion of aluminum from the shotcrete into the bentonite (Fig. C-210). The pH increases slightly in the shotcrete. The high pH front penetrates 7.5 cm into the bentonite after 13 years (Fig. C-211).

Fig. C-212 shows the computed concentrations of the exchanged cations at several times. The concentrations of the exchanged Ca^{2+} and Mg^{2+} increase while that of exchanged Na^{+} decreases. The concentration of the exchanged K^{+} increases near the interface and decreases slightly a few cm from the interface. Fig. C-213 shows a zoom of the predicted concentrations of exchanged Na^{+}, Ca^{2+}, K^{+} and Mg^{2+} in the bentonite near the shotcrete interface in 2015, 1 cm in the bentonite. The exchanged Ca^{2+} concentration at the interface increases while the concentrations of exchanged Na^{+} and Mg^{2+} decrease.

Figures A-214 and A-215 show the computed volume fractions of quartz and cristobalite at several times. The volume fraction of quartz remains constant in the shotcrete while cristobalite dissolves in the bentonite.

Calcite dissolves in the bentonite and precipitates near the bentonite/shotcrete interface. The precipitation front propagates into the bentonite (Fig. C-216).

Fig. C-217 shows the volume fraction of portlandite, which dissolves near the bentonite/shotcrete interface. Neither gypsum nor anhydrite precipitate (Fig. C-218 and Fig. C-219). Fig. C-220 shows the computed volume fraction of ettringite. The model predicts the transient precipitation of ettringite in shotcrete. Ettringite precipitation is very small and non-uniform. This mineral phase dissolves again and only small amounts are present in 2015. This result is somewhat consistent with the experimental observations which indicate the presence of ettringite in shotcrete (Nagra 2015).

Fig. C-221 and Fig. C-222 show the volume fractions of the CSH phases (CSH1.8 and CSH0.8). Model predictions show that CSH1.8 dissolves in shotcrete near the shotcrete/bentonite interface while the precipitation of CSH0.8 in shotcrete is extremely small. These predictions are consistent with the experimental observations of the alteration of CSH.

A front of brucite precipitation in bentonite moves from the shotcrete/bentonite interface into the bentonite (Fig. C-223). Sepiolite shows a similar precipitation front (Fig. C-224). The model does not predict the precipitation of Friedel salt (Fig. C-225).

Fig. C-226 shows the computed porosity calculated from the computed rates of mineral precipitation/dissolution. The porosity decreases slightly in bentonite near the shotcrete/bentonite interface due to the precipitation of brucite, calcite and sepiolite. The porosity in shotcrete, on the other hand, increases near the interface, due mostly to the dissolution of portlandite.

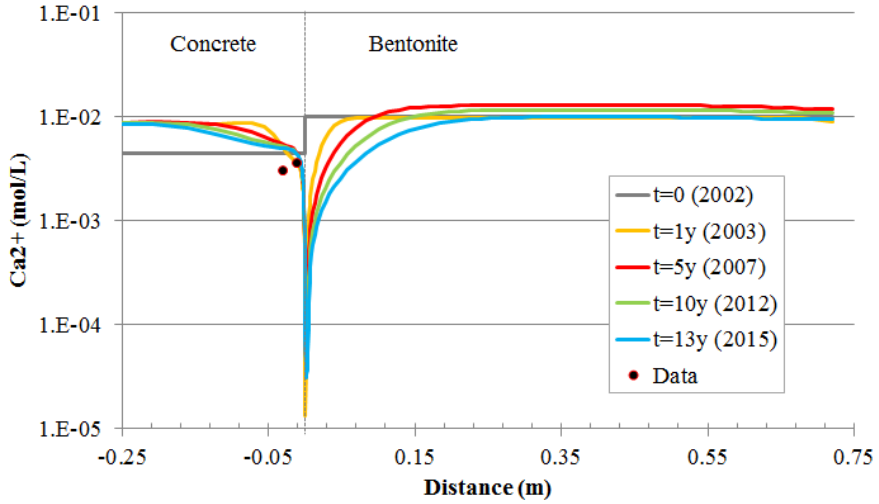

Fig. C-202: Predicted dissolved Ca^{2+} concentrations along the bentonite/shotcrete interface at selected times (lines) and approximate derived aqueous extract data in the shotcrete (symbols)

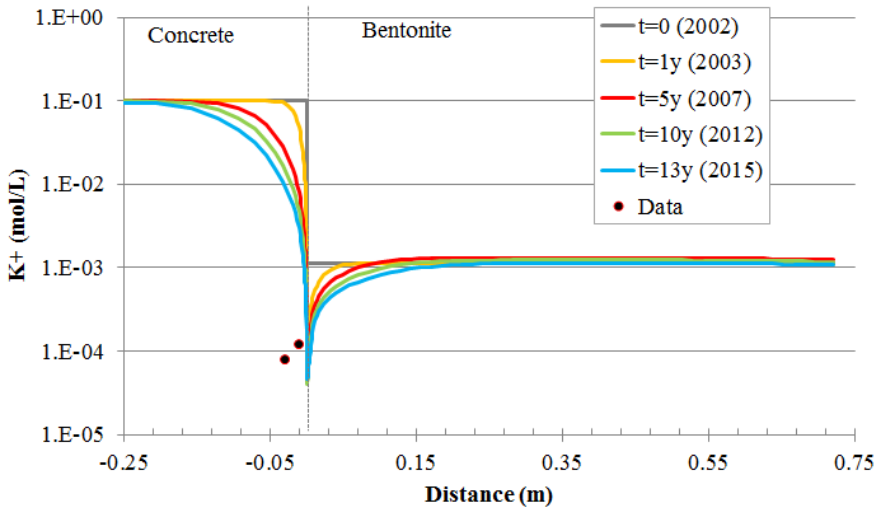

Fig. C-203: Predicted dissolved K^{+} concentrations along the bentonite/shotcrete interface at selected times (lines) and approximate derived aqueous extract data in the shotcrete (symbols)

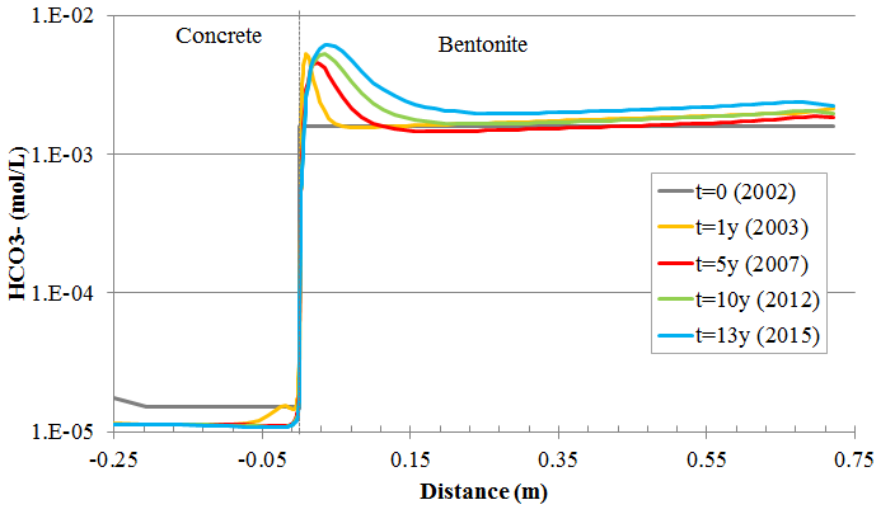

Fig. C-204: Predicted dissolved HCO_3^- concentrations along the bentonite/shotcrete interface at selected times (lines)

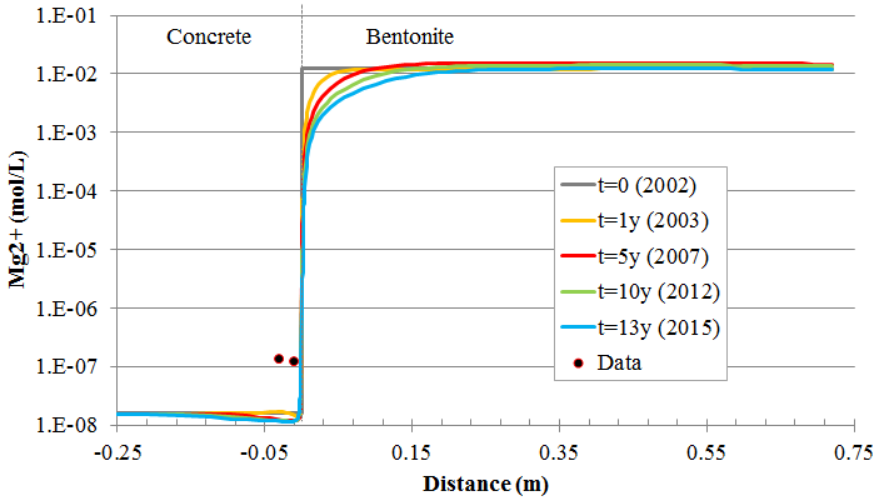

Fig. C-205: Predicted dissolved Mg^{2+} concentrations along the bentonite/shotcrete interface at selected times (lines) and approximate derived aqueous extract data in the shotcrete (symbols)

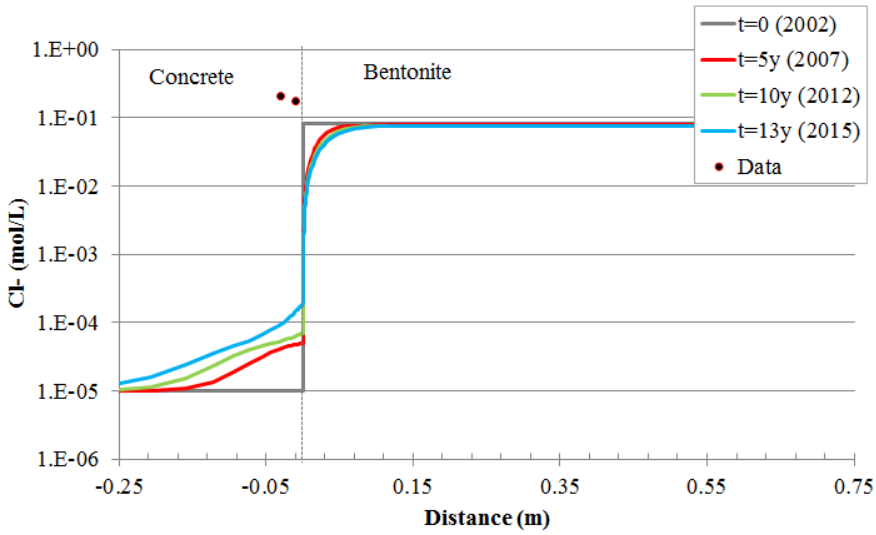

Fig. C-206: Predicted dissolved Cl^- concentrations along the bentonite/shotcrete interface at selected times (lines) and derived aqueous extract data in the shotcrete (symbols)

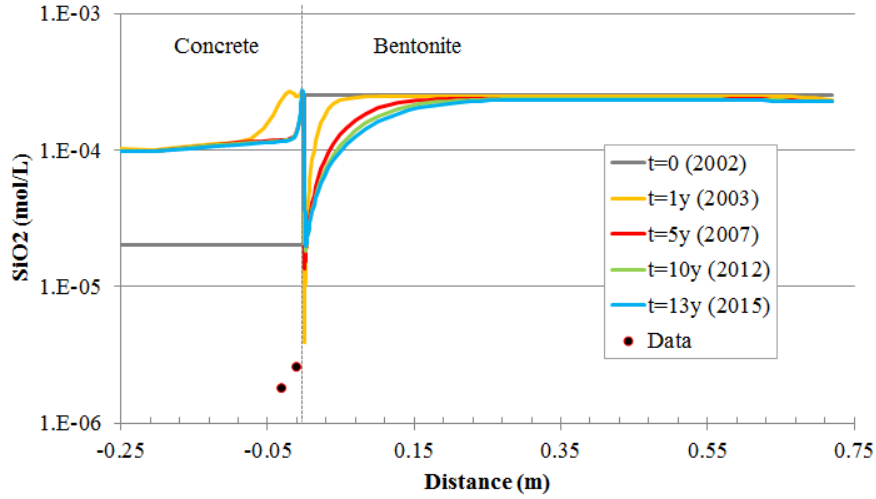

Fig. C-207: Predicted dissolved SiO_2(aq) concentrations along the bentonite/shotcrete interface at selected times (lines) and approximate derived aqueous extract data in the shotcrete (symbols)

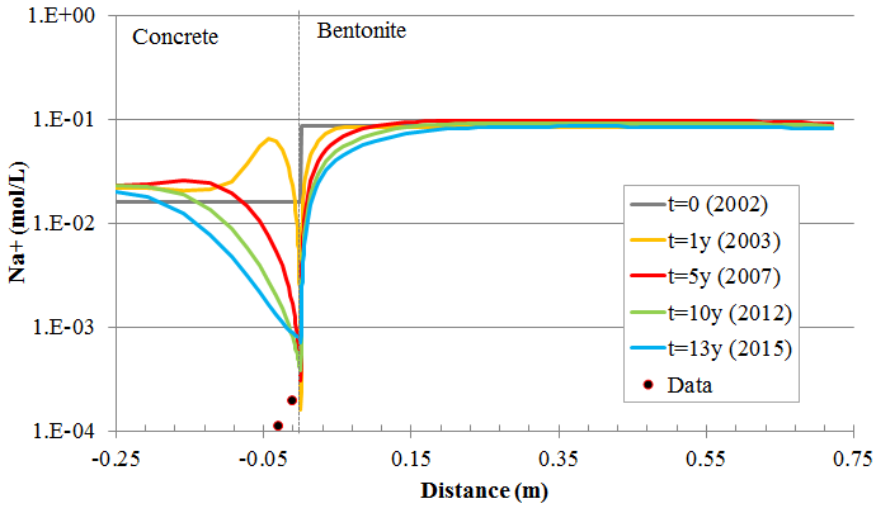

Fig. C-208: Predicted dissolved Na^+ concentrations along the bentonite/shotcrete interface at selected times (lines) and approximate derived aqueous extract data in the shotcrete (symbols)

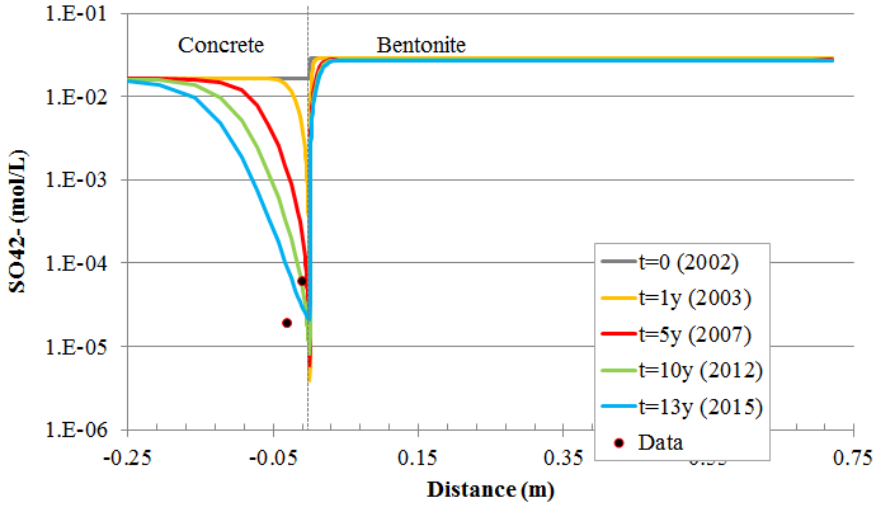

Fig. C-209: Predicted dissolved SO_4^{2-} concentrations along the bentonite/shotcrete interface at selected times (lines) and approximate derived aqueous extract data in the shotcrete (symbols)

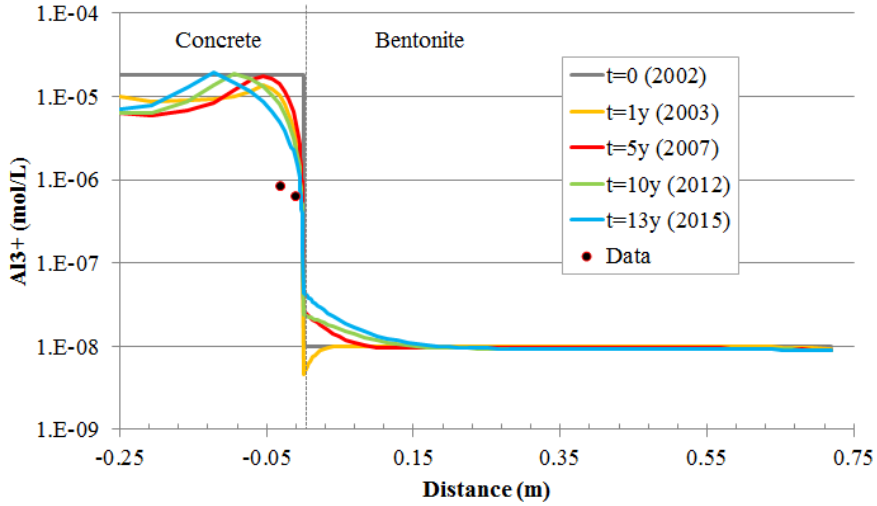

Fig. C-210: Predicted dissolved Al^{3+} concentrations along the bentonite/shotcrete interface at selected times (lines) and approximate derived aqueous extract data in the shotcrete (symbols)

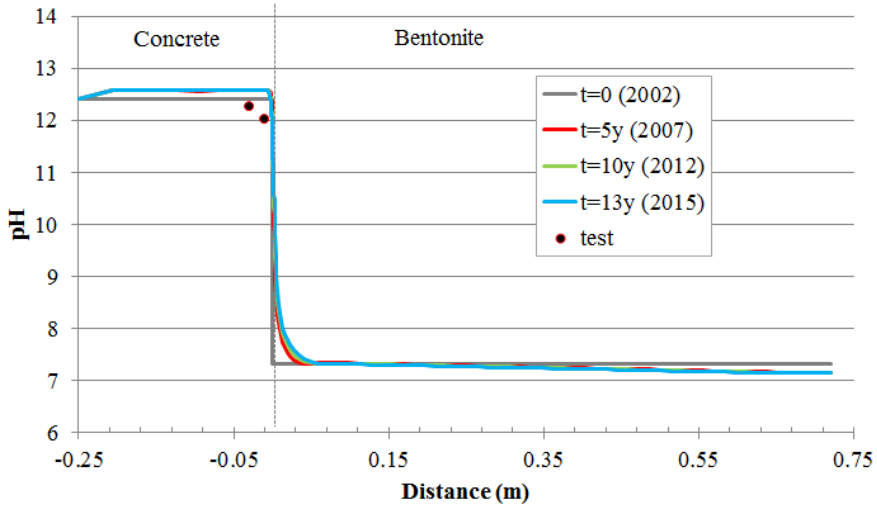

Fig. C-211: Predicted pH along the bentonite/shotcrete interface at selected times (lines) and approximate derived aqueous extract data in the shotcrete (symbols)

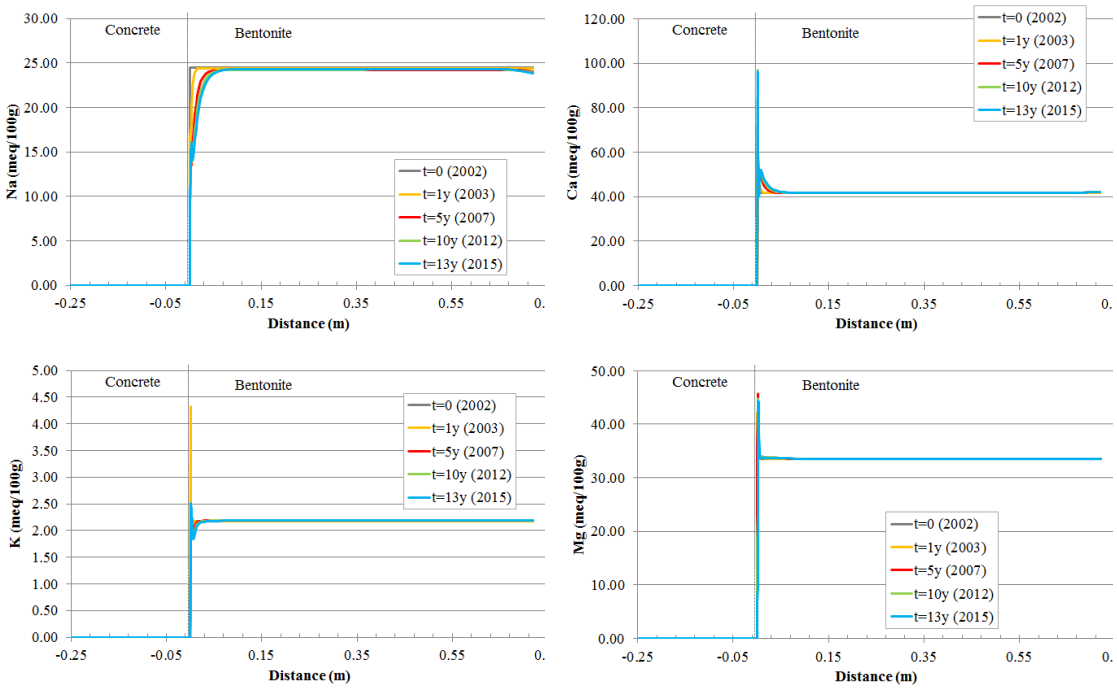

Fig. C-212: Predicted concentrations of exchanged Na^+ (top left), Ca^{2+} (top right), K^+ (bottom left) and Mg^{2+} (bottom right) along the bentonite/shotcrete interface at selected times (values in meq/100 g)

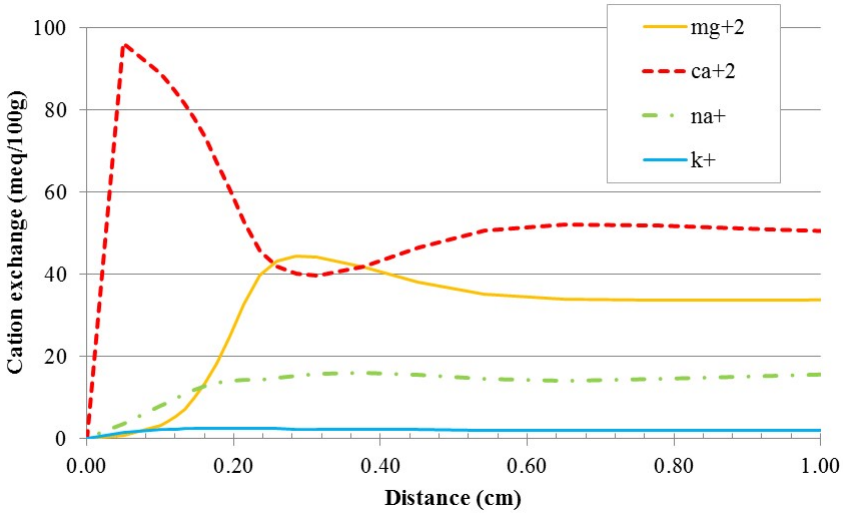

Fig. C-213: Zoom of the predicted concentrations of exchanged Na^+, Ca^{2+}, K^+ and Mg^{2+} in bentonite near the shotcrete interface in 2015 (values in meq/100 g)

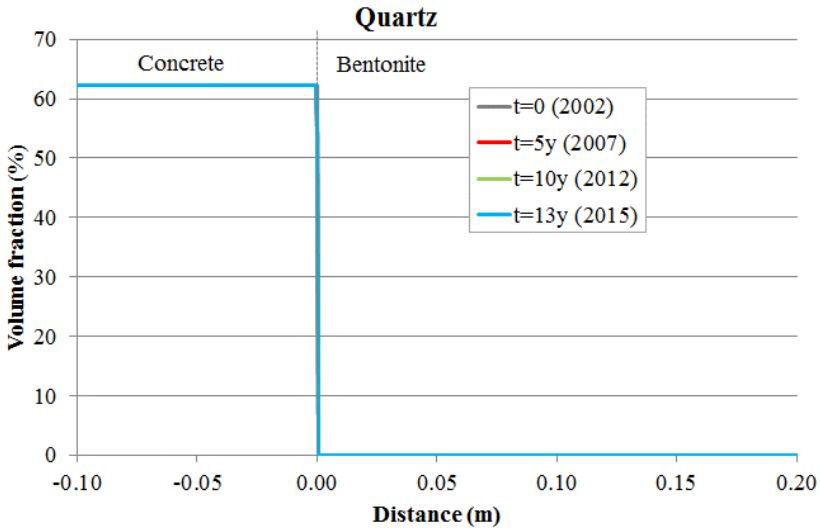

Fig. C-214: Predicted volume fraction of quartz at selected times along the bentonite/shotcrete interface at selected times

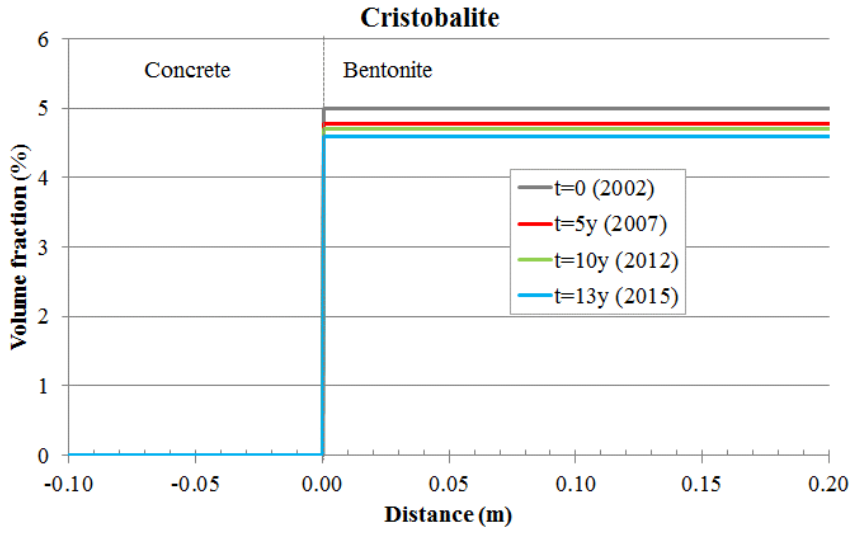

Fig. C-215: Predicted volume fraction of cristobalite at selected times along the bentonite/ shotcrete interface at selected times

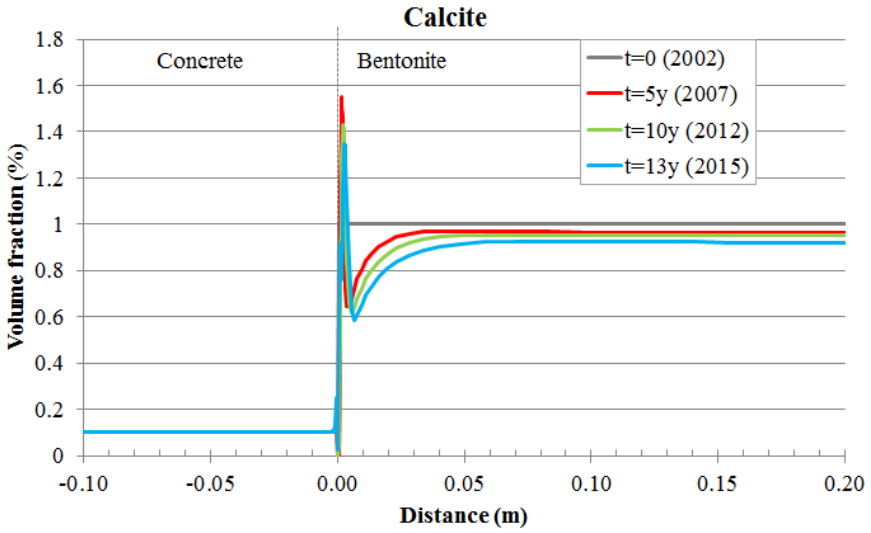

Fig. C-216: Predicted volume fraction of calcite at selected times along the bentonite/shotcrete interface at selected times

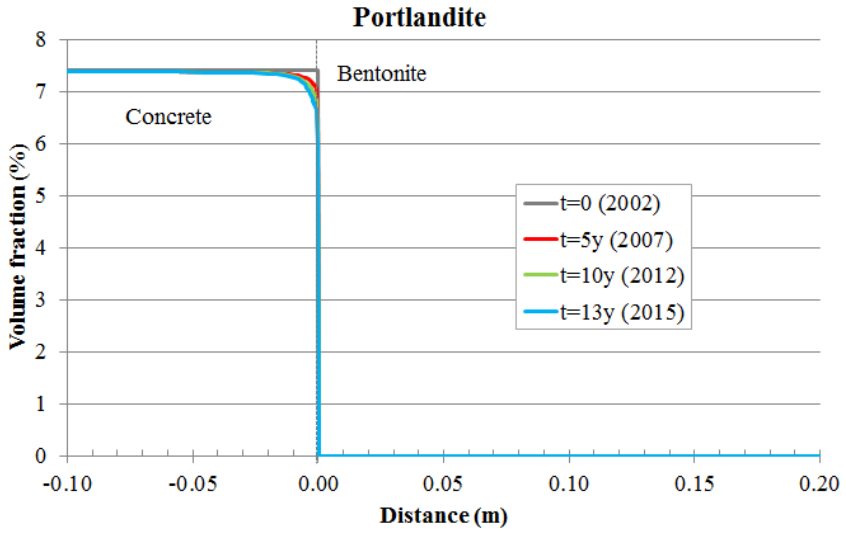

Fig. C-217: Predicted volume fraction of portlandite at selected times along the bentonite/ shotcrete interface at selected times

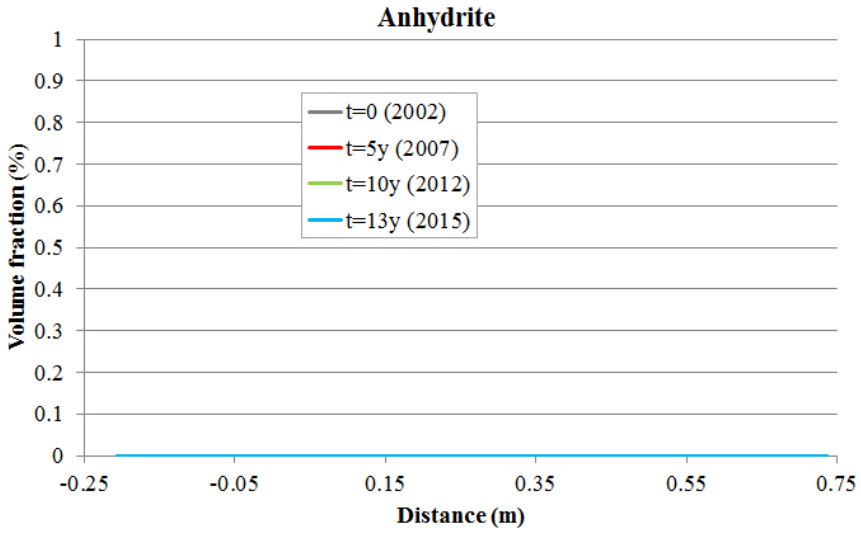

Fig. C-218: Predicted volume fraction of anhydrite at selected times along the bentonite/ shotcrete interface at selected times

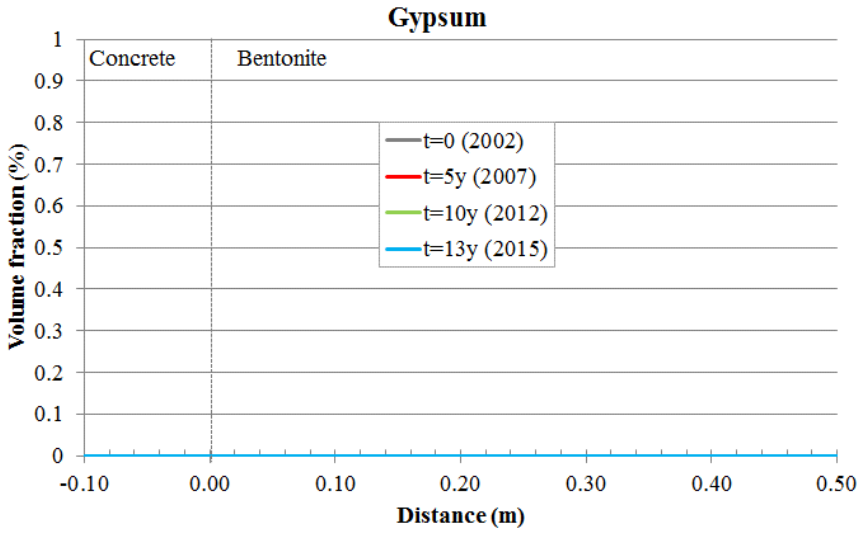

Fig. C-219: Predicted volume fraction of gypsum at selected times along the bentonite/shotcrete interface at selected times

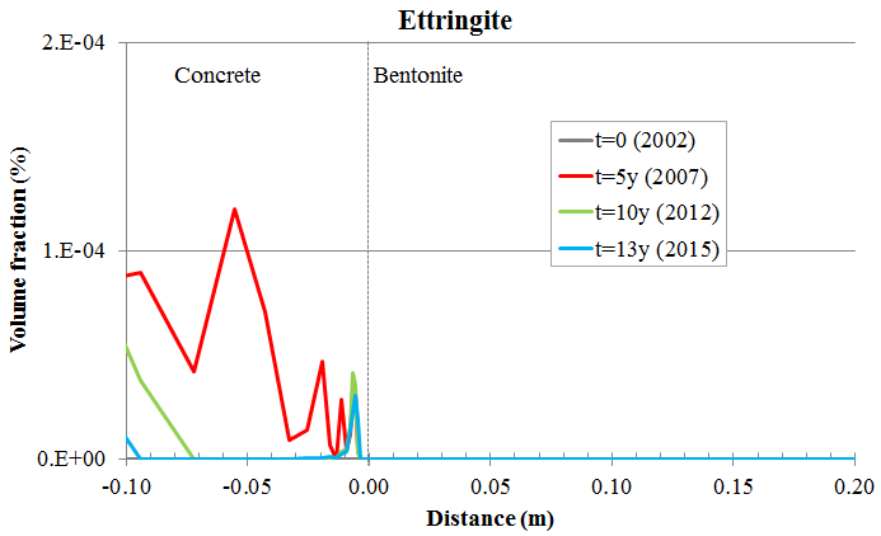

Fig. C-220: Predicted volume fraction of ettringite at selected times along the bentonite/shotcrete interface at selected times

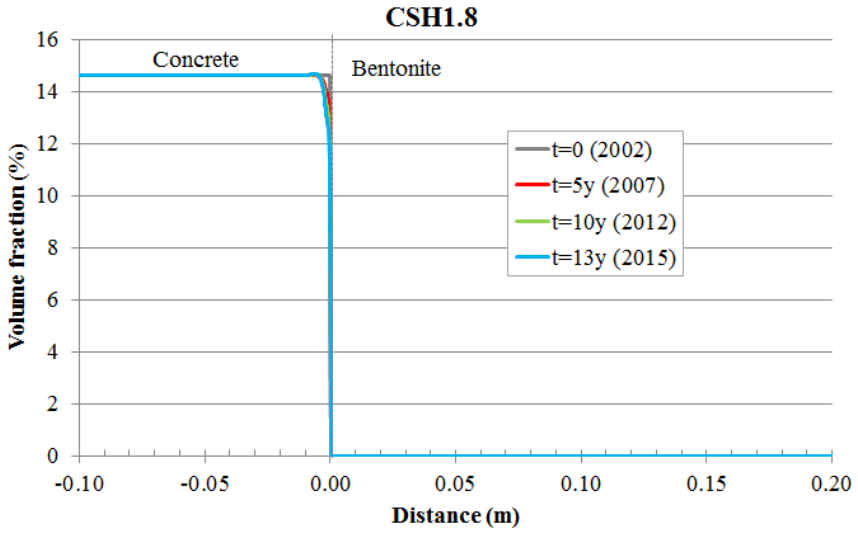

Fig. C-221: Predicted volume fraction of CSH1.8 at selected times along the bentonite/shotcrete interface at selected times

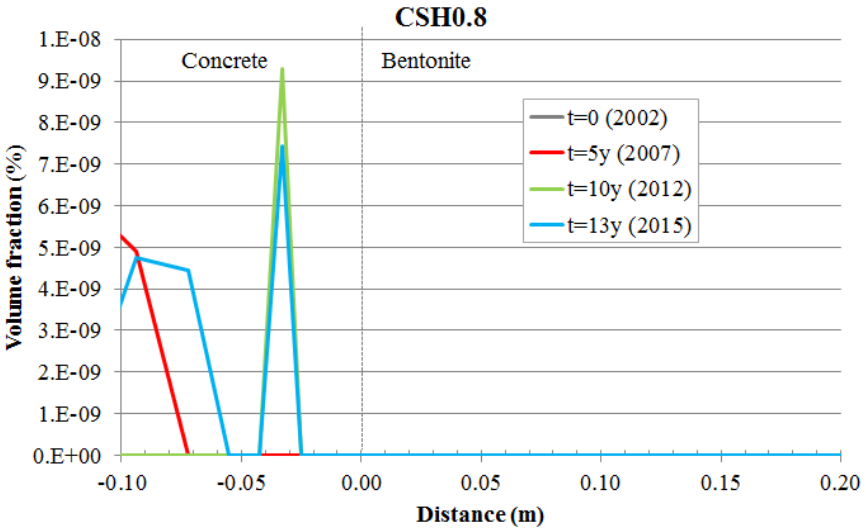

Fig. C-222: Predicted volume fraction of CSH0.8 at selected times along the bentonite/shotcrete interface at selected times

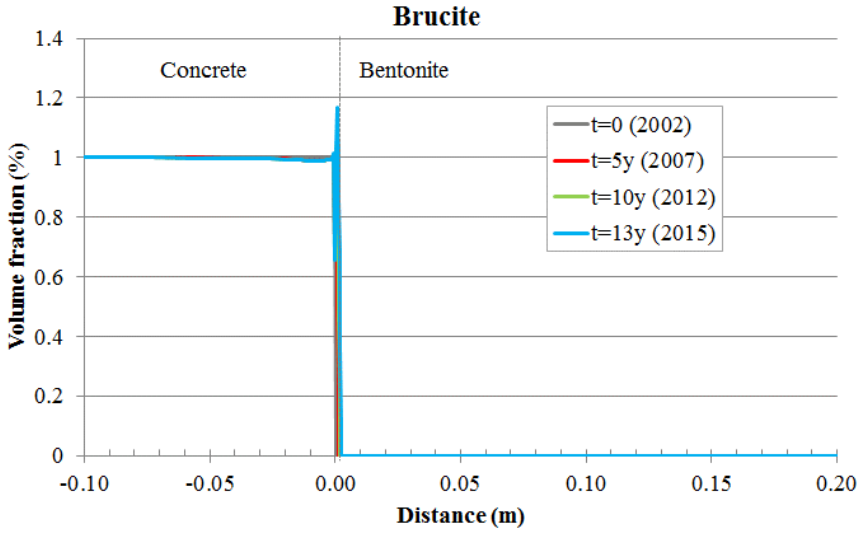

Fig. C-223: Predicted volume fraction of brucite at selected times along the bentonite/shotcrete interface at selected times

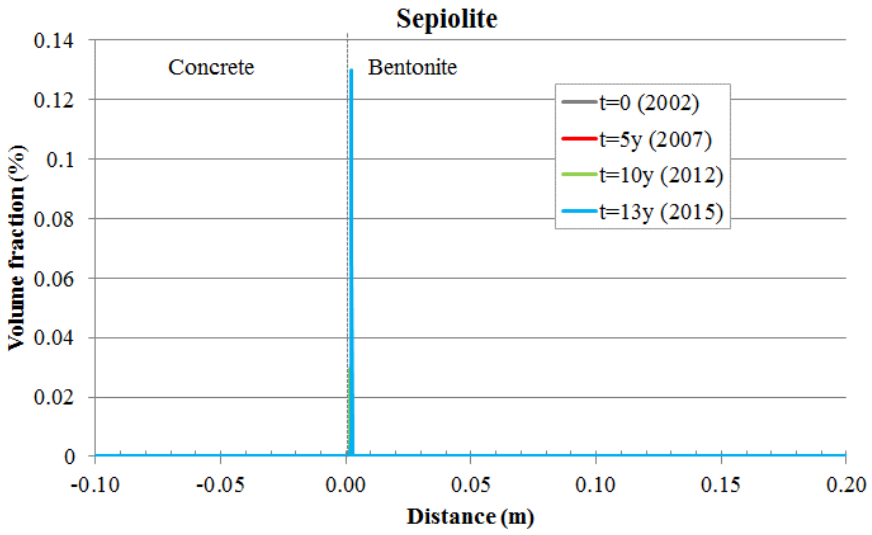

Fig. C-224: Predicted volume fraction of sepiolite at selected times along the bentonite/shotcrete interface at selected times

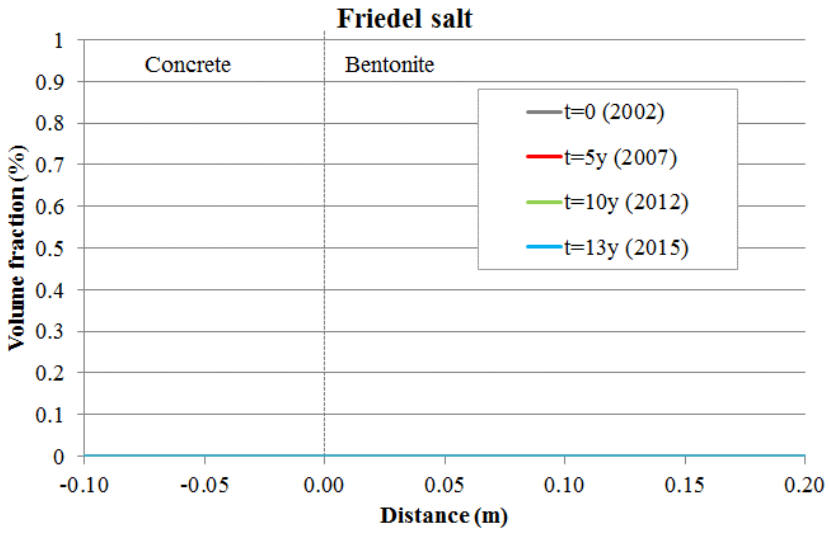

Fig. C-225: Predicted volume fraction of Friedel salt at selected times along the bentonite/ shotcrete interface at selected times

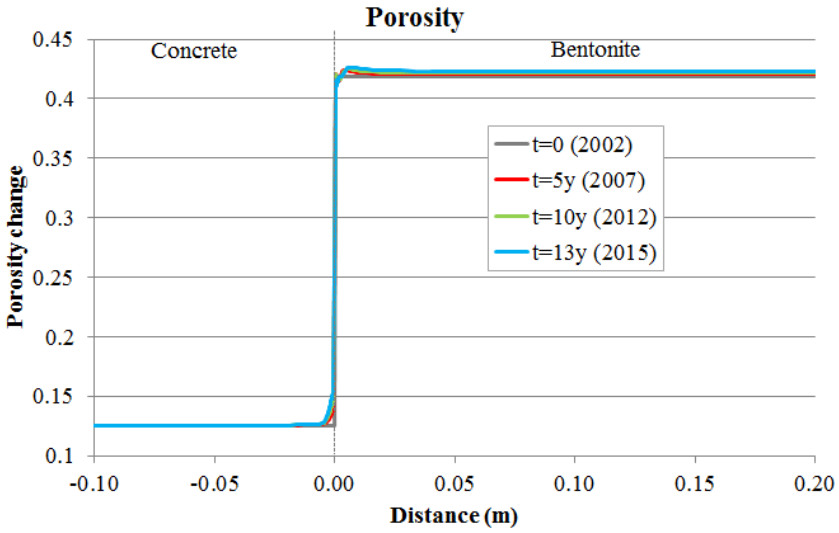

Fig. C-226: Predicted changes in porosity produced by dissolution/precipitation reactions

C.7.5 Conclusions

The geochemical interactions between bentonite and the shotcrete plug have been modelled with a non-isothermal variably-saturated 1D numerical water flow and a multicomponent reactive transport model normal to the interface at a radial distance from the axis of the gallery equal to 0.75 m. A telescopic approach was followed to derive the initial and boundary thermal and hydrodynamic conditions for this 1D model. First, a detailed 2D axisymmetric THM model of the bentonite/shotcrete interface was performed.

Model results show that the computed temperature after 13 years of simulation (from 2002 to 2015) ranges from 24 ºC in the shotcrete to 34 ºC in the bentonite. These computed temperatures compare well with the temperatures measured along the borehole drilled through the shotcrete plug before switching off Heater #2.

Model predictions show that calcite dissolves in the bentonite and precipitates near the bentonite/shotcrete interface. The precipitation front propagates into the bentonite. Portlandite dissolves in the shotcrete interface. Ettringite precipitation is very small and non-uniform. The precipitation of this mineral phase is transient. It subsequently dissolves again and is present only in small amounts in 2015. Neither gypsum nor anhydrite precipitate. CSH1.8 dissolves in the shotcrete near the shotcrete/bentonite interface while CSH0.8 precipitation in the shotcrete is extremely small. Brucite precipitates in the bentonite near the interface. The front of brucite precipitation moves from the bentonite/shotcrete interface into the bentonite. Sepiolite shows a similar precipitation front. The model does not predict the precipitation of Friedel salt.

The porosity decreases slightly in the bentonite near the shotcrete/bentonite interface due to the precipitation of brucite, calcite and sepiolite. The porosity in the shotcrete, on the other hand, increases near the interface due, mostly, to the dissolution of portlandite. The changes in porosity only affect the first 2 cm in the bentonite/shotcrete interface on both sides of the interface.

C.8 General conclusions

C.8.1 Testing and updating THCM model

C.8.1.1 Sensitivity analyses and solute back-diffusion analysis

A 1D axisymmetric THCM model of the FEBEX bentonite was developed within the framework of the FEBEX Project by Zheng et al. (2011) from laboratory tests, online data from the FEBEX mock-up test and online and partial dismantling data from the FEBEX in-situ test in 2002. The THCM model accounts for non-isothermal two-phase flow, heat transfer, mechanical deformation, bentonite swelling and multicomponent geochemical reactive transport.

Several sensitivity runs were performed to quantify the sensitivity of the geochemical predictions to changes in the retention curve of the bentonite, the vapour tortuosity, the dissolution of smectite, and the changes in the boundary conditions caused by the cooling and the dismantling of the test. The results of these sensitivity runs lead to the following conclusions:

1. The computed concentrations of most species in a hot section in 2002 are sensitive to an increase in parameter α of the van Genuchten retention curve of bentonite. The increase in α leads to larger water evaporation and larger solute concentrations near the heater. The pH and the concentration of HCO_3^- are not sensitive to a change in α. The computed concentrations of most species in the cold section, however, lack sensitivity to a change in α.
2. The computed concentrations are not sensitive to smectite dissolution and analcime precipitation because the cumulative dissolution of smectite and precipitation of analcime in 2002 is extremely small.
3. The computed concentrations in 2002 are not sensitive to a change in the gas boundary condition during the dismantling stage. The computed concentrations are sensitive to cooling because the solubility of the minerals and the chemical parameters depend on temperature.
4. The computed concentrations of dissolved Ca^{2+}, K^+, Mg^{2+}, Na^+ and Cl^- near the heater in 2002 increase when the vapour tortuosity increases. However, away from the heater the concentrations decrease when the vapour tortuosity increases. The computed pH and the concentrations of SO_4^{2-} and HCO_3^- are less sensitive to the changes in vapour tortuosity.
5. Solute diffusion from the bentonite into the granite is very sensitive to the effective diffusion coefficients of both bentonite and granite. The effective diffusion, D_e, f in granite used in the previous model was too small. The computed Cl^-, SO_4^{2-}, Na^+ and Ca^{2+} concentrations in the granite with $D_e = 1 \times 10^{-12}$ m^2/s for granite and $D_e = 1.4 \times 10^{-10}$ m^2/s in bentonite are consistent with the Cl^-, SO_4^{2-}, Na^+ and Ca^{2+} concentrations measured in the FUNMIG borehole by Buil et al. (2010).

C.8.1.2 2D axisymmetric THCM model

The 1D axisymmetric THMC model of the FEBEX in-situ test has extended to 2D axisymmetric conditions.

The temperatures computed with the 2D model in the hot section are less than those calculated with the 1D model. The temperatures computed with the 2D model in the cold section are higher than those calculated with the 1D model. The temperatures computed with the 1D model fit the measured data better than the temperatures calculated with the 2D model.

The volumetric water content values computed with the 1D model are larger than those calculated with the 2D model at all radial distances. The volumetric water content values computed with the 1D model fit the measured data better than the volumetric water contents calculated with the 2D model.

The 1D axisymmetric model outperforms the 2D axisymmetric model because the model parameters used to perform the comparison of both models are the parameters calibrated with the 1D axisymmetric model. A detailed calibration of the parameters with the 2D axisymmetric model will surely lead to model results at least as good as or better than the results of the 1D axisymmetric model.

The main conclusions of the sensitivity runs include:

1. The calculated temperatures in the cold part of the bentonite buffer increase slightly with increasing thermal conductivity of bentonite. Similar to the cold section, the calculated temperatures in the hot part of the bentonite buffer increase with increasing thermal conductivity of bentonite.
2. The calculated temperatures in the cold part of the bentonite buffer decrease slightly when the thermal conductivity of granite is increased.
3. An increase of the granite's thermal conductivity affects mostly the computed temperatures near the bentonite/granite interface. Similar to the cold section, the calculated temperatures in the external part of the bentonite buffer decrease when the thermal conductivity of granite is increased. The changes in the computed temperatures in the hot section are larger than the changes in the cold section.

The Cl^- concentrations in 2002 are large near heaters #1 and #2. The largest concentrations are located at the edge of Heater #2. The contour lines are approximately parallel to the axis of the gallery along heaters #1 and #2. At the edges of the heaters, however, the contour lines are no longer parallel to the gallery axis. The computed contour plots of Cl^- concentrations illustrate that the edge effects extend over a distance of 0.5 to 1 m approximately. The Cl^- concentrations in 2015 show a significant decrease compared to the concentrations in 2002 around Heater #2. Large concentrations of Cl^- still remain in the bentonite barrier between the dummy and Heater #2 and between Heater #2 and the end of the gallery.

The Cl^- concentrations computed with the 1D model in a hot section in 2015 are smaller than the concentrations calculated with the 2D model because the bentonite hydration rate calculated with the 1D model is slightly larger than the hydration calculated with the 2D model. In a cold section the concentrations calculated with the 1D model are significantly smaller than the concentrations computed with the 2D model.

C.8.1.3 Updated 1D THCM model

The previous 1D axisymmetric THCM model of the FEBEX in-situ test was improved and updated by: 1) improving the boundary condition at the heater/bentonite interface; 2) refining the spatial discretization of the finite-element mesh; and 3) modifying the solute dispersivities of both bentonite and granite. The revised implementation of the boundary condition leads to more water evaporation than the previous formulation. The computed concentrations of Ca^{2+}, K^+, Mg^{2+}, Cl^- and Na^+ near the heater with the updated model are significantly higher than the concentrations calculated with the reference model. The computed pH and the concentrations of SO_4^{2-} and HCO_3^- with the updated model are similar to those of the reference model.

The improvement in the boundary condition at the heater/bentonite interface led to a significant decrease of the mass balance error. The mass balance error for Cl^- is reduced from 150 % in the previous model to about 20 % in the updated model. The mass balance errors in the model of the cold section are generally smaller than 10 %. The mass balance errors could be reduced further by refining the finite-element grid. However, the computation time increases sharply with a finer spatial discretization. For this reason, at this stage of the project, the mass balance errors of the updated model are deemed acceptable. They will be reduced in future studies.

The computed concentrations of Ca2+, K+, Mg2+, Na+ and HCO3- become smoother when the diffusion coefficients of bentonite are increased by a factor of 10. The profiles of Cl- and SO42- are less sensitive to a change in the diffusion coefficient because the diffusion coefficients of these species are smaller than the diffusion coefficients of the rest of the species. The computed pH is not sensitive to a change in the diffusion coefficients.

C.8.1.4 Comparing the predictions of the updated model with measured thermal and hydraulic data collected from 2002 to 2015

The updated 1D axisymmetric THCM model of the FEBEX in-situ test was compared to gravimetric water content data measured at the dismantling of Heater #1 in 2002 and Heater #2 in 2015 and online temperature, relative humidity, water content, and pore water pressure in the granitic rock data collected during the period from 2002 to 2015.

The comparison of the computed values with measured data leads to the following major conclusions:

1. The numerical model reproduces the main temperature data trends. The computed temperatures near the bentonite/granite interface in hot sections are less than the measured temperatures during the first 2000 days and higher than the measured temperatures after 2000 days. The computed temperature in 2015 is 3 °C higher than the measured temperature at the bentonite/granite interface. The computed temperatures in the cold section C located between Heater #1 and the original concrete plug reproduce the steady increase of temperature before dismantling Heater #1 and the sharp decrease of the temperature after switching off this heater.
2. The computed relative humidity reproduces the general trends of the measured relative humidity data.
3. The computed time evolution of the water content values in the hot section reproduce the time evolution of the measured TDR water content data, except at r = 0.59 m. The best fit of computed values to measured data is achieved at r = 1.04 m, especially at the sensor position on the right side of the tunnel.
4. The computed pore water pressures in the granitic rock are smaller than the measured values due to the heterogeneities of the granitic rock, which are not taken into account in the model and the uncertainty in the prescribed pore water pressure at the external boundary.
5. The predicted water content values in a hot and cold section at the time of dismantling Heater #1 (in 2002) and Heater #2 (in 2015) are within the band of measured data and match the general trend of the measured data.
6. The predicted dry density in a cold and hot section at the time of dismantling Heater #1 (in 2002) and Heater #2 (in 2015) are for the most part within the band of measured data. There are some discrepancies in the hot and cold sections in 2002. The computed dry density

overestimates the measured dry density near the heater (0.7 m < r < 1 m); this discrepancy is not observed in 2015.

C.8.2 Pre-dismantling THCM model predictions

Pre-dismantling THCM model predictions of the geochemical conditions for the hot and cold sections in June 2015 were performed with the updated 1D axisymmetric THCM model. Prediction uncertainties were quantified by sensitivity runs to key model parameters such as the diffusion coefficients of the chemical species.

The main features of the geochemical predictions in a hot section in 2015 include:

1. The predicted Cl^- concentrations in 2015 are largest near the heater due to the evaporation of the bentonite pore water and smallest at the granite/bentonite interface due to the hydration of the buffer with granite pore water, which has a concentration smaller than that of the bentonite. The predicted Cl^- concentrations in 2015 are much smaller than the concentrations in 2002.
2. The predicted concentrations of dissolved cations (Ca^{2+}, Mg^{2+}, Na^+ and K^+) are also large near the heater
3. The predicted concentration of SO_4^{2-} in 2015 increases near the heater and decreases in the rest of the bentonite barrier
4. The computed HCO_3^- is large near the bentonite/granite interface because the hydration of bentonite with granite water induces the dissolution of calcite at the bentonite/granite interface
5. The predicted pH in the bentonite in 2015 is 7.5 near the heater and decreases slightly towards the granite interface

The main features of the geochemical predictions in the cold sections in 2015 include:

1. The predicted Cl^- concentration in 2015 shows a diffusion profile with low concentration in the granite and a high concentration of about 0.16 mol/L in the centre of the bentonite barrier.
2. The predicted concentrations of dissolved cations (Ca^{2+}, Mg^{2+}, Na^+, K^+ and SO_4^{2-}) show diffusion profiles similar to the concentration profile of Cl^-.
3. The predicted concentration of HCO_3^- in the bentonite in 2015 is 10^{-2} mol/L near the granite interface and decreases towards 10^{-3} mol/L at the centre of the barrier.
4. The predicted pH in the bentonite remains sTab. Around 7.5.

The predicted concentrations in the hot sections are very sensitive to an increase by a factor of 10 of the diffusion coefficients. In general, the concentration profiles of most of the chemical species become smoother when the diffusion coefficient is increased. The concentrations decrease near the heater and increase in the rest of the bentonite barrier. The dissolved Ca^{2+} concentration increases everywhere in bentonite because calcite dissolution near the heater is enhanced when the diffusion coefficients of bentonite are multiplied by 10. Such an increase in the Ca^{2+}concentration is accompanied by a decrease in the dissolved HCO_3^- concentration.

The predicted the radial profiles of the Ca^{2+}, K^+, Mg^{2+}, Na^+ and HCO_3^- concentrations in the cold sections become smoother when the diffusion coefficients are increased. The profiles of Cl^- and SO_4^{2-} are also sensitive to a change in diffusion coefficients. However, their sensitivity is much smaller than the sensitivity of other species because the diffusion coefficients of Cl^- and SO_4^{2-} are

much smaller than the diffusion coefficients of the other species. The predicted pH is slightly sensitive to a change in diffusion coefficients.

The mass transfer from granite into the bentonite was quantified with F^-, a chemical species initially present in granite but not present in the bentonite pore water. After 18 years, the predicted concentration of F-is nearly uniform in both bentonite and granite, except near the heater where the predicted concentration of F-is large due to water evaporation. The predicted concentration of F-decreases slightly in granite.

C.8.3 Updating the predictions of tracer migration

Updated predictions of the tracer migration have been presented for: 1) iodide along several radii in Sections 37, 50 and 51 by using a 1D axisymmetric model; 2) borate, europium, perrhenate and selenate at the inner blocks of Section 46 by using 2D models in vertical planes; and 3) caesium and borate at the outer blocks of Section 48 by using 2D models in vertical planes.

The migration of each tracer was simulated separately by taking into account its transport and chemical parameters (accessible porosity, effective diffusion coefficient, distribution coefficient), initial concentration and location.

The predictions of iodide migration reported by Zheng (2006) for Heater #1 in 2002 was updated with the most updated version of the THCM model of the FEBEX in-situ test. The accessible porosity of iodide was subsequently recalibrated. The predictions for Sections 50 and 51 located near the Heater #2 were performed assuming that the heater was switched off in 2015. The pre-dismantling predictions of iodide concentrations in 2015 in Section 37 located near Heater #1 were performed by taking into account that Heater #1 was switched off in 2002.

The model predictions of tracer migration lead to the following conclusions:

1. Large iodide concentrations are predicted near the heater in Sections 50 and 51 located near Heater #2. The iodide concentration in Section 37 near Heater #1 decreased after the heater was switched off in 2002 due to the increase in water content caused by vapour condensation and bentonite hydration.
2. The predicted perrhenate concentrations in 2015 show that this tracer has diffused entirely in the full section.
3. The plumes of the point tracers located in the inner blocks are
   a) Almost circular with an approximate diameter of 8 cm for borate
   b) Semi-circular with an approximate diameter of 20 cm for selenate
   c) Slightly anisotropic with an approximate length of 8 cm for europium
4. The plumes of the point tracers located in the outer blocks are:
   a) Almost circular with an approximate diameter of 7 cm for caesium
   b) Almost circular with a diameter of 10 cm for borate

C.8.4 Predicting the interactions betwwen concrete and bentonite

The geochemical interactions between bentonite and the shotcrete plug were modelled with a non-isothermal variably-saturated 1D numerical water flow and multicomponent reactive transport model normal to the interface at a radial distance from the axis of the gallery equal to 0.75 m. A telescopic approach was followed to derive the initial and boundary thermal and hydrodynamic conditions for this 1D model. First, a detailed 2D axisymmetric THM model of the bentonite/shotcrete interface was performed.

Model results show that the computed temperature after 13 years of simulation (from 2002 to 2015) ranges from 24 ºC in the shotcrete to 34 ºC in the bentonite. These computed temperatures compare well with the temperatures measured along the borehole drilled through the shotcrete plug before switching off Heater #2.

Model predictions show that calcite dissolves in the bentonite and precipitates near the bentonite/shotcrete interface. The precipitation front propagates into the bentonite. Portlandite dissolves in the shotcrete interface. Ettringite precipitation is very small and non-uniform. The precipitation of this mineral phase is transient. It re-dissolves and is present only in small amounts in 2015. Neither gypsum nor anhydrite precipitate. CSH1.8 dissolves in the shotcrete near the shotcrete/bentonite interface while CSH0.8 precipitation in the shotcrete is extremely small. Brucite precipitates in the bentonite near the interface. The front of brucite precipitation moves from the bentonite/shotcrete interface into the bentonite. Sepiolite shows a similar precipitation front. The model does not predict the precipitation of Friedel salt. The porosity decreases slightly in the bentonite near the shotcrete/bentonite interface due to the precipitation of brucite, calcite and sepiolite. The porosity in the shotcrete, on the other hand, increases near the interface due mostly to the dissolution of portlandite. The changes in porosity affect only the first 2 cm on both sides of the interface.

C.9 Recommendations for future work

Coupled THCM predictions of the FEBEX in-situ test were presented in this report. These predictions contain uncertainties. Recommendations for future research work are listed below for each of the tasks presented in this report.

C.9.1 Testing and updating THCM model

The 2D THCM model of the FEBEX in-situ test presented in Chapter C.4 could be improved by calibrating the following parameters to the measured temperatures, relative humidity, and water content values:

1. The thermal conductivities of both bentonite and granite
2. The hydraulic conductivity of the granite and the hydraulic pressure in the granitic rock far from the gallery
3. The retention curve of bentonite
4. The thermal boundary conditions
5. The vapour tortuosity in bentonite

Other model improvements include:

1. Accounting for reactive gases such as $CO_2(g)$ and $O_2(g)$
2. Accounting for the inner-block solute diffusion during the time elapsed since block extraction and water sampling for chemical analyses
3. Improving the estimation of the initial chemical composition of the bentonite pore water and resolving the discrepancies between the data derived from squeezing and those from aqueous extract methods
4. Deepening the analysis of solute back-diffusion from the bentonite into the granite
5. Reducing the mass balance errors of the THCM model by refining the finite-element grid.

C.9.2 Testing the THCM model predictions

The pre-dismantling THCM model predictions of the geochemical conditions for the hot and cold sections in June 2015 should be tested and compared to measured geochemical data including:

1. Radial profiles of the bentonite pore water composition from aqueous extract tests for hot and cold sections. These data should be interpreted with an inverse geochemical model
2. Radial profiles of the bentonite pore water composition from squeezing methods for hot and cold sections
3. Radial profiles of the exchanged cations' concentrations in bentonite for hot and cold sections
4. Mineralogical data for hot and cold sections

C.9.3 Testing the tracer migration predictions

The computed iodide profile is not sensitive to a decrease in the effective diffusion because the diffusion is dominated by hydrodynamic dispersion when the diffusion coefficient is decreased by a factor of 10. The dispersivity used for the bentonite is 0.8 cm. In future studies the sensitivity to the dispersivity should be evaluated.

At this stage of numerical modelling, Cs sorption was modelled with a constant Kd. It is planned to model Cs migration in future studies with a multicomponent cation exchange reactive transport model similar to the model we used for Cs migration in the DR experiment at Mont Terri (Soler et al. 2013, Yi et al. 2015).

The comparison of the predicted tracer concentrations with measured data will provide the basis for the testing and validation of current THCM models for compacted bentonites.

C.9.4 Interactions of bentonite and shotcrete

The predictions of the interactions between bentonite and shotcrete have uncertainties that should be addressed in futures studies. These include:

1. The initial chemical composition of the bentonite in 2002. The pore water composition in 2002 was taken from a previous 1D model at 30 °C. This estimate should be improved.
2. The chemical composition of the shotcrete. A normal concrete CEM I-SR was assumed. However, there are no data on the current composition nor the initial chemical composition of the shotcrete's pore water.
3. The use of a 2D model to study the interactions instead of the simplified 1D model used in this report

The predictions of the model should be tested with measured experimental data such as:

1. Aqueous extract data from the concrete and bentonite. These data should be interpreted with an inverse geochemical model.
2. Mineralogical changes in the concrete and the bentonite
3. Changes in the porosity of bentonite

C.10 References to PART C

AITEMIN (2015): Full Dismantling Sampling Plan (in situ experiment), FEBEX-DP Technical report. Rev. 4. February 2015.

Buil, B, Gómez, P., Peña, J., Garralón, A., Turrero, M.J., Escribano, A., Sánchez, L. & Durán, J.M. (2010): Modelling of bentonite–granite solutes transfer from an in situ full-scale experiment to simulate a deep geological repository (Grimsel Test Site, Switzerland), Applied Geochemistry 25:1797–1804.

Dai Z. & Samper, J. (2006): Inverse modeling of water flow and multicomponent reactive transport in coastal aquifer systems, Journal of Hydrology, vol. 327, pp. 447-461.

Dai Z., Samper, J. & Ritzi, R. (2006): Identifying geochemical processes by inverse modeling of multicomponent reactive transport in Aquia aquifer, Geosphere, vol. 4, pp. 210-219.

Dai, Z. & Samper, J. (2004): Inverse problem of multicomponent reactive chemical transport in porous media: Formulation and Applications. Water Resources Res. 40, W07407. doi:10.1029/2004WR003248.

ENRESA (1998): Bentonita: origen, propiedades y fabricación de bloques. ENRESA Technical Publication PT 04/98 (in Spanish).

ENRESA (2000): Full-scale engineered barriers experiment for a deep geological repository in crystalline host rock FEBEX Project. EUR 19147 EN, European Commission.

ENRESA (2006a): FEBEX: Updated final report 1994-2004. ENRESA Technical Publication PT 05-0/2006.

ENRESA (2006b): FEBEX: Final THG modelling report. ENRESA Technical Publication PT 05-3/2006.

European Commission (EC), (2000): Full-scale engineered barriers experiment for a deep geological repository in crystalline host rock (FEBEX Project). Report of the European Commission, EUR 19147 EN, 403 pp.

Fernández, A.M., Rivas, P. & Cuevas, J. (1999): Estudio del agua intersticial de la arcilla FEBEX. Techn. Report 70-IMA-L-0-44.

Fernández, R., Cuevas, J. & Mäder, U. (2009): Modelling concrete interaction with a bentonite barrier. Eur. J. Mineral., 21, 177-191.

Galíndez, J.M., Molinero, J., Samper, J. & Yang, C.D. (2006): Simulating concrete degradation processes by reactive transport models. J. Phys. IV France 136, 177–188.

García-Gutiérrez, M. (1997): Tracers in the FEBEX Project. Technical Report 70-IMA-L-0-33. CIEMAT 54B50/8/97.

García-Gutiérrez, M., Cormenzana, J.L., Missana, T., Alonso, U., & Mingarro, M. (2011): Diffusion of strongly sorbing cations (^{60}Co and ^{152}Eu) in compacted FEBEX bentonite. Phys. Chem. Earth 36, 1708–1713.

Martín, P.L., Barcala, J.M., & Huertas, F. (2006): Large-scale and long-term coupled thermo-hydro-mechanic experiments with bentonite: the FEBEX mock up test. J. Iberian Geol. 32 (2), 259-282.

Molinero J, Samper, J., Yang, C. & Zhang, G. (2004): Biogeochemical reactive transport model of the Redox zone experiment of the Äspö hard rock laboratory (Sweden), Nucl. Technol., vol. 48, pp. 151-165.

Molinero J. & Samper, J. (2006): Modeling of reactive solute transport in fracture zones of granitic bedrocks, J. Contam. Hydrol., vol. 82, pp. 293-318.

Mon, A., Samper, J., Montenegro, L., Naves, A., Pisani, D. & Fernández, J. (2015): Modelos numéricos acoplados de flujo no isotermo y transporte de solutos reactivos a través de la barrera arcillosa de un almacenamiento geológico profundo de residuos radiactivos, In: Jornadas de Zona no Saturada Vol XII, Silvia Martínez y Antonio Sastre Ed, pp. 267-274. [in Spanish]

Nagra (2015): Minutes of the FEBEXe-FEBEX-DP Partner Meeting Stockholm. September, 2015.

Navarro, V. & Alonso, E.E., (2000): Modelling swelling soils for disposal barriers. Comput. Geotech. 27,19-43.

Navarro, V. (1997): Modelo de comportamiento mecánico e hidráulico de suelos nosaturados en condiciones no isotermas. Ph.D. Dissertation, Universidad Politécnica de Cataluña, 329 pp. (in Spanish).

Rozalén, M.L., Huertas, F.J., Brady, P.V., Cama, J., García-Palma, S. & Linares, J. (2008): Experimental study of the effect of pH on the kinetics of montmorillonite dissolution at 25 ºC. Geochimica et Cosmochimica Acta 72, 4224-4253.

Sacchi, E. & Michelot, J.L. (2000): Porewater extraction from argillaceous rocks for geochemcical characterization. Methods and interpretations. NEA-OECD.

Sakaki, T., Gaus, I. & Schlaeger, S. (2016): Water content measurement with TDR in bentonite blocks, ~ 18-year evolution and verification. Presentation at the FEBEX-DP Project Meeting, May 4, 2016

Samper, J., Mon, A., Montenegro, L., Naves, A. & Pisani, D. (2014a): Coupled THC(m) models of compacted bentonite. International Conference on the Performance of Engineered Barriers: Backfill, Plugs & Seals, Physical and Chemical Properties, Behaviour & Evolution. A Schäfers & S Fahland Ed. BGR, Hannover, Germany, pp. 309-317.

Samper J., Mon, A., Montenegro, L., Pisani, D. & and Naves, A. (2013): Report on testing multiple-continua THC(m) models with laboratory and large-scale tests. PEBS Project Deliverable D3.4-1.

Samper J., Naves, A., Montenegro, L. & Mon, A. (2016): Reactive transport modelling of the long-term interactions of corrosion products and compacted bentonite in a HLW repository in granite: Uncertainties and relevance for performance assessment. Applied Geochemistry 67, 42-51.

Samper J., Yang, C. & Naves, A. (2006): A fully 3-D anisotropic model of DI-B in situ diffusion experiment in the Opalinus clay formation, Physics and Chemistry of the Earth, vol. 31, pp. 531-540, 2006.

Samper J., Zheng, Montenegro, L., Fernández, A.M. & Rivas, P. (2008a): Coupled thermo-hydro-chemical models of compacted bentonite after FEBEX in situ test, Applied Geochemistry vol. 23, pp. 1186-1201.

Samper, J. & Yang, C. (2006): Stochastic analysis of transport and multicomponent competitive monovalent cation exchange in aquifers. Geosphere 2, 102–112.

Samper, J., Delgado, J., Juncosa, R. & Molinero, J. (1998b): Pre-operational THG tracer modelling of the in situ Febex experiment. UDC Technical Report 70-ULC-M-0-2.

Samper, J., Yang, C. & Montenegro, L. (2003): CORE2D version 4: a code for nonisothermal water flow and reactive solute transport. User's Manual. University of La Coruña, Spain.

Sánchez, M, Gens, A. & Guimarães, L. (2012): Thermal–hydraulic–mechanical (THM) behavior of a large-scale in situ heating experiment during cooling and dismantling, Canadian Geotechnical Journal, 49(10): 1169-1195.

Savage, D., Watson, C., Benbow, S. & Wilson, J. (2010): Modelling iron/bentonite interactions. Applied Clay Science 47, 91-98.

Soler, J.M., Wersin, P. & Leupin O.X. (2013): Modeling of Cs diffusion and retention in the DI-A2 experiment (Mont Terri). Uncertainties in sorption and diffusion parameters. Appl Geochem, 33(2013):191–198.

Tachi, Y. & Yotsuji, K. (2014): Diffusion and sorption of Cs^+, Na^+, I^- and HTO in compacted sodium montmorillonite as a function of porewater salinity: Integrated sorption and diffusion model. Geochimica et Cosmochimica Acta, 132, 75–93.

Villar, M.V, Fernández, A.M., Martín, P.L., Barcala, J.M., Gómez-Espina, R. & Rivas, P. (2008a): Effect of heating/hydration on compacted bentonite: test in 60 cm long cells. Colección Documentos CIEMAT.

Villar, M.V., Sánchez, M. & Gens, A. (2008b): Behavior of a bentonite barrier in the laboratory: experimental results up to 8 years and numerical simulation. Physics and Chemistry of the Earth, Vol. 33, Supplement 1, pp. S476-S485.

Yang C., Samper, J. & Montenegro, L. (2008): A coupled non-isothermal reactive transport model for long-term geochemical evolution of a HLW repository in clay, Environmental Geology, vol. 53, pp. 1627-1638, 2008.

Yang C., Samper, J. Molinero, J. & Bonilla, M. (2007): Modelling geochemical and microbial consumption of dissolved oxygen after backfilling a high level radioactive waste repository, Journal of Contaminant Hydrology, vol. 93, pp. 130-148, 2007.

Yi, S, Samper, J., Naves, A. & Soler, J.M. (2015): A single-site reactive transport model of Cs+ for the in situ diffusion and retention (DR) experiment. Environmental Earth Sciences, 74:3589–3601.

Zhang, G., Samper, J. & Montenegro, L. (2008): Coupled thermo-hydro-bio-geochemical reactive transport model of CERBERUS heating and radiation experiment in Boom clay", Applied Geochemistry, vol. 23, pp. 932-949.

Zheng L., Samper, J. & Montenegro, L. (2008a): Inverse hydrochemical models of aqueous extracts tests, Physics and Chemistry of the Earth, vol. 33, pp. 1009-1018.

Zheng, L & Samper, J. (2015): Dual continuum reactive transport with n-th order solute transfer term for structured unsaturated porous media, Comp. Geos, DOI 10.1007/s10596-015-9477-8.

Zheng, L. & Samper, J. (2004): Formulation of the inverse problem of non-isothermal multiphase flow and reactive transport in porous media. In: Miller, C.T., Farthing, M.W., Gray, W.G., Pinder, G.F. (Eds.), Computational Methods in Water Resources, vol. 2. Elsevier, pp. 1317–1327.

Zheng, L. & Samper, J. (2005): Inverse problem of non-isothermal multiphase flow and reactive transport in deformable porous media. In: Samper, J., Paz González, A. (Eds.), VII Jornadas de Investigación en la Zona no Saturada de Suelo, ZNS'05. La Coruña, Spain, pp. 307–313.

Zheng, L. & Samper, J. (2008): A coupled THMC model of FEBEX mock-up test. Physics and Chemistry of the Earth 33, S486-S498.

Zheng, L. (2006): Coupled thermo-hydro-mechanical-geochemical models for structured deformable porous media. Ph.D. Dissertation, Universidad de A Coruña, A Coruña, Spain, 439 pp.

Zheng, L., Samper, J. & Montenegro, L. (2011): A coupled THC model of the FEBEX in situ test with bentonite swelling and chemical and thermal osmosis, J of Contaminant Hydrology 126:45–60.

Zheng, L., Samper, J., Montenegro, L. & Fernández, A.M. (2010): A coupled THMC model of a heating and hydration laboratory experiment in unsaturated compacted FEBEX bentonite, Journal of Hydrology, Vol 386, Issues 3-4, 80-94. 10.1016/j.jhydrol.2010.03.009. ISSN: 0022-1694

Zheng, L., Samper, J., Montenegro, L. & Mayor, J.C. (2008b): Flow and reactive transport model of a ventilation experiment in Opalinus clay, Physics and Chemistry of the Earth, Vol. 33, S486–S498. doi: 10.1016/j.pce.2008.05.012

PART D

LBNL – contribution:
Pre-Dismantling Fully Coupled THMC Models for FEBEX-DP

D.1 Introduction

The most common buffer material for EBS is compacted bentonite, which features low permeability and high retardation of radionuclide transport. The safety functions of EBS bentonite include limiting transport in the near field; damping the shear movement of the host rock; preventing the sinking of canisters (if emplaced in the centre of the tunnel), limiting pressure on the canister and rock, and reducing microbial activity. To assess whether EBS bentonite can maintain these favourable features while undergoing heating from the waste package and hydration from the host rock, we need a thorough understanding of the thermal, hydrological, mechanical, and chemical evolution of bentonite under disposal conditions. While numerous laboratory experiments, field tests, and numerical models have been conducted to improve the understanding of each individual process or coupled THC/THM processes, there is a lack of studies on coupled THMC processes due to the challenges of conducting experiments and developing models that can cover all the THMC processes. Recently coupled THMC models have been developed for a generic disposal system in clayey host rock with EBS bentonite (Liu et al. 2013, Zheng et al. 2014, Zheng et al. 2015b). However, model validation remained difficult for lack of THMC data from long-term, large-scale experiments. The *in-situ* test, which has been ongoing for 18 years, provides a unique opportunity of validating coupled THMC models. In this section, we describe the development of coupled THMC models that interpret the THM data and predict the chemical evolution in bentonite.

D.2 Model development

D.2.1 Simulator

The numerical simulations are conducted with TOUGHREACT-FLAC3D, which sequentially couples the multiphase fluid flow and reactive transport simulator, TOUGHREACT (Xu et al. 2011), with the finite-difference geomechanical code FLAC3D (Itasca 2009). The coupling of TOUGHREACT and FLAC was initially developed in Zheng et al. (2012) to provide the necessary numerical framework for modelling fully coupled THMC processes. It was equipped with a linear elastic swelling model (Zheng et al. 2012, Rutqvist et al. 2013) to account for swelling as a result of changes in saturation and pore-water composition and the abundance of swelling clay (Liu et al. 2013, Zheng et al. 2014). A recent addition to the code is the capability of simulating Non-Darcian flow (Zheng et al. 2015b) and thermal osmosis.

D.2.2 Modelling setup

Because the hydration of bentonite is fairly symmetrical, and radial symmetry has also been observed for heating, we use an axisymmetric mesh (Fig. D-1) to save computation time so that we can focus on the key coupling processes. However, such a model can only be used to interpret and predict the THMC behaviour in the "hot sections", i.e. sections of bentonite block surrounding the heater including Sections 41 – 54 (or more typically Section 49 as in Fig. D-2).

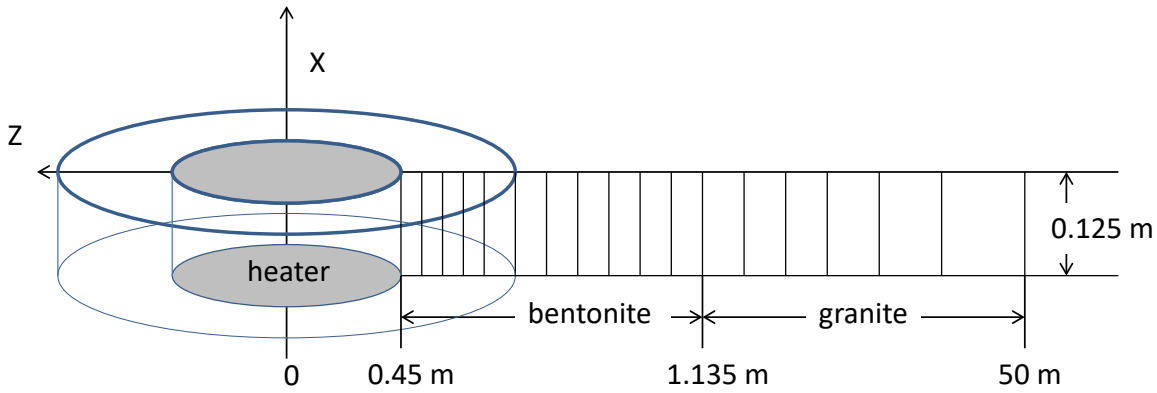

Fig. D-1: Mesh used for the model, not to the scale

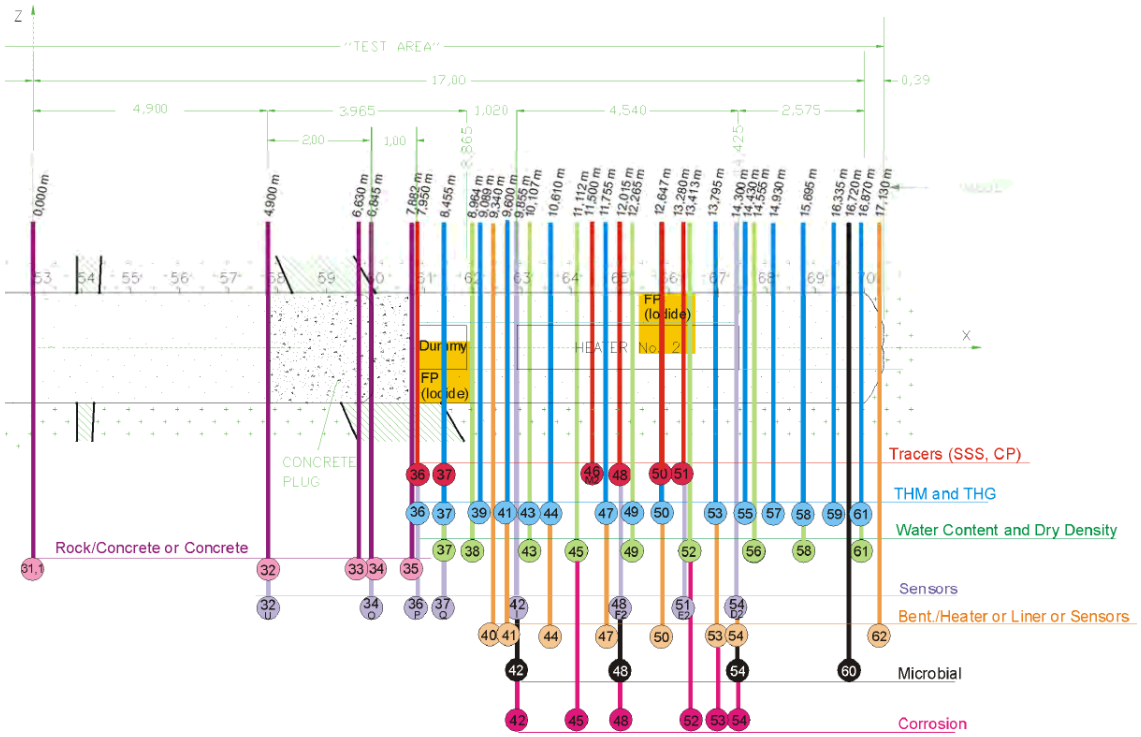

Fig. D-2: Section layout during the dismantling operation of Heater #2 (Detzner & Kober 2015)

The model considers two material zones for the bentonite and granite. The first two nodes (1 and 2) are located on the external wall of the heater (r = 0.45 – 0.46 m). Bentonite is located within 0.45 m < r < 1.135 m. The remaining domain up to 50 m is used to simulate the granite. The simulation time starts on February 27, 1997 and ends on July 1, 2015, a total of 6'698 days (18.3 years).

The initial temperature is uniform and equal to 12 °C. A constant temperature of 100 °C is prescribed at the heater/bentonite interface (r = 0.45 m) while temperature is assumed to remain constant at its initial value of 12 ºC at the external boundary (r = 50 m) because the thermal perturbation induced by the heaters does not extend to this boundary.

The bentonite has a gravimetric water content of 14 % initially, which corresponds to a saturation degree of 55 % and a suction of 1.11×10^5 kPa. The boundary conditions for flow include: 1) no flow at r = 0.45 m and 2) a prescribed liquid pressure of 700 kPa at r = 50 m.

The model assume the bentonite is homogenous. Local features such as sensors and coupons buried in the bentonite may change the local dry density of bentonite, which was not considered in the model. It might affect the local HMC behaviour, but it is not expected to affect the THMC evolution of the entire bentonite barrier.

D.2.3 The TH model

The model considers non-isothermal two phase (air and water) flow, with each individual phase fluxes given by a multiphase version of Darcy's Law. For the vapour flow in the air phase, in addition to Darcy flow, mass transport can also occur by diffusion and dispersion according to Fick's law. Thermal behaviour is relatively well understood because it is less affected by coupled processes in comparison to hydrological and chemical processes and the relevant parameters can be measured reliably. In the current model, both conductive (Fourier's law) and convective heat flux are considered and thermal conductivity is the key parameter. Fig. D-3 shows the measured thermal conductivity for FEBEX bentonite in function of degree of water saturation.

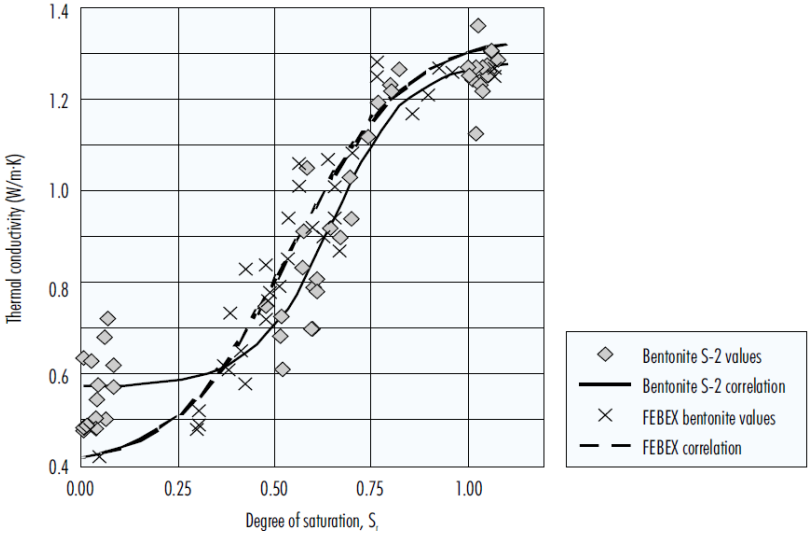

Fig. D-3: Thermal conductivity of FEBEX bentonite as a function of degree of saturation (ENRESA 2000)

Also shown is thermal conductivity for bentonite S-2 which has similar properties to FEBEX bentonite.

The water saturation span the FEBEX bentonite went through (from an initial degree of water saturation 55 – 59 % to 100 %), allows using a linear relationship between thermal conductivity and water saturation. We use a linear relationship implemented in TOUGH2 (Pruess et al. 1999):

$$K_{th} = K_{wet} + S_l(K_{wet} - K_{dry}) \qquad \text{B-1}$$

where K_{wet} is the thermal conductivity at fully saturated conditions, K_{dry} is the thermal conductivity under dry conditions, and S_l is the liquid saturation degree. K_{wet} and K_{dry} are given in Tab. D-1.

In previous modelling work (e.g. Sánchez et al. 2012b; Zheng and Samper 2008), significant effort was invested to find out why the hydration of FEBEX bentonite is slower than predicted by the typical Darcy flow model. Several processes have been proposed to explain the discrepancy between measured data and predictions by the Darcy flow model. These include the permeability decrease due to the dual-structural behaviour of bentonite (Sánchez et al. 2005, 2012b), thermal osmosis, in which a moisture flux induced by the thermal gradient in the bentonite is in the opposite direction of water infiltration from the granite (Zheng et al. 2011), permeability

decreases due to swelling (Zheng & Samper 2008), and non-Darcian flow (Liu & Birkholzer 2012).

In Zheng et al. (2015b), a TH model with non-Darcian flow was developed; the threshold gradient, the key parameter for non-Darcian flow, was calibrated based on a small-scale column test for FEBEX bentonite. However, including non-Darcian flow into the TH model led to a significant underestimation of the relative humidity data in the entire bentonite barrier (even in bentonite near the bentonite/granite interface). Although the relevance of non-Darcian behaviour is clear for saturated flow in clay rock (Liu and Birkholzer 2012 and references cited therein), Zheng et al. (2015b) showed that there were two issues that prevented us from clearly delineating a contribution of non-Darcian flow to water flow in unsaturated clay or bentonite. First and foremost, the calibration of the relative permeability and retention curves overshadows the effect of non-Darcian flow. The non-linear relationship between water flux and hydraulic gradient, which motivates the relevance of non-Darcian behaviour to water flow, is already accounted for, at least partially, by the relative permeability (which in turn is a function of the retention curve) in the flux-gradient relationship for unsaturated flow. However, in most modelling exercises, relative permeability is calibrated based on a Darcy-type flow. As a result, the calibration of the parameters associated with relative permeability overshadows the contribution of non-Darcian flow— the parameters for relative permeability might be "over-calibrated" so that the effect of non-Darcian flow looks irrelevant. For FEBEX bentonite, the relative permeability and retention curve were calibrated based on a Darcy type of flow model (ENRESA 2000), which essentially obviates non-Darcian flow for unsaturated bentonite. Thus, if Darcian flow is added on top of relative permeability that is calibrated based on Darcy flow, we count the non-linearity between flux and gradient double, and consequently the model significantly underestimates the water inflow from granite to bentonite. Second, Cui et al. (2008) reported that threshold gradients are different for different capillary pressure. Further research is needed to take into account the effect of capillary pressure when a threshold gradient is calculated. However, even though we can improve our threshold gradient calculation by taking into account capillary pressure, it is unlikely to eliminate the aforementioned issue of process uncertainties versus parameter uncertainties. Based on the findings from Zheng et al. (2015b) in the models presented in this report, non-Darcian flow was not considered.

The key parameters affecting the hydration of bentonite are the permeability of granite, the relative permeability and retention curves of bentonite, the vapour diffusion coefficient and permeability of bentonite. In Zheng et al. (2015b), the most plausible values for these parameters were discussed and illustrated with sensitivity analyses listed in Tab. D-1.

Granite is a fractured medium and ideally should be represented by fractures and matrix. Just as previous models for in-situ tests (Samper et al. 2008a; Sánchez et al. 2012b), the current model also assumes granite is a homogeneous porous medium, which requires us to use an equivalent permeability. Based on the total water flow at the entire test zone (ENRESA 2000), the permeability of granite is around 5×10^{-18} to 8×10^{-18} m^2. ENRESA (2000) also reports that the most frequent permeability is 1×10^{-18} but deems it is more representative of rock matrix. Zheng et al. (2011) used 8×10^{-18} m^2, Kuhlman & Gaus (2014) estimated a permeability of 6.8×10^{-19} m^2, and Sanchez et al. (2012b) used a surprisingly small value, 8.18×10^{-21} m^2. Based on the published values, it seems that a permeability between 7×10^{-19} to 8×10^{-18} m^2 is plausible. Based on the evaluation in Zheng et al. (2015b), a permeability of 2×10^{-18} m^2 is used (Tab. D-1).

The capillary pressure (retention curve) is calculated by the van Genuchten function as:

$$P_{cap} = -\frac{1}{\alpha}\left(\left[S^*\right]^{-1/m} - 1\right)^{1-m} \qquad \text{B–2}$$

where P_{cap} is the capillary pressure (Pa), $S^* = (S_l - S_{lr})/(1 - S_{lr})$ and S_l is the water saturation, S_{lr} is the residual water saturation. S_{lr} is 0.1 for bentonite and 0.01 for granite. The values of α and m are given in Tab. D-1. The retention curve was fairly well studied for FEBEX bentonite. For example, ENRESA (2000) presented the retention curve for both a drying and wetting path and the van Genuchten function (van Genuchten 1980) was derived with an m-value ranging from 0.3 to 0.6. Kuhlman & Gaus (2014) estimated an m of 0.3 and Zheng et al. (2011) and Sánchez et al. (2012b) use an m of 0.18, which is slightly lower.

The effective permeability of bentonite has been under scrutiny by modelers (e.g. Zheng et al. 2011) due to its critical role in determining the hydration of bentonite. It is the product of intrinsic permeability (k) (or saturated permeability, absolute permeability) and relative permeability (k_r). Relative permeability using $k_r = S_l^3$ (where S_l is water saturation degree) has been consistently used by different models (Zheng et al. 2011, Sánchez et al. 2012b, Kuhlman & Gaus 2014) and we use the same function here. The plausible saturated permeability for FEBEX bentonite in the initial state could be in a range from 1×10^{-21} to 9×10^{-21} m^2 based on various sources (Zheng et al. 2011, Sánchez et al. 2012b, Kuhlman & Gaus 2014, Chen et al. (2009) and we use 2.15×10^{-21} m^2 in the model. However, as demonstrated by Zheng et al. (2015b), a constant intrinsic permeability for bentonite could not explain the relative humidity data in the entire thickness of the bentonite barrier. In the next section, we will discuss the change of permeability as a result of mechanical changes in bentonite.

Tab. D-1: Thermal and hydrodynamic parameters

Parameter	**Granite**	**Bentonite**
Grain density [kg/m^3]	2'700	2'780
Porosity ϕ	0.01	0.41
Saturated permeability [m^2]	2.0×10^{-18}	2.15×10^{-21}
Relative permeability, k_{rl}	$k_{rl} = S$	$k_{rl} = S^3$
van Genuchten $1/\alpha$ [1/Pa]	4.76×10^{-4}	1.1×10^{-8}
van Genuchten m	0.7	0.45
Compressibility, β [1/Pa]	3.2×10^{-9}	5.0×10^{-8}
Thermal expansion coeff. [1/°C]	1.0×10^{-5}	1.5×10^{-4}
Dry specific heat [J/kg- °C]	793	1'091
Thermal conductivity [W/m-°C] dry/wet	3.2/3.3	0.47/1.15
Effective vapour diffusion coefficient (m^2/s)	1.03×10^{-4}	1.03×10^{-4}

D.2.4 Mechanical Model

In current models, we tested two mechanical models for bentonite: a linear swelling model and dual structure Barcelona expansive clay model (BExM).

D.2.4.1 Linear swelling model

The linear swelling models have been used in the generic model evaluation of bentonite barrier in Zheng et al. (2015a; b). The advantage of this method is its simplicity and easy calibration of key parameters, but the disadvantage is that it does not describe the transient state of swelling correctly. For non-isothermal behaviour of unsaturated soils, we may partition the total incremental strain into elastic (ε^e), plastic (ε^p), suction (ε^s), thermal strains (ε^T) and chemical strains (ε^c) (Zheng et al. 2015b):

$$d\varepsilon = d\varepsilon^e + d\varepsilon^p + d\varepsilon^s + d\varepsilon^T + d\varepsilon^c \qquad \text{B–3}$$

where the suction strain represents the strain associated with changes in suction and chemical strain represents the strains associated with a change in chemical conditions, including changes in ion concentration and the abundance of swelling clays.

A linear elastic swelling model essentially defines the suction stress as a function of water saturation:

$$d\varepsilon^s = \beta_{sw} dS_l \qquad \text{B–4}$$

where S_l is the water saturation and β_{sw} is a moisture swelling coefficient.

Under mechanically-constrained conditions and considering the linear relationship between swelling stress and suction strain, $d\sigma_s = 3Kd\varepsilon^s$, we have a swelling stress that is linearly proportional to the saturation:

$$d\sigma_s = 3K\beta_{sw} dS_l \qquad \text{B–5}$$

where K is the bulk modulus. Equation B–5 is what was used for EBS bentonite in Rutqvist et al. (2011). In this report, β_{sw} is 0.238, calibrated using the swelling pressure of 5 MPa for FEBEX bentonite at full saturation. The swelling pressure for FEBEX bentonite ranges from 4.5 MPa (Castellanos et al. 2008) to 7 MPa (ENRESA 2000).

The porosity change in bentonite is given by the following state-surface expression (Lloret & Alonso 1995):

$$e = A + B\ln\sigma' + C\ln(\psi + p^a) + D\ln\sigma'\ln(\psi + p^a) \qquad \text{B–6}$$

where e is the void ratio, which is equal to the volume of voids divided by the volume of the solids; p^a is the atmospheric pressure (Pa), σ' is the mean effective stress (Pa); ψ is the suction (Pa), and A, B, C and D are empirical constants which for the FEBEX compacted bentonite are equal to A = 0.91, B = - 0.0552, C = - 0.0606413 and D = 0.00479977.

The stress-dependence of permeability for low-permeability sedimentary rock is fairly well known and has been studied extensively (e.g. Ghabezloo et al. 2009, Kwon et al. 2001). Many empirical relationships have been put forward to describe the permeability changes with effective stress. One of them is the exponential law (David et al. 1994), which is used in the current model:

$$k = k_0 \exp[-\gamma(\sigma - \sigma_0)] \qquad \text{B–7}$$

where k is the permeability at the effective stress σ, k_0 is the permeability at initial stress σ_0 and is equal to 2.15E-21 m^2; γ is the stress sensitivity coefficient and equal to 1E-7 Pa-1 in the current model based on the calibration against THM data.

D.2.4.2 Dual structure Barcelona expansive clay model (BExM)

The dual structure Barcelona Expansive Clay model (BExM) (Alonso et al. 1999, Sánchez et al. 2005) provide a more mechanistic way to describe the mechanical behaviour of bentonite and has been used to simulate the FEBEX mock-up test (Sánchez et al. 2012a) and in-situ test (Sánchez et al. 2012b). The dual structure BExM was also implemented in TOUGHREACT-FLAC3D and used in this report to simulate the mechanical behaviour of the FEBEX in-situ test.

In the dual structure model, the macrostructure is modelled with a constitutive model for unsaturated soils, such as the Barcelona Basic Model (BBM). The microstructure is incorporated to extend BBM to a dual structure model, which enables simulating the behaviour of expansive soils, such as the dependency of swelling strains and swelling pressures on the initial stress state and on the stress path, strain accumulation upon suction cycles and secondary swelling. Thus, in the dual structure model, the total volume (V), the total void ratio (e), and porosity (ϕ) of the material are divided into a microstructural and a macrostructural part. The microstructure can swell to invade the macro porosity, depending on the mechanical confinement and load level. This is relevant when considering permeability changes during the soil swelling, because fluid flow takes place mostly through the macro porosity, which is not proportional to the total strain and deformation of the expansive soil. Equations to describe the mechanical behaviour of microstructural and macrostructural levels and the interaction between structural levels are given in Zheng et al. (2016).

The parameters of BExM used in these studies are summarised in Tab. D-2. The set of parameters are calibrated based on a compacted bentonite by Lloret et al. (2003) and are used in the numerical analysis for the mock-up test by Sanchez et al. (2012a). In Lloret et al. (2003), the simulation is one-dimensional, which can be treated as an isotropic case in 3D. However, the lateral displacements are constrained in an oedometer test, but the vertical loading is controlled by stresses. Thus, the stress status in oedometer test is anisotropic and the assumption of isotropy is not appropriate for this test. In Sanchez et al. (2012a), although a good agreement between numerical results and observed behaviour during experiments is obtained, the macrostructural bulk modulus of bentonite can reach values as high as 2 GPa. Based on the report by Rutqvist & Tsang (2002), the bulk modulus of the FEBEX bentonite should be in the order of 10 – 100 MPa. Therefore, the bulk modulus values evolve too high during the simulation of Sanchez et al. (2012a). Here we determine the parameters related to macrostructural bulk modulus, κ, which

gives reasonable bulk modulus (in the order of 10 MPa ~ 1'000 MPa), from the observed results during the experiment. In order not to affect the hydraulic effects on macrostructures, we increase the value of the parameter κ_s to keep the same ratio of $\frac{\kappa}{\kappa_s}$ as Lloret et al. (2003) and Sanchez et al. (2012) used in their simulations.

Tab. D-2: Parameters used for a combination of loading paths tests (Lloret et al. 2003, Sanchez et al. 2012a)

Parameters defining the Barcelona basic model for macrostructural behaviour						
$\kappa = 0.018$	$\kappa_s = 0.0036$	$\lambda(0) = 0.08$	$p_c = 0.5$ MPa	$r = 0.90$	$\zeta = 1$ MPa^{-1}	$p_0^* = 6.5$ MPa
$\alpha_a = 1$	$\alpha_0 = 1 \times 10^{-5}°C^{-1}$					
Parameters defining the law for microstructural behaviour						
$\alpha_m = 0.021$ MPa^{-1}	$\beta_m = 2.3 \times 10^{-3}$ MPa^{-1}	$\chi = 1$				
Interaction functions						
$f_c = 1 + 0.9 \tanh\left[20\left(\frac{p_r}{p_0} - 0.25\right)\right]$		$f_s = 0.8 - 1.1 \tanh\left[20\left(\frac{p_r}{p_0} - 0.25\right)\right]$				
$e_{macro} = 0.21$		$e_{micro} = 0.48$				

Note that the parameters (κ and κ_s) related to macrostructural bulk modulus are higher than the original ones used in Lloret et al. (2003) and Sanchez et al. (2012a). All other parameters are set to zero.

D.2.5 Chemical model

The establishment of the chemical model first requires the knowledge of initial chemical conditions in bentonite and granite, i.e., the initial mineralogical and pore water compositions. Extensive mineralogical characterization was conducted by ENRESA (2000) and Fernández et al. (2004). Ramírez et al. (2002) also reported the mineralogical composition of FEBEX bentonite, which is slightly different from that reported by ENRESA (2000). In this report, we take the average of mass fraction reported in ENRESA (2000), Fernández et al. (2004) and Ramírez et al. (2002) and transformed the mass fraction to volume fraction (ratio of the volume for a mineral to the total volume of medium) using a porosity of 0.41 (see Tab. D-3). Note that minerals with zero volume fractions are the secondary minerals that could be formed. A detailed mineralogical composition of granite has not been found in our literature search, probably because the chemical conditions in granite are not supposed to be actively changed by repository conditions. Previous THC models for the *in-situ* test (Samper et al. 2008a; Zheng et al. 2011) only include quartz in the minerals assemblage in granite. Siitari-Kauppi et al. (2007) reported that the Grimsel granite is composed of quartz, K-feldspar, plagioclase and a small amount of "dark material". In the current model, we consider quartz, K-feldspar, plagioclase in granite with their volume fractions listed in Tab. D-3.

Tab. D-3: Mineral volume fraction (dimensionless, ratio of the volume for a mineral to the total volume of medium) of the FEBEX bentonite (ENRESA 2000, Fernández et al. 2004, Ramírez et al. 2002) and granite (Zheng et al. 2011)

Mineral	FEBEX Bentonite	Granite
Calcite	0.00472	0
Smectite	0.546	0.
Chlorite	0.0024	0
Quartz	0.012	0.37
K-Feldspar	0.0059	0.35
Plagioclase	0	0.27
Dolomite	0.0	0
Illite	0.0	0
Kaolinite	0.0	0
Siderite	0.0	0
Ankerite	0.0	0

FEBEX bentonite blocks have an initial gravimetric water content of 13.5 – 14 % (ENRESA 2000). As described in Bradbury & Baeyens (2003), obtaining the pore-water chemistry of compacted bentonite with such a low water content is difficult. Because the concentration of ions for the initial state of compacted bentonite cannot be measured directly, indirect measurement methods must be used. Squeezing and aqueous extract are the most commonly used methods. Squeezing is a straightforward method – pore-water is squeezed out and concentrations are measured. However, pore water cannot be extracted by squeezing from clay samples with gravimetric water contents less than 20 % (Fernández et al. 2001, 2004), which means that squeezing cannot be done for FEBEX bentonite blocks. In an aqueous extract test, a crushed sample is placed in contact with water at a low solid/liquid ratio (ranging from 1:16 to 1:1). After establishing equilibrium, the solid phase is separated and the liquid phase is analysed (Fernández et al. 2001). Geochemical modelling was needed to retrieve the aqueous ion concentrations at low water content (Zheng et al. 2008). Therefore, any uncertainties associated with the geochemical models affect the evaluation of initial aqueous concentration levels at low water content (the water content at the initial state). The model presented in this report uses the pore water composition (see Tab. D-4) derived by Fernández et al. (2001) from aqueous extract data. The pore water composition for granite (Tab. D-4) is taken from Zheng et al. (2011).

Tab. D-4: Pore-water composition (mol/kg water except for pH) of FEBEX bentonite (Fernández et al. 2001) and granite (Zheng et al. 2011)

	EBS Bentonite: FEBEX	**Granite**
pH	7.72	8.35
Cl	1.60E-01	1.31E-05
SO_4^{-2}	3.20E-02	7.86E-05
HCO_3^-	4.1E-04	3.97E-04
Ca^{+2}	2.2E-02	1.81E-04
Mg^{+2}	2.3E-02	1.32E-06
Na^+	1.3E-01	3.76E-04
K^+	1.7E-03	7.80E-06
Fe^{+2}	2.06E-08	2.06E-08
$SiO_2(aq)$	1.1E-04	6.07E-04
AlO_2^-	1.91E-09	3.89E-08

In the chemical model, we consider aqueous complexation, cation exchange, surface complexation and mineral dissolution/precipitation. Aqueous complexes and their disassociation constants for reactions that are written in terms of the primary species in Tab. D-4 are listed in Tab. D-5. These thermodynamic data were taken from Data0.dat.YMPv4.0, an EQ3/6 (Wolery 1993) database qualified by the U.S. Department of Energy for the Yucca Mountain project. Surface protonation reactions are given in Tab. D-6 and cation exchange reactions are given in Tab. D-7.

Tab. D-5: Aqueous complexes and their dissociation constants

Species	**Log K** (25 °C)	**Species**	**Log K** (25 °C)
OH^-	13.99	$MgHCO_3^+$	-1.03
Al^{+3}	-22.88	$CO_2(aq)$	-6.34
$HAlO_2(aq)$	-6.45	CO_3^{-2}	10.33
$NaAlO_2(aq)$	0.75	$CaCO_3(aq)$	7.01
$AlOH^{+2}$	-17.87	KCl(aq)	1.50
$Al(OH)_2^+$	-12.78	$MgCl^+$	0.14
$Al(OH)_3(aq)$	-6.72	$MgSO_4(aq)$	-2.38
$CaCl^+$	0.70	$NaSO_4^-$	-0.81
$CaCl_2(aq)$	0.65	KSO_4^-	-0.88
$CaSO_4(aq)$	-2.10	$NaHSiO_3(aq)$	8.30
NaCl(aq)	0.78	$CaOH^+$	12.85
$FeCl^+$	0.17	NaOH(aq)	14.15
$FeHCO_3^+$	-2.04	$NaCO_3^-$	9.82
$FeCO_3(aq)$	4.88	$NaHCO_3(aq)$	-0.17
$FeCl_4^{-2}$	1.94	$CaHCO_3^+$	-1.04

Tab. D-6: Surface protonation reactions on montmorillonite (Bradbury & Baeyens 2005)

Surface complexation	**Log K**
$mon\_sOH_2^+ = mon\ \_sOH + H^+$	-4.5
$mon\_sO^- + H^+ = mon\ \_sOH$	7.9
$mon\_w1OH_2^+ = mon\_w1OH + H^+$	-4.5
$mon\_w1O^- + H^+ = mon\_w1OH$	7.9
$mon\_w2OH_2^+ = mon\_w2OH + H^+$	-6
$mon\_w2O^- + H^+ = mon\_w2OH$	10.5

Tab. D-7: Cation exchange reactions on montmorillonite and illite (Bradbury & Baeyens 2005)

Cation exchange reaction	**$K_{Na/M}$**
$Na^+ + mon\text{-}H = mon\ \text{-}Na + H^+$	1
$Na^+ + mon\ \text{-}K = mon\ \text{-}Na + K^+$	0.0775
$Na^+ + 0.5\ mon\ \text{-}Ca = mon\ \text{-}Na + 0.5Ca^{+2}$	0.302
$Na^+ + 0.5\ mon\ \text{-}Mg = mon\ \text{-}Na + 0.5Mg^{+2}$	0.302

Tab. D-8: Equilibrium constants for mineral precipitation/dissolution

Primary Mineral	**log(*K*)**	**Secondary Mineral**	**log(*K*)**
Calcite	1.85	Siderite	1.543
Smectite-Na	-34.62	Dolomite	2.524
Quartz	-3.75	Ankerite	-1.035
K-feldspar	-22.91	Illite	-47.33
Albite	-20.133	Chlorite	4.298
Anorthite	-19.19	Kaolinite	-39.9

The equilibrium constants for precipitation/dissolution of primary minerals (minerals that are present initially) and secondary minerals are listed in Tab. D-8. Note that plagioclase is a solid solution with albite and anorthite as its end members. In the current model, we assume plagioclase contains 10 % anorthite and 90 % albite so that there is a quasi-equilibrium between pore water and plagioclase.

Mineral dissolution/precipitation is kinetically controlled. The kinetic law for mineral dissolution/precipitation is given in Xu et al. (2011). The kinetic rates and surface areas for the minerals considered in the model were taken mostly from Xu et al. (2006) (Tab. D-9). However, the illitization rate (the rate of illite precipitation and smectite dissolution) was calibrated (Liu et al. 2013) based on the measured illite percentage in an illite/smectite (I/S) mixed layer from the Kinnekulle bentonite, Sweden (Pusch & Madsen 1995).

Tab. D-9: Kinetic properties for minerals considered in the model (Xu et al. 2006)

Mineral	**A** (cm^2/g)	**Parameters for Kinetic Rate Law**							
		Neutral Mechanism		**Acid Mechanism**			**Base Mechanism**		
		k_{25} (mol/m^2-s)	**E_a** (kJ/mol)	**k_{25}** (mol/m^2-s)	**E_a** (kJ/mol)	**$n(H^+)$**	**k_{25}** (mol/m^2-s)	**E_a** (kJ/mol)	**$n(H^+)$**
Quartz	9.8	1.023×10^{-14}	87.7						
K-feldspar	9.8	3.89×10^{-13}	38	8.71×10^{-11}	51.7	0.5	6.31×10^{-12}	94.1	-0.823
Kaolinite	151.6	6.91×10^{-14}	22.2	4.89×10^{-12}	65.9	0.777	8.91×10^{-18}	17.9	-0.472
Illite	1.18×10^4 (1)	1.66×10^{-13}	105 (2)						
Chlorite	9.8	3.02×10^{-13}	88	7.76×10^{-12}	88	0.5			
Calcite	3.5	1.63×10^{-7}	23.5						
Dolomite	12.9	2.52×10^{-12}	62.76	2.34×10^{-7}	43.54	1			
Ankerite	9.8	1.26×10^{-9}	62.76	6.46×10^{-4}	36.1	0.5			
Smectite -Na	1.18×10^4 (1)	1.66×10^{-13}	105 (2)						

(1) Calibrated based on the field illitization data (Liu et al. 2013)
(2) From Pusch & Madsen (1995)

D.3 Model results

The ultimate goal of using coupled THMC model to interpret the data collected in the FEBEX *in-situ* test is to understand the THMC evolution of bentonite under the repository condition so that we can use the most plausible processes and parameters to describe the behaviour of bentonite. Once the coupled THMC model can simultaneously match the measured temperature, relative humidity, water content, stress, aqueous concentrations, and minerals phase change, we can further use it to predict the long term (e.g. 100,000 years as required by most performance assessment) under different conditions, such as under higher temperature as was done by Zheng et al. (2015a).

In this section, we first present model results from THMC model using the linear swelling model (denoted in the following sections as THMC-LS) and then discuss the results from the model that uses the dual structure BExM (referred as THMC-BExM in the following sections).

D.3.1 THMC model using linear swelling model

D.3.1.1 THM data and model results

In the FEBEX *in-situ* test, some data were collected real time by the sensors buried in the bentonite block such as temperature, relative humidity and stress; and some of them had to be measured in the laboratory using the bentonite sample that were taken after dismantling of test sections, including water content, dry density, concentration of ions in pore water and mineralogical composition. Tab. D-10 list some key dates of the FEBEX *in-situ* test to facilitate the discussion of the model results. The dismantling of Heater #1 in 2002 and Heater #2 in 2015 provides two snapshots of measured water content, dry density, and concentrations of ions in pore water and mineralogical composition, which are very valuable for understanding the temporal evolution of these key data, as shown later in the report. Note that concentrations of ions in pore water and mineralogical composition have been analysed by another partner of the FEBEX-DP project and are not available yet.

Tab. D-10: Timeline of FEBEX in situ test

Event	**Date** (DD/MM/YYYY)	**Time** (day)	**Time** (year)
Beginning of heating	27/2/1997	0	0.0
Shutdown of Heater #1	02/02/2002	1'827	5.0
Sampling after Heater #1 was dismantled	02/05/2002	1'930	5.3
Shutdown of Heater #2	24/04/2015	6'630	18.2
Sampling after Heater #2 was dismantled	03/07/2015	6'700	18.3

On 24 April 2015, Heater #2 was switched off. After a short cool-off time period, dismantling was carried out from the shotcrete towards the bentonite, section by section (see Fig. D-2) and samples were taken for THMC and microbiological characterization. Details about the dismantling of Heater #2 are given in García-Siñeriz et al. (2016).

Fig. D-5 through Fig. D-8 compare the measured temperatures to two simulation results: a TH model and a THMC model with linear swelling (THMC-LS). Because the current model simulates only the "hot" sections that are normally located in the middle of the 4.5 m long heater, we used temperatures measured at section F2 and E2 (see Fig. D-4) surrounding Heater #2 to constrain the thermal calculation. Starting on 27 February 1997, a constant power of 1200 W was applied to each heater for 20 days and then a constant power of 2000 W for another 33 days. After that, the system was switched to the constant temperature mode, allowing the power to fluctuate freely, but the maximum temperature at the surface of steel liner of the heater was maintained at 100 oC. After the shutdown of Heater #1 on 2 February 2002 (1827 days), the temperature field changed, as manifested by the temperature evolution after 1827 days in Fig. D-5 to Fig. D-8. Unfortunately the thermal sensors at radial distances of 0.48 m and 1.09 m failed shortly after 1827 days, but the temperature data from some sensors at a radial distance of 0.8 m (Fig. D-6) and 1.05 m (Fig. D-8) show the decrease in temperature after the shutdown of Heater #1. The model results match well with the temperature data at all the radial distances. Near the steel liner, e.g., radial distance of 0.48 m in Fig. D-5, the temperature is almost the same as at the surface of the steel liner, but it decreases noticeably at a radial distance of 1.09 m (very close to the bentonite/granite interface) after the shutdown of Heater #1 (Fig. D-8). The current model is a 1D axisymmetrical model that is designed to simulate the conditions of "hot" sections. In order to account for the heat dissipation from "hot" sections to "cold" sections, we used a semi-analytical solution implemented in TOUGH2 (Pruess et al. 1999) with an adjusted heat exchange surface area to match the temperature data. After 1827 days, the heat exchange surface area was adjusted again to match the data to mimic further heat loss from Heater #2 when Heater #1 was removed. In general, a fairly good match between the models and data was achieved.

The temperature profiles calculated by TH and THMC model differ only slightly at locations away from the heater. The reason is that thermal conductivity is a function of degree of water saturation and the TH and THMC models give different degrees of water saturation.

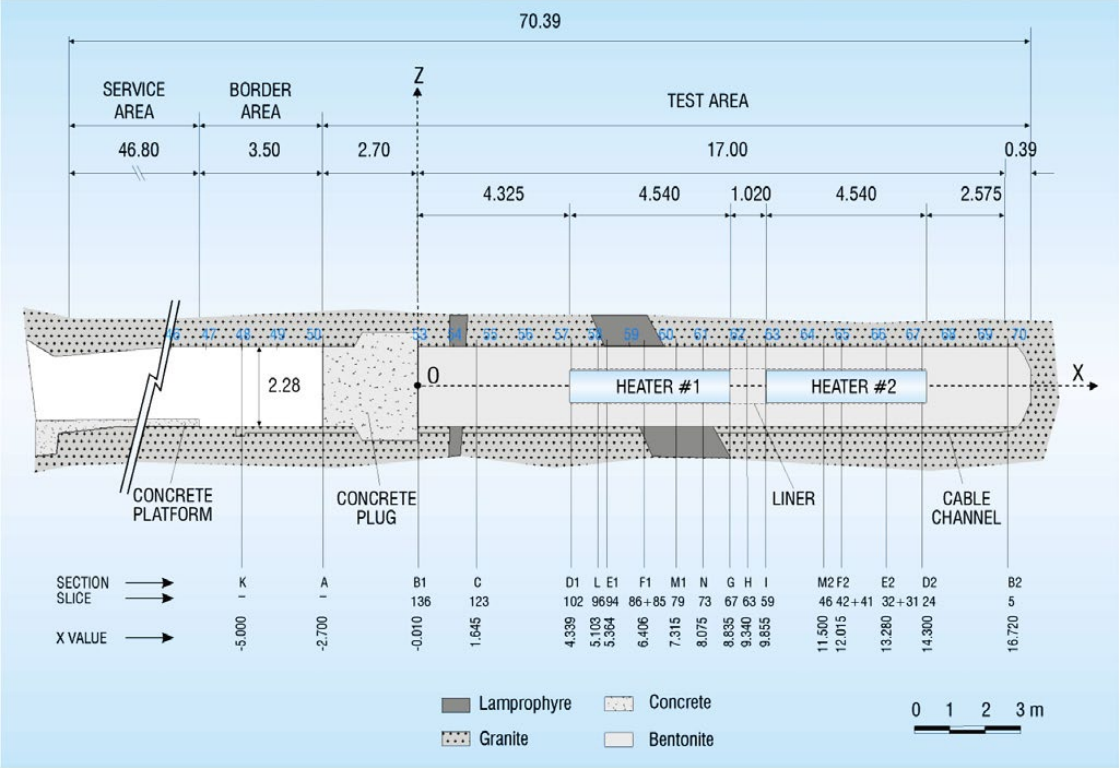

Fig. D-4: The initial configuration of the FEBEX *in-situ* test at the Grimsel underground laboratory (Switzerland) (ENRESA 2000)

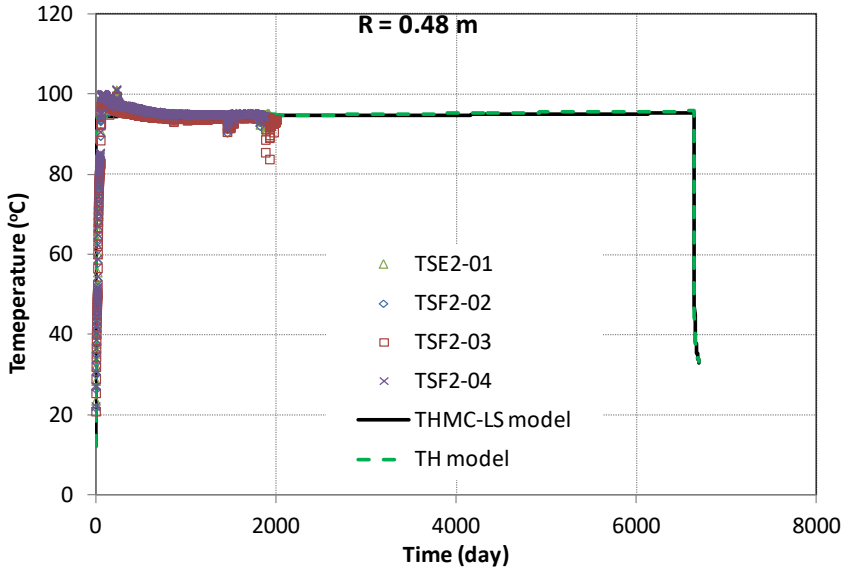

Fig. D-5: Measured temperature by sensors located at a radial distance of 0.48 m in Sections E2 and F2 and model results from the TH model and THMC model with linear swelling (THMC-LS)

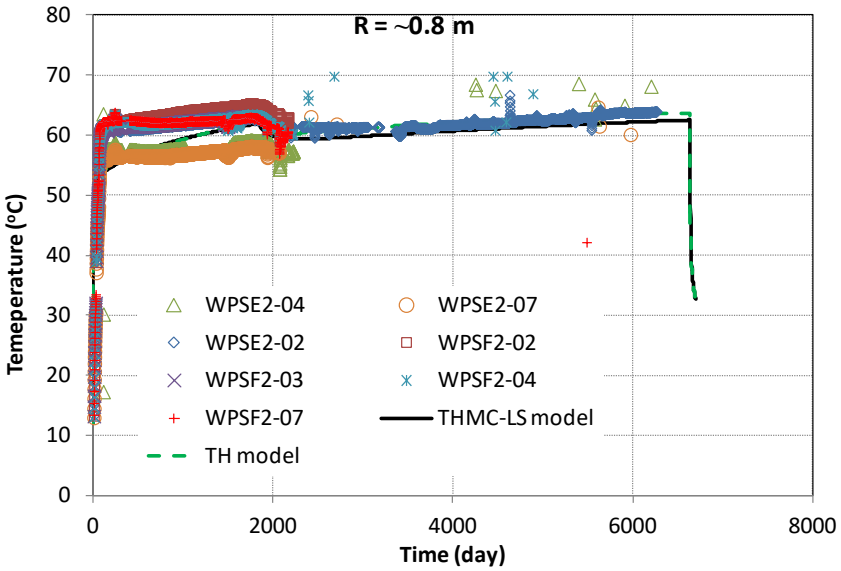

Fig. D-6: Measured temperature by sensors located at a radial distance of 0.8 m in Sections E2 and F2 and model results from the TH model and THMC model with linear swelling (THMC-LS)

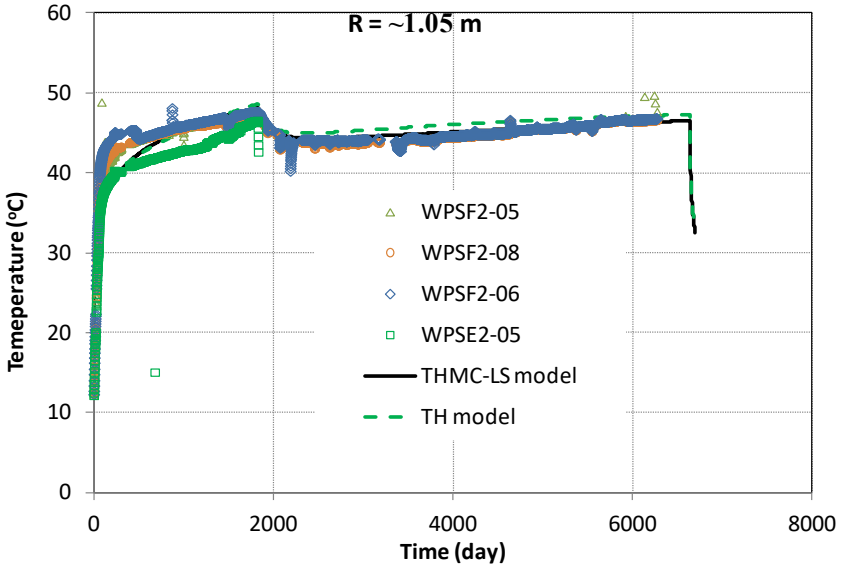

Fig. D-7: Measured temperature by sensors located at a radial distance of 1.05 m in Sections E2 and F2 and model results from the TH model and THMC model with linear swelling (THMC-LS).

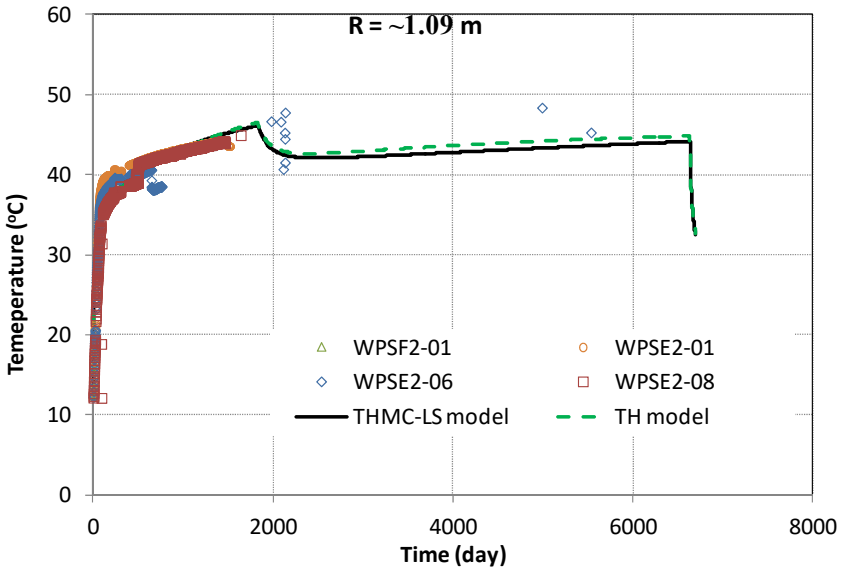

Fig. D-8: Measured temperature by sensors located at a radial distance of 1.09 m in SectionsE2 and F2 and model results from the base TH model.

Relative humidity, water content and dry density are three types of hydrological data that are available so far for comparison with model results. Water content and dry density were measured two times: once after dismantling Heater #1 (in 2002, 5.3 years after the start of heating) and the second time after dismantling Heater #2 (in 2015, 18.3 years after the start of heating).

For the water content and dry density data, in this report we select data from Sections 18, 28 and 29 (Zheng et al. 2011) (see Fig. D-9 and Fig. D-10 for their locations) and Sections 22 and 27 (Daucousse & Lloret 2003) with locations given in Fig. D-10.

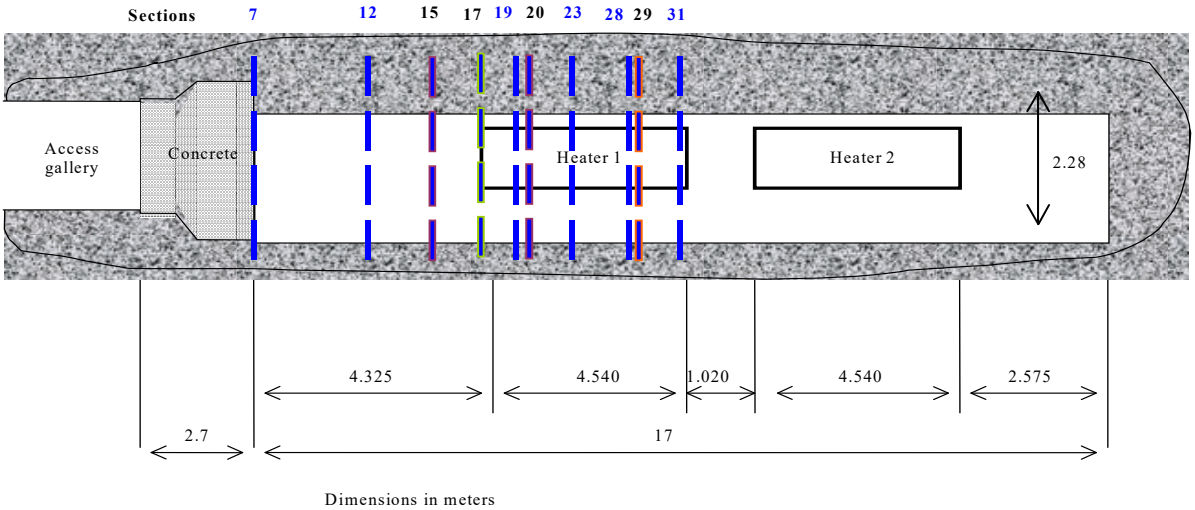

Fig. D-9: Layout of the sampling sections during the dismantling of Heater #1 in 2002

In blue are the common sections for THC and THM analyses (Fernández & Rivas 2003).

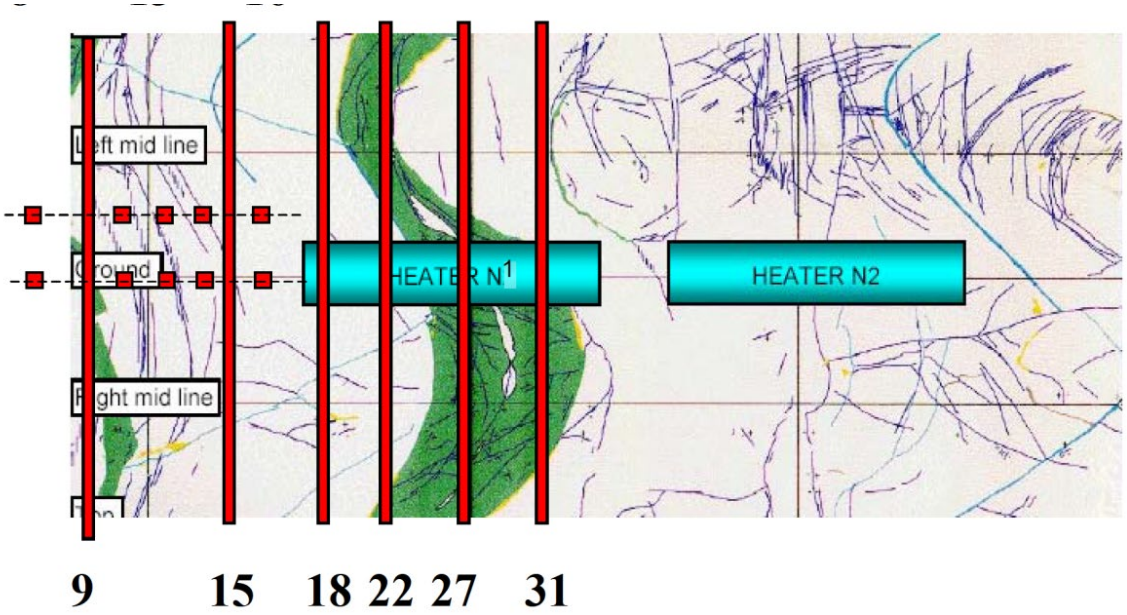

Fig. D-10: Layout of the sampling sections for water content and dry density measurement during the dismantling of Heater #1 in 2002 (Daucousse & Lloret 2003)

After about 5 years of heating and hydration, the bentonite near the heater remains fairly dry, with water contents close to the initial value, whereas bentonite near the granite become fully saturated and has a water content ranging from 25 % to 35 % (Fig. D-11). The TH model with a constant porosity apparently fails to match the measured data at 5.3 years; the model underestimates the water content data near the granite and overestimates the data in the middle of bentonite barrier. If the porosity is constant, the water content of a fully saturated sample is 25 %, the higher measured water content near granite clearly indicates the swelling of bentonite upon hydration from the granite. The THMC model that accounts for the swelling of bentonite and subsequent porosity and permeability changes clearly outperforms the TH model and matches the data at 5.3 years reasonably well. As the heating and hydration continues in the bentonite barrier surrounding Heater #2, water content values near the heater keep increasing and reach about 18 – 19 % at 18.3 years upon the dismantling of Heater #2. Water content values near the granite (about 0.2 m from the bentonite/granite interface) at 18.3 years remained similar to that at 5.3 years because the bentonite had become fully saturated already early on and no more swelling is allowed in the confined gallery. Water content data at 18.3 years are nicely matched by the THMC model across the entire length of the bentonite barrier, but significantly overestimated by the TH model from a radial distance of 0.45 to 0.8 m and underestimated by the TH model from a radial distance of 0.8 m to the bentonite/granite interface.

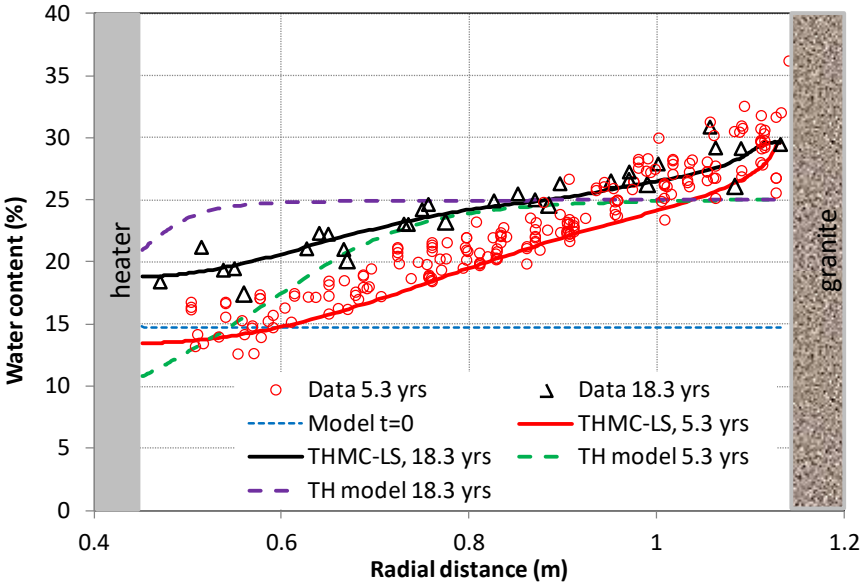

Fig. D-11: Measured water content data at Sections 19, 28 and 29 (Zheng et al. 2011) and Sections 22 and 27 (Daucousse & Lloret 2003) after dismantling Heater #1 ("data 5.3 yrs") and at Section 49 after dismantling Heater #2 ("data 18.3 yrs") and model results from the TH model (Zheng et al. 2015b), THMC model with linear swelling (THMC-LS)

The swelling of bentonite due to hydration is clearly manifested by the measured dry density data. Initially, the FEBEX bentonite blocks have a dry density of 1.7 g/cm^3. Considering the gaps between the bentonite blocks, the average dry density of the bentonite barrier shortly after the test start is estimated around 1.65 g/cm^3. After 5.3 and 18.3 years, the dry density ranges from 1.4 – 1.6 g/cm^3 near the granite, which indicates the swelling of bentonite. For bentonite near the heater, dry density is around 1.65-1.75 (Fig. D-12), indicating compression from the outer rings of the barrier. Model results show that the dry density at 5.3 years is higher than that at 18.3 years whereas measured data do not show any clear difference between 5.3 years and 18.3 years. As bentonite continues hydration from granite and water content keeps increasing from 5.3 years to 18.3 years, it is more conceivable that dry density decreases with time. One reason that measured dry densities at 5.3 and 18.3 years do not show clear difference might be measurement procedure. Dry density cannot be measured under *in-situ* conditions in which the bentonite blocks were compressed by a confining stress of about 7-8 MPa. When samples were taken out of the gallery, they essentially underwent an unloading process which altered the volume of samples, i.e. the dry density measured in the laboratory does not necessary represent the *in-situ* conditions anymore. The THMC model seems to match the dry density profile after 18.3 years pretty well (Fig. D-12).

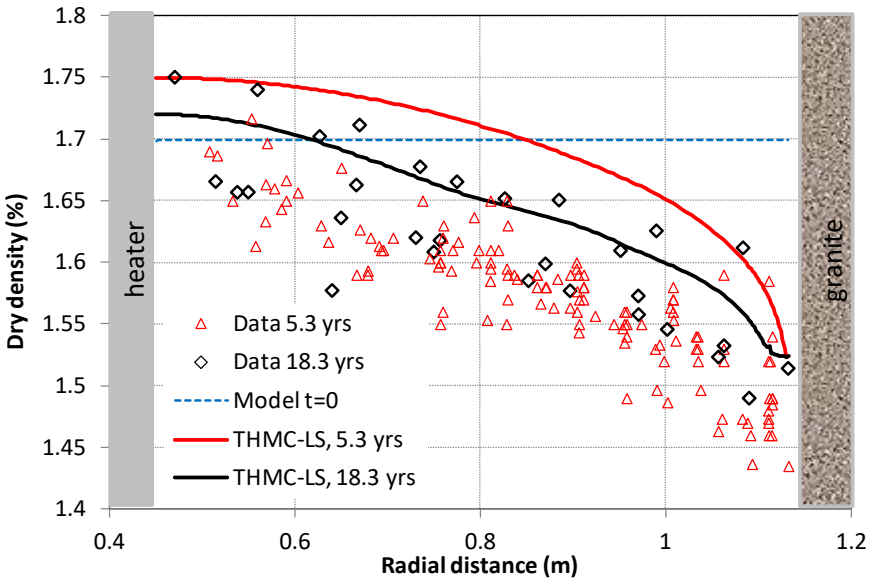

Fig. D-12: Measured dry density data at Sections 22 and 27 (Daucousse & Lloret 2003) after dismantling Heater #1 ("data 5.3 yrs") and at Section 49 after dismantling Heater #2 ("data 18.3 yrs") and model results from THMC model with linear swelling (THMC-LS)

Assuming the solid phase in bentonite is not compressible, porosity can be calculated from dry density with a grain density of 2.78 g/cm^3; these are called ‘inferred porosity data" in Fig. D-13. Model results show an increase of porosity due to the swelling as a consequence of the continuous hydration of the bentonite and match the ‘inferred porosity data" at 18.3 years well (Fig. D-13). Similar to dry density data, porosity data do not show any difference between 5.3 years and 18.3 years. In Fig. D-12 and Fig. D-13, the TH model with a constant porosity of 0.41, apparently, cannot fit the measured dry density and porosity and is therefore not shown here.

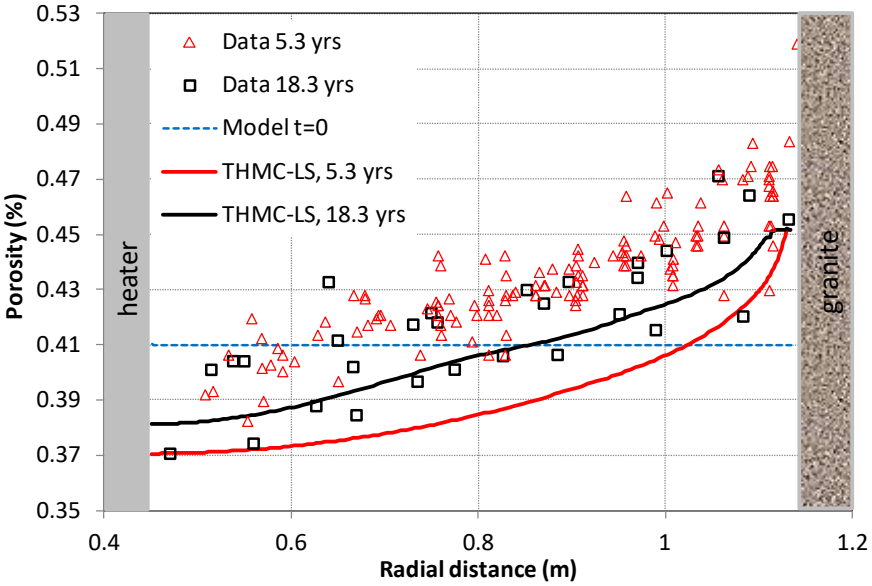

Fig. D-13: Inferred porosity data at Sections 22 and 27 (Daucousse & Lloret 2003) after dismantling Heater #1 ("data 5.3 yrs") and at Section 49 after dismantling Heater #2 ("data 18.3 yrs") and model results from THMC model with linear swelling (THMC-LS).

Unlike water content and dry density, relative humidity data were measured real time by sensors at various positions in the bentonite. These data were grouped by the radial distance of the sensors. Previous modelling exercises (e.g. Zheng et al. 2011) showed that relative humidity near the heater have been overestimated and were the key data to test the models. Unfortunately, most sensors for relative humidity failed for the sections around Heater #2, especially near the heater. For example, as shown in Fig. D-14, sensors at Section E2 (WCSE2-03, WCSE2-04) at a radial distance of ~ 0.52 m only provide data until 147 days. We therefore have to rely on the relative humidity data measured at Section E1 (located around Heater #1) to constrain our model. A fairly good match between model results and relative humidity was achieved. The TH model overestimates the measured relative humidity after about 1000 days and seems to not provide a correct trend of the relative humidity evolution. A better fit between the model and data was obtained by the THMC model. In the THMC model, the permeability decrease due to swelling is responsible for the lower calculated relative humidity near the heater. Another important parameter that controls the relative humidity is the vapour diffusion coefficient. In the base-case THMC model, the vapour diffusion coefficient is 1.03×10^{-4} m^2/s, which is about 5 – 10 fold larger than a typically measured value (e.g. LaManna & Kandlikar 2011). In a sensitivity run based on the THMC-LS model, a vapour diffusion of 2×10^{-5} m^2/s is used and the model results significantly overestimate the data. It is not uncommon to use higher-than-normal vapour diffusion coefficients to interpret moisture movement in an unsaturated medium under non-isothermal conditions, a phenomenon that is called enhanced vapour diffusion (Clifford & Webb 1996).

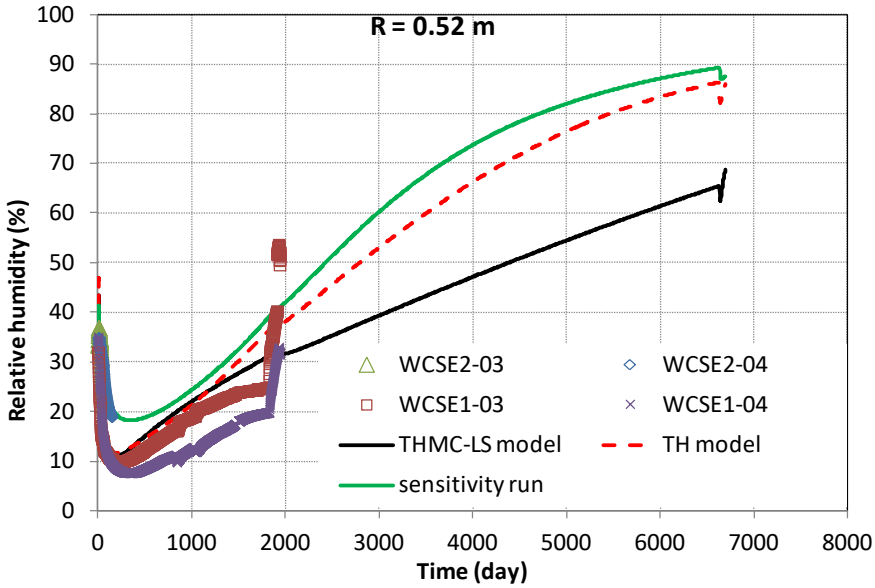

Fig. D-14: Measured relative humidity by sensors located at a radial distance of 0.52 m in Sections E2 and E1 and model results from the TH model (Zheng et al. 2015b), THMC model with linear swelling (THMC-LS) and a sensitivity run that is based on THMC-LS but has a vapour diffusion coefficient that is 5 times lower

Measured relative humidity values in the middle of the bentonite barrier (radial distance of 0.8 m, Fig. D-15) and at the outer rings of the bentonite barrier (Fig. D-16 and Fig. D-17) were adequately matched by both the TH and THMC-LS models. One interesting observation is that the THMC model, albeit having decreased permeability due to swelling at the outer ring area, shows a rapid increase in relative humidity near the granite boundary, which actually match the measured data better than the TH model.

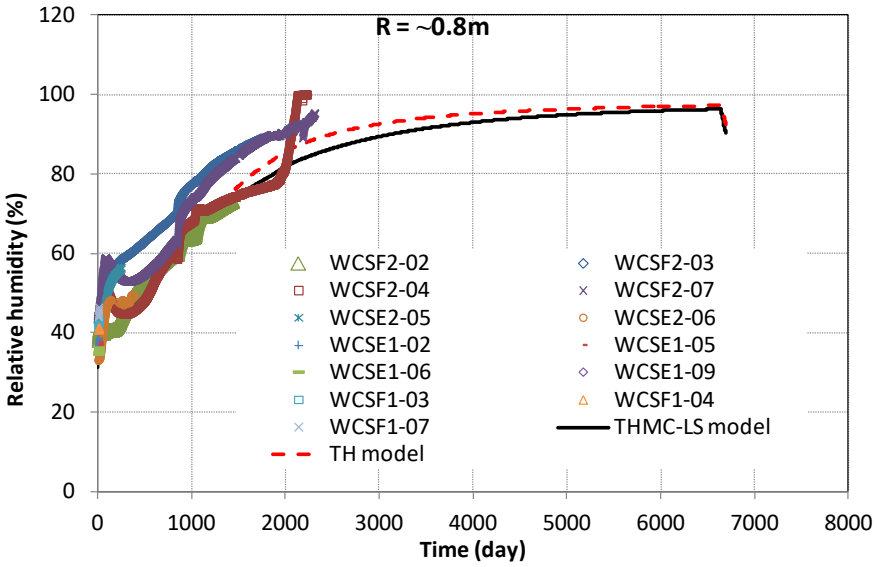

Fig. D-15: Measured relative humidity by sensors located at a radial distance of ~ 0.8 m in Sections E1, E2, F1 and F2 and model results from the TH model (Zheng et al. 2015b) and THMC model with linear swelling (THMC-LS)

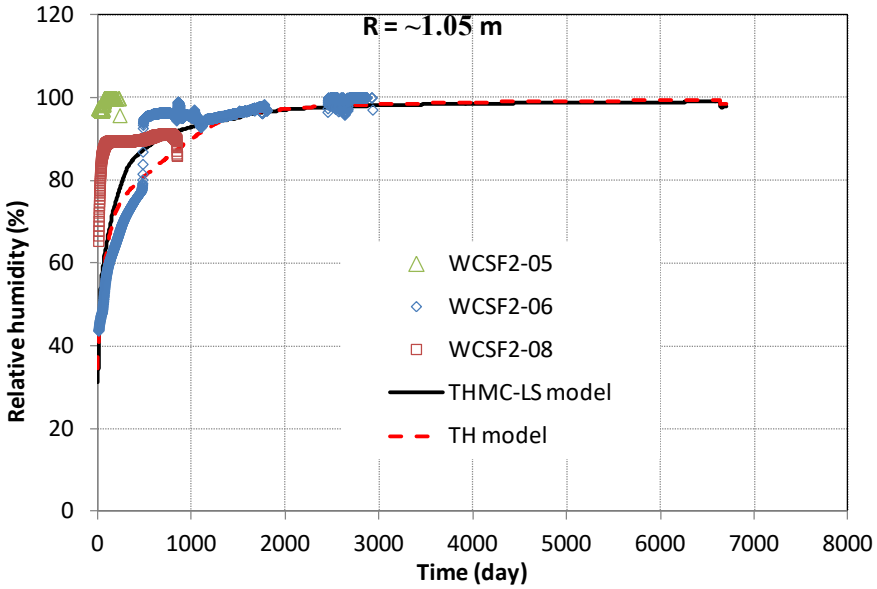

Fig. D-16: Measured relative humidity by sensors located at radial distance of ~ 1.05 m in section F2 and model results from the TH model (Zheng et al. 2015b) and THMC model with linear swelling (THMC-LS)

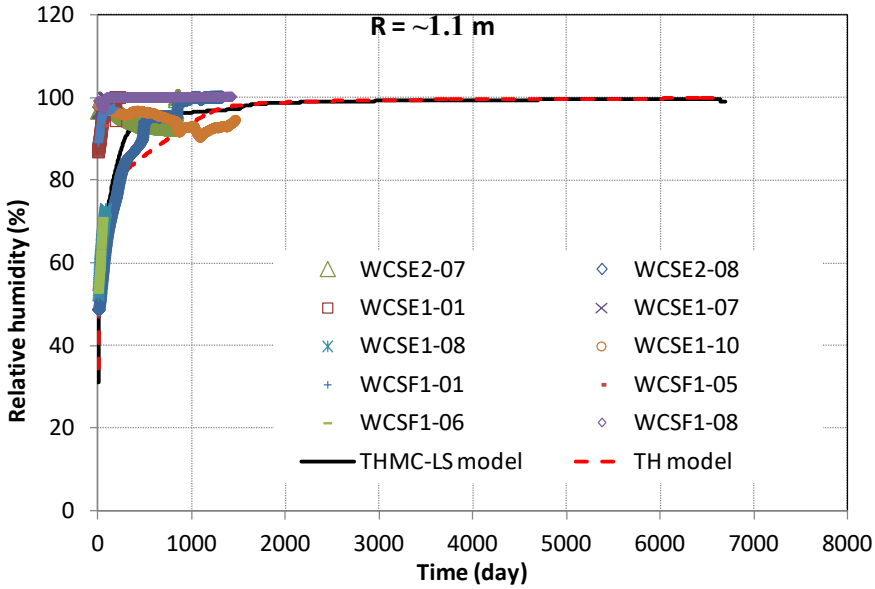

Fig. D-17: Measured relative humidity by sensors located at radial distance of ~ 1.1 m in Sections E1, E2 and F1 and model results from the TH model (Zheng et al. 2015b) and THMC model with linear swelling (THMC-LS)

Sensors for measuring stress were also emplaced in the bentonite block. Although a majority of them stopped functioning, we still were able to extract data at two radial distances: one at 0.5 m, very near the heater and the other at 1.1 m, right at the bentonite/granite interface. No data were available for bentonite in the middle of the barrier. Fig. D-18 and Fig. D-19 show the measured stress and model results. The total stresses in bentonite gradually increase as more water infiltrates into the bentonite. The swelling of bentonite creates a compressive force in the confined gallery, which eventually reaches a plateau as the bentonite barrier is close to being fully saturated, as shown clearly by the data and model result at a radial distance of 1.1 m and to a lesser degree by the data at a radial distance of 0.5 m. It is expected that after the entire bentonite barrier becomes fully saturated, the stress field is fairly homogenous. The THMC model matches the data near the granite reasonably well (Fig. D-19), but overestimates the data near the heater (Fig. D-18). However, it is noteworthy that the stress at a radial distance of 0.5 m might have similar uncertainties as seen in the measured stress at a radial distance of 1.1 m (see Fig. D-19).

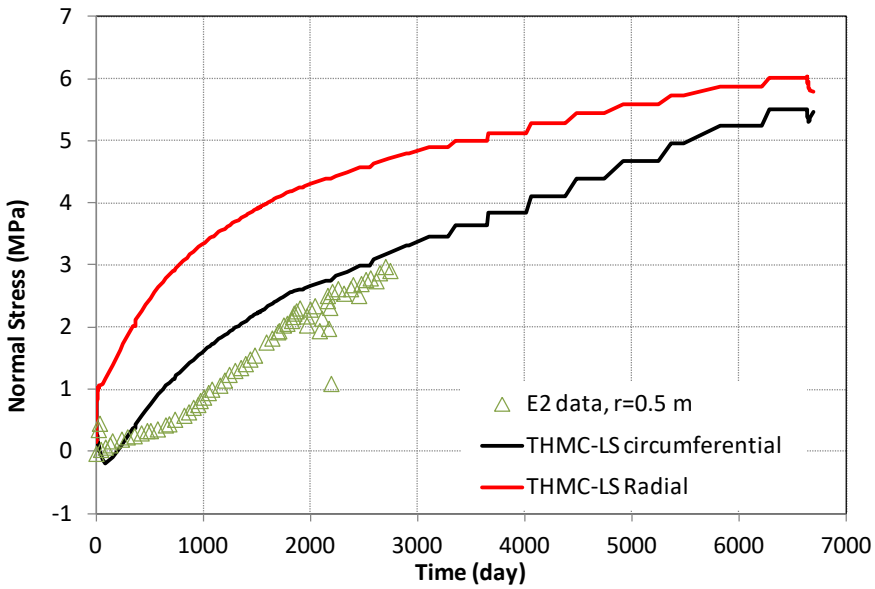

Fig. D-18: Measured stress by sensors located at a radial distance of ~ 0.5 m in Section E2 and THMC model with linear swelling (THMC-LS)

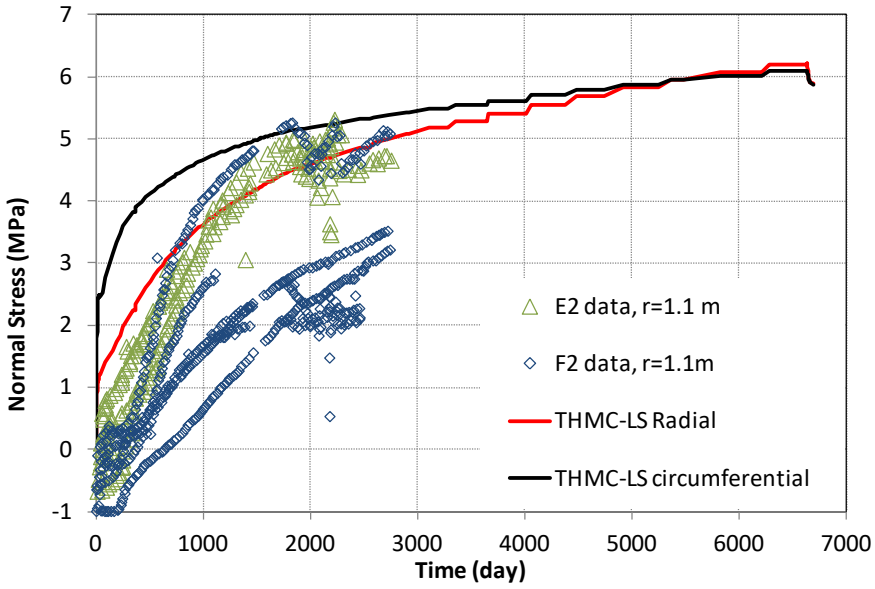

Fig. D-19: Measured stress by sensors located at radial distance of ~ 1.1 m in Sections E2 and F2 and THMC model with linear swelling (THMC-LS)

D.3.1.2 Chemical data and model results

The two dismantling events in the FEBEX in-situ test provide a unique opportunity to check both the spatial and temporal evolution of the geochemistry in bentonite.

After dismantling Heater #1 in 2002, samples were taken along several radii in each section (Zheng et al. 2011). Bentonite samples were taken for THC analyses from three sections surrounding Heater #1: 19, 28, and 29 (see Fig. D-9 for their locations). Each sampling section consists of an outer, central and inner layer of bentonite blocks. Bentonite blocks were preserved immediately after their extraction in plastic films, with two layers of aluminized PET sheets and vacuum-sealed plastic bags. Protection against mechanical damage was used to ensure the integrity of the material (ENRESA 2006). Aqueous extract tests (AET) were used to obtain pore water chemistry for the compacted FEBEX bentonite. AET is a method to quantify the total content of soluble salts of a clay sample. A 1:R AET consists of adding a mass of distilled water equal to R times Ms with Ms the mass of a powdered clay sample. The clay sample and water are stirred during a period of time, usually 2 days, during which water and clay are allowed to equilibrate. Chemical analyses are performed on the supernatant solution after phase separation by centrifugation (Sacchi et al. 2001). In addition to dilution, chemical reactions take place during pore water extraction, which changes the concentrations of dissolved species in a complex nonlinear manner. This makes it difficult to derive the chemical composition of the original pore water from the aqueous extract data (Bradbury & Baeyens 1998, Sacchi et al. 2001). Therefore, geochemical modelling based on mineralogical data is required to derive the dissolved concentrations for the reactive species (Fernández & Rivas 2005, Zheng et al. 2008). Aqueous extract tests and the concentration of exchangeable cations are available for Sections 19, 28 and 29 (Fernández & Rivas 2003). Aqueous extract data from Sections 29 and 19 were interpreted by inverse geochemical modelling (Zheng et al. 2008) and used to test the model predictions (Zheng et al. 2011).

After dismantling Heater #2 in 2015, a similar procedure was taken to measure the pore water composition and mineralogical composition. Because these data will not be available until the end of 2016, we still use the chemical data obtained after the dismantling of Heater #1 to evaluate our THMC models in this report.

Chloride, as a conservative species, is only controlled by the transport processes, i.e. advection and dispersion, which is subsequently dictated by the THM model rather than chemical reactions. In Zheng et al. (2015b), when the THC model failed to match the profile of chloride concentration measured at 5.3 years, it was postulated that adding mechanical processes and the resulting porosity and permeability changes would diminish such a mismatch. Therefore, great effort was dedicated to develop coupled THMC and THM models; they seem to be sufficiently calibrated as shown in the previous sections. However, as shown in Fig. D-20, the THMC model is still unable to match chloride data—it overestimates the concentrations near the granite and underestimates concentrations near the heater. The decrease in permeability at the outer rings of the bentonite barrier in the THMC model leads to less water infiltration and thus less dilution, which is why the THMC model has higher chloride concentration near the granite than the THC model. Less water infiltration also means less evaporation near the heater, which explains why the THMC model has lower chloride concentration near the heater than the THC model. As shown later in the report, finding the right permeability-porosity relationship or considering thermal osmosis might allow the THMC model to match both the THM and chemical data.

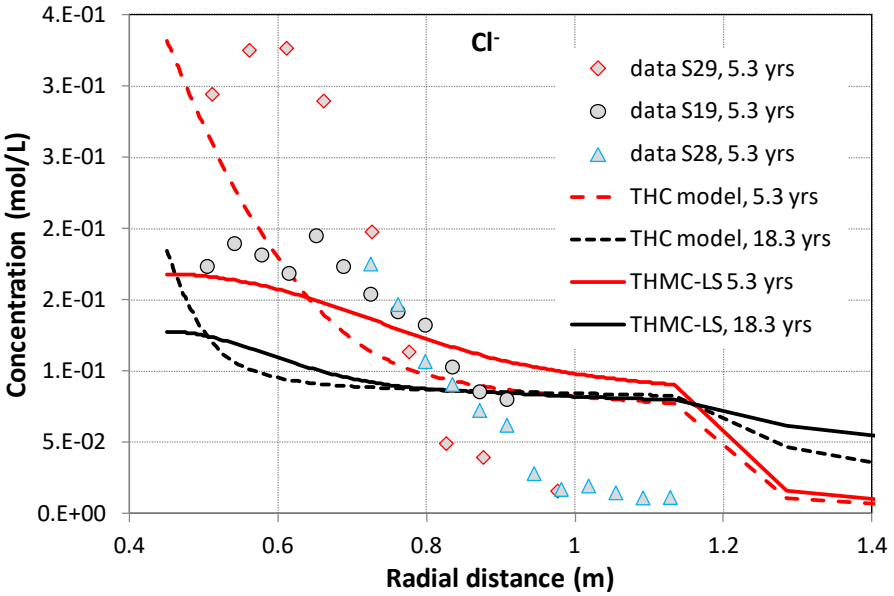

Fig. D-20: The concentration profile of chloride at 5.3 years (Zheng et al. 2011) and model results from the THC model (Zheng at al. 2015b) and THMC model with linear swelling (THMC-LS)

The concentration profiles of major cations are shown in Figures B-21 to B-23. As revealed in Zheng et al. (2015b), the spatial concentration profile of major cations, albeit subject to chemical reactions including cation exchange and minerals dissolution/precipitation, is largely controlled by transport processes and follow the trend of chloride. Chemical reactions alter concentration levels but not the overall trend of the concentration profiles. Similarly, just as the THMC model overestimates the concentration of chloride near the bentonite/granite interface, it also overestimates the concentrations of sodium, calcium, magnesium, and potassium. In addition to the transport processes, sodium concentration could also be affected by cation exchange and dissolution of smectite. However, because the sodium concentration is much higher than other cations and the concentration perturbation of other cations is fairly small, the sodium concentration is not impacted noticeably by cation exchange; the amount of smectite dissolved (Zheng et al. 2015b) is also too small to meaningfully alter the sodium concentration. The THMC model predicts that the concentration of sodium keeps going down until 18.3 years.

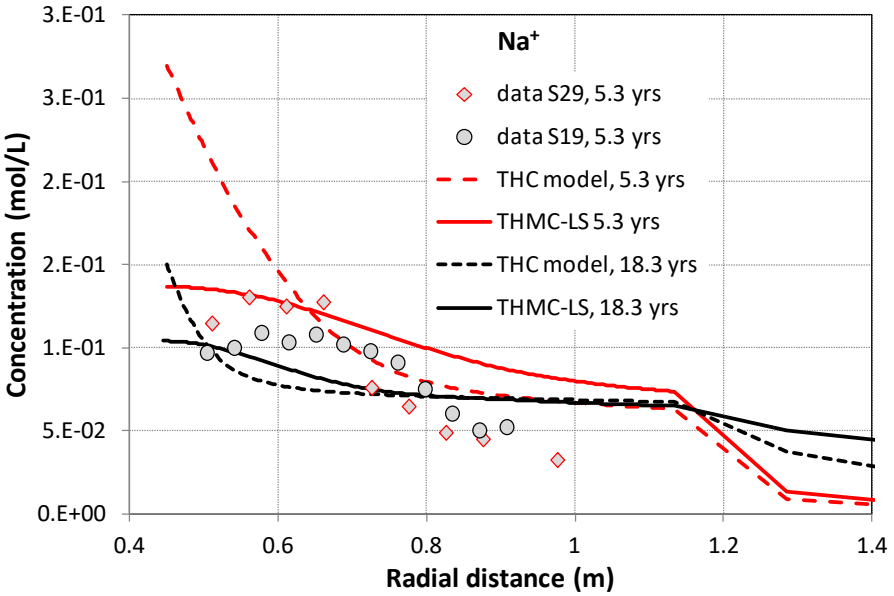

Fig. D-21: The concentration profile of sodium at 5.3 years (Zheng et al., 2011) and model results from the THC model (Zheng at al. 2015b) and THMC model with linear swelling (THMC-LS)

The THMC model, just like the THC model, overestimates the measured calcium concentration across the entire bentonite barrier (Fig. D-22). In addition to the transport processes, the precipitation of dolomite and the dissolution of calcite also affect the concentration level of calcium. Eventually the model needs to delicately balance the pH, bicarbonate, calcium concentration, calcite dissolution, and dolomite precipitation to capture the concentrations of all of them.

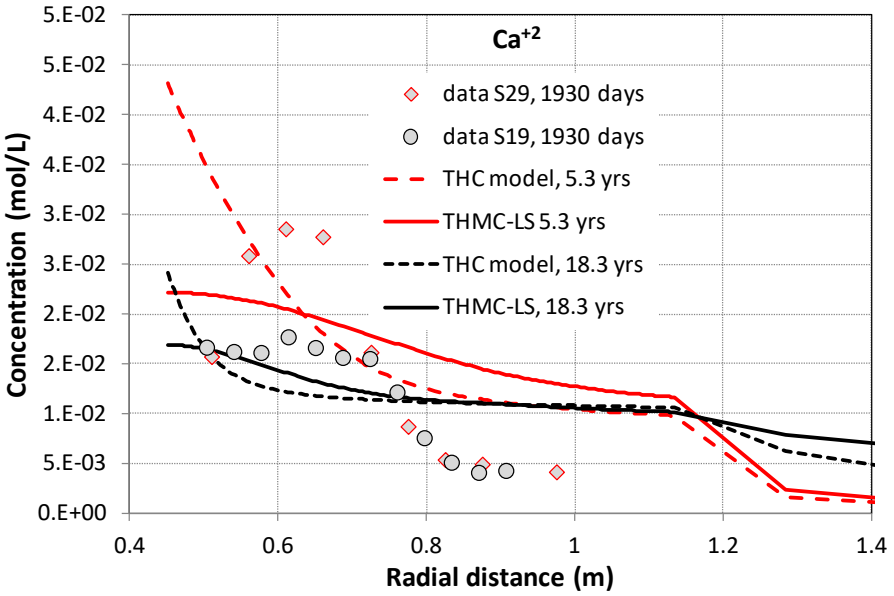

Fig. D-22: The concentration profile of calcium at 5.3 years (Zheng et al. 2011) and model results from the THC model (Zheng at al. 2015b) and THMC model with linear swelling (THMC-LS)

Zheng et al. (2015b) showed that magnesium is involved in the dissolution/precipitation of smectite, the precipitation of dolomite, and cation exchange, but eventually these reactions seem to cancel each other out, and magnesium concentration is largely controlled by the transport processes just like chloride. The discrepancy between the THMC model and magnesium concentration data is similar to other cations (Fig. D-23).

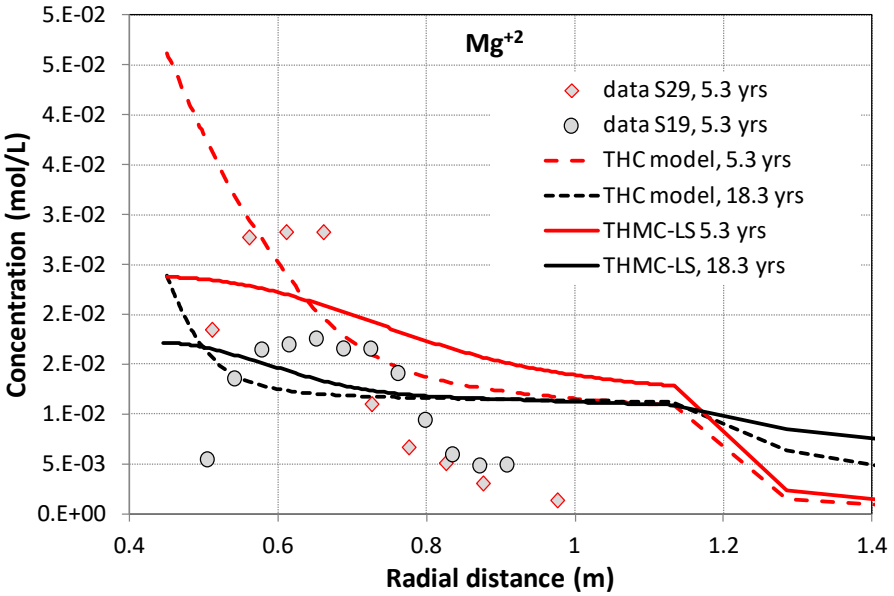

Fig. D-23: The concentration profile of magnesium at 5.3 years (Zheng et al. 2011) and model results from the THC model (Zheng at al. 2015b) and THMC model with linear swelling (THMC-LS)

The computed concentration of potassium from the THC model (Zheng et al. 2015b) that includes chemical reactions is actually lower than that from a sensitivity run that did not consider any chemical reactions. This suggests that some reactions consume potassium in the pore water, such as the precipitation of illite. Although the THMC model overestimates the potassium concentration slightly near the granite, it seems to match the potassium concentration near the heater quite well.

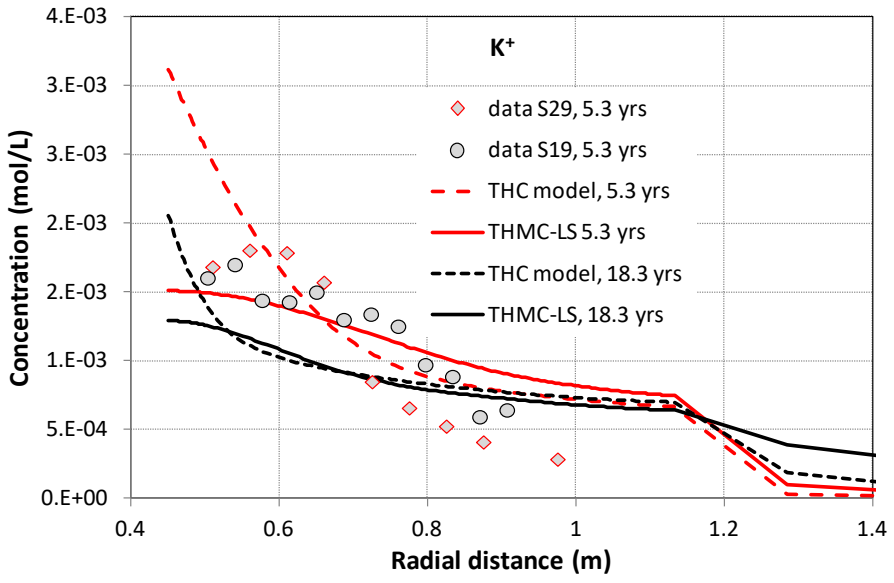

Fig. D-24: The concentration profile of potassium at 5.3 years (Zheng et al. 2011) and model results from the THC model (Zheng at al. 2015b) and THMC model with linear swelling (THMC-LS)

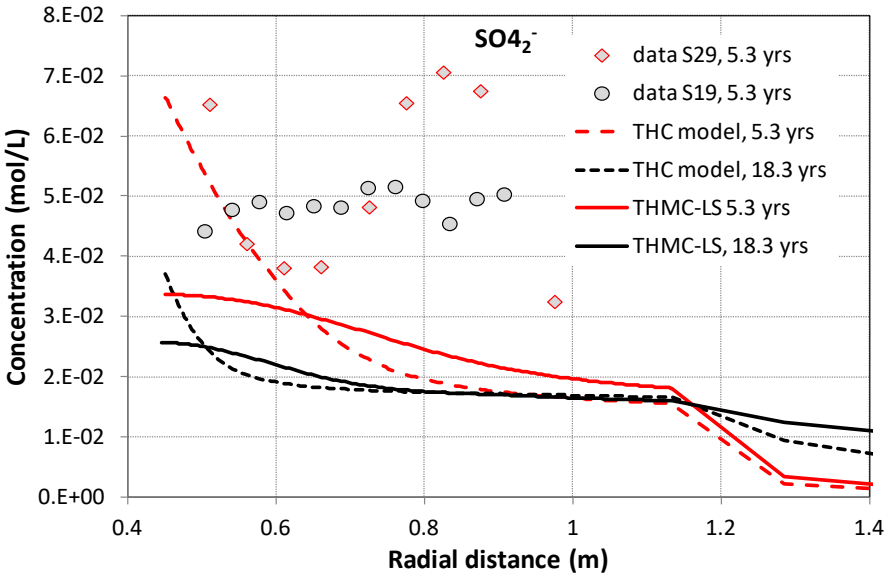

Fig. D-25: The concentration profile of sulphate at 1930 days (Zheng et al. 2011) and model results from the base model

FEBEX bentonite contains a small amount of gypsum (ENRESA 2000). But the amount is very small and gypsum is very soluble, so a small change in water saturation may make gypsum disappear, which makes it debatable whether there is any gypsum initially in the bentonite. The presence of gypsum had been one of the major uncertainties when the pore water compositions were inferred from aqueous extract data under in-situ conditions (Zheng & Samper 2008). Fig. D-25 shows the derived data and model results. Unlike cations, the data for sulphate do not follow the trend of chloride, which indicated strong interference by chemical reactions. In the current model, no gypsum is present in the bentonite. Both the THC and THMC model results underestimate the data. Refinement of the current chemical model is, therefore, needed in the future.

pH is usually very difficult to predict because it involves many reactions. For FEBEX bentonite, pH is mainly regulated by carbonate reactions involving calcite and dolomite and surface protonation reactions. Zheng et al. (2011) showed that surface protonation has strong pH buffering capacity and the model in this report confirms that observation. However, both the THC and THMC models still underestimate the measured pH slightly by 0.1-0.2 unit, which may be attributed to the uncertainties in the initial amount of calcite. Fig. D-27 shows the concentration profile of bicarbonate. Previous modelling (e.g. Samper et al. 2008a,b) showed that the bicarbonate concentration is very sensitive to the alteration of calcite and dolomite and is coupled with pH changes. The current model does not consider the dissolution/exsolution of CO2 gas, which may be a key reaction to explain the underestimation of pH and bicarbonate by the model. Also, as mentioned above, geochemical modelling was needed to obtain the chemical composition of pore water in bentonite under in-situ conditions based on the measured concentrations by aqueous extract (Zheng et al. 2008). However, during the aqueous extract, there was CO2 exsolution that changed the inventory of total carbonate, which was difficult to capture accurately in the geochemical model used to derive the concentration under the in-situ conditions (Zheng et al. 2008). This is another source of uncertainty regarding the pH and concentration of bicarbonate.

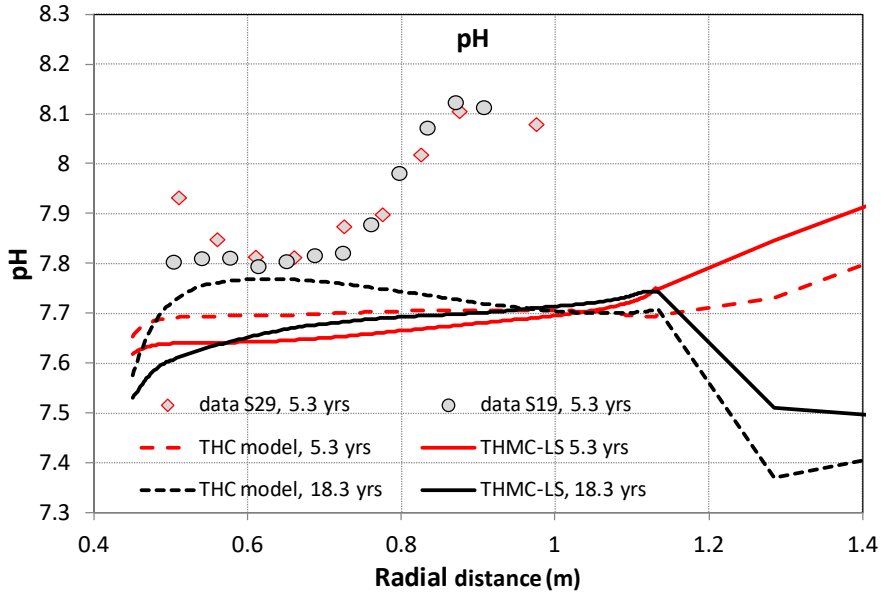

Fig. D-26: The profile of pH at 1930 days (Zheng et al. 2011) and model results from the base model

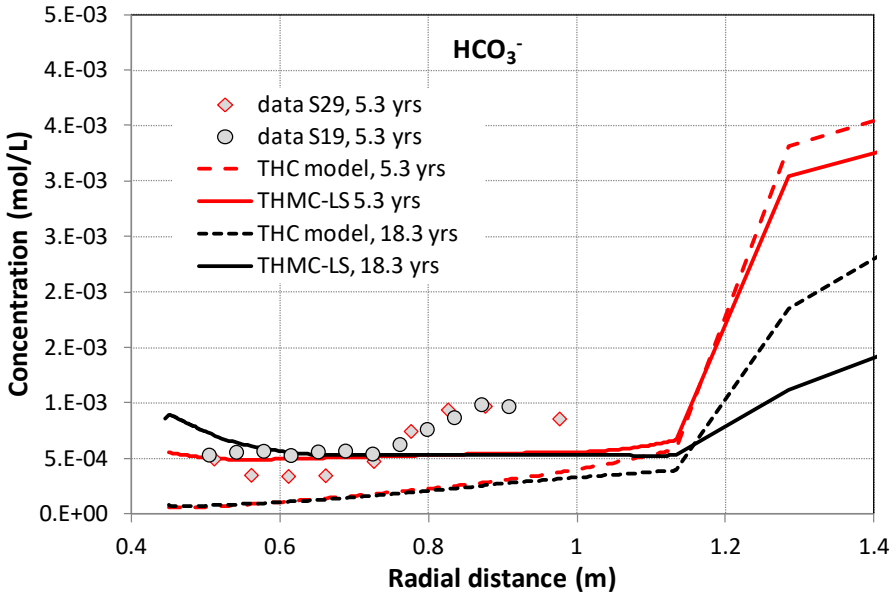

Fig. D-27: The concentration profile of bicarbonate at 1930 days (Zheng et al. 2011) and model results from the base model

Regarding the evolution of concentration of major cations in pore water, after 18.3 years (Fig. D-20 to Fig. D-27) the THMC model predicts lower concentrations across the entire bentonite barrier whereas the THC model predict lower concentration near the heater than that after 5.3 years, but concentrations near granite similar to the level of 5.3 years. Sulphate concentration will be further diluted as more water comes to saturate bentonite (Fig. D-25), but pH and bicarbonate at 18.3 years stay roughly the same as at 5.3 years (Fig. D-26, Fig. D-27).

D.3.2 THMC model using BExM

Conceptually BExM divides the bentonite into a dual structure (Fig. D-28). Such a similar structural concept has been used by other modelers such as Bradbury & Baeyens (2003), Samper & Zheng (2008b) and Zheng & Samper (2015). Swelling takes place predominantly in the microstructure: water molecules enter into the interlayer space and cause an expansion of clay aggregates; water flow, on the other hand, occurs mainly through the macrostructure. The expansion of the microstructure compresses the space of macropore and therefore leads to a reduction in permeability. Such a reduction in permeability would be one of the major reasons that THMC can explain the water content data, which cannot be achieved by TH model. Fig. D-29 shows the measured water content at 5.3 years (dismantling of Heater #1) and 18.3 years (dismantling of Heater #2) and model results by the THMC model using linear swelling (THMC-LS) and BExM (THMC-BExM). Both models have similar water content results and match the measured water content at 5.3 years nicely. However, at 18.3 years, they deviate —THMC-BExM underestimates the water content data whereas the THMC-LS results match the water content data sufficiently well. A close examination of the calculated spatial distribution of permeability (Fig. D-30) and porosity (Fig. D-31) at 5.3 years shows that THMC-BExM has lower permeability than THMC-LS but higher porosity than THMC-LS, which is why THMC-BExM and THMC-LS have similar water content results. At 18.3 years, THMC-BExM has similar total porosity to THMC-LS, but lower permeability than THMC-LS, which explains why THMC-BExM computes lower water content than THMC-LS. Permeability and porosity changes will be further discussed in the next section.

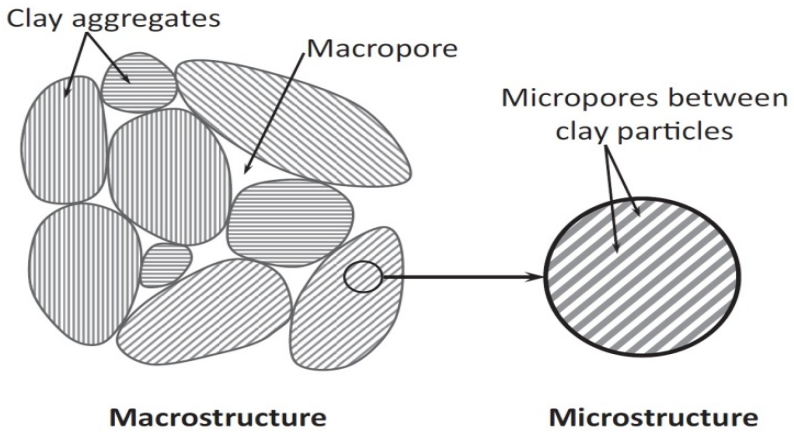

Fig. D-28: Schematic representation of the two structural levels considered in the dual structure BExM (Vilarrasa et al. 2015).

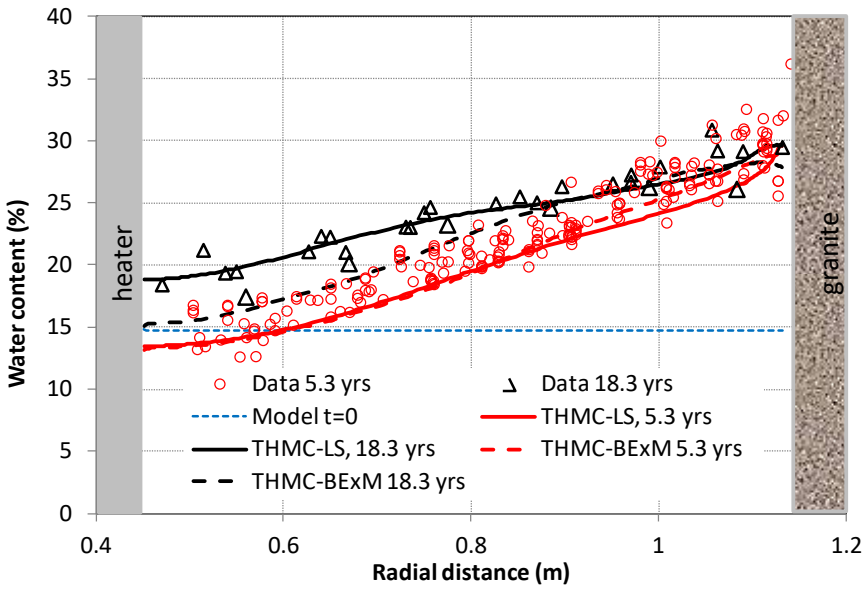

Fig. D-29: Measured water content at 5.3 years (dismantling of Heater #1) and 18.3 years (dismantling of Heater #2) and model results by the THMC model using linear swelling (THMC-LS) and BExM (THMC-BExM)

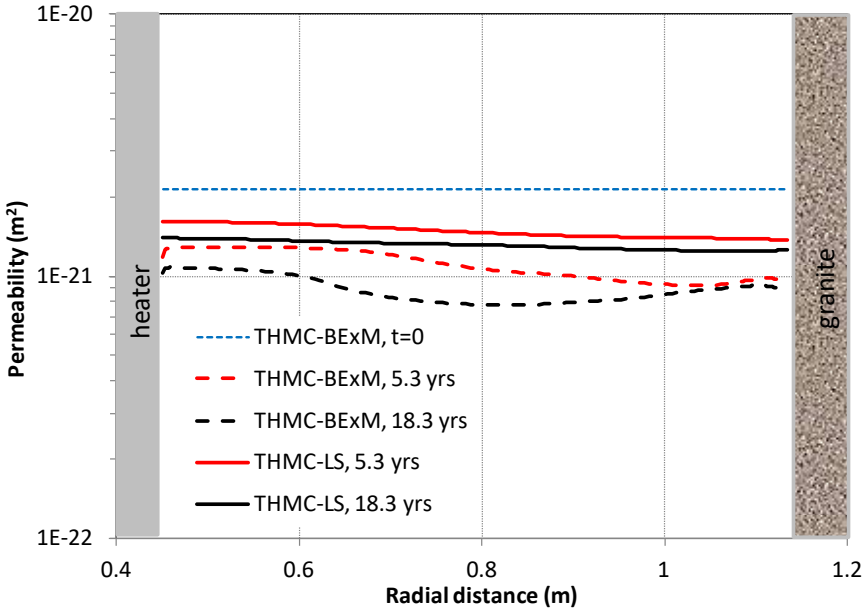

Fig. D-30: Spatial distribution of intrinsic permeability at time zero, 5.3 years (dismantling of Heater #1) and 18.3 years (dismantling of Heater #2) calculated by the THMC model using linear swelling (THMC-LS) and BExM (THMC-BExM)

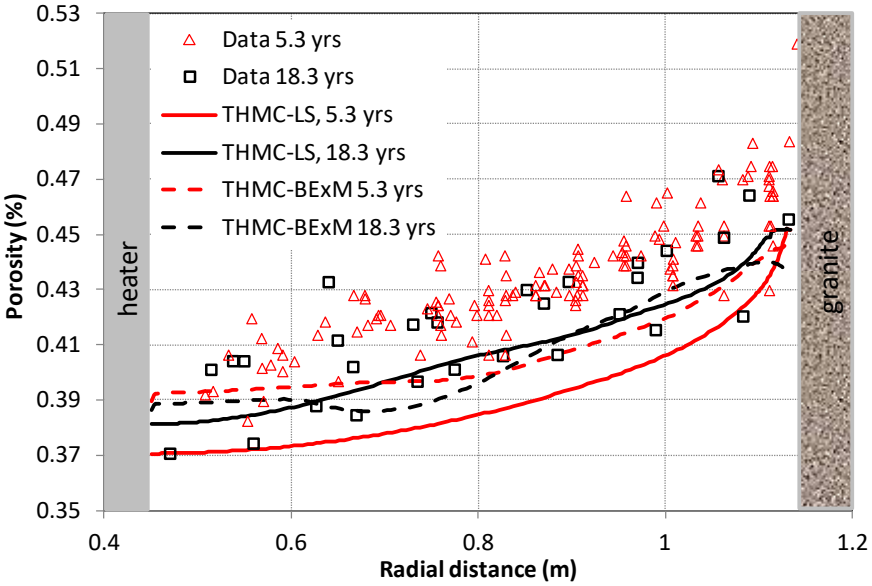

Fig. D-31: Measured porosity at 5.3 years (dismantling of Heater #1) and 18.3 years (dismantling of Heater #2) and calculated porosity by the THMC model using linear swelling (THMC-LS) and BExM (THMC-BExM)

Fig. D-32 shows the dry density data and model results. First, we observe that the data is very scattered, which makes the interpretation difficult. A better measurement procedure might be needed. Second, although the THMC-LS model shows a decrease of dry density from 5.3 years to 18.3 years, observation data show no clear difference between 5.3 years and 18.3 years and neither do the model results by THMC-BExM. In BExM, as suction keeps decreasing upon the hydration of bentonite, the microstructure experiences swelling, but the macrostructure, depending on the local stress state at a given time, could be compressed or expanded, which is why in THMC-BExM, dry densities at 18.3 years are not always lower than that at 5.3 years. On the contrary, THMC-LS uses a linear swelling model, i.e. swelling strain is merely a function of water saturation. As a result, increase in water saturation from 5.3 years to 18.3 years leads to more swelling and subsequently higher porosity and lower dry density. Simply from the goodness-of-fit the measured data dry density, it seems that THMC-BExM outperforms THMC-LS and more likely reflects the reality.

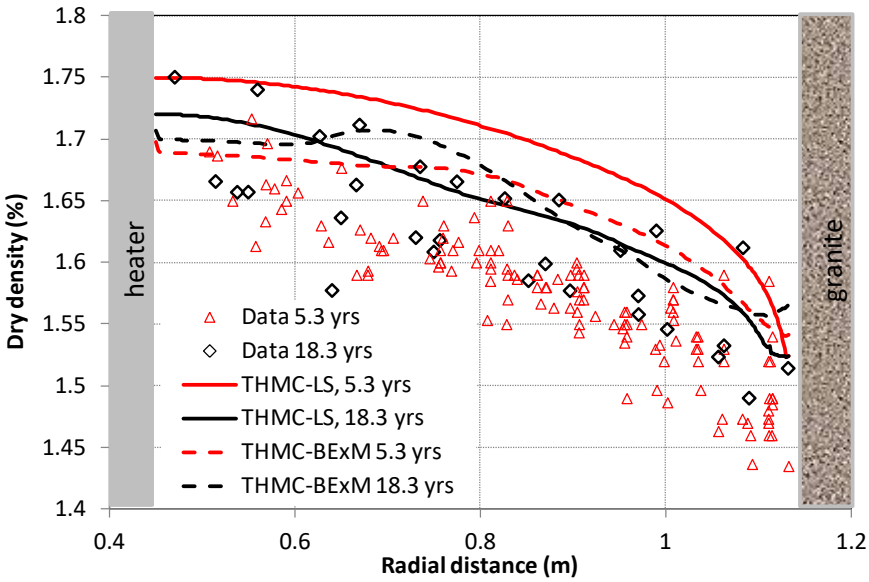

Fig. D-32: Measured dry density at 5.3 years (dismantling Heater #1) and 18.3 years (dismantling Heater #2) and model results by the THMC model using linear swelling (THMC-LS) and BExM (THMC-BExM)

There was a cooling-down period of about 70 days between the time that Heater #2 was switched off and bentonite samples were taken section by section due to operational reasons. During this time period, temperature in the bentonite decreased to about 30 °C (Fig. D-33). This cooling-off period, albeit seemingly very short compared with more than 18 years of operation of the test, has a significant impact on the spatial distribution of water content, as shown in Fig. D-34. Both THMC-LS and THMC-BExM show remarkable re-distribution of water content from 18.2 years to 18.3 years, which is featured by an increase in water content near the heater (roughly with a radial distance < 0.6 m) and a decrease in water content in the middle of bentonite barrier (radial distance from 0.6 to 0.9 m), indicating a moisture movement from the middle of the bentonite barrier towards the heater. Such a phenomenon might be caused by the decreased vapour diffusion upon the disappearance of thermal gradient, or the loss of thermal osmosis.

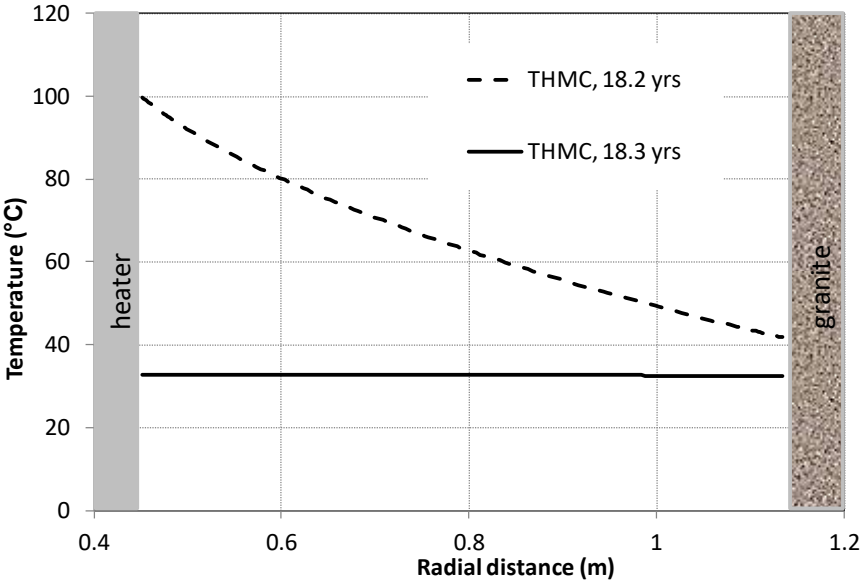

Fig. D-33: Calculated temperature at the time of Heater #2 switch-off (18.2 years) and the time of dismantling (18.3 years)

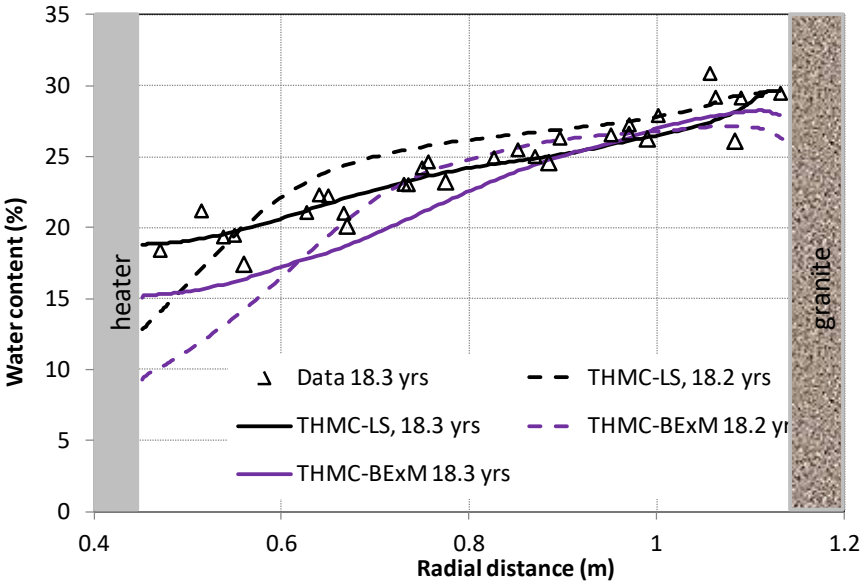

Fig. D-34: Measured water content at 18.3 years (dismantling Heater #2) and model results by the THMC model using linear swelling (THMC-LS) and BExM (THMC-BExM) at the time of Heater #2 switch-off (18.2 years) and at the time of dismantling (18.3 years)

Figures B-35 to B-38 depict the measured relative humidity and values computed with THMC-LS and THMC-BExM at four radial distances. THMC-BExM match the relative humidity data near the heater nicely (Fig. D-35) and outperforms the THMC-LS model, but underestimates the data in the middle of the bentonite barrier slightly (Fig. D-36) and underperforms THMC-LS slightly for the data in the middle of bentonite barrier. THMC-LS and THMC-BExM have similar calculated relative humidity values at the outer rings of the bentonite barrier and both of them match well with measured data.

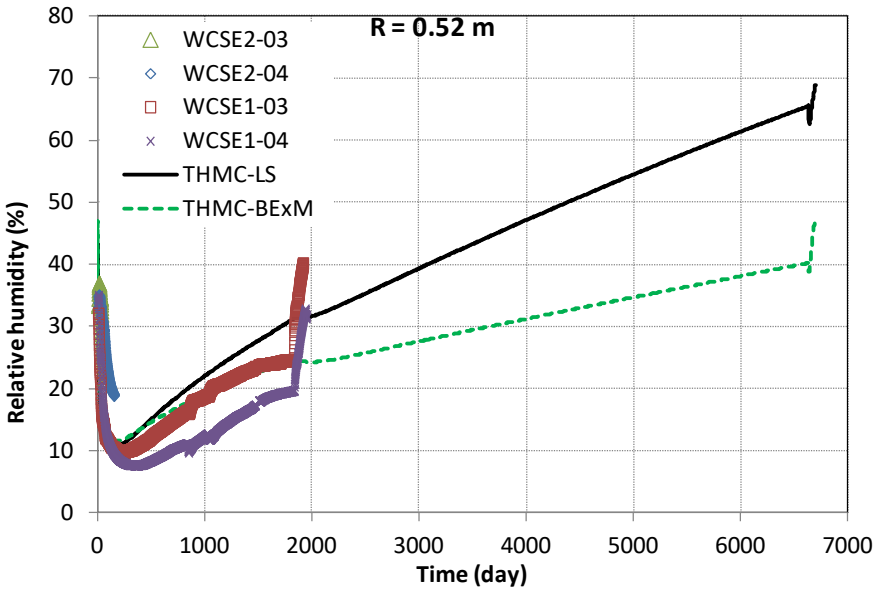

Fig. D-35: Measured relative humidity by sensors located at a radial distance of 0.52 m in Sections E2 and E1 and model results from THMC model using linear swelling (THMC-LS) and BExM (THMC-BExM)

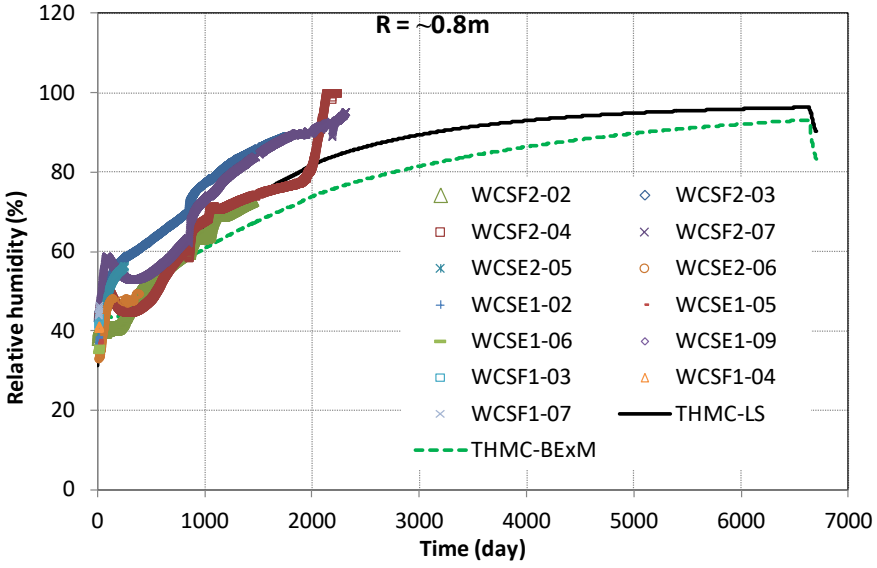

Fig. D-36: Measured relative humidity by sensors located at a radial distance of ~ 0.8 m in Sections E1, E2, F1 and F2 and model results from THMC model using linear swelling (THMC-LS) and BExM (THMC-BExM)

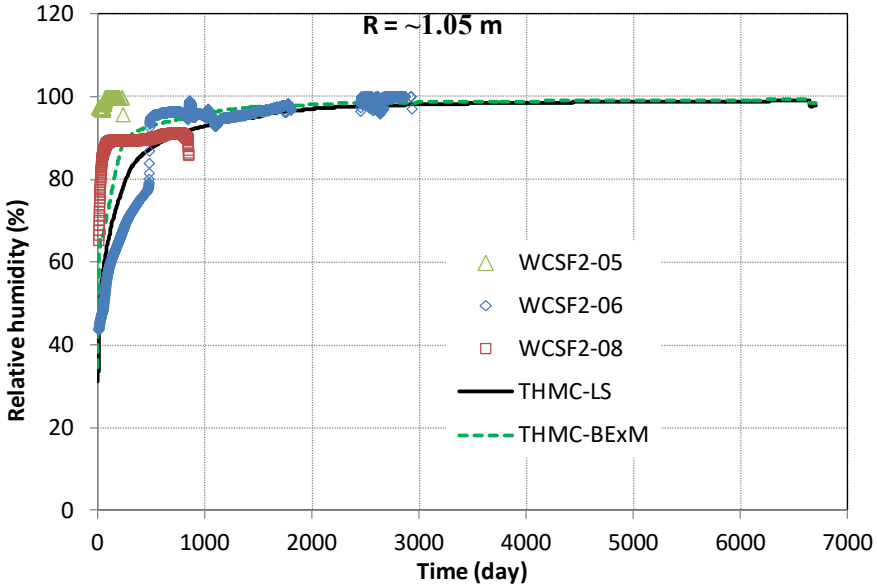

Fig. D-37: Measured relative humidity by sensors located at a radial distance of ~ 1.05 m in section F2 and model results from THMC model using linear swelling (THMC-LS) and BExM (THMC-BExM)

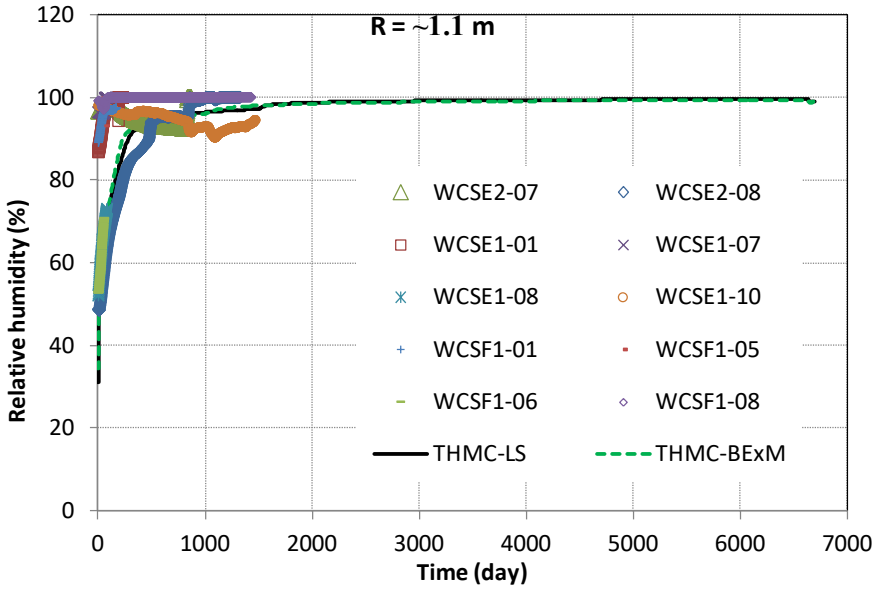

Fig. D-38: Measured relative humidity by sensors located at a radial distance of ~ 1.1 m in Sections E1, E2 and F1 and model results from THMC model using linear swelling (THMC-LS) and BExM (THMC-BExM)

Fig. D-39 and Fig. D-40 show the measured stress and model results by both THMC-LS and THMC-BExM. The expansion of bentonite gradually drives the stress to higher levels, but a rise in stress gradually slows down as the bentonite becomes fully saturated. BExM models that describe the swelling of bentonite more mechanistically, match the stress increase in the beginning better than the linear swelling model that is known to be unable to describe the transient state of swelling.

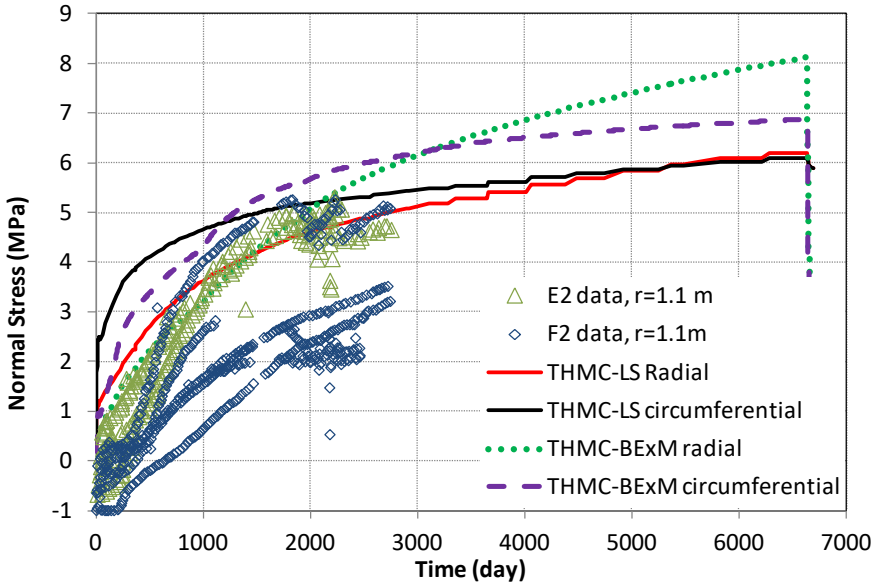

Fig. D-39: Measured stress by sensors located at radial distance of ~ 1.1 m in Sections E2 and F2 and THMC model with linear swelling (THMC-LS)

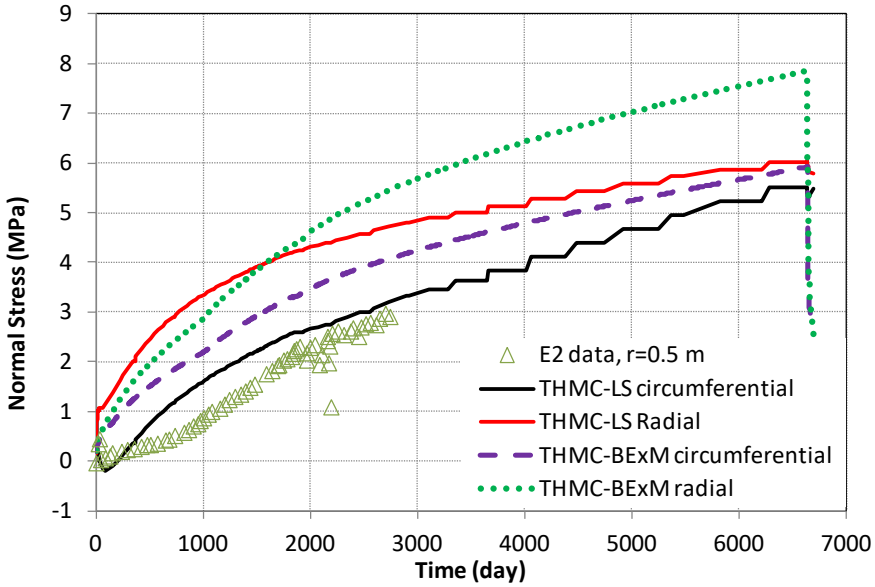

Fig. D-40: Measured stress by sensors located at a radial distance of ~ 0.5 m in Section E2 and THMC model with linear swelling (THMC-LS)

In general, THMC-LS and THMC-BExM yield rather similar results in terms of water content, dry density, relative humidity and stress, despite the difference in calculated permeability and porosity. Considering uncertainties in the measured water content, dry density, relative humidity and stress data, both models seem to be sufficiently calibrated by the THM data; the THMC-BExM may be slightly better. However, as shown in Fig. D-41, THMC-BExM is facing the same problem as THMC-LS: overestimation of the chloride concentration near the granite and underestimation of its concentration near the heater. In fact, THMC-BExM is even worse than THMC-LS with its flatter spatial concentration profile. The fact that current THMC models, either using linear swelling or more complex BExM, reasonably match THM data but fail to explain the chemical data, indicate that the current THMC model is flawed—either some critical coupling relationships were not correctly calibrated or some important processes are missing. This will be further discussed in the next section.

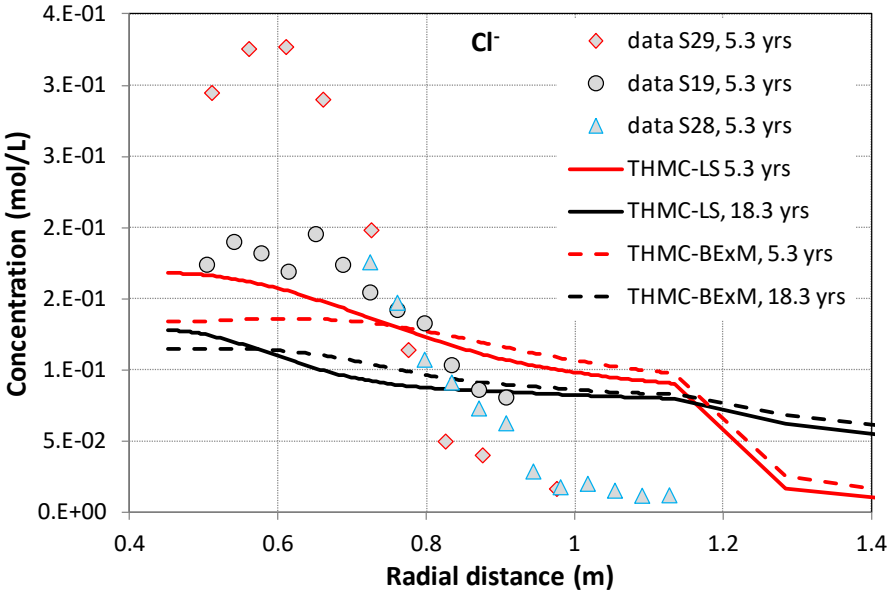

Fig. D-41: The concentration profile of chloride at 5.3 years (Zheng et al. 2011) and model results from the THMC model with linear swelling (THMC-LS) and BExM (THMC-BExM)

D.3.3 Effect of permeability change on chloride concentration

As discussed in Sections D.3.1 and D.3.2, the THMC models using either linear swelling (THMC-LS) or BExM (THMC-BExM) sufficiently match the THM data, but fail to match the concentration profile of chloride at 5.3 years. Chloride is a conservative species; its spatial distribution is controlled exclusively by advection and diffusion. In the THMC-LS and THMC-BExM model shown in Sections D.3.1 and D.3.2, the effective diffusion coefficient is 2E-9 m^2/s. In order to test if the match between the THMC model and chloride data can be improved by adjusting the diffusion coefficient, we conducted a sensitivity run in which the effective diffusion coefficient is reduced to 2E-10 m^2/s. As shown in Fig. D-42, the model with a lower diffusion coefficient significantly overestimates the concentration near the heater although it matches better the concentration near the bentonite/granite interface. More important, neither model is able to match the shape of concentration front (concentration profile from radial distance 0.7 m to 0.9 m). The sensitivity analysis shows that discrepancies between THMC model and chloride data cannot

be resolved by adjusting diffusion. This, in turn, means that advection is not properly calculated in the THMC models. Because advection is totally dependent on the water movement in the bentonite, in this section we re-visit the permeability change in the THMC model to see if we can solve the dilemma that THMC models match the THM data but not the chemical data.

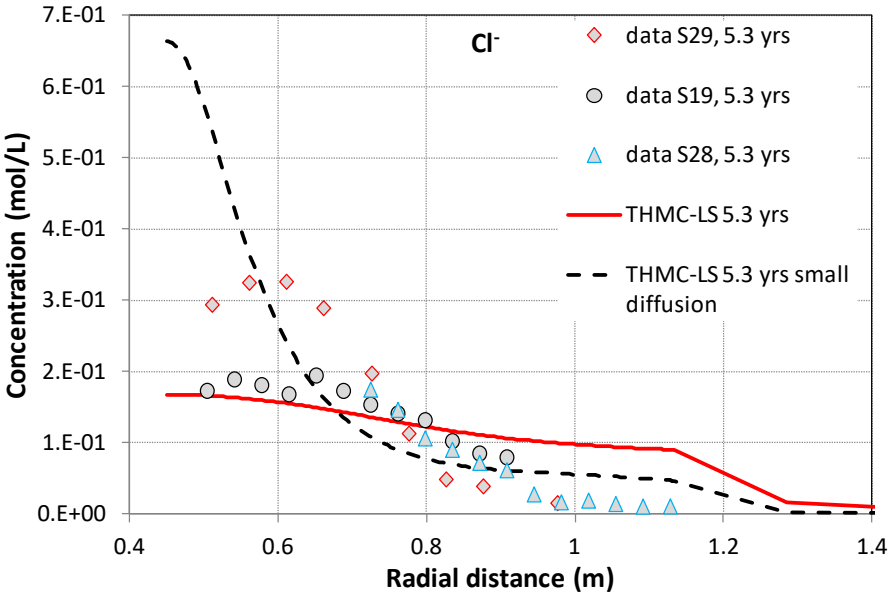

Fig. D-42: The concentration profile of chloride at 5.3 years (Zheng et al. 2011) and model results from the THMC model with linear swelling (THMC-LS) and a sensitivity run in which the effective diffusion coefficient is 2E-10 m^2/s

For water flow in an unsaturated medium, flux is related to pressure gradient via an effective permeability, which is the product of intrinsic permeability (k) (or saturated permeability, absolute permeability) and relative permeability (kr). The relative permeability function of kr = Sl3 has been used for FEBEX bentonite (Zheng et al. 2011, Sánchez et al. 2012b, Kuhlman & Gaus 2014), however, there are uncertainties in the relative permeability function (Tab. D-11): different exponent values were obtained in different tests, ranging from 1.1 to 4.46. In two sensitivity runs shown in Fig. D-43, we used two relative permeability functions with exponent equal to 1.1 and 4, respectively. The concentration profile is flatter if the exponent in the relative permeability function is higher (e.g. equal to 4 in Fig. D-43) and steeper if the exponent in the relative permeability function is higher (e.g. equal to 1.1 in Fig. D-43), but adjusting the relative permeability function is not able match the shape of the concentration front.

Tab. D-11: Exponent in relative permeability law obtained from different type of tests (ENRESA 2000)

Test	Value of n, in $k_r = S_l^n$
Water infiltration in small teflon cells	4.64
Water infiltration in bentonite in contact with granite	3.50
Heat and water flow experiment 1	3.06
Heat and water flow experiment 2	1.10
Heat and water flow experiment 3	1.68

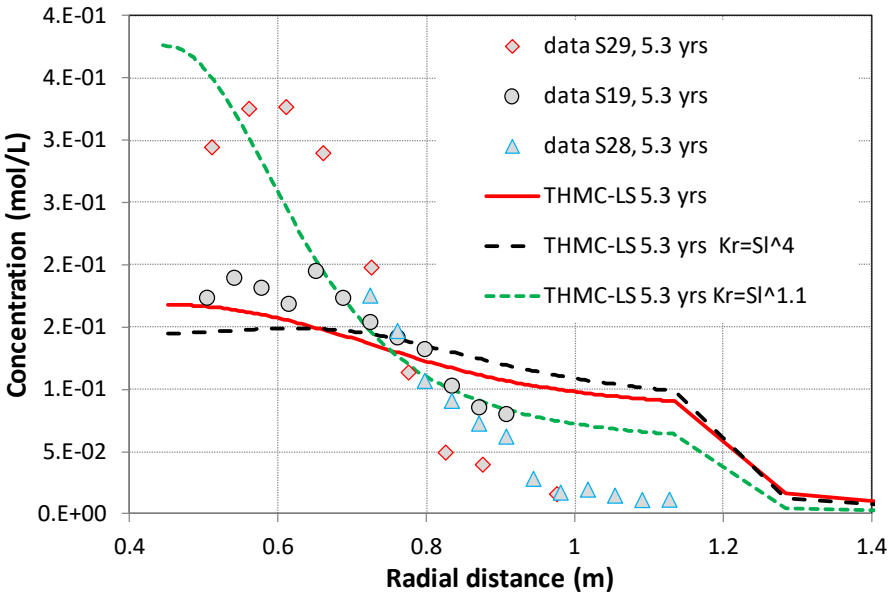

Fig. D-43: The concentration profile of chloride at 5.3 years (Zheng et al. 2011) and model results from the THMC model with linear swelling (THMC-LS) and sensitivity runs in which the exponent in the relative permeability function is 4.4 and 1.1, respectively

After failing to match the concentration profile by adjusting the diffusion coefficient and the relative permeability function, we checked the intrinsic permeability. Intrinsic permeability is usually measured under saturated condition and it is a function of total porosity (Fig. D-44) or dry density (Fig. 3-46) of the FEBEX bentonite. The data from Villar (2002) can be fitted with equation B–8:

$$k = \exp[19(\emptyset - 2.9) \qquad \text{B–8}$$

And the data from ENRESA (2000) can be fitted by Equation B–9:

$$\log k = -2.96\rho_d - 8.57 \qquad \text{B–9}$$

Based on measured dry density after 18.3 years (Fig. D-12), we can calculate the permeabilities across the bentonite barrier at 18.3 years based on Equations B–8 and B–9, which are shown in Fig. D-46. Also shown in Fig. D-46 are the permeabilities from THMC models using linear swelling (THMC-LS) or BExM (THMC-BExM). We can see the THMC models exhibit a different trend than the data — from granite toward the heater, the data show a gradual decrease whereas the models show a gradual increase. Although it is known that permeability values measured in the laboratory are different (typically smaller) than that revealed by large scale model due to a scaling effect, the fact that the model and data exhibit distinct spatial trends in Fig. D-46 clearly reveals that the permeability-porosity relationship used in THMC-BExM or permeability-stress relationship used in THMC-LS needs to be revised to match not only the THM data but also chemical data.

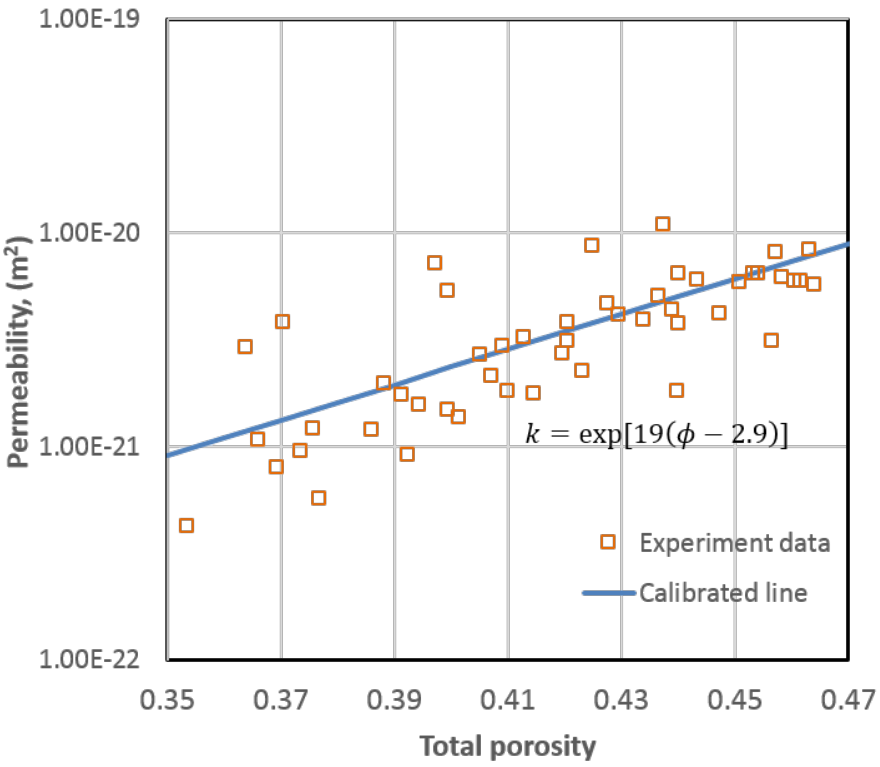

Fig. D-44: Intrinsic permeability as a function of total porosity (Villar 2002)

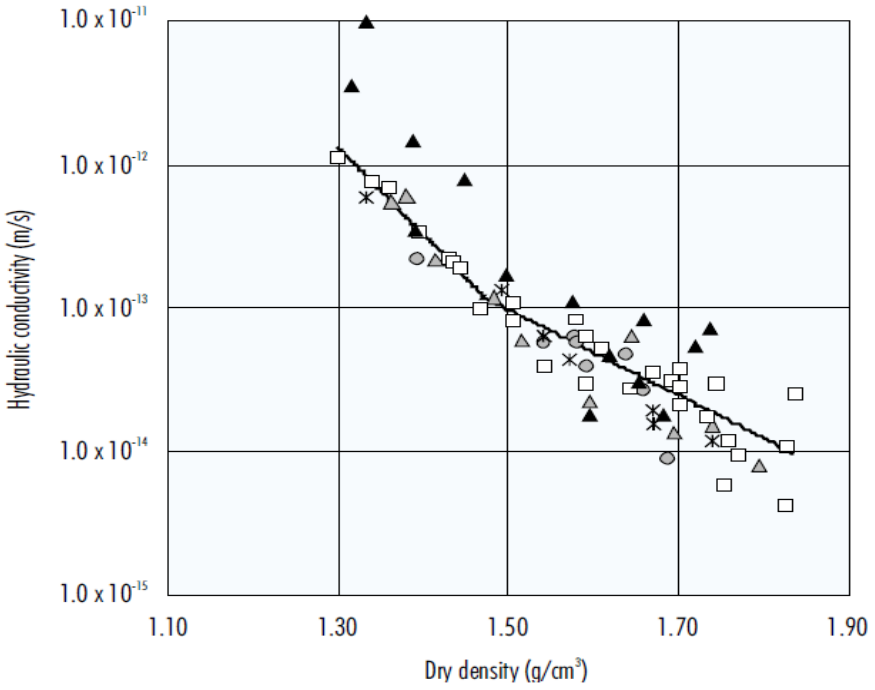

Fig. D-45: Hydraulic conductivity as a function of dry density, which can be fitted with $\log k = -2.96\rho_d - 8.57$ (ENRESA 2000)

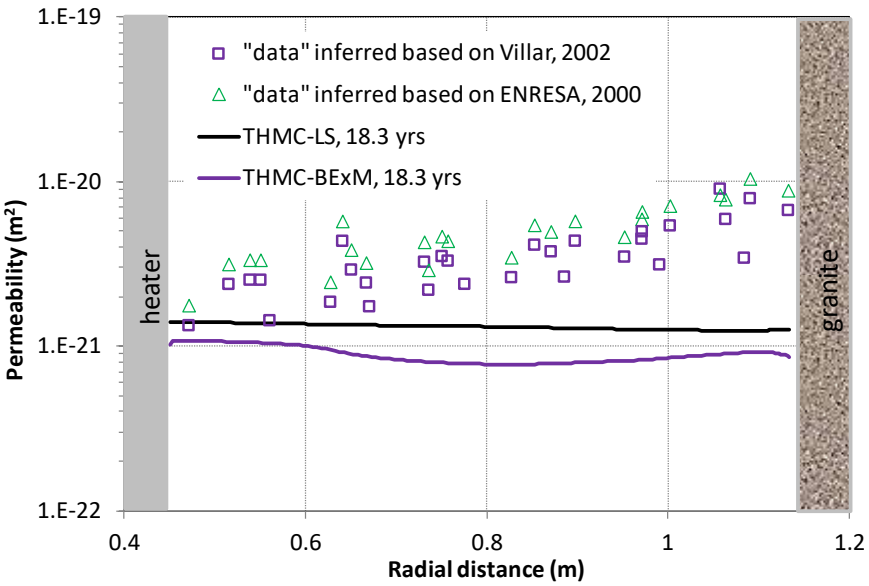

Fig. D-46: Intrinsic permeability calculated from dry density data based on Equation B–8 ("data inferred based on Villar 2002) and based on the Equation B–9 (data inferred based on ENRESA 2000) and the computed permeabilities from THMC-LS and THMC-BExM

We therefore conducted a simulation using Equation B–10 for permeability changes:

$$\log k = (-2.96\rho_d - 8.57)/\alpha \qquad \text{B–10}$$

Equation B–10 is modified from Equation B–9 by adding a factor α of 2.45 to account for the scaling effect (difference in permeability between laboratory measured and field calibrated values). This simulation, named "Model B" in Fig. D-47, is based on the THMC-LS model presented in Section D.3.1. It provides an overall decent match of chloride data at 5.3 years and especially at the concentration front. However, from the middle of the bentonite (radial distance of 0.7) towards the heater, the concentration data plateaus whereas the model results show a monotonic rise. Model B predicts very low concentrations in most parts of the bentonite barrier and very high concentrations close to heater after 18.3 years. Fig. D-48 shows the measured water content and results from "Model B". Although model B matches the measured water content at 5.3 years nicely, it overestimates the data at 18.3 years. In summary, using the revised function for permeability change as has been done in "Model B" leads to a better fit the chloride concentration data but a worse fit to the water content data. An additional process is probably needed for the model to match both THM and chemical data.

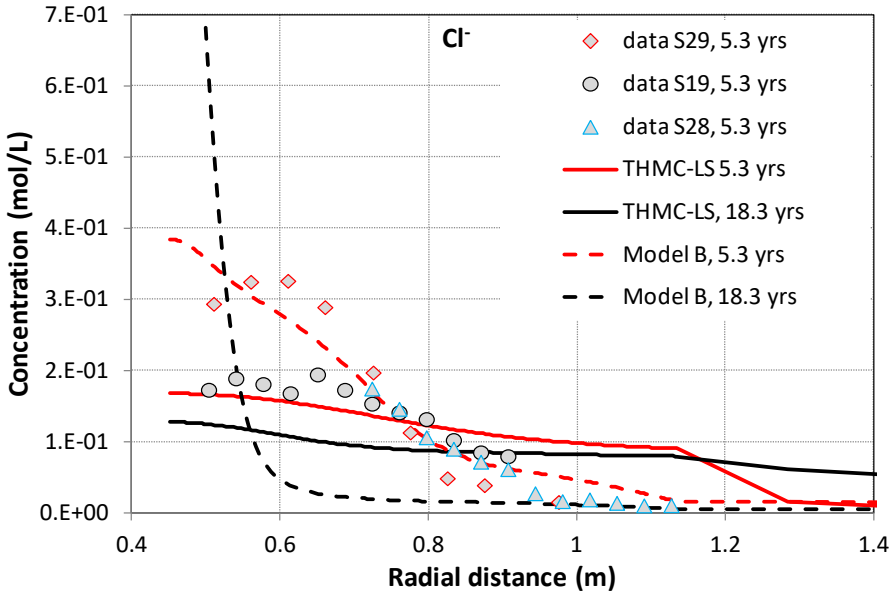

Fig. D-47: The concentration profile of chloride at 5.3 years (Zheng et al., 2011) and model results from the THMC model with linear swelling (THMC-LS) and sensitivity runs (model B) using the Equation B–10 for permeability change

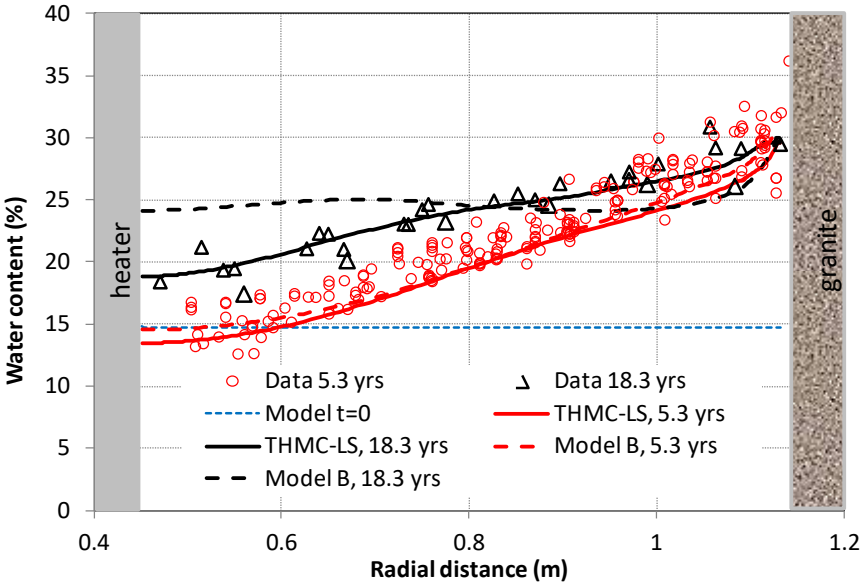

Fig. D-48: Measured water content at 5.3 years (dismantling Heater #1) and 18.3 years (dismantling Heater #2) and model results by the THMC model using linear swelling (THMC-LS) and Model B which is based on THMC-LS but using a different function for permeability change

D.4 Summary

The FEBEX *in-situ* test that lasted more than 18 years is extremely valuable for validating the coupled THMC model and deepening our understanding of the bentonite barrier's evolution over the course of heating and hydration. In the FEBEX-DP project, Heater #2 was dismantled and extensive THMC characterization was conducted. LBNL/DOE joined the FEBEX-DP in 2015. The ultimate goal is to use THMC data from FEBEX-DP to validate THMC models and therefore enhance our understanding of coupled THMC processes in bentonite.

In Zheng et al. (2015b), TH model with non-Darcian flow and the THC model were developed and sensitivity analyses to key parameters were conducted. Model results showed that including non-Darcian flow into the TH model led to a significant underestimation of the relative humidity data in the entire bentonite barrier. In this report, the THC model was extended to THMC models and mechanical processes were simulated using both linear swelling model and dual structure BExM. The results from THMC models match the measured temporal evolution of temperature, relative humidity and stress at several compliance points in the bentonite barrier reasonably well. The measured spatial distribution of water content and dry density at 5.3 years when Heater #1 was dismantled and at 18.3 years when Heater #2 was dismantled, is also well matched. However, the THMC models failed to explain the spatial profile of concentration at 5.3 years. The major findings from current modelling work are as follows:

- As expected, the THMC model outperformed the THC model in terms of matching measured THM data. Permeability and porosity changes due to a mechanical process (swelling) were the key to matching all the THM data.
- The THMC model using a complex double structure BExM (THMC-BExM) did not clearly outperform the THMC model using a linear swelling model (THMC-LS) in terms of matching the measured data. THMC-BExM led to a slightly better fit of measured relative humidity values and stress near the heater and a slightly worse fit to the measured water content and dry density at 18.3 years. Although BExM is a more mechanistic approach and describes structural details of bentonite (the micro- and macrostructure of bentonite), it failed to manifest its superiority to the simple linear swelling model, which is probably due to the fact that THM data including relative humidity, stress, dry density and water content are all macroscopic. Consequently, these data cannot delineate the more mechanistic BExM from a linear swelling model.
- Although the THMC models successfully matched the THM data, they failed to desirably match the measured concentration profile of a conservative species (chloride) at 5.3 years and subsequently the concentration profile of a reactive species. The concentration profiles of cations (calcium, potassium, magnesium and sodium) were largely shaped by transport processes despite the ongoing mineral dissolution/precipitation and cation exchange processes also affecting their concentration levels. The concentration profile of pH, bicarbonate and sulphate were largely determined by chemical reactions.
- Revising the function for permeability changes in the THMC model improved the goodness-of-fit to the chloride concentration profile but deteriorated the fit to water content data. It seemed there was a dilemma that the THMC model cannot match both the THM and chemical data simultaneously, suggesting that additional processes might be needed in the conceptual model.
- The THMC model predicted that concentration levels of major cations and anions at 18.3 years when Heater #2 was dismantled would continue going down in most parts of the bentonite barrier except the area very close to the heater, where the concentration would go

up. This will be compared with concentration data that are expected to be available by the end of 2016.

The following work is planned to finalize the model interpretation of FEBEX in-situ test:

- Thermal osmosis, a moisture movement driven by the thermal gradient, has already been incorporated in the simulator TOUGHREACT-FLAC3D. We will test if the THMC model with thermal osmosis can match both the THM data and the concentration profile of chloride.
- Once the THMC model is calibrated against THM data and measured concentration data at 5.3 years, it will be used to interpret the concentration data for 18.3 years. The chemical model will be finetuned, especially regarding redox condition evolution in the bentonite barrier and bentonite-canister interaction, and evolution of gases such CO_2, CH_4 and H_2.

Ultimately, after the THMC models for FEBEX *in-situ* test are fully validated with data, they will used to explore THMC changes in the long run under higher temperature.

D.5 References to PART D

Alonso, E.E., Vaunat, J. & Gens, A. (1999): Modeling the mechanical behaviour of expansive clays. Engineering Geology 54: 173-183.

Bradbury, M.H. & Baeyens, D. (2005): Modelling the sorption of Mn(II), Co(II), Ni(II), Zn(II), Cd(II), Eu(III), Am(III), Sn(IV), Th(IV), Np(V) and U(VI) on montmorillonite: Linear free energy relationships and estimates of surface binding constants for some selected heavy metals and actinides. Geochimica et Cosmochimica Acta 69(4): 875-892.

Bradbury, M.H. & Baeyens, D. (1998): A physicochemical characterisation and geochemical modelling approach for determining porewater chemistries in argillaceous rocks. Geochimica et Cosmochimica Acta 62, 783–795.

Bradbury, M.H. & Baeyens, D. (2003): Porewater chemistry in compacted resaturated MX-80 bentonite. Journal Contaminant Hydrology 61, 329–338.

Castellanos, E., Villar, M.V., Romero, E., Lloret, A. & Gens, A. (2008): Chemical impact on the hydro-mechanical behaviour of high-density FEBEX bentonite. Physics and Chemistry of the Earth, Parts A/B/C 33, Supplement 1(0): S516-S526.

Chen, Y., Zhou, C. & Jing, L. (2009): Modeling coupled THM processes of geological porous media with multiphase flow: theory and validation against laboratory and field scale experiments. Computers and Geotechnics 36 (8), 1308–1329.

Clifford, K.H. & Webb, S.W. (1996): A Review of Porous Media Enhanced Vapor-Phase Diffusion Mechanisms, Models, and Data – Does Enhanced Vapor-Phase Diffusion Exist? Sandia National Laboratories Albuquerque, NM. SAND96-1198

Cui, Y.J., Tang, A.M., Loiseau, C. & Delage, P. (2008): Determining the unsaturated hydraulic conductivity of a compacted sand-bentonite mixture under constant-volume and free-swell conditions. Physics and Chemistry of the Earth 33, S462-S471

Daucousse, D & Lloret, A. (2003): Results of "in situ" measurements of water content and dry density, Technical report, Polytechnic University of Catalonia, 70-UPC-L-5-012.

David, C., Wong, T.F., Zhu, W. & Zhang, J. (1994): Laboratory measurement of compaction-induced permeability change in porous rocks: Implications for the generation and maintenance of pore pressure excess in the crust. Pure Appl. Geophys. 1994;143:425-456.

Detzner, K. & Kober, F. (2015): FEBEX-DP drilling and sampling report Sections 32-34, Internal report, AN15-714, Nagra.

ENRESA (2000): Full-scale engineered barriers experiment for a deep geological repository in crystalline host rock FEBEX Project, European Commission: 403.

ENRESA (2006): FEBEX: Updated final report. ENRESA Tech. Publ. PT 05-0/2006, 589 pp.

Fernández, A.M., Baeyens, D., Bradbury, M. & Rivas, P. (2004): Analysis of the porewater chemical composition of a Spanish compacted bentonite used in an engineered barrier. Physics and Chemistry of the Earth, Parts A/B/C 29(1): 105-118.

Fernández, A.M. & Rivas, P. (2003): Task 141: post-mortem bentonite analysis. geochemical behaviour. CIEMAT/DIAE/54520/05/03, Internal Note 70-IMA-L-0-107 v0.

Fernández, A.M. & Rivas, P. (2005): Pore water chemistry of saturated FEBEX bentonite compacted at different densities. In: Alonso, E.E., Ledesma, A. (Eds.), Advances in Understanding Engineered Clay Barriers. A.A Balkema Publishers, Leiden, The Netherlands, pp. 505–514.

Fernández, A.M., Cuevas, J. & Rivas, P. (2001): Pore water chemistry of the FEBEX bentonite. Mat. Res. Soc. Symp. Proc. 603, 573-588.

García-Siñeriz, J.L., Abós, H., Martínez, V., De la Rosa, C., Mäder, U. & Kober, F. (2016): FEBEX-DP Dismantling of the Heater #2 at the FEBEX "in situ" test. Nagra Arbeitsbericht NAB 16-11.

Ghabezloo, S., Sulem, J., Guédon, S. & Martineau, F. (2009): Effective stress law for the permeability of a limestone. Int. J. Rock Mech. Min. Sci. 2009;46:297-306.

Itasca, (2009): FLAC3D, Fast Lagrangian Analysis of Continua in 3 Dimensions, Version 4.0, Minneapolis, Minnesota, Itasca Consulting Group.

Kuhlman, U. & Gaus, I. (2014): THM Model validation modelling of selected WP2 experiments.

Kwon, O., Kronenberg, A.K., Gangi, A.F. & Johnson, D. (2001): Permeability of Wilcox shale and its effective pressure law. J. Geophys. Res.-Sol. Ea.;106:19339-53.

LaManna, J. M. & Kandlikar, S.G. (2011): Determination of effective water vapor diffusion coefficient in pemfc gas diffusion layers. International Journal of Hydrogen Energy 36(8): 5021-5029.

Liu, H.H. & Birkholzer, J. (2012): On the relationship between water flux and hydraulic gradient for unsaturated and saturated clay. Journal of Hydrology 475: 242-247.

Liu, H.H., Houseworth, J., Rutqvist, J., Zheng, L., Asahina, D., Li, L., Vilarrasa, V., Chen, F., Nakagawa, S., Finsterle, S., Doughty, C., Kneafsey, T. & Birkholzer, J. (2013): Report on THMC modeling of the near field evolution of a generic clay repository: Model validation and demonstration, Lawrence Berkeley National Laboratory, August, 2013, FCRD-UFD-2013-0000244.

Lloret, A. & Alonso, E.E. (1995): State surfaces for partially saturated soils, In proceedings of the International Conference on Soils Mechanics and Foundation Engineering, Balkema, pp. 557-562.´

Lloret, A., Villar, M.V., Sánchez, M., Gens, A., Pintado, X. & Alonso, E.E. (2003): Mechanical behaviour of heavily compacted bentonite under high suction changes. Géotechnique; 53(1):27–40.

Pruess, K., Oldenburg, C. & Moridis, G. (1999): TOUGH2 User's Guide, Version 2.0, Lawrence Berkeley National Laboratory, Berkeley, CA.

Pusch, R. & Madsen, F.T. (1995): Aspects on the illitization of the kinnekulle bentonites. Clays and Clay Minerals 43(3): 261-270.

Ramírez, S., Cuevas, J., Vigil, R. & Leguey, S. (2002): Hydrothermal alteration of "La Serrata" bentonite (Almeria, Spain) by alkaline solutions. Applied Clay Science 21(5–6): 257-269.

Rutqvist, J. & Tsang, C.F. (2002): Coupled Thermohydromechanical Analysis of FEBEX in Situ test with ROCMAS, Swedish Nuclear Power Inspectorate Research Team Report to DECOVALEX Task 1 Coordinator, PART B-THM modeling of the bentonite. Lawrence Berkeley National Laboratory, Berkeley, CA, USA.

Rutqvist, J., Ijiri, Y. & Yamamoto, H. (2011): Implementation of the Barcelona Basic Model into TOUGH–FLAC for simulations of the geomechanical behavior of unsaturated soils. Computers & Geosciences 37(6): 751-762.

Rutqvist, J., Zheng, L., Chen, F., Liu, H.-H. & Birkholzer, J. (2013): Modeling of Coupled Thermo-Hydro-Mechanical Processes with Links to Geochemistry Associated with Bentonite-Backfilled Repository Tunnels in Clay Formations. Rock Mechanics and Rock Engineering: 1-20.

Sacchi, E., Michelot, J.L., Pitsch, H., Lalieux, P. & Aranyossy, J.F. (2001): Extraction of water and solution from argillaceous rock for geochemical characterisation: methods, processes, and current understanding. Hydrogeology Journal 9, 17–33.

Samper, J., Zheng, L. Montenegro, L., Fernández, A.M. & Rivas, P. (2008a): Coupled thermo-hydro-chemical models of compacted bentonite after FEBEX in situ test. Applied Geochemistry 23(5): 1186-1201.

Sánchez, M., Gens, A. & and Olivella, S. (2012b): THM analysis of a large-scale heating test incorporating material fabric changes. International Journal for Numerical and Analytical Methods in Geomechanics 36(4): 391-421.

Sánchez, M., Gens, A. & Guimarães, L. (2012a): Thermal–hydraulic–mechanical (THM) behaviour of a large-scale in situ heating experiment during cooling and dismantling. Canadian Geotechnical Journal 49(10): 1169-1195.

Sánchez, M., Gens, A., Guimarães, L. d N. & Olivella, S. (2005): A double structure generalized plasticity model for expansive materials. International Journal for numerical and analytical methods in geomechanics 29: 751-787.

Siitari-Kauppi, M., Leskinen, A., Kelokaski, M., Togneri, L. Alonso, U., Missana, T. & García-Gutiérrez, M. (2007): Physical Matrix Characterisation: Studies of Crystalline Rocks and Consolidated Clays by PMMA Method and Electron Microscopy as Support of Diffusion Analyses. CIEMAT Technical Report, 1127, December 2007.

van Genuchten, M.T. (1980): A closed-form equation for predicting the hydraulic conductivity of unsaturated soils. Soil science society of America journal 44(5): 892-898.

Vilarrasa, V., Rutqvist, J., Martin, L.D. & Birkholzer, J. (2015): Use of a Dual-Structure Constitutive Model for Predicting the Long-Term Behavior of an Expansive Clay Buffer in a Nuclear Waste Repository. International Journal of Geomechanics 0(0): D4015005.

Villar, M.V. (2002): Thermo-hydro-mechanical characterisation of a bentonite from Cabo de Gata: a study applied to the use of bentonite as sealing material in high-level radioactive waste repositories. ENRESA, Madrid. Technical Publication 01/2002.

Wolery, T.J., (1993): EQ3/6, A software package for geochemical modelling of aqueous systems, Version 7.2. Lawrence Livermore National Laboratory, USA.

Xu, T., Sonnenthal, E., Spycher, N. & Pruess, K. (2006): TOUGHREACT: A Simulation Program for Non-isothermal Multiphase Reactive Geochemical Transport in Variably Saturated Geologic Media. Computers and Geosciences 32: 145-165.

Xu, T., Spycher, N., Sonnenthal, E., Zhang, G., Zheng, L. & Pruess, K. (2011): TOUGHREACT Version 2.0: A simulator for subsurface reactive transport under non-isothermal multiphase flow conditions. Computers & Geosciences 37(6): 763-774.

Zheng, L., Kim, K., Xu, H. & Rutqvist, J. (2016): DR Argillite Disposal R&D at LBNL. FCRD-UFD-2016-000437, LBNL- 1006013.

Zheng, L., Rutqvist, J. Kim, K. & Houseworth, J. (2015b): Investigation of Coupled Processes and Impact of High Temperature Limits in Argillite Rock. FCRD-UFD-2015-000362, LBNL-187644.

Zheng, L. & Samper, J. (2008): A coupled THMC model of FEBEX mock-up test. Physics and Chemistry of the Earth, Parts A/B/C 33, Supplement 1: S486-S498.

Zheng, L. Rutqvist, J., Steefel, C., Kunhwi, K., Chen, F., Vilarrasa, V., Nakagawa, S., Zheng, J., Houseworth, J. & Birkholzer, J. (2014): Investigation of Coupled Processes and Impact of High Temperature Limits in Argillite Rock. FCRD-UFD-2014-000493, LBNL-6719E

Zheng, L., Li, L., Rutqvist, J., Liu, H. & Birkholzer, J.T. (2012): Modeling Radionuclide Transport in Clays. Lawrence Berkeley National Laboratory. FCRD-URD-2012-000128

Zheng, L., Rutqvist, J., Birkholzer, J. & Liu, H.-H. (2015a): On the impact of temperatures up to 200 °C in clay repositories with bentonite engineer barrier systems: A study with coupled thermal, hydrological, chemical, and mechanical modeling. Engineering Geology 197: 278-295.

Zheng, L., Samper, J. & Montenegro, L. (2008): Inverse hydrochemical models of aqueous extracts tests. Physics and Chemistry of the Earth, Parts A/B/C 33(14–16): 1009-1018.

Zheng, L., Samper, J. & Montenegro, L. (2011): A coupled THC model of the FEBEX in situ test with bentonite swelling and chemical and thermal osmosis. Journal of Contaminant Hydrology 126(1–2): 45-60.

PART E

Clay Technology (CT) – contribution:
Pre-Dismantling Modelling of FEBEX
An Interlayer Approach

E.1 Introduction

This appendix summarises Clay Technology's contribution to modelling the chemical evolution of the FEBEX test. Focus has been on an adequate treatment of interlayers – the pore type which dominates compacted bentonite materials. Thus, transport and chemistry in these pores have been accounted for, as well as the chemical equilibrium between interlayers and external water (groundwater).

E.2 The homogeneous mixture model

The so-called homogeneous mixture model (HMM) is adopted. In this model all water in bentonite is assumed to be located in montmorillonite interlayer spaces – the slit-like nanometer wide pores between adjacent montmorillonite particles. The HMM contrasts the traditional approach to modelling bentonite in that it assumes mobility and reactivity of ions in the interlayer pores. In traditional modelling, ions residing the in the interlayer are instead treated as sorbed (in the sense that they are immobilized) on specific sites (Zheng et al. 2011). This type of sorption is typically referred to as exchange sorption, and cations residing in interlayers are often referred to as exchangeable cations.

More recently developed models treat the exchangeable cations with a combination of sorption on specific sites, and so-called electric double layers (Tournassat & Steefel 2015). An electric double layer is assumed to develop on certain mineral surfaces in the bentonite and is characterized by a lower electrostatic potential compared to an external solution. The effect of a lowered electrostatic potential (whose origin is the negative charge of the montmorillonite particles) is an enhancement of cation and a reduction of anion concentrations. The equilibrium between the electric double layers and bulk water solution in these types of models are typically treated by solving the Poisson-Boltzmann equation or by making a Donnan equilibrium approach.

The HMM, in contrast, requires no treatment of internal equilibrium between different model compartments, as it is postulated to contain only one type of pores. However, equilibrium between bentonite and the external water solution becomes central; it is treated by a general Donnan equilibrium framework, here referred to as ion equilibrium.

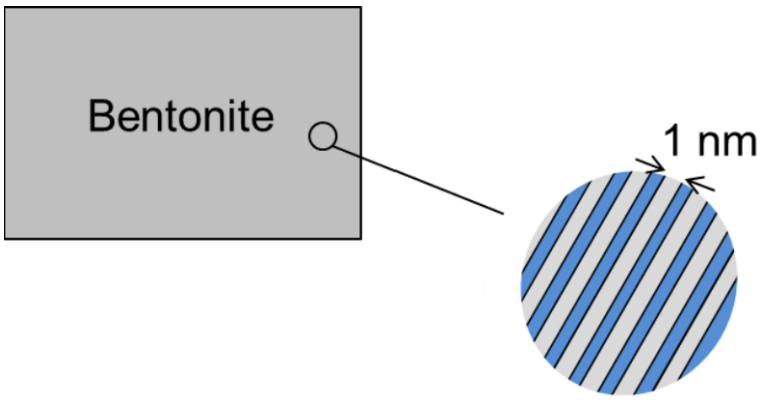

Fig. E-1: In the homogeneous mixture model, all water in the bentonite is assumed to be located in interlayer pores

E.2.1 Interlayer transport

In this work, Fick's law is assumed to govern diffusion in the bentonite. Thus, the diffusive flux of species i is assumed to be directly proportional to the gradient in concentration of that species in the interlayer pore (Birgersson & Karnland 2009) (superscript "int" is used to label interlayer quantities)

$$\vec{J}_i = -\phi \cdot D_c \cdot \nabla c_i^{int} \qquad \text{C–1}$$

Here, ϕ denotes porosity, and D_c is the diffusion coefficient. Since Fickian diffusion is assumed, all species have the same value of D_c. In a more general description, the mobility of different species is coupled via the electric field, in accordance with the Nernst-Planck equation. If all mobilities are put equal, however, the Nernst-Planck description reduces to the Fickian description here adopted (equation C–1).

E.2.2 Ion equilibrium

The system of interest here is bentonite in contact with an external solution via a semi-permeable component, as schematically illustrated in Fig. E-2. It is important to note that the separating component is impermeable for the clay but not for water or ions – in practice this component is e.g. a metal filter or the rock interface in the FEBEX test. The confinement of the clay particles, implies a difference in electrostatic potential between the external solution and bentonite (see Fig. E-2). This potential difference will here be referred to as the Donnan potential and labeled $\phi^\star$. Note that $\phi^\star$ is a negative quantity.

The bentonite will be assumed to have constant density throughout its compartment, quantified by the mean water-to-solid-mass ratio, w. The bentonite is furthermore characterized by its cation exchange capacity, CEC, which quantifies the amount of exchangeable cations in terms of charge equivalents per kg dry clay. This amount of cations can be converted to an interlayer concentration unit as

$$m_{IL} = \frac{CEC}{F\,w} \qquad \text{C–2}$$

where $F = 1$ eq/mol (Faraday's constant).

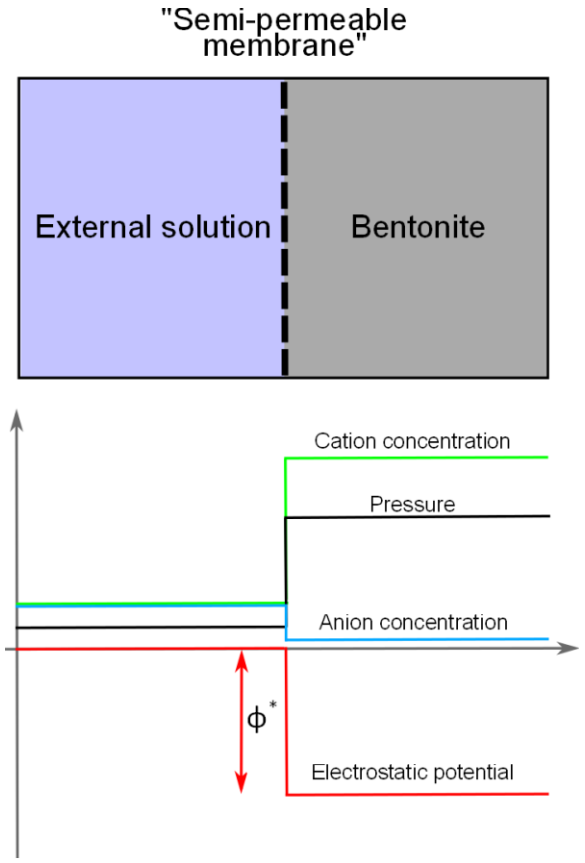

Fig. E-2: Schematic illustration of the system considered in the present work

The electro-chemical potential for an aqueous specie i in an electrostatic potential ϕ is

$$\mu_i = \mu_i^0 + RT \cdot \ln a_i + F \cdot z_i \cdot \phi \qquad \text{C–3}$$

where a_i and z_i respectively is activity and valency of the species, R is the universal gas constant, T absolute temperature, and μ_i^0 a reference potential. In chemical equilibrium, the electro-chemical potential is equal everywhere, and applying the above formula to our system gives

$$\ln a_i^{ext} = \ln a_i^{int} + \frac{F \cdot z_i}{RT} \cdot \phi^{\star} \qquad \text{C–4}$$

Here, and throughout the chapter, the superscripts "ext" and "int" respectively are used for quantities in the external solution and the bentonite.

Equation C–4 can be rewritten as

$$a_i^{int} = f_D^{-z_i} \cdot a_i^{ext} \qquad \text{C–5}$$

where a "Donnan factor" has been defined

$$f_D = e^{\frac{F \cdot \phi^\star}{RT}} \qquad \text{C–6}$$

Equation C–5 can be expressed also in terms of molalities

$$m_i^{int} = \Gamma_i \cdot f_D^{-z_i} \cdot m_i^{ext} \qquad \text{C–7}$$

where

$$\Gamma_i = \frac{\gamma_i^{ext}}{\gamma_i^{int}} \qquad \text{C–8}$$

is the ratio between the activity coefficients in the external solution and the bentonite for the species under consideration. Given the internal molalities for all involved charged species, the requirement of zero net charge in the bentonite can be stated as:

$$Q_{net} = \sum_i z_i \cdot F \cdot m_i^{int} \cdot M_w + Q_{surf} = 0 \qquad \text{C–9}$$

where M_w denotes bentonite water mass, and Q_{surf} total surface charge of montmorillonite in the bentonite. Q_{surf} can be calculated from the cation exchange capacity

$$Q_{surf} = -CEC \cdot M_s \qquad \text{C–10}$$

where M_s is bentonite solid mass.

The requirement of zero net charge can thereby be expressed as

$$\sum_i z_i m_i^{int} - m_{IL} = 0 \qquad \text{C–11}$$

where m_{IL} is given by equation C–2. Combining equations C–7 and C–11 gives an equation for f_D

$$\sum_i z_i \Gamma_i \, m_i^{ext} \cdot f_D^{-z_i} = m_{IL} \qquad \text{C–12}$$

which is to be solved given a complete specification of the external concentrations (m_i^{ext}) and a value of m_{IL}.

E.2.3 Interlayer chemistry

If chemical processes should be considered in the HMM, there is no choice but to assume these processes to occur in interlayer pores. This strongly contrasts to other modelling approaches, that all basically postulate chemical processes to occur only in bulk pore water.

There is, however, no rationale for excluding the possibility of aqueous chemistry in interlayer pores – especially not in compacted bentonite, which under all relevant circumstances is dominated by such pores. Here, a description is outlined of the adopted approach to interlayer chemistry.

A general chemical reaction may be written

$$\sum \nu_i \cdot M_i = 0 \qquad \text{C–13}$$

where ν_i is the stoichiometric coefficient for species M_i (ν_i is negative for reactants and positive for products). The equilibrium condition for this reaction in an interlayer is:

$$\mathrm{K^{int}} = \prod \left(\mathrm{a_i^{int}}\right)^{\{\nu_i\}\sum \nu_i} \qquad \text{C–14}$$

where $\mathrm{K^{int}}$ denotes the equilibrium constant for the reaction. $\mathrm{K^{int}}$ is identical to the equilibrium constant for the reaction in an ordinary aqueous solution ($\mathrm{K^{bulk}}$), which is seen by also assuming equilibrium with an external solution; equation C–14 can then be rewritten using external activities (equation C–7), giving:

$$K^{int} = \prod \left(f_D^{-z_i}\right)^{\nu_i} \cdot \left(a_i^{ext}\right)^{\nu_i} = K^{bulk} \cdot f_D^{-\sum z_i \nu_i} = K^{bulk} \cdot f_D^0 = K^{bulk} \qquad \text{C–15}$$

where we have utilized that charge is conserved in the reaction ($\sum z_i \nu_i = 0$). In the present framework, the description of chemistry in the interlayer is hence identical to that in ordinary aqueous solutions. This means in particular that existing thermodynamic databases can be used directly also for interlayer chemistry. That said, it should be kept in mind that the presence of interlayer activities in equation C–14 means that the resulting chemistry in an interlayer may be very different from the chemistry in a corresponding bulk solution.

E.3 FEBEX bentonite

E.3.1 Ion content

Tab. E-1 shows the analysed exchangeable ion content in FEBEX clay as reported by Huertas et al. (2000). Here, these data are used to assess the initial cation concentrations in the FEBEX. To simplify the analysis, potassium is neglected.

Tab. E-1: Exchangeable cations in FEBEX bentonite

From Huertas et al. (2000)

Ion	**Cation occupancy** (eq/kg)
Na	0.31
Ca	0.35
Mg	0.34
K	0.02

Huertas et al. (2000) also report the results of analysing aqueous extracts of FEBEX bentonite at solid-to-liquid mass ratios between 1 and 1/16. Here, these data are used to assess the total chloride and sulphate inventory of the bentonite. Fig. E-3 shows the corresponding amounts of anions recalculated to relate to the amount of clay. It is seen that chloride and sulphate respectively show relatively constant values of ca. 20 and 10 mmol per kg dry clay; these values are adopted for the present modelling. The carbonate content, on the other hand, increases with increasing water content and consequently has a more complicated chemical behaviour (related to e.g. calcite dissolution or atmospheric carbon). In the present model carbonates will, however, be neglected.

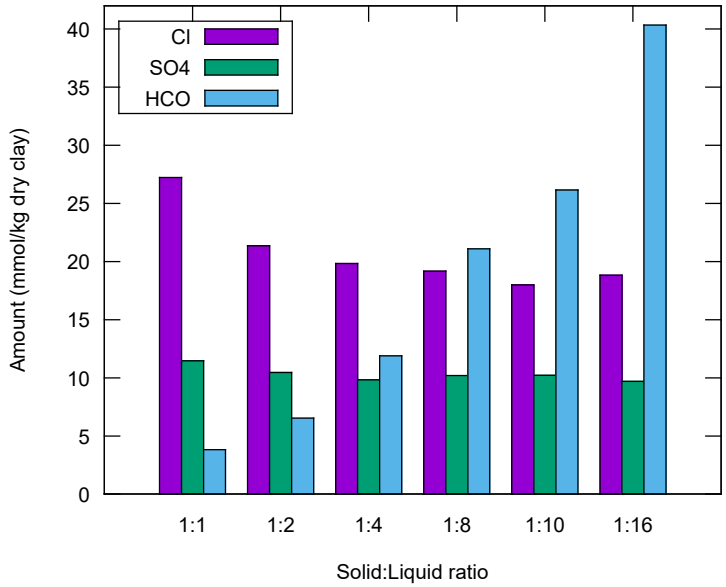

Fig. E-3: Total amount of Cl, SO_4, and HCO analysed in FEBEX bentonite

Data recalculated from Huertas et al. (2000)

From the aqueous extract tests and the analysis of exchangeable cations, initial values for the total amount of substance in the present model for FEBEX bentonite are as stated in Tab. E-2.

Tab. E-2: Adopted total ion content in the present model for FEBEX bentonite

Ion	**Amount** (mol/kg dry clay)
Na	0.34
Ca	0.175
Mg	0.175
Cl	0.02
SO_4	0.01
CEC[1)]	1.0

[1)] Cation exchange capacity, measured in mol monovalent charge per kg dry clay.

All the chloride is assumed to be present in the interlayers in dissolved form, while the sulphate is assumed to be partitioned between the solution and a gypsum mineral phase. The model is thus calibrated by requiring equilibrium between the mineral and the interlayer pore solution. The gypsum equilibrium calculation is summarised in Tab. E-3. The interlayer activity coefficients fitted in this calculation are used generally in the modelling of the FEBEX test.

Tab. E-3: Summary of calculation of gypsum equilibrium in interlayer. $f_D = 0.193$

The adopted concentrations of species Ca^{2+}, Mg^{2+}, Na^{+}, and Cl^{-} are adopted from the values in Tab. E-2. Species SO_4^{2-}, $CaSO_4^0$, $MgSO_4^0$, $NaSO_4^-$ are calculated using the equilibrium constants listed in Tab. E-4. Concentration unit is mM.

	Int	**Ext**
Ca^{2+}	583.33	25.63
Mg^{2+}	583.33	25.63
Na^{+}	1096.54	209.67
Cl^{-}	60.0	286.14
SO_4^{2-}	4.77	11.64
$CaSO_4^0$	4.68	4.68
$MgSO_4^0$	6.17	6.17
$NaSO_4^-$	0.52	2.68
γ_{Ca}	0.35	0.30
γ_{Mg}	0.35	0.30
γ_{Na}	0.75	0.74
γ_{Cl}	0.68	0.74
γ_{SO_4}	0.03	0.30
γ_{CaSO_4}	1	1
γ_{MgSO_4}	1	1
γ_{NaSO_4}	1	1
Water-to-solid mass ratio	0.3	-

Tab. E-4: Equilibrium constants used in gypsum equilibrium calculation (referring to molar units)

Reaction	**log K**
gypsum $\rightleftarrows Ca^{2+} + SO_4^{2-}$	-4.58
$Mg^{2+} + SO_4^{2-} \rightleftarrows MgSO_4^0$	2.37
$Ca^{2+} + SO_4^{2-} \rightleftarrows CaSO_4^0$	2.25
$Na^{+} + SO_4^{2-} \rightleftarrows NaSO_4^-$	0.7

The gypsum solubility in the interlayer is calculated to 16.13 mM. This value is used in the subsequent transport calculation of the FEBEX test. Note that the solubility is approximately equally partitioned over the three species SO_4^{2-}, $MgSO_4^0$, and $CaSO_4^0$. Note further that this solubility corresponds to ca. 5 mM total sulphate per kg dry clay. Thus, approximately the same amount of sulphate (5 mM per kg dry clay) is in mineral form in the clay (Tab. E-2).

E.3.2 Squeezing

Quite a lot of analyses of ion content in bentonite have been conducted using the so-called squeezing technique. The idea is presumably that a bentonite sample is assumed to behave as a "sponge", and that by applying a certain pressure to it, part of its pore water is expelled and can be analysed. However, such an interpretation is dependent on the assumption that bentonite contains bulk water, and that this is what is expelled when a sample is squeezed. Accordingly, results of squeezing tests are typically reported as if the expelled solution directly represented bulk pore water, possibly adjusted for presumed cation exchange sorption.

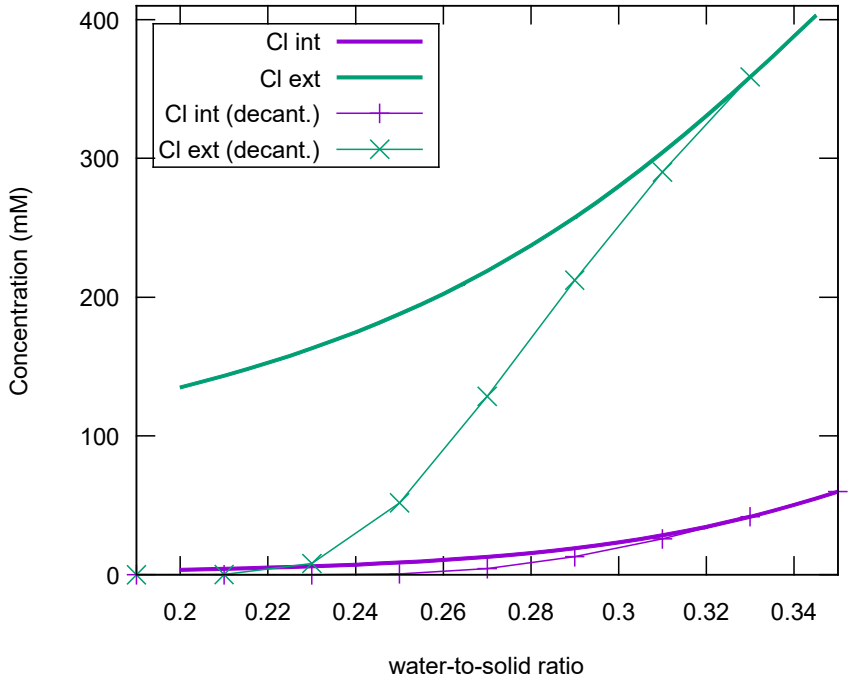

Fig. E-4: Result of simulating a squeezing experiment using the homogeneous mixture model

The model assumes an initial water-to-solid mass ratio of 0.35, an initial (interlayer) chloride concentration in the bentonite of 60 mM, and a cation exchange capacity of 1.0 eq/kg dry clay. All activity coefficient ratios (equation C–8) have been put equal to unity. Note how the external chloride concentration – measured in the expelled water – completely differs from the actual concentration in the clay. Note also that the actual concentrations obtained differ depending on how the squeezing is performed: the thick lines show the result when the expelled water is assumed to accumulate in the external solution while the thin lines show the result when the expelled solution is assumed decanted at certain occasions (indicted by crosses).

From the view of the HMM it is clear that results from squeezing experiments must be interpreted radically different: rather than directly representing the actual pore solution (interlayer solution), the expelled solution strives for equilibrium with the remaining bentonite system, in accordance with the ion equilibrium framework presented in section E.2.2. Thus, from the perspective of the HMM, a squeezing test basically represents a rather complicated procedure for achieving ion equilibrium between bentonite and an external solution – complicated in the sense that the water of the external solution is expelled from the bentonite itself. Note that it is not a priori ensured in a squeezing experiment that the bentonite and the external solution are in (chemical) equilibrium at a certain point in time. In the following analysis, however, we will assume that this is the case.

Note further that, according to the HMM, the result of a squeezing experiment will depend on the way it is performed. This is illustrated in Fig. E-4, which shows the result of simulating the squeezing of a Na-bentonite sample of initial water-to-solid mass ratio 0.35, and initial chloride concentration of 60 mM. The thick lines in this diagram show the internal and external chloride concentrations as a function of water-to-solid mass ratio of the bentonite, under the assumption that the expelled water and ions are kept in the external compartment (the volume of this solution then increases with decreasing water-to-solid mass ratio of the bentonite). The thin lines in Fig. E-4 shows the same quantities, but under the assumption that the expelled solution is removed at certain occasions (indicted by the crosses).

An ion equilibrium analysis thus demonstrates that the composition of the expelled solution generally is very different from the composition of the remaining interlayer solution. Furthermore, although the results also show that there is a relation between the two solution compositions, this relation is complex (requiring the use of the full ion equilibrium calculation framework) and depends on details of how the squeezing test is performed. In general, it is therefore a challenging task to infer the composition of an interlayer pore solution from the results of squeezing tests. Nevertheless, an attempt to simulate the squeezing of FEBEX bentonite is presented in Fig. E-5 together with experimental data from Huertas et al. (2000).

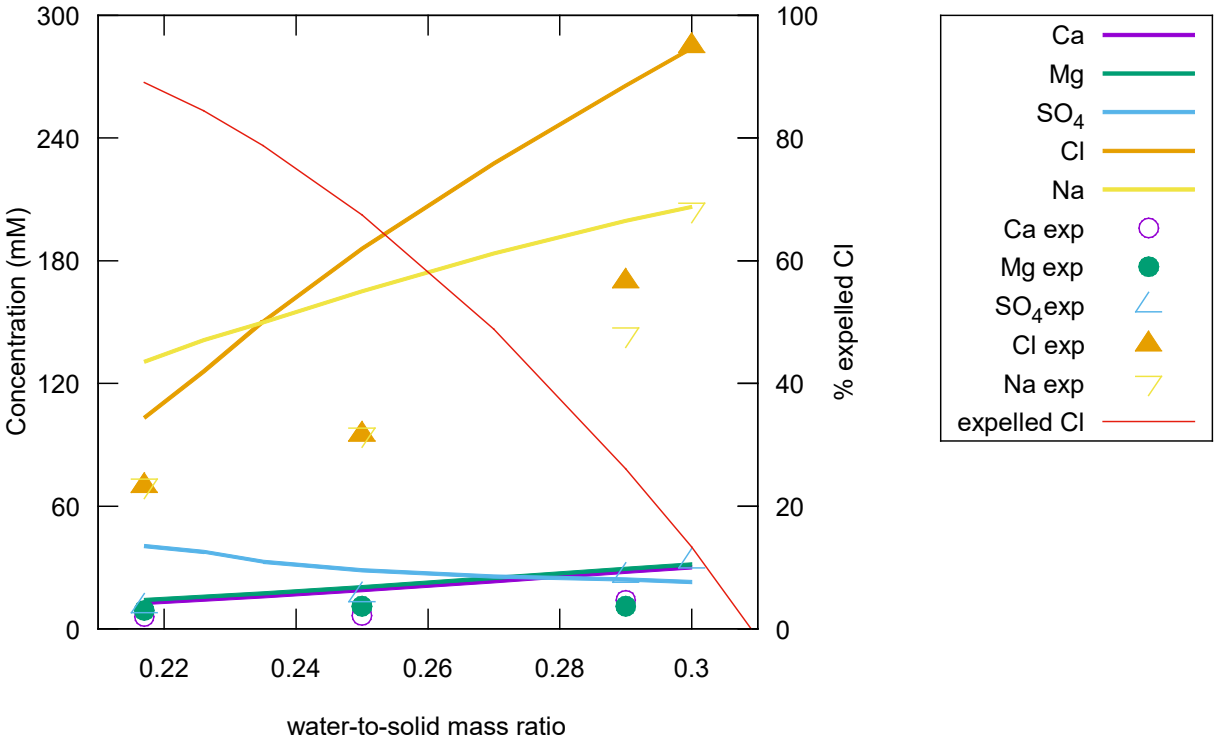

Fig. E-5: Results of simulating squeezing of FEBEX bentonite using the adopted material model. Shown are also experimental data from Huertas et al. (2000)

The values at water-to-solid mass ratio 0.30 correspond to the values in Tab. E-3. Although the simulation in several aspects agrees qualitatively with the experimental results – sodium and chloride concentrations are much larger than calcium, magnesium and sulphate concentrations, and falls with decreasing water-to-solid mass ratio – it may be noted that the simulation gives quite substantially different results as compared to measurements. There are in particular two conspicuous differences between experiment and simulation.

Firstly, much more chloride (and accompanying sodium) is being expelled in the simulation. However, as the total amount of chloride in the simulation was calibrated by empirical data (aqueous extracts, see section E.3.1), it is rather the experimental values which deviate from "expectation" – while the model has expelled approximately 90 % of the chloride at water-to-solid ratio 0.217, substantial amounts are apparently left in the clay according to the experimental results. This may indicate that the bentonite and the external solution actually are not in chemical equilibrium during the experiment. This suspicion is strengthened by the fact that the bentonite is certainly not in hydro-mechanical equilibrium during the test – the expected "swelling pressure" for FEBEX bentonite at water-to-solid mass ratio 0.22 is below 20 MPa, while the applied pressure was 80 MPa (Huertas et al. 2000).

Secondly, the sulphate concentration in the extracted solution is experimentally observed to drop with decreasing water-to-solid mass ratio. In the simulation, on the other hand, the external sulphate concentration is increasing with decreasing water-to-solid mass ratio. This may indicate that the model treats sulphate chemistry too simplistic. However, again, it cannot be dismissed that the disagreement between simulation and experiment indicates non-equilibrium conditions in the latter. In particular, since sulphate species presumably diffuse slower than chloride, and since substantial amounts of chloride were observed to still reside in the bentonite, it can be suspected that sulphate equilibrium was not achieved in the squeezing experiment.

E.4 Simulation of FEBEX in-situ experiment

Using the ion and gypsum content as calibrated in the previous section, a reactive transport calculation of the FEBEX in-situ experiment was conducted. Due to limitations of the numerical tools, the model is planar 1D and only takes into account gypsum dissolution and transport of species Ca, Mg, Na, Cl, and SO4. Furthermore, the model does not consider the thermal problem, i.e. constant temperature is assumed throughout (the only mean by which temperature influences the simulation is on the choice of diffusion coefficient), and the water saturation of bentonite was not simulated (saturation is assumed throughout). On the other hand, the simulation accounts for chemistry and transport in the interlayer pores in accordance with the HMM, and the simulation consequently gives information on the influence of allowing these processes.

E.4.1 Boundary condition

Ion equilibrium between the assumed groundwater and the bentonite in the FEBEX experiment is shown in Tab. E-5. From this table we can see that if the Grimsel groundwater has time to completely equilibrate with the FEBEX bentonite, a basically pure Ca-bentonite, completely devoid of excess salt, would result. However, as the groundwater is very dilute, tremendous amounts of water are required to reach this state (1'000 - 10'000 m^3). The interface between bentonite and rock consequently constitutes a substantial mass transfer resistance.

Tab. E-5: Adopted groundwater composition and the corresponding clay composition at chemical equilibrium. Concentration unit is mM. $f_D = 0.014$

Ion	G.W. concentration	Eq. clay concentration
Na	0.69	63.0
Ca	0.14	1746
Mg	0.001	7.7
Cl	0.4	0.008
SO_4	0.06	0.000

In the simulation this mass transfer resistance is modelled by means of a spurious porous component. The mass transfer resistance of this component can be varied by simply varying its porosity, which does not have to be restricted to be lower than unity – the resistance can thus be made small by choosing values much larger than 1, and it can be made infinite by setting this porosity to zero. The model schematics are pictured in Fig. E-6. The heater/bentonite interface is treated as a closed boundary here.

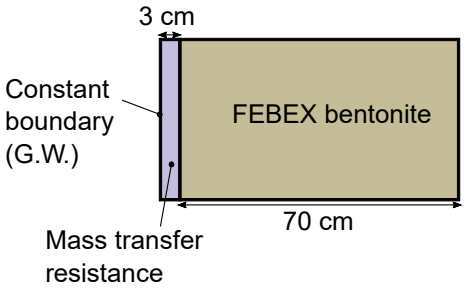

Fig. E-6: The model

E.4.2 The prediction

Fig. E-7 shows the resulting calcium and chloride concentration profiles after simulating the system for 5000 days with diffusion coefficient $D_c = 3 \cdot 10^{-10}$ m/s2. This diagram shows that the transition from a "closed" to an "open" boundary for chloride occurs at relative transfer conductance in the range of $10^{-5} - 10^{-4}$, while the same transition for calcium occur in the range 0.1 – 10. This very large difference in transfer capacity for an anion and a cation is expected – especially with the very low ionic strength of the ground water – and is a direct consequence of the large absolute value of the Donnan potential (f_D is approaching zero). In this case, the interlayer concentration of calcium is orders of magnitude larger than the corresponding groundwater value, while the opposite is true for chloride (see Tab. E-5). The situation is completely analogous to the filter mass transfer limitation experienced in cation tracer through-diffusion tests at low ionic strength (Glaus et al. 2007, Molera & Eriksen 2002).

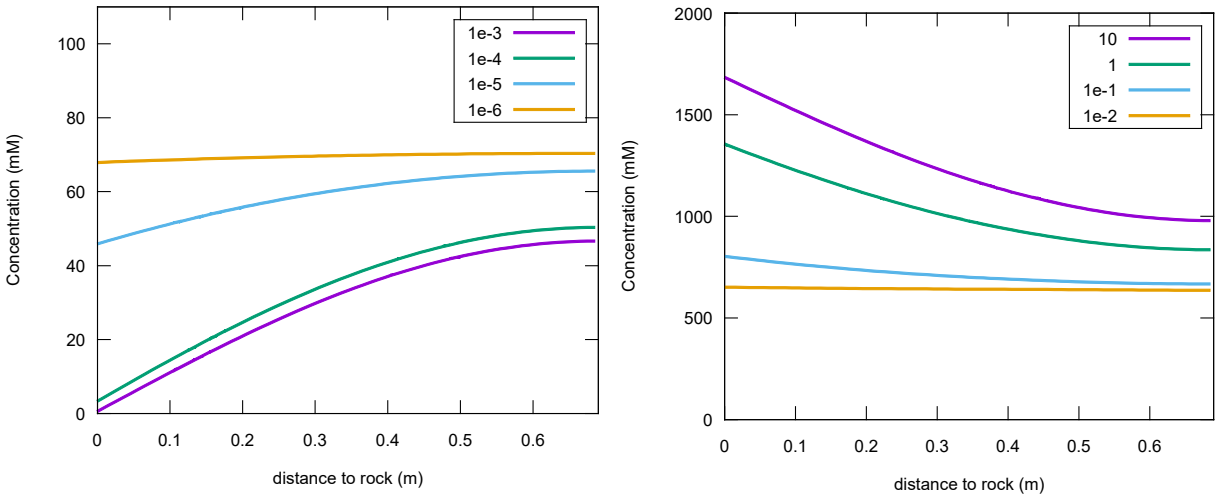

Fig. E-7: Chloride and calcium profiles after 5000 days of simulation for various relative values of mass transfer conductance (inverse resistance) at the rock/bentonite interface

In the simulation, the choice of a relative mass transfer factor of 0.001 is made. This choice – which is basically a guess – corresponds to a boundary open for chloride but practically closed for calcium. Furthermore, in the simulation the solubility of gypsum is set to the constant value of 16.13 mM (see section E.3.1). A simulation time of 5000 days was chosen. This is shorter than

the lifetime of the FEBEX test which is ca. 18 years. But since the saturation phase is not covered by the present modelling, and since it can be expected that transport is strongly suppressed before the clay has increased its water content, the simulation length was reduced by approximately 4 years. The diffusion coefficient was set equal to $D_e = 3 \times 10^{-10}$ m/s^2. This is somewhat larger than what is typically measured for small ions at room temperature (Bourg & Tournassat 2015), and is motivated by the elevated temperature. The result of the simulation is shown in Fig. E-8.

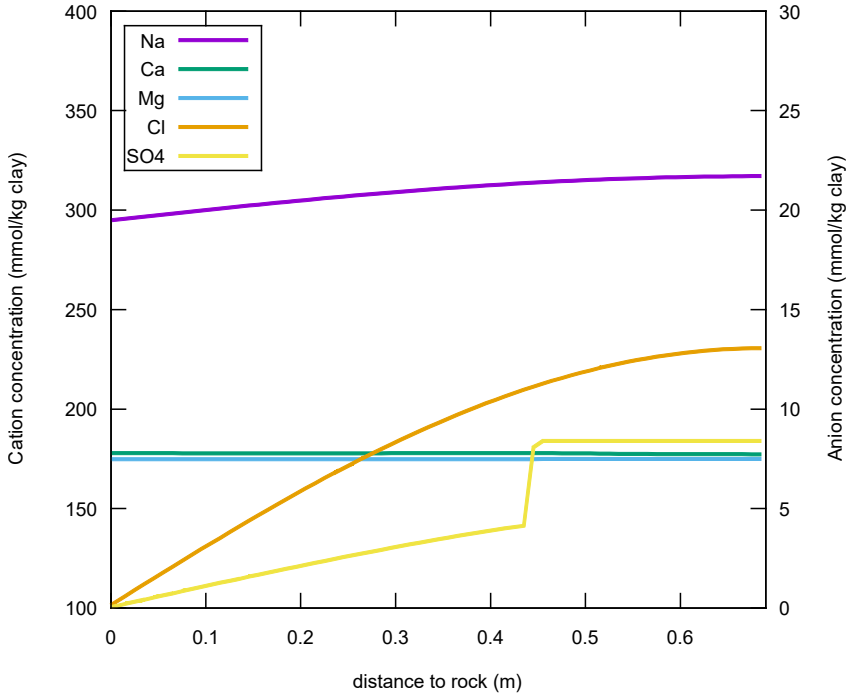

Fig. E-8: The prediction

The length of the modelled domain is 0.7 m, which corresponds to the distance between rock wall and heater surface in the FEBEX test. It should be emphasized, however, that the present simulation is made in a 1D plane and is, therefore, only an approximation to the cylindrical geometry of the bentonite surrounding the heaters. Alternatively, the simulation approximately represent the axial dimension of the inner part of the test hole. Although such a representation has planar geometry, however, it is not strictly one-dimensional as the extension of the modelling domain is comparable to the hole diameter.

Fig. E-8 reveals a pronounced chloride profile, accompanied by a similar profile of sodium. That sodium, rather than magnesium, is the cation diffusing out, is natural since the low ionic strength promotes divalent ions in the clay – note that this ion exchange effect is captured in the present simulation although no sorption model is involved.

Furthermore, the simulation reveals a sulphate profile due to dissolution and diffusion of gypsum. For the specific parameter choices of the model, all gypsum dissolves in a range of approximately 0.4 m closest to the rock wall (indicated by the step in the sulphate profile in Fig. E-8).

E.5 Refererences to PART E

Birgersson, M. & Karnland, O. (2009): Ion equilibrium between montmorillonite interlayer space and an external solution - Consequences for diffusional transport. Geochim. Cosmochim. Acta 73, 1908–1923.

Bourg, I.E. & Tournassat, E. (2015): Self-Diffusion of Water and Ions in Clay Barriers, in: Christophe Tournassat, E.I.S., Ian E. Bourg and Faqpza Bergaya (Ed.), Developments in Clay Science, Natural and Engineered Clay Barriers. Elsevier, pp. 189–226.

Glaus, M.A., Baeyens, D., Bradbury, M.H., Jakob, A., Van Loon, L.R. & Yaroshchuk, A. (2007): Diffusion of 22Na and 85Sr in Montmorillonite: Evidence of Interlayer Diffusion Being the Dominant Pathway at High Compaction. Environ. Sci. Technol. 41, 478–485.

Huertas, F., Fuentes-Cantillana, J.L., Jullien, F., Rivas, P., Linares, J., Fariña, P., Ghoreychi, M., Jockwer, M., Kickmaier, W., Martínez, M.A., Samper, J., Alonso, E. & Elorza, F.J. (2000): Full-scale engineered barriers experiment for a deep geological repository for high-level radioactive waste in crystalline host rock (FEBEX project): Final report. (No. EUR 19147 EN). European Commission.